



GEETHANJALI COLLEGE OF ENGINEERING AND TECHNOLOGY

Striving towards perfection

Department of Electronics and Communication Engineering



Research Articles Published in Journals in the Academic Years

2020 - 21

2019 - 20

2018 - 19

GEETHANJALI COLLEGE OF ENGINEERING AND TECHNOLOGY**Department of ECE****Research Articles Published in Journals**

2020-21						
S.No.	Name of the Faculty	Title of the paper	Title of the Journal	Vol No. Issue No	Month and Year	Page No.
1.	U. Appalaraju	Improved Convolutional Neural Network Based Cooperative Spectrum Sensing for Cognitive Radio	KSII Transactions on Internet and Information Systems	Vol.15 Issue 6	June-2021	1
2.	M. Anand	Weed detection using image processing	Annals of Romanian Society for Cell Biology	Vol. 25 Issue 6	May-2021	21
3.	P. Chandra Prakash Reddy	Analyzing Patient Health Information Based on IoT Sensors With AI	Annals of Romanian society for cell biology	Vol.25 Issue 6	May-2021	29
4.	B.Ramu	A study of deep learning based brain tumor segmentation strategies for mri image	Annals of Romanian society for cell biology	Vol.25 Issue 6	May-2021	37
5.	B. Sreelatha	Smart extension cord using node MCU	PENSEE International Journal	Vol. 51 Issue 04	April-2021	54
6.	Dr. B.L.Prakash	A General Evaluation of Dermis Sores Identification using MOR-WAVELET Transforms	Turkish Journal of Computer and Mathematics Education (TJCME)	Vol. 12 Issue 4	April-2021	63
7.	Dr. P. Sudhakar	Optimisation of Cloud Seeding Criteria Using a Suite of Ground-Based Instruments	Book chapter in Lecture Notes in Electrical Engineering Springer	Vol. 722	April-2021	70
8.	Dr. P. Sudhakar	COVID-19 Social Distancing with Speech-Enabled Online Market Place for Farmers	Book Chapter in Lecture Notes in Networks and Systems Springer	Vol. 176	March-2021	75
9.	G.Sree Lakshmi	A Framework for Decimal Floating Point Multiplier Using Vinculum Multipliers	Book Chapter in New Insights into Physical Science Book Publisher International	Vol. 13	March-2021	89
10.	M. Laxmi M. sowjanya	Design of Smart Garbage Monitoring System	International Journal of Advanced research in Engineering and Technology	Vol.12 Issue 3	March-2021	99
11.	M. Sowjanya M Laxmi	Age Progression using Delaunay Triangulation	International Journal of Advanced research in Engineering and Technology	Vol.12 Issue 3	March-2021	104

12.	P. Chandra Prakash Reddy A R L Padmaja	Delivery collection of parcels with smart shipment container using arduino	International journal of electrical engineering and technology	Volume 12 Issue 3	March-2021	110
13.	B. Sreelatha	Recent developments in code compression techniques for embedded systems	ELSEVIER, Materials Today: Proceedings	-	March-2021	117
14.	A. Shanker	Implementation of simple PWM/PPM generator for microcontroller using Verilog	International Journal of Advanced Research in Engineering and Technology (IJARET)	Vol.12 Issue 3	March-2021	122
15.	U. Appalaraju	DynMAC Based Spectrum Handoff Algorithm for Deterministic Multihop Industrial Networks	Journal of Green Engineering	Vol.11 Issue 3	March-2021	128
16.	Dr R V Durga	Suboptimal Multi-user Receivers Detection Algorithms	GIS Science Journal	Vol.8 Issue 3	March-2021	149
17.	Dr.B.L.Prakash	Smart Garbage monitoring and air pollution Controlling system	International Journal of Advanced Research in Engineering and Technology	Vol.12 Issue:3	March-2021	158
18.	Dr. V. Satyasrinivas	Single Point Positioning Accuracy of Combinations combined GPS/Galileo	GIS SCIENCE JOURNAL	Vol. 8 Issue 2	Feb-2021	164
19.	Dr. S. Vallisree	Modeling and performance optimization of two-terminal Cu ₂ ZnSnS ₄ -silicon tandem solar cells	International Journal of Energy Research	-	Feb-2021	177
20.	M. Anand B. Ramu	Automatic identification of brain tumor using Matlab by fuzzy C means clustering	International Journal of Advanced Research In Engineering and Technology	Volume 12 Issue 2	Feb-21	188
21.	R Odaiah M Krishna	Design of an area efficient 16-bit logarithmic multiplier	International Journal of Advanced Research in Engineering and Technology (IJARET)	Vol12 Issue2	Feb-2021	191
22.	Dr.P.Spandana	Automatic classification of mammograms using 2D-discrete wavelet transform and feature selection methods	Journal of critical reviews	Vol. 7 Issue18	Dec -2020	199
23.	Dr. S Suryanarayana	Hybrid Power Gating Technique In FinFET Based Memory for High Speed Applications	Sambodhi	Vol. 43 Issue 3	Dec -2020	205

24.	Dr. R.V.Durga	Performance analysis of MIMO System capacity with various Receiver Architectures	International Journal of Grid and Distributed Computing	Vol. 13 Issue. 2	Dec-2020	208
25.	Dr. R.V.Durga	The Mimo System Capacity Analysis with Various Detectors and Different Modulation Scheme	International Journal of Grid and Distributed Computing	Vol. 13 Issue. 2	Dec-2020	219
26.	Dr. S. Saritha	MRI brain tumor segmentation with slic and convolutional neural networks	Journal of critical reviews	Vol. 7 Issue 19	Aug-2020	231

2019-2020						
S.No.	Name of the Faculty	Title of the paper	Title of the Journal	Vol No. Issue No	Month and Year	Page No.
1.	Dr. S. Saritha, Dr.C.V.Narasimhulu	Segmentation of Tumour using PCA based Modified Fuzzy C Means Algorithms on MR Brain Images	international journal of imaging systems & technology	-	May-2020	240
2.	Dr C V Narasimhulu Professor	Modified Euler Frobenius Halfband Polynomial Filter based Dual-Tree Complex Wavelet Transform and Metaheuristic Optimization Algorithms for Image Denoising along with Artificial Neural Networks	International Journal of Advanced Science and Technology	Vol. 29 Issue 6	Apr-20	249
3.	Dr.P.Srihari Professor	Sumulti Codes- A Binary Forward Error	International Journal of future generation communication and networking	Vol. 13 Issue 1	Apr-20	271
4.	Dr C V Narasimhulu Professor	Dual Stage Bayesian Network with Dual-Tree Complex Wavelet Transformation for Image Denoising	Journal of Engineering	Vol. 8 Issue 1	Mar-20	277
5.	Dr C V Narasimhulu Professor	Design and Implementation of Low Complexity Circularly Symmetric 2D FIR Filter Architectures	Multidimensional Systems & Signal Process (MULT)	-	Mar-20	302
6.	Dr C V Narasimhulu Professor	Denoising Images by Dual Tree Complex wavelet Transform combined with Metaheuristic Optimization Algorithms	International Journal of Innovative Technology and Exploring Engineering (IJITEE)	Vol. 9 Issue 4	Feb-20	328
7.	Dr. S. Vallisree	Investigations of carrier transport mechanism and junction formation in Si/CZTS dual absorber solar cell technology	Applied Physics A	-	Feb-2020	335
8.	S.Jyothirmayee B.Ramu	Border Guard Spy Robot	Test Engineering and Management	-	Dec- 2019	345
9.	S. Krishna Priya B.Jugal Kishore M Krishna Chaitanya	Design and Research of Rectangular, Circular and Triangular Microstrip Patch Antenna	International Journal of Innovative Technology and Exploring Engineering (IJITEE)	Vol. 8 Issue 12S	Oct-2019	349

2018-2019						
S.No.	Name of the Faculty	Title of the paper	Title of the Journal	Vol No. Issue No	Month and Year	Page No.
1.	U Appala Raju Dr C V Narasimhulu	Implementation of MAC Protocol for Analysis of Traffic in Smart Cities	Journal of Advanced Research in Dynamical & Control Systems,	Vol. 11 Special Issue 6	Jun-19	355
2.	Dr C V Narasimhulu	Implementation of Low Power and Memory Efficient 2D Finite Impulse Response Filter architecture	International Journal of Recent Technology and Engineering	Vol. 8 Issue 1	May-19	364
3.	Dr. C Venkata Narasimhulu	Rice Grains Categorization using Neural Network	International Journal for Research in Applied Science & Engineering Technology (IJRASET)	Vol. 7 Issue V	May-19	373
4.	Ch Suresh Kumar RVNR Suneel Krishna	Design and Analysis of Dual Frequency Pentagon Shaped Slotted Microstrip Patch Antenna using HFSS Software	Pramana Research Journal	Vol. 9 Issue 4	May-19	376
5.	Prof O.V.P.R. Shiva Kumar Prof B. Hari Kumar	An Effective Low Power Frequency Synthesizer for On-Chip Clock Generation	International Journal of Research	Vol. VIII Issue IV	Apr-19	380
6.	Dr. B. L. Prakash	Implementation of Remote Medical Nursing Monitoring System using Arduino	Anveshana's International Journal of Research in Engineering and Applied Sciences	Vol. 4 Issue 4	Apr-19	389
7.	Dr.C.Venkata Narasimhulu	Robust Video Watermarking Using a Hybrid Algorithm of SVD and DWT with Secured QR Code	Journal of Emerging Technologies and Innovative Research (JETIR)	Vol. 6 Issue 4	Apr-19	393
8.	B Sreelatha	Smart Apartment With Automatic Water Management And Security Alert System	Paramana Research Journal	Vol. 9 Issue 4	Apr-19	399
9.	R Odaiah	Data Hiding Using JPEG Steganography	International Journal Of Innovative Science And Research Technology	Vol. 4 Issue 4	Apr-19	403
10.	R Odaiah I.Naresh, K.Sai Krishna Reddy and M.Prince Titus	Accident Detection With Mems and Alert System for Medical Emergency	Anveshana's International Journal of Research in Engineering and Applied Sciences	Vol. 4 Issue 4	Apr-19	408
11.	Dr C V Narasimhulu Professor	A Unit Plane Edge on-off Slope Algorithm Based Fast LTVR Restoration Analysis	International Journal of Engineering & Technology(UAE)	-	Nov-18	412

Improved Convolutional Neural Network Based Cooperative Spectrum Sensing For Cognitive Radio

Appala Raju Uppala^{1*}, Venkata Narasimhulu C², and Satya Prasad K³

¹ Research Scholar, Department of ECE, Jawaharlal Nehru Technological University
Kakinada Andhra Pradesh, India

Associate Professor, Geethanjali College of Engineering and Technology,
Hyderabad, Telangana, India

[e-mail: rekharajuppala2009@gmail.com]

² LORDS Institute of Engineering and Technology, Hyderabad,
Telangana, India

[e-mail: narasimhulucv@gmail.com]

³ Vignan's Foundation for Science, Technology & Research
Guntur, India

[e-mail: prasad_kodati@yahoo.co.in]

*Corresponding author: Appala Raju Uppala

*Received October 24, 2020; revised January 29, 2021; accepted May 16, 2021;
published June 30, 2021*

Abstract

Cognitive radio systems are being implemented recently to tackle spectrum underutilization problems and aid efficient data traffic. Spectrum sensing is the crucial step in cognitive applications in which cognitive user detects the presence of primary user (PU) in a particular channel thereby switching to another channel for continuous transmission. In cognitive radio systems, the capacity to precisely identify the primary user's signal is essential to secondary user so as to use idle licensed spectrum. Based on the inherent capability, a new spectrum sensing technique is proposed in this paper to identify all types of primary user signals in a cognitive radio condition. Hence, a spectrum sensing algorithm using improved convolutional neural network and long short-term memory (CNN-LSTM) is presented. The principle used in our approach is simulated annealing that discovers reasonable number of neurons for each layer of a completely associated deep neural network to tackle the streamlining issue. The probability of detection is considered as the determining parameter to find the efficiency of the proposed algorithm. Experiments are carried under different signal to noise ratio to indicate better performance of the proposed algorithm. The PU signal will have an associated modulation format and hence identifying the presence of a modulation format itself establishes the presence of PU signal.

Keywords: Cognitive radio, Cooperative spectrum sensing, Primary user, Simulated annealing, Neural network.

1. Introduction

In cognitive radio (CR) networks, the spectrum resources have become highly scarce [14] with the rapid advancement of 5G paradigm in advent of wireless connectivity technology [34]. Spectrum allocation will limit and avoid the interference between cognitive radio devices and licensed primary users to authorize a better methodical usage of the wireless radio spectrum [43]. The interface between spectrum availability and its development has been emerged as a potential growth in cognitive radio. Efficient granting of unused spectrum to unlicensed users is an important problem [28]. The identified licensed users are called primary users (PUs) [31] and unlicensed users are called secondary users (SUs) [25]. The main aim of spectrum sensing is to detect the spectrum holes of enormous number of primary users in the network [34]. A new spectrum sensing method which can distinguish all types of primary users based on the inherent ability has been proposed in this paper. It utilizes improved convolutional neural network with simulated annealing (SA) to discover the quantity of neurons in each hidden layer of the primary users. In addition, we discover the LSTM spectrum sensing that combines CR networks with CNN. The deep learning methods solve the optimization problem of forecasting the number of neurons. The proposed algorithm utilizes SA to discover reasonable number of neurons with low unpredictability in each layer of the completely associated CNN.

1.1 Current State of the Art and Motivation

Spectrum sensing is categorized into two types namely individual spectrum sensing and cooperative spectrum sensing. In individual spectrum sensing, only one secondary user can sense to know how many spectrum holes are available at a particular time. But in cooperative spectrum sensing, the secondary users can sense a bunch of available spectrum holes thereby improving the execution [33]. Energy detection is an important method used in spectrum sensing because of its less computational and execution complexities even with drawbacks in finding out the noise and the signal. Energy detection can be done by means of energy comparison between the received signals in specific frequency bands for setting a proper decision threshold [20]. Therefore, the output gives prior knowledge of the PU in this method of detection and causes signal to noise ratio (SNR) [26]. Non-parametric blind spectrum sensing like Censored Anderson Darling (CAD) [9], likelihood ratio statistics (LRS-G2G2) [30] and Anderson Darling test [41] is proposed in the literature. The occupancy patterns in PU activities consists of a number of factors like time, location and frequency band [3]. The individual SUs characteristic changes the channel condition of the spectrum. We used cooperative spectrum sensing (CSS) to predict the error and to conquer this issue. The results from numerous individual spectrum sensing data of secondary users are used for finding the availability of PU. Cooperative spectrum sensing (CSS) is used to overcome the channel impacts, to exploit location diversity and to recognize a weak primary signal [10].

Nowadays deep learning has become one of the popular algorithms compared to other conventional methods due to its performance gain [18][36]. In a deep neural network (DNN), the near ideal strategy is to change over the information of the contemplated measure of sample data by back-propagation algorithm. The major benefits of CR are cognitive ability that denotes the learning nature of the radio networks. This method is same as the machine learning (ML) system. Hence, ML systems are applied to CR networks [7][2][4]. Besides CNN [24], the orthogonal frequency division multiplexing (OFDM) based CR receiver detects

the OFDM signal of the primary users. Hence, cognitive radio receiver is outfitted with different antenna-based energy detectors [19]. For DNN-based detection structure, the DNN-based likelihood probability proportion test (DNN-LRT) is proposed in [24].

Several spectrum sensing algorithms are presented by numerous researchers all over the world. For instance, CNN based cooperative spectrum sensing is used on wireless data. The authors addressed a deep cooperative sensing with CSS method for convolutional neural network in [22]. Authors in [23] have proposed a covariance matrix-aware CNN (CM-CNN)-based spectrum sensing algorithm. Additionally, the creators in [45] have proposed the fire-feature reuse detection convolutional neural network. The above-mentioned methods have good accuracy and problem solving skills when compared to other machine learning algorithms. On the other hand, it has its own limitations in predicting the available spectrum. To get rid of this issue, long short-term memory (LSTM) design has implemented a traditional method of recurrent neural network (RNN) for time and arrangement issues [23]. LSTM comprises some gates which have a neuron that readily arranges its verifiable data and the traffic type data [11] can be resolved precisely with LSTM. Moreover, LSTM based spectrum sensing (LSTM-SS) with CNN is proposed for CR networks. Further, CR users obtain beneficiary advantages from the PU in spectrum sensing decisions. Finally, we can find out the presence of PU by using this method.

An improved method has been introduced in deep learning methods. Yet, there is an issue with this neural network that the computational cost is very high [17]. For example, to shift through the noise we utilized advancement of an autoencoder to pack data from the info layer. To improve the results, we additionally found the hereditary algorithm which predicts an enlarged structure for deep learning scheme. In order to develop a powerful detecting approach, the proposed calculation receives deep neural system and metaheuristic calculations called simulated annealing for deep neural network (SADNN).

1.2 Contributions

The contribution of this paper is discussed below.

- (1) First, the proposed method introduces deep learning-based spectrum sensing indicator to utilize CNN to exploit the energy connection features from the covariance framework of detecting information. Then, the arrangement of energy correlation features the comparison between various detecting periods of the LSTM. Hence, the action patterns of PUs can be learned.
- (2) Secondly, the proposed strategy could investigate the discriminative features to additionally improve the detection performance. The LSTM structure is used to exploit the PU activity pattern. The proposed CNN-LSTM structure is free from signal-noise model assumptions. To make LSTM with fair high SNR, the preparation data set is set-up to incorporate the data at exceptionally low SNRs in varying values.
- (3) Finally, the best boundaries of convolutional neural network are chosen by simulated annealing algorithm to improve the exactness of recognition and limit the computational multidimensional nature.

1.3 Paper Organization

The rest of this paper is structured as follows. Section 2 briefly depicts the background methodology. Section 3 describes the system model. CNN-LSTM is proposed in Section 4. Experimental outcomes are examined in Section 5 and in Section 6, conclusions are finally summarized.

2. Background Methodology

The major problem in cognitive radio is raised due to the inadequacy of spectrum resources and mismanagement of spectrum [35]. Adapting techniques like cyclo-stationary detection (CD), matched filter detection (MFD), energy detection (ED) and ML techniques enhance the functioning of CSS in cognitive radio systems. Energy detection is one of the traditional schemes that recognize all forms of primary users inside the transmission range of a CR user. Especially, the OFDM based CR receiver recognizes the primary user OFDM signal where CR receiver is furnished by different antenna-based energy detectors [19]. The two basic types of spectrum sensing in cognitive radio setup are cyclo-stationary detection and energy detection. Both of these techniques detect the licensed users in cognitive radio setup. Analysis of these two techniques is carried out in [37] to bring an improved technique for primary user identification. Cooperative spectrum sensing in OFDM dependent on energy recognition in multiple-input multiple-output (MIMO) cognitive radio sensor networks is implemented. Soft combination of the observed energy estimates various cognitive radio users is examined. OFDM based MIMO cognitive radio network recognizes the OFDM signal with multiple antenna detector of the CR receiver. It resulted in the critical development of primary user identification of the square law combining with energy detection of a MIMO cognitive radio sensor networks [46].

Machine learning techniques are adopted in several works [32][13] to allow CR users to be trained about the nature of the system. This can be carried out by techniques that use both supervised and unsupervised learning approaches or only supervised learning approach. In the first type, algorithms like k means which uses PU transmission patterns and statistics such as energy statistic and probability vector are used. Then, the identification of primary user is done by training the classifier using labelled training data [40]. In the second case, the primary user can be recognized by using classifiers like K-nearest neighbour (KNN), support vector machine (SVM) or naïve bayes. The effectiveness of these machine learning algorithms is completely dependent on feature selection. In case of KNN classifier, spectrum sensing features are needed for K neighbour classes. A test case is then ordered into one of the K neighbours based on larger part casting a vote. The voting depends on the statistical data picked up for pointing out the separation between the test case and the training instances. The separation ought to be determined precisely and really reflects the classifying classes [16].

Artificial neural network (ANN) based spectrum sensing (SS) is advanced to evaluate the database and to prepare the ANN to distinguish between signal and noise [51]. In cognitive radio, spectrum sensing has been considered as an ideal method to sense the availability of primary users in the network. Here, ANN analysis is to detect the signals and hence performance error has been occurred [36]. Due to this limitation, cooperative spectrum sensing is proposed in the duty cycle detection model for primary users [29].

Deep learning algorithms for parallel CNN-LSTM spectrum sensing is proposed where the signal and the noise prepare the model to detect multiple signals. Different patterns were performed to reveal the accuracy of the proposed scheme that does not require earlier information of the licensed user [27]. At that point, deep cooperative sensing (DCS) includes the first CSS system dependent on a CNN. In DCS, the framework for combining the individual detecting consequences of the SUs is found out freely with a CNN utilizing prepared detection tests, whether or not the individual detection outcomes are quantized. Furthermore, spectral and spatial correlations of detecting the results are considered as CSS in DCS [22].

Currently, spectrum sensing addresses much on deep learning algorithm. CNN-LSTM detector uses CNN for energy correlation to extract the information. The sensing information

of different periods is inserted as an input for LSTM to identify the primary user activity [49]. The blind spectrum sensing technique that depends on deep learning is composed of three types of neural systems like convolutional neural networks, long short-term memory and fully connected neural networks [15]. DNN-based likelihood probability proportion test is tested in DNN-based detection frameworks. DNN-based system is used as the input of a CNN to present a covariance matrix-aware CNN (CM-CNN)-based spectrum sensing algorithm [24].

The sensing performance in deep neural networks got increased but there are no strategies to analyse the variables of deep learning and to solve the optimization. Additionally, DNN is proposed to find out the quantity of neurons in the layer [20, 47 & 8]. Systems like autoencoder can be used to resize the information (dimensionality decrease) data to limit the disadvantages [21]. An unsupervised learning algorithm named genetic algorithm (GA) is utilized in [48] to recognize the best structure of DNN. Simulated annealing based deep neural network is utilized to improve the precision rate and to build up a beneficial detecting strategy by picking the best limits.

In spite of the fact that countless spectrum detecting strategies are accessible in the literature, every method has restriction in any of the three fundamental CR necessities like low detection time, low multidimensional nature and precision of identification. Strategies like cyclostationary feature detection (CFD) and OFDM require earlier information on PU signal in which CR situation is not fitting. Majority of other spectrum detection methods are incredibly mind boggling with high inactivity which is unacceptable for mechanical sensor and actuator systems. Therefore, it is important to structure a detecting procedure which is anything but difficult to execute and identify all types of PU signals. Subsequently, this article has proposed another spectrum sensing procedure that can identify a wide range of PU signals (both solid and feeble, with or without earlier data) with low unpredictability and improved determinism. However, CNN-LSTM is free from signal to noise model presumptions. To make LSTM with fair high SNR, the preparation informational index is set-up to incorporate information at low SNR in changing extents. SA is utilized to discover an appropriate quantity of neurons for every layer of a completely associated DNN. It upgrades the correct value in taking care of the specific enhancement issue. Contrasted with efficiently listing technique, it can discover the rough arrangement inside a sensible time. The proposed novel spectrum detecting strategy is planned for identifying the PU with least time and improved exactness.

3. System Model

Cognitive radio network comprises of PUs and SUs. The SUs in the CR network consider the spectrum band to sharply get to the white space. Here, two metrics such as $H0$ and $H1$ were considered with respect to the condition of the PUs in Equation (1 & 2). In this, $H0$ represents the absence of PU and $H1$ signifies the time of PU presence.

$$H1 : x(n) = s(n) + u(n) \quad (1)$$

$$H0 : x(n) = u(n) \quad (2)$$

Where $x(n)$ is the n -th received signal, $s(n)$ indicates the signal from PU, $u(n)$ signifies the additive white Gaussian noise (AWGN) sample. The spectrum sensing works on a principle that an unlicensed secondary user can utilize the spectrum resources when a licensed user is inactive or absent. Thus, the exhibition of spectrum sensing is assessed by the probability of detection and the probability of false alarm. The detection probability is the probability of choosing $H1$ when $H1$ is valid; the probability of false alarm is the probability that the choice is $H1$ when $H0$ is valid. In cooperative spectrum sensing, the secondary user

can sense a bunch of available spectrum holes to sense the execution. Hence, the statistical covariance can be calculated using a limited number of signal samples. For notation simplicity, we consider the case of single sensor with $M=1$. Fig. 1 shows the system model of cooperative spectrum sensing.

3.1 Pre-Processing

To represent as a simple process, we illustrate the entire received signal samples in the u -th detecting time interval as in Equation (3).

$$M_i = \{ M_i(1), \dots \dots \dots M_i(N) \} \tag{3}$$

In deep learning algorithms, labelled training data is needed where the training data of the proposed method is defined as given in Equation (4).

$$M = \{(M_1, l_1), (M_1, l_2), \dots \dots \dots (M_n, l_n)\} \tag{4}$$

Where, n is the size of the training set and l_n is the label. The label is the actual PU activity state corresponding to M_n . The real primary user activity state corresponds to M_n as the computation difficulty of the neural network is partially linked with the size of the input M_n . Furthermore, M_n is created from monotonous sampling of comparative dispersion which has overabundant information. Subsequently, we pre-process the sensing samples before contributing into the neural network. The labelled training data can be obtained by cooperating with the PU. The fundamental fact of PU activity must be known.

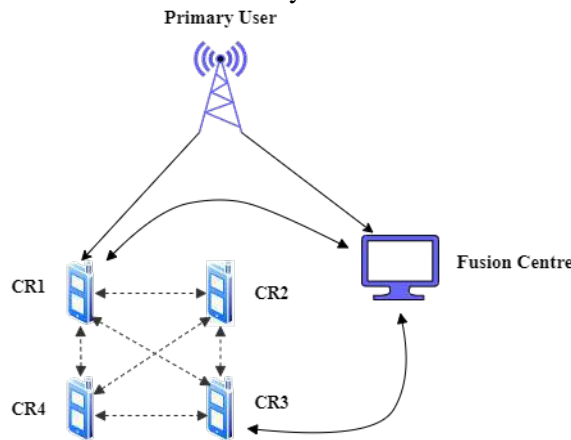


Fig. 1. System model of cooperative spectrum sensing

3.2 Sample Covariance Matrix

Sample covariance matrix is one of the adaptable statistics which inherently consolidates diverse discriminative i.e., energy, eigenvalues and non-diagonal elements. Hence, sample covariance matrix is proposed to act as an input to the neural network even though it does not have the energy correlation data of the sensing samples. Here, the sample covariance matrix is mentioned in Equation (5).

$$P_s = \frac{1}{Z} N_m N_m^J \tag{5}$$

So, the pre-processed training dataset is expressed as in Equation (6).

$$P_s = \{(P_1, l_1), (P_1, l_2), \dots \dots \dots (P_m, l_m)\} \tag{6}$$

Where, P_m denotes the sample covariance matrix and l_m indicates the corresponding label. N_m represents all the received signal samples in the m^{th} sensing period. m is the size of the training set, Z is the signal sample based on the PU activity, J is the channel index between PU and SU. Additionally, various sensing period of the spectrum sensing is processed to predict on-off strategy of the PU. In this paper, the proposed CNN extracts the energy correlation features from the covariance matrices created by the sensing data. At that point, the energy-correlation function contributed to various sensing periods are taken as input and processed for generalized neural networks to study the activities of the primary user.

4. Spectrum Sensing by Improved Convolutional Neural Network

4.1 Proposed Method

The improved neural network possesses the ability to remove the features and map the values. The three-layer structure such as input layer, hidden layer and output layer faces enormous number of issues in the variables. CNN is a multilayer structure where the characters are predicted by itself. Moreover, it is a feed forward network with structural parts of the neural network. The problem in this network is solved by using simulated annealing based hidden layer modelling. The extracted features from the convolution and pooling layer of CNN are passed to the LSTM layer. At last, CNN-LSTM model is used to predict the generated output of the network. The result and analysis of this proposed model can be demonstrated by few performance metrics.

4.2 Dataset Construction

Labelled training data is acquired by PU, while the PU activity is recognizable. To detect the execution process, we contemplate four digitally balanced families as the candidate set. Three different sets namely the training set, validation set and test set are considered. A wide range of SNR is sort out between -20dB and 18dB with a break of 1dB to deal with most of the executed situations. The AWGN information is created as noise information in the training set. Then, 100 samples are taken as training set for each SNR. The highlights of dataset factors are shown in [Table 1](#).

Table 1. Dataset generation

Modulation family	FSK, PAM, PSK, QAM
Signal length	1024
Over sampling rate of signals	2
Roll of factor	0.35
No. of SNR levels	20
Range of SNR	-20db to 18db
Samples taken per modulation type	8000

In this method, 5000 samples are taken for each SNR that ranges between 20 db and 18 db. There is similar number of PU signal and AWGN sequence. The generated information is split into training and testing datasets. [Fig. 2](#) shows the dataset construction.

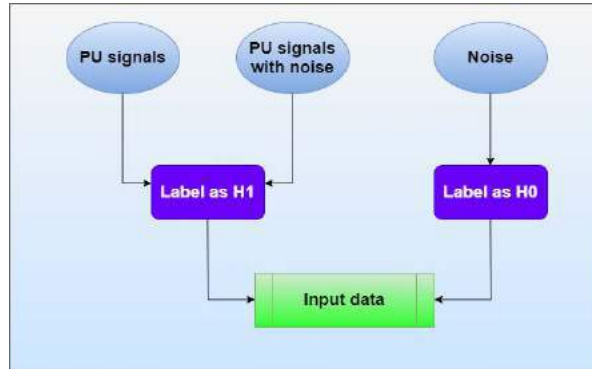


Fig. 2. Dataset construction

4.3 Long Short-Term Memory (LSTM)

Hochreiter et al. [11] proposed an LSTM as a specific variant of recurrent neural network. RNNs use the best gradient descent technique for learning about the research. However, it has its own limitation as gradient vanishing or detonation problem. To avoid these limitations, LSTM network has been introduced. The cell structure of LSTM unit is displayed in Fig. 3. It is comprised of three gates in particular input gate i , forget gate f and output gate o . The computation procedure of LSTM unit at time t is denoted.

$$I_S = \sigma(Y_i a_s + V_i d_{s-1} + g_i) \quad (7)$$

$$F_S = \sigma(Y_f a_s + V_f d_{s-1} + g_f) \quad (8)$$

$$O_S = \sigma(Y_o a_s + V_o d_{s-1} + g_o) \quad (9)$$

Equations (7-9) explain the operation of input gate i , forget gate f and output gate o in which I_S , F_S , O_S are the activation functions. g_f is the offset term of forgetting gate.

$$C_S = F_S \bullet C_{s-1} + i_t \bullet \tanh(Y_c a_t + V_c d_{s-1} + g_c) \quad (10)$$

$$O_S = \sigma(Y_o a_s + V_o d_{s-1} + g_o) \quad (11)$$

Equations 10 and 11 determine the cell state and the hidden state. The variable a_t denotes the critical qualities of electric energy consumption and the output pooling layer at time t . C_S is the hidden unit memory, d_s is the corresponding unit output, a_s is the unit input, Y and V are the weights, g is bias variables, ' \bullet ' indicates the Hadamard product and $\sigma[\]$ means the activation function (tanh). LSTM algorithm is explained in Pseudocode 1.

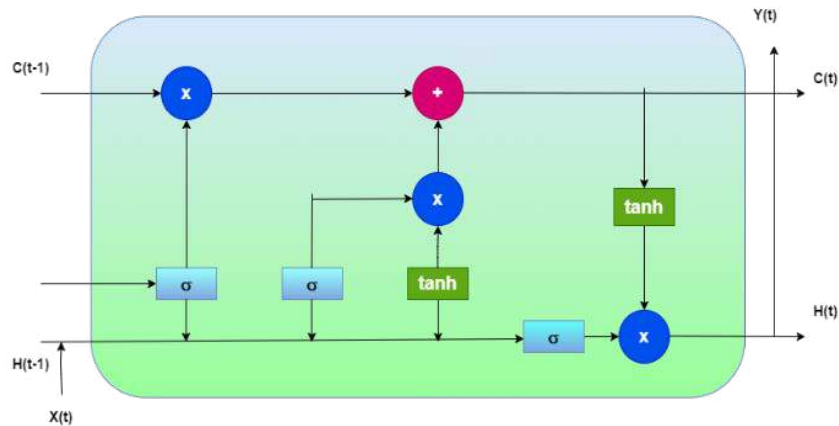


Fig. 3. LSTM structure

Pseudo code 1: LSTM

```

Input = data
// initialization
Initialize (batch size, sequence length, embedding, number of layers, hidden size)
LSTM = LSTM (embedding, number of layers, hidden size)
Hidden layer = model (number of layers, hidden size, batch size)
LSTM out, Hidden layer = LSTM (data, Hidden layer)
Fully connected layer = linear (hidden size, output size)
Fully connected out = LSTM out * Fully connected layer
Output = fully connected out

```

4.4 Simulated Annealing for Convolutional Neural Network

The main aim of SA is to find out the exact directions to delineate an assumed arrangement during the iterative process. When related to other methodologies, it is much better because of its accurate and low computational time. As seen in pseudocode 2, it comprises some associated factors: initialization, neighbour selection, evaluation of output, where t denotes the temperature. The neighbour selection operator of SA is assumed to change the search direction; evaluation operator estimates the number of solutions generated by neighbour selection. As appeared in lines 6–8 of Pseudocode 2, the search path of SA is related to probabilistic acceptance criterion. The temperature t will be refreshed towards the end of every emphasis to diminish the diversity gradually with the goal of SA to few specific locales.

Pseudocode 2: Simulated Annealing (SA)

```

// Initialization
Initialize Maximum Iteration (M), Temperature (t)
X = initial solution
For i=1: M
    While stopping criteria not met
        Y = neighbour selection
        E = evaluation
        If probabilistic acceptance criteria is met
            X = Y
        End
    End while
    Update Temperature (t)
     $T = \alpha \times T$ 
End for

```

As shown in Pseudocode 3, the proposed dual algorithm integrates simulated annealing with CNN to form a unique search algorithm. The flow chart of SA-CNN is shown in [Fig. 4](#). The input is considered as data D and t is another input parameter to determine the strategies of SA algorithm. Therefore, the proposed method is same as simple SA which plays the important role in determining the CNN solution. The initial role of SA is to predict the quantity of neurons in every hidden layer of the CNN. Hence, the identified outcome Y of simulated annealing moves to the CNN structure and demonstrates certain illustration to examine the best model in the network. The proposed method will decide whether to keep the result Y or not to determine the number of neurons. Then, as usual, the temperature t will update the iterations at the end of the algorithm. The temperature gets updated by geometric reduction law as ($T = \alpha \times T$, Where T is taken as 50^0 C and α reduction temperature is 0.95). As temperature raises slowly, the neurons in the hidden layer gets affected. At certain temperature, the neurons have very low sound of spikes which finally gets discharged. In spite, SA will converge to some particular regions to improve the results for better structure of convolutional learning algorithm. The hidden layer in CNN gets affected by a metaheuristic algorithm (SA).

SA finds the number of neurons in each layer of CNN to enhance the execution of CNN. Finally, the proposed CNN algorithm as shown is utilized to estimate the occurrence of primary user.

Pseudocode 3: CNN-SA

```

Input: data
// initialization
Initialize maximum iteration (M), Temperature (t)
X = initial solution\
While stopping criteria not met
    Y = neighbour selection
    Assign number of hidden neurons in
    W = initial weight
    E= initial error

While
    CNN= network (W, E)
    E= calculate error
    End
F = MSE (network, data)
    If probabilistic acceptance criteria is met
        X = Y
    End
Update temperature (t)
    T= $\alpha \times T$ 
End
Output = CNN

```

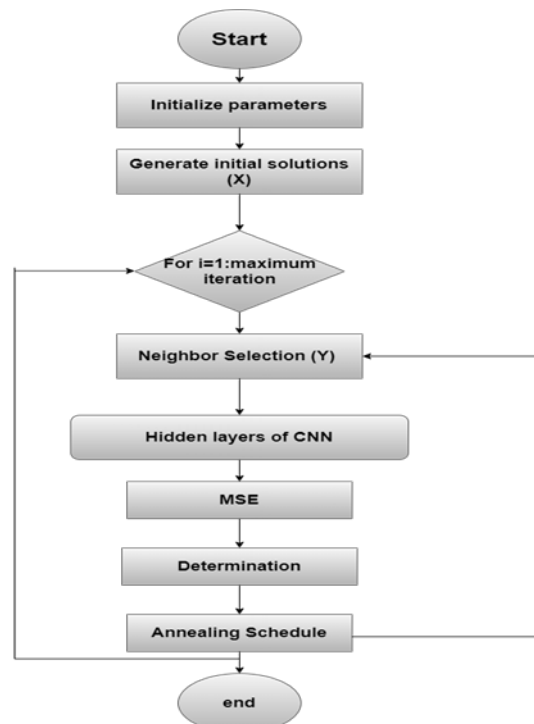


Fig. 4. SA CNN

4.5 CNN LSTM Network Structure

CNN-LSTM network structure is displayed in [Fig. 5](#). The proposed CNN-LSTM network can obtain complex spatial and temporal features. CNN can extract features among several

variables and LSTM layer can perform appropriate modelling with the temporal information. LSTM is the last layer of CNN-LSTM structure that stores important data extracted over CNN. LSTM provides a solution for preserving the long-term memory by consolidating memory units that can update the previous hidden state. This makes temporal features on long-term sequence.

The sample covariance matrices are complex which can be seen as two-layer process. The energy of the covariance matrix under state H0 is concentrated to the diagonal components in the real part while H1 energy is dispersed over the imaginary part and the real part. This visual distinction in covariance matrices under H0 and H1 makes the CNNs appropriate for studying the energy and correlation features out of the information. In CNN-LSTM module, sensing the data of CNN extracts features from the covariance matrices. The sequence of energy correlation features corresponding to numerous sensing periods are taken as the input of LSTM. The vectorized output consisting of energy and correlation features of the CNN sensing period are used as input to the LSTM cells. Likewise, the following strategy is to remove the time dynamic features in the array of sensing periods. Hence, the last output of LSTM cell is comprised of energy, correlation and time dynamic features of the sensing period is input into a thick layer to modify the output measurement as indicated by the quantity of information classes. Hence, PU activity pattern can be acquired.

4.6 Network Training

First introduce weights and biases in all convolution kernels. The forward propagation with the training set output O is determined. At that point, the CNN can become familiar with the error E through contrasting the output O with the labels y . Assume the quantity of sample set as S and the quantity of the sample types as c . We can compute the error E as per the equation (12).

$$E^S = \frac{1}{2} \sum_{m=1}^S \sum_{i=1}^c (y_i^m - o_i^m)^2 \quad (12)$$

CNN tests converges as stated by the value E . If it converges, then the training is finished. If it is not, then the residual δ of the output is analysed. Given the activation function f , the residual and the relu function is identified as activation function in the experiment. The residues can go from output layer to front layer. From Equation (13), residual can be calculated from each layer in which δ^l is the residual of the l^{th} layer.

$$\delta^l = ((W^l)^T \delta^{(l+1)}) \cdot f'(z^l) \quad (13)$$

Update the weights and bias in each layer with the learning rate α as in Equations (14) and (15).

$$W^l = W^l - \alpha \cdot \delta^{(l+1)} (a^l)^T \quad (14)$$

$$B_i^l = B_i^l - \alpha \cdot \delta^{(l+1)} \quad (15)$$

CNN continuously runs the above process to get an ideal outcome. It sends feature vector into NN for computing the training set. At any cost, the training set of a neural network is mathematically high. So, the performance is needed to be enhanced. To overcome this limitation, the introduced SA algorithm is used to find out the total quantity of neurons in the CNN. This solves the specific optimization problem and gives better accuracy rate.

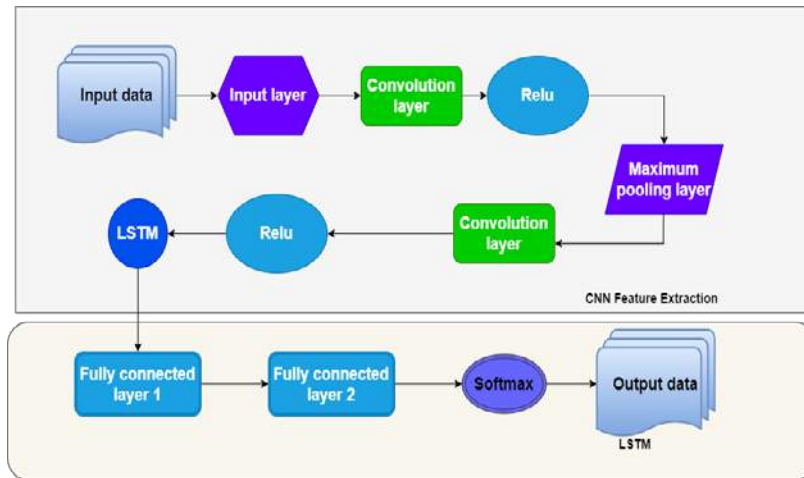


Fig. 5. CNN LSTM Structure

Pseudocode 4: CNN-LSTM

```

Input: data
// Initialization
Initialize random weight, w
// Training
Train network for training dataset
While  $i < \text{maximum iteration}$ 
     $N = \text{net}(\text{Updated weight})$ 
     $e = \text{evaluate}(\text{data}, N)$ 
     $i = i + 1$ 
End
// Testing
Output = test ( $N$ , data)

```

5. Experimental Setup

The proposed CNN-LSTM based spectrum sensing technique has been implemented in MATLAB R2018a. The datasets used in the proposed technique consist of SNR value in the range of -20db to 18db. The dataset is created with enormous samples with low SNR value. The aim of the proposed method is to point out the occupancy of PU signal even in low SNR value. Hence, 80% samples are maintained with low SNR value and 20% samples with high SNR range. Experiment is carried out by differentiating the number of training samples. Finally, a total number of 5000 samples are maintained for training process. The dataset composition is presented in [Table 2](#).

Table 2. Composition of dataset

Dataset	Label	Samples	Total
Training	H0	2500	5000
	H1	2500	
Testing	H0	250	500
	H1	250	

Specific parameters and the network architecture are chosen for the best performance of detector. The parameter setting used in the proposed CNN LSTM structure and the network architecture is presented in [Table 3](#) and [Table 4](#).

Table 3. Composition of dataset

Parameter	value
Learning rate	0.0005
Dropout rate	0.1
Mini Batch size	25
Number of epochs	200
Number of hidden layers	6
Activation function	Relu
Loss function	Mean Squared Error (MSE)
Training set	5000
Testing set	500

Table 4. Network architecture

Activation	Relu
Optimizer	Adam
Convolutional layer 1+relu	250
Maximum pooling	2 x 2
Convolutional layer 2+relu	500
LSTM nodes	124
Fully connected layer 1	62
Fully connected layer 2	2

5.1 Performance Evaluation

Here, we assess the proposed CNN-LSTM spectrum sensing for its demonstration. The detection probability (P_d) and the false alarm probability (P_f) are validated for assessing the proposed strategy. Signal information about the test dataset is taken individually from the system to determine P_d and P_f . It accurately arranges the signal, for example, (H_1) is separated by the absolute number of PU signal models to decide P_d . In LSTM network, the AWGN sequence samples are inserted and the P_f is obtained. At any point, it could not predict H_0 where it was separated by AWGN sequence samples. The demonstration of the invented CNN LSTM structure for changing SNR ranges is introduced in **Fig. 6 - 10**. From the given experimental analysis, it is demonstrated that the proposed spectrum sensing strategy beats the current approaches.

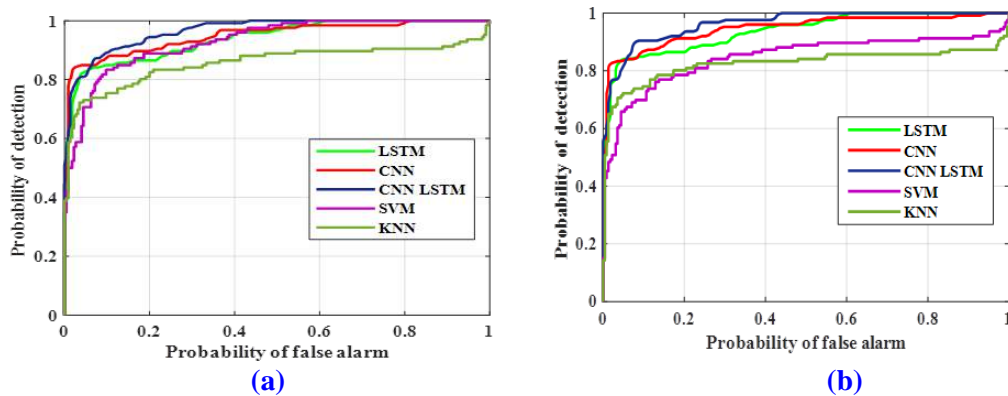
**Fig. 6.** Probability of detection (P_d) Vs Probability of false alarm (P_f) (a) SNR=-12db (b) SNR= -14db

Fig. 6(a) shows the analysis of Pd (vs.) Pf under a dataset with SNR=-12db. It illustrates that the proposed CNN-LSTM method beats other sensing methods with less SNR. This is achieved due to the temporal characteristics available in the signal of the proposed CNN-LSTM method. The scientific reason behind the proposed CNN-LSTM method is their standard architecture of the network. Even though ANN has a shallow neural network, the LSTM has chain network. SVM considers the spatial temporal detector. The proposed method is the combination of deep neural network and looping structures. The elements are unrolled in a continuous manner in which other techniques do not perform this function.

The signal to noise ratio is set as -14db in **Fig. 6(b)** to reveal the features of the proposed CNN-LSTM detector under different values. It represents that the CNN LSTM method has high density value when compared to other techniques like CNN and LSTM. The high false alarm probability in the existing KNN and SVM means that there is a less availability of primary users to use the spectrum holes. The proposed method contains various discriminative features that have the ability to extract features of matrix shaped data. CNN itself has the quality of relieving graphical features but it is not good at specifying the temporal features. Therefore, the proposed method of CNN-LSTM is good at sensing the temporal characteristics in the signal where other methods are unable to do so.

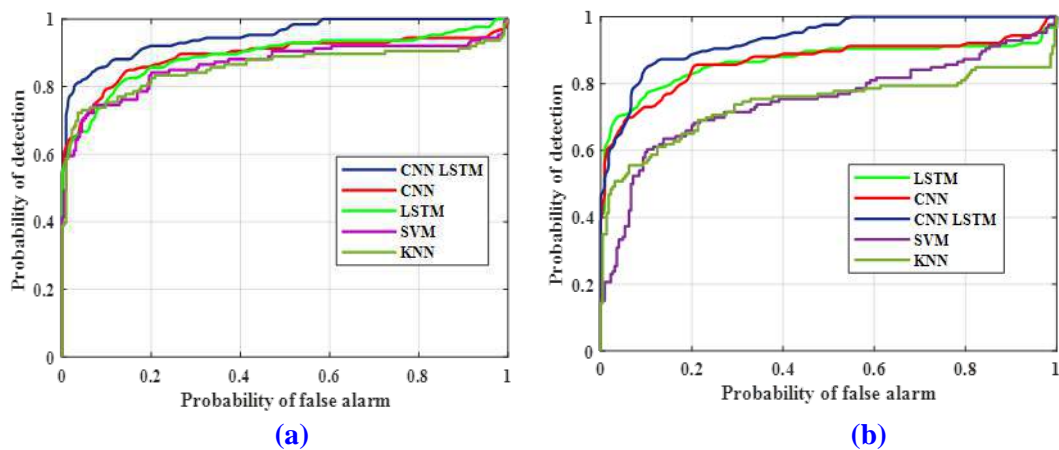


Fig. 7. Probability of detection (Pd) vs. Probability of false alarm (Pfa) (a) SNR = -16db (b) SNR = -18db

The data is kept same for all three methods with SNR of -16db as shown in **Fig. 7(a)** to demonstrate a reasonable comparison with the proposed CNN LSTM method and other techniques. This is further used to verify whether Pd (vs.) Pfa has high and accurate detection value. The major reason that the proposed CNN-LSTM method overcomes similar existing strategies as LSTM and CNN is due to the design and working principle of CNN-LSTM method. The deep feature extraction and fair detection capability of the proposed method extracts all features of the signal. From the plot, we can derive that the proposed CNN-LSTM method has high detection value than the other methods at a low SNR of -16 db. The proposed method has high probability of detection value than the machine learning algorithm namely KNN and SVM. Note that in **Fig. 7(b)**, it shows the test statistics of the CNN LSTM technique by using the training set containing SNR value of -18db. It is shown that the proposed method has high detection value when compared to other proposed method like CNN, LSTM, SVM and KNN. The high performance detection is due to the CNN-LSTM structure which is free from signal to noise model. It simultaneously performs both energy correlation and temporal

primary user detection. Though, CNN only performs to learn spatial features and LSTM performs only temporal features. The sensing efficiency of KNN and SVM classification speed is minimal. Hence, the invented method has best Pd (vs.) Pf even in the SNR value which is shown in Fig. 7(b).

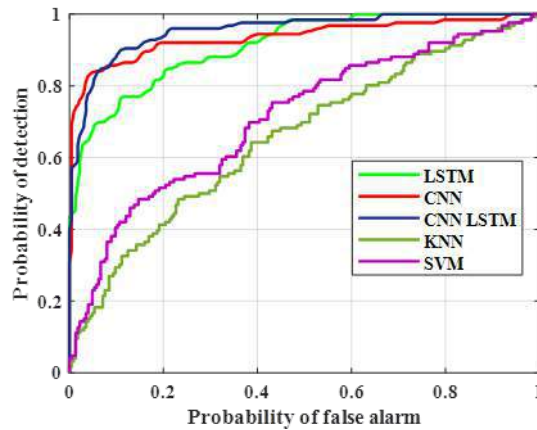


Fig. 8. Probability of detection (Pd) vs. Probability of false alarm (Pf) (SNR=-20db)

To execute the performance of the proposed CNN-LSTM with the existing methods, we evaluate the graph which shows Pd (vs.) Pf in Fig. 7 with the SNR value of -20db. This different SNR performance shows the best accuracy schemes of CNN-LSTM method. The data flow in LSTM is structured by the Gate layer as it performs extremely in temporal data. The CNN structure evaluates the energy correlation features where CNN-LSTM took all the hidden characteristics from both the invented information which definitely LSTM and CNN neglected to do as such. As well as the supervised machine learning techniques KNN, SVM algorithm required more time for training the classifier.

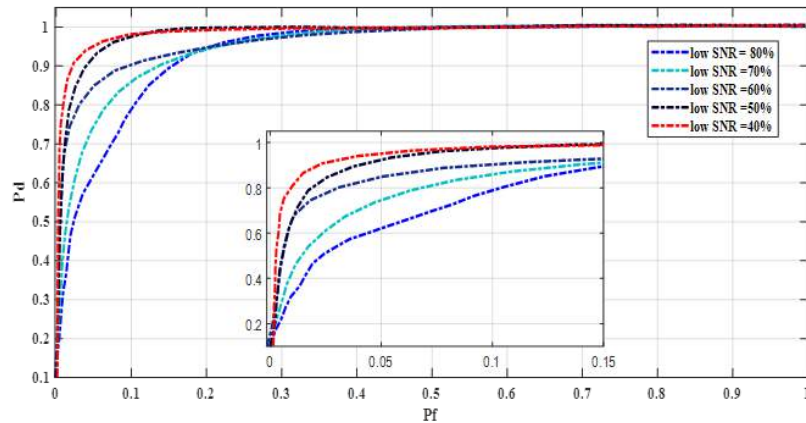


Fig. 9. Pd Vs Pf for various training samples

The creation of training set notably affects Pd and Pf from Fig. 9. For different SNR training sets, the Pf and Pd got enlarged. As the quantity of samples and level of samples in low SNR go is expanded, Pf and Pd likewise increment. The magnitude of the primary user signal is noted to be noise at low SNR. Network, in this manner, consider that it is difficult to separate the primary user signal and noise. This is exploited because the temporal correlation is placed in this method so that the plotted graph shows high detection value for the low SNR range at various samples for the proposed CNN LSTM work.

The detection probability of various techniques for different SNR values is shown in **Fig. 10**. The various SNR values are compared with detection probability of different techniques like CNN, LSTM, SVM and KNN. When the SNR values get reduced, the detection probability also gets decreased. The proposed spectrum sensing method provides high probability of detection when compared with other techniques. This seems that the CNN-LSTM has good temporal dependency and it outperforms other schemes as shown in the bar diagram.

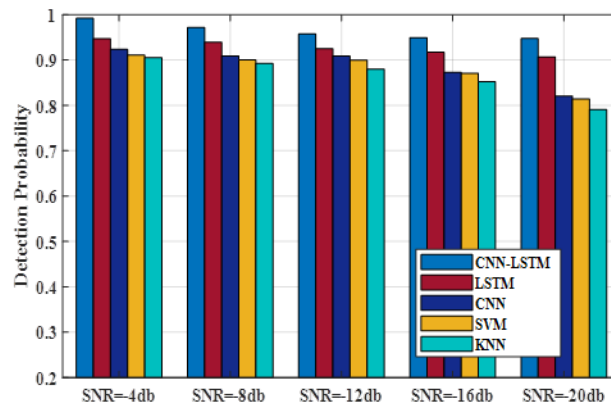


Fig. 10. Detection Probability

The effectiveness of the proposed CNN-LSTM algorithm is verified under various SNR ranges. A graph has been plotted between P_d (vs.) Signal to Noise Ratio for the five convolutional schemes and is shown in Figure.11. When compared to the existing methods namely CNN, LSTM, SVM and KNN, the proposed technique CNN LSTM has a high-performance detection algorithm. It is mainly caused due to the use of temporal dependency of the proposed technique where the existing methods fail to do so because CNN can predict only the spatial features. The supervised techniques like SVM and KNN have higher training module time. So, both the matrix correlation features are needed to find out the presence of primary user.

6. Conclusion

The cognitive radio system shows great impact in developing a good implementation of networks. The determinism includes both spectrum sensing and spectrum handoff algorithms. Though there are various spectrum sensing strategies demonstrated in the previous implementation, the technique which satisfies both ease of implementation and accuracy need to be developed. Hence, a spectrum sensing algorithm with improved CNN LSTM is proposed in this paper. The principle used in this approach is that any PU signal will have a modulation format associated with it and hence identifying the presence of a modulation format itself establishes the presence of PU signal. This approach is able to effectively sense the PUs presence. The experimental results are carried out in MATLAB. In this proposed technique, probability detection is considered as one of the important parameters for the efficiency of the method. Simulation results were carried out under different SNRs to indicate improved execution of the invented algorithm. The methodology can be additionally improved by using different optimizing techniques to determine the best hidden layer size of the network so that complexity can be further reduced thereby identifying PU presence more effectively.

References

- [1] H. M. A. Abdullah, and A. V. S. Kumar, "HFSA-SORA: Hybrid firefly simulated annealing based spectrum opportunistic routing algorithm for Cognitive Radio Ad hoc Networks (CRAHN)," in *Proc. of 2017 International Conference on Intelligent Computing and Control (I2C2)*, 2017. [Article \(CrossRef Link\)](#)
- [2] A. Agarwal, S. Dubey, M. A. Khan, R. Gangopadhyay, and S. Debnath, "Learning based primary user activity prediction in cognitive radio networks for efficient dynamic spectrum access," in *Proc. of SPCOM*, pp. 1-5, June 2016. [Article \(CrossRef Link\)](#)
- [3] A. Al-Tahmeesschi, M. Lopez-Benitez, J. Lehtomaki, and K. Umebayashi, "Investigating the Estimation of Primary Occupancy Patterns under Imperfect Spectrum Sensing," in *Proc. of 2017 IEEE Wireless Communications and Networking Conference Workshops (WCNCW)*, 2017. [Article \(CrossRef Link\)](#)
- [4] F. Azmat, Y. Chen, and N. Stocks, "Analysis of spectrum occupancy using machine learning algorithms," *IEEE Trans. Veh. Technol.*, vol. 65, no. 9, pp. 6853-6860, September 2016. [Article \(CrossRef Link\)](#)
- [5] S. Badrinath, and V. U. Reddy, "A hybrid energy detection approach to spectrum sensing," in *Proc. of 2009 First UK-India International Workshop on Cognitive Wireless Systems (UKIWCWS)*, December 2009. [Article \(CrossRef Link\)](#)
- [6] Chun-Wei Tsai, Chien-Hui Hsia, Shuang-Jie Yang, Shih-Jui Liu and F. Zhi-Yan, "Optimizing hyperparameters of deep learning in predicting bus passengers based on simulated annealing," *Applied Soft Computing Journal*, vol. 88, 2020. [Article \(CrossRef Link\)](#)
- [7] C. Clancy, J. Hecker, E. Stuntebeck, and T. O'Shea, "Applications of machine learning to cognitive radio networks," *IEEE Wireless Communication*, vol. 14, no. 4, pp. 47-52, August 2007. [Article \(CrossRef Link\)](#)
- [8] L. Deng, "A tutorial survey of architectures, algorithms, and applications for deep learning," *APSIPA Trans. Signal Inform. Process.*, vol.3, pp.1-29, 2014. [Article \(CrossRef Link\)](#)
- [9] Dhaval Patel and Yogesh Trivedi, "Non-parametric Blind Spectrum Sensing Based on Censored Observations for Cognitive radio," *Journal of Signal Processing Systems*, vol. 78, pp. 275-281, March 2015. [Article \(CrossRef Link\)](#)
- [10] A. Ghasemi, E. S. Sousa, "Collaborative spectrum sensing for opportunistic access in fading environments," in *Proc. of the 1st IEEE International Symposium on New Frontiers in Dynamic Spectrum Access Networks (DySPAN '05)*, pp. 131-136, November 2005. [Article \(CrossRef Link\)](#)
- [11] S. Hochreiter and J. Schmidhuber, "Long short-term memory," *Neural Comput.*, vol. 9, no. 8, pp. 1735-1780, November 1997. [Article \(CrossRef Link\)](#)
- [12] W. Huixin, M. Duo, and L. He, "Analysis and Simulation of the Dynamic Spectrum Allocation Based on Parallel Immune Optimization in Cognitive Wireless Networks," *The Scientific World Journal*, pp. 1-8, 2014. [Article \(CrossRef Link\)](#)
- [13] Hurmat Ali Shah and Insoo Koo, "Reliable Machine Learning Based Spectrum Sensing in Cognitive Radio Networks," *Wireless Communications and Mobile Computing*, 2018. [Article \(CrossRef Link\)](#)
- [14] Jiandong Xie, Jun Fang, Chang Liu, Xuanheng Li, "Deep Learning-Based Spectrum Sensing in Cognitive Radio: A CNN-LSTM Approach," *IEEE Communications Letters*, vol. 24, no. 10, pp. 2196-2200, 2020. [Article \(CrossRef Link\)](#)
- [15] Kai Yang, Zhitao Huang, Xiang Wang and Xueqiong Li, "A Blind Spectrum Sensing Method Based on Deep Learning," *Sensors*, vol. 19, no. 10, pp. 2270, March 2019. [Article \(CrossRef Link\)](#)
- [16] Karaputugala Madushan Thilina, Kae Won Choi, Nazmus Saquib, and Ekram Hossain, "Machine Learning Techniques for Cooperative Spectrum Sensing in Cognitive Radio Networks," *IEEE Journal on selected areas in communications*, vol. 31, no. 11, pp. 2209-2221 November 2013. [Article \(CrossRef Link\)](#)
- [17] S. Kirkpatrick, C.D. Gelatt, and M.P. Vecchi, "Optimization by simulated annealing," *Science*, vol. 220, no. 4598, pp. 671-680, May 1983. [Article \(CrossRef Link\)](#)

- [18] A. Krizhevsky, I. Sutskever, and G. E. Hinton, "Imagenet classification with deep convolutional neural networks," in *Proc. of NIPS Stateline NV*, pp. 1097–1105, December 2012.
- [19] V. Kuppusamy, and R. Mahapatra, "Primary user detection in OFDM based MIMO Cognitive Radio," in *Proc. of 3rd International Conference on Cognitive Radio Oriented Wireless Networks and Communications*, 2008. [Article \(CrossRef Link\)](#)
- [20] M. Lakshmi, R. Saravanan, and R. Muthaiah, "Energy Detection Based Spectrum Sensing For Cognitive Radio Using Fusion Rules," *International Journal of Scientific & Engineering Research*, vol. 4, no. 6, June 2013.
- [21] M. Långkvist L. Karlsson, A. Loutfi, "A review of unsupervised feature learning and deep learning for time-series modelling," *Pattern Recognit, Lett.*, vol. 42, pp.11–24, 2014. [Article \(CrossRef Link\)](#)
- [22] W. Lee, M. Kim, and D. H. Cho, "Deep Cooperative Sensing: Cooperative Spectrum Sensing Based on Convolutional Neural Networks," *IEEE Transactions on Vehicular Technology*, vol. 68, no. 3, pp. 3005-3009, March 2019. [Article \(CrossRef Link\)](#)
- [23] Z. C. Lipton, J. Berkowitz, and C. Elkan, "A critical review of recurrent neural networks for sequence learning," 2015.
- [24] C. Liu, J. Wang, X. Liua, and Y. C. Liang, "Deep CM-CNN for Spectrum Sensing in Cognitive Radio," *IEEE Journal on Selected Areas in Communications*, vol. 37, no. 10, pp. 2306-2321, October 2019.
- [25] X. Lu, P. Wang, D. Niyato, and E. Hossain, "Dynamic Spectrum Access in Cognitive Radio Networks with RF Energy Harvesting," *IEEE Wirel. Communication*, vol. 21, no. 3, pp. 102–110, 2014.
- [26] Mangesh V Deshmukh , Dr. Mrs. Shruti Oza, "Spectrum Sensing based on Energy Detection for Cognitive Radio using FPGA," vol. 08, no. 05, May 2019.
- [27] Mingdong Xu, Zhendong Yin, and Mingyang Wu, "Spectrum Sensing Based on Parallel CNN-LSTM Network," in *Proc. of 2020 IEEE 91st Vehicular Technology Conference (VTC2020-Spring)*, 2020.
- [28] J. Mitola and G. Q. Maguire, "Cognitive radio: Making software radios more personal," *IEEE Pers. Commun.*, vol. 6, no. 4, pp. 13-18, August 1999. [Article \(CrossRef Link\)](#)
- [29] Ouchra Senadji and Kevin Chang, "Detection of dynamic primary user with cooperative spectrum sensing," in *Proc. of 21st European Signal Processing Conference (EUSIPCO 2013)*, May 2014.
- [30] Patel D. K. and Y. N. Trivedi, "LRS-G2G2 Based Non-parametric Spectrum Sensing for Cognitive Radio," in *Proc. of International Conference on Cognitive Radio Oriented Wireless Networks*, vol. 172, pp 330-341, 2014.
- [31] H, S. Reyes, N. Subramaniam, N. Kaabouch, and W. Chen, "A spectrum sensing technique based on autocorrelation and Euclidean distance and its comparison with energy detection for cognitive radio networks," *Comput. Electronics journal Eng.*, vol. 52, pp. 319-327, 2016. [Article \(CrossRef Link\)](#)
- [32] Saber Mohammed, El Rharras Abdessamad, and Saadane Rachid, "An Optimized Spectrum Sensing Implementation based on SVM, KNN and TREE Algorithms," in *Proc. of International Conference on Signal-Image Technology & Internet-Based Systems*, 2019.
- [33] P. Sharma and V. Abrol, "Individual vs cooperative spectrum sensing for Cognitive Radio Networks," in *Proc. of 2013 Tenth International Conference on Wireless and Optical Communications Networks (WOCN)*, 2013.
- [34] Shree Krishna Sharma, Mohammad Patwary, Symeon Chatzinotas, Bjorn Ottersten, and Mohamed Abdel-Maguid, "Repeater for 5G Wireless: A Complementary Contender for Spectrum Sensing Intelligence,".
- [35] S. Haykin, "Cognitive radio: brain-empowered wireless communications," *IEEE Journal on Selected Areas in Communications*, vol. 23, no. 2, pp. 201–220, 2005. [Article \(CrossRef Link\)](#)
- [36] K. Simonyan and A. Zisserman, "Very deep convolutional networks for large-scale image recognition," *arXiv preprint arXiv*, pp.1409.1556, 2014.

- [37] Z. Sun, Q. Wang, and C. Che, "Study of Cognitive Radio Spectrum Detection in OFDM System," in *Proc. of 2010 Asia-Pacific Conference on Wearable Computing Systems*, 2010. [Article \(CrossRef Link\)](#)
- [38] Y. J. Tang, Q. Y. Zhang, and W. Lin, "Artificial Neural Network Based Spectrum Sensing Method for Cognitive Radio," in *Proc. of 2010 International Conference on Computational Intelligence and Software Engineering*, 2010. [Article \(CrossRef Link\)](#)
- [39] C. W. Tsai, C. H. Hsia, S. J. Yang, S. J. Liu, and Z. Y. Fang, "Optimizing hyper parameters of deep learning in predicting bus passengers based on simulated annealing," *Applied Soft Computing Journal*, vol. 88, no. 106068, 2020. [Article \(CrossRef Link\)](#)
- [40] Vaibhav Kumar, Deep Chandra Kandpal, and Monika Jain, "K-mean Clustering based Cooperative SpectrumSensing in Generalized_μ Fading Channels," in *Proc. of 2016 Twenty Second National Conference on Communication (NCC)*, 2016. [Article \(CrossRef Link\)](#)
- [41] H. Wang, E. H. Yang, Z. Zhao, and W. Zhang, "Spectrum sensing in cognitive radio using goodness of the testing," *IEEE Trans.Wireless Communication*, vol. 8, no. 11, pp. 5427-5430, November 2009.
- [42] B. Wang and K. J. R. Liu, "Advances in cognitive radio networks: a survey," *IEEE Journal on Selected Topics in Signal Processing*, vol. 5, no. 1, pp. 5–23, 2011. [Article \(CrossRef Link\)](#)
- [43] Wangjam Niranjana Singh and Ningrinla Marchang, "A Review on Spectrum Allocation in Cognitive Radio Network," *International Journal of Communication Networks and Distributed Systems*, vol.23, no.2, pp.172 – 193, March 2018.
- [44] J. B. Wei, S. Wang and H. T. Zhao, "Cognitive wireless networks: key techniques and state of the art," *Journal on Communications*, vol. 32, no. 11, pp. 147–158, 2011.
- [45] Wei Li, Kai Liu, Lin Yan, Fei Cheng, YunQiu Lv, and LiZhe Zhang, "FRD-CNN: Object detection based on small-scale convolutional neural networks and feature reuse," *Scientific Reports*, vol. 9, no. 1, 2019. [Article \(CrossRef Link\)](#)
- [46] Wei Ma, Mu Qing Wu, Dong Liu, and Meng Ling Wang, "User sensing based on MIMO cognitive radio sensor networks," in *Proc. of 2009 2nd IEEE International Conference on Computer Science and Information Technology*, 2009. [Article \(CrossRef Link\)](#)
- [47] Xianghui Cao, Xiangwei Zhou, Lu Liu, and Yu Cheng, "Energy-Efficient Spectrum Sensing for Cognitive Radio Enabled Remote State Estimation Over Wireless Channels," *IEEE Transactions on Wireless Communications*, vol. 14, no. 4, April 2015.
- [48] L. Xie and A. Yuille, "Genetic CNN," in *Proc. of the IEEE International Conference on Computer Vision*, pp. 1388–1397, 2017. [Article \(CrossRef Link\)](#)
- [49] J. Xie, J. Fang, C. Liu, and X. Li, "Deep Learning-Based Spectrum Sensing in Cognitive Radio: A CNN-LSTM Approach," *IEEE Communications Letters*, 2020.
- [50] T. Xu, M. Zhang, and H. Hu, "Harmonious Coexistence of Heterogeneous Wireless Networks in Unlicensed Bands: Solutions from the Statistical Signal Transmission Technique," *IEEE Vehicle. Tech. Mag*, vol. 14, no. 2, pp. 61–69, June 2019. [Article \(CrossRef Link\)](#)
- [51] R. G. Yelalwar, and Y. Ravinder, "Artificial Neural Network Based Approach for Spectrum Sensing in Cognitive Radio," in *Proc. of International Conference on Wireless Communications, Signal Processing and Networking (WiSPNET)*, 2018.



Appala Raju Uppala received the Diploma in Electronics and Communication Engineering from Govt. Polytechnic College, Narsipatnam in 1997, A.M.I.E Degree in ECE from Institution of Engineers India, Kolkata in 2004, and Master of Technology from Jawaharlal Nehru Technological University (JNTU), Hyderabad in 2007, and Pursuing the Ph.D degree from department of ECE, Jawaharlal Nehru Technological University (JNTU), Kakinada, India. He has published more than 12 technical papers in national and international journals and Conferences. His areas of interest Analog Electronics and Design, Cognitive Radio System, Communication and signal processing.



C. Venkata Narasimhulu received B.Tech degree in Electronics and Communication Engineering from S V University, Tirupathi in 1995 and Master of Technology in Instrumentation & Control Systems from REC, Calicut in 2000 and Ph.D. from JNTU, Kakinada in 2013 in the area of signal Processing. He has published more than 45 technical papers in national and international Journals and Conferences. His interested areas are Signal Processing, Cognitive Radio, Image processing and medical image processing etc.



K. Satya Prasad received B Tech. degree in Electronics and Communication Engineering from JNTU college of Engineering, Anantapur, in 1977 and M. E. degree in Communication Systems from Guindy college of Engineering, Madras University, in 1979 and Ph.D from Indian Institute of Technology, Madras in 1989. He has published more than 150 technical papers in different National & International conferences and Journals and Authored one Text book. His areas of Research include Communications Signal Processing, Image Processing, Speech Processing, Neural Networks & Ad-hoc wireless networks etc.

Weed Detection Using Image Processing

M Anand^{1*}, P Vijaya Mary², G Archana³, P Charith⁴

¹Assistant Professor, Geethanjali College of Engineering and Technology, Hyderabad India

^{2,3,4} Students, Geethanjali College of Engineering and Technology, Hyderabad India

*manand.ece@gcet.edu.in

ABSTRACT

As the increase in the world population the demand of the Soya production and other is also increases. In order to increase the growth of the Soya in the Soya crop it is necessary to detect the weed in the Soya crop and the barren land to minimize the growth of weed so that the growth of the Soya can be improved. Weed detection is one of the important factors to be analysed. Unmanned Air Vehicle (UAV) is used to get data acquisition of Soya crop in different phases so that high quality of RGB images can be captured. The proposed method facilitates the extraction of weed, Soya, and barren land in the Soya crop field using background subtraction. The result shows that background subtraction method is good for detection the weed, barren land, and Soya.

Key words: UAV, RGB, CNN

INTRODUCTION

Weeds are an all too common occurrence in lawns and gardens. While some may be deemed useful or attractive, most types of weeds are considered a nuisance. Learning more about weed control and detection can make it easier for gardeners to decide whether these weeds should be welcomed or if they must go. Let's take a look at some common weed plants and when or what weed control methods may be necessary. By definition, a weed is known as "a plant in the wrong place." For the most part, these plants are known more for their undesirable qualities rather than for their good ones, should there be any. Weeds are competitive, fighting your garden plants or lawn grass for water, light, nutrients and space. Most are quick growers and will take over many of the areas in which you find them. While most types of weeds thrive in favourable conditions, native types may be found growing nearly anywhere the ground has been disturbed. In fact, they may even offer clues to your current soil conditions.

One of the newest and most researched technologies nowadays is deep learning. Deep learning is a technique used to create intelligent systems as similar as possible to human brains. It has made

a big impact in all types of domains such as video, audio and image processing. On the other hand, agriculture is humanity's oldest and most essential activity for survival. The growth of population during the last years has led to a higher demand of agricultural products. To meet this demand without draining the environmental resources the agriculture uses, automation is being introduced into this field. The present project aims to merge both concepts by achieving autonomous weed recognition in agriculture this goal will be reached by using new technologies such as Open CV, FarmBot and Python programming, image processing, deep learning and Artificial Neural Networks (ANNs).

LITERATURE REVIEW

Agriculture has always been an essential activity for survival. Over the last century, and more specific, over the last 15 years, agriculture has started to mechanise and digitise due to this evolution and automation, labour flow was almost totally standardised. Nowadays, after introducing robotics and artificial intelligence into agriculture there is no need of standardization, robots are working collaboratively with humans and learning from them how to realize the basic agriculture tasks such as weed detection, watering or seeding.

Weed detection is one of those basic agriculture tasks that are being automatized and digitised, in this case, because of toxicity related to herbicides so, reducing human intervention will make possible a decrease in the use of herbicides, increasing health care. To achieve this, robots able to detect plants and classify them into crop or weed are now introduced into agriculture. This implementation has been done in multiples studies such as Dankhara. Where Internet of Things (IoT) is applied into an intelligent robot to differentiate crop and weed remotely IoT is present in the communication between a Raspberry Pi, where the processing is done and the camera and sensors are connected, and the Data Server, where the Raspberry Pi sends the information obtained.

Machine learning (ML)

Machine learning is the scientific study of algorithms and statistical models that computer systems use to perform a specific task without using explicit instructions, relying on patterns and inference instead. It is seen as a subset of artificial intelligence. Machine learning algorithms build a mathematical model based on sample data, known as "training data", in order to make

predictions or decisions without being explicitly programmed to perform the task. Machine learning algorithms are used in a wide variety of applications, such as email filtering and computer vision, where it is difficult or infeasible to develop a conventional algorithm for effectively performing the task.

CNN ALGORITHM IMPLEMENTATION

Convolutional Neural Network has had ground breaking results over the past decade in a variety of fields related to pattern recognition; from image processing to voice recognition. The most beneficial aspect of CNNs is reducing the number of parameters in ANN. This achievement has prompted both researchers and developers to approach larger models in order to solve complex tasks, which was not possible with classic ANNs. The most important assumption about problems that are solved by CNN should not have features which are spatially dependent. In other words, for example, in a face detection application, we do not need to pay attention to where the faces are located in the images. The only concern is to detect them regardless of their position in the given images. Another important aspect of CNN is to obtain abstract features when input propagates toward the deeper layers.

SUPPORT VECTOR MACHINE ALGORITHM

Support Vector Machine or SVM is one of the most popular Supervised Learning algorithms, which is used for Classification as well as Regression problems. However, primarily, it is used for Classification problems in Machine Learning. The goal of the SVM algorithm is to create the best line or decision boundary that can segregate n-dimensional space into classes so that we can easily put the new data point in the correct category in the future. This best decision boundary is called a hyper plane. SVM chooses the extreme points/vectors that help in creating the hyper plane. These extreme cases are called as support vectors, and hence algorithm is termed as Support Vector Machine. Consider the below diagram in which there are two different categories that are classified using a decision boundary or hyper plane.

METHODOLOGY

This project work describes the methodology for weed detection process in soya crops. It follows ten steps. The task flow is shown in Figure 1. The tasks and process represents the steps of the algorithm. Our algorithm includes the following steps

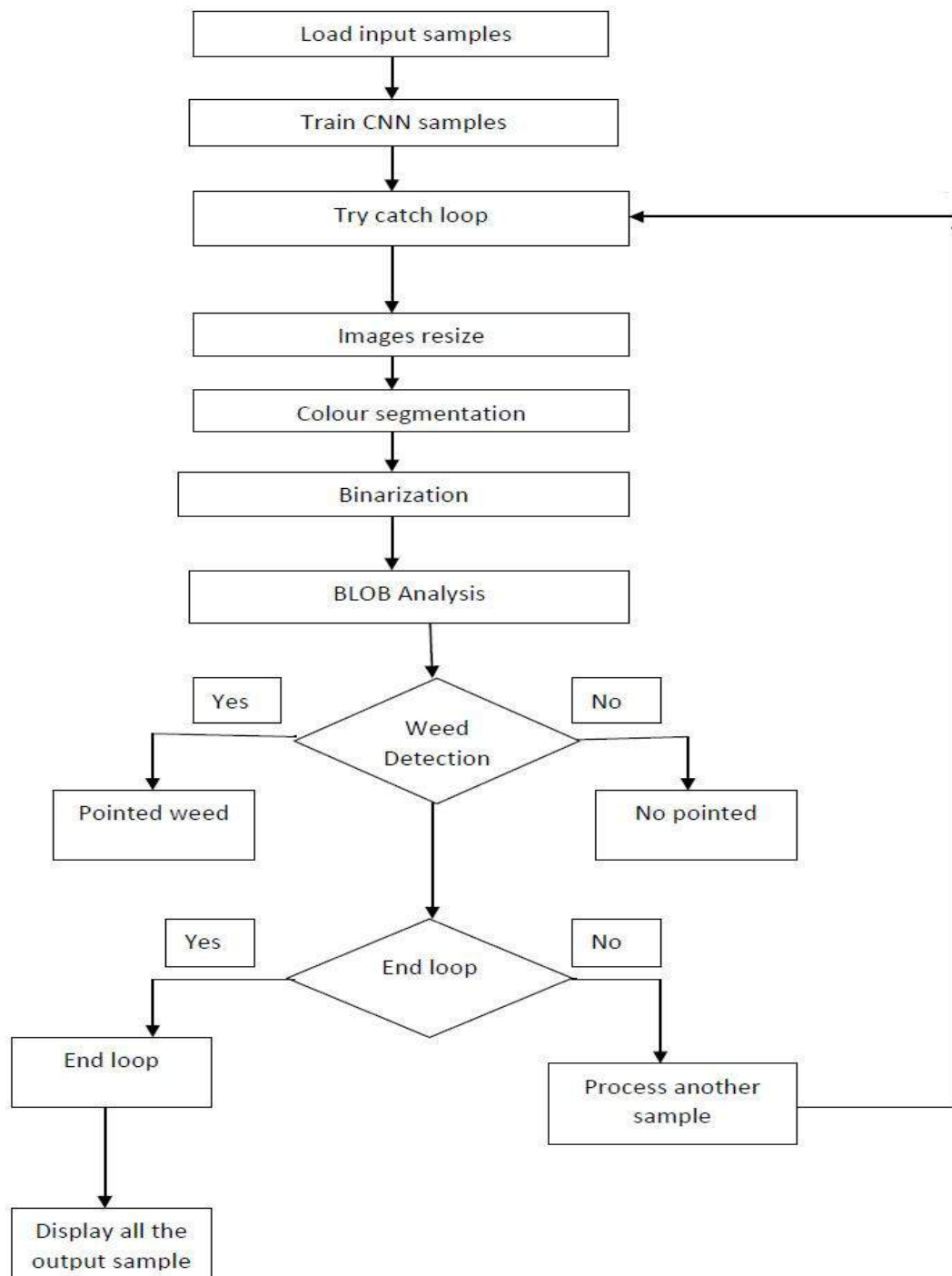


Fig: 1 Flow chart

Method of Data Collection

In this project, we attempt to build a classifier that can identify the weed based on the module we built. The data collection is the primary data which we take data manually by our self. The data collected has been check one by one before taking it as input data. There are 2 classes named as crop and crop weed will be classified and each of the class contains 123 images. From the 80% of images used for training and 20% of images used for validation and testing. Hence there are 99 images for training and 24 images for testing

RESULTS

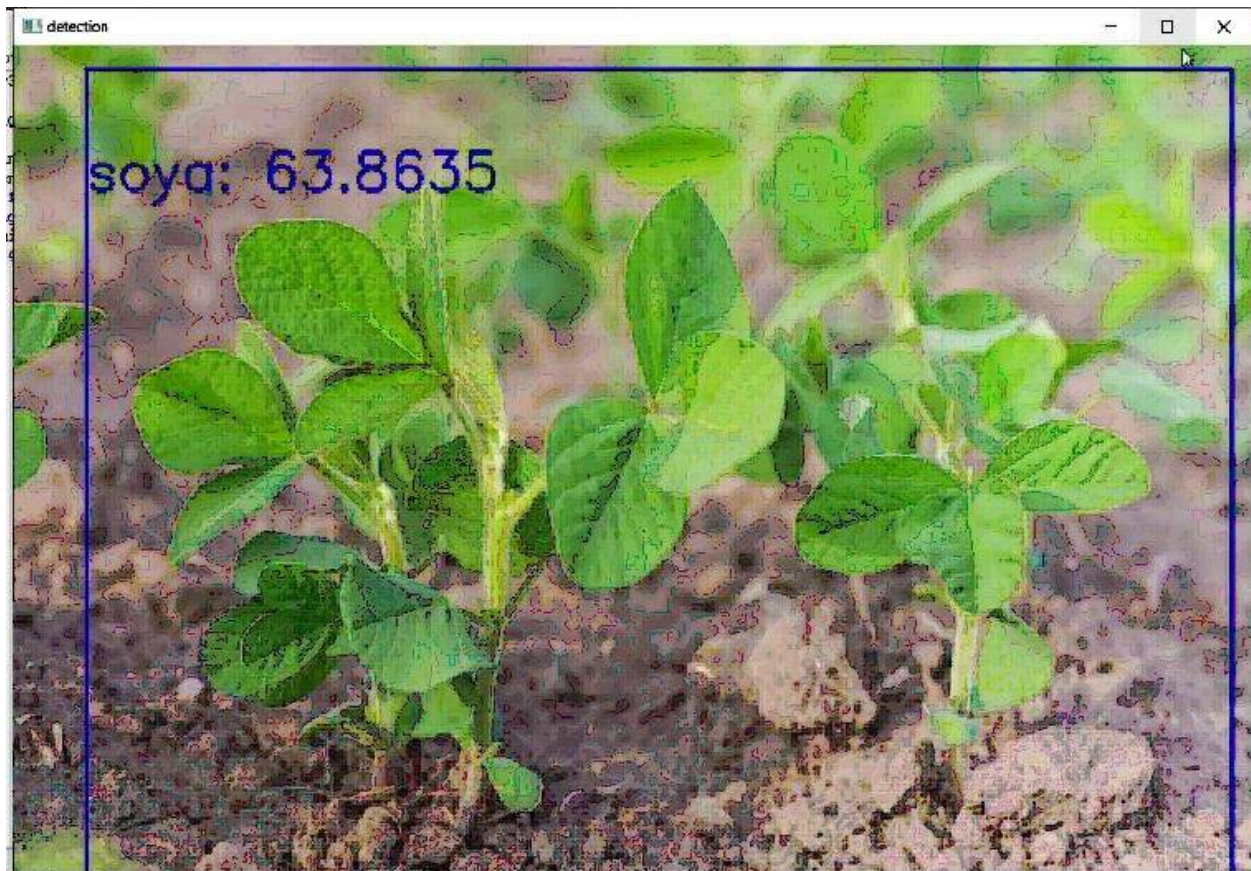


Fig: 2 Soya crop detection.

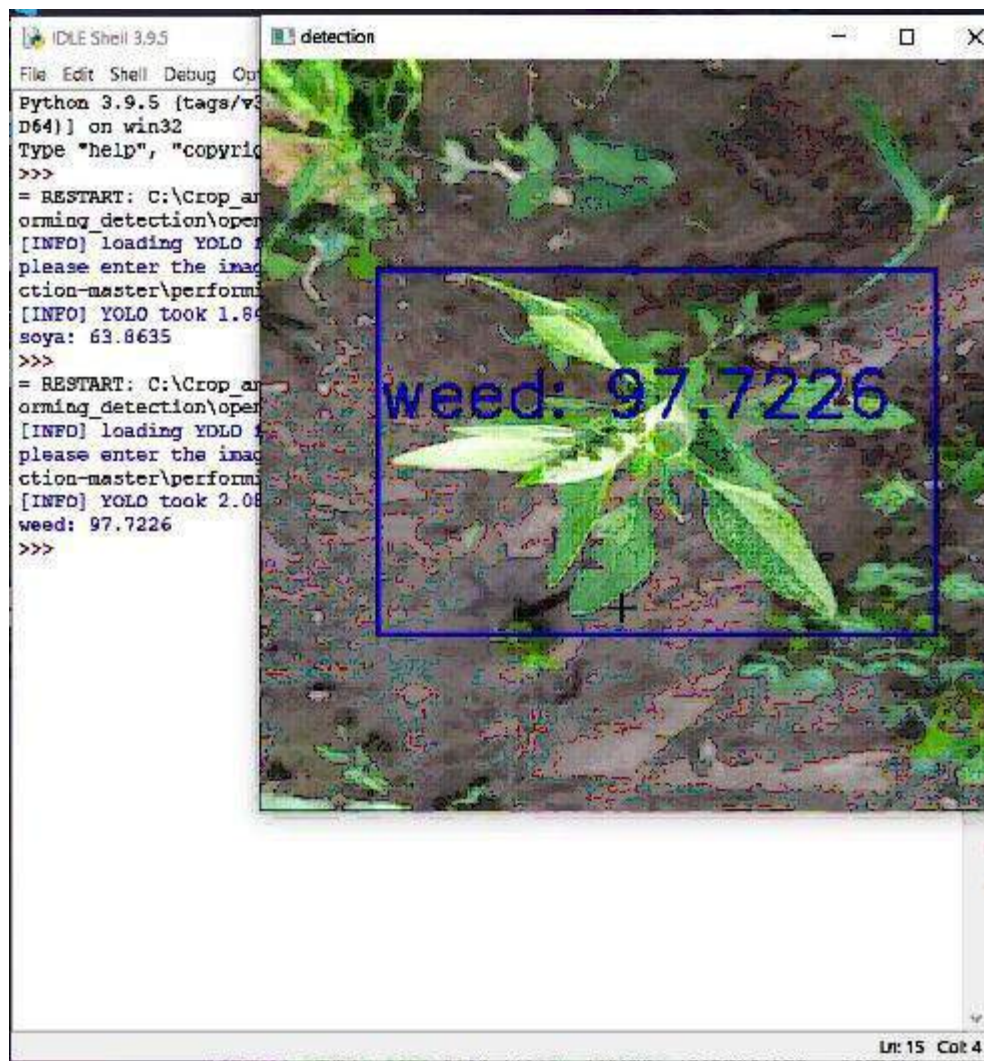


Fig. 3 Weed detection in soya crop.



Fig. 4 Percentage of soya and weed detection.

CONCLUSION AND FUTURE WORK

Although the detection was good enough but still there exist a room for the improvement in the result. Convolution Neural Network (CNN) can be applied in the future research for better result. In stage when the weed and Soya colour are same convolution network (CNN) can be produced much better result. The limitation in the above proposed research that was faced was sunlight light intensity issue because of the variation in the captured image was quite high. This can be overcome when the similar research was done in a very controlled environment. Better camera can be used in order to capture much better image with different sensor in order to overcome the problem that arise due to sunlight variation and shadows.

REFERENCES

- [1] K.Kantipudi , C.Lai , C.Hong. Min , Ron C. Chiang (2018). Weed Detection among Crops by Convolutional Neural Networks with Sliding Windows. Conference Paper.
- [2] Ana I. de Castro, Jorge Torres-Sanchez, Jose M. Pena, Francisco M.Jimenez-Benes, Ovidu Csillik and Francisca Lopez-Granados(2018). An Automatic Random Forest-OBIA Algorithm for Early Weed Mapping between and within Crop Rows Using UAV Imagery,21(17),pp.25-29.
- [3] S. J. Leghari, U. A. Leghari, G. M Laghari, M. Buriro, F. A. Soomro, “An overview on various weed control practises affecting crop yield”, Journal of Chemical, Biological and Physical Sciences, Vol.6, No. 1, pp. 59-69, 2015
- [4] International Survey of Herbicide Resistant Weeds, available at: <http://www.weedscience.org/default.aspx>
- [5] F. Ahmed, H. A. Al-Mamun, A. S. M. Hossain Bari, E. Hossain, P. Kwan, “Classification of crops and weeds from digital images: A support vector machine approach”, Crop Protection, Vol. 40, pp. 98-104, 2012
- [6] S. Mallick, Blob Detection Using OpenCV (Python, C++), available at: <https://www.learnopencv.com/blob-detection-using-opencv-python>
- [7] M. Weis, M. Sokefeld, “Precision crop protection-the challenge and use of heterogeneity”, In: Detection and Identification of Weeds, first ed. SpringerVerlag, pp. 119–134, 2010
- [8] T. Rumpf, C. Romer, M. Weis, M. Sokefeld, R. Gerhards, L. Plumer, “Sequential support vector machine classification for small-grain weed species discrimination with special regard to

Cirsium arvense and Galium aparine”, Computers and Electronics in Agriculture, Vol. 80, pp. 89-96, 20

- [9] P.Sakthi, P.Yuvarani(2018),Detection and Removal of Weed between Crops in Agricultural Field using Image Processing, 5(1), pp. 1-13.
- [10] P.Sakthi, P.Yuvarani (2018). Detection and Removal of Weed between Crops in Agricultural Field using Image Processing.Electronics and Instrumentation Engineering, 118(8), 201-206.

Analyzing Patient Health Information Based on IoT Sensors with AI

P. Chandra Prakash Reddy¹, – K. Prashanth², T. Sai Chandana³, J. Srikanth⁴

¹Assistant Professor, Geethanjali College of Engineering and Technology, Hyderabad India 2,3,4

Students, Geethanjali College of Engineering and Technology, Hyderabad India

ABSTRACT:

The IOT devices utilizes the several sensor devices that are able to collect a large volume of data in different domains which are processed by AI techniques to make the decision about the assistance problems. Among several applications, in our project, IOT with AI is used to examine the healthcare sectors to improve patient assistance and patient care in the future direction. An IOT sensor with AI is used to predict the exact patient details such as fitness tracker, medical reports, health activity, body mass, temperature, and other health care information which helps to choose the right assistance process. The patient information which is shared in the cloud environment is accessed and processed by applying the optimized machine learning techniques. It further examines the patient's details from the previous health information which helps to predict the exact patient health condition in the future direction. In this system, doctor and care takers can observe patient without exactly visiting the patient actually.

We proposed a nonstop checking and control instrument to screen the patient condition and store the patient information in sever utilizing Wi-Fi Module based remote correspondence. And furtherly they can upload medicines and medical reports on the web server which after can be accessed by the patient anywhere at anytime. It is very much easy process and convenient for both the doctors and patients. The efficiency of IOT sensor with an AI-based health assistance prediction process is developed by using the MATLAB tool. Monitoring and recording of various medical parameters of patient outside hospitals has become widespread phenomena. The reason behind this project is to design a system for monitoring the patient's body any time using internet connectivity. The function of this system is to measuring some biological parameter of the patient's body like Temperature, Heartbeat, Blood pressure, by using sensors and the sensors will sense the body temperature, heartbeat and blood pressure of the patient and sends the values to IOT Cloud platform through WIFI-Module. All information about the patient health will be stored on the cloud ,it enables the doctors to monitor patient's health, Where the doctor can contineously monitor the patient's condition on his smart phone. This system is based on client server application in which server stores data collected from client, role of client is to collect proper data from patient & transfer it to server. A remote health monitoring system using IoT is proposed where the authorized personal can access these data stored using any IoT platform and based on these values received, the diseases are diagnosed by the doctors from a distance. The

results showed that this project can effectively use WiFi technology to monitor patient health status. And the power consumption of Wi-Fi module can be reduced as much as possible

Key words: Embedded system, IoT, Patient monitoring system, Microcontroller.

INTRODUCTION

Internet of Things (IOT) and Artificial Intelligence (AI) plays a vital role in the upcoming years to improve the assistance systems. Now a days Internet of Things (IOT) is one of the effective and emerging technologies because it helps to interconnect computing devices and objects that can transfer the data from one place to another place. Most people thought that the diagnosis of diseases and patient assistant system consumed more amounts. Also, they thought that hospital services are not packet friendly which means, accessibility. Therefore, IOT sensor-related services were provided to the health care sectors for improving the people's hospitality in terms of ensuring accessibility. In addition, the IOT sensor-based disease diagnosis process enhanced the quality of treatment effectively. The main reason for utilizing IOT sensor devices in health devices was the patient workflow which was successfully maintained by using effective technologies and facilities. IoT sensor-based healthcare services. More ever, the IoT sensor helps to improve communication without requiring.

The utilized technologies increased data interoperability, data movement, information exchange, and machine-machine communication effectively. Due to the effective utilization of technologies and connectivity protocols, the patients' unnecessary visits were reduced, improving planning and allocations. Unlike the cloud storage, the IoT sensor device collected the patients' information and stored it until the physician retrieved it or the patient did the clinical analysis. In addition, the device itself had the data-driven analytic tool which generated the graph according to the deviations which improved the decision-making process with minimum errors. Once the gathered medical information had any threatening activities or characteristics, then, the on-time alert was provided via the medical device. This alarm related data was transmitted to the physician for making the real-time tracking system and sending the alert message to the linked devices. Based on the alert, the respective treatment was provided, and the decision was handled successfully for enhancing the people life span. According to the discussion, it clearly showed that the IoT sensor device effectively monitored the patient's activities, alerting, tracking, providing better treatment, and improved patient care completely. From the analysis, it clearly stated that the IoT sensor device completely used to monitor the patient in the remote activity. The remote-based activity ensured the patient treatment also provided the drugs based on the disease effectively. Based on the discussion, several smart devices such as hearable, ingestible sensors, drug storage.

LITERATURE SURVEY

According to the different author opinion, healthcare applications have enhanced using the internet of things (IoT) because it effectively collected the patients' information in real-time application. More ever, for attaining the remote monitoring process, the IoT sensor was very useful. It reduced the complication rate and enhanced the treatment procedure. Even though, the assistance rate should be further improved with minimum complexity and maximum accuracy. For attaining this, in this work, an optimized artificial intelligence technology with the internet of things is used. Based on the discussion, iterative golden section optimized deep belief neural network approach is used to examine the IoT sensor based collected patients' health information. The detailed study of the work is discussed in further chapters.

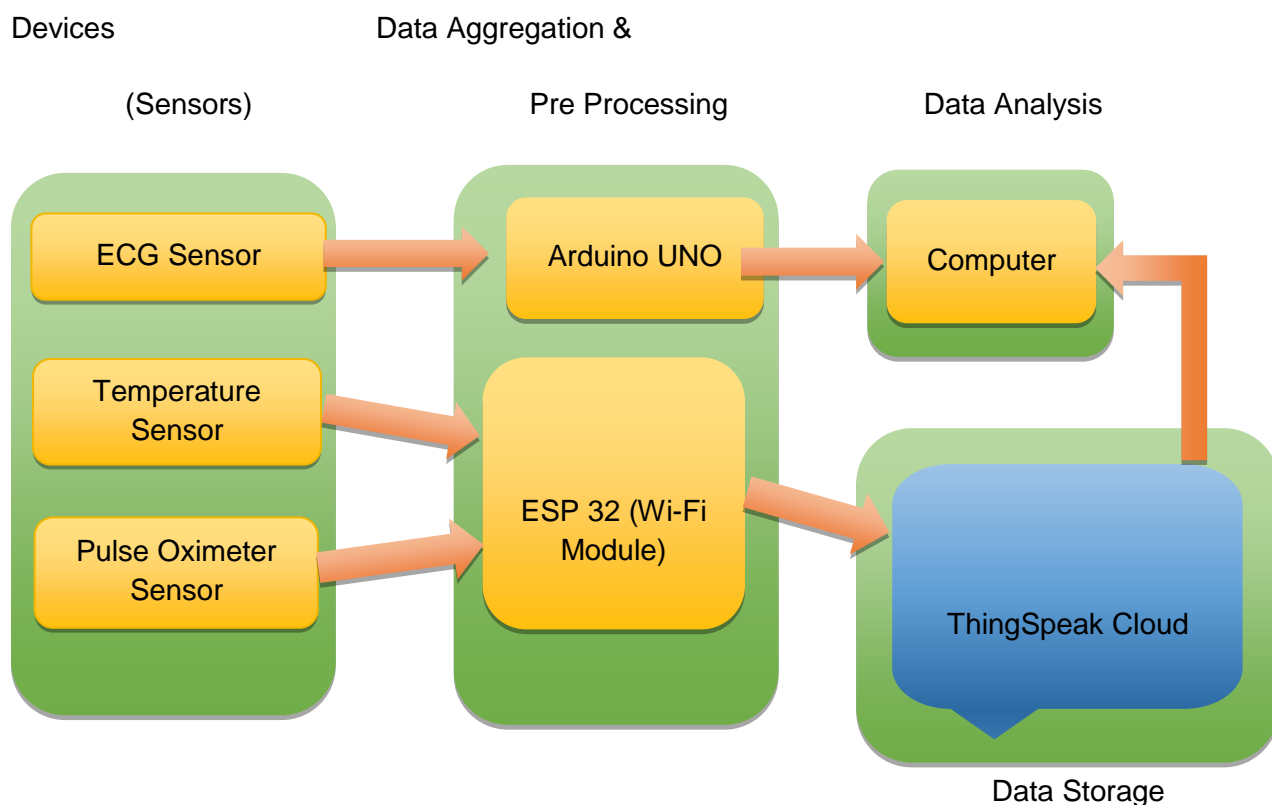
There are various vital parameters in this system. They are ECG, Heart Rate, Heart Rate, Pulse Oximetry. The Tele-medical System is the system which focuses on the system which focuses on the measurement and evaluation of these vital parameters. In android smartphones there are two different designers of a (Wireless) Body Networks, The Real Time System Features Several Capabilities. Data Acquisition in the (W) ban plus the use of the smartphone sensors, Data Transmission and Emergency Communication with first responders and clinical server. It is very important to save the Energy Efficient Sensors. This can be compensated. In the first ZigBee based approach, sensor nodes acquire physiological parameter perform signal processing and data analysis and transmit measurement value to the coordinator node. Sensors are connected via cable to an Embedded System in the second deign. In the both types of system, Bluetooth is used for transferring the data to an android based smartphone.

PROPOSED SYSTEM

As we are dealing with E-Health Care Monitoring System, our system design is based on the Wireless Sensor Networks (WSN) and Smart Devices. It is very important to have strong networks between doctor, patient, and care givers judges the condition of the patient. Sensors are used to monitor the patient surrounding as well as health, these sensors are medical and environmental sensors. Sensors are relayed to the prior devices through the transmitter and them to the end user. In this system, doctor and care takers can observe patient without exactly visiting the patient actually. We proposed a nonstop checking and control instrument to screen the patient condition and store the patient information in sever utilizing Wi-Fi Module based remote correspondence. And furtherly they can upload medicines and medical reports on the web server which after can be accessed by the patient anywhere at any time. It is very much easy process and convenient for both the doctors and patients. With the help of this data, doctors can understand and observe patient from private home i.e., patient to public health care Centre patient. This is the cost reducing technique. We have also defined the sets of add on services which include real time health advice and action (Retina) and parent monitoring.

This paper describes the implementation of a Telemedicine System for Patient Monitoring using Mobile Telephony, using this application any patient can be monitored with Rs232 interface. The system proved to be quick and reliable. Therefore, it represents an applicable solution to Telehomecare. Additionally, the high costs involving the conventional internment and the frequent problems in patient transporting do necessary a different way of providing good medical care. This system is based on client server application in which server stores data collected from client, role of client is to collect proper data from patient & transfer it to server. A remote health monitoring system using IoT is proposed where the authorized personal can access these data stored using any IoT platform and based on these values received, the diseases are diagnosed by the doctors from a distance.

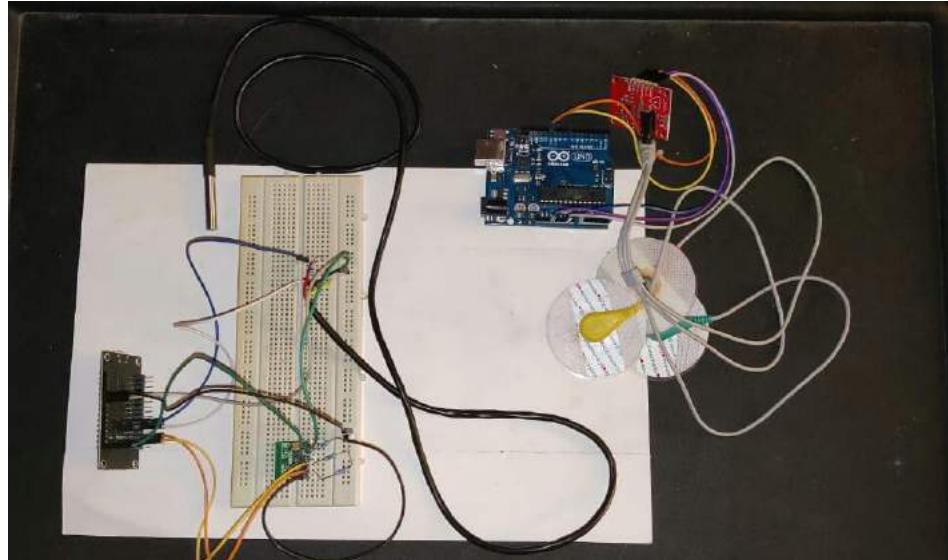
Block diagram



As we can see in the above block diagram, there are four blocks namely Devices (Sensors) block, Data Aggregation and Pre-Processing block, Data Storage block and Data Analysis block. In the first block we are having ECG Sensor, Temperature Sensor and the Pulse Oximeter Sensor. All these three sensors will be enabled and the data from ECG Sensor is given to Arduino UNO. The remaining two sensors' data is fed to ESP 32 (Wi-Fi Module). Next, we are writing the sensors data from ESP 32 to Thing Speak Cloud i.e., we are storing the data. Thereafter, the computer will read the data from Thing Speak Cloud and performs data analysis. Similarly, the computer will also read the ECG Sensor data from Arduino UNO and gives out the resultant ECG graph.

The reason that we are not giving the ECG Sensor data to Thing Speak because, we cannot get the ECG graph in online mode.

CIRCUIT DIAGRAM



COMPARE THE DATA WITH STANDARD HEALTH CONDITIONS

Next step is to compare the obtained results with the standard health conditions. The standard health conditions of a healthy human being are :-

- The normal core body temperature of a healthy, resting adult human being is stated to be at 98.6 degrees fahrenheit or 37.0 degrees celsius. Though the body temperature measured on an individual can vary, a healthy human body can maintain a fairly consistent body temperature that is around the mark of 37.0 degrees celsius.
- A normal resting rate for a healthy adult is between 60 and 100 beats per minute (bpm). Human heart rates vary enormously with age, general health and physical exertion.
- A normal ECG is the one that shows sinus rhythm. Sinus rhythm may look like a lot of little bumps, but each relays an important action in the heart. The typical frequency range of ECG signals of healthy human in BPM can range from 0.5-100 Hz, sometimes reaching up to 1khz

Pulse Rate	Body Temperature		
	Low	Normal	High
Low	Bradycardia & Hypothermia	Bradycardia	Bradycardia & Fever

Normal	Hypothermia	Healthy	Fever
High	Tachycardia & Hypothermia	Tachycardia	Tachycardia & Fever

Table Standard Health Conditions

APPLICATIONS

- ECG monitoring.
- Temperature monitoring.
- Pulse rate monitoring.

Other notable applications such as:

1. Glucose level monitoring.

2. Medication management.

3. Asthama monitoring.

4. Mood monitoring.

5. Wheelchair management.

6. Oxygen saturation monitoring.

7. Rehabilitation.

ADVANTAGES

- Simultaneous reporting and monitoring.
- Affordable price.
- End to End connectivity.
- Accurate data analysis.
- Remote medical assistance.
- Tracking system.
- Alert system.

- Improved decision-making process with minimum errors.
- Increased data interoperability.
- Effective machine to machine communication.

LIMITATIONS

- Accurate power supply should be given to pulse oximeter in order to avoid voltage fluctuations.

CONCLUSION

The system introduced smart healthcare to monitor the basic important signs of patients like heart rate, body temperature. The rate of success between the observed data and actual data is approximately greater than 95% for all cases of the developed healthcare system. The system is very useful in the case of infectious disease like a novel coronavirus (COVID-19) treatment. The developed system will improve the current healthcare system that may protect lots of lives from death. In our project, an IoT based health monitoring system was developed. These sensor values are then sent to a medical server using wireless communication. These data are then received in an authorized personal smart phone with IoT platform. With the values received the doctor then diagnose the disease and the state of health of the patient. The Internet of Things facilitates that the individual prosperity parameter data is secured inside the cloud, stays in the hospital and reduced for conventional routine examinations and most important that the health can be monitored and the disease can be diagnosed by the doctor at any instant. These sensor values then will be sent to a medical server using wireless communication. Thus, with the help of IOT sensors and AI, the patient assistance has been improved to a reasonable extent.

FUTURE SCOPE

IoT after getting the hold of many domains like Enterprises, Retails, Government, industrial, IoT is finally booming the healthcare domain also. Perhaps, no other sector has taken the great benefits of the Internet of Things than healthcare. Be it for doctors, researchers, patients or insurers, IoT in healthcare is actually a vibrant force. Doctors can now monitor patients' health and improvement continuously while patients, on the other hand, can connect with their doctors easily. Specialists and researchers got the chance to confer with one another across the globe about difficult health cases. Though technology cannot stop the population from aging or eradicating chronic diseases but it can at least make healthcare easier in a pocket. Hence, it is not wrong to say that Healthcare is one of the most exciting yet challenging verticals for IoT transformation while posing great future scope of IoT in Healthcare. With it, IoT app development is also gaining momentum in the healthcare domain. Before going any further, it will be wise to check out the stats for the IoT market trends to validate how the technology is

changing different domains. Once done with that, understanding how the technology is fueling healthcare will not be a task.

REFERENCES

1. Oliver and F. Flores-Mangas, “HealthGear: A real-time wearable system for monitoring and analyzing physiological signals,” Apr. 2020.
2. Cloud and IOT based disease prediction and diagnosis system for healthcare using Fuzzy neural classifier, 2020.
3. Valsalan P, Surendran P, IOT based breath sensor for microbacterium tuberculosis, Journal of Advanced Research in Dynamical and Control Systems, 2020.
4. S. Bhaskar, K.P. Sridhar and R. Kumar for based spearman rank correlation of cranial nerve palsy detection in MIOT environment, 2019.
5. Tae-Yoon Kim, Sungkwan Youm, Jai-Jin Jung, Eui-Jik Kim, “Multi-hop WBAN Construction for Healthcare IoT”, 2019 International Conference on Platform Technology and Service.
6. Rajendran T et al. “Recent Innovations in Soft Computing Applications”, Current Signal Transduction Therapy. Vol. 14, No. 2, pp. 129 – 130, 2019.
7. Senthil Kumar Mohan and Chandrashekar Thirumalai – “IOT platform for real time multichannel ECG monitoring and classification with Neural Networks”, IEEE Access, 2018.
8. Valsalan P, Manimegalai P, Analysis of area delay optimization of improved sparse channel adder, Pakistan Journal of Biotechnology, 2017.
9. Junaid Mohammed, Abhinav Thakral, Adrian Filip Ocneanu, Colin Jones, Chung-Horng Lung, Andy Adler, “Internet of Things: Remote Patient Monitoring Using Web Services and Cloud Computing”, 2017 IEEE International Conference on Internet of Things (iThings 2014), Green Computing and Communications (GreenCom2014), and Cyber-Physical-Social Computing (CPSCoM 2017).
10. Charalampos Doukas, Ilias Maglogiannis, “Bringing IoT and Cloud Computing towards Pervasive Healthcare”, 2016 Sixth International Conference on Innovative Mobile and Internet Services in Ubiquitous Computing.
11. Vandana Milind Rohokale, Neeli Rashmi Prasad, Ramjee Prasad, “A Cooperative Internet of Things (IoT) for Rural Healthcare Monitoring and Control”, 2014 Center for TeleIn Frastuktur, Aalborg University.

A Study of Deep Learning-Based Brain Tumour Segmentation Strategies for MRI Image

B. Ramu¹, Dr. Navjot Rathour²

ECE, PhD Scholar, Lovely Professional University Punjab, India

ECE, Professor, Lovely Professional University Punjab, India

Corresponding Author E-mail:ramu0604.ece@gcet.edu.in

ABSTRACT

The segregation of irregular tissues from normal brain tissues, such as brain tumour segmentation, is one of the most essential and fundamental activities of any brain tumour identification scheme. Interestingly, the tumor in tumor analysis domain has been effectively used in the principles of medical image processing to computerize the center steps, i.e. detection, segmentation and classification for a approximant brain tumor finding, particularly on Magnetic Resonance images. It is more invasive to study for its noninvasive properties for imaging. Identification or recognition systems assisted by computers are suitable complicated and are present an unbolt issue because of variations in tumor forms, areas, and size. Important study performance, mechanical brain tumor detection techniques based it's on previous completed works of various experts in biomedical image processing and flexible computing as well as classification and their combinations. Different methods are used to identify the brain tumor using images of Magnetic Resonance Image is analyzed in the article, along with robustness & problems found with every to notice different types of tumors in brain.

In the existing methods of classification/segmentation, detection be as well confer with heart on the merits and demerits of the approaches to biomedical imaging area in every mode the reason of the study provided at this point is to support the analyst to get the necessary quality of brain tumor type and identify different brain classification and techniques is which are very successful and for spotting brain tumor a choice is tumor brain diseases. The script covers the most applicable techniques, procedures, functioning system, preference, limitations, and possible MRI image tumor in brain detection snags. It is effort to recap the existing state of the art with admiration into various forms of tumors will assist researchers to pursue future directions.

Keywords: Segmentation, MRI, Deep Learning, CNN, ANN

I. INTRODUCTION

According to the World Health Organization's most recent figures, brain tumour disease is the most frequent form of cancer death worldwide. the advance diagnosis a mind tumor saves the patient from death and helps treat patients on time but this is not always accessible to people, Glioma can be considered the most dangerous tumors in the central nervous systems systems (CNS)is primary brain tumor. In present years the world health organization amend the edition 'LGG (Low grade glioma) and high grade glioma (HGG) glioblastomas will exhibit compassion propensities in 2016 adoptive the state of two forms of glioma tumours is LGG (Low grade glioma) and high grade glioma (HGG) glioblastomas.

A new tool is used for the field of biomedical engineering gives awareness about the various healthcare observations. A deep learning is a one of the part of AI system; it able of conduct advanced dimensional data and is capable in focused on the right features. Tumor it is a very complex disease: a multifaceted cell has more than hundred billion cells; each cell acquires mutation fully. Finding of tumor particles in experiment is easily done by using MRI or CT. Brain tumors can also be detected by MRI, however, deep learning techniques provide a better approach to do segmentation of the brain tumor images. Deep Learning models are roughly positive by in sequence managing and communication designs in biological nervous system. Classification plays a leading role in detection of brain tumor.

Neural network is creating a well-organized rule for classification. To achieve image medical data of neural network is trained to used the a convolution algorithm, for classification of an image Multilayer perception is proposed. In this review article, the brain images are categorized into two types: normal and abnormal. This article emphasizes the significance of categorization and characteristic selection approach for predict the head tumor. This classification is completed by machine learning technique acting are like support vector machine ANN, and Neural Deep network. It might be famous that more than one method can be practical to the segmentation of tumor.

The several samples images of a brain tumor are classified with deep learning algorithms, convolution deep neural network and multi-layer observation. Analysis imaging of tumor in brain it's to obtain the most major information, it help to medical identification of patient for good quality treatment, in imaging analysis errors come into view at feature extraction, image size and also display the enlargement to the brain tumor disease cells is unmanageable that type of disease is called as tumor. The tumor a variety of types and have more character these are cure with different type of therapy's' [in 2013, Guptha and Shringirishi]. MR image segmentation can be biological part of a person being in a body and such as blood vessel in the spine, heart, brain, , and knee and the segmentation is the procedure of removing reassuring detail from diagnostic photographs that are one-of-a-kind.

A key intend for segmentation is to split a image into uniform and no overlapping location of similar properties they are strength, Texture, color, and intensity that gives the segmentation results of on each image of label then recognize the area borders in uniform region and it is a set of bias field, contours noise, and unfair level cause are the

problems and a difficult job in the procedure for brain tumor images.

MRI image is the most important and trendy to get entire detailed of image of dissimilar parts of the brain and its very-known for study and detect irregular change in the tissues with a good contrast we compare previous modality name CT computer tomography The gaining parameter of MRI can be used to for various brain tissues to get dissimilar gray values. Generally the researches may use MRI images of brain segmentation of in medical therapeutic applications, the recent study it is unified in a tumour located in the brain in an exacting, this tumors appear as irregular tissue are found in only certain areas of the brain, according to the recent research.

A segmentation of the brain tumor has different methods are characterized on different ideology segmentation normal tissues in brain are exposed in below figure1. In the field of biomedical the MRI segmentation techniques mention below as.

- Physical Segmentation is a technique for separating people into groups based on their physical characteristics.
- Semi-automated segmentation
- Segmentation that is fully automated
- Mixture segmentation of image

In the first method is manual segmentation method refers the when an professional human operator label the picture and segmentation the restrictions which are perceptually applicable, these segmentation goal to shade and the area of the body structure tagging by hired hand, this done in the way it is part-by-part volumetrically images [in 2000 pham et al.], According to reports, the physical segmentation mechanism is extremely accurate.. These techniques are in used for tumor brain segmentation to sketch these limits structure to the concern in detects lesion with various labels, Physical segmentation, is to assess the results is a time taking process to the operator to find the results by within the cell or intera variability studied.

By beat these trouble in manual segmentation, superior methods are emerged as fully automatic and semiautomatic method. Mechanical segmentation refer to the development to part assign limits mechanically by a PC aid systems, the process of a semiautomatic segmentation as cutting the segmented borders The ROI (Region of Interest) is described by to the operator in this semi-automated segmentation. As an example, method as easy inter active objects removal we apply on image to gate output for a good border fit of the picture, a number of input factor to be given by human specialist in perceptive study of content to get a action reply from to the computing software, the main process is Initialization, feedback response and evaluation of semiautomatics sectionalization (Shi et al., 2011). Completely automated segmentation strategies provide better results than semi-automated approaches.

A full routine segmentation playing with no human function assist segmentation is to resolute In the complete automated segmentation procedure, the processor combines the previous information and artificial percept in the algorithms. Crossed segmentation is the compilation of any number of segmentation methods to show the improved result in terms of consistency and computational time.. Various classification method are thresholding edge base, region-based, classification methods modify models this type of method are classify into supervise and unverified methods, The supervised method are the representation to a classifier like SVM (support vector machine), ANN (artificial neural network), and Bayes classifier are examples of artificial neural networks. An unsupervised method are the representation of clustering algorithm like fuzzy clustering (FCM), k men's algorithm and Markova random field (MRF) algorithm, and atlas based segmentation. In the medical area is a visible increase in the volume of data and usual models cannot manage it efficiently there is a continue work The collection and processing of massive medical data are important aspects of medical image analysis.

Present years deep learning methods are very important key function in the medical image data analysis of using machine learning early tumor area its export to the radiologist, we use biopsy is gives to find weather the tissue is benign or malignant, not like the tumors start somewhere The biopsy of the brain tumour is not performed somewhere else in the body. get previous to the end of the brain operation is performed. The diagnosis get more accurately by using biopsy helps obtain high image quality of the complex brain tissue and to get an accurate characteristic and proof of a medical procedure and bias its tough build good clinical system tool segmentation for classification of brain tumor in MRI images. [1]

A new expertise is development for particularly in the medical industry, machine learning and artificial intelligence it's having had a positive effect. it provide very good support tool for medical department, as well as medical imagining. Different automated learning approach is applied to segmentation and classification to process MRI to support the radiologist's result, one of supervised technique to classify a tumor requires exact expertise to extract optimal features and selecting domain. [2]. In coming recent time unverified approach has get experts interest in not only for their outstanding performance but also the mechanically generate features increase in the amount of error Deep learning (DL) models have recently emerged is one of the very most effective techniques for imaging of biomedical study such as segmentation, reconstruction, Milica et al a new technique is projected for segmentation of brain tumor used three types of tumor CNN (convolutional neural network) architecture.

This one is based on a small developed network its already used in pretrained network is tested using MRI T1 weighted images. In the models overall performance has evaluated using current four methods: between two combined database and two tenfold cross support methods, total ability of the model has tested the tenfold cross validation is gives best values has agreed The consistency of record-by-record cross validation with a larger sample has 96.56%. Gliomas high grade (HGG) and Low-Grade Gliomas (LGG) are two types of gliomas. (LGG), here Low glioma is slowly-growing tumour, and High glioma grows quickly, which explains why HGG is a deadly bug. According to the

central nervous system (CNS) a current poll of the Canadian people from 2009–2013 people diagnosed with HGG and aged 44-20 years has contain a 19% continued existence rate with therapy after 14 months analysis of diagnosis. Fig1 gives the sharing of survival rates between various types of brain tumors.

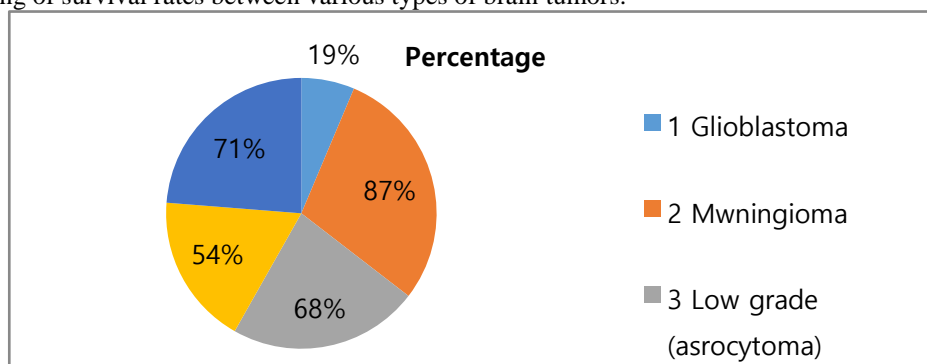


Figure1: The above pie chart is for patients aged 20-44 and with their survival rates

The connectivity pattern between neurons in convolucional networks is inspired by biological processes [3] as it resembles the organizing of an animal image cortex. The Artificial Network (ANN) was first used to analyses data from digital images, but it needed a domain would have to be a specific. Experts or scholars should physically pick and remove features from digital images until providing the data to ANN.

CNN came to the save through streamlining difficult task of selecting the features. CNN it is the most outstanding kind of the ANN encouraged by natural image detection events [4]. In the field of image processing, CNN does have a extra of applications pattern recognition and classification [5]. CNN's architecture was revealed in the late 1980s. LeCun improved CNN in the late 1990s, but the ConvNet architecture implemented in the twenty-In comparison to traditional computer vision (CV) processes, the 21st century has taken CNNs to a new extreme, with a fault rate of error 15.3 percent. CNN has a major influence on medical imaging as well as a variety of other fields such as artificial intelligence, machine vision, and digital image processing. Even though a large number of deep learning algorithms have been introduced in the past decades, CNN is of the majority trendy method used for image analysis because of the layered architecture CNN is a cable news network., like ANN, and a news outlet.CNN, unlike ANN, uses adaptive method to learn provides advanced of features on through a back propagation. Furthermore, different CNN, ANN does not have full linked of neurons for a all layers; with last layer will be the only fully connected layer. The building blocks of CNN are first Convolution layers, 2nd one is pooling layers, and last one is completely connected layers the building blocks in CNN [7]. Here the first layer convolution layer is responsible of extracting features. Traditionally, this layer is in control of the convolution mechanism a activation and function, which separates it from ANN.

II. LITERATURE REVIEW

In the previous few years, fellow researchers had place a lot of work in developing convolucional neural network a number of articles gives on studying the description of machine learning algorithms [8], table 1 trying to give explanation the multilayered network methodology used back propagation and update weights, a comprehensive analysis of relevant literature is presented, together with the methodology. The results, and future processes and directions of the CNN and other neural networks, and also use in Algorithms for machine learning and deep learning is briefly discussed. Their research paved in image segmentation is the way future research. It's been recognized that obtaining an boundary is a essential element of successful segmentation [9], Regular segmentation, and many scientists using by edge detection to find the best regions in an image that is a usually defined as segmentation the of image into a needed separation. Edge-based segmentation is introduced to Canny and his colleagues, which has used best smooth filter to keep the edges as performing image segmentation.

Here an effort to track the achievement of he performed a pilot study. Optimizations have been used to grip the spatially sparse components of a handwriting recognition segmentation and algorithm the parts have been used a picture to be used as a layer input in CNN algorithms. AM. Hasan et al [10] suggested a deep Siamese convolution neural network-based Alzheimer's disease treatment strategy. stage classification that yielded promising results in terms classification. Images of a brain could be used to differentiate among healthy adults those who have a disease. Reference introduced a thresholding technique that has since become a popular segmentation technique.

They recommended the aforementioned limitation by creating system for Optimization techniques. Integrated multidisciplinary systems' design and stability, their proposed concept is based The gradient knowledge strategy (KG) for chronological order is based on the Gibbs estimation approach and produces the major predicted one-time improvement in the design process [11]. This process requires by selecting a threshold value, the white and grey scale values are clean or manipulated. Among the most well-known threshold strategies are the Maximum entropy method, Otsus method, and k-means clustering The selected threshold value serves as a dividing line between input values above and below it are finally displayed. In present era, thresholding techniques are widely used.

In a recent study, researchers divided an image into computed tomography (CT), magnetic resonance imaging

(MRI), imaging, and (PET) positron emission tomography (PET), the Convolutional Recurrent Neural Network (CRNN) was introduced. It is a mixture of RNN and CNN. The two main key features in CRNN are: the feed forward layer supplies the output and the recurrent layer introduces the derived functionality. The performance has improved as a result of improved back propagation.

A layer-based DL approach was proposed in [12] to identify various brain tumour forms and grades using a CNN.

Brain tumours are divided employing Transfer learning and fine tuning focused on deep convolutional neural networks [13]. A research recently summarized the CNN apparatus (layers, ReLU, dropout, reaction, and pooling) and its operating mechanism; this study is an assessment of scale invariant function transformations (SIFT) in inclusion. They were using a data set of over one million images with over a 1000 category. They used a 50,000-image training set and a 50,000-image testing set to train and validate their method, and they used a technology that decreased error rates about 2%. Furthermore, when researchers were hoping to build a supervised learning-based Support Vector Machine (SVM), discriminative classifiers come to the rescue in the case of hyper planes. Using a brain atlas and manual intervention, a new analysis used Least Square Support Vector Machine to distinguish between White Matter (WM) and Grey Matter (GM) areas (LS-SVM) [14]. Later, researchers have begun to exploit the multilayered combined multidimensional methodology.

The below figure gives the whole image of brain tumor different types



Figure 2: Types of Brain tumors

The concept and design of the proposed model for MRI image segmentation/classification are seen in the diagram below

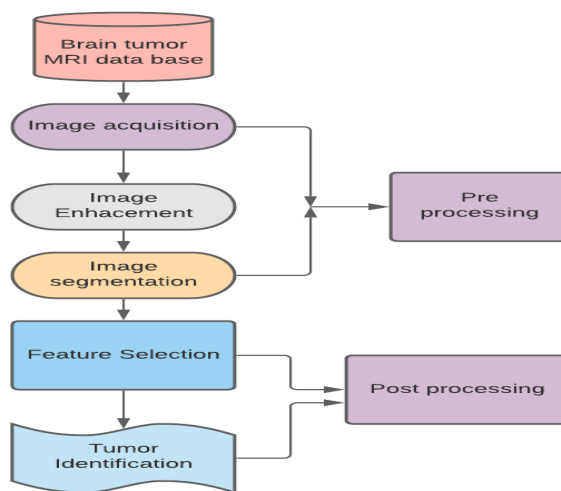


Figure 3: Flow Chart of Basic Method of the Brain Tumor Identification/Segmentation

Preprocessing

It is important in the medical profession to obtain specific photographs in order to make correct diagnoses. The origins of artifact acquisition, such as MRI, PET, and CT, have an effect on the excellence of the medical images. In the actual images of an MRI scan, there might be a number of unnecessary and insignificant bits. Rician noise has an effect

on MRI. Rician noise is signal based and difficult to eliminate. To maintain the initial image properties, image preprocessing technique such as scanning, contrast enhancement, and skull stripping is used.

Segmentation

Regions of Interest (ROI) are extracted from digital images using segmentation. It is important to tell between the tumour areas from to the brain MRI. Different supervised and unsupervised approaches for segmentation exist, such as thresholding, soft computation, atlas-based, clustering, neural networks, and so on. Adaptive, national, Otsu's, and histogram-based thresholding approaches are all examples of thresholding. Clustering without supervision-means and Fuzzy C means are examples of strategies. It effectively segments of Gray Matter (GM), and White Matter (WM), Cerebrospinal Fluid (CSF) MRI images in the brain (CSF). Segmentation is also done using bio-inspired algorithms including Particle Swarm Optimization (PSO) and a Genetic Algorithm (GA). CNN, Mask-RNN, and other deep learning architectures Unet have exposed to get better segmentation accuracy over traditional methods.

A image of digital image, such as an MRI image, can be represented as a two-dimensional function, $x(w, z)$, with the spatial coordinates x and y and the value of x at any given point. The image's intensity or grey level at that stage is (w, z) . A pixel in a picture is a dot symbol a pixel is a picture element. $M \times N$ matrix, A is yet another name for the function x , while M the digits M and N represent the number of rows and columns, respectively, respectively. Image segmentation is the process of separating a image digital into several disjoint segments, with its own set of properties, in computer vision. It's also used to locate objects in images and also limits. This is achieving by assigning values to each pixel. (w, z) , a label in an picture a basis on certain character or computed attributes, such like as colour, texture or intensity.

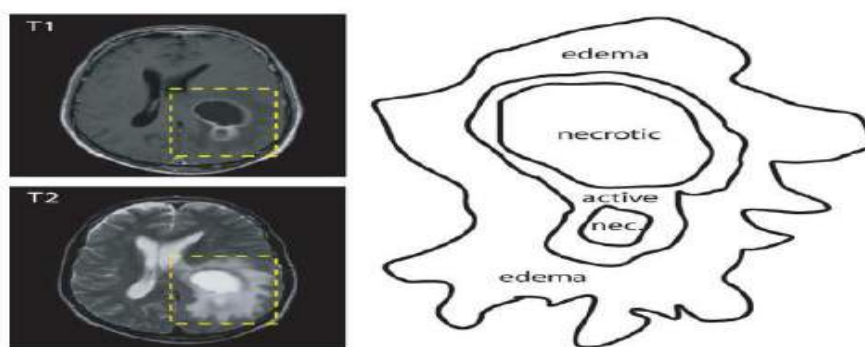


Figure4: Example for brain cancer labeled.

Above shown Figure4 is the aim classification of brain tumor to determine the position and extend of tumour region.

- Tumour tissue that is actively growing;
- Tissue which is necrotic (dead);
- The absence of edoema (tumor nearby swelling)

This is achieved by comparing usual areas to abnormal tissues. Because they infiltrate surrounding tissues, some tumours, such as glioblastomas, are difficult of tell between from normal tissues. Image modalities with variation are frequently used as a solution. In figure 4 In teach, MRI modalities (T1 with contrast and T2) are used to precisely identify tumour areas.

Feature Extraction

MRI features such as form texture, wavelet, and Gabor are extracted during feature extraction. The Gray-Level-Co-occurrence Matrix (GLCM) of second order is used by the majority of researchers, arithmetical approach for shaping texture features such as energy, correlation, and contrast, among others. Discrete Wavelet Transform is used to remove wavelet characteristics (DWT). It is added to the raw image, and the approximation coefficients are extracted and chosen as the function vector. [15] Formalized paraphrase it have been observed that handcrafted characteristics, as well as automated features produced by deep learning techniques' such as CNN, ResNet, and Capsule network, perform well. Formalized paraphrase PCA and GA are used to decrease the number of features. [16]

Classification

Brain tumours are categorizing into two types of tumors Benign and Malignant tumours. Glioma, Meningioma, and Pituitary tumours are the three forms of malignant tumours. Glioma is classified into four categories by the World Health Organization, as seen in Fig5.

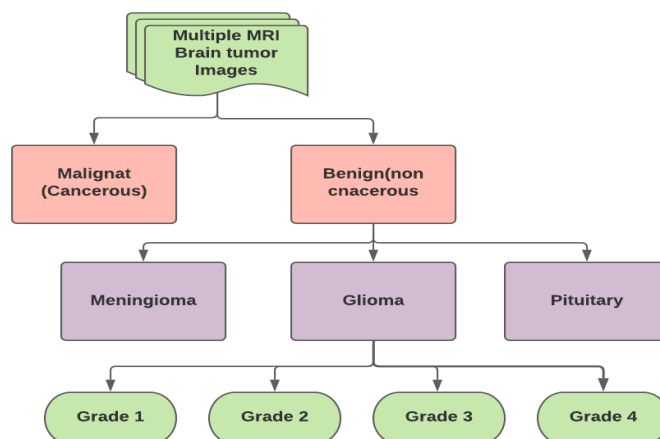


Figure 5: Types of Brain Tumors

Deep Learning

An input layer, an output layer, hidden layers, and hidden layers are all present in neural networks, hyper parameters, are widely used for deep learning. It is a process of supervised classification in which the kernel convolved around the input image to generate feature maps. Automatic segmentation and function extraction may be supported by DL. Aside from its success in medical disease diagnosis, it has some drawbacks, such as the need to create complex algorithms, tune hyper parameters, require a huge volume of data for testing, and need more training time and expense.

According to a recent analysis, comprehensive To solve the issue of big data supply, data augmentation techniques such as rotation, cropping, scaling, and transforming are used. A pre-trained neural network is used in transfer learning approaches to retrieve similar characteristics is applied to an application-specific dataset. For cancer prediction, existing transfer learning models such as VGG19, LetNet, GoogleNet, ResNet, and AlexNet are used. Deep learning, mainly the convolutional neural network-based system, has achieved the most advanced output for medical image semantic segmentation [17].

A two-pathway CNN model with a local image block as feedback was suggested by Havaei et al. To figure out what each pixel's mark will be, response used in a sliding window fashion. ResNet made use of the efficient bottleneck structure for impressive results.

Ronneberger et al. proposed the first and most widely used medical image semantic segmentation tool, known as "U-Net." Since then, U-Net has grown in popularity and is now widely used in medical imaging and computational pathology. Xu et al. suggested a new deep network known as LSTM multi-modal UNet, which combines multi-model UNet and convolution LSTM. Multi-modal UNet employs high density encoders and decoders to fully leverage multi-modal data, whereas convolution LSTM employs sequential information within neighboring slices. Dong et al. used a deep atlas complex with a knowledge accuracy restriction to segment the 3D left ventricle in order to deal with high dimensional data and a lack of annotation data. Heinrich et al. created OBELISK-Net, novel convolutional architecture for segmenting 3D multi-organ images. Li et al. Used a new adversarial model based on a multi-stage learning move toward to segmentation various three-dimensional spinal structure from multi-modal MRI images. Their findings further indicate that deep learning has exceptional success in resolving 3D medical image segmentation and has become an important part of medical image processing, being the first option for a number of of medical image segmentation application. Furthermore, Brain tumour segmentation methods focused on deep learning have shown strong segmentation outcomes. The following is the a review of segmentation-based treatments to brain tumours Learning at a deeper level approaches for brain tumour segmentation have recently achieved state-of-the-art segmentation precision. Ping Liu et al. demonstrated a The Deep Supervised 3D Squeeze-excitation V-Net (DSSE-V-Net) will segment brain tumours automatically from multi-modal MRI images. On the 2017 BraTS,

Kamnitsas et al. obtained excellent results and suggested EMMA, a rigorous segmentation incorporating multiple models that used an adaptive architecture with several individual training models. EMMA, in particular, merged DeepMedic [20] and U-Net models and incorporated their segmentation predictions. In 2018, Myronenko took first place in BraTS18 with a 3D encoder-decoder concept built on ResNet. To extract multi-scale background details, Zhou et al. ensembled several different networks and used shared backbone weights. For the actual autism spectrum disorder dataset, the authors used the k-nearest neighbour classifier in. They considered the issue of MRI data's huge volume and sophistication. They suggested using the adaptive independent subspace analysis (AISA) approach to detect significant electroencephalogram behaviour in MRI scan data for this purpose. Using the AISA system, they achieved 94.7 percent accuracy. Khan et al. developed an automatic multi-modal classification system for brain tumour type classification using deep learning. They first used linear contrast stretching with edge-based histogram equalisation and the discrete cosine transforms (DCT). They then used transfer learning to perform deep learning function extraction.

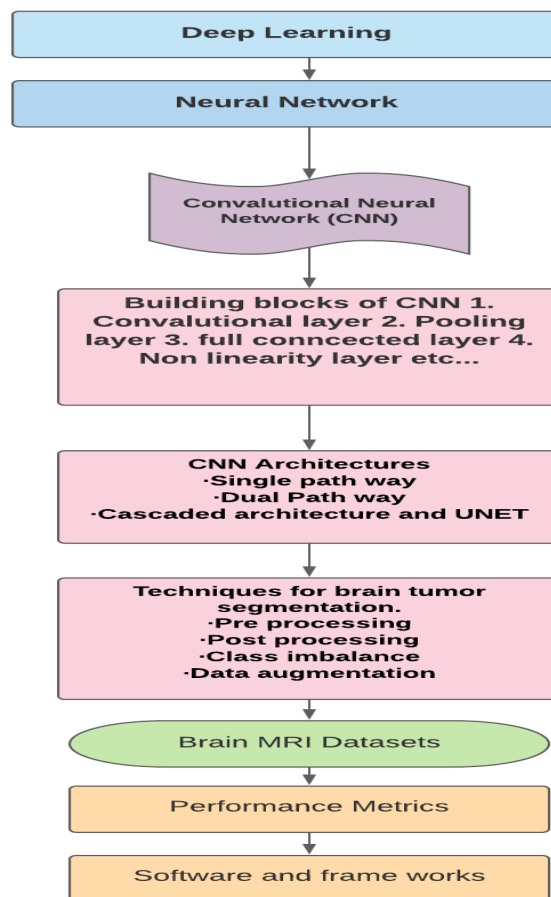


Figure 6: Steps and Architectures is a deep learning algorithm for brain tumour segmentation.

Chen et al created a high-efficiency 3D CNN for real-time dense volumetric segmentation, based on the multi-fiber unit for enabling knowledge flow between classes. Previous research has explicitly shown the anatomical regions of the brain can be classified using deep learning algorithms. Nonetheless, because of the use of multi-layer 3D convolutions, these 3D CNN architectures have a high computing overhead. As a result of shortcomings in some of the previous models, we were compelled to suggest a new system. We suggest a novel network for resolving the issue of brain tumor segmentation and employ multiple techniques for reducing network parameters order to allow efficient use of multi-modalities and depth knowledge.

III. BRAIN TUMOUR PREDICTION USED CUTTING-EDGE MACHINE LEARNING AND DEEP LEARNING ALGORITHMS

Deep learn has been described by researchers as an increasing machine learning methods are a subset of a machine learning methods. Deep neural networks can study gradable character from a input images instead of using pre-defined hand-crafted features. A rugged likeness of segmentation brain tumour algorithms based on standard and deep learning. Deep learning strategies require a large amount of training data to be effective prevent over-fitting and large computational power in order to go faster the training procedure. Deep learning approaches have attained state-of-the-art efficiency in a variety of domains, including target recognition and natural language processing, when joint with efficient strategies for weight initialization and optimization. A large amount of training data is needed for deep learning approaches. Deep learning has recently been applied to medical image recognition tasks such as chest x-ray detection by a number of researchers and breast image analysis. Recurrent and convolutional neural networks are two well-known deep learning approaches.

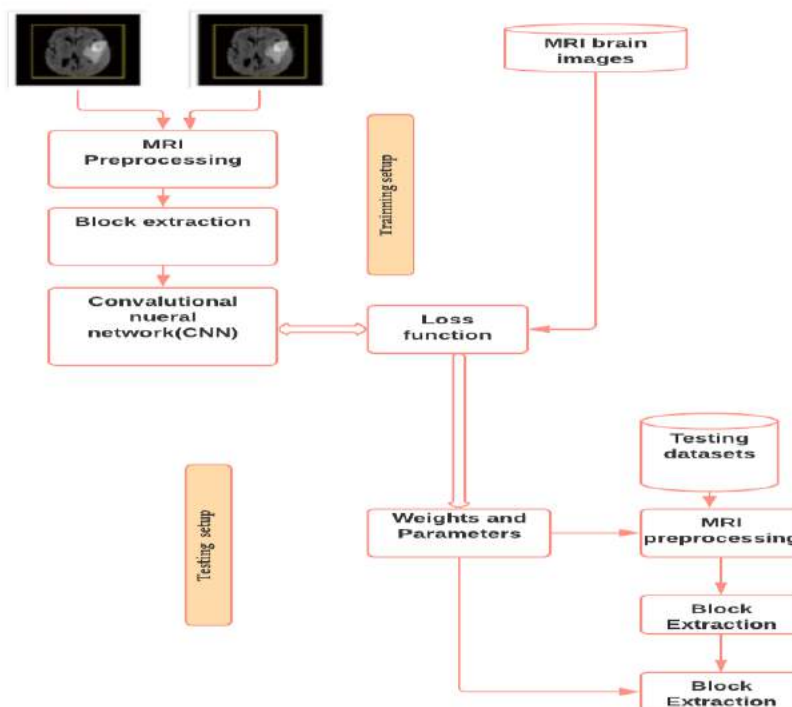


Figure 7: Deep CNN Flow chart

The literature contains a number of machine learning techniques for brain tumour segmentation and detection using MRI. Hasan et al. suggested a method for classifying MRI brain scans with deep and handcrafted image features. For statistical feature extraction, pre-processed MRI is added to a transformed GLCM. CNN performs automatic feature extraction. SVM classifier with a600 axial MRI scans, 10 fold cross-validation revealed 99.30 percent accuracy. When compared to other transfer learning networks such as AlexNet and GoogleNet, the proposed approach worked well by integrating MGLCM and CNN functions. A Naive Bayes-based brain tumour detection method employs maximum entropy segmentation based on thresholds.

The device is evaluated on the REMBRANDT dataset, which comprises 114 MRI. The suggested procedure that has advantage of being able to locate a tumour in any region in the brain, including the temporal lobe. Introduces a novel method for brain tumour detection focused on full blurry entropy segmentation and CNN. On MRI, Single Image Super Resolution is used to improve resolution. On the BRATS2018 and RIDER datasets, SVM classification reaches 98.3 percent and 97.9 percent accuracy, respectively. With the combination of handcrafted and deep features, the proposed concept has shown positive results. On the CE-MRI dataset, pre-trained GoogleNet for deep feature extraction is evaluated for 3 type classification into Glioma, Meningioma, and Pituitary tumours using KNN and SVM classifiers with accuracy of 97.8 percent and 98 percent accordingly. The accuracy of a brain tumour classification technique based on a multinomial logistic regression The BRATS 2017 dataset was used to validate the model, which included 48 images. However, the system's accuracy should be validated on larger datasets.

Keerthana et al. propose an intelligent method for early diagnosis of brain tumours. Noise reduction and skull stripping are performed first, followed by threshold foundation. SVM is given GLCM texture features to classify tumours into three categories: regular, benign, and malignant. With the GA-SVM classifier, the device performs well. GA is used for tumour segmentation in an efficient optimization strategy for brain tumour classification. SVM is given GLCM texture functionality with a precision of 91.23 percent.

Polly et al. planned a method for classifying HGG and LGG brain tumours using k-means segmentation. PCA is used to choose 10 related features from a collection of wavelet features. SVM is used to differentiate among regular and irregular videos. SVM classifier is used to identify HGG and LGG tumours in pathological images once more. The proposed method has 99 percent accuracy for 440 pictures, but it needs to be tested for larger images.

IV. DISCREPANCY FROM EARLIER SURVEYS

In current years an amount of prominent Table I lists medical image processing polls, as well as recent associated studies and summary papers. An examination of early state-of-the-art technologies Prior to 2013, there was no such thing as state-of-the-art. Brain tumour segmentation approaches were presented in, where the majority of the methodologies proposed prior to 2013 used traditional machine learning techniques, with handcrafted components, such as clustering and region-growing methods In 2014, Liu et. al. published on a review for MRI-based brain tumour classification. There is no deep learning approach used in this survey. A survey published to summaries deep learning-based medical image processing methods. This survey covers large research on medical image processing as well as other in-depth studies. Strategies for segmenting of brain tumors based on machine learning. Bernal et al.

available the results of a revision on the application of deep convolutional neural networks to the retrieval of brain images The use of deep learning convolutional neural networks, recurrent networks, and deep generative models, for example, were not included in this survey.

Akkus et. al. published a survey of deep learning methods for segmentation on brain MRI images. The approaches discussed in are largely focused on convolutional neural networks, with no description of other deep learning methods. They have failed to address critical issues such as datasets and data collected before and after A research on deep learning in health-care was recently published by Esteva et al. This analysis compiled findings on how deep learning in computer vision, natural language processing, and reinforcement learning can be used to improve performance, simplified approaches facilitate healthcare application. A new survey on semantic and object detection and segmentation was conducted in, giving additional implication on object finding and semantic segmentation.

Table 1: Brief explanation on previous published DCNN-based classifiers and the presentation

Task and year	Tumor type	Image type	Model name	Model description	software	cases	Performance
Classification 2020	- Glioma - Meningioma - Pituitary - Glioblastoma	MRI	SixDCNN Architecture	A possible study of Deep learning techniques used to categorise multigrade brain tumours.	-CAFFE -NVIDIADI GITS	-121 -306 4 -49 -274	VGGNet received precision of 0.93 on multi-grade brain tumours and precision of 0.94 on brain tumour public results.
	- Astrocytoma - Mixed-glioma - Oligodendroglioma - Glioblastoma	H&EHISTOLOGY	DeepSurvNet	The classification of brain cancer patients' survival rates using a deep convolutional neural network	- ML Python - ML TensorFlow - ML Keras	400 9	0.99 precision 0.80 precision
	- GBM - LGG - Gliomas(Grade II to IV)	H&EHistology	GAN-based ResNet50*	Gliomas' IDHstatus forecast by using the GAN model for data growth and Resnet50 as a prognostic model	- Python software - TensorFlow software	200 66	accurateness:0.88 precision:0.93
	- GLIOMA - MENINGIOMA - PITUITARY	MR (T1 WEIGHTED CONTRAST-ENHANCED)	18 DCNN layer*	categorization by using 18 layer DCNN-based replication on MR images Meningioma, glioma, and pituitary tumors	NA	3064	0.99 precision 0.98 Sensitivity

Classification 2020	- GLIOMA - MENINGIOMA - PITUITARY	MRI (t1 WeightedContrast-Enhanced)	22 DCNN layers*	categorization based on MRI images using a 22-layer DCNN-based replica	R2018a MATLAB	3064	0.96 precision
	LGC HGC	T2 weighted MR	FLSCBN	normal vs abnormal categorization of used by a DCNN five layers based model on MRI image	Software Python Software Tensorflow Software Keras	4500 281	0.89 precision 0.3 FA 0.7: MA
	Glioma	MRI	AlexNet, linear SVM	tumor texture features a mixed DCNN architecture combining and Pert mutations using age radiomic features	Pytorch	2035 2000	precision 1. 0.95 precision 2. 0.99
	Glioma Meningioma Pituitary	MR T1 weighted	GResNet	Resnet34-based model is Using a of global Average pooling and an MR-based adjusted loss feature	PYTORCH	3064	0.95 precision
	Meningioma Metastasis Glioma is a type of cancer that affects the brain. Astrocytoma is a type of cancer that affects the cells	T1,T2,FLAIR for MR images	MDCNN	Metastasis Meningioma Glioma and Astrocytoma tumors	NA	320	0.96 Accuracy
GBM LGG	H&E HISTOLOGY	CNN Deep NETWORK	Based on H&E histological images, DCNN was used.	Software Python Tensorflow	220	precision. 90	
Classification 2020	Glioma Meningioma Pituitary	MR T1 weighted	KECNN	using a mixed approach of DCCN and extreme learning based on MR images	NA	3065	correctness. 0.93

Glioma Meningioma Pituitary	MR I T1 weighted	CapsNet	Using developed a classification system for meningioma and glioma tumours. CapsNet is a collaborative effort between CapsNet	NA	3064	Accuracy. 0.86
Glioma Meningioma Pituitary	MR T1 weighted(W CE)	CapsNet	MR images based on the CapsNet architecture were used to classify meningioma and glioma tumours.	Python Software keras	3064	precision. 0.91
Tumor (N/A) Non tumor(Normal)	MRI	Trained Pre DCCN	Categorization of brain tumours vs. non-tumors using a pre-trained DCNN based on MR images	python	NA	precision. 0.97

Frame work and software

To simplify the deep learning workflow, developers and engineers have often focused on free-source software platform, this concept creation to testing to manufacture deployments. This separation gives some of the common frameworks used in machine learning the articles that were analysed.

Theano is a free source python platform designed for quick calculation of comprehensive dataflow arithmetical terms that can be compile and execute on both CPUs and GPUs. Furthermore, this method has been used by science community to perform machine learning of research however it's not just mechanical. It's not a parser for arithmetical expressions written in NumPy-like syntax, rather than a learning by framework. Many clever software packages have been built on top of Theano, such as Pylearn2, Keras software, bricks, and a Lasagne, to take advantage of its ability as a strong arithmetic source of control. A library Pylearn2 is machine learning method developed on top of the Theano platform that is free and open-source. It gained attention after winning a transfer learning competition and applying numerous cutting-edge computer idea of benchmark, the collection emphasises consistency and extensibility, allow researcher to easily apply random models of machine learning. unluckily, there is no longer involved creator for the library, and it has since slipped behind other successfully managed frameworks, such as Keras.

Caffe is an C++ and deeplearning platform has be originally designed for a computer idea application but has since expanded to other fields such as astronomy, robotics, and a neuroscience It includes a detailed kit tool of a building a deep network learning pipeline, from planning to output implementation of the processing is accompanied by good documented instances. Furthermore, architecture includes performances of common Deep network learning and building blocks of location models allow accelerated exploration of cutting-edge deep learning approaches. Rather than being hard-coded, models are described in config files, guaranteeing distinction of image and execution.

Pytorch is one more complete free software deep learning

system. It is design methodology shifted away from describe and execute, as seen in a lot of frameworks that generate a motionless conceptual grid before operation the model. Although this solution an efficient, to compromises accessibility, debugging easiness, and versatility.in its place, Pytorch take an crucial approach, energetically building the computational graph and allow the model to be idiomatically described in accordance with the Python programming style.

The architecture also allows for a smooth transition from analysis to manufacturing, dispersed training, and model execution on edge devices.

Tensorflow is a dispersed deep learning framework for major applications that use machine learning The app enables the use of dataflow graphs on a variety of formats, including mobile devices and large-scale systems, dispersed networks, with small to modification. Is an architecture theory was used to shorten the model.Parallelism within a single computer as well as parallelism through thousands of distributed networks It includes a comprehensive toolkit for rapid exploration of cutting-edge deep learning frameworks, a smooth change from testing to varied applications, and the visualization and debug of extensive models.

Keras is a sophisticated API is a deep learning application that is rapidly increasing in popularity. While it at first support several data-flow chart back ends, such as Theano, it is tightly integrated into the Tensorflow2 system eco. It provides reliable and easy APIs for easily experimenting with new model and using Tensorflow2 to export models for use in browsers and mobile devices. Furthermore, it includes structure blocks and pertained a cutting-edge template and a wide range of machine learning domains Because of an its ease of use, a user centered approach, and thorough confirmation, the software has been adopted by the business and research community.

Data set

In earlier period of 5 years there has been researches are measured in automatic brain tumor segmentation using deferent researchers are used various algorithms and methods as research output is grow, for the object evolution is big challenge why because the developers are used private data set with different attributes. As BARTS (segmentation of multi modal brain tumor image) is emerging to calculate the performance accuracy by with public data set. The below tabel1 is gives the summary of recently used data set segmentation for brain tumor. As per the Medical image compute and computer assisted interference (MICCAI) they gives the medical research community we access the public brain tumor data set in the starting it is around It has increased to over a year after 50 image scans of glioma patience.

Table 2: Report on a study of a widely used public dataset for brain tumour segmentation

Datasets type	Year	Total	Data Training	Data Validation	Data Testing
BRATS 2019	2019	653	335	127	191
BRATS 2018	2018	542	285	66	191
BRATS 2017	2017	477	285	46	146
BRATS 2016	2016	391	200	-	191
BRATS 2015	2015	252	201	0	52
BRATS 2014	2014	238	201	10	38
BRATS 2013	2013	60	35	10	25
BRATS 2012	2012	50	35	10	15
Decathlon[70]	-	750	484	-	266

In the top of table gives an idea of different BraTs challenge held in year 2012 given by A comparison of low grade glioma and high grade glioma was made using a brain MRI data set.

V. COMPARISON TABLE FOR STUDIED RESEARCHES

Table 3: This tables is gives the summary of different researches work and future Expansion

Ref.	Survey title	Published journal & year	Result & Future Expansion
1	Deep learning segmentation for a survey of state-of-the-art brain tumor	Journal of Imaging MDPI 2021	This paper have gives different building blocks state of art tools methods for 'algorithms for automatic brain tumour segmentation' Many segmentation algorithms' poor performance is due to a lack of large-scale medical training datasets.

2	The most up-to-date technology is used. Stem tumour segmentation using the CNN optimizer in magnetic resonance images	Brain Sciences MDPI 2020	In this paper a comparative analysis is observed in CNN to find segmentation of brain tumor. Here a made a comparison is on available public data set MRI brain BraTs2015 images both graphical and quantitative results are gives consistency. In the future, we'll compare this state-of-the-art optimizer to with to find brain tumor segmentation using multiple CNN architectures.
3	multi-fibe Recurrent network for 3D MRI segmentation on brain tumor	MDPI2021Symmetry	This paper the entire tumor and the tumor the enhancing tumor they can get dice scores of 78.72%, 83.65%, 89.62% relatively. Considering the 3D context they also compare with the previous methods the reduction of parameters the training time and execution time is to long due to complexity of methods .In future we will modify this method to get its ability to generalization and improve the speed of training for improve the segmentation
4	Using template-based k means and an improved fuzzy c means clustering algorithm, automatic human brain tumour identification in mri images is possible.	MDPI 2019 Big data and Cognitive computing	For this paper to compare the how much time to take find the brain tumor using conventional method and TKFCM method here the proposed method TKFCM method it will take less time Brain tumor detect and accuracy of the method 25.64%, 7.69%, 5.12%,2.56%, 17.9%. In future we analyze to apply More features that can be used to identify brain tumours and increase accuracy, but it may take a long time.
5	A systematic MRI approach for segmentation on brain tumor localization and using deep learning and active contouring	Journal of Healthcare Engineering Hindawi 2021	Provided a user-defined initial guessed boundary, In ChanVese brain tumour segmentation using MRI, active contour algorithms are used to achieve better and more precise object boundaries. It is important to provide a reasonably reliable estimate.algorithm. For effective segmentation, start with the initial region of interest search field. We used the bounding box that was generated after The ChanVese algorithm uses a faster R-CNN as the initial boundary to simplify the entire brain tumour segmentation process.
6	Localization and Detection of early-stage multiple brain tumors using a hybrid technique of patch-based processing, k-means clustering and object counting	international journal of biomedical imaging Hindawi 2020	In this article, the researchers present an idea about how to identify and localise early stage brain tumours in MRI images using an artificial approach known as k means clustering patch dependent processing and tumour evolution. This technique was used on about 20 brain MRI actual images that had already been detected by laboratories, as well as a massive tumour that this method was able to detect at an early stage.

7	An intelligent diagnosis method of brain MRI tumor segmentation using deep convolutional neural network and SVM algorithm	Hindawi computational and mathematical methods in medicine2020	The researchers introduced a new technology for finding a Deep convolutional neural network Fusion SVM algorithm and Deep convolutional neural network Fusion SVM algorithm are used to segment brain tumours. this paper give a comparative simulation results for Public dataset and self made data experiment and they achieve results CNN, DCNN f SVM, and SVM of 26 patients respectively. Despite this, the proposed methods have drawbacks, such as a long measurement time. The future analysis background will be how to solve the algorithm and reduce the running time.
8	A framework for brain tumor segmentation and classification using deep learning algorithm	International Journal of Advanced Computer Science and Applications2020	In this article, experts are offered a technique for detecting brain tumours and grading tumours using MRI into meningioma and glioma is suggested by preprocessing, skull stripping, and brain segmentation, graded into malignant or benign using CNN based Alex net method and they achieved precision of 0.937, recall of 1, and f-means 0.967, while using CNN based Google net method they achieved precision of 0.95, recall of 1, and f-means
9	Using magnetic resonance imaging and deep learning to classify brain tumours	Journal of Critical Reviews2020	The author suggested a Recurrent neural network architecture for tumour detection that has a 90% accuracy rate. A RNN is a kind of ANN in which nodes from a directed graph are connected in a temporal series.
10	Brain image segmentation using machine learning brain detection of tumor	International research journal of engineering and technology 2020	This approach may only be used to enhance tumours with distinct enhancing edges. Only two labels are used in this method: object and context. One of the few disadvantages of graph-based approaches is that they are difficult to apply to multi-label problems.
11	Deep learning based brain tumor segmentation: a survey	2020	In this paper the researches are apply a different deep learning techniques for brain tumor classification it's a big task in the deep learning is a power full method for future learning of brain tumor and they presented a comprehensive review and finalized the deep learning based brain tumor segmentation .In future a deeply investigation is need for comprehensive survey of deep learning based brain tumor segmentation.
12	Detection and diagnosis of brain tumors using deep learning convolutional neural networks	Wiley2020	In this research paper the inventors invites a new method is Deep convolutional neural network architecture finding the tumor affected area in the brain and the proposed method achieved the brain tumor accuracy up to 97.7% . In Future we same CNN method for identifying the tumor region in thermal scanned brain images

13	A study on brain tumor detection and segmentation using deep learning techniques	Journal of computational and theoretical nanoscience2020	The classified tumor gives a better result to diagnose the tumor with less computational time. The medical department gets an enhanced knowledge to diagnose the tumor of patient. In future work segmentation of skull region to predict the brain tumor at early stages with better computation rate.
15	An overview of deep learning in medical imaging focusing on MRI	Elsevier 2020	A detailed examination of deep learning methods for medical image analysis.
16	A review on brain tumor diagnosis from mri images: practical implications, key achievements, and lessons learned	Elsevier 2021	Normal databases for tumour identification and classification are needed. In addition, the three processes must be integrated into a single completely automated method for brain tumour diagnosis that is more scientifically beneficial. Methods for a more accurate diagnosis.
17	Review of mri-based brain tumour image segmentation using deep learning methods	Elsevier2016	Future enhancements and modifications to CNN architectures, as well as the inclusion of complementary knowledge Other imaging modalities, such as PET, MRS, and Diffusion Tensor Imaging (DTI), can be used to improve existing approaches, leading to the development of clinically effective automatic glioma segmentation.
18	Brain tumour classification using deep learning neural networks	Sciencedirect 2017	In the future, the positive results obtained with the DWT may be used with the CNN to compare the results.

VI. CONCLUSION

With different deep learning approaches to segment brain tumors' is a precious and difficult process. Since deep learning techniques have a strong feature learning capacity, automated image segmentation gains multiple ways. In this article, we researched and published a detailed survey of applicable Brain tumour segmentation methods focused on deep learning. Brain tumour segmentation using deep learning approaches is structurally classified and summarized. We thoroughly researched this assignment and addressed some main issues such as the advantages, disadvantages on various processes, Linked datasets, pre- and post-processing, and calculation metric. At the conclusion of this survey, we even forecast future research paths.

REFERENCE

- [1] Tirivangani Magadza, and Serestina Viriri, Deep Learning for Brain Tumor Segmentation A Survey of State-of-the-Art; J.Imaging2021, 7, 19.[<https://doi.org/10.3390/jimaging7020019>]
- [2] Muhammad Yaqub , Jinchao Feng , M. Sultan Zia, Kaleem Arshid, Kebin Jia, Zaka Ur Rehman and Atif Mehmood State-of-the-Art CNN Optimizer for Brain Tumor Segmentation in Magnetic Resonance Images, Brain Sci. 2020, 10, 427.[<https://pubmed.ncbi.nlm.nih.gov/32635409/>]
- [3] Yue Zhao , Xiaoqiang Ren, Kun Hou and Wentao Li Recurrent Multi-Fiber Network for 3D MRI Brain Tumor Segmentation, Symmetry 2021, 13, 320.[<https://www.mdpi.com/2073-8994/13/2/320>]
- [4] Md Shahariar Alam, Md Mahbubur Rahman, Mohammad Amazad Hossain, Md Khairul Islam, Kazi Mowdud Ahmed, Khandaker Takdir Ahmed, Bikash Chandra Singh and Md Sipon Miah, Automatic Human Brain Tumor Detection in MRI Image Using Template-Based K Means and Improved Fuzzy C Means Clustering Algorithm, Big Data Cogn. Comput. 2019, 3, 27[https://www.mdpi.com/2504-2289/3/2/27/review_report]
- [5] Dhanashri joshi, hemlata channe, a survey on brain tumor detection based on structural MRI using deep learning and machine learning techniques. International journal of scientific & technology research volume 9, issue 04, april 2020.[<https://www.ijstr.org/paper-references.php?ref=IJSTR-0420-34239>]
- [6] Zhihua liu, long chen, lei tong, feixiang zhou, zheheng jiang, qianni zhang, caifeng shan, xiangrong Zhang, ling li, huiyu zhou, deep learning based brain tumor segmentation: A survey, journal of latex class files, vol. 14, no. 8, august 2015.[<https://arxiv.org/abs/2007.09479>]

- [7] Dr.R.C.Suganthe, G.Revathi, S.Monisha, R.Pavithran, deep learning based brain tumor classification using magnetic resonance imaging, journal of critical reviews. Issn- 2394-5125 vol 7, issue 9, 2020.[<http://www.jcreview.com/?mno=111627>]
- [8] Wentao wu ,daning li,jiaoyang du,xiangyu gao,wen gu,fanfan zhao, Xiaojie feng,and hong yan, an intelligent diagnosis method of brain mri tumor Segmentation using deep convolutional neural network and Svm algorithm, hindawi Computational and mathematical methods in medicine Volume 2020, article id 6789306, 10 pages.
- [9] Mohamed nador and walid obaid, detection and localization of early-stage multiple brain tumors using a hybrid technique of patch-based processing, k-means clustering and object counting, hindawi international journal of biomedical imaging volume 2020, article id 9035096, 9 pages,[<https://doi.org/10.1155/2020/9035096>]
- [10] AM.Hasan,HA. Jalab,F. Meziane, HKahtan,ASA Ahmad, combine Deep and Handcrafted Image character for MRI Brain Scan Classification, IEEE Access, pp. 79959–79967,2019.[<https://ieeexplore.ieee.org/stamp/stamp.jsp?arnumber=8736208>]
- [11] HT. Zaw, N. Maneerat, KY. Win, detection of Brain tumor based on Naïve Bayes classification, International Conference on Engineering, Applied Sciences and Technology, pp.1-4,2019[<https://www.jetir.org/papers/JETIR2104081.pdf>]
- [12] AK. Anaraki ,A.Moosa ,F. Kazemi MRI-based brain tumor grades classification and grading via convolutional neural networks and genetic algorithms, Biocybernetics and Biomedical Engineering, pp.63-74,2019[<https://www.ijstr.org/paper-references.php?ref=IJSTR-0420-34239>]
- [13] N. Gupta , P. Khanna, A non-invasive and adaptive CAD system to detect brain tumor from T2-weighted MRIs using customized Otsu’s thresholding with prominent features and supervised learning, Signal Processing Image Communication, pp.1-9,2017
- [14] S.Deepak ,PM. Ameer, Brain tumor classification using deep CNN features via transfer learning, Computers in Biology and Medicine, pp.1-7,2019[DOI:10.3390/s21062222]
- [15] Ronneberger, O.; Fischer, P.; Brox, T. U-net: Convolutional networks for biomedical image segmentation. In Lecture Notes in Computer Science, Proceedings of the International Conference on Medical Image Computing and Computer-Assisted Intervention, Munich, Germany, 5–9 October 2015; Springer: Cham, Switzerland, 2015; pp. 234–241[<https://arxiv.org/abs/1505.04597>]
- [16] Heinrich, M.P.; Oktay, O.; Bouteldja, N. Obelisk-net: Fewer layers to solve 3D multi-organ segmentation with sparse deformable convolutions. *Med. Image Anal.* 2019, 54, 1–9.[<https://pubmed.ncbi.nlm.nih.gov/30807894/>]
- [17] Shaik Naseera, G.K. Rajini, B. Venkateswarlu, Jasmin Pemeena Priyadarisini M, A Review on Image Processing Application in Medical Field, *Research J. Pharm. and Tech.* 10(10): October 2017.[[www. rjptonline.org](http://www.rjptonline.org)].
- [18] M. Muthumeenakshi. An Application of Pentagonal Valued Hesitant Fuzzy Set in Medical Diagnosis. *Research J. Pharm.and Tech* 2016;9(10):1823-1826.
- [19] V. N. Dange, S. J Shid, C.S. Magdum, S.K. Mohite. A Review on Breast cancer: An Overview, *Asian J. Pharm. Res.* 2017; 7(1);49-51.
- [20] Zhao, Y.X.; Zhang, Y.M.; Liu, C.L. Bag of Tricks for 3D MRI Brain Tumor Segmentation. In *Brainlesion: Glioma, Multiple Sclerosis, Stroke and Traumatic Brain Injuries*; Lecture Notes in Computer Science; Crimi, A., Bakas, S., Eds.; Springer International Publishing: Berlin/Heidelberg, Germany, 2020; pp. 210–220.
- [21] A. Kabir Anaraki, M. Ayati, and F. Kazemi, “Magnetic resonance imaging-based brain tumor grades classification and grading via convolutional neural networks and genetic algorithms,” *Biocybernetics and Biomedical Engineering*, vol. 39, no. 1, pp. 63–74, 2019.
- [22] J. Ker, L. Wang, J. Rao, and T. Lim, “Deep learning applications in medical image analysis,” *IEEE Access*, vol. 6, pp. 9375–9389, 2018.
- [23] A. Isin, C. Direkoğlu, and M. Şah, “Review of MRI-based brain tumor image segmentation using deep learning methods,” *Procedia Computer Science*, vol. 102, pp. 317–324, 2016.
- [24] H. Dong, G. Yang, F. Liu, Y. Mo, and Y. Guo, “Automatic brain tumor detection and segmentation using U-net based fully convolutional networks,” *Communications in Computer and Information Science*, vol. 1, pp. 506–517, 2017.
- [25] J. Cheng, W. Huang, S. Cao et al., “Enhanced performance of brain tumor classification via tumor region augmentation and partition,” *PLoS One*, vol. 10, no. 10, Article ID e0140381, 2015.
- [26] R. Kumar and A. M. Arthanariee, “Performance Evaluation and comparative Analysis of Proposed Image Segmentation Algorithm,” *Indian Journal of Science and Technology*, vol. 7, no. 1, pp. 39–47, 2014.
- [27] J. Liu, M. Li, J. Wang, F. Wu, T. Liu, and Y. Pan, “A survey of MRI based brain tumor segmentation methods,” *Tsinghua Science and Technology*, vol. 19, no. 6, pp. 578–595, 2014.
- [28] N. B. Bahadure, A. K. Ray, and H. P. _ethi, “Image analysis

- for MRI based brain tumor detection and feature extraction using biologically inspired BWT and SVM,” *International Journal of Biomedical Imaging*, vol. 2017, Article ID 9749108, 12 pages, 2017.
- [29] Li, H.; Li, A.; Wang, M. A novel end-to-end brain tumor segmentation method using improved fully convolutional networks. *Comput. Biol. Med.* 2019, 108, 150–160.
- [30] Glorot, X.; Bengio, Y. Understanding the Difficulty of Training Deep Feedforward Neural Networks. In *Proceedings of the Thirteenth International Conference on Artificial Intelligence and Statistics*, Chia Laguna Resort, Sardinia, Italy, 13–15 May 2010; Volume 9, pp. 249–256.
- [31] Pereira, S.; Pinto, A.; Alves, V.; Silva, C.A. Brain Tumor Segmentation Using Convolutional Neural Networks in MRI Images. *IEEE Trans. Med. Imaging* 2016, 35, 1240–1251.
- [32] Casamitjana, A.; Puch, S.; Aduriz, A.; Sayrol, E.; Vilaplana, V. 3D Convolutional Networks for Brain Tumor Segmentation. In *Proceedings of the MICCAI Challenge on Multimodal Brain Tumor Image Segmentation (BRATS)*, 2016; pp. 65–68. Available online,
- [33] Mlynarski, P.; Delingette, H.; Criminisi, A.; Ayache, N. Deep learning with mixed supervision for brain tumor segmentation. *J. Med. Imaging* 2019, 6, 034002.
- [34] Iqbal, S.; Ghani Khan, M.U.; Saba, T.; Mehmood, Z.; Javaid, N.; Rehman, A.; Abbasi, R. Deep learning model integrating features and novel classifiers fusion for brain tumor segmentation. *Microsc. Res. Tech.* 2019, 82, 1302–1315.

SMART EXTENSION CORD USING NODE MCU

B.Sreelatha (Associate Professor ,ECE Department ,Geethanjali College of Engineering and Technology / JNTUH, Cheeryala(V) Keesara(M), Medchal Dist.,Telangana, INDIA,sree.0474@gmail.com)

Subrat Mohanty (Project Engineer,WIPRO, subratmohanty17@gmail.com)

Maneesh Kumar (Software Engineer, Capgemini,maneeshkumar0913@gmail.com)

P.Surya Teja-(Assistant System Engineer,TCS,suria.teja999@gmail.com)

ABSTRACT

With advancement of Automation Technology, life is getting simpler and easier in all aspects. In today's world automatic systems are being preferred over manual system. With the rapid increase in the number of users of internet over the past decade, made internet as a part and parcel of life. Internet of Things (IoT) is the latest and emerging internet technology. It is a growing network of everyday object-from industrial machine to consumer goods that share information and complete tasks while busy with other activities. Wireless Home Automation system (WHAS) using IoT is a system that uses computers or mobile devices to control basic home functions, facilitate automation through internet from anywhere around the world. Automated home is also called as Smart Home. It is meant to save the electric power and human energy. This paper is IoT based which works on internet to operate the Smart Extension Cord sockets individually from any part of world with ease using the application. The application is user friendly which will help the user to easily ON/OFF the sockets and can also set the timer for individual socket, which will notify after the time is complete.

This work is done with the help of Node MCU, Relays, Google Assistant, Firebase Cloud, MIT App Inventor and IFTTT. We implemented an application using which any user can operate it very easily with the help of active internet connection.

KEYWORDS

Firebase Cloud, Google Assistant, IFTTT, MIT App Inventor, Node MCU

1. INTRODUCTION

Demand response (DR) program support demand side management so as to reduce power consumption in residential and commercial buildings by considering time of use, real time pricing and critical peak pricing. In the residential sector, the technology developed for DR strategy is Home Energy Management System (HEMS) which helps to reduce electricity bill and peak demand by scheduling the home electrical appliances based on priority, comfort level and preference setting. A HEMS involves any device or product that analyze energy consumption, control and monitor home electrical appliances.

Many smart devices like smart meters and smart plugs that been used to support intelligent buildings, to assist homeowners to control the electrical appliances remotely using their smart phone and help to take decisions about energy consumption. Smart grid technologies are used to provide real-time energy consumption to consumer and utility and it provides two way communications between the grid and customers. Smart meter is one of the monitoring device in a smart grid system connected at the home entrance to allow active participation of consumer to manage power delivery and reduce its cost. A smart plug sits between the wall outlet and the electrical appliance and it is used to control and monitor appliances remotely. Furthermore, it allows user for optimizing the usage of appliance and benefit lower energy consumption by remotely scheduling or turning ON/OFF the appliance in a room via tablet or smart phone using ZigBee communication. Non-smart appliances should also be considered for energy management systems and therefore it is necessary to find a practical solution to connect non-smart appliances to a controller. So, the design of smart plugs forms a network of distributed sensing nodes, which provide remotely switch loads (ON/OFF) and control the electrical appliances in a HEMS. In this paper is a prototype of smart plug which is developed by using a stand-alone device supported with Zigbee wireless communication for implementing a HEMS in smart homes. A node is connected to a home appliance and it is used for sending power consumption data of each device by means of ZigBee communication to a data collection device such as personal computer.

2. SOFTWARES AND HARDWARE COMPONENTS

2.1 Node MCU

Node MCU is an open source firmware for which open source prototyping board designs are available. The name "Node MCU" combines "Node" and "MCU" (micro-controller unit). The term "Node MCU" strictly speaking refers to the firmware rather than the associated development kits. Both the firmware and prototyping board designs are open source.

2.2 RELAYS

A relay is an electrically operated switch. It consists of a set of input terminals for a single or multiple control signals, and a set of operating contact terminals. The switch may have any number of contacts in multiple contact forms, such as make contacts, break contacts, or combinations thereof.

2.3 GOOGLE FIREBASE

Firebase is a Google's database platform which is used to create, manage and modify data generated from any android application, web services, sensors etc.

2.4 GOOGLE ASSISTANT

Google Assistant is an artificial intelligence-powered virtual assistant developed by Google that is primarily available on mobile and smart home devices. Unlike the company's previous virtual assistant, Google Now, the Google Assistant can engage in two-way conversations.

2.5 MIT APP INVENTOR

It uses a graphical user interface (GUI) very similar to the programming languages Scratch (programming language) and the Star Logo, which allows users to drag and drop visual objects to create an application that can run on mobile devices. In creating App Inventor, Google drew upon significant prior research in educational computing, and work done within Google on online development environment

2.6 IFTTT: [IF THIS THEN THAT]

If This Then That, also known as **IFTTT**, is a free web based service that creates chains of simple conditional statements, called applets. An applet is triggered by changes that occur within other web services such a Gmail, Facebook, Telegram, Instagram or Pin Interest

3. ALGORITHM

3.1 Methodology

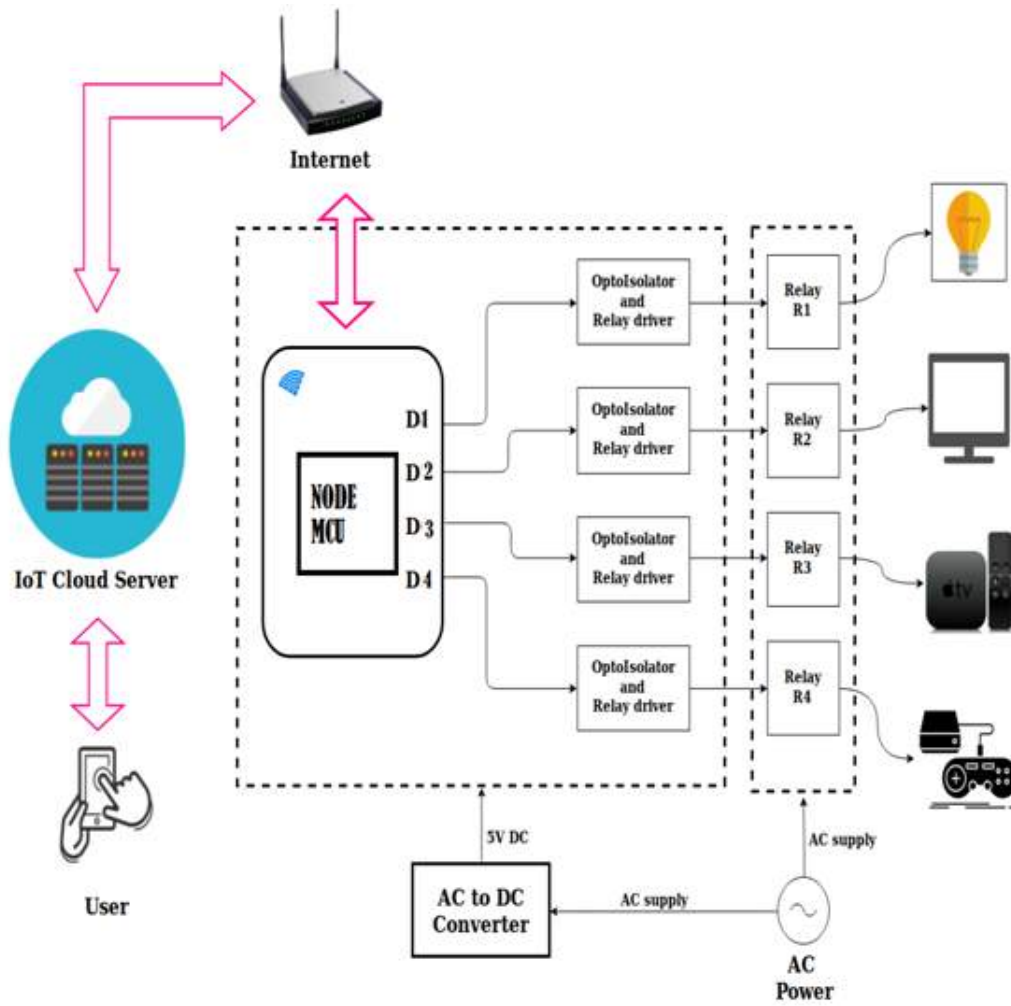
In this project the main components used are NodeMCU and Relays. The NodeMCU is connected to the relay through jumper wires. NodeMCU consists of an inbuilt Wifi Module which has to be connected to a good internet connection. The digital pin of the NodeMCU provides the relay with input and the relay performs operation accordingly. The Power supply is provided to the NodeMCU as well as the relay module.

On the other hand, the NodeMCU is connected to another relay module which controls different sockets. The NodeMCU is programmed to control different type of appliances through an application. The digital pins on the NodeMCU (D1, D2, D3, D4, D5) are connected to the input pin of the relay. The relay provides the output of certain commands given by the user to turn the appliances ON and OFF.

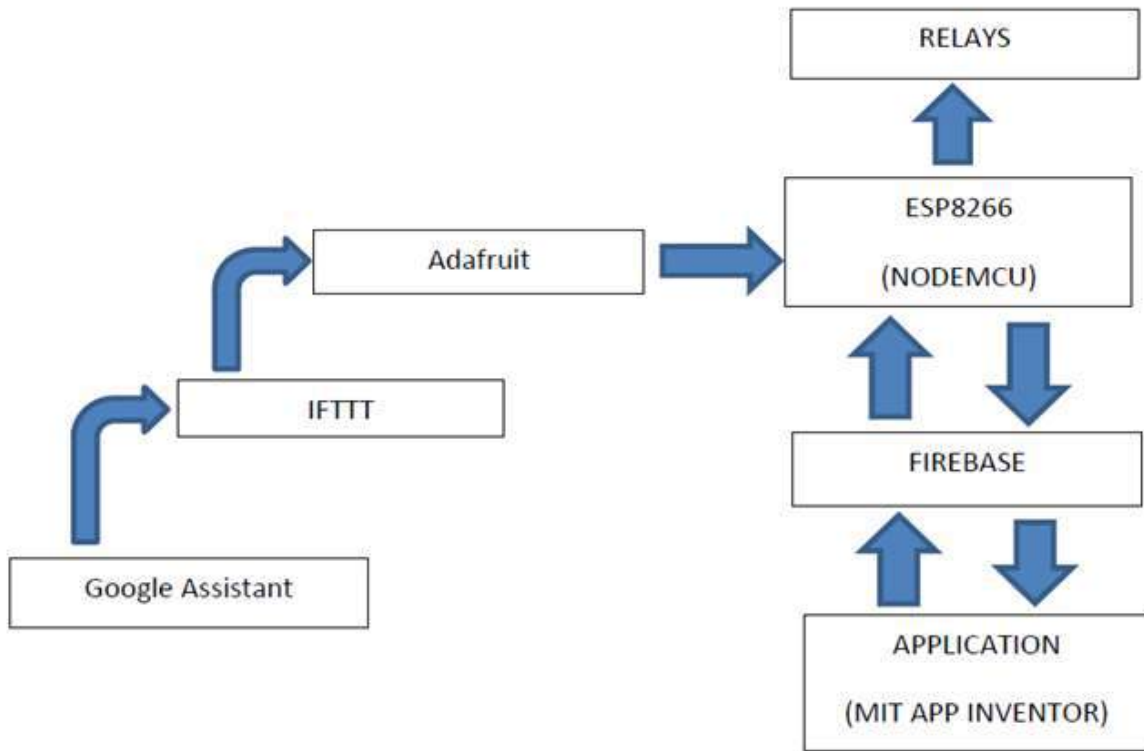
The application is designed to be connected to the same IP as the Wi-Fi module so that exchange of signals can take place, the user selects an appropriate command through the application which sends signals to the NodeMCU through which the signal is forwarded to the relay, which is programmed to perform certain actions which includes controlling the appliances, when signals are received.

The mobile application is developed using Android IDE and MIT App Inventor that helps us to create an interface between the Node MCU and the mobile device. The application has various options to choose from, the user decides what commands to forward to the NodeMCU. The Wi-Fi module (NodeMCU) receives signal from the application, when the user opens the application and can control the appliances from anywhere if he/she is connected to the internet.

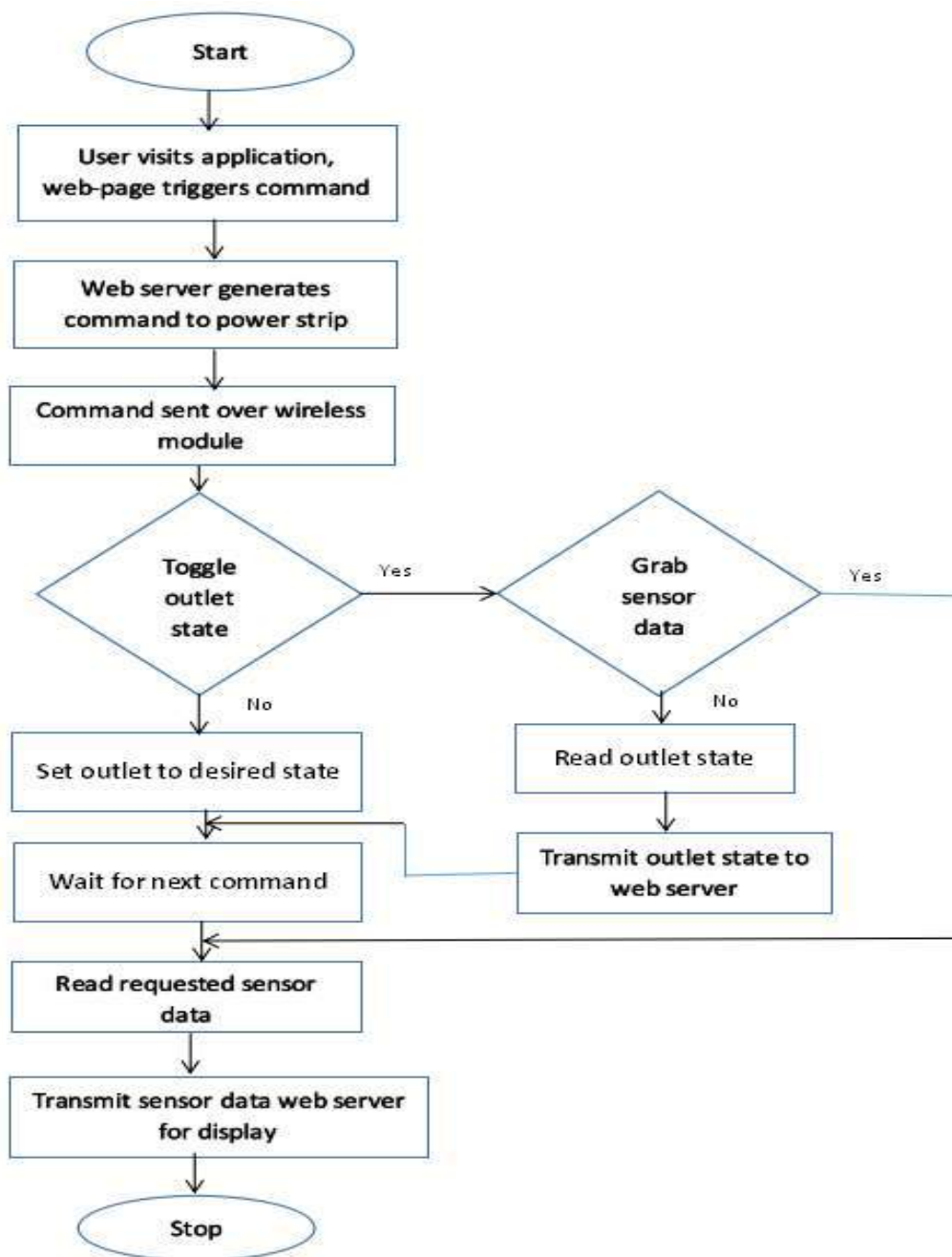
3.2 BLOCK DIAGRAM



3.3 FLOW DIAGRAM



3.4 FLOWCHART



4. Conclusion

Using this we created a working model which works efficiently with the help of internet. The sockets are Switching ON/OFF with the help of the Application as well as with the commands on Google Assistant. Having such smart Technologies installed at home or at workplace very drastically reduces the human effort and also have some control on things like wastage of power. Our project can be beneficial in the long run, as the interface is user friendly and can be operated by people of any age. Currently the research in the field of IoT and its implementation will improve the quality of life of human civilization .Today IoT is

being implemented everywhere like Smart city, smart environment, smart business process, smart agriculture, security and emergencies , domestic and home automation and health-care.

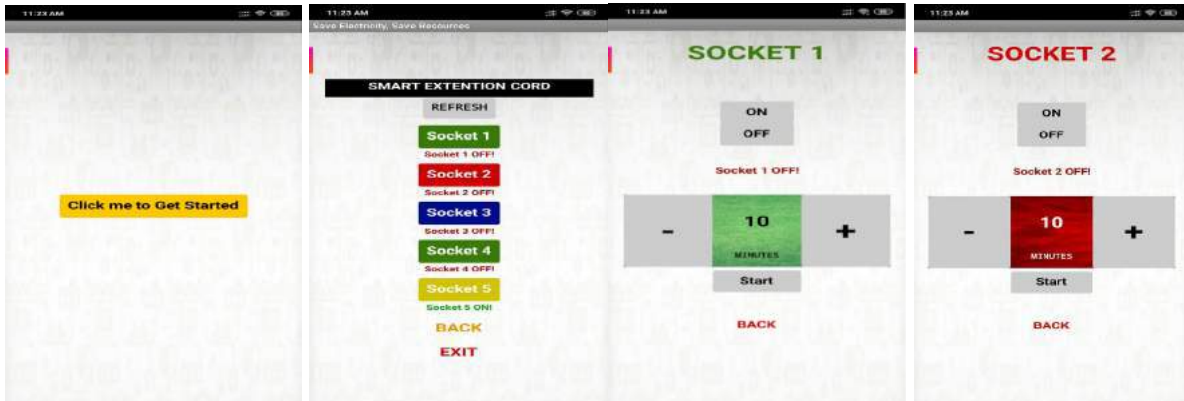


Figure 4.1.1: Pages of Mobile Application

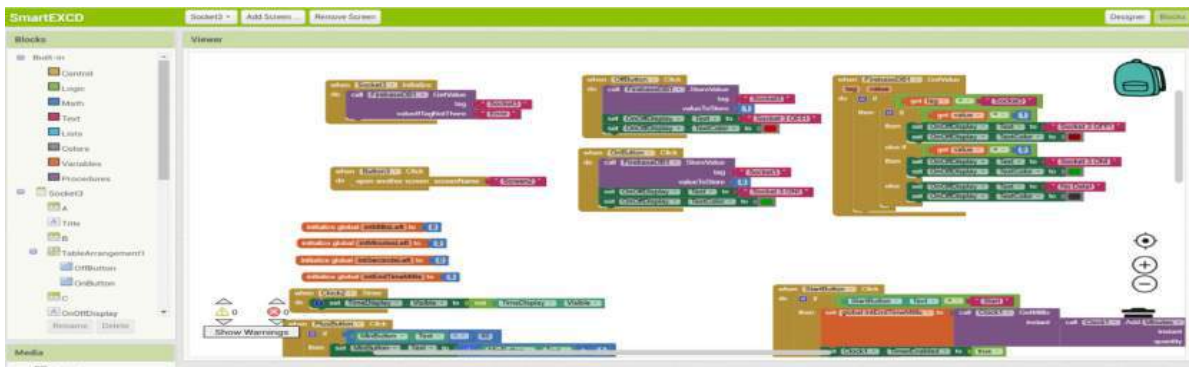


Figure 4.1.2: Back-end Work of Each Page of the Android Application in MIT APP Inventor.

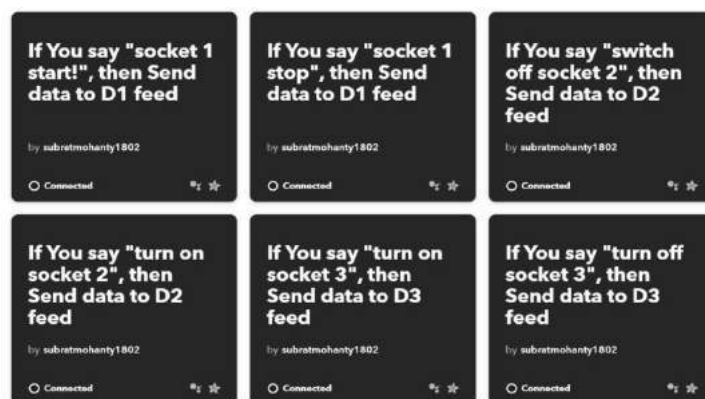


Figure 4.1.2: IFTTT commands

5.REFERENCES

1. Vikram, K. S. Harish, M. S. Nihaal, R. Umesh, A. Shetty and A. Kumar, "A Low N Cost Home Automation System Using Wi-Fi Based Wireless Sensor Network Incorporating Internet of Things (IoT)," 2017 IEEE 7th International Advance Computing Conference (IACC), Hyderabad, 2017, pp. 174-178.

2. N. Kushiro, S. Suzuki, M. Nakata, H. Takahara and M. Inoue, "Integrated residential gateway controller for home energy management system," in IEEE Transactions on Consumer Electronics, vol. 49, no. 3, pp. 629-636, Aug. 2003
3. V. H. Bhide and S. Wagh, "i-learning IoT: An intelligent self learning system for home automation using IoT," 2015 International Conference on Communications and Signal Processing (ICCSP), Melmaruvathur, 2015, pp. 1763-1767.
4. K N. Vinay Sagar, Kusuma, "Home Automation Using Internet of Things", International Research Journal of Engineering and Technology (IRJET), vol. 2, no. 3, July 2015.
5. Rohit Sharma, Pankaj Singh, Abhishek Singhal "Two Different Authentication Protocol for Rfid Credit Card Security", in Journal of Engineering and Applied Sciences, ISSN 1816-949x Vol 12, Issue – 22, Page – 6006 – 6012, 2017.
6. Mohamed Abd El-LatifMowad, Ahmed Fathy, Ahmed Hafez "Smart Home Automated Control System Using Android Application and Microcontroller" International Journal of Scientific & Engineering Research, Volume 5, Issue 5, May-2014 ISSN 22295518.
7. Sook-Ling Chua and Stephen Marsland and HansW. Guesgen "Behaviour Recognition in Smart Homes Sook" Proceedings of the Twenty Second International Joint Conference on Artificial Intelligence

A General Evaluation of Dermis Sores Identification using MOR-WAVELET Transforms

CH. Kranthi Rekha^a, Dr Rajeev Shrivastava^b, Dr. Sanjay Kumar Suman^c, Dr. L. Bhagyalakshmi^d, B. Leelaram Prakash^c

^aResearch Scholar, KL University, Vijayawada, Assistant Professor Bharat Institute of Engineering and Technology, Hyderabad email: sk1101143@gmail.com

^bAssociate Professor, Department of Electronics and communication engineering Bharat institute of engineering and technology Hyderabad, email: rajeev2440130@gmail.com.

^cProfessor, Dept. of ECE, Bharat Institute of Engineering and Technology, Hyderabad, email: prof.dr.sanjaykumarsuman@gmail.com.

^dProfessor, Dept. of ECE, Rajalakshmi Engineering College, Chennai, email: Prof.Dr.L.Bhagyalakshmi@gmail.com.

^eProfessor, ECE, Geethanjali College of Engineering and Technology, Hyderabad, email: prakashvignan4368@gmail.com

Article History: Received: 10 January 2021; Revised: 12 February 2021; Accepted: 27 March 2021; Published online: 28 April 2021

Abstract: Dermis Canker detection is one of the significant image processing approach utilized in finding the Dermis sores, for example, malignancy and other pigmented sores. Because of the trouble and subjectivity of human understanding, mechanized examination of dermoscopy pictures has become a significant exploration territory. One of the most significant strides in dermoscopy picture investigation is the mechanized discovery of sore outskirts. In this paper we propose a novel approach for fringe recognition of sores in dermoscopy pictures. To begin with, the shading input picture is changed over into a dim level picture. At that point, the wavelet coefficients of dark level picture are determined. The wavelet coefficients are adjusted utilizing inclination of each wavelet band and a nonlinear capacity. The upgraded picture is acquired from the opposite wavelet change of altered coefficients. Morphology administrators are utilized to fragment the picture; lastly the injury is distinguished by a mechanized calculation. The outcomes show that the proposed technique has a low rate fringe error in a greater part of Dermis injuries.

Keywords: Discrete Wavelet Transform, Fringe error, Morphology, Dermis Sores, Malignancy

1. Introduction

A crucial difficulty the medical practitioners facing is to identify the frequent cause of deaths due to dermis diseases not identified at early stages. As indicated by the W.H.O, there are around one million dangerous malignancy cases and more than sixty thousands demise instances of harmful malignancy around the globe every year [1]. Dermis is the comparatively bigger organ in the human body, which comprises of the 3 principal layers: Dermis, epidermis, and hypodermis. The Dermis has a significant job in the soma securing about external influenced parameters, for example, microscopic organisms, heat changes, and presentation to bright radiation (U.V.R) [2]. U.V.R is one of the well-known grounds that take to dermis malignant growth. These U.V.R beams are sufficiently amazing to arrive at our slough layer in the dermis and harm the D.N.A which drives at last to Dermis disease. The postponement from the hour of harm and the malignant growth can be numerous years.

The expression "Dermis disease" refers to three distinct conditions that are recorded underneath in rising request of mortality:

1. Basal cell carcinoma (or basal cell carcinoma epithelioma)
2. Squamous cell carcinoma (the principal phase of which is called actinic keratosis)
3. Malignancy.

Malignancy is commonly the genuine type of dermis lymphoma since it will spread in general (metastasize) all through the body rapidly.

Dermatologists are confronting urgent issues in confirming the threatening malignancy by utilizing dermoscopy. The determination by utilizing dermis-surface microscopy is not exact and sets aside some effort to give the last finding. Timely malignancy discovery may expand the likelihood of testing threatening malignancy up to ninety percentage. In the year 1994, Franz Nachbaur [3] proposed a clinical dermoscopy strategy for malignancy identification known as *abcd* rule. This standard was surveyed by a scoring condition for every assessment technique. The *abcd* rule works just for melanocytic injuries.

As of late PC frameworks helped practitioners in malignancy recognition. The greater part of the identification frameworks comprises of five principal steps: picture securing, pre-processing, highlight extraction, arrangement,

lastly assessment. There are many distributed papers which center principally around the order frameworks to separate between threatening malignancy and amiable injuries. The article is intended to contemplate the identification frameworks of malignancy that rely upon one of these component extraction strategies: Discrete wavelet transforms (dwt), wavelet packet transforms (wpt) and gabor wavelet transform (gwt). Harmful Lymphoma is hard to be perceived relying just upon vision. There are three principal points in this investigation: Right off the bat, to consider the past strategies that utilized wt and dwt. Secondly to distinguish harmful malignancy with amiable nevus dependent on the drawing out of features by utilizing wpt and wavelet entropy (we) calculation. At the end to decide the best boundary outputs with certain analysis.

2. Related Works

WT has been utilized for picture preparing [13]. Since two decades the modification on the malignancy recognition frameworks has been studied. In the mid 2000 century, wavelets in malignancy recognition have been used by researchers from many years. In the accompanying writing, we will talk about the normal and various strategies for every 5 years.

Hutokshi Sui et al. proposed the method of surface highlight extraction for order of malignancy. The testing strategy utilizes picture handling methods furthermore, man-made consciousness. Pre-preparing is never really input dermis pictures and the picture is divided utilizing referencing technique. From the highlighted portion of picture, few highlights are separated at that point utilizing SVM classifier [6].

M.R.Patil et al, proposed a work on Non-Obtrusive *abcd* observing of Threatening Malignancy utilizing Picture Prepared in MATLAB. He proposed two significant components of a non-invasive time span programmed dermis injury investigation framework for the main location and bar of dermis malignant growth. The essential portion is a time frame mindful to encourage clients prevent dermis consume brought about day light. The picture obtaining, hair discovery what's more, rejection, sore division, includes extraction, and arrangement which is remembered for programmed picture investigation module goes under the subsequent part. The yield is prudent, and the exactness got for kind hearted, different also, dermis malignant growth is more than ninety percent [7].

Terrance DeVries et al, proposed a technique for dermis Sore Characterization utilizing profound multi scale convolutional neural systems. This methodology used an Origin v3 organize pre-prepared on the ImageNet dataset, which is calibrated for dermis injury order utilizing two distinct sizes of info pictures. It is demonstrated that, subsequent precision for malignancy order is less than 1 and for Seborrheic Keratosis is near to 1 [8].

Adri'a Romero L'opez, accomplished a job dependent on the issue of programmed dermis sore identification, especially on malignancy identification, and it is finished by put in semantic division and arrangement from dermoscopic pictures. Utilizing cutting edge strategies to characterize pictures, the impeccably sectioned pictures accomplish 76.66% exactness, while the precision improves to 81.33% when utilizing unsegmented pictures. The affectability is recorded at 84% when utilizing unsegmented pictures and increments to 85.33% when utilizing entirely divided pictures [9].

E. Nasr-Esfahani et al. introduced a work on Malignancy acknowledgment by investigation of clinical pictures utilizing Convolutional Neural System. The CNN classifier, which is set up by enormous number of preparing tests, perceives between malignancy and kind hearted cases. To the extent the exactness of assurance, the outcomes exhibit that the proposed strategy is predominant in relationship with the cutting-edge strategies [10].

3. Methodology

In this paper a general method of detection of boundary of the lesion is performed. The method involves using morphology and wavelets to extract proper boundary by resizing the image. In this area, we present the system embraced in our proposed approach for the division of sores from Dermis within the sight of relics like Dermis lines, vessels, gel and hairs. The proposed calculation comprises of three phases which incorporates: pre-preparing stage for picture improvement alongside hair location/inpainting for antique expelling; division of the injury territory utilizing wavelet-based methodology and afterward at long last post processing stage for improving division results.

In this work the data set is taken from DERMIS and DERMQUEST webs. More than 50 images were tested and boundary detection is been successful.

A. Morphological approaches for images:

A morphological activity is (thoughtfully) characterized by moving a window over the parallel picture to be adjusted, so that it is inevitably focused over each picture pixel, where a nearby consistent activity is performed. Opening expels little items from the frontal area (generally taken as the splendid pixels) of a picture, setting them out of sight, while closing evacuates little gaps in the forefront, changing little islands of foundation into closer view. These methods can likewise be utilized to discover explicit shapes in a picture.

Understand that morphology in this research is explicitly with regards to dermatology. Morphology in dermatology is characterized as the general appearance and structure of a specific Dermis sore in any case of its capacity, etiology or pathophysiology. Morphology can be additionally isolated into essential and auxiliary morphology. As indicated by, Dermis injuries can be gathered into two classifications, essential and auxiliary morphologies. Essential morphologies contrast in shading or surface furthermore, are either obtained from birth, for example, moles or Dermis colorations, or during an individual's lifetime, as for the situation of irresistible ailments and unfavorably susceptible responses. Optional morphologies then again are injuries that outcome from essential Dermis sores, either as a characteristic movement or on the other hand because of disturbing the essential sore. Because of this nature, the morphologies have been found to be essential for classification.

In spite of the tremendous measure of writing examining Dermis sores and morphology, various sources will in general rundown various arrangements of morphologies. Despite these various postings, the portrayal of every morphology is reliable among various references, so any of the references can be chosen and used. For this examination, a subset from the arrangement of morphologies as recorded by [Bic12a] and appeared in Fig. 1 is being utilized. This subset of morphologies was picked to expand the utilization of the information assembled for the exploration. [Wel08a] gave the accompanying brief portrayal of the essential morphologies recorded by [Bic12a]:

- Bulla - a liquid filled delineated height of Dermis that is over 0.5 cm in distance across
- Macule - a little level region with shading or surface contrasting from encompassing Dermis
- Nodule - a strong mass in the Dermis that is touched or raised and is, in distance across both width and profundity, more noteworthy than 0.5 cm
- Papule - a strong rise of Dermis that is under 0.5 cm in distance across
- Patch - a huge level territory with shading or surface varying from encompassing Dermis
- Plaque - a raised region of Dermis without considerable profundity yet is more prominent than 2 cm in distance across
- Pustule - an apparent aggregation of discharge in Dermis
- Vesicle - a liquid filled delineated height of Dermis that is under 0.5 cm in breadth
- Wheal - a white raised compressible and blurred region regularly encompassed by a red flare

As the depictions for every morphology show, morphology in the dermatological sense isn't just alluding to shape yet in addition alluding to visual characteristics, for example, size, shading, surface, and height. Moreover, since no metric information will be used in this examination, the framework is constrained in segregating between morphologies. Another restriction is that this examination centers around Dermis injuries that are marked as one morphology just, though cases wherein a specific Dermis injury can be characterized under numerous morphologies (for example a maculopapular rash has a place with both macule and papule) are not utilized in this examination.

B. WAVELETS FOR IMAGE PROCESSING:

Wavelets are a more general way to represent and analyze multiresolution images. Wavelets are very useful for image compression (e.g., in the JPG-2000 standard) and removing noise. The basic approach to wavelet-based image processing is given as follows: [14]

- i. Two-dimensional wavelet transform of the given image is calculated using the formula.
- ii. The transform coefficients are adjusted automatically if the criteria are not reached
- iii. Then inverse wavelet transform is computed.
- iv. The obtained results are evaluated and compared for efficient disease identification.

The wavelet transform has comparable properties to Fourier transform as a numerical strategy for Dermis sores examination, the essential contrast between both is that wavelets are restricted in both time and recurrence, while the standard Fourier transform is just limited in recurrence [14]. At the point when computerized Dermis sore images are seen or prepared at different goals, the Discrete Wavelet Transform (DWT) is the scientific device

of decision. Being a productive and exceptionally natural system for the portrayal and capacity of multi-resolution archive pictures, the DWT gives incredible understanding into a Dermis sores spatial and recurrence quality.

The wavelet transform is essential to give a minimal portrayal of Dermis sores that are constrained in time and it is extremely useful in depiction of edge and line that are exceptionally restricted.

Mathematically Discrete Wavelet transform denoted by $w(j, k)$ is given as,

$$w(r, s) = \int_p f(p)2^{\frac{p}{2}}\psi(2^p p - s)dt \tag{1}$$

The method is evaluated using a fringe error calculated between transformed image and reconstructed image.

4. Results And Discussion

The proposed method is the combination of morphology and wavelets resulted in good identification of borders of the lesion region, which will be useful for easy diagnosis for medical practitioners.

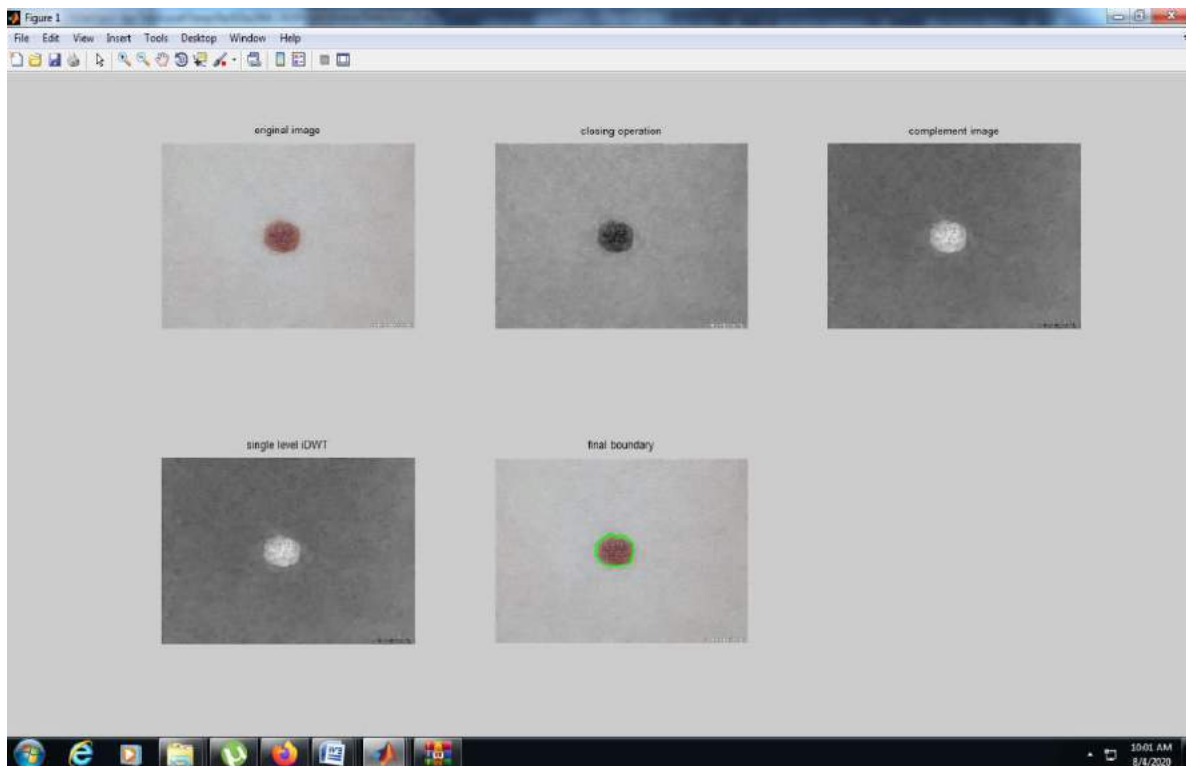


Fig. 1 Morphological operations and wavelets for fringe detection of a Dermis lesion of image Th3.jpg with fringe error 1.19%

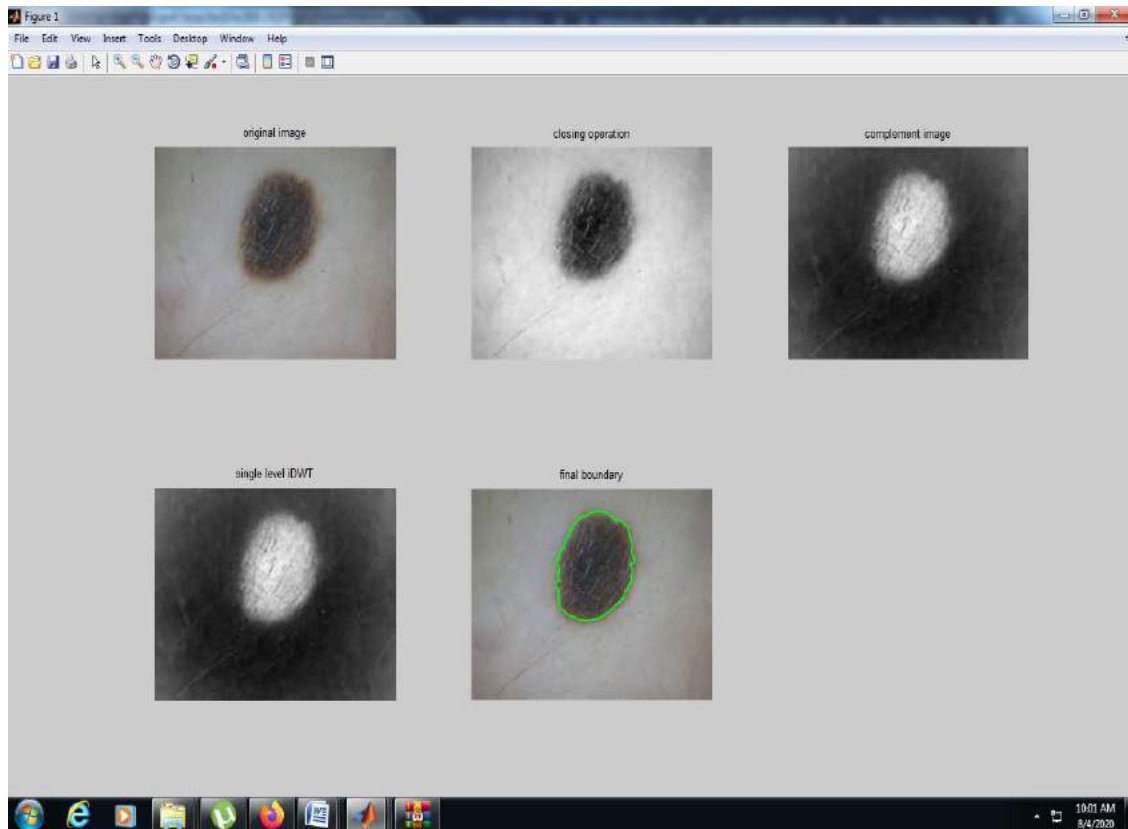


Fig. 2 Morphological operations and wavelets for fringe detection of a Dermis lesion of an image Th5.jpg with Fringe error 2.003%

The percentage border error is given by

$$FE = \frac{Area(AF \oplus MF)}{Area(MF)} 100\% \tag{2}$$

FE, AF, and MF stand for fringe error, Automatic fringe and Manual fringe, respectively. Automatic fringe is the binary image of the lesion border obtained by the propose method, Manual fringe is the binary image of the manual border of the lesion, \oplus is the Exclusive-OR operation that gives the pixels for which the Automatic fringe and Manual fringe disagree, and Area(I) denotes the number of pixels in the binary image I. The proposed method is tested on a set of 100 dermoscopy images.

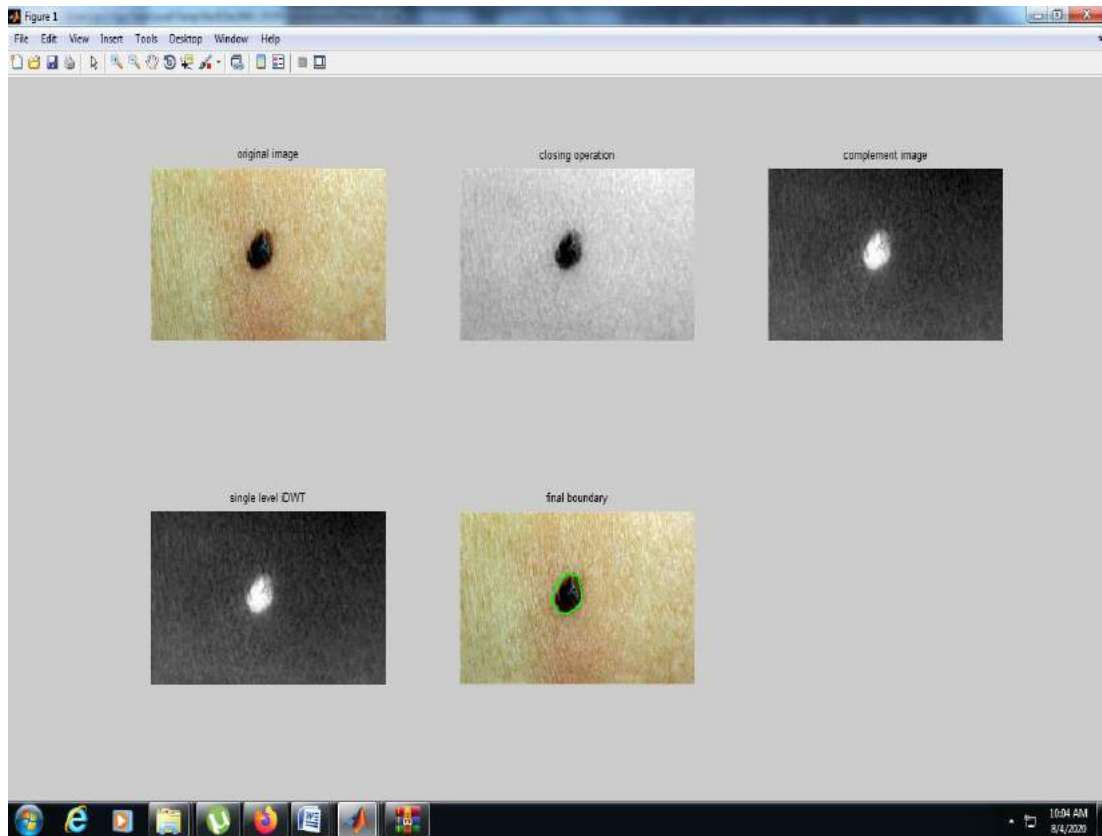


Fig. 3 Morphological operations and wavelets for fringe detection of a Dermis lesion of an image Th4.jpg with fringe error 2.34%

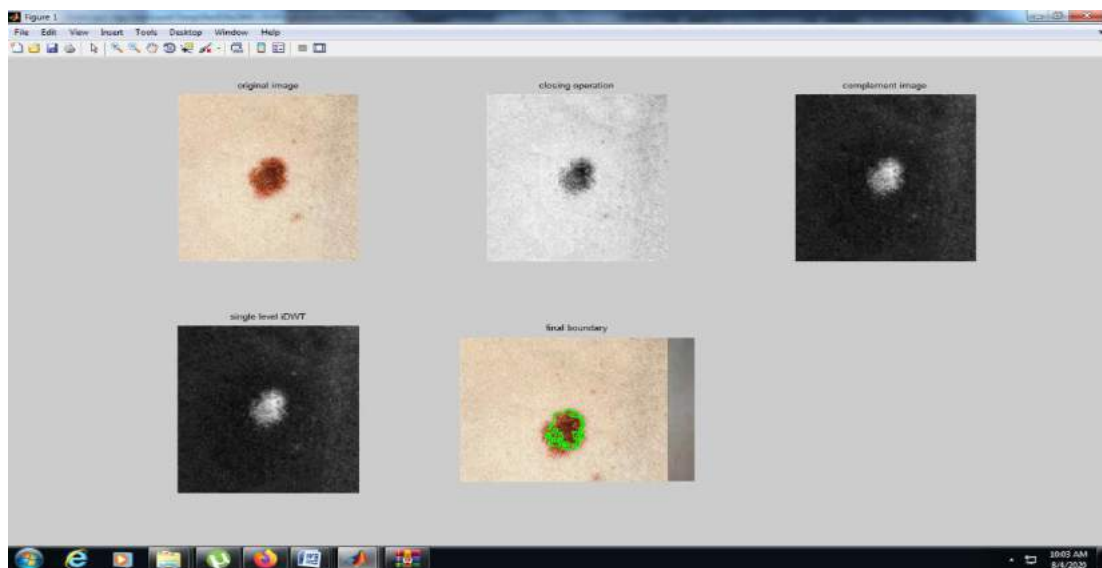


Fig. 4 Morphological operations and wavelets for fringe detection of a Dermis lesion of an image Th11.jpg with fringe error 3.1%

5. Conclusion

A new strategy dependent on wavelet transform and morphology is introduced in the current work for sore fringe identification of dermis sore from dermoscopy pictures. The fringe miscalculation is shown for the pictures in which hair ventures into the canker. The inconvenience of the introduced technique is that it can't distinguish more than one sore in a picture. The proposed strategy can be created so as to diminish the fringe mistake of sore where hairs ventures into the injury and furthermore it could recognize more than one sore in picture.

References

1. R. L. Siegel, K. D. Miller and A. Jemal, "Cancer statistics, 2016," *CA: a cancer journal for clinicians*, vol. 66 (1), pp. 7-30, 2016.
2. American Cancer Society, "Malignancy Dermis Cancer," 20 March 2015. [Online].
3. [3] Nikhil Cheerla and Debbie Frazier, "Automatic Malignancy Detection Using Multistage Neural Networks," *International Journal of Innovative Research in Science, Engineering and Technology*, vol. 3(2), pp. 9164 – 9183, 2014.
4. Santosh. A and Sadashivappa. G, " Statistical Analysis of Dermis Cancer Image–A Case Study," *Int. J Electron Commun Eng.*, vol. 3(3), pp. 1-10, 2014.
5. Jeyanthi Kamalakkannan, Bhavani Sankari. S, "Detection of Malignant Dermis Cancer Based on Automated Image Analysis and Classification", *International Journal of Innovative Trends and Emerging Technologies*, vol. 1(1), May 2015.
6. Hutokshi Sui, Manisha Samala, Divya Gupta, Neha Kudu, 'Texture Feature Extraction for Classification of Malignancy,' *International Research Journal of Engineering and Technology*, vol.5(3), pp. 1026-1029, 2018.
7. M.R.Patil, AboliGhonge, Mansi Dixit, Deep Joshi, "Non-Invasive ABCD Monitoring of Malignant Malignancy Using Image Processing in MATLAB," *International Research Journal of Engineering and Technology*, vol. 4(3), pp. 1074-1081, 2017.
8. Terrance DeVries, Dhanesh Ramachandram, "Dermis Lesion Classification Using Deep Multi-scale Convolutional Neural Networks," *Computer Vision and Pattern Recognition*, arXiv:1703.01402v1 [cs.CV], 4 Mar 2017.
9. Adri`a Romero L`opez, "Dermis Lesion Detection from Dermoscopic Images Using Convolutional Neural Networks," *Universitat Polit`ecnica de Catalunya, BarcelonaTech*, January 2017.
10. E. Nasr-Esfahani, S. Samavi, N. Karimi, S.M.R. Soroushmehr, M.H. Jafari, K. Ward, K. Najarian, "Malignancy Detection by Analysis of Clinical Images Using Convolutional Neural Network," *Annual International Conference of the IEEE Engineering in Medicine and Biology Society*, 2016, pp. 1373-1376.
12. ISIC, "ISIC Archive : The International Dermis Imaging Collaboration: Malignancy Project," *ISIC*, 5 Jan 2016. [Online]. Available: <https://isicarchive.com/#>. [Accessed 20 Jan 2018].
13. Mariam A.Sheha, MaiS.Mabrouk, AmrSharawy, "Automatic Detection of Malignancy Dermis cancer using Texture Features," *International Journal of Computer Applications*, vol. 42(20), pp. 22-26, 2012.
14. Chang T, Kuo CJ. Texture analysis and classification with tree-structured wavelet transform. *IEEE Trans. Image Process.* 1993;2(4):429-441.
15. Manish T. Wanjari, Dr. Mahendra P. DHore, "Document image segmentation using wavelet and Gabor filter techniques," *IOSR Journal Computer Engineering (IOSR-JCR)*, NCRTCSIT-2016.

Optimisation of Cloud Seeding Criteria Using a Suite of Ground-Based Instruments



P. Sudhakar, K. Anitha Sheela, and M. Satyanarayana

Abstract All fresh-water, whether on the surface or underground, comes from the atmosphere in the form of precipitation. Nevertheless, a large volume of water present in the clouds is never transformed into precipitation on the ground. This has prompted researchers to explore the possibility of augmenting water supplies by the use of “cloud seeding” technique to initiate and accelerate the precipitation process. The seeding technique is expected to provide an increase in precipitation from the cloud and provide rain almost immediately at the targeted region/ location. This is done by dispersing suitable substances into the cloud that serve as cloud condensation or ice nuclei. Although many projects around the world have successfully demonstrated a considerable increase in precipitation due to seeding, majority of the projects, however, yielded inconclusive results on precipitation enhancement [1]. The reason for this inconsistency is that the physical mechanisms of aerosol effects on cloud and precipitation development are much more complex than anticipated earlier. There are many ongoing operational cloud seeding programs and the number has been steadily increasing with time. Despite this, there is still a great need for more intensive FIELD experiments to standardize the cloud seeding technology for increased reliability and enhancement of precipitation from clouds. The technology of rain enhancement is based on the science of cloud physics with major linkages reaching

P. Sudhakar (✉)

Department of ECE, Geethanjali College of Engineering & Technology, Cheeryal (V), Keesara (M), Hyderabad 501301, India
e-mail: sudhakar.lidar@gmail.com

K. A. Sheela

Department of ECE, JNTUH College of Engineering Hyderabad (Autonomous), Hyderabad 500085, India
e-mail: kanithasheela@gmail.com

M. Satyanarayana

Ananth Technologies Ltd (ATL), Hyderabad 500081, India

Department of ECE, VNR Vignana Jyothi Institute of Engineering & Technology, Hyderabad 500090, India

M. Satyanarayana

e-mail: drsatanarayana.malladi@gmail.com

© Springer Nature Singapore Pte Ltd. 2021

T. Laxminidhi et al. (eds.), *Advances in Communications, Signal Processing, and VLSI*, Lecture Notes in Electrical Engineering 722, https://doi.org/10.1007/978-981-33-4058-9_33

373

into mesoscale and boundary layer meteorology, weather forecasting, diffusion and turbulence, physical chemistry, aerosol physics, statistics, and instrumentation [2–4]. In this paper, we present the details of the multi-wavelength dual polarization lidar being used and the methodology to monitor the various cloud parameters involved in the precipitation process.

Keywords Cloud seeding · Precipitation · Rain enhancement · Dual polarization lidar

1 Statement of the Proposed Research and Method of Implementation

The success of the cloud seeding process can be predicted with confidence if the processes and the chain of events involved, leading to precipitation are fully understood and monitored in real time. It is proposed to monitor the cloud characteristics and measure these events in real time to decide on the go/ no go criteria for seeding to increase the efficacy in inducing and increasing precipitation. One of the important criteria for the timing of the seeding is the knowledge of microphysical properties of the clouds in real time when the seeding of the material is done in the clouds. The direct monitoring of the ice water balance of the clouds will yield valuable information on the right conditions for seeding to obtain efficient precipitation. Background aerosol, water vapor, and other meteorological parameters also play a crucial role in the precipitation process involved in cloud seeding operations [5]. The main goal of the proposed work is to precisely measure the physical conditions and chain of events in precipitation development in real time using a suite of ground-based instruments consisting of cloud radar, polarization diversity and aerosol lidar, automatic weather station, and other supporting equipment. A series of field experiments are to be conducted in the real-time conditions of the clouds. From these experiments, the right conditions of the clouds for seeding will be optimized. From the data obtained on the optimized seeding conditions, it is proposed to make the cloud seeding technology as a regular operational and reliable technique for rain enhancement.

2 Objective of the Research

One of the main goals of the proposed research on rain enhancement is to firmly establish the physical chain of events in precipitation development so that the perturbations both intentional and inadvertent can be understood and quantified through field experiments. The research addresses the common fundamental understanding of aerosol, cloud, and precipitation processes that helps progress in other important research areas including quantitative precipitation forecasting. The research also envisages fundamental research on seeding materials through experimental investigations [6].

3 Detailed Methodology

Field experimentations are required for monitoring the nearby aerosols, meteorological parameters, and cloud chattels in the real-time atmosphere for optimizing the standards for seeding to enhance the precipitation at the stressed region. Towards this, it is proposed to conduct a series of cloud seeding experiments in arid and semiarid regions to establish the optimized conditions of the cloud for seeding. It is proposed to use also a Multifunctional Dual Polarization Llidar in measurements of the microphysical characteristics of clouds, aerosols, and water vapor in the laboratory [7, 8]. The Lidar provides simultaneous measurements on cloud structure, particles, humidity, temperature, and also, more importantly, the background aerosol system which plays an important role in cloud formation and precipitation. The formation of the cloud droplets from the aerosols after seeding depends on many factors of the seeding material including the chemical composition, number concentration, size distribution, etc. The meteorology and topography of the location are also important for seeding operations. As such the following commercially available ground-based instruments are proposed to be used for real-time monitoring and optimization of seeding methods.

4 Multi-Wavelength Dual Polarization LIDAR and Cloud RADAR

- It is proposed the above for integrated measurements of cloud characteristics and precipitation process and to measure the Temporal and Spatial variation of size distribution functions of aerosols, microphysical properties of Clouds and Water Vapor, the Nd: YAG dual polarization lidar will be used [9].
- The system is transportable and can be setup within 24 h at the required location.
- It can make the measurements both day and night by having sufficient signal-to-noise ratio, even in broad daylight conditions.
- The required software for characterizing the aerosols and clouds and measurement of water vapor with good vertical resolutions in real time is provided as required for the cloud seeding program.
- The whole equipment will be fitted on a Mobile Platform in a Truck with a facility to enclose the equipment in an air-conditioned environment along with a Power Generator facility to carry out the research experiments at different locations.
- It is proposed to conduct an investigation on the clouds using Multi-wavelength Dual Polarization Lidar and Cloud Radar (35 GHz/ 95 GHz) during the period of cloud seeding operations over the targeted areas.
- Measurement of the size and distribution of cloud condensation nuclei (CCN) that is released artificially after burning the flares, containing Silver iodide/ Dry ice/ Calcium Chloride are carried out.

- The size distribution can be optimized after different trials of success.
- The occurrence frequency of various clouds will be derived using the Cloud RADAR data collected during the period of cloud seeding program [10].

5 Integration of Data Obtained by LIDAR and Cloud RADAR Simultaneously in the Field for Optimization of Seeding Methods

- The results obtained from the simultaneous observations of both RADAR and LIDAR can be used to understand the influence of size distribution of aerosols on the size of the cloud droplets.
- As the Multi-wavelength Dual polarization lidar able to distinguish the type of aerosol present at different altitudes the data of different types of aerosols present at different altitudes can be used to understand the influence of the various types of CCN on the rainfall enhancement process. The results obtained in the entire observations will be analyzed and the conditions for optimization of cloud seeding techniques will be arrived.

Automatic Weather Station (AWS)

Standard commercially available AWSs are to be located at different stations in the target area to obtain real-time information on various meteorological parameters when the cloud seeding field experiments are conducted

Seeding methodology

It is proposed to use the aircraft and drone platforms to seed the clouds with selected materials at the appropriate altitude and time. Aircraft seeding is a well established procedure and is being applied for the purpose in many countries successfully. Recently, drones are being used with additional advantages successfully for seeding operations in USA.

It is thought-provoking to recognize that wide-ranging information is accessible in ancient *VEDIC* literature on the usage of '*HOMAM*' for inducing rain at the vital sites. The method comprises the spreading of various materials into the cloud region by burning the material in fire ponds, especially setup on the ground. It is proposed to conduct simultaneously the seeding operations from the ground using this technique also. This technique is expected to be very expedient and cost-effective for seeding clouds.

6 Conclusion

The design details of a dual polarization lidar used for characterizing the microphysical properties of clouds are described. The methodology used in the characterization of clouds to understand the precipitation processes in cloud seeding techniques is described in this research article.

References

1. Zoljoodi M, Didevarasl Ali (2013) Evaluation of cloud seeding project in Yazd Province of Iran using historical regression method. *Nat Sci* 5(6):1006–1011. doi:<http://dx.doi.org/10.4236/ns.2013.59124>
2. Krishnakumar et al (2014) Lidar investigations on the optical and dynamical properties of the cirrus clouds in the UTLS region at a tropical station Gadanki, India (13.5°N, 79.2°E)". *J Appl Remote Sens* 8(1):083659. doi: <https://doi.org/10.1117/1.jrs.8.083659>
3. Krishnakumar V, Satyanarayana MV, Radhakrishnan SR, Mahadevan Pillai VP, Raghunath K, Venkat Ratnam M et al (2011) Investigations on the physical and optical properties and their role in the nucleation of cirrus clouds using lidar at Gadanki (13.50 N, 79.20E). *J Appl Remote Sens* 5:053567. doi: <https://doi.org/10.1117/1.3662877>
4. Meenu S, Rajeev K, Parameswaran K (2011) Regional and vertical distribution of semitransparent cirrus clouds and cloud top altitudes over tropical Indian region derived from CALIPSO data. *J Atmos Solar Terr Phys* 73(13):1967–1979. doi: <https://doi.org/10.1016/j.jastp.2011.06.007>
5. Radhakrishnan SR, Satyanarayana M, Presennakumar B, Mahadevan Pillai VP, Murthy VS (2008) Measurement of water vapor in the lower atmosphere at a coastal station, Trivandrum (80 N, 770E) using a high resolution Raman lidar. *Indian J Radio Space Phys* 37:353–359
6. Drofa AS, Ivanov VN, Rosenfeld D, Shilin AG (2010) Studying an effect of salt powder seeding used for precipitation enhancement from convective clouds. *Atmos Chem Phys* 10(1): 8011–8023. doi: <https://doi.org/10.5194/acp-10-8011-2010>
7. Parameswaran K et al (2003) Lidar observations of cirrus cloud near the tropical tropopause: temporal variations and association with tropospheric turbulence. *Atmos Res* 69(1–2): 29–49. doi: <http://dx.doi.org/10.1016/j.atmosres.2003.08.002>
8. Sunilkumar SV et al (2003) Lidar observations of cirrus clouds near the tropical tropopause. *Atmos Res* 66(3):203–207. [http://dx.doi.org/10.1016/S0169-8095\(02\)00159-X](http://dx.doi.org/10.1016/S0169-8095(02)00159-X)
9. Sassen K (2000) Lidar backscatter depolarization technique for cloud and aerosol research. In: Mishchenko ML, Hovenier JW, Travis LD (eds.) *Light scattering by nonspherical particles: theory, measurements, and geophysical applications*. Academic Press, San Diego, CA, p 393
10. Göke S, Ochs III HT, Raube RM (2007) Radar analysis of precipitation initiation in maritime versus continental clouds near the Florida coast: Inferences concerning the role of CCN and giant nuclei *J Atmos Sci* 64:3695–3707

COVID-19 Social Distancing with Speech-Enabled Online Market Place for Farmers



D. Mohan, K. Anitha Sheela, and P. Sudhakar

Abstract Corona virus (COVID-19) has been rampant in most countries across the world, leading to a global crisis, and it has been so dangerous because of its ability to spread through any medium especially when there is physical contact of any object. So, this puts many people including the farmers and the customers at a bigger risk when they sell or buy products physically in a market place. This is a major challenge to an Indian farmer today to sell the product at the right price at the right time. Moreover, social distancing is the need of the hour, and hence, it is an even bigger challenge to monitor the market place to avoid physical contact. Also, many initiatives by governments, local bodies, and cooperative societies to eliminate the intermediaries are not turning effective due to the non-awareness, non-accessibility, ignorance, and ease of usage difficulties. Keeping the current pandemic situation in mind and social distancing being the need of the hour, this paper proposes a speech-enabled interactive voice response (SEIVR) wherein the farmer and the customer can sell and buy products online, i.e., without any physical contact. In the current technology era, online market platforms like Amazon, Flipkart, and Olx are effectively cutting short these supply-chain overheads by establishing a direct connection between buyer and seller. Hence, the proposed implementation of a speech-enabled interactive voice response (SEIVR)-based online market place for farmers which even ensure social distancing will help to reduce the spread of the virus. The objective of this work is to build an agriculture-based mobile application with speech-enabled interactive voice response (SEIVR) based on speech recognition application with the Telugu language as a case study.

Keywords COVID-19 · Corona virus · Agricultural information system · Voice-enabled mobile application · Speech recognition · Speech-enabled IVR · Sphinx · Acoustic model · Language model · Photic dictionary

D. Mohan (✉) · P. Sudhakar
ECM Department, Sreenidhi Institute of Science and Technology, Hyderabad, India
e-mail: mohan.aryan19@sreenidhi.edu.in

K. A. Sheela · P. Sudhakar
ECE Department, JNTUH College of Engineering, Kukatpally, Hyderabad, India
e-mail: kanithasheela@jntuh.ac.in

© The Editor(s) (if applicable) and The Author(s), under exclusive license
to Springer Nature Singapore Pte Ltd. 2021

S. Shakya et al. (eds.), *Proceedings of International Conference on Sustainable Expert Systems*, Lecture Notes in Networks and Systems 176,
https://doi.org/10.1007/978-981-33-4355-9_3875

1 Introduction

COVID-19, a deadly virus, has created a pandemic situation with its widespread outburst and put the entire world in a crisis. It has been so deadly and severe because of its ability to spread through any medium especially when there is physical contact involved. This has pushed us into a situation where social distancing has become a mandatory norm. With social distancing being the need of the hour, it has changed the way businesses are running especially in the field of agriculture where farmers sell products physically in a crowded market place. To avoid physical contact, it is imperative to adopt digital technology into the field of agriculture to avoid the spread of the deadly virus. Keeping the current pandemic situation in mind and social distancing being the need of the hour, this paper proposes a speech-enabled interactive voice response (SEIVR) wherein the farmer and the customer can sell and buy products online, i.e., without any physical contact. In this context, the adoption of information communication technology-enabled information support systems for supportable development in the agricultural expansion is very important for developing countries such as India, where agriculture is still the Indian economy's most significant field. Given the country-wide expansion of telephone and mobile networks, with easy access to smart mobile devices and access mobile data services, initiatives are now being introduced by both the government and the private sector [1] to develop and fund smart agriculture-related solutions.

With a similar context, the work is presented on developing a speech-based mobile application for “*Speech-Enabled IVR-Based Online Market Place for Farmers*” in the Telugu language. A robust automatic speech recognition (ASR) engine automatically recognizes voice queries in the form of spoken commodity names in the Telugu language at runtime, to generate text outputs for commodity variety collection, product searching, etc.

The application developed serves end-users both in rural and urban areas, especially those who are not computer literate or find it hard to access the same data during busy working hours. In reality, the rural end-users of this application include mostly semi-literate, non-tech savvy farmers, and agro-producing sellers who mainly earn their livelihood by selling farm-grown products on local markets. In comparison, price knowledge for customers helps smart customers to have equal offers when purchasing agricultural commodities. This speech-based mobile application is therefore unique in its way to encourage both farmers, and consumers through one single application.

This paper is organized as follows, and Sect. 2 explains the related work of the existing system; Sect. 3 discusses proposed work and key issues on application design, and it describes the application overview and architecture. Section 4 deals with the framework for designing a speech recognition system. Section 5 illustrates a detailed result analysis and assessment study. Finally, conclusions were made from the obtained results which are depicted in Sect. 6, and future directions for the expansion of this work presented in Sect. 7.

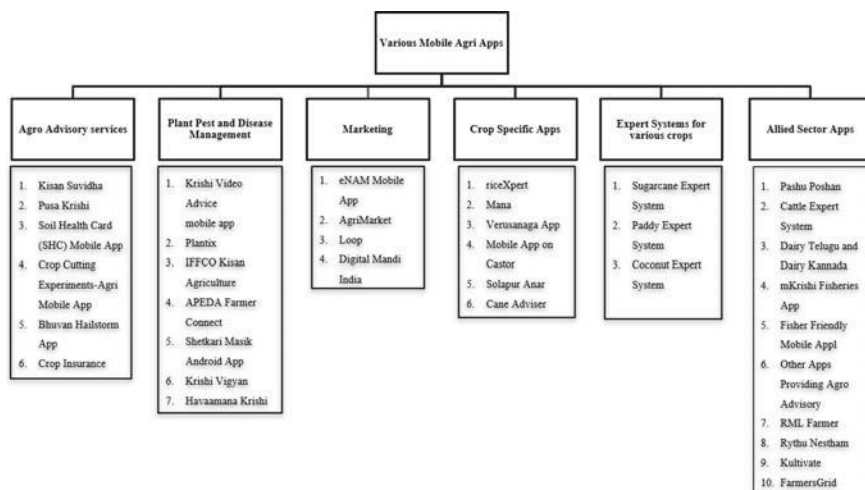


Fig. 1 Available mobile applications in indian agriculture and allied sectors [2]

2 Related Work

Currently available mobile applications in the Indian agriculture sector, the government of India, for the benefit of farmers and other stakeholders, has launched a range of online and mobile-based applications to disseminate information on agricultural-related activities, free of charge. These in the “mkisan.gov.in” Web site. There are also applications established by agricultural institutions, private sector, non-governmental organizations.

All these existing applications are menu-driven/touch-tone keypad-based systems, which is not easily handled by low literacy farmers (Fig. 1).

3 Proposed Work

The proposed work is primarily focused on building the user interface for agricultural-related technologies to support agriculture activities and conversational systems for low-literate users. More broadly it implements the speech recognition system, and its output is evaluated using created speech database by using real-time Google speech recognition engine as well as on CMU’s sphinx speech recognition engine (Fig. 2).

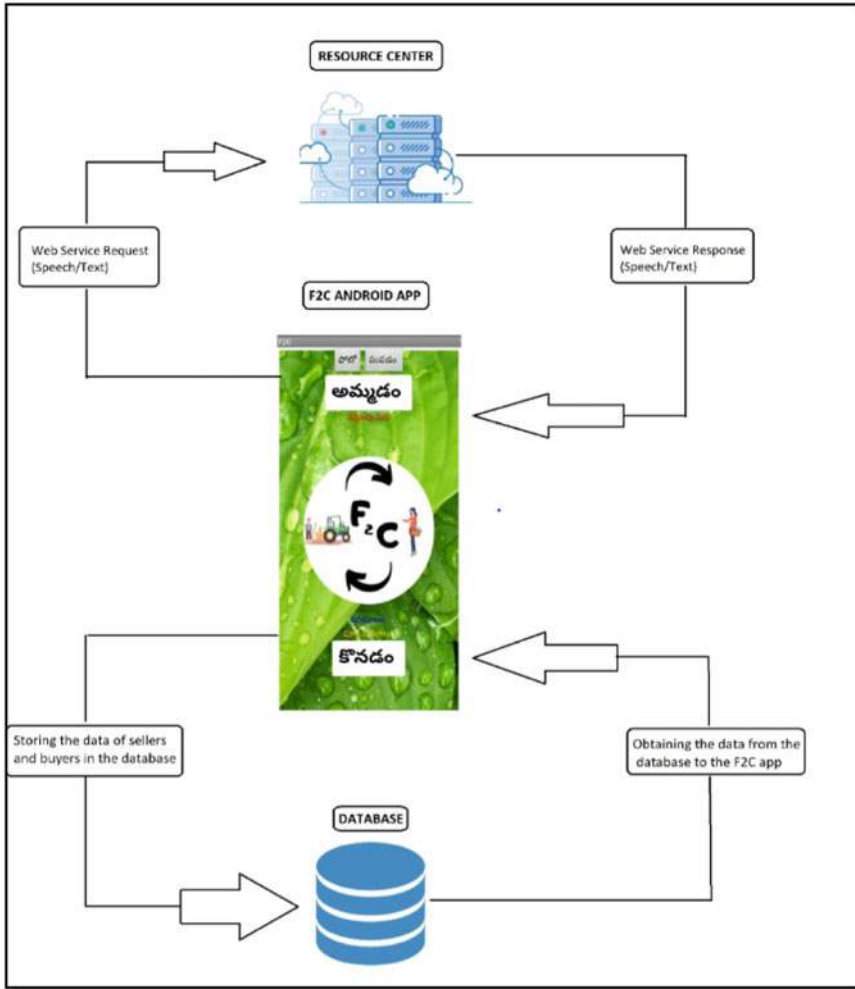


Fig. 2 General block diagram of the application

3.1 Key Issues on Application Design

Major issues being discussed and decided during the design of the developed application are as follows, and connecting stakeholders are a simple, responsive interface with an efficiently configured core framework allows for easy use by all stakeholders (government department, farmer, consumer) and therefore communicating with each of them equally. Access modality in various access modalities like touch-type-listen, speak-see, and speak-listen are included in the design to attract literate as well as semi-literate end-users. User preferences for language, input-output modality, service

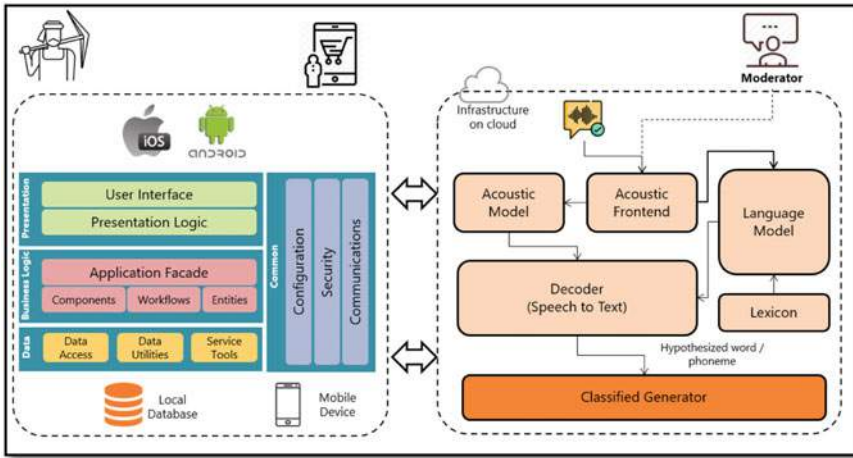


Fig. 3 Technical architecture

type, etc., are recorded while user registration and maintained until the next change. The content quality design should ensure completeness, reliability, and timeliness (important for the agriculture domain) of the information to be provided. The core technology such as application-based colorful user interface is underlying client-server architecture, and the latest ASR technology in the application core to add flexibility and ease of access.

3.2 APPLICATION Overview and Architecture with Detailed Process Flow

3.2.1 Technical Architecture

The overall design of the mobile application depends on three basic components, namely Android-based user interface software, Web service to which the application communicates, and An authentic online information source. Figure 3 demonstrates the entire framework architecture with data flow within the core modules.

3.2.2 Application Flow

When the farmer opens the Application –home screen with a mike button (ready to supply message), then by one-click—application collects details (product name, quantity, and price). Next in interactive mode farmer responds to simple questions in native language (one-word answers). The application processes speech inputs

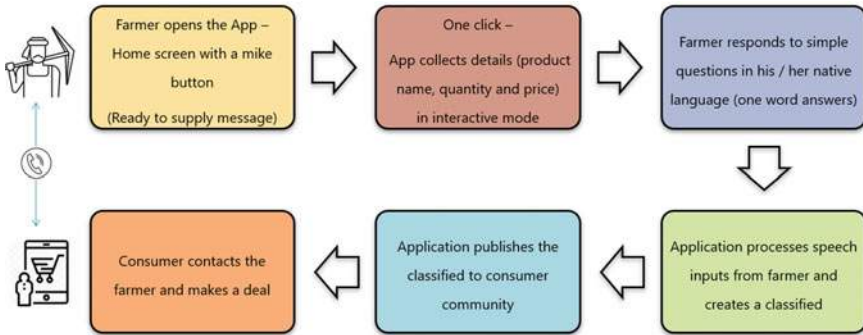


Fig. 4 Application flow

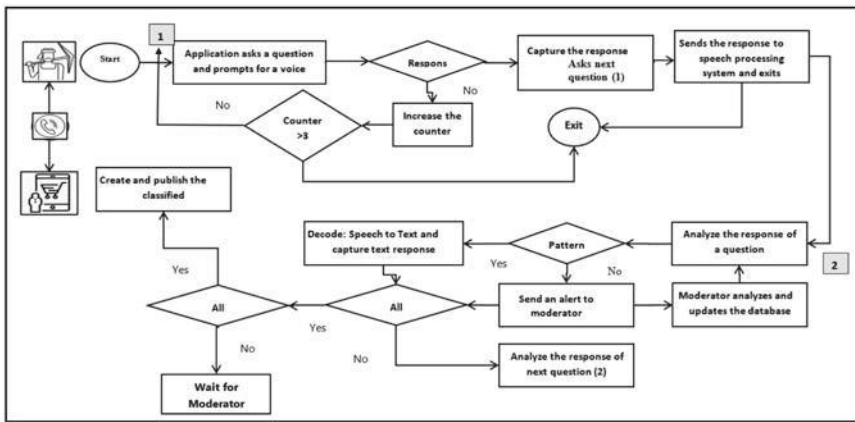


Fig. 5 Detailed process flow

from the farmer and creates a classified then publish the classified to the consumer community. The consumer contacts the farmer and makes a deal (Figs. 4 and 5).

4 Frame Work for Designing Speech Recognition System

CMU’s Sphinx has been primarily used as a proof of concept [3] for our proposed designed mobile Application, i.e., “Speech-Enabled IVR-Based Online Market Place for Farmers mobile Application” (Fig. 6).

Stages involved in the design of speech recognition system [4] are:

- Stage 1: Preparation of Speech database
- Stage 2: Design of the Vocabulary
- Stage 3: Design of the Grammar Rule

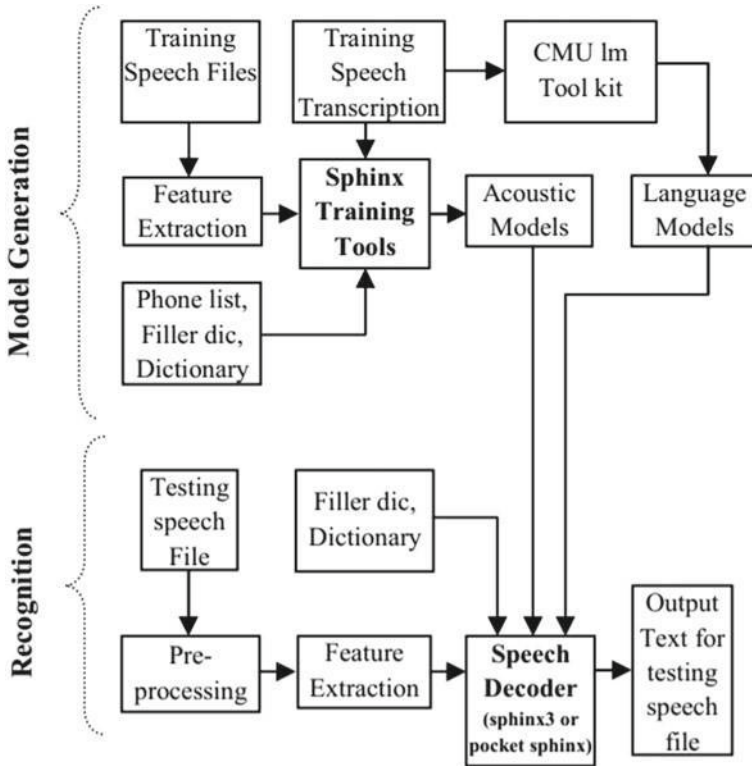


Fig. 6 Model generation diagram for speech recognition system

Stage 4: Generation of Acoustic Model

Stage 5: Generation of Language Model.

The acoustic model (AM) and language model (LM) are generated with the help of a training database using sphinx training tools. The sphinx decoder (Sphinx-3) performs speech recognition.

4.1 Database Preparation

The agricultural data collection process is for data collection primarily aims to collect isolated words such as rice, wheat, vegetable names, quantity, and price (Fig. 7).

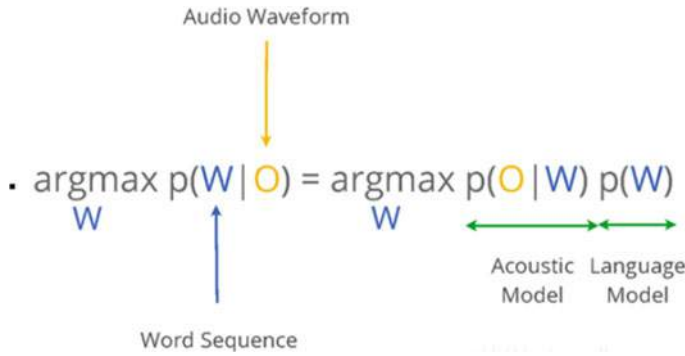


Fig. 7 Mathematical description of speech recognition system [15]

4.1.1 Design of the Vocabulary

Phonemes are important speech sound units for any language. So, to have a Telugu language phone list is prepared and it should contain all the phonemes of Telugu varnamala with the help of the Baraha tool [6, 7].

4.1.2 Design of the Grammar Rule

Dictionary is known as the mapping table which maps a word to a sequence of phones. It is important in performing speech recognition. All the unique words of the training and testing speech file transcriptions are included in the phonetic dictionary [8, 9].

4.2 Feature Extraction

The process of extracting vocal tract parameters form the speech signal is known as feature extraction. The main purpose of extraction of the feature is to generate the sequence of vectors describing the speech signal’s spectral and temporal nature.

Generating AM and LM model during the training, mel frequency cepstral coefficients (MFCC) are used [10–12].

4.3 Acoustic Model (AM)

The acoustic model can be known as the phoneme model because the output of the acoustic model is “phone sequence.” The acoustic model gives the likelihood of various phonemes at different time instant [4, 13, 14].

4.4 Language Model (LM)

The language model gives the probability of appearing one phone after another phone [4]. This work language model is generated using the CMU SLM tool kit [13–15].

5 Results

This work has been carried with real-time Google voice search as well as with CMU’s Sphinx speech recognition system. The testing was carried out on 20 farmers of which 10 were male farmers and 10 were considered female farmers. The speech recognition accuracy of the system is measured with the following performance metrics such as accuracy of recognized words and the rejection rate. The male and two female speaker’s speech samples were used in the deployed system’s testing. The way to carry out the speech recognition test is tabulated with few test samples (from the available speech database consider only a few speech samples for demonstration purpose).

(a) **Accuracy of recognized words is defined as follows:**

$$\text{Accuracy} = \frac{\text{No. of correctly recognized speech samples}}{\text{Total no. of test samples}} \times 100$$

The experimental results of only a few samples of speech are given below. They correctly recognized samples are denoted with T (True), and those speech samples that are not recognized are labeled as F (False). The experimental results of only a few samples of speech are given below. They correctly recognized samples are denoted with T (True), and those speech samples that are not recognized are labeled as F (False) (Tables 1 and 2).

(b) **Rejection Rate:** The error rate of total test samples that are being falsely recognized is calculated as follows: (Table 3)

$$\text{Accuracy} = \frac{\text{No. of correctly recognized speech samples}}{\text{Total no. of test samples}} \times 100$$

The graph of correct acceptance rate (CAR) versus correct rejection rate(CRR) shows that the word recognition rate is greater than the word rejection rate. The graph of the CAR CRR shows that the word recognition rate is greater than the word rejection rate (Fig. 8).

Table 1 Speech recognition test results

Words	No. of speech samples	1 st Speaker	2nd Speaker	3rd Speaker	4th Speaker	5th Speaker
గోధుమలు Word1	1	T	T	T	T	T
	2	T	T	T	T	F
	3	T	T	F	T	T
	4	T	T	T	T	T
	5	T	T	T	T	T
బిడు కిలోలు Word2	1	T	T	T	T	T
	2	T	T	T	T	T
	3	T	T	T	T	T
	4	T	T	T	F	T
	5	T	T	T	F	T
వంద రూపాయలు Word3	1	T	T	T	T	T
	2	F	T	T	T	F
	3	T	F	F	T	T
	4	T	T	T	T	T
	5	F	T	T	T	T

Table 2 Correct recognition accuracy

Words	1 st Speaker (%)	2nd Speaker	3rd Speaker (%)	4th Speaker (%)	5th Speaker (%)	Average accuracy (%)
గోధుమలు Word1	100	100	100	80	80	92
బిడు కిలోలు Word2	100	100	100%	60	100	92
వంద రూపాయలు Word3	60	80	100	100	100	88

5.1 Results Analysis Using CMU's Sphinx-3

The performance is evaluated with CMU's Sphinx-3. Speech recognition is carried out using a speech database of 20 farmers (Table 4).

M = Male; F = Female

Table 3 Rejection rate

Words	1 st Speaker (%)	2nd Speaker (%)	3rd Speaker (%)	4th Speaker (%)	5th Speaker (%)	Average accuracy (%)
గోధుమలు Word1	0	0	0	20	20	8
బదు కిలోలు Word2	0	0	0	40	0	8
వంద రూపాయలు Word3	40	20	0	0	0	12

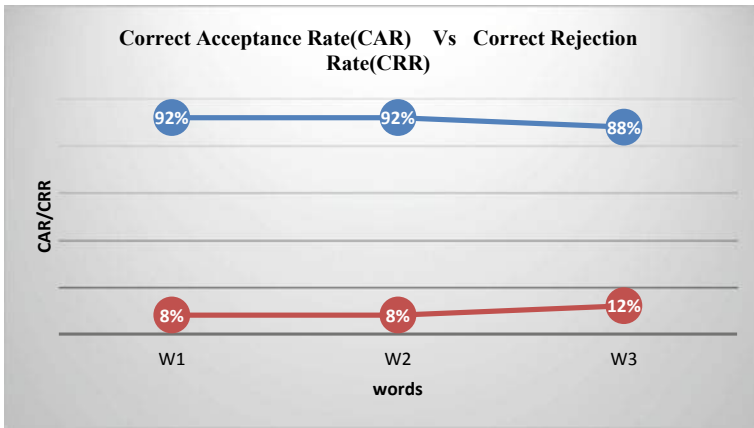


Fig. 8 Graph -CAR/CRR versus Words

Table 4 Speech recognition accuracy and rejection rates using CMU’s Sphinx-3 on male and female speech samples

Training	Testing	Accuracy of recognized words (%)	Rejection rate (%)
10 (M + F)	12 (M + F)	95	5
10 (M + F)	7F	90	10
10 (M + F)	8 M	97	3

Table 5 Speech recognition accuracy and rejection rate on male and female speech data

Training	Testing	Accuracy of recognized words (%)	Rejection rate (%)
10 (M + F)	12 (M + F)	92	8
10 (M + F)	7F	88	12
10 (M + F)	8F	95	5

5.2 Results from the Field Study with Real-Time Google Voice Search

Initially, the farmers are trained on the application for a few minutes, where the application's target and the task are demonstrated with the help of a real-time voice search application are explained. Then, collect the feedback from formers for the pre- and post-experiment, respectively (Table 5).

Result analysis is carried out in two conditions. One is a studio environment like no-noise condition, and the other one is in real-time where noise occurred. The speech recognition accuracy is higher for male speakers, and normally, it is lower for female speakers. The error rate is higher for women than for men. This could be because the pitch frequency is usually higher for female speakers and separating formant and pitch from female speakers' speech is a very difficult task.

The results of the collected data are shown in Tables. This work is carried out on the same speech data set for both the methods, and from observations of the assessment, results of the accuracies are somewhat higher and rejection rates are lower for CMU's Sphinx as it is a non-real-time setup and another one is the real-time environment, which is to be expected.

6 Conclusion

In this research work, an application is developed with the Telugu speech recognition module for the online market place for farmers. The application allows farmers to sell their products with a voice search system which even ensures social distancing will help to reduce the spread of the virus. Test results show more than 90 percent accuracies for both real-time and non-real-time scenario. Investigation results display that this application performs well for isolated word queries even in noisy field conditions.

7 Future Scope

This research can be expanded to process continuous word voice queries so that applications of live voice chat related to agriculture such as soil preparation and crop advisory can be built in a similar line as well.

Acknowledgements This is the collaborative research work of JNTUH and SNIST and funded by JNTUH under the scheme of “Collaborative research project under TEQIP-III.”

References

1. Saravanan, R., Bhattacharjee, S.: Mobile phone applications for agricultural extension in India. In: Worldwide mAgri Innovations and Promise For Future. New India Publishing Agency, pp. 1–75. (2013)
2. Mobile App Empowering Farmer-Published by the Director General on behalf of the National Institute of Agricultural Extension Management (MANAGE), Hyderabad, India. Vol.1 No.2 (2017)
3. CMU Sphinx project by Carnegie Mellon University, Pittsburgh, USA (2018). <https://cmusphinx.sourceforge.net/>
4. Picone, J.W.: Signal modeling techniques in speech recognition. Proc. IEEE **81**, 1215–1247 (1993)
5. Website <https://www.ffmpeg.org/>
6. <https://www.speech.kth.se/wavesurfer/>
7. Website <https://www.baraha.com/>
8. Ramana, A.V., Laxminarayana, P., Mythilisharan, P.: Real time ASR with HMM word models for Telugu. In: Proceedings of the International Conference on Recent Advances in Communication Engineering, Osmania University, December 20–23 (2008)
9. Deller, J.R., Hansen, J.H., Proakis, J.G.: Discrete Time Processing of Speech Signals. Prentice Hall, NJ (1993)
10. Benesty, J., Sondhi, M.M., Huang, Y.A.: Handbook of Speech Processing. Springer, New York (2008)
11. Volkmann, J., Stevens, S., Newman, E.: A scale for the measurement of the psychological magnitude pitch. J. Acoust. Soc. Am. **8**, 185–190 (1937)
12. The Carnegie Mellon University Statistical Language Modeling (SLM) Toolkit. https://www.speech.cs.cmu.edu/SLM_info.html
13. Aker, J.: Dial “A” for agriculture: using information and communication technologies for agricultural extension in developing countries. In: Conference on Agriculture for Development Revisited, University of California at Berkeley (2010)
14. Ram Reddy, M., Laxminarayan, P., Ramana, A.V.: Transcription of Telugu TV news using ASR. Published In: 2015 International Conference on Advances in Computing, Communications and Informatics (ICACCI) (2015)
15. https://medium.com/@Alibaba_Cloud/interspeech-2017-series-acoustic-model-for-speech-recognition-technology-c7cea164d654

A Frame Work for Decimal Floating Point Multiplier Using Vinculum Multipliers

G. Sreelakshmi^{1*}, Kaleem Fatima² and B. K. Madhavi³

DOI: 10.9734/bpi/nips/v13/6866D

ABSTRACT

IEEE Decimal floating point format play an important role in many financial, tax, account, commercial and internet based applications for which binary floating point format is not suitable. IEEE Standards Association approved a revision to the IEEE 754-1995 format to IEEE 754-2008 which includes specifications for DFP formats and operations. This paper broadens our past work on floating point multiplier utilizing proficient vinculum multipliers for mantissa multiplication and vinculum adders for adding exponents.

Keywords: Signed Digit; floating point multiplier; Urdhav Triyagbhyam; VBCD multipliers.

1. INTRODUCTION

Designing of hardware units for decimal arithmetic is a growing interest among researchers to achieve better latency and throughput for highly complex, accurate fast computation required in business and commercial applications. The basic binary number system can be used for decimal arithmetic operations but it requires conversions at both ends. These conversions will take significant amount of processing time which increase delay. Binary and Decimal number system supports integer and fractional parts in numbers and the system which uses fractional numbers may result in lack of accuracy which in turn has a greater negative impact on commercial, financial and tax applications. To solve these problems, interest in hardware design of decimal arithmetic is growing. This has led to the incorporation of specifications of decimal arithmetic in the IEEE-754 2008 standard for floating-point arithmetic [1]. With high performance and low resource usage it is expected to facilitate the implementation of business applications [2,3]. In DFP formats, multipliers play an important role in multiplication of mantissas. Among all arithmetic operations, multiplication is a complex operation. To speed up this operation, different methods were explained in the literature: Mixed Binary and BCD Approach [4], Multiplication via Carry Save Addition [5], Efficient Partial Product Generation [6], using Radix-10 multipliers [7,8,9], Parallel Decimal Multipliers [10,11,12,13], Compressor Trees for partial product reduction [14], Multi operand Decimal Adders [15,16], Redundant BCD and Signed Digit Adders [17,18], High performance Vedic decimal multiplier using binary to BCD converter [19], Vinculum BCD Multiplier (VBCD multiplier) [20,21]. In our earlier approach in [20], we had proposed a vinculum BCD multiplier based on Ten's complement method [22,23]. There also we used vertical cross wire method to generate partial products but the generated partial products were checked for +ve or -ve and if it is -ve, it was passed through Ten's complemented circuit and those products were given to the adder circuit.

In this paper floating point multiplication using vinculum multiplier is proposed. The number system we used is vinculum number system $\{-4, 5\}$ in which -ve numbers are represented in two's complement form [24]. In this method mantissas are multiplied using vinculum multipliers and exponents are added using vinculum adders and simple xor gate is used to identify sign bit of the resultant floating point

¹Geethanjali College of Engineering and Technology, Hyderabad, India.

²Muffakamjah College of Engineering and Technology, Hyderabad, India.

³Siddhartha Institute of Engineering and Technology, Hyderabad, India.

*Corresponding author: E-mail: gantisiriphd@gmail.com;

multiplier. Terms like NaN (Not a Number), overflow, underflow, and normalization were explained with the help of examples and simulation results were shown for various inputs.

The outline of the paper is organized as follows. In Section 2, review of decimal multiplication, vertical and cross wire method used in generation of partial products were discussed. In section 3 is focused on Vinculum binary coded multipliers and in section 4 Floating point multiplier is discussed along with Results, Conclusions and Future scope in section 5.

2. REVIEW OF BCD REPRESENTATIONS AND DECIMAL MULTIPLICATION

Vazquez and E. Antelo implemented a BCD multiplier using a recoding technique [7]. Signed-Digit (SD) Radix5 was employed to recode one of the input operands of the multiplier for the generation of the partial products. 6-Input LUTs and fast carry chains in Xilinx FPGAs were used to generate the building blocks and the decimal adders. Another SD-based decimal multiplier approach was proposed in [18]. The recoding was based on SD Radix10. BCD4221, 5211 and 5421 converters were used for the partial product generation. BCD4221-based compressors and adders were utilized in this approach. Although the BCD4221-based operations are similar to binary operation, the recoding and the different code conversions still lead to delay and resource cost.

- 1) SD Radix10 Recoding and Decimal multiplier based on BCD-4221/5221. In this method author assumed both multiplier and multiplicand to be unsigned BCD decimal integers of n digits each. The product $P = x * y$ is a non redundant BCD format with $2n$ digits. They used BCD4221/5211 in recoding [13].
- 2) Redundant BCD Representation and Decimal Partial Product Generation and Reduction:

In this method author used the same BCD 4221 and BCD5211 encodings to reduce partial product reduction [12,13]. It is passed through a pre-computed correction, binary CSA tree structure, decimal sum correction blocks and 3:2 compressors to get final BCD 8421 corrected sum with 2d digits [14,15].

- 3) Decimal Multiplier using Hybrid BCD codes: In this design author uses various types of BCD codes like 4221, 5211, ODDS, XS-3 and XS-6 codes [13] in which binary partial product reduction trees are non-fixed size.

The above method uses the weighted codes where conversions are required from one code to other code.

2.1 Vertical and Cross Wire Method (Urdhav Triyagbhyam)

It is an ancient method which is very simple and suitable for both binary and decimal number systems. It follows the principle of divide and conquer method where large module is divided into small modules of regular structures [20, 21]. This feature became an advantage in designing VLSI architectures. This method is very efficient for high speed applications [22]. Fig. 1 shows an example of two digit multiplication using Urdhav Triyagbhyam method.

3. Binary Coded Vinculum Multiplier

Multiplication mainly consists of three stages: the generation of partial products, the fast addition (reduction) of partial products and the final carry propagate addition.

3.1. Vinculum Number Representation

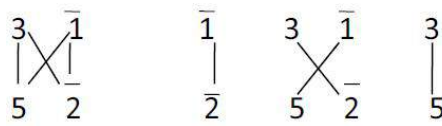
It's a Vedic mathematics of representing numbers. It allows only the digits from 0 to 5 either in +ve form or in -ve form. The higher order numbers from 6 to 9 must be converted into its equivalent numbers. In our method we selected the two's complement representation to denote -ve numbers. Instead of 6,7,8,9 the equivalent less complex digits $\bar{4}, \bar{3}, \bar{2}, \bar{1}$ are included in the set of vinculum

numbers. Therefore the new vinculum number system is $\{0, 1, 2, 3, 4, 5, \bar{4}\}$. These digits are represented in binary using 4 bits each [24].

3.2 Generation of Partial Products

Single digit VBCD multiplier is developed using LUT where all partial products are saved in memory as shown in Fig. 2. The maximum value of the partial product generated by single digit is +25 (5×5) and in BCD the maximum value generated is 81 (9×9). Very less combinations are available in proposed number system method which is simple and faster. This forms the basic multiplier for all other higher multipliers.

$$3\bar{1} * 5\bar{2} = 141\bar{2}$$



Step1: $\bar{1} \times \bar{2} = 02$
 Step2 & 3: $3 \times \bar{2} + \bar{1} \times 5 + 0 = \bar{1}1$
 Step 4: $3 \times 5 = 15 + \bar{1} = 14$
 Result: 141 $\bar{2}$

Fig. 1. Two digit multiplication using vertical cross wire method

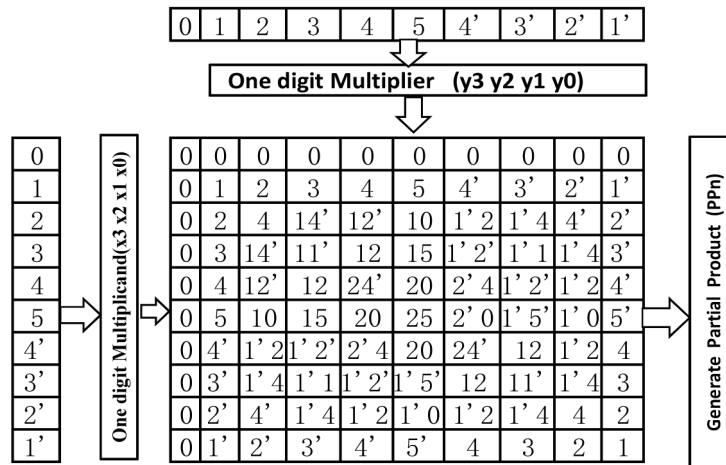


Fig. 2. One digit VBCD multiplier

3.3 Two and Four Digit VBCD Multiplier Architecture

Fig. 3 shows an example of 2 digit Vedic multiplier with the pictorial representation of addition of partial products along with their intermediate sum and carry bits of various levels to get their final product using VBCD parallel Adders [26]. Fig. 5 shows the basic 2×2 digit Vedic multiplier. Multiplier and Multiplicand are the two inputs to the system which produces four partial products. These four partial products are passed through parallel VBCD adder [26] for addition. The output of the adder is nothing but Final Result. The addition process is explained in next paragraph.

3.4 Example for 4 Digit Vedic BCD Multiplier

The above figure shows an example of 4 digit BCD multiplication using vertical cross wire method only by divide and conquer method. In this each digit is sub- divided into 2 digits and multiplication is performed as shown in above figure.

Fig. 7 shows the pictorial representation of addition of partial products their intermediate sum and carry bits of various levels to get their final product.

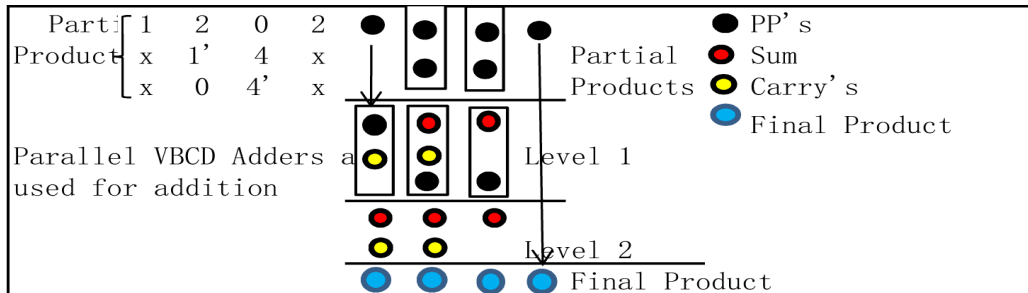


Fig. 3. Addition of partial products using VBCD parallel adders

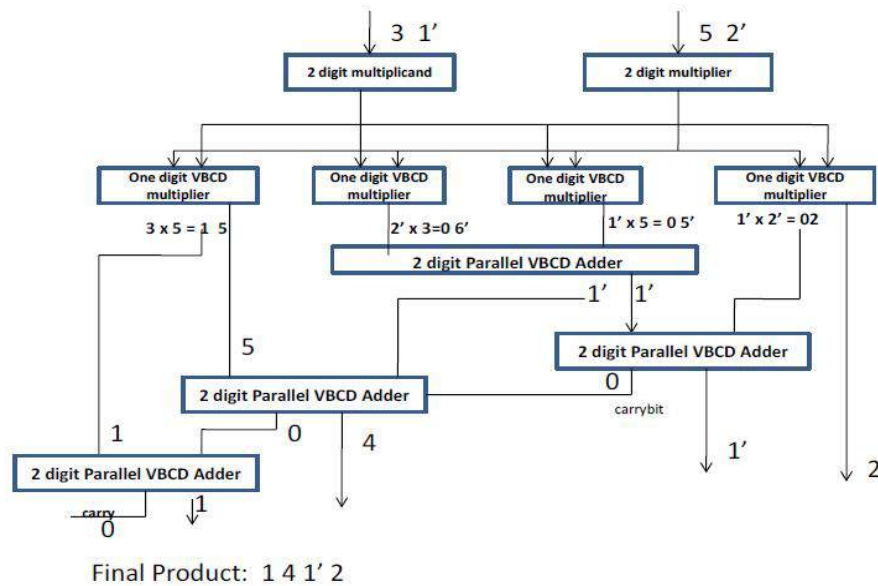


Fig. 4. Two digit Vedic BCD multiplier

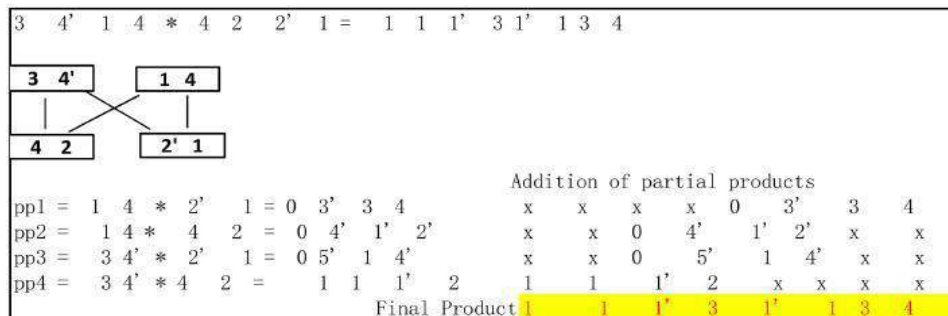


Fig. 5. Example for 4 digit multiplication

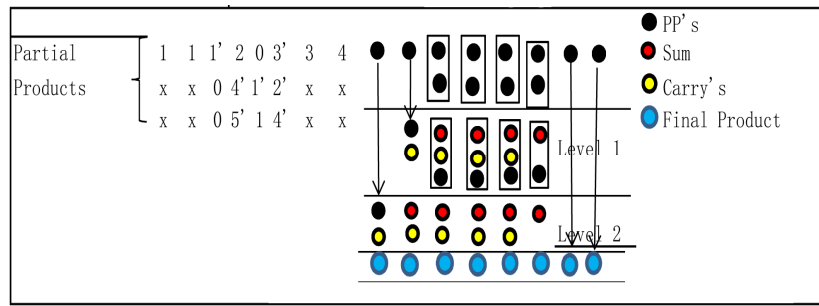


Fig. 6. Addition of partial products using parallel adder

It was observed that as the number of digits increases BCD adders increases but the number of levels or stages remains same because it generates only four partial products always.

3.4.1 Four digit VBCD multiplier architecture

Fig. 7 illustrates 4×4 multiplication using 2×2 digit Vedic multiplier (divide and conquer approach). Using this approach we will get only four partial product rows at any time there by addition becomes simple and faster. Four digit VBCD adders are used to add partial products and the output of the adder structure becomes Final product of 8 digits (32 bits).

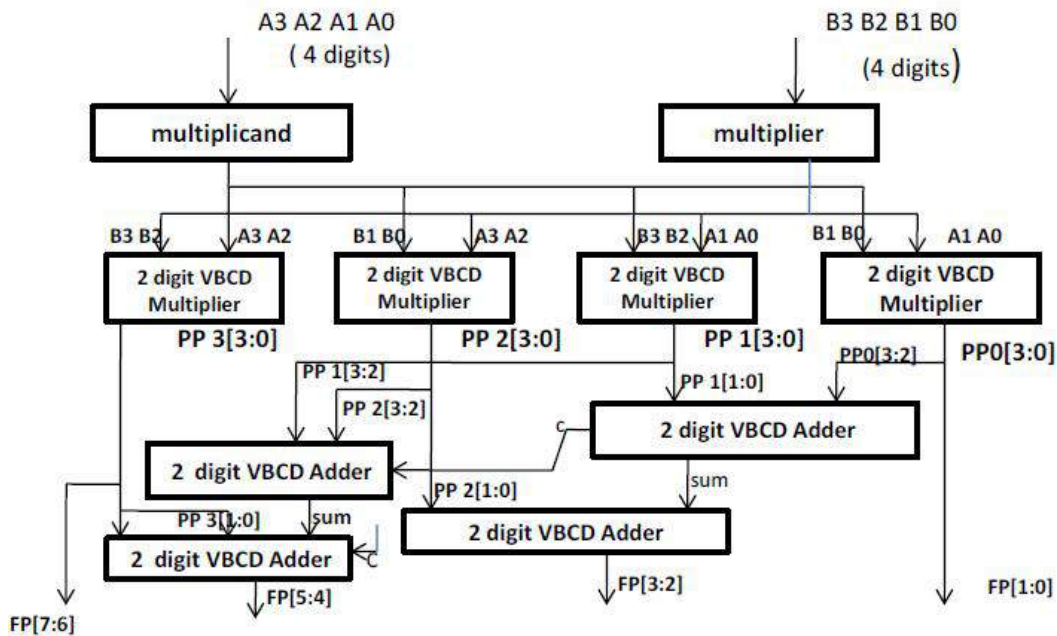


Fig. 7. Four digit VBCD multiplier

3.5 Adder Structures for Adding Partial Products

Efficient adders were designed to add partial products for high performance and less delay. Literature gives various adder structures like simple simple Ripple carry adder, CLA, Carry Save Adders etc to complex prefix adder structures like Kogge stone, Brent kung adders etc, compressor logics (3:2 to 7:2 compressors), parallel Adders, Multi operand adders. Our proposed method uses 3 different methods to add partial products.

3.5.1 First method (VBCD Parallel Adder)

In this method we used signed parallel adders to add partial products. The input to the adder may be +ve or -ve numbers which produces a valid vinculum sum. The advantage of signed digit adders are carry depends only on i -th stage for i th bit addition as shown in Fig. 9 which means only one bit delay exists. This concept was explained more clearly in refs [25, 26] and Fig. 10 shows an N -digit parallel adder in which $i + 1$ stage depends only on i^{th} stage output.

3.5.2 Second method (Multi Operand VBCD Adders)

It uses Multi-operand signed digit adders to add partial products. Minimum depth of the adder is two which means we require two operands to add also known as parallel adder and maximum we went up to 8 operands as shown in Fig. 11 and Fig. 12 with 4, 8, 16, 32 bit operands. 4×4 digit multiplier uses 4 rows with 7 columns. The maximum depth for 4 digit multiplier is 5 along with previous carry bit. So we used 5:2 multi operand adder with 5 inputs and two outputs sum and carry. We observed that delay is reduced when compared to first method. Fig. 13 explains addition of partial products using multioperand adder concept for the example which is shown in Fig. 6.

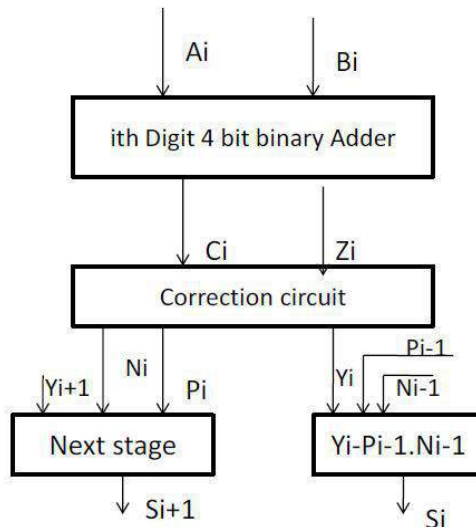


Fig. 8. Decimal adder at i^{th} digit

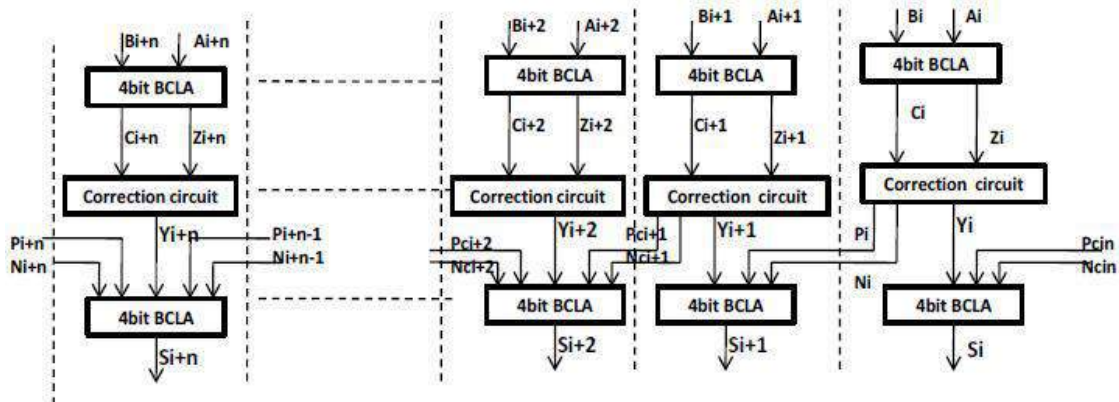


Fig. 9. N-digit parallel adder

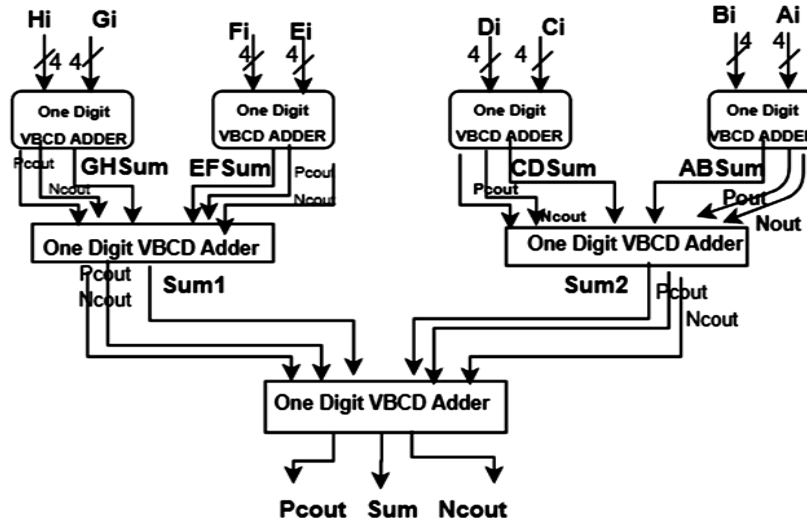


Fig. 10. Multi operand adder

4. FLOATING POINT MULTIPLIER

IEEE 754-2008 format Single Precision Format

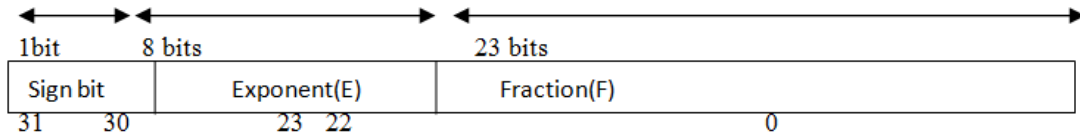


Fig. 11. Single precision decimal floating point format

The above format consists of three fields namely Sign field of 1bit which gives information of +ve or –ve and 8 bits of Exponent field where the maximum range of numbers that can perform arithmetic operation can be in the range of $+10^{55}$ and -10^{44} 23 bits of Fractional field. The maximum Value of mantissa is $F=555555$ and minimum value of mantissa is $F=5\bar{4}\bar{4}\bar{4}\bar{4}\bar{4}$. If we are going to add these fractional parts then we can call it as Floating Point Adder, if we subtract fractional parts then its equivalent to Floating point Subtractor and if we multiply two fractional parts it's called Floating point Multiplier. Using this format we can perform any arithmetic operation like Addition, subtraction, multiplication and Division. In this chapter we concentrated more on Floating point Decimal multipliers and the same is compared with the conventional decimal floating point multipliers. As a part of this chapter we also discussed about Floating point Adders and subtractors.

Sign Field: The most significant bit of the format is used as sign bit and if it is logic high '1' it indicates the number is –ve and if it is logic '0' it gives +ve number. By passing the sign bit of two numbers to xor gate we can find out the resultant as +ve or –ve number.

Exponent field: 8 bits are reserved under this field which indicates that if both numbers are either +ve or –ve Exponents must be added and if both are different exponents are subtracted.

Fraction field: 23 bits are reserved under this field where actual operation of numbers are either added or subtracted or multiplied. Multipliers are most important unit in any processor and consume lot of delay in getting its output. Lot of research is taking point in reducing delay. For this various concepts like Fast Adders, Parallel Adders, Booth Algorithm, Vedic Algorithm and many more exists in literature. In the proposed Floating point Multiplier we used Signed Digit multiplier for multiplying fractional part.

- maximum value of mantissa that can accommodate 6 digit number $m=555555$ and minimum value of mantissa than can accommodate with 6 digit is $5\bar{4}\bar{4}\bar{4}\bar{4}\bar{4}$
- Exponent: In IEEE format 8 bits are reserved for exponent and the min and max values of exponent are $\bar{4}\bar{4}$ and 5 5.
- Hence the maximum floating point number in vinculum number system is 555555×10^{55} and the minimum floating point number in vinculum number system is $5\bar{4}\bar{4}\bar{4}\bar{4}\bar{4} \times 10^{\bar{4}\bar{4}}$

Not a Number (NaN): when any one of the input is zero output is zero and is termed as Not a Number

- Example:

A= 0_0000_0000_000_0000_0000_0000_0001;

B= 0_0000_0010_000_0000_0000_0011_0010_0001;

Final Product = 0_0000_0101_0000_0000_0000_0000_0000

Under flow: Under flow occurs when the result enters into out of range.

Example: $a= 333 \times 10^{\bar{4}\bar{4}}$ and $b=333 \times 10^{\bar{4}\bar{4}}$

Product= $111\bar{1}\bar{1}\bar{1} \times 10^{\bar{1}\bar{3}\bar{4}}$ (1 indicates underflow)

$a=0_1100_1100_000_0000_0000_0011_0011_0011;$

$b=0_1100_1100_000_0000_0000_0011_0011_0011;$

Final Product: 0_0001_0010_001_0001_0001_1111_1111_1111;

Overflow: Overflow occurs when the result exceeds the maximum value or range. It is indicated by overflow flag.

Example: $a= 333 \times 10^{55}$ and $b=333 \times 10^{55}$

Product= $111\bar{1}\bar{1}\bar{1} \times 10^{110}$ (1 indicates over flow)

$a=0_0101_0101_000_0000_0000_0011_0011_0011;$

$b=0_0101_0101_000_0000_0000_0011_0011_0011;$

Final Product: 0_0001_0000_001_0001_0001_1111_1111_1111;

Normalization can be defined as non zero digit in most significant digit.mul_out is before normalization and shft_data is after normalization.

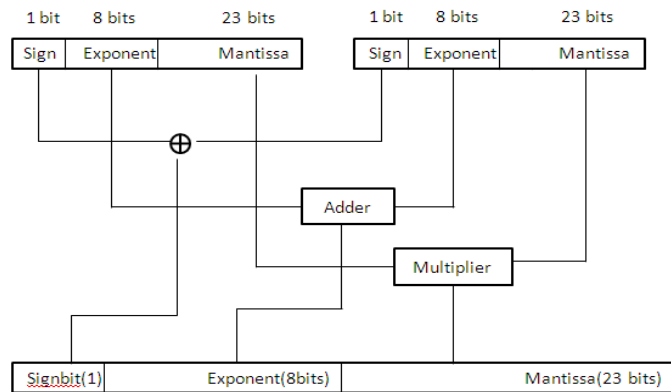


Fig: Floating point Architecture

Table 1. Decimal Floating Point Multiplier delay and area report

DFP Format	Vinculum DFP	
	Delay(ns)	Cellusage
Single Precision	16.03	882
Double Precision	28.402	7060

Simulation results of Floating point multiplier is shown in Table 1.

The decimal floating point multiplier design is described at gate level in verilog HDL, simulated and synthesized by Xilinx 14.2i simulator tool.

5. CONCLUSION AND FUTURE SCOPE

In this paper we implemented floating point multiplier using Vinculum binary coded number systems in which we used VBC adders and multipliers for designing. In future we can design VBC Arithmetic unit, Division algorithms, MAC architectures and Fused multiply and Add units.

COMPETING INTERESTS

Authors have declared that no competing interests exist.

REFERENCES

1. Cowlshaw MF. Decimal floating-point: Algorithm for computers. Proceedings 2003 16th IEEE Symposium on Computer Arithmetic, Santiago de Compostela, 15-18 June. 2003;104-111. DOI: <https://doi.org/10.1109/ARITH.2003.1207666>
2. IEEE Std 754(TM)-2008. IEEE standard for floating-point arithmetic. IEEE Computer Society, Washington, DC; 2008.
3. Aswal M, Perumal G, Prasanna GNS. On Basic financial decimal operations on binary machines. IEEE Transactions on Computers. 2012;61:1084-1096. DOI: <https://doi.org/10.1109/TC.2012.89>
4. Dadda L. Multioperand parallel decimal adder: A mixed binary and BCD approach. IEEE Transactions on Computers. 2007;56:1320-1328. DOI: <https://doi.org/10.1109/TC.2007.1067>
5. Erle MA, Schulte MJ. Decimal multiplication via carry-save addition. Proceedings IEEE International Conference on Application-Specific Systems, Architectures, and Processors ASAP 2003, The Hague, 24-26 June. 2003;348-358. DOI: <https://doi.org/10.1109/ASAP.2003.1212858>
6. Erle MA, Schwarz EM, Schulte MJ. Decimal multiplication with efficient partial product generation. Proceedings of 17th IEEE Symposium on Computer Arithmetic, Cape Cod, MA, 27-29 June. 2005;21-28. DOI: <https://doi.org/10.1109/ARITH.2005.15>
7. Vazquez EA, Bruguera J. Fast Radix-10 multiplication using redundant BCD codes. IEEE Transactions on Computers. 2014;63:1902-1914. DOI: <https://doi.org/10.1109/TC.2014.2315626>
8. Lang T, Nannarelli A. A Radix-10 combinational multiplier. 2006 Fortieth Asilomar Conference on Signals, Systems and Computers, Pacific Grove, CA, 29 October-1 November. 2006;313-317. DOI: <https://doi.org/10.1109/ACSSC.2006.354758>
9. Dadda L, Nannarelli A. A variant of a Radix-10 combinational multiplier. 2008 IEEE International Symposium on Circuits and Systems, Seattle, WA, 18-21 May. 2008;3370-3373.
10. Gorgin S, Jaberipur G. A fully redundant decimal adder and its application in parallel decimal multipliers. Microelectronics Journal. 2009;40:1471-1481. DOI: <https://doi.org/10.1016/j.mejo.2009.07.002>
11. Jaberipur G, Kaivani A. Improving the speed of parallel decimal multiplication. IEEE Transactions on Computers. 2009;58:1539-1552. DOI: <https://doi.org/10.1109/TC.2009.110>
12. Vazquez EA, Montuschi P. Improved design of high-performance parallel decimal multipliers. IEEE Transactions on Computers. 2010;59:679-693. DOI: <https://doi.org/10.1109/TC.2009.167>

13. Cu X, Lui W, Dong W, Lombardi F. A parallel decimal multiplier using hybrid Binary Coded Decimal (BCD) codes. IEEE 23rd Symposium on Computer Arithmetic (ARITH), Santa Clara, CA, 10-13 July. 2016;150-155.
DOI: <https://doi.org/10.1109/ARITH.2016.8>
14. Castellanos D, Stine JE. Compressor trees for decimal partial product reduction. Proceedings of the 18th ACM Great Lakes Symposium on VLSI, New York, NY, 4-6 May. 2008;107-110.
DOI: <https://doi.org/10.1145/1366110.1366137>
15. Vazquez, Antelo E. Multi-operand decimal addition by efficient reuse of a binary carry-save adder tree. Conference Record of the 44th Asilomar Conference on Signals, Systems and Computers, Pacific Grove, CA, 7-10 November. 2010;1685-1689.
16. Kenney RD, Schulte MJ. High-speed multi operand decimal adders. IEEE Transactions on Computers. 2005;54:953-963.
DOI: <https://doi.org/10.1109/TC.2005.129>
17. Shirazi DY, Yun Y, Zhang CN. RBCD: Redundant binary coded decimal adder. IEE Proceedings—Computers and Digital Techniques. 1989;136:156-160.
DOI: <https://doi.org/10.1049/ip-e.1989.0021>
18. Svoboda. Decimal adder with signed digit arithmetic. IEEE Transactions on Computers, C-18, 212-215; 1969.
19. Mehta AK, Gupta M, Jain V, Kumar S. High performance Vedic BCD multiplier and modified binary to BCD converter. Annual IEEE India Conference, Mumbai, 13-15 December. 2013;1-6.
DOI: <https://doi.org/10.1109/INDCON.2013.6725995>
20. Sreelakshmi G, Fatima K, Madhavi BK. Implementation of high speed Vedic BCD multiplier using vinculum method; 2016.
21. Tirthaji SBK. Vedic Mathematics. Motilal Banarsidass, Delhi; 1965.
22. Vestias MP, Neto HC. Parallel decimal multipliers using binary multipliers. Proceedings IEEE VI Southern Programmable Logic Conference, Ipojuca, 24-26 March. 2010;73-78.
DOI: <https://doi.org/10.1109/SPL.2010.5483001>
23. Sutter G, Todorovich E, Bioul G, Vazquez M, Deschamps J.-P. FPGA implementations of BCD multipliers. International Conference on Reconfigurable Computing and FPGAs, Quintana Roo, 9-11 December. 2009;36-41.
24. Sreelakshmi G, Fatima K, Madhavi BK. A novel approach to the learning of vinculum numbers in two's compliment method for BCD arithmetic operations. IEEE Conference ICCMC 2018, IEEE Conference Record #42656; 2018.
25. Sreelakshmi G, Ahmed MS, Fatima K, Madhavi BK. Efficient signed digit decimal adder. IEEE Conference ICDCS 2018, Coimbatore, 16-17 March; 2018.
26. Sreelakshmi G, Fatima K, Madhavi BK. Hybrid signed digit parallel and multi operand BCD adders; 2018.

Biography of author(s)



G. Sreelakshmi

Geethanjali College of Engineering and Technology, Hyderabad, India.

She did her Masters in Engineering from Osmania University, Hyderabad in the field of Digital Systems in 2008 and Bachelor of Engineering from JNTU Anantapur in 2002. She is having 17 years of academic experience and started her career as an Assistant professor in Department of Electronics and Communication Engineer in 2003 and became Associate professor in 2008. She served as In charge HOD, Internal BOS member, established various labs and handled more than 15 subjects for UG and PG students. She carried out various works related to NBA and NAAC accreditations during her service. She is currently pursuing her PhD in the field of VLSI from JNTU Hyderabad, Telangana. She is the author and co-author of more than 25 papers in various fields in reputed journals and conferences. She had presented papers in prestigious IEEE conferences at

National and International level. She acted as a reviewer for an International journal JCSC (Journal of Circuits Systems and Computers). Her research interest includes several aspects in Computer Architectures, Digital VLSI, Testing and Verification and developing new Arithmetic circuits. She is a member of IEEE and Circuits and System Society, Fellow of IETE and Life member of ISTE. She organized various Student Development programs and workshops at various levels.



Dr. Kaleem Fatima

Muffakamjah College of Engineering and Technology, Hyderabad, India

She completed her PhD from Osmania University, Hyderabad in the field of VLSI. She is having 22 years of experience in teaching. She served as Head of the Department. Her research interest are Digital Design, Semi-Custom/full custom VLSI Design for applications in Digital systems, Digital Communications, Image processing and Signal Processing, Hardware Routing accelerators for VLSI CAD, Embedded Systems design. She is a senior member of IEEE, acted as chair person for Circuits and Systems Chapter, Member of IETE and ISTE. She is having a couple of papers in reputed journals and international journals.



Prof. B. K. Madhavi

Siddhartha Institute of Engineering and Technology, Hyderabad, India.

She completed her PhD from JNTUH, Hyderabad in 2007 under guidance of X vice chancellor Prof. Dr..K.Lal Kishore from JNTUA, in the area of Low Power VLSI Design. She had a total of 30 years of teaching and, 16 years of research experience. She worked in various positions as a Principal, Dean, Head of the department of ECE and as R&D Director/Advisor in JNTUH affiliated Engineering Colleges. Presently, she is working as a Professor in Siddhartha Institute of Engineering and Technology, Ibrahimpatnam, Hyderabad. Under her guidance, 10 more Scholars are working and are in progress for their Ph.D. She is one of the authors of the recently published IGI Global publisher book and the title of the book is “*Major Applications of Carbon Nanotube Field-Effect Transistors (CNTFET)*”. She is a Life member of Professional bodies like ISTE and IETE.

© Copyright (2021): Author(s). The licensee is the publisher (Book Publisher International).

DISCLAIMER

This chapter is an extended version of the article published by the same author(s) in the following journal. Circuits and Systems, 9: 87-99, 2018.



DESIGN OF SMART GARBAGE MONITORING SYSTEM

M. Laxmi

Associate Professor, Geethanjali College of Engineering and Technology, Hyderabad, India

M.Sowjanya

Associate Professor, Geethanjali College of Engineering and Technology, Hyderabad, India

Sreenivas Kondapally

Student, Geethanjali College of Engineering and Technology, Hyderabad, India

Katakam Sahithi

Student, Geethanjali College of Engineering and Technology, Hyderabad, India

CH. Samhith Reddy

Student, Geethanjali College of Engineering and Technology, Hyderabad, India

ABSTRACT

Rapid increase in Urbanisation and Globalisation has led to an upsurge in the levels of solid waste production. The 21st century has notarised increased levels of garbage which not only degrades the environment but has severe implications at the societal level like deterioration of health of both human and animals in and around. Hence, it is the need of the hour to take time and build an efficient, effective and a well-organised mechanism to detect, monitor and manage the waste production. The traditional approach to waste management as we witness is time-consuming, cumbersome and heavily dependent on human effort which is not in sync with the updating technology. Smart Cities equipped with Smart Garbage Monitoring Systems can be one of the potential solutions to overcome these issues. A Smart City is assimilation of several integrated Internet of Things (IoT) Subsystems, of which Smart Garbage Monitoring System is one. One of the main applications is to eliminate the problems posed by the solid waste by designing a smart garbage monitoring system. The aim of this project is to design a cost-effective system which optimises waste collection and reduces fuel consumption thereby mitigating the cost requirement considerably. The system monitors the bin levels and informs the same via a web-page. This in turn conveys the information to the garbage collectors. Results thus produced verify accurate real time monitoring of garbage levels.

Key words: Internet of Things, Smart City, Solid Waste Management.

Cite this Article: M. Laxmi, M.Sowjanya, Sreenivas Kondapally, Katakam Sahithi and CH. Samhith Reddy, Design of Smart Garbage Monitoring System, *International Journal of Advanced Research in Engineering and Technology (IJARET)*, 12(3), 2021, pp. 366-370.

<http://iaeme.com/Home/issue/IJARET?Volume=12&Issue=3>

1. INTRODUCTION

Overflowing garbage bins have been a major cause of concern for residents in developing countries. With increase in population, the state of cleanliness with respect to garbage management is degrading tremendously. With the already prevailing diseases, the open containers are proving to be a breeding place for germs and insects. Traditionally, municipalities operate on weekly routes to pick up trash on designated days, regardless of whether the containers are full or not.

This paper aims to optimise waste collection and reduce fuel consumption. The project makes use of an Arduino UNO micro-controller (ATmega 328P), GSM Module (SIM 900A), Ultrasonic Sensor, Temperature and Humidity Sensor, RFID Reader and Tags. The sensors are interfaced to the micro-controller. The ultrasonic sensor placed over the bin detects the garbage level of the bin and compares with the threshold limit. The information so obtained is sent to the webpage via a cellular network which displays the garbage, temperature and humidity levels. The vehicle owner has to flash his RFID card so that who, when and at what time garbage bin was emptied is known. It will help to curb laziness of the municipality's garbage collectors. The system designed is cost-efficient and compact. This makes the system portable and easily adaptable for the current needs.

This paper automates the waste management effectively. IoT refers to communication paradigm in which a network of connected physical devices communicate and exchange information or data among themselves without human intervention. IoT has revolutionized the current networking systems. Internet of Things provides an infrastructure for all the information, gathered by various sensors when they are connected to a microcontroller. Both manufactures and consumers have benefitted from the advancement in IoT. It has helped in providing value added services thereby enhancing the product life cycle.

Essentially, this paper is about collecting the most amounts of materials in the least amount of time to reduce costs and emissions along the way. Additionally, this paper is supposed to work with any type of container and any type of waste, including mixed materials, paper, glass, metals and fluids.

2. REQUIRED TOOLS

2.1 Hardware Required

Arduino Uno (ATmega 328P): The Arduino Uno is an opensource microcontroller board based on the Microchip ATmega328P microcontroller. The board is equipped with sets of digital and analog input/output (I/O) pins that may be interfaced to various expansion boards (shields) and other circuits. The board has 14 digital I/O pins (six capable of PWM output), 6 analog I/O pins, and is programmable with the Arduino IDE (Integrated Development Environment), via a type B USB cable. It can be powered by the USB cable or by an external 9-volt battery, though it accepts voltages between 7 and 20 volts.

Ultrasonic Sensor: The Ultrasonic Sensor is used to measure the distance with high accuracy and stable readings. It can measure distance from 2cm to 400cm or from 1 inch to 13 feet. It emits an ultrasound wave at the frequency of 40KHz in the air and if the object will come in its way then it will bounce back to the sensor. By using that time which it takes to strike the object and comes back, you can calculate the distance.

Distance can be measured by equation: $\text{Distance} = (\text{Time} * \text{sound speed}) / 2$.

Temperature and Humidity Sensor: DHT11 is a Humidity and Temperature Sensor, which generates calibrated digital output. DHT11 can be interface with any microcontroller like Arduino, Raspberry Pi, etc. and get instantaneous results. DHT11 is a low-cost humidity and temperature sensor which provides high reliability and long-term stability.

It uses a capacitive humidity sensor and a thermistor to measure the surrounding air, and outputs a digital signal on the data pin.

RFID Reader Module: The RC522 is a 13.56MHz RFID module that is based on the MFRC522 controller from NXP semiconductors. The module can support I2C, SPI and UART and normally is shipped with a RFID card and key fob. It is commonly used in attendance systems and other person/object identification applications.

GSM Module: The SIM900A is a readily available GSM/GPRS module, used in many mobile phones and PDA. The module can also be used for developing IOT (Internet of Things) and Embedded Applications. SIM900A is a dual-band GSM/GPRS engine that works on frequencies EGSM 900MHz and DCS 1800MHz. SIM900A features GPRS multi-slot class 10/class 8 (optional) and supports the GPRS coding schemes CS-1, CS-2, CS-3 and CS-4.

2.2 Software Required

Arduino IDE: The Arduino Integrated Development Environment (IDE) is a cross platform application (for Windows, MAC OS, LINUX) that is written in functions from C and C++. It is used to write and upload programs to Arduino compatible boards, but also, with the help of third-party cores, other vendor development boards.

The source code for the IDE is released under the GNU General Public License, version 2. The Arduino IDE supports the languages C and C++ using special rules of code structuring. The Arduino IDE supplies a software library from the Wiring project, which provides many common input and output procedures. User-written code only requires two basic functions, for starting the sketch and the main program loop, that are compiled and linked with a program stub `main()` into an executable cyclic executive program with the GNU toolchain, also included with the IDE distribution. The Arduino IDE employs the program `avrdude` to convert the executable code into a text file in hexadecimal encoding that is loaded into the Arduino board by a loader program in the board's firmware. By default, `avrdude` is used as the uploading tool to flash the user code onto official Arduino boards.

Adafruit.io is a cloud service. Adafruit IO is a platform designed to display, respond, and interact with designed unit data. It also keeps data private (data feeds are private by default) and secure.

3. BLOCK DIAGRAM

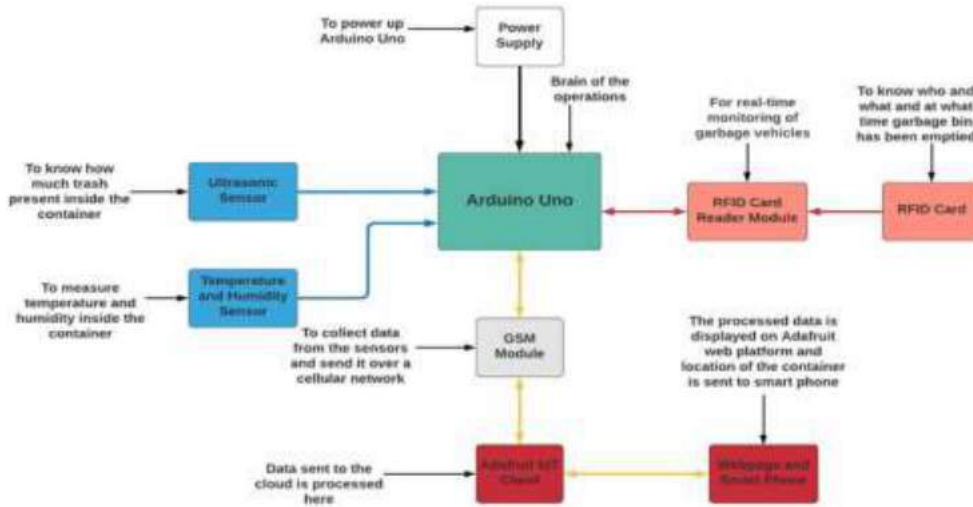


Figure 1

4. OPERATING PROCEDURE

Ultrasonic Sensor will shoot sonar waves to know how much trash is inside the container.

.DHT11 The temperature and humidity sensor’s readings will be helpful to account for any activity (fungal, bacterial etc.) taking place inside the container

Data collected from the sensors are sent over a cellular network for analysis and displayed on Aadafruit web platform.

A list of containers to be collected is then sent to workers/drivers to plan an efficient route.

The worker has to flash his RFID card so that who, when and at what time garbage bin were emptied will be known.

5. FLOWCHART

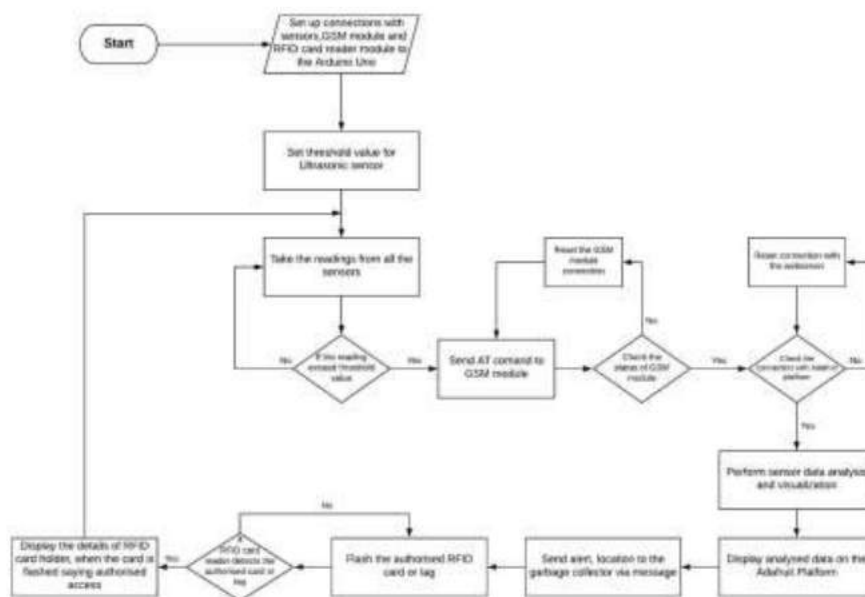


Figure 2

6. CONCLUSION

We can monitor the garbage bins and notify about the level of garbage collected in the garbage bins. It also measures decomposition levels of garbage which helps to overcome the breeding grounds of flies and mosquitoes. The information will be sent to the municipal authorities as a preventive measure. It helps in keeping our Environment clean & green. This paper helps to optimise waste collection and reduce fuel consumption with low cost and less effort.

7. RESULT

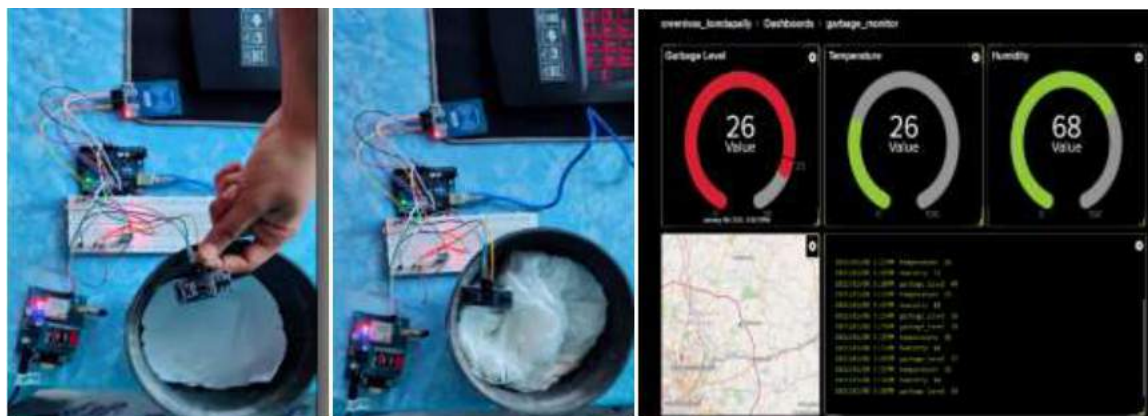


Figure 3

REFERENCES

- [1] C. K.M. Lee, T. Wu, International Conference on Industrial Engineering and Engineering Management, 798 (2014)
- [2] Kanchan Mahajan, Prof.J.S.Chitode,” Waste bin monitoring system using integrated technologies” an IRJET in july 2014.
- [3] Narendra Kumar G., Chandrika Swami, and K. N. Nagadarshini, “Efficient Garbage Disposal Management in Metropolitan”, Cities Using VANETs Journal of Clean Energy Technologies, Vol. 2, No. 3, July 2014.
- [4] Kirti Pille, Raziya Maniyar, Nutan Bade and J.M.Bakliwal “SOLID WASTE MANAGEMENT SYSTEM”, National Conference on “Internet of Things: Towards a Smart Future” & “Recent Trends in Electronics & Communication” (IOTTSF-2016), in Association With Novateur Publication 17th -18th, Feb. 2016.
- [5] Krishna Nirde, Prashant S.Mulay, Uttam M.Chaskar” IOT based solid waste management system for smart cities” an ICICCS in 2017.



AGE PROGRESSION USING DELAUNAY TRIANGULATION

M Sowjanya

Associate Professor, Geethanjali College of Engineering and Technology, Hyderabad, India

M Laxmi

Associate Professor, Geethanjali College of Engineering and Technology, Hyderabad, India

K Bhavya Reddy

Student, Geethanjali College of Engineering and Technology, Hyderabad India

ABSTRACT

Age is a factor which determines the changes that take place in a human body both physically and mentally. As the age increases, the features of human changes accordingly. That changes can be either for a period or entire life. Suppose the height of human, generally, increases up to a certain age of 18-21 and stops changing later. So, age cannot be determined by the height. But few features like the elasticity of skin, hair nature, skin texture, etc., changes throughout the life. Age progression can be used extensively in several applications.

Age progression can be used to show the likely current appearance of a missing person from a photograph many years old. For example, it is widely used as a forensics tool by the law enforcement. In some cases, age and appropriate face image plays a crucial role. Suppose there's a criminal committing crime been caught when he was 20 and subjected to an imprisonment. When he was 60, he was caught again committing crimes. In this scenario if the police suspected him to be behind certain crimes in the past 40 years and wanted to verify, then they will need pictures of the criminal at 30 years of age 40 years of age and so on.

This project will solve such issues by generating expected images of criminal at required age. Using the concepts of node points and triangulation, we morph the image and change the age in both the directions. The inputs to be taken are two images at different ages and output will be a video showing the transitions in age by moving the shape and color blending sliders in the MATLAB

Key words: Age progression, Forensics, Node points, Triangulation, Morph, Blending sliders

Cite this Article: M Sowjanya, M Laxmi and K Bhavya Reddy, Age Progression using Delaunay Triangulation, *International Journal of Advanced Research in Engineering and Technology (IJARET)*, 12(3), 2021, pp. 583-588.

<http://iaeme.com/Home/issue/IJARET?Volume=12&Issue=3>

1. INTRODUCTION

Quite often we want to see how our appearance has changed from a baby up to now all through the ages. More interestingly, as we reach old age, we're wondering how our face would regress. Children to adults and adults to old age are the two main age progression types. It is also possible to combine the two categories as a child will become an adult and then proceed to grow older.

There are films in motion pictures in which children become adults. The opposite age progression process is called as age regression, showing how a person becomes younger. The project takes advantage of several techniques from Computational Photography.

First, image morphing, the project's main contribution, is outlined throughout the project to demonstrate morphing technique. Second, multiple image processing methods can be used to align images input, acquire points of features, and build a interactive UI application. Third, a significant contribution to the project is also facial recognition. While implementing the method of face detection is beyond the scope of this project, it is possible to obtain the results of the method by manually clicking the corresponding facial points. Age progression can be accomplished using image morphing, a popular algorithm used in digital image processing. While the output image may not be as realistic as the original, it can serve as a good approximation of the progression of age. In addition, image morphing includes multiple parameters that enable users to control the output image appearance. Finally, we wanted to create an application which takes either two or three input photographs of a person at different ages, possibly one at a old age, young and the other when the person is a child. By taking these images at same angle and manually plotting facial points we can show the age progression of the person at the given age frame.

2. REQUIRED SOFTWARE TOOLS

PC Installed with MATLAB software

3. PROPOSED METHODS

The process starts with identifying suitable images to morph. The block diagram and detailed explanation is given below

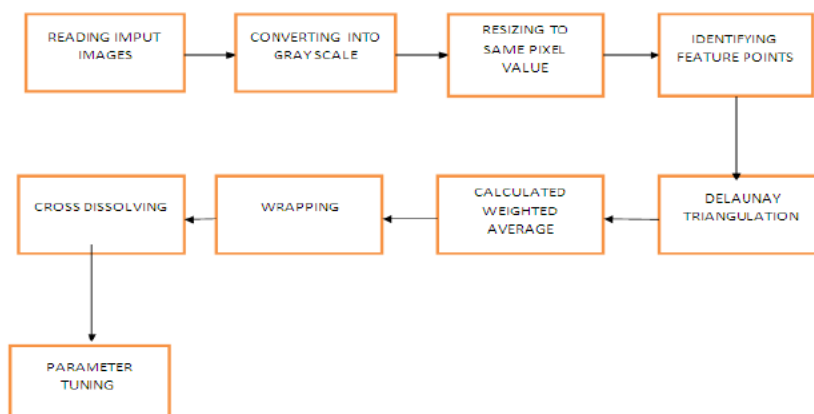


Figure 1

3.1 Choosing Input Images

Application needs three images to perform morphing. The maximum deviation in angle between images should be less than 15 degrees. If it is more than that the morphing will not work as expected. Images are read in matlab by using imread command and stored into a variable.



Figure 2

3.2 Converting into Gray Scale

RGB images cannot be processed easily in morphing tools because of complex matrix formation. Processing complicated values is a time-taking and not reliable.



Figure 3

3.3 Resizing Images

To perform perfect morphing, images should be of same pixel size and same quality. Unless quality and size are same, performing morphing is not an easy task. So all this images are converted to 256 x 256 pixel size.



Figure 4

3.4 Plotting Feature Points

Feature points are the points on an image which describes the change in pixel value. In a face the feature points should cover the entire face and a part of their off face features. These feature points acts as vertices in the upcoming steps.

3.5 Identifying Feature Points and Storing Feature Points



Figure 5

Feature points are stored in excel sheet for easy and smooth transmission of flow. It is copied from output console to an excel sheet. From fileread command in MATLAB, the points are collected back to MATLAB to proceed to nextsteps.

4. DELAUNAY TRIANGULATION

A triangulation of a set of points P in 2D is a set of triangles T whose:

- Vertices are collectively P
- Union is the convex hull of P
- Interiors do not intersect each other

The Delaunay triangulation for a set of points P , in 2D is the triangulation $DT(P)$ of P such that no point falls in the interior of the circumcircle of any triangle (the circle that passes through all three of its points) in $DT(P)$.

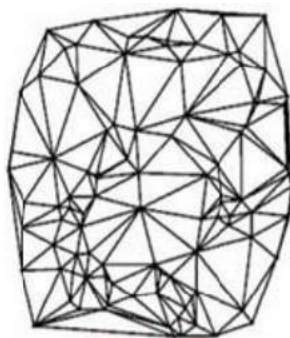


Figure 6

5. RESULT

5.1 Input



Figure 7

5.2 Output

A GUI interface has been developed where three images of a person at different stages of life is given as input. This project shows the change of features in a persons face over the course time. This is done by tuning the shape blending and colour bending parameters.

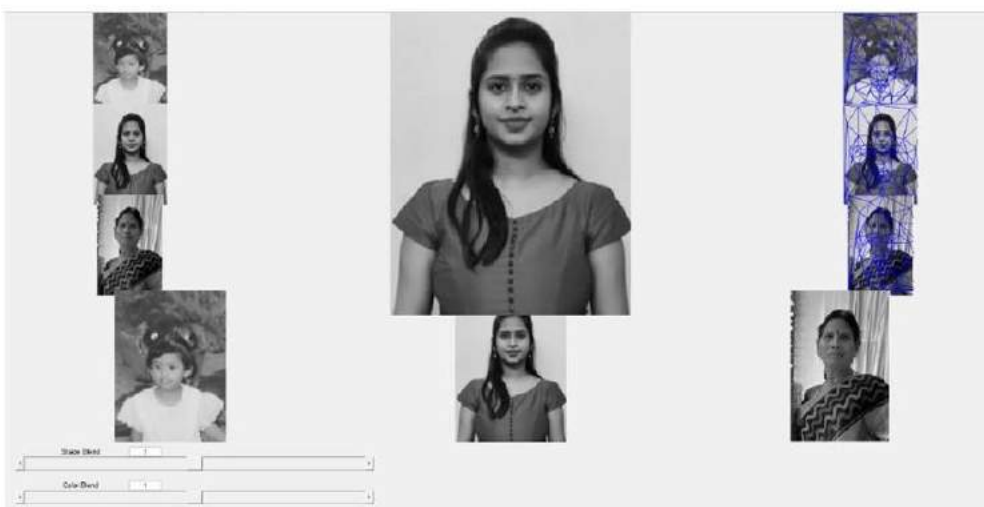


Figure 8

6. CONCLUSION

Give a person portrait picture, we developed an interactive application showing how the person changes from a baby face into an elder face. Even though the realistic facial appearance of this application is limited, the output images reflect the change in facial structure, features as well as texture. We hope to study more about using computer vision and image processing for this field in the future. As for the project, we pleased with the results while have fun playing with the application on different faces. This technique of image morphing is widely used and can be used in motion pictures or cinema industry. This can be extended using computer vision application and it can be developed as a mobile application as a fun or recreational application. Despite the explosive growth of morphing in recent years, the subject of morphing among multiple images has been neglected. So, morphing among multiple images can be performed in future

REFERENCES

- [1] Liu, X., Zhou, F.: Improved curriculum learning using SSM for facial expression recognition. *Vis. Comput.*
- [2] Jilani, S.K., Ugail, H., Bukar, A.M., Logan, A., Munshi, T.: A machine learning approach for ethnic classification: the British Pakistani face, In: *International Conference on Cyberworlds (CW)*, vol. 2017, pp. 170–173 (2017)
- [3] Chu, Y., Zhao, L., Ahmad, T.: Multiple feature subspaces analysis for single sample per person face recognition. *Vis. Comput.* 35(2), 239–256 (2019).
- [4] Zhi, R., Liu, M., Zhang, D.: A comprehensive survey on automatic facial action unit analysis. *Vis. Comput.* 36(5), 1067–1093 (2020).



DELIVERY COLLECTION OF PARCELS WITH SMART SHIPMENT CONTAINER USING ARDUINO

P. Chandra Prakash Reddy

Assistant Professor, Geethanjali College of Engineering and Technology
Hyderabad India

Amirineni Rama L. Padamaja

Assistant Professor, Geethanjali College of Engineering and Technology
Hyderabad, India

I. Sangeetha

Student, Geethanjali College of Engineering and Technology, Hyderabad, India

M. Vishal

Student, Geethanjali College of Engineering and Technology, Hyderabad, India

ABSTRACT

The proliferation of online shopping has introduced a number of problems for the customer not present in what we might call the traditional shopping experience. One of the big new problems is how to handle the receiving of a parcel when not at home. A common practice by couriers is to leave a message indicating their failed attempt to deliver your package due to door lock or leave it in the care of the local neighbors (or not so local) post office. This then introduces a new problem of finding the time to collect your package from a place which is only open during the hours which most people work. What is needed is a way to receive a package at home even when no one is there. This would mean providing a secure location in which the package can be stored until someone gets home to collect it.

In our modern busy lifestyles, we are often not having enough time to respond to our routine activities like – answering a person at the door or collecting a door delivery. To handle such situations we propose a solution by automating the parcel collection unit. This system presents a low cost, less time-consuming, safe and effective implementation of Smart Box System through the wireless sensor networks. A special device, called a hardware kit is realized and designed for this purpose. When the parcel is placed inside the box, it is sensed through the optical (IR) sensors and the door will be automatically closed and simultaneously a message will be sent to the android device that the parcel is put in the smart box. In addition, a vibration sensor is also placed in

the smart box to identify and inform the android device when any one tries to take away the smart box.

Keywords: Internet of Things, barcode, online shopping, unavailability of customer, IoT based parcel collection, home automation, Smart Sensor Box

Cite this Article: P. Chandra Prakash Reddy, Amirineni Rama L. Padamaja, I. Sangeetha and M. Vishal, Delivery Collection of Parcels with Smart Shipment Container using Arduino, *International Journal of Electrical Engineering and Technology (IJEET)*, 12(3), 2021, pp.35-41.
<http://iaeme.com/Home/issue/IJEET?Volume=12&Issue=3>

1. INTRODUCTION

The basic idea is to introduce technology into our lives for monitoring issues which demand our personal presence. By doing so we aim at providing a reliable and user friendly solution to problems incurred during online shopping. A standalone smart box is designed which receives and stores the intended parcel so that the customer can retrieve it as and when required. In our modern busy lifestyles we are often not having enough time to respond to our routine activities like – answering a person at the door or for collecting a door delivery. To handle such situations we propose a solution by automating the parcel collection unit. This project discusses the part of IoT (WiFi) in home sophistication, the proposed approach for automating the parcel delivery collection, the working and design of the system.

This system presents a low cost, less time consuming, safe and effective implementation of Smart Box System through the wireless sensor networks.

Wi-Fi communication patterns come with excellent features of robust (strong) digital communication. This can enable variable bit rate for desired purposes like voice or data. 802.11n operates on both the 2.4 GHz and the lesser-used 5 GHz bands. Support for 5 GHz bands is optional. It operates at a maximum net data rate from 54 Mbit/s to 600 Mbit/s.

Smart mailbox is an important part of a future house where all deliveries are notified. This allows the user to track the delivered goods in real-time. It will also prove helpful for the elderly, people living in sparsely populated areas and farms with faraway mailboxes.

2. LITERATURE SURVEY

IoT based Smart Delivery Box secured delivery Box which generates OTP for every active session and notifies the customer about the systematic process flow till the session is terminated. The system performs as a secured Box with minimum operational delay. Time based One Time Password increases the authenticity of the delivery vault. Global system for mobile communication module is used to send text messages since GSM network has an advantage of covering wider area of operation even during mobility of the customer.

This system presents a low cost, less time consuming, safe and effective implementation of Smart Letter Box System through the wireless sensor networks which makes the use of obstacle sensors. A special device, called a hardware kit is realized and designed for this purpose. Obstacle sensors have IR transmitter and IR receiver. IR transmitter transmits the rays. When the rays fall on to the object then it gets reflected to the IR receiver, it results that the object is detected. In the existing system users are notified by sending a text message through a SIM card, but here we introduce Android Application which gives the notification through the internet. The paper illustrates the description of this device the android application which receives the notification .This system reduces the Human efforts.

3. PROPOSED SYSTEM

In the system we implemented a smart system letter box, in which the hardware kit is used to notify the user that a letter has arrived. The mobile application is used to receive the notification. Here the obstacle sensor is used to detect the object (letter). The RTC clock is used to store the time of the delivery of the letter. GSM module is used to send the notification through message and the GPS detects the location at which address the letter has been received. We have used Android operating system in this system which has lot of features integrated in it. MySQL database is used to store the records. This database is easy to maintained records

The Internet of Things concept is much broader in the sense that everyday objects that did not previously seem electronic are connected to the internet via sensors. The proposed approach uses the integration of IoT, cloud and mobile application for the automation process. The idea is to introduce a Smart Freight Box (SFB) which will be able to verify and accept the ordered parcel as well as acknowledging the customer and the e-retailers.

4. ANDROID APPLICATION

Android application system: Android is an open handset Alliance. It is a mobile operating system developed by Google which is based upon the Linux kernel. Software stack in android operating system consist of java application which is based on object oriented-application

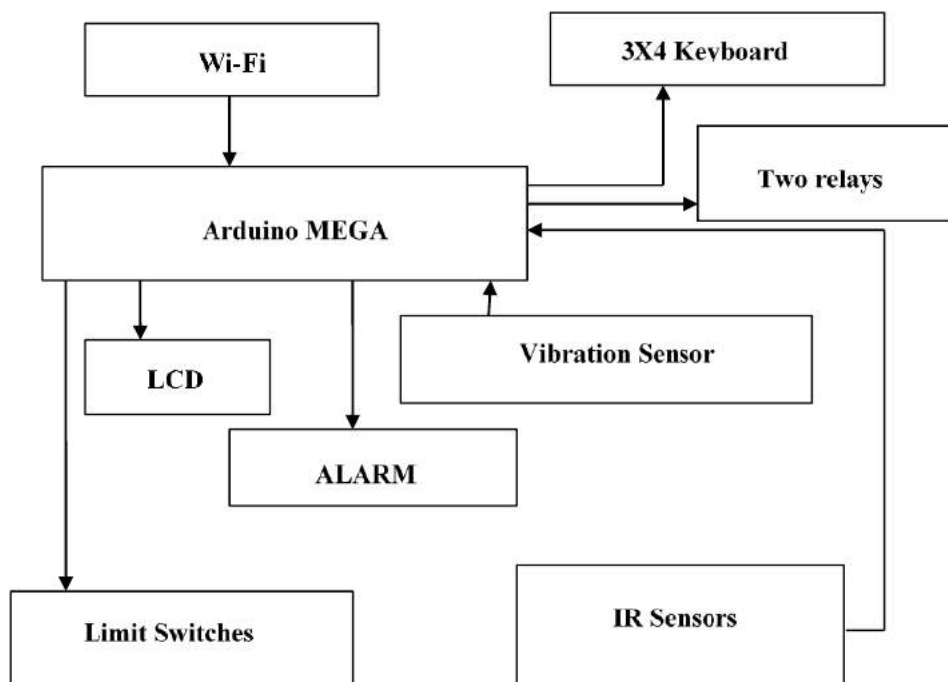


Figure 1 Block diagram of smart box for parcel delivery collection using Arduino

A smart letter box system is accessed anywhere and at any time .The record can be accessed using the android mobile operating system .The report generated message is stored in the server database. Mobile application is developed and installed in the mobile and the message generated with the hardware kit which has GSM in it.

Letter box system is actually an indication system it shows indications whenever a letter arrives in the letter box .Ref 2. It works using the concept of Obstacle detection. In this arrangement IR Transmitter and IR Receiver are placed near to each other, whenever any obstacle (i.e. Letter) comes in front of the obstacle sensor the rays get reflected and thus we get

the output as HIGH. Thus the letters have been detected in the Letter the Box. Thus the letter has been detected in the Letter the Box.

In the days of technology the postman still comes to our house to deliver the letters, courier and parcels. Because the things courier and parcels cannot be sent via email and by any other electronic media. So to get notification of letter delivery in our mail box here we design an intelligent letter box that provides notification of delivery of letters in our mail box through the message to our smart phone or GSM mobiles.

5. WIFI TECHNOLOGY

Wi-Fi (or, incorrectly but commonly, WiFi) is a local area wireless technology that allows an electronic device to participate in computer networking using 2.4 GHz UHF and 5 GHz SHF ISM radio bands. The Wi-Fi Alliance defines Wi-Fi as any "wireless local area network" (WLAN) product based on the Institute of Electrical and Electronics Engineers' (IEEE) 802.11 standards". However, the term "Wi-Fi" is used in general English as a synonym for "WLAN" since most modern WLANs are based on these standards. "Wi-Fi" is a trademark of the Wi-Fi Alliance. The "Wi-Fi CERTIFIED" trademark can only be used by Wi-Fi products that successfully complete Wi-Fi Alliance interoperability certification testing.

Many devices can use Wi-Fi, e.g. personal computers, video-game consoles, smart phones, digital cameras, tablet computers and digital audio players. These can connect to a network resource such as the Internet via a wireless network access point. Such an access point (or hotspot) has a range of about 20 meters (66 feet) indoors and a greater range outdoors. Hotspot coverage can comprise an area as small as a single room with walls that block radio waves, or as large as many square kilometers achieved by using multiple overlapping access points.

6. KEYBOARD INTERFACING

The keyboard is designed with 12 keys, out of these 12 keys 10 keys are utilized for 0 to 9 numbers to enter the time data in hours and minutes, the 11th key is used to clear when the wrong digit is typed and the 12th Key is used as the enter key. This keyboard is designed to form a matrix of rows and columns.

The microcontroller accesses both rows and columns through ports. When any key is pressed, a row and a column make a contact (short circuited). Otherwise there is no connection between rows and columns. The microcontroller (consisting of processor, RAM and EPROM, and four I/O ports) takes care of hardware and software, when the keyboard is interfaced to it. In this concept, the microcontroller scans the keys continuously and automatically identifies the activated key. The activated key information is stored in the internal RAM of the microcontroller. Finally, it is the function of the microcontroller to scan the keyboard continuously to detect and identify the key pressed.

As mentioned above the keyboard is designed with 12 keys and all these are configured in 3X4 Matrix form, meaning three rows and four columns. For this purpose seven I/O lines of microcontroller are engaged with this keyboard. The information generated by this keyboard is fed to the microcontroller through two different ports. The rows are connected to one port and columns are connected to another port for identifying the activated key. By pressing the corresponding keys one after another in a sequence, the controller will display in the LCD and check the time data with the RTC for activating the alarm.

The time information produced by the keyboard by pressing the corresponding code keys is fed to the microcontroller to store into its RAM. To detect a pressed key, the micro-controller makes high all rows by providing logic high at input, and then it reads the columns. If the data read from all the column pins is zero, no key has been pressed and the process continues until

a key press is detected. When any key is pressed, the micro-controller detects and goes through the process of identifying the key. Starting with the top row, the microcontroller reads all the columns. If the data read is all zeros, no key in that row is activated and the process is moved to the next row. This process continues until the row is identified. After identification of the row in which the key has been pressed, the next task is to find out which column the pressed key belongs to. This can be achieved, because the micro-controller knows at any time which row and column are being accessed. The keyboard interfacing diagram with the controller is shown below.

The keyboard contains press to ON type micro-switches having two pins and remains in normally open condition. When the key is pressed normally, open contact gets closed to generate a logic signal and this signal is fed to the microcontroller. These switches are nothing but feather touch keys, popularly known as 'Push buttons' or 'Push-to-ON' switches.

7. OBSTACLE SENSING CIRCUIT DESIGNED USING IR SENSORS

The Obstacle Sensing circuit is designed with IR Sensors for detecting the parcel is placed inside the smart box. The obstacle-sensing block is designed with LM567 IC; to this oscillator frequency can be adjusted. When the circuit is energized it starts producing a continuous chain of square pulses. The output of this oscillator is amplified and fed to an IR LED. This LED radiates the signal into air and depending on the signal strength or radiating power, the range can be increased. The IR signal delivered from the IR LED transmitted in a line like a laser beam, this beam is invisible and harmless. The output of IR-Receiver is (proportional to reflected wave) found for matching (comparing) with that of transmitted wave, and then the output of the IC will become low automatically (If both are equal then output of this IC becomes low). The output of this tone decoder IC is fed to the microcontroller.

The basic function of the detector circuit is by radiating energy into space through IR LED and detecting the echo signal reflected from an object. The reflected energy that is returned to the IR sensor indicates the presence of an object which is within the range. A portion of the transmitted energy is intercepted by the target and re-radiated in many directions. The radiation directed back towards the system is collected by the receiving LED to produce a high signal at Pin No.8 of LM567 IC. The output of the receiver is fed to the Microcontroller. Whenever the controller receives a high signal from the reference point, the microcontroller energizes the voice chip to announce the information. The following is the diagram of the sensing circuit.

8. ARDUINO MEGA CONTROLLER

The Arduino Mega 2560 is a microcontroller board based on the ATmega2560. It has 54 digital input/output pins (of which 15 can be used as PWM outputs), 16 analog inputs, 4 UARTs (hardware serial ports), a 16 MHz crystal oscillator, a USB connection, a power jack, an ICSP header, and a reset button. It contains everything needed to support the microcontroller; simply connect it to a computer with a USB cable or power it with an AC-to-DC adapter or battery to get started. The Mega 2560 board is compatible with most shields designed for the Uno and the former boards.

- Arduino Mega 2560 is a Microcontroller board based on Atmega2560. It comes with more memory space and I/O pins as compared to other boards available in the market.
- There are 54 digital I/O pins and 16 analog pins incorporated on the board that make this device unique and stand out from others.
- A crystal oscillator of 16MHz frequency is added to the board.

- This board comes with a USB cable port that is used to connect and transfer code from computer to the board.

9. RESULT

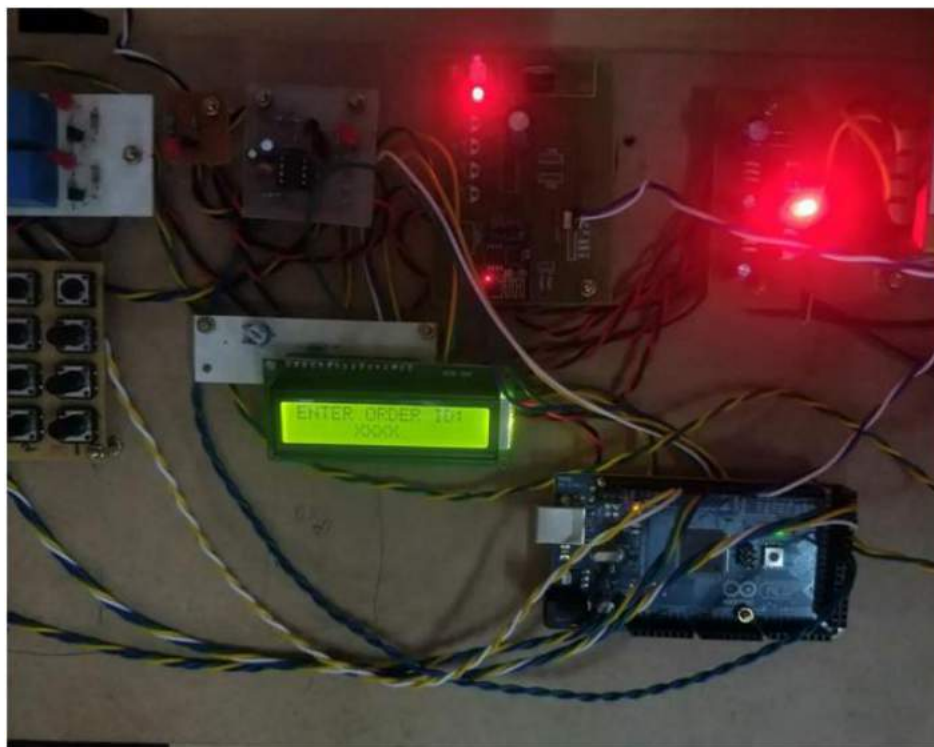


Figure 2

10. ADVANTAGES

- Enhanced security and safety.
- Less human errors.
- Providing a contactless identification and tracking.
- Real-time delivery status.
- Less money and time spent on tracking and handling of the package

11. CONCLUSION

The aim of engineering studies is to increase the quality of living by constant innovation and research. Introducing technology into common man's life by exploiting the advancements in technology an effort has been made to simplify the delivery procedure which usually involves a lot of human effort and time. Currently handling of packages, tracking and delivery is a major concern for delivery and logistics companies An attempt has been made by realizing the vacuum that exists and a fully automated receiver system has been developed which is to be installed in customer premises.

The project work is designed and developed successfully. For the demonstration purpose, a prototype module is constructed; and the results are found to be satisfactory. While designing and developing this proto type module, Since it is a prototype module, much amount is not invested. The whole machine is constructed with locally available components some of the modifications must be carried out in design to make it a real working system.

FUTURE SCOPE

- With the blooming of IoT (Internet of Things) tracking of packages becomes easier. Using the internet instead of GSM services also reduces the cost for communication.
- The box could be built inside the wall so that only receiving compartment lid is visible to outside world thus providing an extra security to the package and the box itself.
- The box can be paired with artificial intelligence like Alexia or Google Assistant.
- Further improvisation could be made by adding biometric verification at the customer premises.

REFERENCES

- [1] <http://postscapes.com/internet-of-things-award/connected-home-products/>
- [2] <http://www.cisco.com/web/strategy/docs/gov/everything-for-cities.pdf>
- [3] http://en.wikipedia.org/wiki/Internet_of_Things.
- [4] <http://whatis.techtarget.com/definition/Internet-of-Things>.
- [5] <http://www.wired.com/2013/05/internet-of-things-2/>.
- [6] Zhiyong Shi, "Design and implementation of the mobile internet of things based on tdsdmanetwork" published on 17-19th December 2010 in Information Theory and Information Security (ICITIS), 2010 IEEE International Conference.
- [7] K. Nirosha, B. Durga Sri, Ch. Mamatha and B. Dhanal axmi, Automatic Street Lights On/Off Application using IO T, International Journal of Mechanical Engineering and Technology, 8(8), 2017, pp. 38–47.
- [8] B. Durga Sri, K. Nirosha, P. Priyanka and B. Dhanal axmi, GSM Based Fish Monitoring System Using IOT, International Journal of Mechanical Engineering and Technology 8(7), 2017, pp. 1094–1101.
- [9] Hariharr C Punjabi, Sanket Agarwal, Vivek Khithani, Venkatesh Muddaliar and Mrugendra Vasmatkar , Smart Farming Using IoT , International Journal of Electronics and Communication Engineering and Technology , 8(1), 2017 , pp. 58–66.
- [10] S. Nithya, Lalitha Shree, Kiruthika and Krishnaveni, Solar Based Smart Garbage Monitoring System Using IOT, International Journal of Electronics and Communication Engineering and Technology, 8(2), 2017, pp. 75–80



Contents lists available at ScienceDirect

Materials Today: Proceedings

journal homepage: www.elsevier.com/locate/matpr

Recent developments in code compression techniques for embedded systems

Dumpa Prasad^a, P. Rahul Reddy^b, B. Sreelatha^c, Koya Jeevan Reddy^d, Sudharsan Jayabalan^e, Asisa Kumar Panigrahy^{e,*}

^a Department of Electronics and Communication Engineering, Sasi Institute of Technology and Engineering, Tadepalligudam, India

^b Department of Electronics and Communication Engineering, Geethanjali Insititue of Science & Technology, Nellore, India

^c Department of Electronics and Communication Engineering, Geethanjali College of Engineering & Technology, Keesara, Telangana 501 301, India

^d Department of Electronics and Communication Engineering, Sreenidhi Institute of Science and Technology, Yamanapet, Ghatkesar, Telangana 501 301 India

^e Department of Electronics and Communication Engineering, Gokaraju Rangaraju Institute of Engineering & Technology, Hyderabad 500090, Telangana, India

ARTICLE INFO

Article history:

Received 8 February 2021

Received in revised form 18 February 2021

Accepted 21 February 2021

Available online xxxxx

Keywords:

Embedded systems

PDA

Code compression

LUT

Compressed instructions

ABSTRACT

Embedded applications software code is increasingly growing in size. Whereas the entire code of all control panels in a car provided for roughly a few 100 K code lines a decade ago, a single control panel such as the engine control can now have up to 1million code lines. With these help of good approach, common scenarios are developed for other, even for mobiles, embedded systems like PDA's, cell phones etc. However, increasing software size requires greater memory and can therefore raise the cost of an embedded system considerably. The starting of this pattern was already established in the early 1990 s. The compressed code is created by compressing the binary numbers using a code compression tool (at the time of design) is stored in the instruction memory of the embedded devices. The compressed instructions are decompressed and implemented by the processor at the time of startup. One of the serious challenges is that the tables will become wide in size and therefore decrease the benefits of compressing the code that could be accessed. Although the whole research in this area has mostly concentrated on improving greater code compression without specifically targeting the issue of wide look-up table sizes.

© 2021 Elsevier Ltd. All rights reserved.

Selection and peer-review under responsibility of the scientific committee of the International Conference on Materials, Manufacturing and Mechanical Engineering for Sustainable Developments-2020.

1. Introduction

An extremely slower processor and limited memory sizes are commonly utilized by embedded devices to reduce costs. There is also an approximately 5 billion embedded microprocessors are being used now-a-days, as per the World Semiconductor Trade Statistics Blue Book. The major determinant for the rising prevalence of embedded device- driven portable devices like (Personal Digital Assistants) and web-platform mobile phones is the global expansion of their implementation, example the world demand for embedded devices will rise from about \$1.6 billion in 2004 to \$ 3.5 billion to 2009 a Average Annual Growth Rate(AAGR) of 16%. Because due to the requirements of the embedded industry,

the memory chip of the embedded device must be tiny, various techniques are utilized to minimize the size of the embedded software by encoding it inactive and then decoding it active. In the field of individual instruction problem use generally a RISC processor, the concept of utilizing code compression as a method for chip size mitigation in microprocessors has most triggered concern. Furthermore many developments in IC integration techniques to explore another direction which surely impedes the speed of processing[1-7].

The method of compression of code can be utilized when the ISA (Instruction Set Architecture) may or may not be defined. When the ISA ids defined, to create the decoders hardware, the code compression algorithm uses the data in opcode or instruction format. In this situation, the compression ratio will be increased, as the amount and type of operands can be minimized as according o the operation specified by the opcode in the instruction format. If the ISA is not defined, the code compression method implements

* Corresponding author.

E-mail address: asisa@griet.ac.in (A. Kumar Panigrahy).

conventional methods of data compression, which rely only on instruction values or byte sequence data. In this scenario, the decoder is easier than before because it does not consider the instruction format. The only drawback is that the compressed code is not as effective as the approach with a particular ISA. Compressed instructions and decoding tables are created when a code compression method is utilized. Approximately 40 percent of the memory specifications for the compressed program could be the size of the decoding table, while the other 60 percent are covered by the encoded instructions.

Greater volume and expensive embedded devices developers as the industry demands single-chip approach to satisfy constraints such as lower devices cost, higher flexibility, higher efficiency level and lower consumption of power requirements for highly complicated applications, the industry faces many design problems. Code compression/decompression has appeared as an significant area for solving some related sections of these issued in embedded system design. It is possible to decompress beyond the CPU for example between L2 cache and main memory or between L2 cache and CPU or within the CPU as a part of fetch or decoding the unit of instruction. In any event, only sections of the entire code will be decompressed at a time for example, at the instruction level or block level to reduce the memory complexity. As a step after code initialization, the code is compressed and then extracted into Flash or ROM from where it is inserted into the main memory or L2 cache during the devices reset. That means that it is not possible to modify the program and that it must be set. But the software program changes, then it are appropriate to encrypt the code again and destroy the ROM or Flash again. Usually, this is not a limitation for embedded systems that do not allow user to modify the program. The main objective in code compression has historically been to minimize the size of the instruction memory, but recent techniques have proved that it can also lead to performance improvements for an embedded device.

Recently, VLIW algorithms have been very common especially for single processing (Texas Instruments for example, the star core DSP VLIW DSP of TMS 320C6X and Lucent appears to take more program memory than traditional DSP and high bandwidth instructions. To provide multiple operations per cycle, a pre-fetch algorithm is required. Even though entire research in this field has primarily focused on improving greater compression of code without explicitly targeting the problem of large table sizes of look-ups.

Yuan Xie et al. (2001) The cost of decompression could destroy all the advantages from compression in the code compression [8]. In the code compression for the new VLIW technology, the size of decoder and speed are very significant. In this paper, they have taken benefits of the isolation of coding and modeling in the arithmetic coding, and also discussed about the trade-off between compression ratio and also the design of the decompression structure as shown in Fig. 1. They have simplified less than 10 percent of

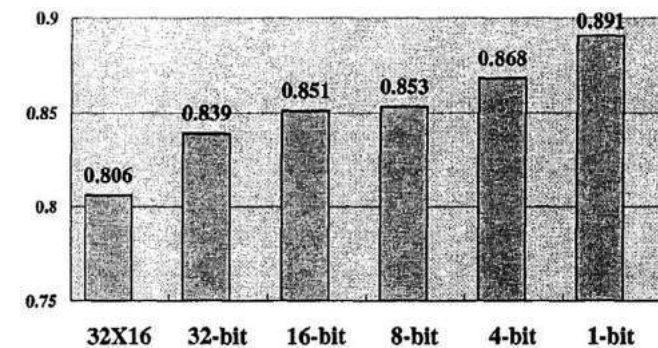


Fig. 1. Compression ratio for dissimilar structures [8].

the compression ratio, but the design of the decoder is much lesser than others. One more benefit of utilizing this simplified model is that even if the application changes, the decompression device cannot be a application specific and hence does not requires any changes.

Luca Benini et al. (2002) They have introduced two different types of encrypted techniques one is profile driven and other is differential as they are defined by portable hardware applications and they compared their results with compression techniques they have observed a some alternatives of Lempel [9]- Ziv encoder. To maintain energy avoidance in core-based embedded devices, they have proposed a new technique called HW-application based data compression. They have implemented a novel data compression structural paradigm and many compression techniques. Based on the particular compression technique memory traffic and energy consumption decrements are achieved in the cache-to-memory path of devices connected to traditional benchmarks which are in a scale of 4.2 percent – 35.2 percent.

Haris Lekatsas et al. (2002) In this paper they have introduced a new decompression modules as a structure, development and testing the hardware that enables an embedded devices to operate utilizing compressed binary code [10]. Within a single cycle and without using any extra cycle time lag, kit is the initial operating prototype model that decompresses instructions. As hardware model containing decompression machine, a cache, CPU, peripherals and memory, the entire devices are operating. They have noticed a performance improvement of up to 63 percent with a 25 percent average across a wide variety of applications as depicted in Fig. 2.

Mikael Collin et al. (2003) They proposed an enhancement to ISA, RISC, with instructions of variable length, generating a greater density of information without affection the programmability [11]. They have introduced a strategy of 8, 16 and 24 instruction bits followed by LUTs within the processor which is based on the evaluation of flexible instruction utilization and assertion locality of set of SPEC CPU 2000 applications. This proposed method shows 20 to 30 percent drop in main memory application and results indicates that small instructions consists of up to 60 percent of including all executed instructions. For the complete data path and memory devices, the total energy consumptions is up to 15 percent and for the path of instruction fetch is up to 20 percent.

Chang Hong Lin et al. (2004) For the VLIW code compression, they have suggested a new variable-sized block technique. Fixed-sized blocks, typically works by using code compression and its performance is restricted by the size of small blocks (Fig. 3) [12]. Branch blocks have larger blocks for code compression, which are instructed between two consecutive reasonable branch goals. They

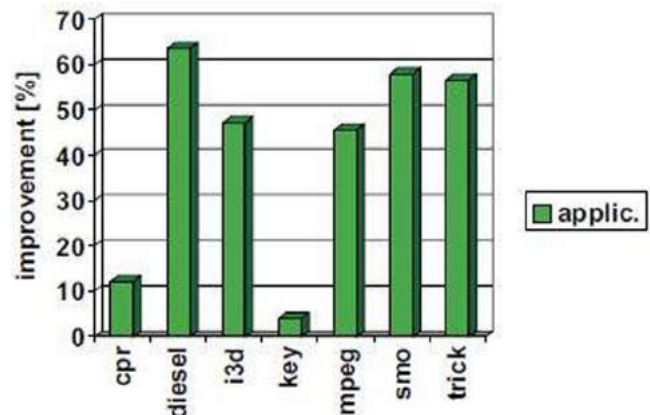


Fig. 2. Better performance development for each application [10].

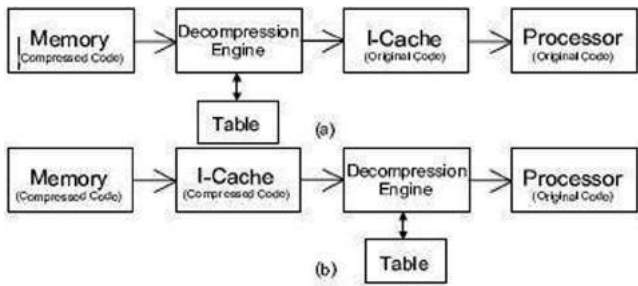


Fig. 3. Two feasible code decompression models (a) Pre-cache, (b) Post-cache [12].

proposed a compression systems based on LZW and selected code that uses branch blocks as the compression module. The compression ratio is around 83 percent and 75 percent accordingly. Low power is accomplished by the limited memory used to store code of compressed source. This system has very less cost of decompression and greater bandwidth of decoding with acceptable compression ratios compared with previous results. Parallel decompression may also be applicable to these techniques, because these are more suitable for VLIW architecture.

Haris Lekatsas et al. (2005) They have proposed a new compression/decompression models for binary data operating on embedded devices [13]. This technique is special because it also treats binary code and data in a single way, although the issue of encoding data returns back to memory is not solved by previous literature on embedded software compression. In order to decode the input byte sequences and replacing them with table indices, and they also provided a new approximation. In accordance with

their model, this technique will enable very quick compression/decompression and very efficiently compresses separate files. These results show that the overall size, which includes hardware cost is reduced by 51 percent or more, thus maintaining the output cost within 11.5 percent of the initial uncompressed program as illustrated in Fig. 4.

Talal Bonny et al. (2006) To enhance the design effectiveness of embedded applications, the proposed study utilizes code compression [14]. Generally they have proposed a different technique and different design which are required for the process of decompression known as look-up tables. Still now no other research have not concentrated on reducing the look-up tables but they have proved by reducing the look-up tables also has a major effect on total bandwidth which is based on hardware decompression systems. They have implemented a new as well as powerful hardware system based on canonical Huffman coding. They have minimized the size of look-up tables up to 45 percent by utilizing Lin-Kernighan method and also reduced LUT's efficiency without using ISA as shown in Fig. 5.

Seok-Won Seong et al. (2006) Embedded systems are restricted by the memory requirement. This problem is solved by data compression approaches by minimizing the code size of programs for application [15]. Dictionary-based code compression methods are common because both offer good compression ratios and faster decompression systems. By recognizing the errors, newly proposed approaches enhance traditional dictionary-based compression. This paper provides two significant improvements:- i) it offers a basis for cost-benefits analysis to improve the compression ratio by developing more matching patterns, and ii) it uses bit masks to build an effective code compression approach to enhance the compression ratio without adding any decompress-

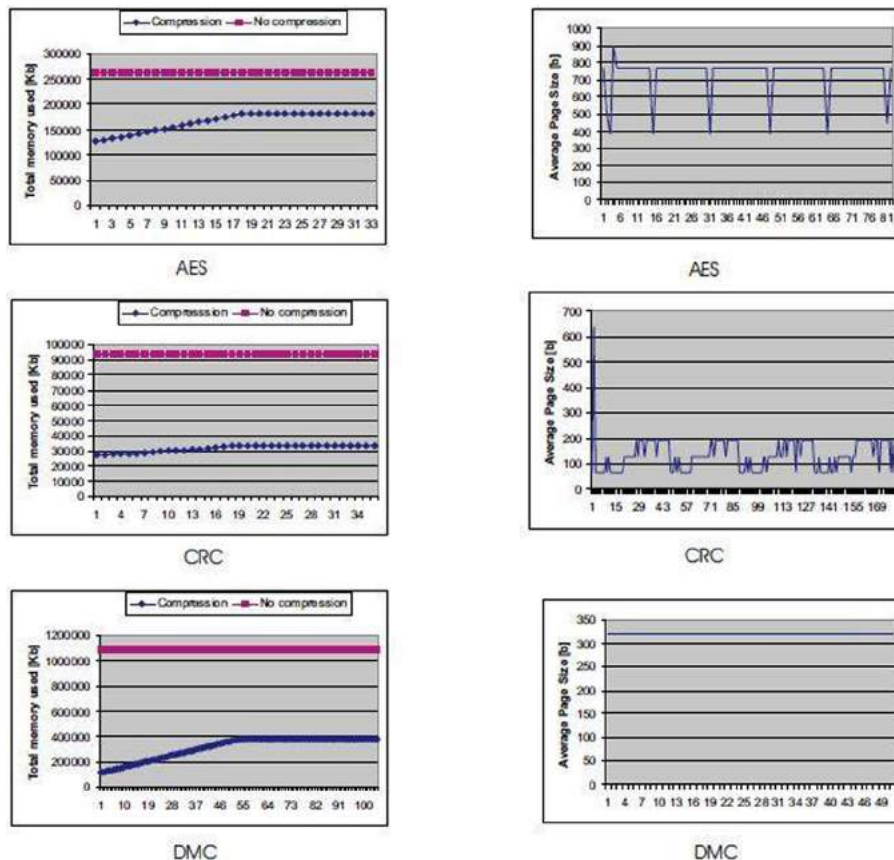


Fig. 4. (a) Memory handling and (b) normal page size vs time [13].

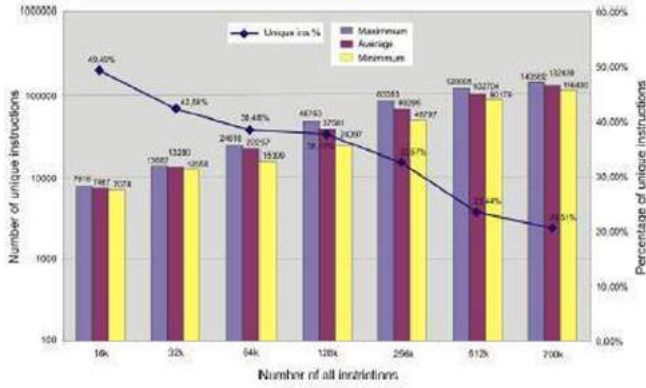


Fig. 5. LUT sizes for dissimilar applications [14].

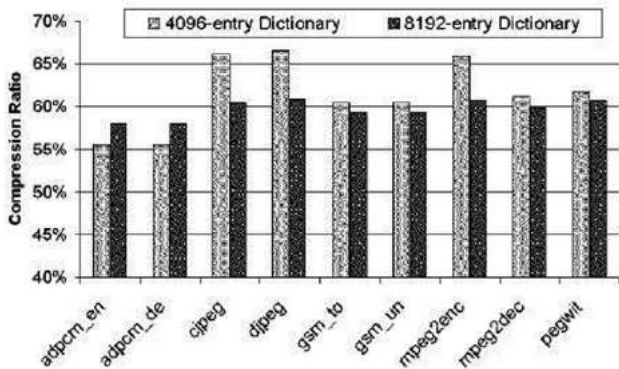


Fig. 6. Compression ratios for dissimilar benchmarks [15].

sion retributions as depicted in Fig. 6. They have utilized a new application from different areas to illustrate the utility of their method and optimized them for a wide range of technologies. This strategy breaks the current dictionary-based technologies by an

average of 15 percent offering a 55 percent- 65 percent of compression ratio.

Talal Bonny et al. (2007) The density of code in embedded technology structure is an important condition because it not only decreases the demands for limited memory of resources but also helps to enhance further significant structure specifications such as performance and power consumption [16]. This paper is focused on canonical Huffman coding which is a new and effective hardware method which includes all type of numerical hardware techniques. They have applied his proposed methods to three main embedded hardware architectures such as MIPS, ARM and Power PC. They have achieved a total compression ratio of 52 percent for ARM, 49 percent for MIPS, 55 percent for Power PC along with LUT overhead without including ISA information as shown in Fig. 7.

Talal Bonny et al. (2008) One of the essential constraints of embedded systems plan is to minimize the size of code of embedded systems [17]. Regarding to size, code compression will supply with considerable economy. So in this paper, they have proposed a new and effective hardware technique. In some particular operations, this technique explores the advantages of re-encoding the leftover bits (called as re-encodable bits) in the instruction formant to increase the compression ratio. Re-encoding these bits will further decrease the size of decrypted table by higher than 37 percent and also they have achieved compression ratios as lower as 44 percent. They have used a standard set of devices and simulated the performance and tried these applications into two main embedded processors such as MIPS and ARM. By using MIPS processor, they have gained 45 percent compression ratio (Fig. 8) and by using ARM processor they have gained 48 percent of compression ratio, but the performance of proposed method is not much effective.

2. Conclusion

Finally this paper concludes with several research techniques are surveyed including all the compressed and decompressed structures used in embedded systems. It provides a brief overview of several significant finding with respect to existing methods. This paper shows different techniques proposed in the existing papers and also shows their advantages and disadvantages also to improve more complexity in future research work.

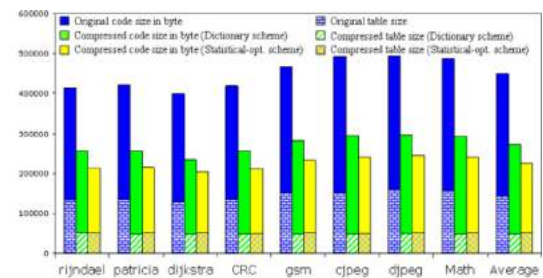
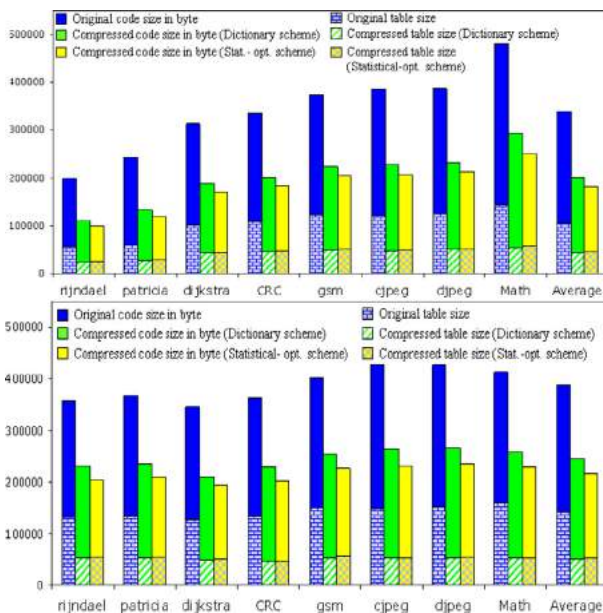


Fig. 7. (a), (b) and (c) Comparison results for ARM, MIPS and Power PC and (d) shows time taken in cycles for original and compressed code [16].

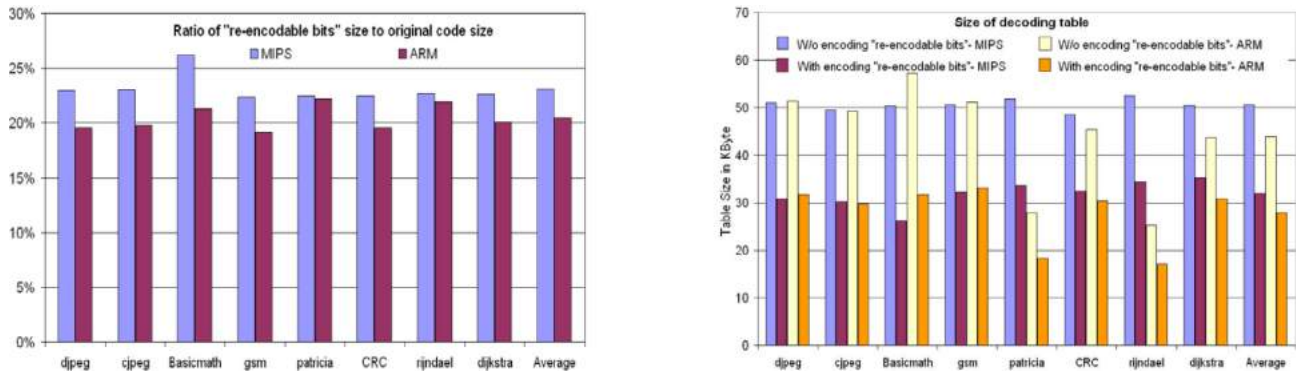


Fig. 8. (a) Re-encodable bit size ratios, (b) Decoding table size for MIPS and ARM [17].

Declaration of Competing Interest

The authors declare that they have no known competing financial interests or personal relationships that could have appeared to influence the work reported in this paper.

References

- [1] A.K. Panigrahi, S. Bonam, T. Ghosh, Shiv Govind Singh, and Siva Rama Krishna Vanjari. "Ultra-thin Ti passivation mediated breakthrough in high quality Cu-Cu bonding at low temperature and pressure.", *Materials Letters* 169 (2016) 269–272.
- [2] A.K. Panigrahy, K.-N. Chen, Low temperature Cu-Cu bonding technology in three-dimensional integration: An extensive review, *Journal of Electronic Packaging* 140, no. 1 (2018).
- [3] A.K. Panigrahi, T. Ghosh, S.R.K. Vanjari, S.G. Singh, Demonstration of sub 150° C Cu-Cu thermocompression bonding for 3D IC applications, utilizing an ultrathin layer of Manganin alloy as an effective surface passivation layer, *Materials Letters* 194 (2017) 86–89.
- [4] A.K. Panigrahi, T. Ghosh, S.R.K. Vanjari, S.G. Singh, Oxidation Resistive, CMOS Compatible Copper-Based Alloy Ultrathin Films as a Superior Passivation Mechanism for Achieving 150 C Cu-Cu Wafer on Wafer Thermocompression Bonding, *IEEE Transactions on Electron Devices* 64 (3) (2017) 1239–1245.
- [5] A.K. Panigrahy, T. Ghosh, S.R.K. Vanjari, S.G. Singh, Surface density gradient engineering precedes enhanced diffusion; drives CMOS in-line process flow compatible Cu-Cu thermocompression bonding at 75° C, *IEEE Transactions on Device and Materials Reliability* 19 (4) (2019) 791–795.
- [6] C.h. Dadaipally Pragathi, M. Usha Kumari, T. Usha Rani, S. Kumar, P. Tatiparti Padma, S. Kumar, A.K. Panigrahy, Simplistic approach to alleviate noise coupling issues in 3D IC integration, *Materials Today: Proceedings* 33 (2020) 4007–4011.
- [7] Banothu Rakesh, Kailaas Mahindra, Marri Sai Venkat Goud, N. Arun Vignesh, Tatiparti Padma, and Asisa Kumar Panigrahy. "Facile approach to mitigate thermal issues in 3D IC integration using effective FIN orientation." *Materials Today: Proceedings* 33 (2020): 3085–3088.
- [8] Y. Xie, W. Wolf, H. Lekatsas, Compression ratio and decompression overhead tradeoffs in code compression for VLIW architectures, in: *International Conference on ASIC, 2001*, pp. 337–340.
- [9] L. Benini, D. Bruni, A. Macii, E. Macii, Hardware-assisted data compression for energy minimization in systems with embedded processors, in: *Proceedings of the conference on Design, Automation & Test in Europe DATE02, 2002*, pp. 449–453.
- [10] H. Lekatsas, J. Henkel, V. Jakkula, Design of an One-cycle Decompression Hardware for Performance Increase in Embedded Systems, *Design Automation Conference DAC'02 (2002)* 34–39.
- [11] M. Collin, M. Brorsson, Low Power Instruction Fetch using Profiled Variable Length Instructions, in: *Proceedings of the IEEE International SoC Conference, 2003*, pp. 183–188.
- [12] C. Lin, Y. Xie and W. Wolf. LZW-based code compression for VLIW embedded systems. *Proceedings of the Design, Automation and Test in Europe conf. (DATE04)*, pp. 76–81, 2004
- [13] H. Lekatsas, J. Henkel, V. Jakkula, S. Chakradhar, A unified architecture for adaptive compression of data and code on embedded systems, in: *Proc. of 18th. International Conference on VLSI Design, 2005*, pp. 117–123.
- [14] T. Bonny and J. Henkel. Using Lin-Kernighan Algorithm for Look-Up Table Compression to Improve Code Density. *Proc. of the 16h Great Lakes Symposium on VLSI-(GLSVLSI'06)*, pp. 259–265, Philadelphia, USA, April 2006
- [15] Seong and P. Mishra. A Bitmask-based Code Compression Technique for Embedded Systems. *24th IEEE/ACM International Conference on Computer-Aided Design (ICCAD06)*, pp. 251254, 2006
- [16] T. Bonny and J. Henkel. Efficient Code Density Through Look-up Table Compression. *IEEE/ACM Proc. of Design Automation and Test in Europe Conference (DATE07)*, pp. 809–814, Nice, France, April 2007
- [17] T. Bonny and J. Henkel. Efficient Code Density Through Look-up Table Compression. *IEEE/ACM Proc. of Design Automation and Test in Europe Conference (DATE07)*, pp. 809–814, Nice, France, April 2007



IMPLEMENTATION OF SIMPLE PWM/PPM GENERATOR FOR MICROCONTROLLER USING VERILOG

Shankar A

Associate Professor, Electronics and Communication Engineering
Geethanjali College of Engineering and Technology, Hyderabad, India

Lokeshwari A

UG Student, Geethanjali College of Engineering and Technology, Hyderabad, India

Manohar B

UG Student, Geethanjali College of Engineering and Technology, Hyderabad, India

Pranavi S

UG Student, Geethanjali College of Engineering and Technology, Hyderabad, India

ABSTRACT

A Pulse Width Modulation (PWM) Signal is a method for generating an analog signal using a digital source. Now-a-days microcontrollers support PWM outputs. A PWM signal consists of two main components a duty cycle and a frequency. The PWM Generator block generates pulses for carrier-based pulse width modulation (PWM) converters using two-level topology. Most of the microcontrollers will have built in timers which helps in generation of PWM signal with various widths. PWM generator helps in controlling the brightness in smart lighting systems by controlling voltage to LED driver connected with LED bulbs. Also helps in controlling the speed of motors by varying voltage supply to it. It is also used as modulation scheme to encode message into pulsing signal for transmission. Pulse-position modulation (PPM) is a form of signal modulation in which M message bits are encoded by transmitting a single pulse in one of possible required time shifts. This is repeated every T-seconds, such that the transmitted bit rate is. bits per second. Used in non-coherent detection where a receiver does not need any Phase lock loop for tracking the phase of the carrier, Used in radio frequency (RF) communication. Also used in contactless smart card, high frequency, RFID (radio frequency ID) tags.

This project demonstrates how a simple and fast a pulse width modulator (PWM) generator and a pulse position modulator (PPM) can be implemented using Verilog programming. It is simulated using ModelSim, a multi-language (hardware description language) simulation environment from Mentor Graphics and tested on FPGA

development board. In the hardware simulation the module for PWM generator can be realized using development board. The board is built around Xilinx Spartan-3E FPGA and Atmel AT90USB2 USB controller. It provides complete, ready-to-use hardware suitable for hosting circuits, ranging from basic logic devices to complex controllers. The FPGA development board allows USB programming through the computer USB port. The program, when run, automatically detects the development board connected to the system, and allows you to program ROM memory in the FPGA board to permanently store the code, or to temporarily program the FPGA with the code. When programmed temporarily, FPGA runs the code as long as it is supplied with power. Once power disconnected, FPGA reverts back to being a blank IC, waiting to be programmed again.

Key words: Pulse Width Modulation (PWM), Pulse Position Modulation (PPM), Verilog HDL, ModelSim, FPGA.

Cite this Article: Shankar A, Lokeshwari A, Manohar B and Pranavi S, Implementation of Simple PWM/PPM Generator for Microcontroller Using Verilog, *International Journal of Advanced Research in Engineering and Technology (IJARET)*, 12(3), 2021, pp. 97-102.

<http://iaeme.com/Home/issue/IJARET?Volume=12&Issue=3>

1. INTRODUCTION

In Power Electronics. Pulse Width Modulation (PWM) is the core for control and has proven effective in driving modern semiconductor power devices. Majority of power electronic circuits are controlled by PWM signals of various forms. (1) PWM is effective and commonly used as control technique to generate analog signals from a digital device like a microcontroller.

The PWM/PPM Generator converts analog input signals to Pulse Width Modulated (PWM) or Pulse Position Modulated (PPM) output signals. Pulse Width Modulation (PWM) Signal is a method for generating an analog signal using a digital source. (1) Now-a-days microcontrollers support PWM outputs. Most of the microcontrollers will have built in timers which helps in generation of PWM signal with various widths. It is commonly used to control average power delivered to a load, motor speed control, generating analog voltage levels and for generating analog waveforms.

In PPM, an analog input signal is sampled a pulse whose position is proportional to the input signal amplitude is generated at each sample point. (2) Both PWM and PPM signals are of constant height (amplitude), and the pulses in PPM signals are of constant width. Although PWM and PPM are more complex forms of message processing than PAM, they still are not considered true digital signals.

Most of the microcontrollers have special pins assigned for PWM as in Arduino-UNO it has 6 PWM pins on it. Similarly, PIC Microcontrollers also have PWM pins but unfortunately 8051 Microcontroller doesn't have this luxury means there's no special PWM pins available in 8051 Microcontroller. But PWM is necessary so we are manually generating the PWM pulse using Verilog. CCP Modules are available with a number of PIC Microcontrollers.

This project demonstrates how a simple and fast pulse width modulator (PWM)/pulse position modulator (PPM) generator can be implemented using Verilog programming. (5) It is simulated using ModelSim, a multi-language (hardware description language) simulation environment from Mentor Graphics and tested on Basys 2 FPGA development board from Digilent. (6)

2. PULSE WIDTH MODULATOR (PWM) / PULSE POSITION MODULATOR (PPM) GENERATOR

The PWM/PPM Generator converts analog input signal to Pulse Width Modulation (PWM) or Pulse Position Modulation (PPM) output signals. In PWM, an analog input signal is sampled, and a pulse whose width (duration) is proportional to the input signal amplitude is generated at each sample point. In PPM, an analog input signal is sampled and a pulse whose position is proportional to the input signal amplitude is generated at each sample point. Both PWM and PPM signals are of constant height (amplitude), and the pulses in PPM signals are of constant width. Although PWM and PPM are more complex forms of message processing than PAM, they still are not considered true digital signals.

Using the PWM/PPM Generator, students can gain an understanding of how PWM and PPM signals are generated. The noise resistance characteristics of PWM/PPM signals can be studied also.

3. PRINCIPLE OF GENERATOR

The Pulse Width Modulation (PWM) and Pulse Position Modulation (PPM) Generators works on two principles one is a counter and a comparator were modulated signal and sawtooth signal form the input to the comparator for analog signal input and digital equivalent of analog input for digital signals. (1) One input of the comparator is fed by the input message or modulating signal and the other input as the analog or digital input which operates at carrier frequency.

The counter produces the carrier frequencies to the comparator and plays a major role in Pulse Width Modulation and Pulse Position modulation during the generation process. In this the message Bits are encoded by transmitting a single pulse in one possible required time shifts into the Microcontroller.

4. PRINCIPLE OF FPGA

Principle for PWM generator can be realized using Basys 2 development board. The board is built around Xilinx Spartan-3E FPGA (9) and Atmel AT90USB2 USB controller. It provides complete, ready-to-use hardware suitable for hosting circuits, ranging from basic logic devices to complex controllers. (4) This board is used, along with the following two software, to allow for effortless programming and debugging of the FPGA board:

- Xilinx ISE Webpack 14.7
- Digilent Adept v2.0 or higher.

Digilent Adept v2.0 or higher program allows USB programming through computer USB port. The program, when runs, automatically detects the development board connected to the system, and allows you to program ROM memory in the FPGA board to permanently store the code, or to temporarily program the FPGA with the code. When programmed temporarily, (5) FPGA runs the code as long as it is supplied with power. Once power disconnected, FPGA reverts back to being a blank IC, waiting to be programmed again. Adept software requires a bitmap file with .bit extension. This is usually created using synthesizer software like ISE from Xilinx or Simplify from Synopsys for logical synthesis. (6) This is where Xilinx ISE webpack is used, is a free software that can be used by anyone. Include the Verilog file into a new project along with a user constraints file (ucf extension).

5. WORKING OF GENERATOR FOR MICROCONTROLLER

The working of the PWM/PPM Generator is simple. It uses one counter and one comparator. The microcontroller unit provides 8-bit input into PWM module. Counter used in the PWM module is 8-bit. It increments it's value on the positive edge of the clock (positive edge

triggered). Comparator used in PWM generator is also 8-bit. Input given to PWM module is compared to the current value of the counter using the comparator. If current value of the counter is greater than the value given to the module as input, PWM output is pulled low. However, if current value of the counter is less than the value given as input to the module, output of PWM generator is pulled high.

Let us take a test case to understand the operation. Suppose, input to PWM module is 128 (10000000_b). Counter is initialized using Reset button, so that output is 0(00000000_b). During the first clock cycle, value of counter and input value to PWM module are compared.

The module finds that, value of counter is less than the value provided. This prompts the module to pull output of PWM generator high. This same paradigm keeps output of the generator pulled high until value of the counter reaches 128 (10000000_b).

In the next clock cycle, after the counter has reached 128, counter increments its value to 129 (10000001_b). Comparator finds that, current counter value is greater than the value provided to PWM module, therefore output must be pulled low.

Changing input to PWM module will consequently change the threshold value, where transition from high to low state occurs. Thus, PWM can be achieved by varying the input provided to PWM

module. When the analog input value is greater than the counter value it is sent to the d flip flop which stores the greater than value. PPM clock (2) is another input given to the d flip flop. After some delay they output of the d flip flop is given to the and gate and when the input is less than or equal to counter output it is given as the second input to the and gate so that during the negative fall of PWM output from high to low then ppm generates the pulse.

6. BLOCK DIAGRAM

Block diagram of the PWM and PPM generator is shown in Fig. Working principle of the generator is simple. It uses one counter and one comparator. The microcontroller unit provides 8-bit input into PWM module. Counter used in the PWM module is 8-bit. It increments it's value on the positive edge of the clock (positive edge triggered). Comparator used in the PWM generator is also 8-bit.

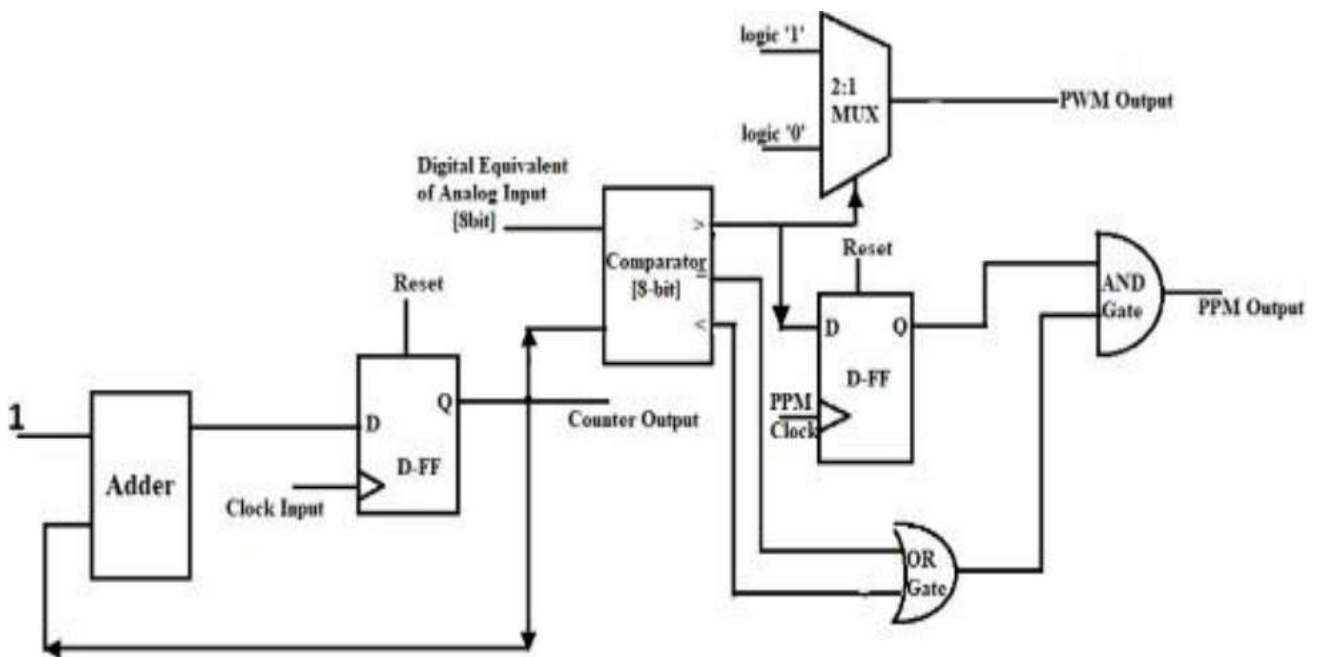


Figure 1 Block diagram of PWM/PPM generator.

In the PWM generator is also 8-bit. (4) Input given to PWM module is compared to the current value of the counter using the comparator. If current value of the counter is greater than the value given to the module as input, PWM output is pulled low. However, if current value of the counter is less than the value given as input to the module, output of PWM generator is pulled high. When the analog input value is greater than the counter value it is sent to the d flip flop which stores the greater than value. Clock 2 is another input given to the d flip flop. After some delay they output of the d flip flop is given to the and gate and when the I/p is less than or equal to counter output it is given as the second input to the and gate so that during the negative fall of PWM output from high to low then PPM generates the pulse.

7. RESULT AND DISCUSSION

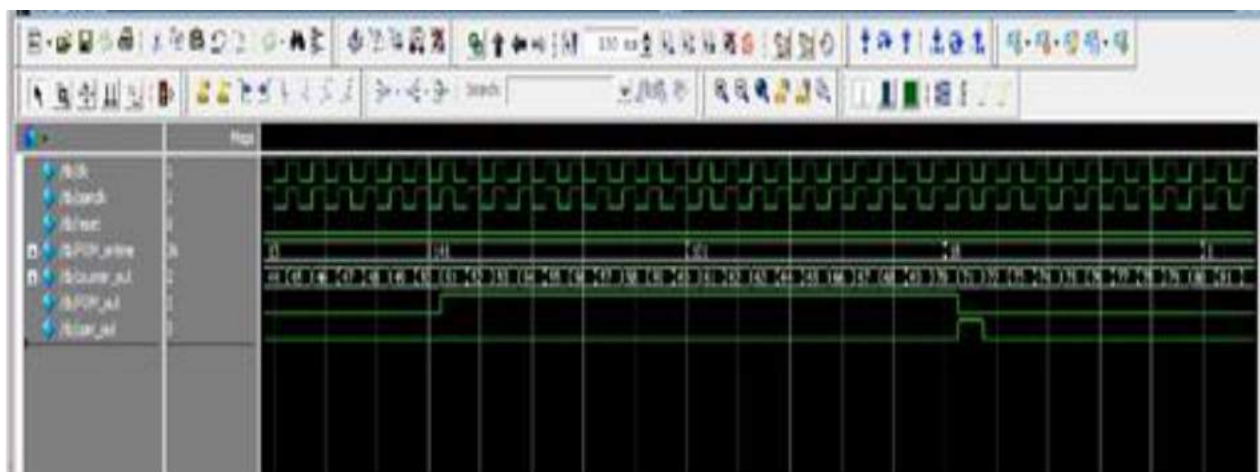


Figure 2

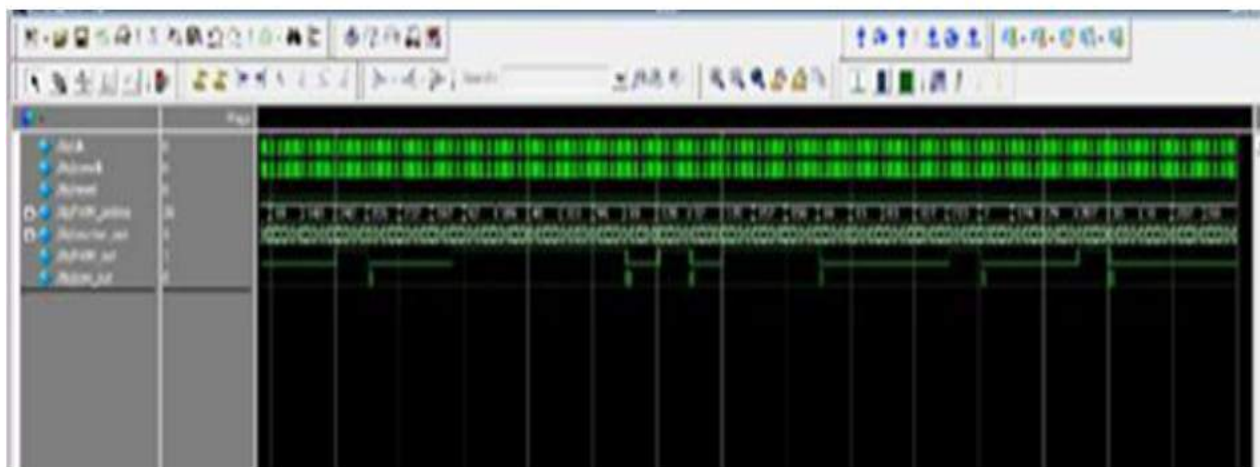


Figure 3 PWM/PPM wave-forms

- This PWM has a maximum operating frequency of 232.504MHz, which allows the most dynamic and fast operation applications to be accommodated.
- Total power dissipated by the design at an operation frequency of 50MHz is 38mW.
- Static power dissipation for 34mW (power required to drive the development board) and the power consumed by the oscillator to produce the clock is 1mW.
- Average power consumed by PWM output is 3mW, which indicates that the design is also power efficient.

8. CONCLUSION

This project demonstrates how a simple and fast pulse width modulator (PWM)/Pulse Position Modulator (PPM) generator can be implemented using Verilog programming. It is simulated using ModelSim, a multi-language (hardware description language) simulation environment from Mentor Graphics and tested on Basys 2 FPGA development board from Digilent.

REFERENCES

- [1] R.M. Jalanekar & K.S. Jog, "Pulse –Width-Modulation Techniques: A Review," IETE journal of research, Vol. 46, No. 3, May-June 2000.
- [2] O. Cadenas, G. Megson, "A clocking technique for FPGA pipelined designs," Journal of Systems Architecture 50, 2004, pp. 687–696.
- [3] M.M. Islam, D. Allee, S. Konasani, A. Rodriguez, "A low-cost digital controller for a switching DC converter with improved voltage regulation," IEEE Power Electronics Letters 2, 2004, pp. 121–124.
- [4] A. Arbit, D. Pritzker, A. Kuperman, R. Rabinovici, "A DSP-controlled PWM generator using field programmable gate array," 23rd IEEE Convention of Electrical and Electronic Engineers, vol. 1, 2004, pp. 325– 328.
- [5] Brian von Herzen, "Signal processing at 250 MHz using high-performance FPGA s," IEEE Transactions on VLSI Systems 6, 1998, pp. 238–246.
- [6] R. Ramos, D. Biel, E. Fossas, F. Guinjoan, "A fixed- frequency quasi sliding control algorithm: application to power inverters design by means of FPGA implementation," IEEE Transactions on Power Electronics 18, 2003, pp. 344–355.
- [7] A.M. Omar, N. Rahim, S. Mekhilef, "Three-phase syn- chronous PWM for flyback converter with power-factor correction using FPGA ASIC design," IEEE Transactions on Industrial Electronics 51, 2004 pp. 96- 106.
- [8] Koutroulis, Eftichios, Apostolos Dollas, and Kostas Kalaitzakis. "High frequency pulse width modulation implementation using FPGA and CPLD ICs." Journal of Systems Architecture 52.6, 2006, pp. 332-344.
- [9] Nouman, Z. "Generating PWM Signals with Variable Duty From 0% to 100% Based FPGA SPARTAN3AN." Electorevue Journal, International Society for Science and Engineering publications 4.4, 2013, pp. 75-79.
- [10] Youichi Ito and Scoichi Kawauchi, "Microprocessor – Based Robust Digital control for UPS with three phase PWM Inverter," IEEE Transactions on Power Electronics, Vol.10, No.2, March 1995.

DynMAC Based Optimized Spectrum Handoff Algorithm for Deterministic Multihop Industrial Networks Modelling

¹AppalaRaju Uppala, ²C Venkata Narasimhulu, ³K Satya Prasad

¹Research Scholar, Department of E.C.E., Jawaharlal Nehru Technological University Kakinada, Andhra Pradesh, India.

¹Associate Professor, Geethanjali College of Engineering and Technology, Hyderabad, Telangana, India. Email : raju.mdl@gmail.com

² LORDS Institute of Engineering and Technology, Hyderabad, Telangana, India. Email : narasimhulucv@gmail.com

³Vignan's Foundation for Science, Technology & Research, Guntur, Andhra Pradesh, India. Email : prasad_kodati@yahoo.co.in

Abstract

Cognitive Radio (C.R.) networks are being used in industrial wireless applications due to their inherent capabilities. The effectiveness of cognitive radio depends on the type of Medium Access Control (M.A.C.) and handoff algorithms used and measured by its deterministic reinstating of transmission channels. However, the applicability of C.R. algorithms for multihop networks is less explored. Hence, in this paper, a deterministic handoff algorithm for multihop networks is proposed with the help of C.R. based M.A.C. A Common Control Channel (CCC) free M.A.C. based on G.I.N.M.A.C. termed as DynMAC (Dynamic M.A.C.) is chosen for experimentation. Unlike conventional DynMAC, new functionality that makes Child Nodes (C.N.) aware of the Global Channel (G.C.) list generated by Sink Node (S.N.) is added in DynMAC of the proposed approach. This, along with the spectrum handoff algorithm, facilitates switching transmission channels on receiving three consecutive errors. DynMAC is evaluated employing network calculus to model its arrival and service curves theoretically. Simulations have been carried out in the Integrated Development Environment (IDE) using DynMAC with and without the proposed spectrum handoff algorithm for both single and multihop networks.

Lognormal shadowing, Rayleigh fading, Rice fading, and interference is considered for finding Cumulative Distribution Function (C.D.F.) of delays and Packet Error Rate (PER). Results indicate that DynMAC when used with the proposed spectrum handoff algorithm, performs better compared to when it is used without the spectrum handoff algorithm. Finally, the proposed approach is compared statistically with other multi-hop-based M.A.C.s in terms of PER for substantiating simulation results. Friedman's test implies that significant differences between M.A.C.s and Holm's Procedure establish the proposed approach's superiority. The confidence level taken for performing a statistical analysis is 0.05, which means that the accuracy of the obtained results is 95%.

Keywords: Cognitive Radio, Industrial Applications, DynMAC, Spectrum Handoff, Determinism, Multi-Hop Networks

1 Introduction

Sensors are generally tiny, battery-powered devices that monitor and record conditions of environments. Conditions include temperature, pressure, humidity, the direction of wind and speed, illumination, the intensity of vibration, the intensity of sound, power line voltage, chemical concentrations, pollutant levels, and vital body functions. The sensors are usually placed in self-governing devices and are collectively referred to as sensor nodes. Sensor nodes are spatially distributed, with the number ranging from a few to several thousand. Connecting sensor nodes through wired networks is time-consuming and labour-intensive, especially when the distance is large. In industrial applications, using cables leads to high maintenance costs and aggregation of many wired equipment, which is dangerous in situations like fire outbreaks [1]. Hence, Wireless Sensor Networks (W.S.N.), which connects sensors wirelessly, is used in industries. International Society of Automation (I.S.A.) specifies six industrial systems: safety systems, closed-loop regulatory and supervising systems, open-loop control systems, alerting systems, and information gathering systems. W.S.N.s perform three basic tasks; collection, processing, and transmission of data [2]. While collection and processing depend on sensor nodes' inherent attributes, transmission works through cooperative action between sensor nodes. Transmission is enabled by various wireless standards like WirelessHART, I.S.A. 100.11a, Zigbee Pro, 6LoWPAN, and IEEE 802.15.4e. However, unlike normal W.S.N.s, Industrial W.S.N.'s has additional requirements such as interoperability, link reliability, service differentiation, a facility for data aggregation, noise resistance, deterministic latency, predictive behaviour, coexistence, support for multiple sources and sinks and application-specific protocols, which are not fully addressed by above standards [3].

Further, industrial machinery produces interference, in which mentioned standards do not guarantee deterministic behaviour. For example, in the fire case, an alarming signal is produced by the corresponding section that should reach the safety section in deterministic time. If not, it will result in human injuries and machine losses. Even extensions of IEEE 802.15.4e and Zigbee Pro are inappropriate in tackling this problem in the presence of interference.

It is a matter of concern in industrial applications which demand real-time capabilities.

Cognitive Radio (C.R.), proposed by J.Mitola [4], is a handy solution for I.W.S.N.'s. C.R. initially finds available channels (spectrum holes), and transmission is initiated in the best free channel. When interference happens, C.R.stops current transmission and switches to another available channel. However, it is not significant as other wireless standards, as the handoff process (a process of stopping transmission in one channel and reinstating in another channel) is not deterministic. Hence,the deterministic handoff process is required for using C.R.s in Industrial W.S.N.'s (I.W.S.N.'s).

Another point of interest is that as the energy range of sensor nodes is less, the transmission range is also less. It makes I.W.S.N.'s operate in a multihop fashion. Each sensor node sends processed information to another sensor node in a multihop scenario where it can be combined or just retransmitted to another node until the destined node is reached. This information sharing process among different nodes is called multi hopping, and such networks are termed multihopnetworks[5]. Other factors that boost the need for multihop networks in I.W.S.N.'s are the small size of sensors, low battery capacity, and limited processing ability. However, studies in C.R. have concentrated on single-hop networks, whereas multihop C.R. networks are gaining interest recently. Hence, in this paper, a deterministic spectrum handoff algorithm for C.R. in multihop networks is proposed[6].

The remainder of the paper is coordinated as follows. Segment 2 sums up associated works. Section 3 describes the mathematical preliminaries of chosen M.A.C. Section 4 elaborates on the proposed spectrum handoff algorithm. Section 5 briefs onthe application of network calculus to DynMAC. Section 6 showsthe results obtained along with its discussion. Section 7 depicts a statistical analysis of the proposed method, and other M.A.C.s and section 8 concludes the paper[7].

2 Related Work

Most wireless standards are based on IEEE 802.15.4 in I.W.S.N.'s as they require low data rate transmission over relatively small distances. On the contrary, IEEE 802.11 is concerned with long-range transmission and data throughput of 2-54 Mbps [8]. WirelessHART is an I.W.S.N. standard that uses IEEE 802.15.4 in the physical layer. In the data link layer, Medium Access Control (M.A.C.) is improved through adding time slots of 10 ms and utilizing Time Division Multiple Access (T.D.M.A.), thereby reducing the number of collisions [9].However, it is specifically used for process automation, and only dedicated links are present instead of shared links that are not suited for deterministic industrial applications. I.S.A. 100.11a has IEEE 802.15.4 physical layer, but the M.A.C. layer is extended with a combination of T.D.M.A. and CSMA. Though determinism is achieved and single hops, as well as multihop topologies, are supported, it has the disadvantage of high implementation cost.

Further, hopping is slow in multihopnetworks, which increase power consumption [10]. Zigbee is another wireless standard launched on top of

IEEE 802.15.4, which has its network and application layers. An extended implementation option is Zigbee Pro which is used for large networks.

Though it supports mesh and cluster tree topologies, it is interoperable only with Zigbee devices. Further, static channel usage increases interference, and there is higher power consumption, limiting its use in multihop networks [11]. 6LoWPAN is a suitable wireless standard for multihop I.W.S.N.s as it is specifically designed for large geographic areas and has low power consumption, computation time, cost, etc. It also works on top of IEEE 802.15.4 physical and M.A.C. layer. However, they are prone to link failures, and performance in the presence of interference is not satisfactory [12]. IEEE 802.15.4e is an advanced version with IEEE 802.15.4 MAC layer amended by taking some functionality from WirelessHART and I.S.A. 100.11a. This approach has latency concerns which make it unsuitable for industrial applications. In state-of-the-art works, authors experimented with an improvement to IEEE 802.15.4e with star topology [13]. However, the extension is limited to single-hop networks and does not work out for multihop networks.

From the analysis, it is clear that all improvements in wireless standards are carried out in the M.A.C. layer. Hence, in our paper, the spectrum handoff algorithm is proposed for multihop networks in the C.R. based M.A.C. context.

Dynamic Slot Allocation based T.D.M.A. (D.S.A.T.) M.A.C. is a CR-MAC proposed to achieve energy-efficient utilization of spectrum [14]. Since it is implemented using single radio, interference, collision, and hidden node problems are not considered. Fair (F) M.A.C. though addresses interference problems, it is inherently designed with the constraint that there are only one primary user and N secondary user, which is not the case in I.W.S.N.s [15]. Hybrid (H) M.A.C. uses a modified CSMA/CA protocol that employs overlay spectrum sharing to access Primary User (PU). Hence, both P.U. and Secondary User (S.U.) transmit at the same time. However, it tolerates only minimum interference [16]. In Grouping and Cooperative sensing (G.C.) M.A.C., S.U.s are grouped into several teams and S.U.s in each team's senses channels jointly. Interference affects the working of M.A.C., questioning its suitability for industrial applications. In Hardware Constrained (H.C.) M.A.C.s, a particular S.U., can either transmit or sense. There is a Common Channel (CC) through which S.U.s share information among each other. But P.U.s tolerate interference from S.U.s to certain degrees. All the above protocols are proposed in the literature for single-hop networks and are of no interest in our approach. Synchronized (SYN) M.A.C. is proposed for multihop networks. Here, all out time is partitioned into constant time spans. In every time allotment, one of the available channels is applied for control signal trades. All matters considered, covered up terminal problems could not be dodged. For reducing interference levels of S.U.s in P.U.s, C.R. Enabled Multi-Channel (CREAM) M.A.C. was put forward in.

In all methods mentioned above, Common Control Channel (CCC) is deployed to control channels. CCC's are meeting points of S.U.s in C.R. networks. When S.U.s become crowded in CCC, performance is decreased as

nodes that are not properly synchronized cannot know the activities of neighbouring C.R. users. These reasons point towards the need for CCC to open C.R.M.A.C. protocols. Song and Xie proposed a QoS Based Broadcast Protocol Under Blind Information for Multi-hop CR networks (QB²IC) [18]. The design considers practical facts such as lack of knowledge of network topology and channel information of S.U.s. In traditional CCC based networks, if a node receives multiple copies of messages from parent nodes, it leads to a collision. In multihop networks, such situations become unavoidable when parent nodes transmit at the same time. But QB²IC protocol tackles it effectively as the receiver can listen to only one channel at a time. However, the approach fails when parents select the same channel for transmission. A Deterministic Real-Time Medium Access (D.R.M.A.C.) for cognitive industrial radio networks is recommended [19]. Though D.R.M.A.C. works for any topology, it is not suitable for multihop networks.

Hence, for implementing the proposed spectrum handoff algorithm, a CCC open C.R. M.A.C. protocol suitable for multihop networks needs to be taken. Dynamic M.A.C. (DynMAC) is found to be the most suited one. DynMAC is based on GINMAC. G.I.N.M.A.C. becomes DynMAC when cognitive capabilities like monitoring environmental conditions, mobility, sharing information, and decision on the best channel are added to G.I.N.M.A.C. The following section provides a detailed description of DynMAC.

3 DynMAC Preliminaries

As DynMAC is based on G.I.N.M.A.C., an overview of the GINSENG Project and G.I.N.M.A.C. is provided, followed by a detailed discussion of DynMAC.

3.1 GINMAC

In G.I.N.M.A.C., tree topology is considered where sensor nodes are child nodes, and the root node is a sink node. Two parameters define the topology of G.I.N.M.A.C., one is maximum hop distance, and the other is a fan-out-degree. Fan-out degree corresponds to several sensor nodes at each level. The fan-out degree at the sink node level is one as there is only one root node in a multihop tree topology. G.I.N.M.A.C. employs offline dimensioning mechanisms, which means sensor nodes possess knowledge of their positions in the topology and parent and child nodes based on their I.D. G.I.N.M.A.C. ensures real-time functions in industrial environments using the T.D.M.A. technique. Each sensor node has different time slots in which it can transmit data to or from the sink node. The slot reserved for one node cannot be used by other nodes. The flow of traffic from sensor nodes to the sink node is termed upstream [20].

Consequently, child nodes require a one-time slot for communicating with the parent node, whereas parent nodes require two slots, one for incorporating information from child nodes and others for its data.

Downstream is the flow of traffic from sink nodes to actuators. The sink sends data to actuators. Hence, sink nodes require at least as many basic slots as that of the number of actuators. Thus, total time slots are the total number of upstream slots and downstream slots. Fig.1 shows a frame structure of G.I.N.M.A.C.

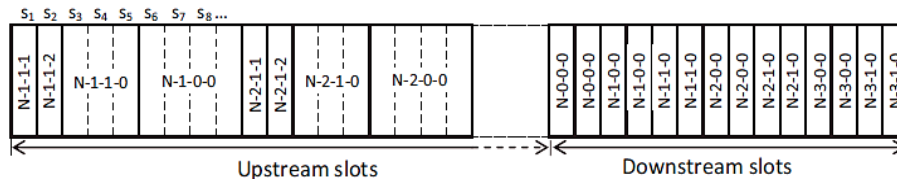


Fig.1. GinmacTdma Frame

3.2 DynMAC INCORPORATED GINMAC

Though G.I.N.M.A.C.can tackle packet loss and improve delivery rate, automatic avoidance of interference in environments where other wireless networks and devices exist is not available. When CC2420 radios are used,interference is avoided to some extent. However, when interference is present in adjacent channels, the mechanism fails. DynMAC tackles these limitations by adding cognitive characteristics to G.I.N.M.A.C. DynMAC monitors environment conditions, assesses the best channel, and share information about the best channel to nodes. By environmental conditions, we mean occupancy of channels. There are various mechanisms to assess it, and in our paper, we use the Received Signal Strength Indicator (RSSI). RSSI is an indicator of the strength of a signal received by each node. It is chosen as this mechanism is available in radios of sensor nodes. Each node obtains RSSI values periodically, thereby providing a good approximation of channel conditions.

GinMAC is a Medium Access Control (MAC) protocol designed to meet the real-time requirements of Wireless Sensor Actuator Networks (WSAN) applications. We present a formal executable specification for the GinMAC protocol in this article. We can specifically capture and evaluate the abstract features of this protocol using this formal executable model. Our platform-independent systematic executable system could be used as a framework for further study of the protocol or any protocol extensions that are made to it.

3.3 Spectrum Sensing, Local Best Channel, and Global Best Channel

During the spectrum,the sensing sink node collects RSSI values of all channels. The number of channels is equal to the number of nodes. The RSSI values obtained periodically are accumulated and stored. Additionally, RSSI values greater than a particular threshold defined by CC2420 radios is separately stored. On completion of spectrum sensing, RSSI values are stored in ascending order. Next,the cost of each channel is calculated by using two sets of information. 1) The sorted RSSI value and 2) the frequency that collected RSSI values are greater than the threshold. The former is termed

RSSI cost and later threshold cost. The RSSI cost for the smallest accumulated RSSI value is 1. The RSSI, as well as threshold costs, are added. When accumulated RSSI changes periodically, the RSSI cost is increased by 1 unit. The final sorted list best channel is chosen by the sink node and informs it to other nodes by broadcasting a control frame with the network's Group Identification (GID) number.

The child nodes repeatedly search all channels for a valid frame from the sink node. Once a frame is detected, GID is checked to verify whether it is from the sink node. If GID matches, child nodes stop searching and join the network by switching to the sink's channel. Additionally, child nodes send a joining frame to the sink node, acknowledging it by sending an acknowledgement frame. However, the channel selected by the sink node might not be the best channel when the network is considered as a whole because the sink node selects the best channel based on its local information only. Therefore, the best channel calculated by the sink node is called the local best channel. The noise and interference may vary considerably between the child and sink nodes. Hence, all nodes should contribute to the process of selecting a channel for communication. But in real environments, all nodes do not join the network at any time. Therefore, the global best channel selection process starts when the network reaches a stable state, i.e., at least one node joins the network other than the sink node. Once the global best channel selection process is started, sink nodes send solicit messages to child nodes asking them to provide channel information. Each node calculates the best channels in the same manner as was discussed earlier and forward them to the sink node. The sink node selects the best channel from available information. If the best channel is different from the current working channel sink node sends switching channel messages to parent nodes, send them to their child nodes. Finally, all nodes operate on the same channel.

3.4 Limitations

However, certain problems arise in DynMAC, which limits its use for deterministic applications. One scenario is that channel switching messages might not be delivered properly to child nodes due to interference. This results in child nodes transmitting in one channel and sink nodes transmitting in another channel, thereby disrupting communication. DynMAC tackles it by making nodes rescan the sink's communication channel if it cannot communicate with its parent for a specific duration. However, this is unusable in deterministic applications as interference may induce prolonged delays in reinstating the same channel across sink and child nodes. The same occurs in the case of communication between child and parent nodes. Secondly, even when transmission occurs in the same channel, interference may occur in the middle of transmission resulting in jamming the channel, thereby losing connectivity. Hence, an algorithm that detects interference and recovers transmission in another available channel in deterministic time is proposed.

4 Proposed Spectrum Handoff Algorithm

As mentioned in section 3, DynMAC sensor nodes work based on offline dimensioning mechanisms. Hence, each node is aware of its parent or child nodes. Once the sink node sends channel switching messages, child nodes send joining frames back to sink nodes. In case of interference, these frames are not received by sink nodes since such frames are not generated, as channel switching messages are not received by child nodes. Hence, if the sink node does not receive a joining frame after sending a channel switching message, it is considered an error.

Similarly, if the parent node does not receive a joining frame from the child node, it is also considered an error. Further, as DynMAC is a traditional M.A.C., slots are reserved for nodes irrespective of whether there are packets to transmit or not. This makes parent nodes unaware of packet loss due to interference as they consider it a lack of packets instead of a loss of packets. This is a matter of serious concern in deterministic real-time industrial applications where every packet is vital. Hence, in the proposed approach, two functionalities are appended. One is a new flag functionality added to child nodes of DynMAC, which informs parent nodes that packets are there to transmit. This flag frame is sent repeatedly until parent nodes are aware of packets' presence in upcoming slots. Therefore, when the flag is active and parent nodes do not receive a packet from child nodes, it is considered an error. Once an error is found, the flag frame is sent back to the child node. Another feature of our proposed approach is that every child node is updated with the sink node's final channel list for selecting the best channels. Hence, when communication is lost child node itself can hop to the best channel without rescanning the sink node. Therefore, errors are detected in the M.A.C. layer. When DynMAC is used for cognitive radio, waiting for a specific time duration to scan the sink node and hop to another channel is not feasible. A consecutive number of errors received is taken as a metric to hop to another channel in our proposed approach. The schematic representation of the proposed handoff algorithm is shown in Fig.2. It represents three instances of communication loss. In the first instance, due to interference, no Joining Frame (J.F.) is generated, and hence there is a loss in communication. After three instances, the Child Node (C.N.) detects Interference; Best Channel (B.C.) selects B.C. and hops to another Channel Hoping (C.H.).

In industrial networks, the number of consecutive errors is chosen to maintain trade-offs between speed and robustness. If any errors are chosen as a condition for hopping, delays become prolonged, thereby failing to meet deterministic requirements. On the contrary, if a small number of errors is chosen, nodes may hop to another channel even when no interference is jamming the channel. For example, if the wireless channel has harsh errors or when packets are transmitted in a dispersive channel, nodes may sense it as

SN	INTERFERENC E	CN	COMMUNICATION	SN	CN	CN	CN	CN
CSM	YES	NO JF	LOST	X	X	-	-	-
CSM	YES	NO JF	LOST	X	X	-	-	-
C.S.M	YES	NO JF	LOST	X	X	ID	BC	CH

Fig.2.Channel Hopping Of Child Nodes When Csm Messages Are Lost Due To Interference

interference. Hence, the number of consecutive errors is chosen in our approach based on the Packet Error Rate (PER) of the channel, thereby maintaining a compromised solution between delay and hopping probability. As shown in Fig.2, Sink Node (S.N.) sends Channel Switching Messages (C.S.M.) to Child Nodes (C.N.). Interference makes C.S.M. not reach C.N. As a result, no Joining Frames (J.F.) is generated by C.N., and communication is lost, which is indicated by errors in S.N. and C.N. It must be noted that the first two errors are not considered as interference due to earlier mentioned trade-offs. Once three consecutive errors take place, interference is detected (I.D.). Next, C.N. selects Best Channel (B.C.) from S.N.'s global channel list, and Channel Hopping is done.

CN FLAG	INTERFEREN CE	PN	CN FLAG	INFO	PN	CN	CN	CN	CN
ACTIVE	YES	NO PACKET S	SEND BACK TO CN	LOS T	X	X	-	-	-
ACTIVE	YES	NO PACKET S	SEND BACK TO CN	LOS T	X	X	-	-	-
ACTIVE	YES	NO PACKET S	SEND BACK TO CN	LOS T	X	X	ID	BC	CH

Fig.3. Channel Hopping Of Child Nodes When Packets Are Lost Due To Interference

Fig.3 shows channel hopping of child nodes when packets are lost due to interference. Once packets are there to transmit, C.N. sends flag frames to Parent Nodes (P.N.). Interference makes packets not reach C.N. nodes. Therefore, information is lost, and P.N. sends back flag frames to C.N. Once three consecutive errors take place, interference is detected (I.D.). Next, C.N. selects Best Channel (B.C.) from S.N.'s global channel list, and C.H. is facilitated. Finally, the sink nodes, as well as other nodes, start operating on

the same channel. This operation type enables DynMAC to detect interference and hop to the next channel deterministically without rescanning S.N. or carrying out spectrum sensing. Thus, the proposed handoff algorithm ensures time-bound in delay traffic, and since DynMAC used to evaluate it is not based on CCC, problems due to external interference are avoided.

5 Application of Network Calculus to DynMAC Based Spectrum Handoff Algorithm

Network calculus is used to characterize traffic arrival and the ability of the proposed system to handle that traffic theoretically. The arrival curve characterizes traffic arrival, and the service curve characterizes traffic handling ability. In the case of static T.D.M.A., the arrival curve for periodic traffic is given in Equation (1).

$$\alpha(t) = L \left\lceil \frac{t}{T} \right\rceil \tag{1}$$

Where T is the flow period, and L is packet length. In the service curve case, for determining minimal guaranteed flow, the T.D.M.A. frame should be analyzed. As mentioned in previous sections, for DynMAC, each node is assigned a particular slot to transmit. The frame length is given in Equation (2). It should be noted that DynMAC frame length is longer than G.I.N.M.A.C. as C.R. algorithms consume more time.

$$c = \sum_{k=1}^M t_{slot} + t_{sync} \tag{2}$$

Where M is the number of nodes in a network, t_{slot} is slot length and t_{sync} is synchronization time. Therefore, the service curve can be estimated by Equation (3).

$$\beta(t) = B. \max\left(\left\lfloor \frac{t}{c} \right\rfloor t_{slot}, t - \left\lfloor \frac{t}{c} \right\rfloor (c - t_{slot})\right) \tag{3}$$

Bis linked transmission capacity, a T.D.M.A.C. service and arrival curve plot for traffic flow whose inter-arrival time equals frame duration is shown in Fig.4.

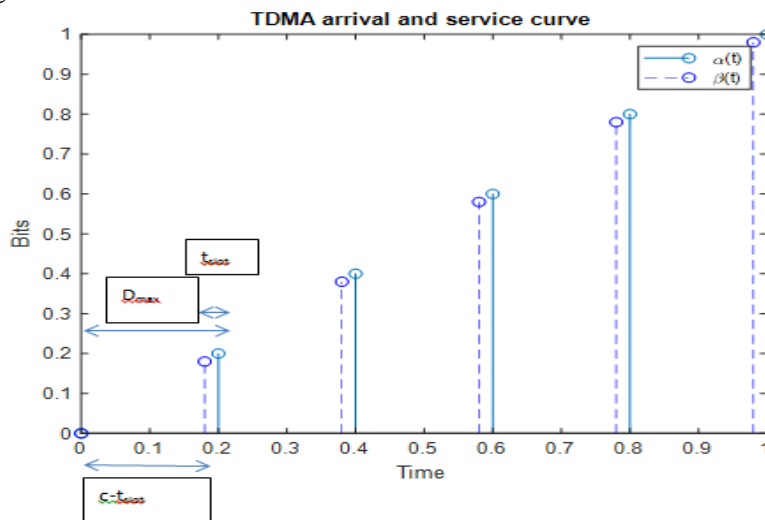


Fig.4. TDMA Arrival And Service Curve

As DynMAC adds cognitive capabilities to the G.I.N.M.A.C., two slots are added to the G.I.N.M.A.C. frame for spectrum sensing. Fig.5 shows the G.I.N.M.A.C. frame with two additional slots for single and multihop networks.

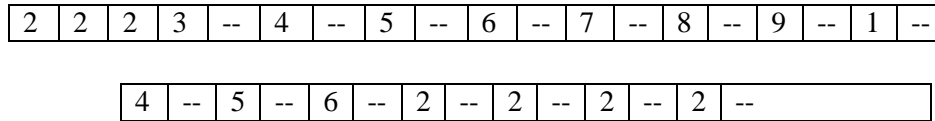


Fig.5. Ginmac Frame With Two Additional Slots For Single Hop And Multihop Networks

From Fig.5, it is clear that the node can wait for a maximum of 3 slots to access the medium. Hence, the maximum time which a node takes to access the medium is $c - 3.t_{slot}$. When a medium is accessed, the node has three chances to send packets. Therefore, the service curve $\beta(t)$ is given in Equation (4).

$$\beta(t) = B. \max\left(\left\lfloor \frac{t}{c} \right\rfloor t_{slot}, t - \left\lceil \frac{t}{c} \right\rceil c\right) \quad (4)$$

The service and arrival curves of DynMAC are jointly plotted in Fig.6.

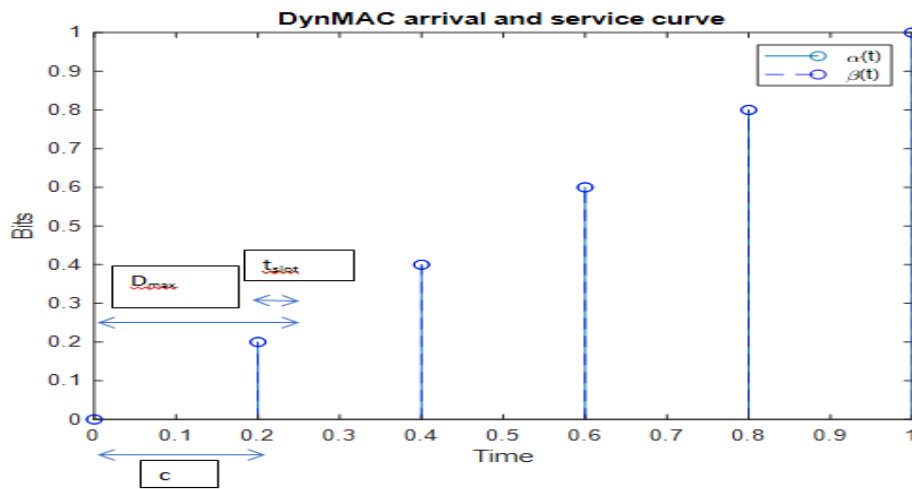


Fig.6. Arrival And Service Curves For DynMAC

The horizontal distance between the service and arrival curves gives maximum delay, as shown in Equation (5).

$$D_{max} = c + t_{slot} \quad (5)$$

The full-time nodes take to access medium in multihop networks is similar to that of single-hop networks. However, due to two hops, the maximum time between transmission and reception of packets between nodes is $21.t_{slot}$. For example, from Fig.6, if node 4 transmits a packet to node 2 in the initial slot, it might not be traced at node one till the last slot of node 2. Hence, the DynMAC multihop network's service curve can be depicted as in Equation (6), and maximum delay is given in Equation (7).

$$\beta(t) = B. \max\left(\left\lfloor \frac{t}{c} \right\rfloor t_{slot}, t - \left\lceil \frac{t}{c} \right\rceil (c + 20.t_{slot})\right) \quad (6)$$

$$D_{max} = c + 21 \cdot t_{slot} \quad (7)$$

5.1 Multi-Hop DynMAC with Spectrum Handoff

As a result of spectrum handoff, though interference is detected, the delay is increased compared to normal multihopDynMAC. This is because the time is taken for interference avoidance, and data gets accumulated in the queues. This is considered while obtaining service curves. Therefore, the maximum delay is given by Equation (7).

$$D_{max} = c + T_{BC} + T_{CH} + 21 \cdot t_{slot} \quad (8)$$

Where T_{BC} is the time taken to find the best channel and T_{CH} is channel hopping time.

The maximum delay in Equation (8) is greater than Equation (7) attributed to the spectrum handoff process. Delay is sacrificed for achieving determinism and detecting interference. The following section gives a detailed description of simulation results obtained for the proposed DynMAC based spectrum handoff algorithm.

6 Results and Discussion

The simulations were carried out in C++ based Integrated Development Environment (IDE). The nodes were randomly placed in 100m x 100m square to imitate real-time industrial multihop topology. All nodes are simulated based on the IEEE 802.15.4 physical layer. The proposed DynMAC based spectrum handoff algorithm is evaluated in terms of PER and delay. In industrial wireless scenarios, fading is one of the major factors that influence packets' transmission and reception. For simulation purposes, they are often modelled as a random process. Fading can be slow or fast. Slow ones are termed shadowing and occur when the path between transmitter and receiver is obstructed. They are modelled, as shown in Equation (9).

$$PL(d) = PL(d_0) + 10n \log_{10} \left(\frac{d}{d_0} \right) + X_{\sigma} \quad (9)$$

Where $PL(d_0)$ is path loss in dB at a distance d_0 , $PL(d)$ is path loss in dB at an arbitrary distance d and X_{σ} is zero-mean random variables with standard deviation σ . Fast fading occurs as a result of small changes in results between transmitter and receiver. In our approach, we used Rayleigh fading and Rician fading to model fast fading, as shown in Equation (10).

$$PL(d) = \sigma - \sqrt{-2 \log U} \quad (10)$$

Where U is uniform distributed numbers in the interval [0 1]. Rician fading is similar to that of Rayleigh fading except that the Line of Sight (L.O.S.) component is present. The arrival rate is modelled according to stationary traffic, as mentioned in network calculus. Further, other networks may coexist in a networking environment leading to interference. Hence, WiFi interference was also considered for simulations. Table 1 shows the PER of DynMAC with a spectrum handoff algorithm for both single-hop and multihop networks under lognormal shadowing, Rician fading, and Rayleigh Fading.

Table 1: DynMACFor Different Fading Environments

	Single Hop			Multihop		
	Lognormal Shadowing	Rician Fading	Rayleigh Fading	Lognormal Shadowing	Rician Fading	Rayleigh Fading
DynMAC	190	590	16300	3300	3700	5300
DynMAC with spectrum handoff	150	510	15700	3110	3300	4900

From Table 1, it is clear that DynMAC inherently gives small PERs in single-hop networks for lognormal shadowing and Rician Fading. This is because there is no L.O.S., and received power is exponentially distributed in the presence of shadowing. In Rician fading, a stronger L.O.S. component leads to the rare occurrence of deep fades resulting in low PERs. The error rate is much higher in the Rayleigh fading channel attributed to the Rayleigh channel's time-varying envelope that decreases the system's instantaneous PER. In multihop networks, packet error probability increases with the number of hops, as is evident from PER values. DynMAC, when used in single-hop networks with spectrum handoff, shows low PERs compared to normal DynMAC. But its effect is more profound in multihop networks, proving that the proposed handoff algorithm is suitable for multihop networks under fading environments. Fig.7 shows the performance of DynMAC in the presence of interference for single-hop and multihop networks.

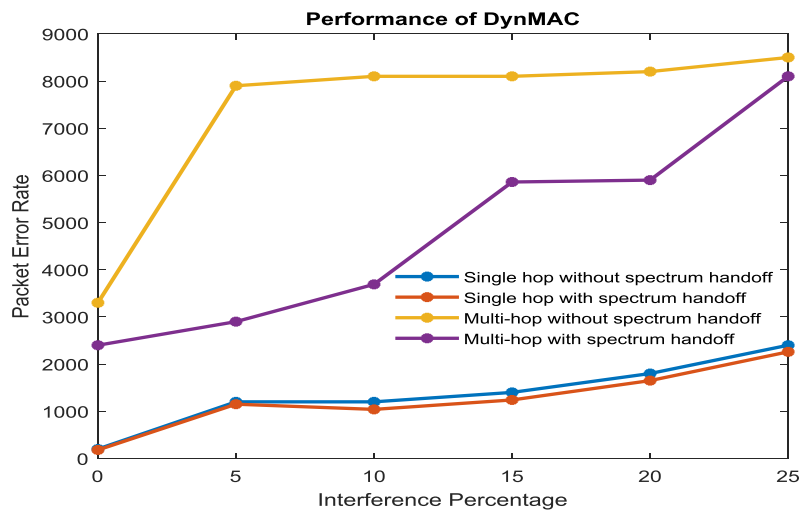


Fig.7. Performance Of Dynmac With And Without Proposed Spectrum Handoff Algorithm For Single And Multihop Networks

From Fig.7, it is obvious that single-hop networks with handoff produce the least PER in environments affected by interference, whereas multihop networks without spectrum handoff produce the highest PER. In the case of both single-hop and multihop networks, the proposed algorithm is found to decrease PER. However, the approach should be validated in terms of delay, which is significant in deterministic industrial applications. Fig.8 and Fig.9 shows the delay of DynMAC with and without the proposed handoff algorithm in lognormal fading environments.

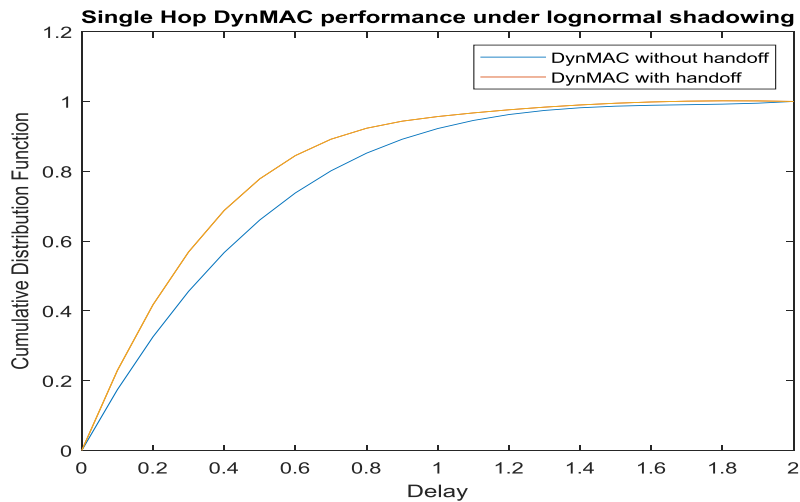


Fig.8. Delay For Lognormal Shadowing In Single Hop Networks

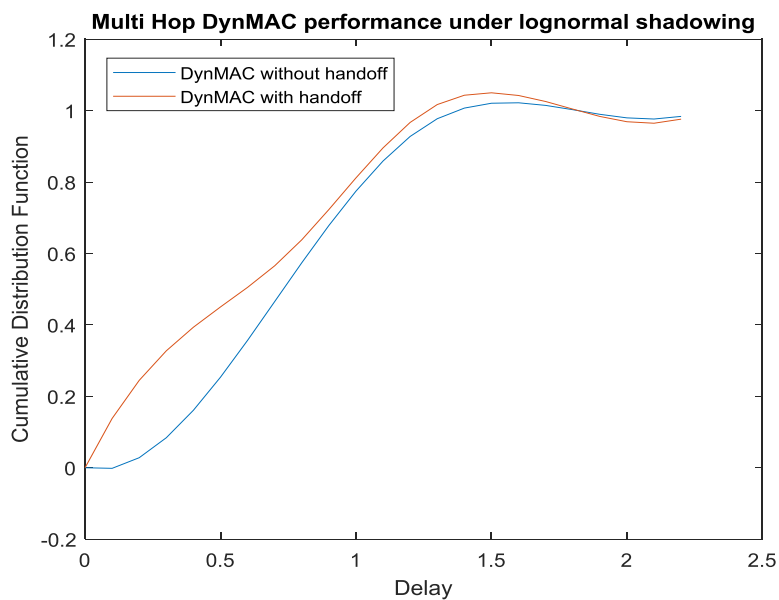


Fig.9. Delay For Lognormal Shadowing In Multihop Networks

In single-hop networks, the proposed spectrum handoff algorithm shows better delay performance than a network that used normal DynMAC. Further, the algorithm maintains its performance in multihop networks too.

However, the delay is increased in multihop networks as the number of hops is more. The decrease in delay in the proposed approach can be attributed to flag functionality and provision provided to C.N.s for selecting the best channel, unlike conventional DynMAC, where S.N. is solely responsible for selecting the best channel. Fig.10 and Fig.11 show delays in frames for Rayleigh fading environments.

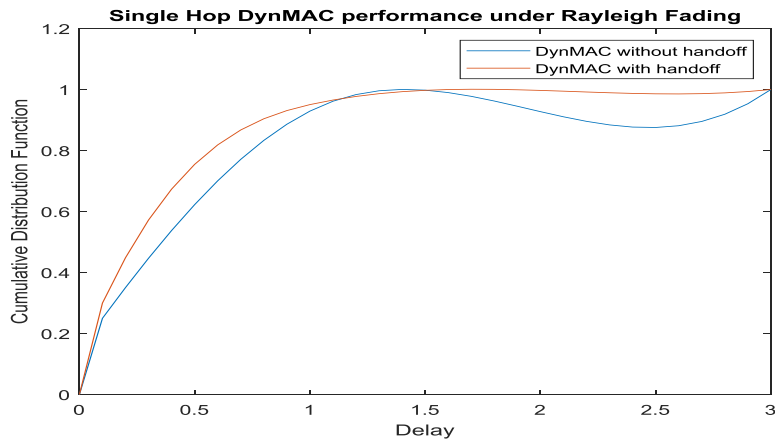


Fig.10. Delay For Rayleigh Fading In Single Hop Networks

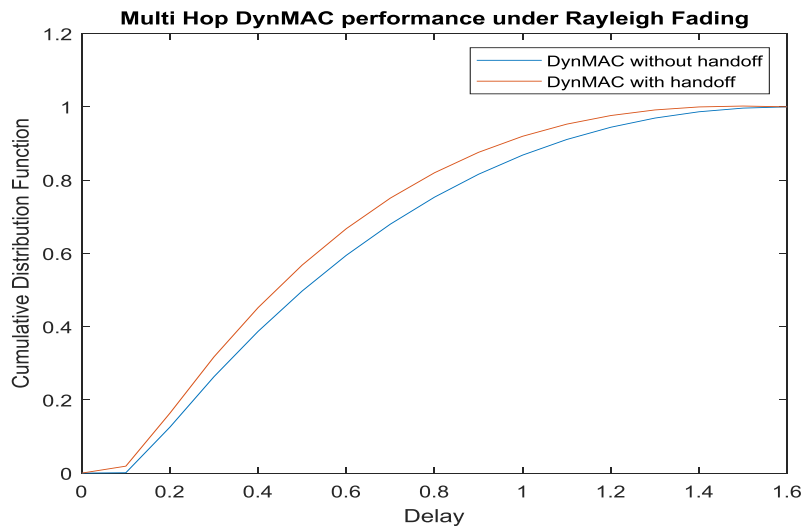


Fig.11. Delay For Rayleigh Fading In Multihop Networks

It should be noted that delays are higher in Rayleigh fading channel compared to lognormal shadowed channels. In Rayleigh fading, many objects are present in the environment that scatters signals before getting to the receiver. However, the proposed algorithm shows better performance in Rayleigh environments, too, owing to additional functionalities added in

DynMAC along with usage of three consecutive errors for hopping to the next channel by C.N.'s. Rice fading is not discussed as it provides results similar to that of lognormal shadowing.

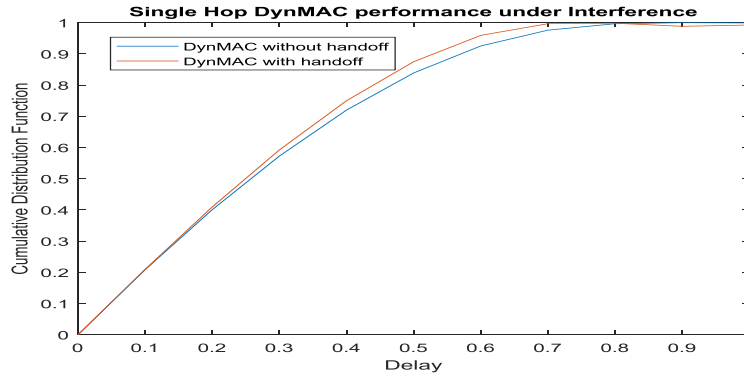


Fig.12. Delay For Single Hop Networks In The Presence Of Interference

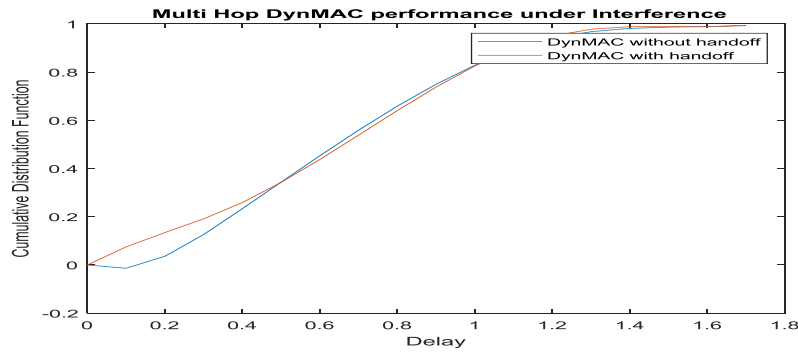


Fig.13. Delay For Single Hop Networks In The Presence Of Interference

Fig.12 and Fig.13 shows the cumulative distribution function of the proposed algorithm at 25% interference. When M.A.C. is used without a spectrum handoff algorithm, it increases delay. On the other hand, when used, a C.R. system capable of detecting interference and hopping to another channel in a deterministic time is created. Additionally, resultant delays of the proposed algorithm are similar to that of interference-free environments. From the overall analysis of delay and PER, the proposed spectrum handoff algorithm ensures determinism and robustness against interference. This also establishes its suitability in industrial wireless sensor and actuator networks. To validate simulation results, statistical analysis is carried out in the following section by comparing PER of the proposed approach with other M.A.C. approaches.

7 Statistical Analysis

Statistical analysis is performed on obtained results to establish the proposed method's superiority over other methods that are otherwise unclear from graphical representations. Since we compare methods whose variables

are ordinal dependent, the Friedman test is employed to find significant differences. We chose PER of multihop networks to perform statistical analysis as it is significant in our study. Table 2 provides PERs of five different M.A.C.s viz priority M.A.C., G.I.N.M.A.C., QB2IC, DynMAC and DynMAC with handoff under increasing rates of interference.

Table 2: PERs OF MACs At Different Levels Of Interference

Interference	Priority MAC	GINMAC	QB2IC	DynMAC	DynMAC with Handoff
0%	2500 (3)	800 (1)	56000 (5)	3300 (4)	2400 (2)
5%	3100 (3)	2400 (1)	57500 (5)	7900 (4)	2900 (2)
10%	3700 (2)	6600 (3)	63800 (5)	8100 (4)	3690 (1)
15%	5900 (2)	20800 (4)	63800 (5)	8100 (3)	5860 (1)
20%	6600 (2)	51700 (4)	67600 (5)	8200 (3)	5900 (1)
25%	9000 (3)	123800 (5)	63800 (4)	8500 (2)	8100 (1)
Total Rank	15	18	29	20	8
Average Rank	2.5	3	4.83	3.33	1.33

Each algorithm is ranked from 1 to 5 based on its values, the least PER being given the first rank and the highest being given the last rank. The ranks are then averaged. The Friedman test's first step is to define a null hypothesis that states that there are no significant differences between groups.

$H_0 = \text{There are no significant differences between groups}$

Now Friedman statistic is obtained from Equation (11).

$$FM = \frac{12}{N * k * (k + 1)} * \sum R^2 - [3 * N * (k + 1)] \quad (11)$$

Where N is the number of interference variations, k is the number of M.A.C.s under studies, and R is the total rank value of each column. Substituting N , k , and R we get a value of 15.6 for F.M. Now, for the same N and k values and $\alpha = 0.05$, the Chi-Square table gives FM critical value 11.07. Since obtained FM value is greater than FM critical value null hypothesis is rejected, thereby proving that significant differences exist between methods. The significance of the proposed algorithm is found by employing Holm's procedure as a post hoc test. As in the Friedman test, a null hypothesis is stated initially.

$H_0 = \text{All MACs have the same performance}$

Initially, the z value is calculated using Equation (12)

$$z = \frac{R_i - R_j}{SE} \quad (12)$$

Where R_i is the average rank of DynMAC with handoff and R_j is the average rank of other M.A.C.s and $SE = \sqrt{\frac{k(k+1)}{6N}}$. The probability values are obtained from a table of the normal distribution for each z value. Finally, p -values are compared with $\alpha/(k - i)$ values. When $\alpha/(k - i)$ values are greater than the p -value, the null hypothesis is rejected. Table 3 summarizes Holm's procedure.

TABLE 3: HOLM'S PROCEDURE

i	MAC	z-value	p-value	$\alpha/(k - i)$	Null Hypothesis
1	Priority MAC	-1.2817	0.0999	0.0125	Not Rejected
2	GINMAC	-1.8294	0.0337	0.016	Not Rejected
3	QB2IC	-3.8340	0.000063	0.025	Rejected
4	DynMAC	-2.1909	0.0142	0.05	Rejected

From Table 3, it is clear that the proposed algorithm outperforms DynMAC and QB2IC. However, Holm's procedure shows that Priority M.A.C. and G.I.N.M.A.C. have performance closer to the proposed algorithm. This is because Holm's procedure considered average ranks of M.A.C.s rather than total ranks as in the Friedman test, which leads to a reduction in differences of values between M.A.C.s as they are limited to 0 to 6 intervals. However, it is clear from Table 3 that at higher levels of Interference, G.I.N.M.A.C. shows large deviations from the proposed algorithm. On the other hand, priority M.A.C. though maintaining a considerable performance, the absence of handoff algorithms makes it unsuitable for deterministic applications.

Hence, statistical analysis confirms the effectiveness of the proposed algorithm over other states of the art methods.

8 Conclusion

The deterministic capabilities of cognitive radio lead to its popularity in wireless sensor applications. But the idea of using cognitive radio and existing wireless standards in deterministic industrial scenarios has gained interest recently. Though applied to single-hop networks, its applicability in multihop networks needed attention. Moreover, the use of cognitive radio in conventional standards showed lower performance. Further, the absence of deterministic handoff algorithms hindered its development and deployment. Hence, in this paper, a spectrum handoff algorithm based on one of the advanced M.A.C.s known as DynMAC for multihop networks is presented. The approach can detect interference in the middle of transmission and hops to another channel in deterministic time. The suitability of DynMAC is analyzed with the help of network calculus. Simulations were carried out for the proposed algorithm considering both single-hop and multihop networks under different fading and interference environments to determine packet error rate and delay. The results indicate better performance of the proposed algorithm, which is verified by statistical analysis. The capability to avoid interference deterministically adds robustness to the system, thereby assuring its use in industrial wireless sensor and actuator networks. As an extension, the system's response to non-stationary traffic considering both single and multihop networks will be studied in the future.

References

- [1] A.J.Watt et al., “Wireless Sensor Networks for monitoring underwater sediment transport”, *Science of the Total Environment*, Vol. 667, pp. 160–165, 2019.
- [2] S.Kharb and A.Singhrova, “Next-Generation Networks”, *Advances in Intelligent Systems and Computing*, 2018.
- [3] J.Mitola AND G.Q.Maguire, Jr, “Cognitive Radio: Making Software Radios More Personal”, *IEEE Personal Communications*, Vol. 6, no. 4, pp. 13-18, 1999.
- [4] C.Campbell et al, “Comparison of IEEE 802.11 and IEEE 802.15.4 for Future Green Multichanne Multi-radio Wireless Sensor Networks”, *International Journal of Communication Networks and Information Security*, Vol. 3, no. 1, pp. 96-103, 2011.
- [5] K.S.J.Pister and L.Doherty, “TSMP: Time Synchronized Mesh Protocol”, *IASTED International Symposium Distributed Sensor Networks*, pp. 691-698, 2008.
- [6] Group, W.W, “Draft standard ISA100. 11a. In: Internal Working Draft, International Society of Automation, 2008.
- [7] Available Online : <http://www.zigbee.org/>
- [8] IETF IPv6 over Low power WPAN, Available Online: <https://datatracker.ietf.org/wg/6lowpan/documents/>
- [9] W.Y. Lee et al, “Distributed fast beacon scheduling for mesh networks”, *8th IEEE International Conference on Mobile Ad-hoc and Sensor Systems*, 2011.
- [10] N.K.Verma and A.Roy, “DSAT-MAC: dynamic slot allocation based TDMA MAC protocol forcognitive radio networks”, *Ninth International Conference on Wireless and Optical Communications*, 2012.
- [11] Y.Zhao et al., “FAMC: A fair MAC protocol for coexisting cognitive radio networks”, *IEEEI NFOCOM*, 2013.
- [12] N.Faruk, “Performance analysis of hybrid MAC protocol for cognitive radio networks”, *International Journal of communications, network and system sciences*, Vol. 6, no. 1, pp. 18-28, 2013.
- [13] Yi Liu et al., “An efficient MAC protocol with selective grouping and cooperative sensing in cognitive radio networks”, *IEEE Transaction on Vehicular Technology*, Vol. 62, no. 8, 2013.
- [14] J. Jia et al., “HC-MAC: a hardware constrained cognitive MAC for efficient spectrum management”, *IEEE Journal of selected areas in communications*, Vol. 26, no. 1, pp. 106-117, 2008.
- [15] Y. R. Kondareddy and P. Agrawal, “Synchronized MAC protocol for multi-hop cognitive radio networks”, *IEEE International Conference on Communications*, 2008.

- [16] X Zhang and H Su, "CREAM-MAC: cognitive radioenabled multi-channel MAC protocol over dynamic spectrum access networks", IEEE Journal of selected topics in signal process, Vol. 5, no. 1, pp. 110-123, 2011.
- [17] Y.Song and J.Xie, "QB2IC: A QoS-Based Broadcast Protocol Under Blind Information for Multihop Cognitive Radio Ad Hoc Networks", IEEE Transactions on Vehicular Technology, Vol. 63, no. 3, pp.1453-1465, 2014.
- [18] P.M.Rodriguez et al., "Spectrum Handoff Strategy for Cognitive Radio-based MAC for Real-time Industrial Wireless Sensor and Actuator Networks", Computer Networks, Vol. 152, pp. 186-196, 2019.
- [19] L.H.A.Correia et al., "DynMAC: A resistant MAC protocol to coexistence in wireless sensor network", Computer Networks, Vol. 76, pp. 1-16, 2015.
- [20] A.R.Uppala, C.V.Narasimhulu and K.S. Prasad, "Implementation of MAC Protocol for Analysis of Traffic in Smart Cities", Implementation of MAC Protocol for Analysis of Traffic in Smart Cities, Vol.11, no. 6, pp. 1349-1357, 2019.

Biographies



AppalaRaju.Uppala received the Diploma in Electronics and Communication Engineering (E.C.E.) from Govt. Polytechnic College, Narsipatnam, the A.M.I.E Degree in E.C.E. from Institution of Engineers India, Kolkata, the M Tech degree from Jawaharlal Nehru Technological University (J.N.T.U.), Hyderabad, and Pursuing the Ph.D. degree from department of E.C.E., Jawaharlal Nehru Technological University (J.N.T.U.), Kakinada, India. His areas of interest include Analog Electronics and Design, Cognitive Radio System, Communications and signal processing.



C. VenkataNarasimhulu received B.Tech degree in Electronics and Communication Engineering from S V University, Tirupathi in 1995 and Master of Technology in Instrumentation & Control Systems from R.E.C., Calicut in 2000 and Ph.D. from J.N.T.U., Kakinada in 2013 in the area of signal Processing. He has published more than 25 technical papers in

national and international Journals and Conferences. His interested areas are Signal Processing, Image processing and medical image processing etc.



K. Satya Prasad received B Tech. degree in Electronics and Communication Engineering from J.N.T.U. college of Engineering, Anantapur, in 1977 and M. E. degree in Communication Systems from Guindy college of Engineering, Madras University, in 1979 and Ph.D from Indian Institute of Technology, Madras in 1989. He has published more than 139 technical papers in different National & International conferences and Journals and Authored one Text book. His areas of Research include Communications Signal Processing, Image Processing, Speech Processing, Neural Networks & Ad-hoc wireless networks etc.

Suboptimal Multi-user Receivers Detection Algorithms

R V Durga^{1,2}, A McLauchlin¹

¹*Department of Electronics and Communication Engineering, University of Hertfordshire, College Ln, Hatfield AL10 9AB, UK.*

²*Geethanjali College of Engineering and Technology (Autonomous), Cheeryal (V), Keesara (M), Medchal Dist., Telangana - 501 301, India.*

Abstract: Current innovation tries to consistently advance. This movement prompts a ton of examination in any critical region of progress. There is a developing number of end-users in the remote range which has prompted a requirement for improved transmission capacity and BER esteems. At the end of the day, new advancements which would expand the limit of remote frameworks are ending up being an essential purpose of examination in these cutting-edge times. Furthermore, in these modern times, new technologies are proved as research's crucial point that increases the wireless systems' capacities. There have been many multi-user detectors in which the MMSE conducts several linear detector as well as the *n-stage* PIC overcoming the SIC. The assessed detectors were investigated, taking into account even the correlative composition of MAI found in CDMA. In case of high users number as well as because it's basically a matched filters' bank, the limits in multipath and noise occurrence render its use redundant in complicated modern detectors like a traditional linear detector. The MMSE detector are used as a detector's improvement. Therefore, the combination of its collection as one of the linear detectors with other sensors types was investigated. The technology's new field today enables wireless networks to be interpreted as well as explored by many applications. Owing to its wide use within the industry, the software used to simulate this project is MATLAB.

Keywords- Multi User Detection, Single Input- Single Output (SISO) Systems, Successive Interference Cancellation, Parallel Interference Cancellation, Multiple Access Interference.

1 Introduction

Today's telecommunications industries' main goal is data, voice as well as their combination's information's reception and transmission; with higher data rates as well as providing considerably low interferences. Wireless networking is one of the fast-growing media largely due to the appeal it offers to end users: mobility. In terms of the development of technology, wireless communication's premature usage as a medium of voice communication must be re-assessed to meet the increasing market for multimedia and text messaging, as used by cell phones. This need created a demand for extremely high data speeds that cannot be provided solely because of the signal interference and finite radio spectrum. Even though wired networks give these preferential rates, connectivity and instantaneity lack the requisite advantages, so research into the achievement of these wireless systems has become a critical research field in today's world.

Excellence is strived by the present world. This feature allows to obtain the most network space, latency and low errors. The last feature of the identification includes multiple people. It is a mixture of methods used to minimize the errors in a contact system's 'receiving' end. The requirement for wider speeds and bandwidths produces the need for recipients that represent minimal errors is of significant importance to MUD. The multi-user scans are a blend of algorithms that easily detects the received multi-user signals. This functionality makes it possible to serially process various MUD combinations to obtain higher error rates and the more visual variations, the more difficult it is. In SISO systems for multi-user detection, the present work offers an overview of the most commonly used techniques. Various SIC, MMSE and ZF detectors combinations were evaluated in order to identify the detector combination.

Multi-user receivers can never match the received signals to optimal match [1]. The Optimum Maximum “Likelihood Sequence Estimation Receiver (MLSE)” offers an approach to a perfect match. This receiver has their key limitations in comparison to the system's compute sophistication and the cumulative number of consumers grows exponentially [1]. The optimal CDMA user was obtained by Verdu in 1986 [1]. The implementation of multifunctional identification by Schneider in 1979 was seven years earlier [1] pre-empted. The best recipient is a matched filters’ bank to provide user amplitude calculations to a Viterbi decision algorithm for the first-order. Verdu showed mathematically that the optimized receiver has a substantial boost in efficiency relative to the traditional setup, but with the largest number of users in the system, its deployment costs have risen dramatically. This also posed a challenge because the system was greatly complicated. Consequently, detectors are currently planned to be less costly and less robust but now the best detector is used as a benchmark for future solutions. An estimate of the receiver is known to mitigate this significant challenge, leading to the evaluation of “suboptimal” recipients. In Figure 1, you can screen large sizes with multi-user receivers.

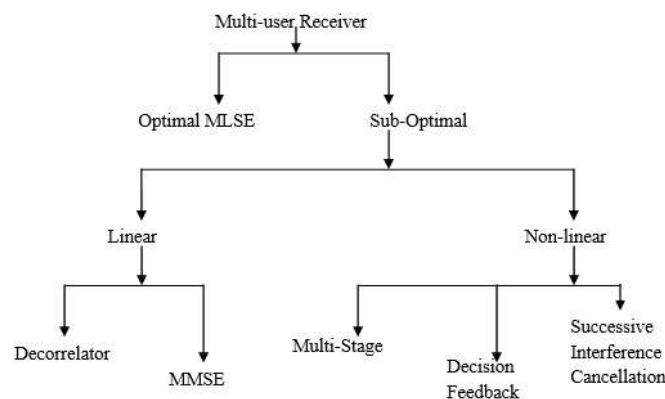


Figure 1: Various MUD Configurations

The corresponding advantages and drawbacks are possessed by the various receiver types; thus, it is significant to provide an insight within their theoretical behavior. Two variants occur, linear and non-linear, as seen in Figure 1. In evaluating certain receiver identification algorithms, the architecture obstacles to be addressed are:

- Limitations under Practical Operating Conditions
- Performance versus Complexity
- Linear versus Non-Linear
- Asynchronous versus Synchronous
- Near Far Resistance

2. Implementation

2.1 Multi-user Detectors for SISO Systems

Signal identification at the receiving end usually utilized in the “single-user” case. When MU transmission advantages arise, that is Figure 2, there is also a requirement for an effective multi-user identification. In the case of existing single-user systems the new 'balanced filter' detector is not appropriate for detecting multimedia signals alone; this is because “Multiple Access Interference (MAI)” is present in the multi-user signals. The deleted signal’s BER is disrupted by MAI when utilizing traditional matched filters as the active users’ number

grows. The MAI is screened off and handled as noise by the matching filters. This MAI also has pieces of the signal, but helpful information is discarded when deciding the exact signal value.

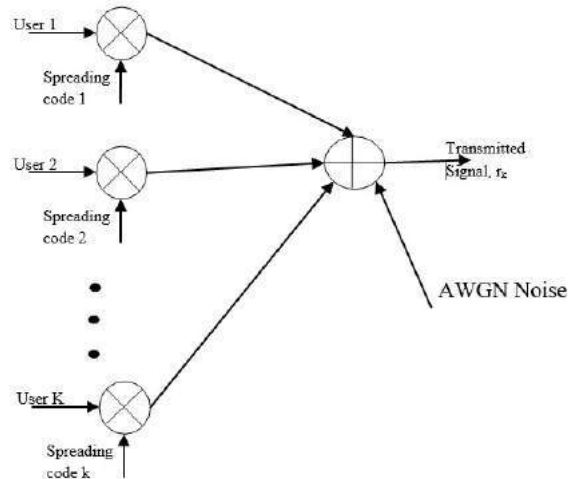


Figure 2: Transmitter of Multi User Detection with CDMA

As referred to above-mentioned Figure 1 MUD receiver classification tree, sub-optimal detectors are primarily of two types. To promote and settle on the option of detectors to use, it is significant to consider the core principles, disadvantages and advantages of devices. For both linear and non-linear situations, the most typical detector configurations were investigated.

2.1.1 Linear Detectors

The linear MU detectors aim at developing decision statistic's refined set with reduced MAI observed by every user, aims at performing a linear operation on the outputs of matched filters, therefore turn out to be near-far resistant. The most commonly used two detectors are mentioned as:

2.1.1.1 The De-correlating Detector

It transforms the outputs of matched filters from the initial stage linearly. It de-correlates the user's signals to distinguish the user, e.g. mechanism used to decrease the self-relation within the signals or cross-correlations in a group of signal and retain another communication facets. This method is done by measuring the cross similarity values of the PN code type as well as storing them in a $K \times K$ matrix (it is discovered to have complexity of K^2). The respective filter outputs' vector is then multiplied by the opposite [2]. Since channel parameters' previous knowledge does not apply, the recipient is insensitive to the near-far effect. The recipient achieves a substantial value in contrast with the traditional paired filter recipient, although the decorrelation mechanism poses a significant drawback to better noise statistics. Because of this downside, the linear detectors studied were ignored.

2.1.1.2 The MMSE Detector

The de-correlating detector is identical in its function in comparison to the first stage linear transformation of the matching filter outputs. The detector's purpose is to minimize the

average square error among the real data as well as the detected data that is the filter performance. This characteristic resulted in making the MMSE detector more desirable as compared to the detector when noise is amplified. The disadvantage attributable to this characteristic is that the channel parameters must be known [3]. It was observed [4] that a better BER (bit error rates) is possessed by the MMSE than the de-correlator, but at the limit; that is, while the noise level falls to zero, it is similar to the de-correlator's output. A significantly lower almost-far resistance has also been shown [5] [6].

The Least Squares detector is another very useful linear detector which is commonly used. In order to minimize the amount of the squared error, this is similar to the MMSE. The mistake is the subtraction from the initial signal [1] of the observed signal.

2.2 MUD Algorithm for the Linear Detectors

The utilized equations' derivation is as below:

- By utilizing the one-shot demodulation assumption: vector $r(i)$ represents the K users' i^{th} data symbol, where filter's output matched with s_k is represented by k^{th} component in the interval is stated as:

$$r_k(i) = \int_{iT}^{(i+1)T} s_k(t-iT)r(t)dt, \quad k = 1, 2, \dots, K \quad (1)$$

- The received discrete-time signals are represented in vector form at the i^{th} symbol instance by assuming every N chip samples as:

$$r(i) = SAb(i) + n(i) \quad (2)$$

- As to the symbol interval's selection, i statistical invariance is discovered by discrete-time signal, $r_k(i)$; removal of indices is done deprived of generality loss. Therefore, Equation (2) can be represented in vector form as:

$$r = S\theta + n \quad \text{where } \theta = Ab \quad (3)$$

S represents an N by K matrix which holds all K users' signature sequences and θ comprises of the sum of the transmitter bits and their corresponding amplitudes. With [8] and (3), the general equation of linear multi-user detection can be described under as

$$\hat{\theta} = Cr = CS\theta + Cn \quad (4)$$

For the k^{th} user case:

$$\hat{\theta}_k = C_k s_k \theta_k + \sum_{j \neq k} C_k s_k \theta_j + (Cn)_k \quad (5)$$

where, from the received signals for the k^{th} user estimates $\hat{\theta}_k$ are obtained by utilizing the filter, C_k . Also, within the signal, MAI presence and ambient noise's contribution is shown by the

equation. The correspondence of filter C_k is observed to linear detector's transfer function. For the three examined detectors that are MMSE, least squares and matched filter are the $\hat{\theta}_k$ derivations.

$$\begin{aligned}\hat{\theta}_{MF} &= S^T r \\ \hat{\theta}_{LS} &= (S^T S)^{-1} S^T r \\ \hat{\theta}_{MMSE} &= [SA^2 S^T + \sigma^2 I]^{-1} SA r\end{aligned}\quad (6)$$

Where, user spreading sequences are represented by S

2.3 Non-Linear Detectors

As in linear detectors, nonlinear multi-user detectors act on the corresponding philtre outputs in a nonlinear way. The most advanced detectors have been tested in recent years. Following is a short summary of their core concepts.

2.3.1 Successive Interference Cancellation (SIC)

This algorithm first determines the strongest user, substitutes him / her from the signal received, and after that detects the most powerful user. You should do so in two ways. It will firstly extract the soft information from the signal received; it contributes to minimal to no error propagation, but it acquires a noise effect accumulating for vulnerable users. Secondly, hard information may be eliminated from processed signals that contribute to little to no noise accumulation due to the potential distribution of errors. Successive interference cancellation may be achieved circularly at the cost of low convergence and therefore higher complexity. The MAI has been diminished and the issue is almost / far greater. The most effective and the most accurate cancellation is the cancellation of the best signal [9]. The SIC algorithm will then most likely be influenced by an error distribution as the most accurate cancellation. Channel estimates at the recipient are also required [9]. The cancellation parallel interference detector, PIC, is another version of this interference detector.

2.3.2 Parallel Interference Cancellation (PIC)

The PIC detector often includes the removal of other users' interference, close to its predecessor. As its name implies; compared to the SIC series subtraction, the PIC detector cancels the MAI predictions in parallel (i.e. simultaneously) from the output of the matching philtre. Its efficiency primarily depends on the estimates of original signal as well as at the source channel estimates are needed. If both consumers are getting the same pressure (e.g. under regulation of power), it works better than SIC [10].

2.3.3 Decision Feedback Equalizer (DFE)

The "DFE (Decision Feedback Equalizer)" is a famous nonlinear equalization technique. The DFE is a very popular one. In the majority of instances, a linear equalizer and a non-linear decision component's combination resulted in DFE. The DFE's aim is to provide both a FIR feed filter and a feedback filter to reduce the interference of the residual inter-symbol, ISI. Due to the need for picosecond resolution of decisions in Feedback direction, in

multi-gigabit networks, the DFE is difficult to enforce. DFE conducts linear detectors in terms of efficiency but primarily the difficulty of their implementation and some error propagation problems constitute the big drawback [11]. The particular project consists of combining the MUD techniques' various numbers. Thus, there is a need of every technique's proper dissemination.

3 Simulation and Results

3.1 Simulation of Linear Detectors

The technology's new field today enables wireless networks to be interpreted as well as explored by many applications. Owing to its wide use within the industry, the software used to simulate this project is "MATLAB." This Programme is user-friendly and is intended to provide engineers and scientists with the best approximation possible to model every day activities. The project aim is very precise but execution is very complex since multiple communication mechanisms are interconnected. Following are the major phases used in this project:

- For single carrier CDMA, designing as well as simulating linear multi-user detectors
- Combining a PIC receiver with the selected linear detector
- By using a MIMO architecture, it is extended
- Through Sphere Decoding Algorithm's incorporation total performance is improved

The following simulations sum up the initial process of the experiment. The contrast included two large linear detectors of industries, the MMSE and Least Squares detector, which were the traditional mixed filters detector in combination. MMSE and PIC have integrated the optimal alternative and measured their success.

This was obtained by means of MATLAB to compare the following three sensors; the MMSE detector, least squares detector and conventional matched filter.

- BER vs. number of Users, as represented in Figure 3.
- BER vs. S/N Ratio, with distinct users' number, as represented in Figure 4 & 5.

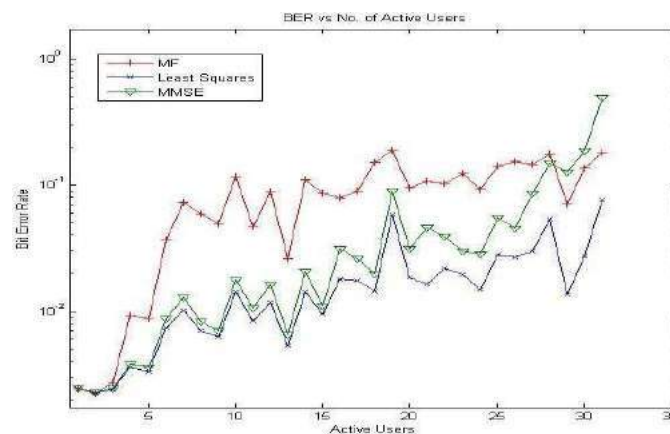


Figure 3: Bit Error Rate Versus Number of Users

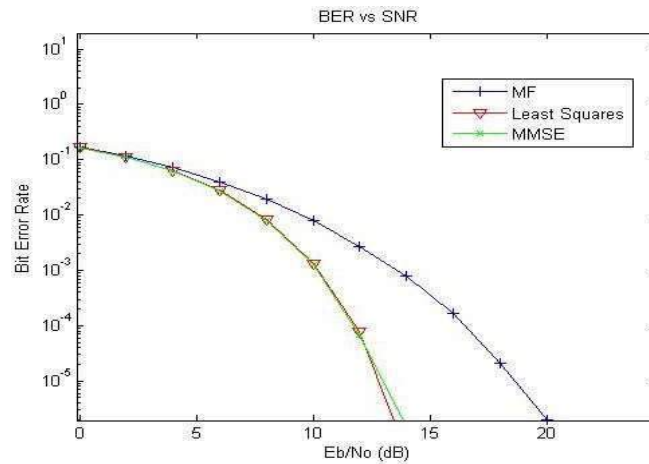


Figure 4: Bit Error Rate Versus Signal-to-Noise Ratio with user count 5

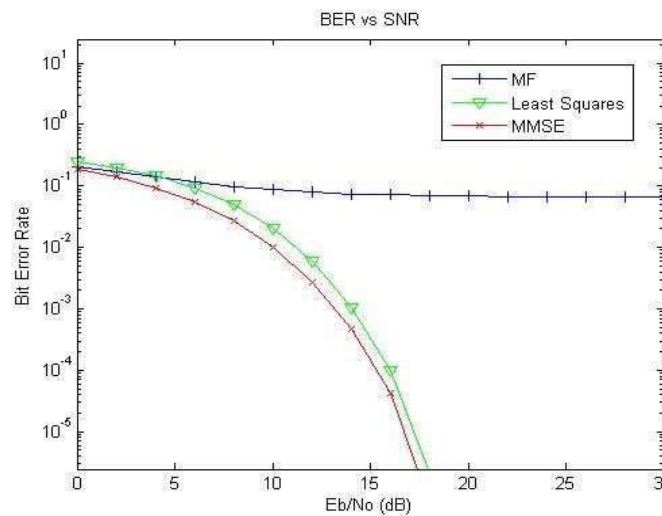


Figure 5: Bit Error Rate Versus Signal-to-Noise Ratio with user count 10

The Fig.3, 4 as well as Fig.5 results explicitly illustrate the benefits that the MMSE detector provides in contrast to the traditional mixed filter detectors as well as lowest square. These statistics indicate that MMSE offers a better SNR for a growing number of users as well as provides better BERs. The statistics illustrate the need to identify multiple users, as the traditional mixed filter deteriorate with active users' growing number. In Fig.5, the MF calculation indicates a high rate of roll-off relative to Figure 4, which is historically the MF calculation.

3.2 Simulation of Non-Linear Receiver Combinations

The early simulations have shown that when compared with their previously described predecessors, MMSE provides substantial enhancements. The ever-growing need for higher data speeds, however, demands much greater BER upgrades. The combination of the MMSE and PIC algorithms, which have also been researched in previous literature, [4], is envisaged for this reason. An N-stage System has been studied for a receptor with this configuration. The BER values increase with rising PIC measures can be seen very clearly in Figure 6. However, it is worth noting that with phase numbers that lead to tradeoffs at times of system design, the

complexity of the PIC system increases. The MMSE stage addition to the PIC algorithm also indicates in figure 6 that the BER value is higher. However, compared with the standalone PIC simulations, this implementation enhanced simulation performance.

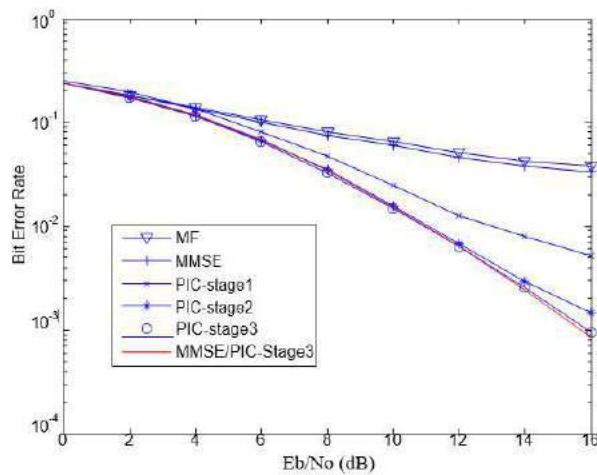


Figure 6: Bit Error Rate for n-stage PIC Detector

It is significantly noted that as $\sigma \rightarrow 0$ that means wireless channel which is noiseless; simply a simple PIC algorithm is approximated by the MMSE/PIC because of the reason that a matched filter is approximated by the MMSE counterpart.

4. Conclusion

There have been many multi-user detectors in which the MMSE conducts several linear detector as well as the *n-stage* PIC overcoming the SIC. The assessed detectors were investigated, taking into account even the correlative composition of MAI found in CDMA. In case of high users number as well as because it's basically a matched filters' bank, the limits in multipath and noise occurrence render its use redundant in complicated modern detectors like a traditional linear detector. The MMSE detector are used as a detector's improvement.

PIC and SIC algorithms also outweigh their MMSE and MF counterparts. It is also shown. The MMSE / PIC detector's principal appeal is how to boost the signal receiving by interfering with the incident device noise.

References

- [1] S. Verdu, "Minimum Probability of Error for Asynchronous Gaussian Multiple Access Channels," IEEE Trans. Info. Theory, vol. IT-32, no.1, pp 85 -96, 1986.
- [2] D. Landers and L. Rogge, "Identically distributed uncorrelated random variables not fulfilling the WLLN", Bull. Korean Math. Soc. 38 (2001), No. 3, pp. 605–610.
- [3] X. Wu, T. C. Chuah, B. S. Sharif, and O. R. Hinton, "Adaptive robust detection for CDMA using a genetic algorithm," Inst. Electr. Eng. Communications, vol. 150, pp. 437–444, Dec. 10, 2003.
- [4] A. Paulraj, R. Nabar and D. Gore, Introduction to Space-Time Wireless Communications, 2003, ISBN: 0-521-82615.2.
- [5] I. Land, I. Graell, A. Amat, A. L.K. Rasmussen, "Bounding of MAP decode and forward relaying", 2010 IEEE International Symposium on Information Theory Proceedings (ISIT), pgs 938 – 942. June 2010.

- [6] L.L. Scharf. Statistical Signal Processing – Detection, Estimation and Time Series Analysis. Adison Wesley, 1991.
- [7] G. J. Foschini and Michael. J. Gans, "On limits of wireless communications in a fading environment when using multiple antennas". Wireless Personal Communications. January 1998.
- [8] Institute of Electrical and Electronics Engineers, IEEE Standard 802.11a: Wireless LAN Medium Access Control (MAC) and Physical Layer (PHY) Specifications: High-Speed Physical Layer in the 5 GHz Band, 1999.
- [9] Institute of Electrical and Electronics Engineers, IEEE Standard 802.11a: Wireless LAN Medium Access Control (MAC) and Physical Layer (PHY) Specifications: High-Speed Physical Layer in the 5 GHz Band, 1999.
- [10] Y. G. Li, N. Seshadri, and S. Ariyavisitakul, "Channel estimation for OFDM systems with transmitter diversity in mobile wireless channels," IEEE J. Select. Areas Commun., vol. 17, pp. 461–471, Mar. 1999.



SMART GARBAGE MONITORING AND AIR POLLUTION CONTROLLING SYSTEM

Dr. B. L. Prakash

Professor, Geethanjali College of Engineering and Technology,
Hyderabad, Telangana, India

N. Swetha

Student, Geethanjali College of Engineering and Technology
Hyderabad, Telangana, India

P. Gopi

Student, Geethanjali College of Engineering and Technology
Hyderabad, Telangana, India

P. Kavya

Student, Geethanjali College of Engineering and Technology
Hyderabad, Telangana, India

ABSTRACT

Garbage monitoring system helps to eradicate or minimize the garbage disposal problem and helps to manage unwanted material leftover in the various places in the city, hospitals, houses, public areas etc. This paper presents the design and implementation of smart garbage monitoring system. Monitoring of garbage level only is not sufficient to make city environment clean and odor free but also free from harmful gases. If level of garbage bin remains below threshold value for long period then it causes smell, and it is unhygienic to people living nearby. To avoid this, we need to monitor gases generated by the garbage bin. One of the objectives of design is sensing unit at garbage bin, which is battery operated, so that it can be portable and easy for connecting.

Key words: Limit Switch, Gas Sensor, Arduino-UNO, Smart Waste Collection Monitoring and Air Pollution alerting system.

Cite this Article: B. L. Prakash, N. Swetha, P. Gopi and P. Kavya, Smart Garbage Monitoring and Air Pollution Controlling System, *International Journal of Advanced Research in Engineering and Technology (IJARET)*, 12(3), 2021, pp. 698-703.

<http://iaeme.com/Home/issue/IJARET?Volume=12&Issue=3>

1. INTRODUCTION

In the proposed system, we get the information about bin level and harmful gases by using limiting switch and gas sensor respectively. Limiting switch is used to continually access garbage bin data which is useful to monitor the level of garbage bin if it increases the threshold value then the system blinks red LED otherwise green LED. If any harmful gases like Ammonia and smoke are detected by using gas sensor then we get the message to the mobile and gives the location of that dustbin by using GPS technology. Then immediately truck driver can collect the garbage in the bin.

1.1 Effects of Release of Harmful Gases

Pollutants produced by backyard burning of trash are released primarily into the air, and close to ground

level where they are easily inhaled-with no pollution controls. Burn barrel air emissions include Carbon Monoxide (CO), Carbon dioxide (CO₂), and Nitrogen Oxides (NO). Smaller amounts of more poisonous gases and substances are commonly detected in the smoke: viz. Benzene, Styrene, Formaldehyde, Polychlorinated Di-Benzo-Di-Oxins (PCDDs or "Dioxins"), Polychlorinated Di-Benzofurans (PCDFs or "Furans"), Polychlorinated Biphenyls (PCBs), and heavy metals such as Lead, Mercury, and Arsenic. Air is the most useful thing for every living being. Researching on this serious issue this system's main purpose is to estimate the quality of air for people and many other living things which exist on earth. It is very important to know how much safe we are and how the weather and climate have changed due to air pollution.

1.2 Technological Advancement

A sensor is a device that measures physical input from its environment and converts it into data that can be interpreted by either a human or a machine. Most sensors are electronic but some are simpler, such as a glass thermometer, which presents visual data. People use sensors to measure temperature, gauge distance, detect smoke, regulate pressure and a numerous of other uses. A GSM MODEM or GSM module is a hardware device that uses GSM mobile technology to provide a data link to a remote network. From the view of the mobile phone network, they are essentially identical to an ordinary mobile phone, including the need for a SIM to identify themselves to the network.

GPS is a system of 30+ navigation satellites circling around earth. The information regarding the location of the bin releasing harmful gases can be obtained as they constantly send out signals. A GPS receiver in the mobile phone receives these signals.

Once the receiver calculates its distance from four or more GPS satellites, it can figure out where the corresponding bin is. One of the major gas sensors which is responsible for the most air pollution mostly is being used in the system to know the best result of the whole condition of the air. Once the sensor detects the specified gas then automatically it alerts the Municipal authorities by sending SMS stating the exact location of the bin using GPS.

A limit switch is an electromechanical switch that consists of an actuator mechanically linked to a set of contacts. When an object meets the actuator, the device operates the contacts to make or break an electrical connection.

2. SYSTEM DEVELOPMENT

Limiting Switch plays a vital role in garbage monitoring system. Limiting Switch is the mechanical switch which converts mechanical energy into electrical energy. If the bin is full of garbage, then the switch triggers and blinks Red led this shows that the garbage is full. If the garbage is not filled, then switch does not trigger and blinks Green LED it means there is limited

garbage in the bin. Negative terminal of the battery is connected to the common pin of limit switch and positive terminal is given to anodes of both Green and Red LED. Cathode of Red LED is connected to Normally Open (NO) of a switch and battery.

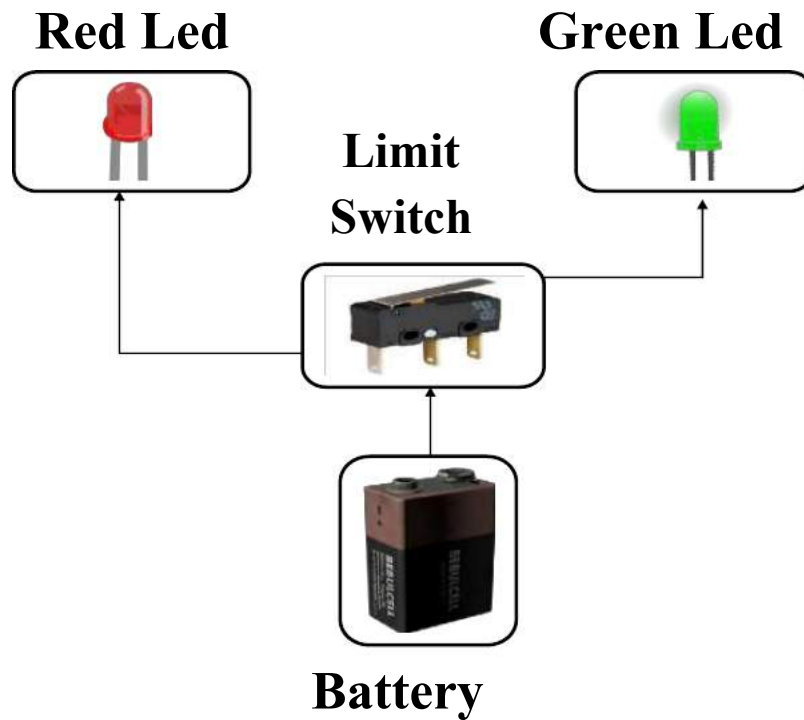


Figure 1 Block Diagram of Garbage Monitoring System

Arduino is the main block of the air pollution controlling system where the entire operation depends on the Arduino. Arduino will collect the data from the Gas Sensor based on the threshold value of the gas. The user will get notified about the status of the bin through SMS with the help of SIM900A GSM Module. If there are no harmful gases like Carbon Monoxide and Smoke there will be no alerting message from the bin. The truck driver gets both latitudinal and longitudinal position of bin through the GPS Module.

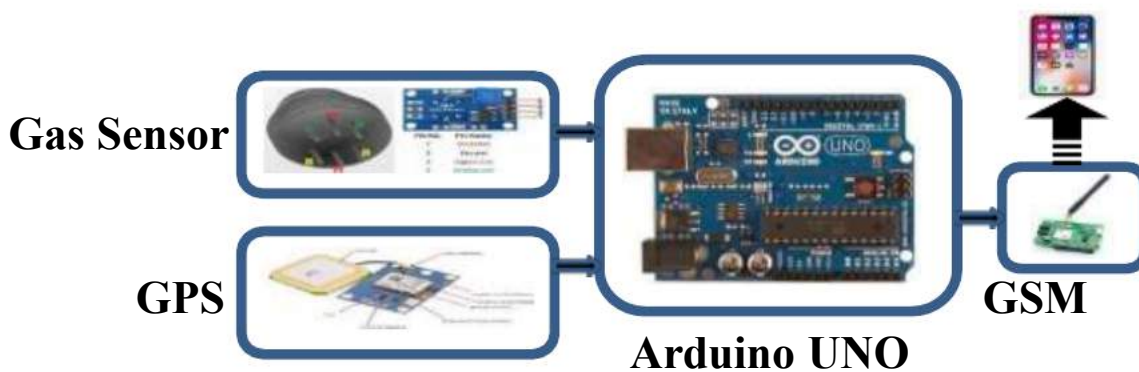


Figure 2 Block Diagram of Air Pollution Controlling System

Flow Chart

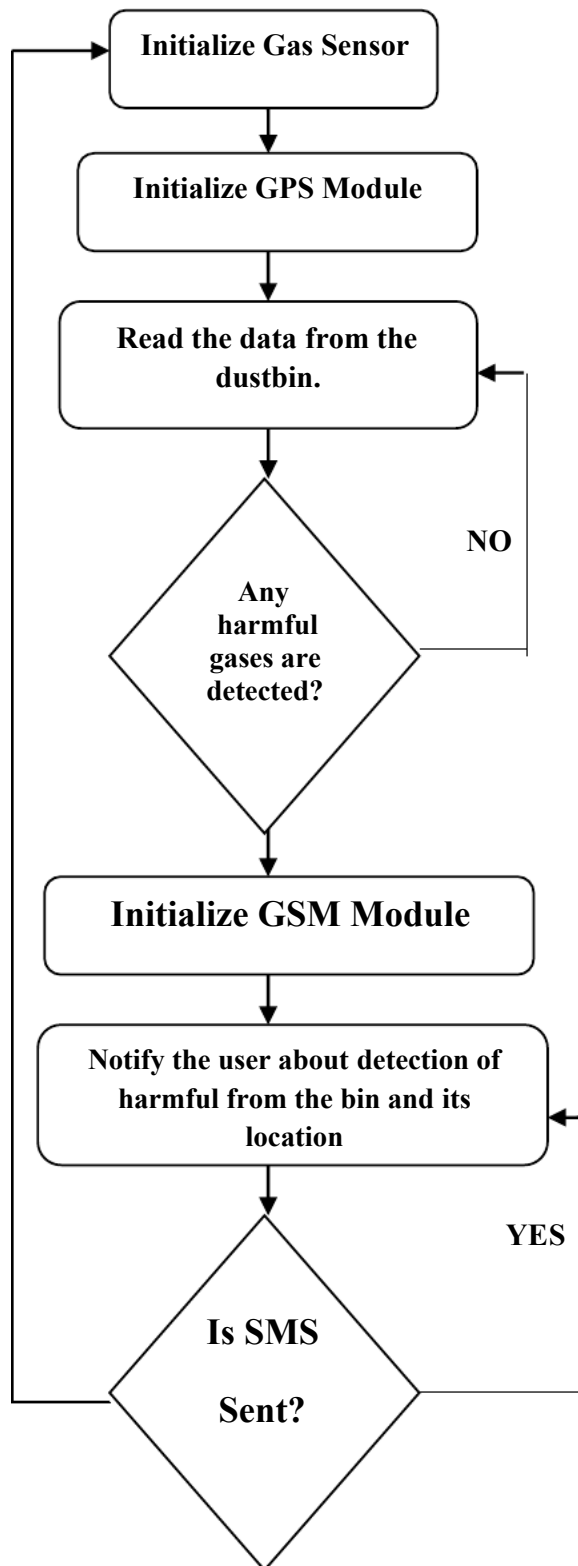


Figure 3 Flow chart of the proposed system

3. DESIGN



Figure 4 Connections in the project

- As shown in the block diagram given in Fig 2 the connections should be made.
- The threshold value of the gas sensor is set to predefined value.
- The Gas Sensor will continuously sense the gases in the bin.
- If any harmful gases have been detected and its value is greater than the threshold value, then the Arduino turns ON and sends alerting SMS to the user by stating the location of the bin.
- As shown in the Fig 1 of garbage monitoring system connection should be made accordingly.
- Limiting Switch should be placed on the top of the bin which is attached to the lid.
- If there is no dust or dust is not filled Limit switch does not get triggered and then Green LED blinks.
- If garbage is filled in the dustbin then Limiting switch triggers and gives Red LED.

4. RESULTS



Figure 5 Blinking of LEDs

If garbage is not filled in the bin, then GREEN LED blinks. If entire bin is filled with garbage, then Limiting switch triggers Red LED.

Longitude: 78.5784 Latitude:
17.5065 Harmful gas has been
detected. Please, empty the bin

Figure 6 SMS from GSM Module

If harmful gases like smoke, Carbon Monoxide are detected then user gets notified with SMS alert with the longitude and latitude position of the bin.

5. APPLICATIONS

- This methodology when implemented in real time can be used in the smart cities.
- This is also helpful in the government project of ‘Swachh Bharat Abhiyan’.

6. MERITS AND DEMERITS

6.1 Merits

- A reduction in the number of waste collections needed by up to 80%, resulting in less manpower, emissions, fuel use and traffic congestion.
- Improved environment (i.e., no overflowing bins and less unpleasant odors).
- The cost & effort are less in this system.
- Very simple circuit.
- Can help in reducing overflowing bins.
- Reduces harmful gases in the bins.
- Makes city environment clean and hygiene.

6.2 Demerits

- Cannot detect liquid waste.
- Consumes more Power Supply.

7. CONCLUSION

This paper is the implementation of Smart garbage and air pollution management system project using sensors, microcontroller, GSM, and GPS. This system assures the cleaning of dustbins soon when the garbage level reaches its maximum. This system also helps to monitor the fake reports and hence can reduce the corruption in the overall management system. This reduces the total number of trips of garbage collection vehicle and hence reduces the overall expenditure associated with the garbage collection. It ultimately helps to keep cleanliness in the society.

Therefore, the smart garbage management system makes the garbage collection more efficient and makes our environment free from harmful gases in the bin.

REFERENCES

- [1] D. D Mondal, Rutuja Deshpande, Pooja Bhagat, Gitanjali Bandal, “A System detecting an Air Pollution and tracking using GPS & GSM”, “International Research Journal of Engineering and Technology (IRJET)”
- [2] Norfadzlia Mohd Yousuf, Aiman Zakwan Jidin and Muhammad Izzat Rahim, “Smart Garbage Monitoring System for Waste Management”, www.mateconferences.org/articles/mateconf/pdf/2017/11/mateconf_etic2017_01098.pdf Publication, California, 33-35.

Single Point Positioning Accuracy of Combinations combined GPS/Galileo

Satya Srinivas Vemuri

Geethanjali College of Engineering and Technology, Cheeryal(V), Telangana, India

Abstract

GNSS provides the position information Geographical Information systems (GIS). The precise positioning capability ensure the successful application of GNSS and its demand for GIS applications. Single point positioning (SPP) is widely used for applications including surveying, Mapping (most common use of GIS) and vehicle navigation. The effect of ionosphere on the GNSS signals is the largest and most unpredictable source of error. The availability of new civilian coded signals on multi-frequency for Galileo (E1, E5a, E5b) and GPS (L2C, L5) systems have given an opportunity to utilize the code-phase measurements to form dual linear combinations to correct for refractive effects due to ionosphere. The advantage of ionosphere-free linear model is that it can be used directly in least squares adjustment to obtain accurate position solution. Code-phase observations are used instead of using carrier-phase observations that are ambiguous. The attainable accuracies of stand-alone GPS and combined GPS/Galileo are evaluated by considering ionosphere-free combinations of civil codes on L1/L2, L1/L5 and E1/E5a frequencies. The results show that attainable positional accuracy of SPP solution is improved. The 3D positional accuracy of combined GPS/Galileo is less than 2 meters.

Keywords: GPS, GALILEO, Ionosphere-free linear combination, Position domain Single point positioning and Position error

1. Introduction

The modern GNSS receivers are designed to track more number of satellites corresponding to different constellations. The interoperability of GNSS and availability of multi-frequency signals of distinct center frequencies with new civilian codes, aid in removal of majority of refractive effects of ionosphere on these signals. The work reported by Cocard and Geiger (1992), Han and Rizos (1996), Odjick (2003) and Richert et al., (2017) is focused in measurement domain and that to using carrier-phase measurements. Taking the advantage of new civilian coded signals of GPS and Galileo, the analysis is carried out to evaluate how these linear combinations affect the positional accuracy. Table 1 depicts broadcasting signals and their frequencies of these two systems (Hofmann et al., 2008).

TABLE 1: GPS and Galileo signals

S.No.	GPS	Galileo
1.	L1(1575.42 MHz)	E1 (1575.42 MHz)
2.	L2(1227.60 MHz)	E5a (1176.45 MHz)
3.	L5 (1176.54 MHz)	E5b (1207.14 MHz)

It is envisaged that that all receivers in the International GNSS (IGS) network will be capable of tracking modernized GPS signals (L2C and L5) and Galileo signals to ensure highest- quality of GNSS related standards (conventions), data, and products. Receiver developers are also less interested in codeless and semi-codeless tracking with the availability of new civilian codes on multiple frequencies with backward compatibility to L1C/A. "U.S Airforce intend to discontinue receivers with feature encrypted P(Y) code by 2020". Therefore, the evaluation of accuracy of point positioning using dual-frequency measurements is essential. Single point positioning (SPP) technique involves determining absolute 3D coordinates using standalone GNSS receiver, which is desired in applications such as surveying, geographical Information Systems (GIS), marine (port navigation requirement) and aviation. The main motivation behind undertaking the current research is to understand the reliability of GNSS positional accuracy for SPP with new civilian signals. The investigation aims at study of attainable accuracies due to dual frequency ionosphere-free combinations of new civilian code measurements of GPS and Galileo. The unsmoothed code phase measurements data obtained from receiver are utilized to perform standalone GPS and combined GPS/Galileo single point positioning (SPP) on epoch by epoch basis. An overview of GNSS systems and observation equations used by receiver to compute position are presented in subsequent sections.

2. GNSS systems and observation equations

Global Navigation Satellite Systems usually referred with the acronym GNSS, which is intended to include all the existing and planned satellite systems aimed at navigation purpose. GNSS is a worldwide precise time and position determination system that includes one or more satellite constellations along with other augmentation systems. The positioning and timing capabilities based on Global Navigation Satellite Systems (GNSS) extend their service in many advanced applications such as aviation, tracking of space borne objects, location based services (LBS), fleet management etc. There are currently two operational GNSS, one is the GPS, which is operated by U.S Department of Defense (DoD) and the other is GLONASS (Globalnaya Navigatsionnaya Sputnikovaya Sistema), which is operated by Russian DoD. One more GNSS, Galileo in Europe is under development, which is a joint initiative of European Commission (EC) and the European Space Agency (ESA). As on date 9 satellites are providing services. Further, Several SBAS and Regional systems are planned in various parts of the world and are operational, such as WAAS (U.S.A), EGNOS (Europe), Beidou (China), MTSAT (Japan) and GAGAN (India), QZSS(Japan), IRNSS/NavIC (India) (Jacob, 2007). The GNSS receivers are designed to track the signals of multi-constellation to obtain better positional accuracy. The primary measurements of tracking channels are code and carrier phase pseudoranges, Doppler and signal strength. The range between the user and three or more satellites is required for computation of three dimensional position of user. This range can be measured using code phase, carrier phase and/or doppler measurements of GNSS signals. The code/phase measurements are affected by atmospheric delays, satellite-receiver hardware delays, drift in clocks, multipath etc. The relation between these influences on GNSS code and carrier phase measurements are expressed as observation equations (Blewitt, 1997; Seeber, 2003).

2.1. Code phase measurement

The Delay Locked Loop (DLL) of GPS receiver generates the PRN code and will try to align with the code sequence of signal transmitted from the satellite. The time difference of signal transmission and reception multiplied with velocity of light gives the range. This method of range computation requires synchronization of clocks at the satellite and receiver. However, this is not possible because satellites use atomic clocks that are highly accurate and stable when compared to inexpensive clocks used in receivers. Therefore, the range measured is referred as pseudorange and is written as,

$$PR_{code} = R + c(dt_s - dt_\tau) + dt_{SIS} + B + Mp \quad (1)$$

PR_{code} : Code measurement (m),

R : True range (m),

c : Speed of propagating wave (m/s),

dt_s : Satellite clock bias (s),

dt_τ : Receiver clock bias (s),

dt_{SIS} : Atmospheric propagation delay (m),

B : Hardware delay in the satellite and the receiver (m)

Mp : Multipath (m)

2.2. Carrier phase measurement

The Phased Lock Loop (PLL) in the GPS receiver measures beat phase of the signal. The beat phase at time "t" is obtained by taking the difference between the phase of transmitted signal and local oscillator generated phase at that instant of time. Since, only fractional part of phase is measured by the receiver, the unknown integer number of phase cycles traversed has to be estimated. Therefore, the phase based measurements are ambiguous. The positional accuracy achieved by using the phase measurements depends on consistency of „ambiguity resolution technique“ applied. The carrier phase equation can be written as,

$$PR_{carrier} = R + c(dt_s - dt_\tau) + dt_{SIS} + N_{L1/L2} \lambda_f + B + Mp \quad (2)$$

where,

$PR_{carrier}$: Carrier measurement (m), $N_{L1/L2}$: Integer ambiguity (cycles), and

λ_f : Wave length of carrier frequency (m)

2.3. Doppler measurement

Integrated Doppler measurements (‘ F_{di} ’) can be used to determine range rate between the user and GPS satellite. It is the measure of total number of carrier cycles of doppler shift for a given time interval. This includes not only the frequency shift due to relative motion of satellite with respect to the user but also drifts in the satellite as well as receiver clocks.

$$F_{di} = \int_{t_1}^{t_2} f_{di}(t) dt \quad (3)$$

The doppler shift (f_{di}) is expressed as,

$$f_{di} = \frac{1}{\lambda_f} (v_{Ri} \cdot u_{si} - v_{si} \cdot u_{si}) + f_{bc} \quad (4)$$

where,

v_{Ri} : User velocity vector

u_{si} : Unit satellite direction vector

v_{si} : Satellite velocity vector

f_{bc} : Receiver reference oscillator clock error

Forming the linear combinations of the code and/or carrier phase observations on multi-frequency signals is useful in several aspects of GNSS data-processing and analysis. The mitigation and modelling of biases and systematic errors in measurements comes under processing. Several algorithms using zero, single, double and triple difference techniques are developed with various linear combinations of dual frequency data for static and kinematic applications (Xu Guochang, 2007; Xu Guochang, 2002). Major errors that can be eliminated using linear combination are Ionospheric delay, noise and multipath. As the orbital error and tropospheric delay are frequency independent, linear combination of observations cannot be used to reduce these errors (Cocard and Geiger, 1992).

3. Linear combinations of observations

By developing various linear combinations of multi-frequency phase or code data an optimal Pseudo-observation can be derived. The optimal combination will aid in elimination or mitigation of GNSS errors. Several linear combinations are proposed using GPS L1/L2 data. The various linear combinations are, narrow-lane, ionosphere-free, wide-lane, semi-widelane, and geometry-free combinations etc., (Wubben et al., 1985; Urquhart L., 2009; Han and Rizos, 1999). Usually linear combinations are formed from zero-difference or double difference code or carrier phase observations. A few widely used linear combinations and their significance are discussed in this section.

3.1. Ionosphere-free linear combination

This linear combination eliminates the effect of ionosphere (1st order) partially. The 2nd and 3rd order Ionospheric affects still remains. This is widely used in time and frequency transfer applications. The noise in the derived measurements is less, and is useful for smoothing of code/carrier measurements to reduce the effect of noise and multipath. The double-difference ionosphere-free observables, eliminates integer ambiguity term. Therefore, this is not suitable in kinematic differential positioning applications, where there is necessity of ambiguity resolved carrier phase measurements. A linear combination using additional signals of GPS modernization plan (L2C, L5), a triple frequency approach is capable of resolving ambiguities (Hatch et al., 2000). The possible ionosphere-free combinations using GPS frequencies (dual and triple) can be found in open literature (Lee, 2008; Defraigne and Petit, 2003). The ionosphere-free linear combination using un-differenced or zero-difference L1/L2 can be written as,

$$L_{if} = \frac{1}{f_{L1}^2 - f_{L2}^2} (f_{L1}^2 \cdot L_1 - f_{L2}^2 \cdot L_2) \quad (5)$$

Typically, this combination has wavelength of 11 cm. A similar form of equation using code measurements can be derived to estimate P_{if} .

3.2 Geometry-free combination

This linear combination eliminates the effect of troposphere, true range between satellite and receiver, satellite clock and receiver clock effects as well. This is used for estimation of ionospheric delay which is a function of Total Electron Content (TEC), which varies subject to time, season, latitude and solar activity. But, the measured quantities are affected by noise, multipath and Differential Code Bias (DCB) or Inter-Frequency Bias (IFB) of satellite and receiver. The geometry-free linear combination using un-differenced or zero difference L1/L2 can be written as,

$$L_{GF} = (L_1 - L_2) \quad (6)$$

Typically, this combination has wavelength of 5.4 cm. A similar form of equation using code measurements can be derived. Appropriate techniques are required in order to remove the effect of DCBs. The DCB is dependent on the type/class of GPS receiver. The receivers are categorized based on code tracking data (P1, C1, P2, X2 (C1+(P2-P1)) etc). The code bias corrections for various linear combinations for different code tracking data receivers can be found in Dach et al., (2007). The DCBs formulae are defined for L2C (i.e., C2) as well.

3.3. Wide-lane combination

This linear combination is widely used for cycle slip detection (Petovello, 2007). The double differenced processing of wide-lane observables aid in precise estimation of integer ambiguity. The wide-lane linear combination using un-differenced or zero difference L1/L2 can be written as,

$$L_{wl} = \frac{1}{f_{L1} - f_{L2}} (f_{L1} \cdot L_1 - f_{L1} \cdot L_2) \quad (7)$$

Typically, the wavelength is around 86 cm. The noise in observations is large and also the ionospheric delay is many times more when compared with that on L1. A similar form of equation using code measurements can be derived to estimate wide-lane code.

3.4. Narrow-lane linear combination

This linear combination is used to mitigate the measurement noise and multipath. Resolving narrow-lane ambiguities is difficult due to shorter wavelength (10.6 cm). The wide-lane linear combination using un-differenced or zero difference L1/L2 can be written as,

$$L_{NI} = \frac{1}{f_{L1} + f_{L2}} (f_{L1} \cdot L_1 + f_{L2} \cdot L_2) \quad (8)$$

A similar form of equation using code measurements can be derived to estimate narrow-lane code.

3.5. Melbourne-Wubben linear combination

This linear combination removes the signal in space errors, satellite and receiver clock error and geometry. The noise of the observations depends on the quality of code phase measurements. This is used for cycle slip detection and even to resolve wide-lane ambiguities. Typically, the wavelength is around 86 cm. Both code and carrier phase measurements are used in Melbourne-Wubben linear combination and it is written as (Wubben, 1985),

$$L_{WM} = \frac{1}{f_{L1} - f_{L2}} (f_{L1} \cdot L_1 - f_{L2} \cdot L_2) - \frac{1}{f_{L1} + f_{L2}} (f_{L1} \cdot P_1 + f_{L2} \cdot P_2) \quad (9)$$

Several new linear combinations can be developed and the properties of existing linear combinations can be improved by multi-frequency approach. The linear combinations code and carrier phase data of other satellite navigation systems such as GLONASS (G1, G2 and G3), Galileo (E1, E2, E5 and E6), and COMPASS/Beidou (E1, E2, E5b and E6) can be used with the GPS signals for an optimal navigation solution. This combination eliminates or mitigates errors that are limiting desired accuracy levels of satellite positioning technology. However, the interoperability and compatibility of these systems must be considered for precise GNSS services (Richert and El Sheimy, 2007).

4. Dual frequency approach: GPS and Galileo

The ionosphere-free linear combination of GPS dual frequency code measurements can be written as,

$$R_{f_{L1/L2}} = \frac{1}{f_{L1}^2 - f_{L2}^2} (f_{L1}^2 \cdot R_1 - f_{L2}^2 \cdot R_2) \quad (10)$$

$$R_{f_{L1/L5}} = \frac{1}{f_{L1}^2 - f_{L5}^2} (f_{L1}^2 \cdot R_1 - f_{L5}^2 \cdot R_5) \tag{11}$$

$$R_{f_{L2/L5}} = \frac{1}{f_{L2}^2 - f_{L5}^2} (f_{L2}^2 \cdot R_2 - f_{L5}^2 \cdot R_5) \tag{12}$$

where,

R_1 : Pseudorange on L1 (m), R_2 : Pseudorange on L2 (m), R_5 :Pseudorange on L5 (m), $R_{f_{L1/L2}}$: Ionosphere-free pseudorange of L1/L2, $R_{f_{L1/L5}}$: Ionosphere-free pseudorange of L1/L5, $R_{f_{L2/L5}}$: Ionosphere-free pseudorange of L2/L5.

$$R_{f_{E1/E5a}} = \frac{1}{f_{E1}^2 - f_{E2}^2} (f_{E1}^2 \cdot R_{E1} - f_{E5a}^2 \cdot R_{E5a}) \tag{13}$$

$$R_{f_{E1/E5b}} = \frac{1}{f_{E1}^2 - f_{E5b}^2} (f_{E1}^2 \cdot R_{E1} - f_{E5b}^2 \cdot R_{E5b}) \tag{14}$$

The notations in Eq.(13) and (14) are similar to that of Eq.(11) and (12), but are for Galileo ranging signals. Table 2 shows the ionosphere-free coefficients of dual-frequency of GPS (L#) and Galileo (E#) observables (Refer to pg.616 GNSS handbook).

Table 2 coefficients of linear combinations

Signals	Coeff1	Coeff2
L1+L2	2.5457	1.5457
L1+L5	2.2606	1.2606
L2+L5	2.5312	1.5312
E1+E5a	2.2606	1.2606
E1+E5b	2.4220	1.4220

5. GNSS positioning and satellite geometry

The GNSS receiver measures ranges to all the satellites in-view and estimate the user’s 3-D position (latitude, longitude and height). The user position in earth centered earth fixed coordinate (ECEF) system is represented as x_u, y_u and z_u , and the visible Satellites are designated as x_i, y_i and z_i (where $i=1, 2, 3, 4$) in the same coordinate system as the user. Fig.1 depicts principle of operation, trilateration principle based on TOA (Ref). Taking into consideration the time difference (Δt) between the satellite signal transmission “ t_i ” ($i=1, 2, 3, 4$) and signal received time in the receiver “ t_u ”. 3D position and time offset are obtained by simultaneously solving the nonlinear equations using Bancroft method and expressed as (Bancroft, 1985),

$$(x_u - x_i)^2 + (y_u - y_i)^2 + (z_u - z_i)^2 = c(t_i - t_u + \Delta t)^2 \tag{15}$$

The quadratic equation in Eq.3 is similar to Lorentz inner product of a multivariate vector of dimension 4 ($X=[x \ y \ z \ b]^T$). A least square solution solves the normal equation. With sufficient number of satellites (minimum four), this method provides a direct solution of first position fix without “a prior knowledge” of location information of the receiver. The technique is iterated applying tropospheric corrections to improve the solution and is computationally efficient (Sanz Subirana et al., 2013).

In order to achieve higher performance ‘Kalman filter’ technique is applied further to smooth the Least Square solutions and to provide accurate position estimate along with the confidence level. The key parameters of the for filter process are state variables, measurement equation and process equation. The state vector (X_k) contains current position ($S_k=[x \ y \ z]_k$), velocity ($V_k = [V_x \ V_y \ V_z]_k$), acceleration ($A_k=[\alpha_x \ \alpha_y \ \alpha_z]$), clock bias ($B_k=[b]_k$) and drift. ($D_k=[b']_k$). Measurement equation is nonlinear and includes corrected pseudoranges (ρ_c) of visible satellites from different error sources (Viz. Ionosphere, Troposphere etc), and has a quadratic relationship with the state parameters. Whereas, process equation is linear, that relates current state to the preceding state. The algorithm is implemented with initial guess for system state (X_0) and covariance (P_0). These are values are updated

by an iterative procedure. The following expressions describe the application of KF for PVT and absolute error in position estimate.

1. State vector $(X_k)=[S_k V_k A_k B_k D_k]$ (16)

2. The measurement equation contains the pseudoranges of satellites visible and is given as,

$$Z=\rho \tag{17}$$

3. Observation matrix ‘H’ is defined as a function of satellite and receiver position at this instant. A- prior coordinates of receiver at the moment are used.

4. The following KF process steps are tailed,

State propagation: $(X_k^- = \varphi_k X_{k-1}^+)$ (18)

5. Error covariance propagation: $(P_k^- = \varphi_k P_k^+ \varphi_k^T + Q_k)$ (19)

6. State update: $(X_k^+ = X_{k-1}^- + X_k [Z_k - h_k(X_k^-)])$ (20)

7. Error covariance update $(P_k^+ = [I - K_k H_k] P_k^-)$ (21)

8. Kalman gain expressed as,

$$K_k = P_k^- H_k^T [H_k P_k^- H_k^T + R_k]^{-1} \tag{22}$$

Iteratively the X and P are updated.

6. Dilution of precision

The accuracy of navigation solution depends not only on elimination or mitigation of various error sources, but also on the visible satellite geometry (i.e. Dilution of Precision (DOP)). DOP is computed from the design matrix ‘A’ elements (Eq.), which contains X, Y, Z (ECEF) coordinates of satellite vehicles visible at an instant of time. The co-factor matrix (Q_X) is derived from (Langley, 1992; Sarma et. al., 2010),

$$Q_X = (A^T A)^{-1} \tag{23}$$

The subscript ‘X’ signifies the result in ECEF coordinate system. Q_X is a [4x4] matrix and the elements of the matrix are as follows

$$Q_X = \begin{bmatrix} q_{xx} & q_{xy} & q_{xz} & q_{xt} \\ q_{xy} & q_{yy} & q_{yz} & q_{yt} \\ q_{xz} & q_{yz} & q_{zz} & q_{zt} \\ q_{xt} & q_{yt} & q_{zt} & q_{tt} \end{bmatrix} \tag{24}$$

The diagonal elements of the Q_X matrix are used to compute following DOPs:

Horizontal DOP (HDOP) : $\sqrt{q_{xx} + q_{yy}}$ (25)

Vertical DOP (VDOP) : $\sqrt{q_{zz}}$ (26)

Position DOP (PDOP) : $\sqrt{q_{xx} + q_{yy} + q_{zz}}$ (27)

Geometry DOP (GDOP) : $\sqrt{q_{xx} + q_{yy} + q_{zz} + q_{tt}}$ (28)

Time DOP (TDOP) : $\sqrt{q_{tt}}$ (29)

In order to define HDOP and VDOP, the transformation of ‘Q_X’ matrix to local coordinates (n, e, u) is essential. Position error is related to DOP is given as,

Position error = user range error × DOP (30)

DOP is multiplicative factor and unit less quantity, lesser the value better the positional accuracy.

7. Position error

The error in the estimated position of GNSS receiver is usually described by terms accuracy and precision. The degree of closeness of an estimate to its true position, which is an unknown value is accuracy and precision is the degree of close of observations to their mean value. The commonly used measures to quantify accuracy and precision are circular error probability (CEP), root mean square error (RMSE), and distance root mean square (DRMS) error. There are three different approaches to describe position error such as formal accuracy, predicted accuracy and measured accuracy (Sanz Subirana et al., 2013). The formal errors rely on statistical characterization of errors and linear model used for position estimation. This gives the uncertainty of the error estimates but not the actual error. The predicted accuracy is based on satellite-receiver geometry and involves calculations using only standard deviation of measurements by evaluating Dilution of Precision (DOP) parameter. Whereas, actual range measurements are used to assess accuracy of position estimate in local coordinates (East, North, UP (ENU)) in case of measured error. The error in ENU coordinates are assessed using above discussed linear models of ionosphere-free linear combinations. The RMS vertical and horizontal (2-D) errors are analyzed to determine the measured accuracy of ionosphere-free linear combination of GNSS signals and expressed as,

$$2D\text{-horizontal error} = \sqrt{\frac{1}{n} \sum_{i=1}^n \Delta E_i^2 + \Delta N_i^2} \quad (31)$$

$$RMS\text{vertical error} = \sqrt{\frac{1}{n} \sum_{i=1}^n \Delta U_i^2} \quad (32)$$

$$3D\text{-RMS error} = \sqrt{\frac{1}{n} \sum_{i=1}^n (\Delta E_i^2 + \Delta N_i^2 + \Delta U_i^2)} \quad (33)$$

8. Methodology

To estimate the position dual frequency ionosphere-free linear combination of code-phase are used rather using single frequency carrier/code phase measurements. Bancroft method and Kalman filter techniques are applied with the derived pseudorange measurements of ionosphere-free combination. The measurements are corrected for other error sources orbit (considering precise orbits), clock and troposphere. The antenna is placed in multipath-free environment and therefore, almost insignificant. Triple-frequency linear combinations of GPS and Galileo are used to calculate/test multipath at the site (Yedukondalu and Satya srinivas, 2017). The absolute error in position estimation is computed for the linear combinations depicted in table 2, in standalone GPS case (L1C/A - L2C), (L1C/A - L5) and in case of combined GPS/Galileo, (L1C/A - L5) / (E1-E5a) observations are used.

9. Experimental setup and data acquisition

Multi-frequency GNSS receiver of make Septentrio, Nv (Model: PolaRxs pro) capable of tracking GNSS (GPS, GLONASS, Galileo) and SBAS (WAAS, GAGAN, EGNOS) satellite signals was setup at Geethanjali College of Engineering and Technology (GCET), Hyderabad, India. Fig.1. depicts the antenna at top of the building and the receiver connected to HP workstation for continuous data acquisition. The raw data is recorded in Rinex format (Version 3.0). Two files both the observation file and navigation file are obtained for analysis. The data sampling interval is 60s. Eight days (28th September 2018 to 4th October 2018) is considered for the analysis. Investigated the positional accuracies of dual frequency ionosphere-free linear combinations of GPS and combined GPS-Galileo for Single point positioning (SPP).

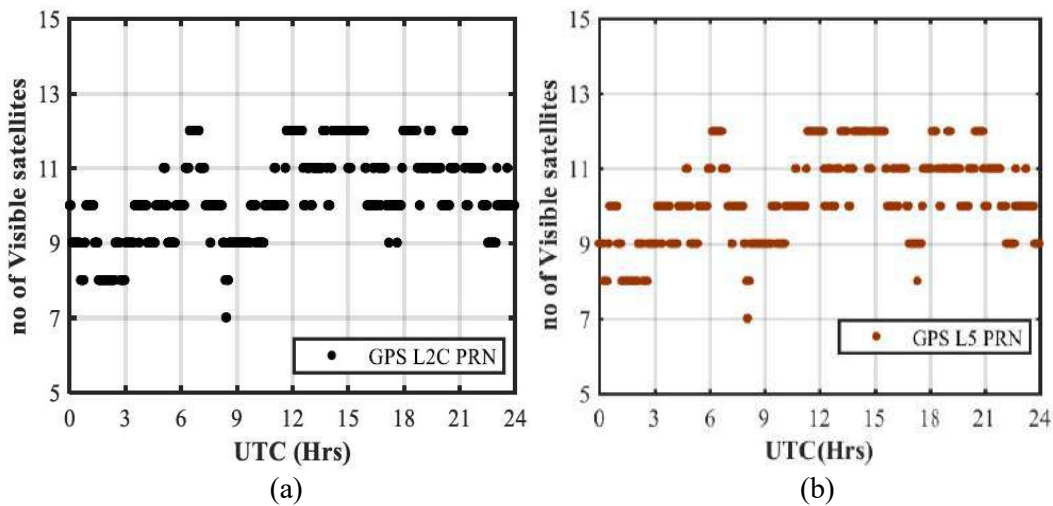


Figure 1. Septentrio PolaRxs-Pro GNSS receiver and antenna setup at GCET, Hyderabad

10. Results and discussion

The present GPS constellation has 19 satellites (PRN: 01, 03, 05, 06, 07, 08, 09, 10, 12, 15, 17, 24, 25, 26, 27, 29, 30, 31, 32) with L2C capability and 12 satellites (PRN: 01, 03, 06, 08, 09, 10, 24, 25, 26, 27, 30, 32) with L5 capability. The visibility of the satellite at GCET site for a typical day (DoY:272) are depicted in Fig.2 for L1C/A/L2C and L1C/A/L5. From Fig.2 (a) and (b), it is evident that a minimum of 7 and maximum of 12 are visible with L2C and L5 capability. The total satellite visibility has increased for combined GPS L1/L5 and Galileo E1/E5a combination (Fig.2c). A minimum of 10 and maximum of 19 satellites are visible. It is anticipated that the GPS constellation with full L5 operational capability will obviate the need for code less and semi-code less receivers by facilitating receivers with L5 in combination with L1. Therefore, in evaluating the combined GPS-Galileo positioning, L1/L5 combination is used for GPS.

As depicted in Fig.2(d) the satellite visibility drops even less than 4 at several epochs for stand-alone Galileo (E1/E5) at the site. Therefore, the performance evaluation for this case is not assessed. Satellite geometry is also a constrain that limit the attainable positional accuracy. The HDOP, VDOP, PDOP and TDOP for the satellite visibility of Fig.2 (a), (b) and (c) is depicted Fig.3 (a), (b) and (c) respectively.



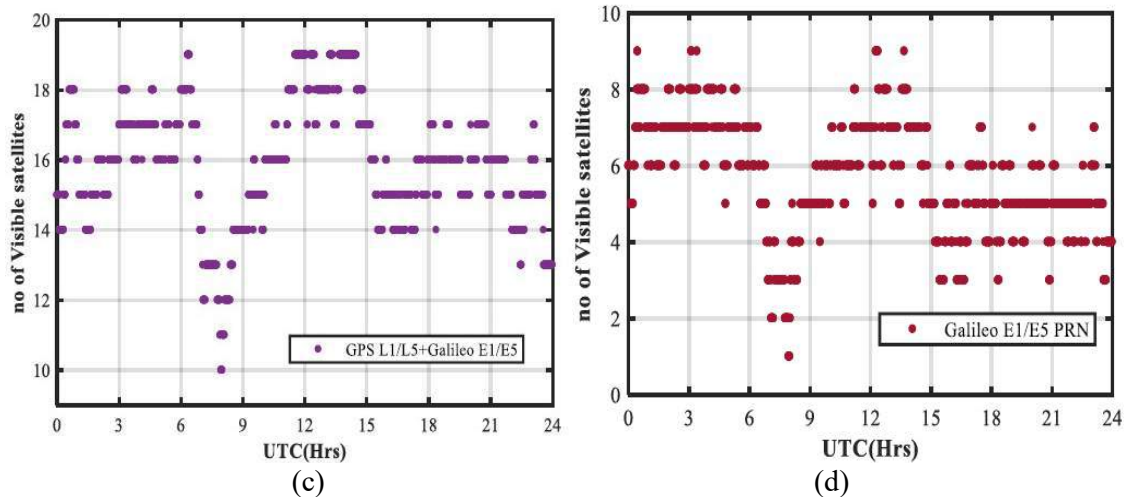


Figure 2. GPS and Galileo Satellites Visible at GCET (a) GPS L1/L2C PRN, (b) GPS L1/L5 PRN, (c) Combined GPS/Galileo PRN and (d) Galileo E1/E5 PRN

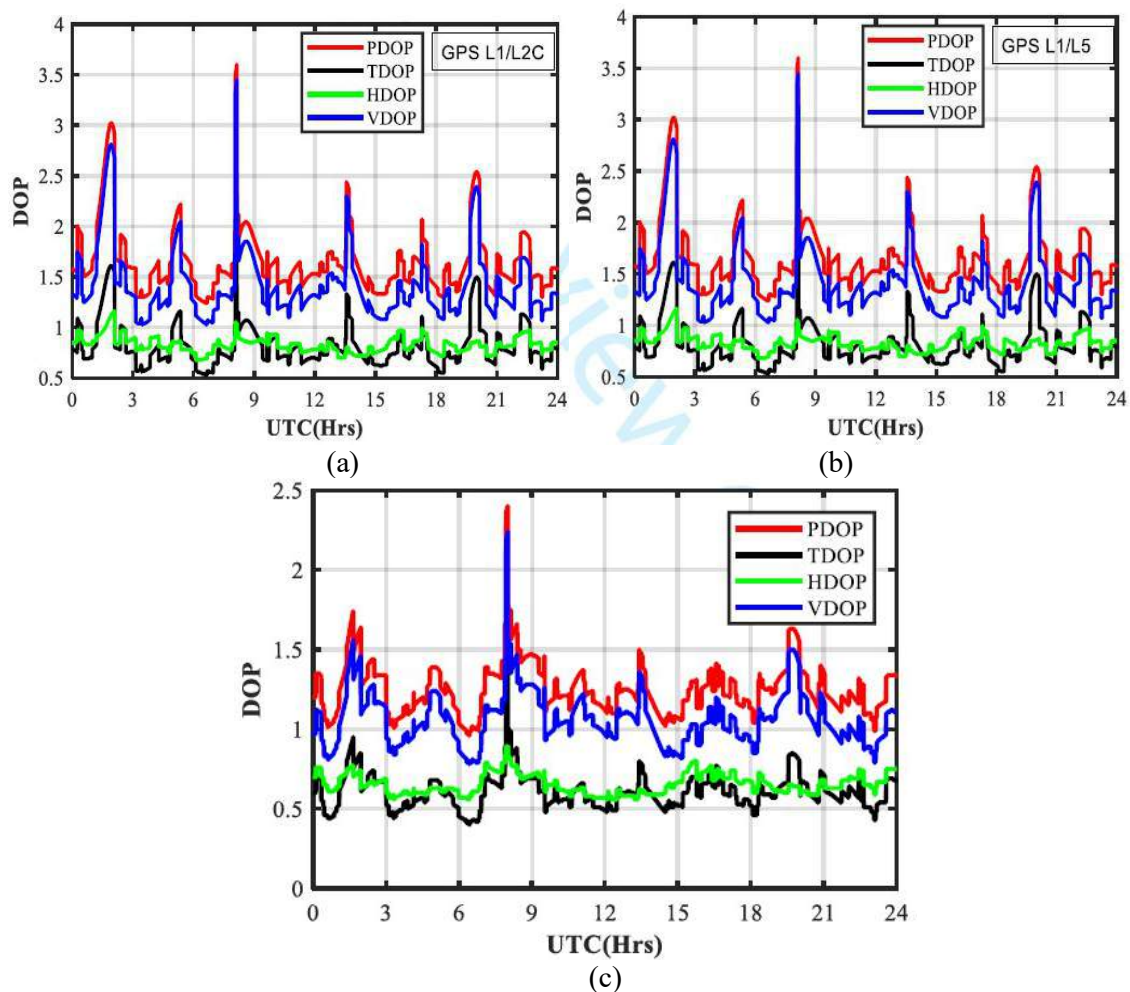


Figure 3. Epoch wise DOPs for visible satellites of (a) GPS L1/L2C (b) GPS L1/L5 and (c) GPS L1/L5 and Galileo E1/E5 combined

It can be observed from tables 3-5 that the DOP values are comparatively small for combined GPS+Galileo system than that of both the cases of GPS (L1/L2C and L1/L5). The minimum, maximum PDOP are 0.96, 2.40 and 1.2, 3.5 for combined constellation and GPS respectively. The position domain analysis is performed by evaluating measured error in local coordinate systems (east-north-up (ENU)). The error in estimated position is calculated by taking difference from the average position.

Table 3 Minimum, Maximum, Mean and Standard deviation of DOPs of GPS L1/L2C

DOPs	Min.	Max.	Mean	Std.
HDOP	0.65	1.12	0.81	0.09
VDOP	1.05	3.40	1.40	0.36
PDOP	1.20	3.52	1.62	0.37
TDOP	0.60	1.98	0.84	0.25

Table 4 Minimum, Maximum, Mean and Standard deviation of DOPs of GPS L1/L5

DOPs	Min.	Max.	Mean	Std.
HDOP	0.68	1.16	0.82	0.07
VDOP	1.03	3.45	1.41	0.34
PDOP	1.24	3.60	1.64	0.32
TDOP	0.53	2.15	0.81	0.21

Table 5 Minimum, Maximum, Mean and Standard deviation of DOPs of GPS+Galileo

DOPs	Min.	Max.	Mean	Std.
HDOP	0.56	0.89	0.65	0.06
VDOP	0.78	2.24	1.06	0.17
PDOP	0.96	2.40	1.25	0.16
TDOP	0.40	1.43	0.60	0.11

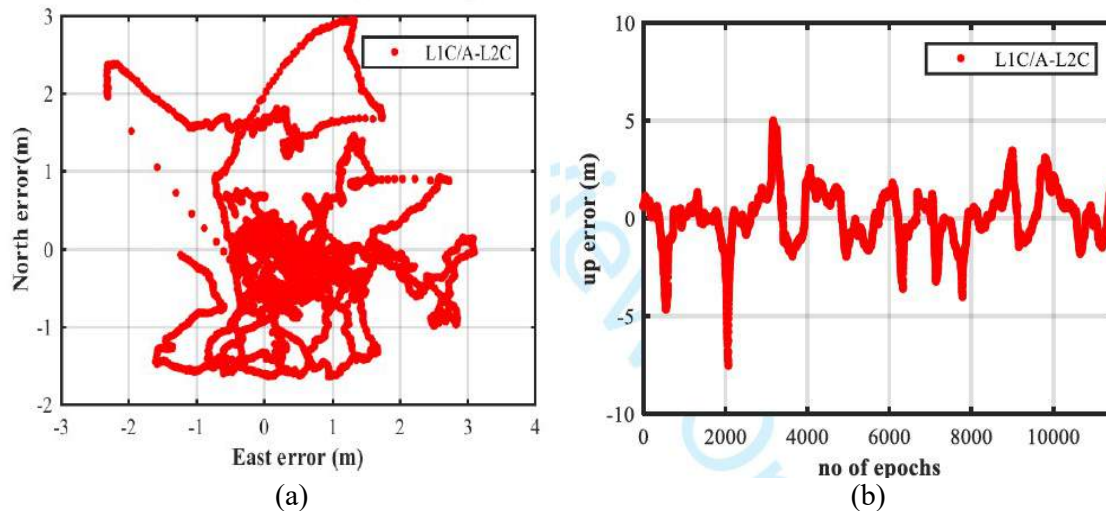


Figure 4. Position error for GPS L1C/A-L2C (a) Horizontal error and (b) Vertical error

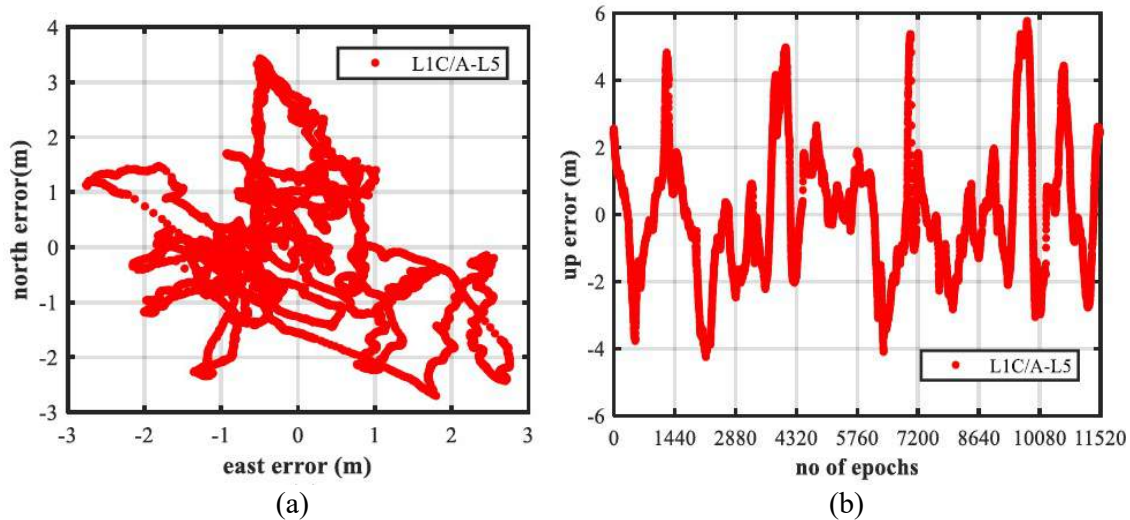


Figure 5. Position error for GPS L1C/A-L5 (a) Horizontal error and (b) Vertical error

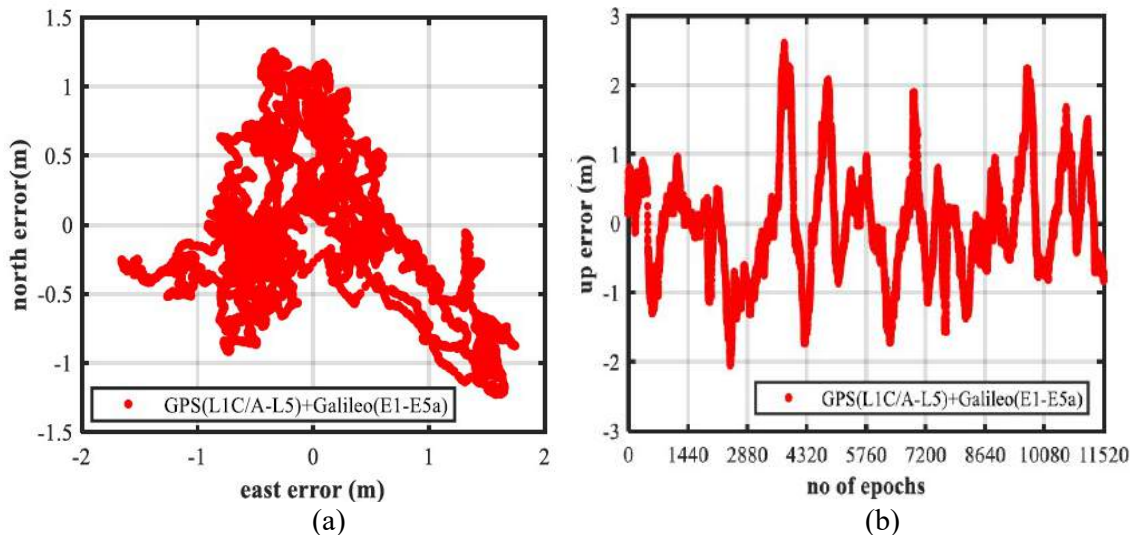


Figure 6. Position error for dual system (a) Horizontal error and (b) Vertical error

The horizontal and vertical position error in ENU coordinates are presented in Figs.4-6. The descriptive statistics are depicted in table 6. The maximum error in east, north and up coordinates are 1.74m, 1.24m and 2.59m respectively when position is estimated using dual system (Table 6). From table 7, 2-D RMS error of 2-4meters is evident due to code-phase ionosphere-free combination of modernized GNSS signals. The 3D-RMS position error is about 8.9m and 6.3m for L1-L5 and L1-L2C respectively. The attainable SPP accuracy is less than 2m (Table 7) with dual-system (GPS+Galileo). The ECEF coordinates of the GCET site with this accuracy are 1199419.584 m, 5965113.838 m and 1908094.934 m. The geodetic coordinates are 17.52o, 78.63o and 464.21 m.

Table 6 Descriptive statistics of position error along east, north and up axes

Linear Combination	East Error		North Error		Up Error	
	Min.	Max.	Min.	Max.	Min.	Max.
GPS L1C/A-L2C	-2.32	3.10	-1.65	2.79	-7.55	4.99
GPS L1C/A-L5	-2.75	2.76	-2.71	3.42	-4.26	5.74
GPS L1C/A-L5 + Galileo E1-E5a (Dual system)	-1.65	1.74	-1.23	1.24	-2.05	2.59

Table 7 Measured accuracy: RMS vertical, horizontal (2D), and 3D position

Linear Combination	GPS L1C/A-L2C	GPS L1C/A-L5	GPS L1C/A-L5 + Galileo E1-E5a (Dual system)
RMS vertical error (m)	1.40	1.95	0.80
2D-RMS horizontal error (m)	2.77	3.59	1.08
3D-RMS error (m)	6.34	8.94	1.84

12. Conclusions

The results show that Galileo in combination with GPS will aid in improving overall positional accuracy. The attainable accuracy in 2D and 3D position is observed to be less than 2 meters (Table 7). In near future, Galileo with full constellation and GPS with more satellites of L5/L2C capability, the accuracy, robustness and consistency of navigation solution is expected to improve. The results are encouraging and may find useful for future implementation of dual frequency Ground Based Augmentation systems (GBAS) as well. The attainable 2-D RMS accuracy of code-phase combination of modernized GNSS signals (L1/L5 and L2C/L5) is about 3-4 meters. On average of 10 and 16 satellites are visible for stand-alone GPS and combined GPS/Galileo case respectively. There is substantial improvement in DOP as well. The maximum PDOP for stand-alone GPS is 3.5 and in case of combined GPS/Galileo it is 2.4. The point positioning horizontal accuracy (2D RMS) of GPS/Galileo is observed to be within 1 meter most of the time (Figure 6), which seems to meet the accuracy requirement of port navigation.

Acknowledgment

This work was supported by the Department of Science and Technology, New Delhi. Vide sanction letter No:SR/FTP/ES-156/2014,dated:4th September 2015.

References

1. Bancroft, S. An Algebraic Solution of the GPS Equations. *EEE Trans. on Aerospace and Electronic Systems*, Vol. AES-21, No.7, pp.56-59, 1985.
2. Cocard, M., and A. Geiger. Systematic Search for all Possible Widelaners. *Proceedings of the Sixth International Geodetic Symposium on Satellite Positioning*, Columbus Ohio March 17-20, 1992, pp. 312-318, 1992.
3. Dach, R., Urs Hugentobler, Pierre Fridez, and Michael Meindl. *Bernese GPS Software Version 5.0. User Manual*, Astronomical Institute, University of Bern, Bern, Switzerland, 2007.
4. Defraigne, P., and G. Petit. Time Transfer to TAI Using Geodetic Receivers. *Metrologia*, Vol.40, pp.184-188, 2003.
5. Geoffrey Blewitt. Basics of the GPS Technique. *Geodetic Applications of GPS: Observation Equations*, Swedish Land Survey, pp.1-46, 1997.
6. Han, S., and C. Rizos. Improving the computational efficiency of the ambiguity function algorithm. *Journal of Geodesy*, Vol. 70, No. 6, pp330-341, 1996.
7. Han, S., and Rizos, C. The Impact of Two Additional Civilian GPS Frequencies on Ambiguity Resolution Strategies. *Proc. of IONNTM*, Cambridge, Massachusetts, Satellite Division of the Institute of Navigation, Fairfax, Va., pp.315-321, 1999.
8. Hein, G. *GNSS Interoperability: Achieving a Global System of Systems or Does Everything Have to be the Same?*, Inside GNSS, 2006.
9. Hofmann-Wellenhof, B., Lichtenegger, and Wasle. *Global Navigation Satellite Systems – GPS, GLONASS, GALILEO and More*. Springer-Verlag Wien New York, 2008.
10. J. Sanz Subirana, J.M. Juan Zornoza and M. Hernández-Pajares. *GNSS Data Processing: Fundamental and Algorithms*. ESA Communications, 2013.
11. Jacobson, L. *GNSS Markets and Applications*, London, Artech House Inc., 2007.

12. K. Yedukondalu and V. Satya Srinivas. Analysis and Estimation of Multipath Interference using Dual and Triple Frequency GNSS Signals. IEEE Applied Electromagnetics Conference, 19-22 Dec., Aurangabad, 2017.
13. Lee, J. GNSS Precise Point Positioning Approach Based on Dual Code Linear Combination, American Geophysical Union, 2008.
14. M. Cocard, A. Geiger: Systematic search for all possible widelanes, Proc. 6th Int. Geod. Symp., Satellite Position., Columbus, pp. 312–318, 1992.
15. Odijk, D. Ionosphere-Free Combinations for Modernized GPS. Journal of Surveying Engineering, Vol.129, No.4, pp.165–173, 2003.
16. Patrick Henkel and Christoph Gunther. Three frequency Linear combinations for Galileo. IEEE workshop on Positioning, Navigation and Communication, Hannover, Germany, 2007.
17. Petovello, M.G. Narrow-lane: Is It Worth It?, GPS Solutions, pp.187-195, 2006.
18. R. Hatch, J. Jung, P. Enge, B. Pervan. Civilian GPS: The benefit of three frequencies. GPS Solutions, vol. 3, No.4, pp.1-9, 2000.
19. R.B. Langley, Dilution of precision. GPS World, Vol. 10, No.5, pp. 52–59, 1999.
20. Rajat Acharya. Understanding Satellite Navigation. Elsevier, Academic Press, 2014.
21. Richard B. Langley, Peter J.G. Teunissen, and Oliver Montenbruck. Principles of GNSS. Handbook of GNSS, Springer International Publishing, pp.3-23, 2017.
22. Richert, T., and N. El-Sheimy. “Optimal linear combinations of triple frequency carrier phase data from future global navigation satellite systems. GPS Solutions, Vol. 11, No. 1, pp.11-19, 2007.
23. Sarma, A.D, Quddusa Sultana, and V. Satya Srinivas. Augmentation of Indian Regional Navigation Satellite System to Improve DOP. The Journal of Navigation, The Royal Institute of Navigation, Vol.63, pp.313-321, 2010.
24. Seeber, G. Satellite Geodesy. 2nd ed., Walter de Gruyter, Berlin, New York, 2003.
25. Strang, G., and Kai Borre. Linear Algebra, Geodesy, and GPS. Wellesley- Cambridge press, 1997.
26. Urquhart L. An Analysis of Multi-Frequency Carrier Phase Linear Combinations for GNSS. Senior Technical Report, Department of Geodesy and Geomagnetism Engineering, Technical Report, No.263, University of New Brunswick, Fredericton, New Brunswick, Canada, 2009.
27. Wubbena, G. Software Developments for Geodetic Positioning with GPS Using TI 4100 Code and Carrier Measurements. Proceedings of 1st International Symposium on Precise Positioning with the Global Positioning System, Edited by Clyde Goad, US Department of Commerce, Rockville, Maryland, pp.403–412, 1985.
28. Xiaoying Gu And Bocheng Zhu. Detection and Correction of Cycle Slip in Triple-Frequency GNSS Positioning. IEEE Access, Vol.5, pp.12584-12595, 2017.
29. Xu Guochang. GPS Data Processing With Equivalent Observation Equations. GPS Solutions, Springer-Verlag, 2002.
30. Xu Guochang. GPS Theory, Algorithms and Applications, Springer-verlag, Berlin, Heidelberg, 2007.



V. SATYA SRINIVAS, was born in Guntur, India, in November 1981. He received the Ph.D. degree in electronic and electrical engineering from Jawaharlal Nehru Technological University Hyderabad, India, in 2014 and Master’s degree in communication engineering from Osmania university in 2007. He was awarded CSIR senior research fellowship in 2010. He was associated Research and Training Unit for Navigational Electronics, Osmania University, Hyderabad, India and Space Science Radio Engineering, University of Electro- Communications, Japan. He is currently an

Associate Professor of electronics and communication engineering with the Geethanjali College of Engineering and Technology, Hyderabad. He has thirty publications to his credit in journal and conference proceedings. His research interests include GNSS Point Positioning algorithm development and application, multi-GNSS ionospheric modeling and software defined radio. Dr. Satya Srinivas is a Member of IEEE; USA, Life Member of IETE and ISTE; India.

Modeling and performance optimization of two-terminal $\text{Cu}_2\text{ZnSnS}_4$ -silicon tandem solar cells

Vallisree Sivathanu¹  | Thangavel R² | Trupti Ranjan Lenka³

¹Department of Electronics and Communication Engineering, Geethanjali College of Engineering and Technology, Hyderabad, India

²Department of Physics, Indian Institute of Technology (ISM), Dhanbad, India

³Department of Electronics and Communication Engineering, National Institute of Technology Silchar, Silchar, India

Correspondence

Trupti Ranjan Lenka, Department of Electronics and Communication Engineering, National Institute of Technology Silchar, Silchar 788010, Assam, India.

Email: trlenka@ieee.org

Summary

A dual-junction $\text{Cu}_2\text{ZnSnS}_4$ -Silicon (CZTS-Si)-based tandem configuration is modeled and analyzed for its viability as a solar cell. The top and bottom modules in the tandem structure are validated by comparison with experiment. Initially, the designed tandem structure yields very low efficiency of 3.18%, and the various loss mechanisms are identified and investigated. The current mismatch between top and bottom cells and parasitic absorption (photon losses) are suggested to be the major causes limiting the short circuit current and hence the efficiency of the device. We optimize the material parameters within experimentally achievable limits in order to obtain current matching, and the optimized thicknesses of copper zinc tin sulfide (CZTS) and silicon (Si) absorbers are found to be 150 nm and 250 μm , respectively. The simulation results revealed that the photon losses are reduced, and overall absorption in the longer wavelength region has enhanced with the replacement of cadmium sulfide (CdS) by zinc sulfide (ZnS) buffer and careful optimization of the front layers of the device. The maximum predicted efficiency of tandem structure is >20% by minimizing the recombination centers within the experimentally obtainable ranges and improving the carrier separation process.

KEYWORDS

current losses, CZTS, photon losses, silicon, tandem solar cell

1 | INTRODUCTION

Crystalline silicon-based solar cells conquered the photovoltaic market in the past decades. Nowadays, the tandem solar cells have gained popularity as it possesses the capability of surpassing the Shockley-Queisser efficiency limits. As a result, the recent technology focuses on combining the thin film technology with silicon in tandem structure where thin films act as top cell absorbers focusing toward the achievement of efficiency enhancement of the device. Blanker¹ reported a two terminal tandem configuration which utilizes copper indium gallium selenide (CIGS) thin film as top cell absorber and hydrogenated amorphous silicon absorber layers in bottom cell. The

tandem structures designed with cadmium zinc telluride (CdZnTe) and cadmium telluride (CdTe) in combination with silicon as a bottom cell absorber were reported by.^{2,3} An analytical model has been developed for kesterite-based tandem solar cells in Reference 4. Also, researchers have studied the performance of perovskite-based tandem solar cells for various topologies and configurations.^{5,6} Ferhati et al have studied the perovskite/CZTS tandem solar cell and reported efficiency of 17%.⁷ Amran et al have reported a monolithic configuration of perovskite/silicon solar cell with efficiency of 29% by employing a special hole-selective layer in the perovskite module.⁸ Zhao et al reported a bulk-passivation technique for lowering the band gap of perovskite absorber

materials toward the development of all-perovskite tandem solar cells.⁹ Also, various configurations of all-perovskite tandem structures are reviewed in Reference 10. The absorber material in the top cell should possess band gap in the range 1.6 to 1.9 eV for tandem configuration with silicon having band gap in the range of 1.1 eV as a bottom cell absorber.¹¹ Out of all the thin film absorber materials suitable for top cell, copper zinc tin sulfide (CZTS) material has gained increased attention owing to tunable band gap, abundance of zinc and tin, and low cost, and it possess absorption coefficient $> 10^4 \text{ cm}^{-1}$.^{12,13} Both silicon and CZTS materials are good absorbers¹⁴ and hence can be connected in tandem configuration for improving the open circuit voltage and maximize spectrum utilization. Also, the tunneling material for the tandem structure should possess both electrical coupling capability between the top and bottom modules and pass on the longer waves to the bottom cell. Hence, a transparent conducting oxide can be considered as suitable candidate for the tunneling material in the tandem structure. However, various undesirable effects such as current mismatch, differences in refractive index, lattice mismatch, and other losses may prevent the achievement of high efficiencies.⁷ Hence, the present work focuses on the modeling of silicon-CZTS tandem structure, identifying the various loss mechanisms contributing to low efficiency. The various undesired losses are mitigated step by step by

following a methodology in Figure 1 which is not reported elsewhere. The structure of this paper is as follows: The methodology used for design and optimization of CZTS-Si dual-junction solar cell is discussed in Section 2. The individual sub-cell simulations are described in Section 3.1, and dual-junction simulation and identification of loss mechanisms are discussed in Section 3.2. Mitigation of various loss mechanisms and prediction of maximum attainable efficiency of the proposed tandem structure are discussed in Sections 3.3 to 3.5.

2 | SIMULATION APPROACH

The proposed methodology for the design and optimization of dual-junction CZTS-Si tandem solar cell is illustrated in Figure 1. Initially, the top and bottom cells were modeled and validated by experimental fitting. Then, the tandem structure is modeled, and the various loss mechanisms are identified. The maximum attainable efficiency is predicted after mitigating the loss mechanisms. CZTS absorber material is chosen for the top cell as it possesses tunable band gap property of approximately 1.6 eV. The single-junction and the dual-junction simulations are carried out using ATLAS 2D simulator¹⁵ where the Poisson's equation and carrier continuity equations are self consistently solved to evaluate the potential at each and every

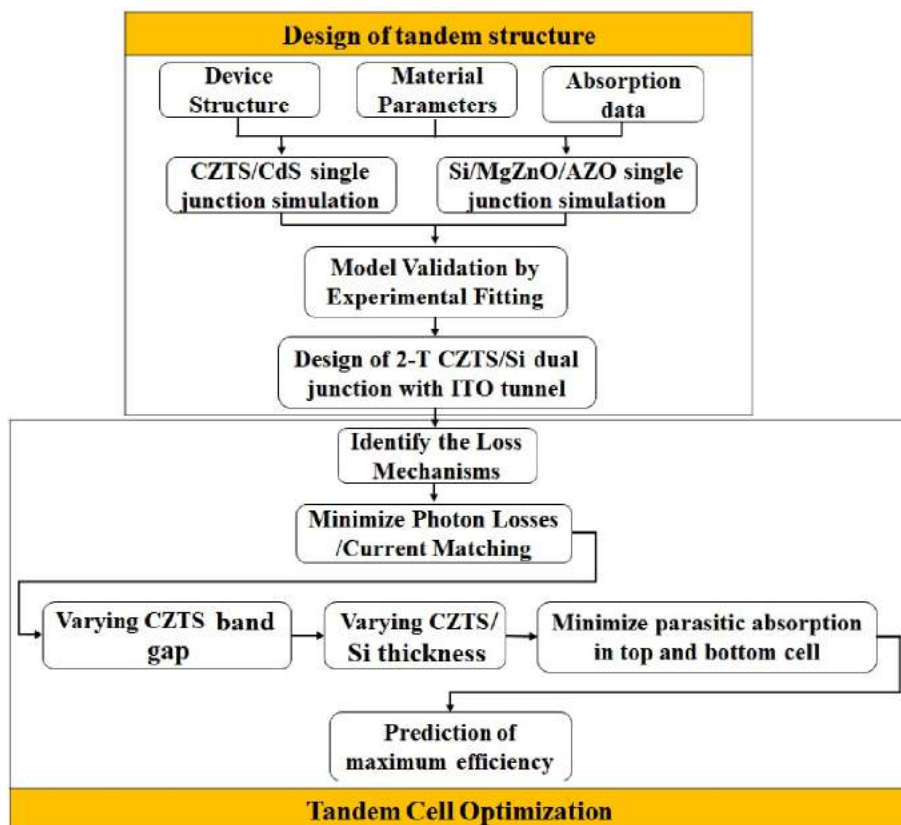


FIGURE 1 Proposed methodology for the CZTS-Si tandem solar cell design and optimization [Colour figure can be viewed at wileyonlinelibrary.com]

mesh point. SRH recombination mechanism is used to obtain the recombination statistics^{15,16} to account for the phonon transitions and radiative recombination is incorporated for direct band gap materials by specifying the radiative recombination rate coefficient. Auger recombination is considered for both top and bottom cell absorber materials.

Initially, the propagation of light is described by ray tracing optics for simulating the individual sub-cells where the optical intensity is obtained from the real part of refractive index and the photo-generated carrier concentration at each grid point is calculated from the imaginary part of refractive index. Then, the transfer matrix method is used for simulating the tandem CZTS–Si solar cell structure because it provides accurate solution for simulating electromagnetic wave propagation through a layered medium by relating the tangential components of electric and magnetic fields at the multilayer boundaries.¹⁵ This method relates the electric field amplitudes of transmitted and reflected wave to the incident wave amplitude. The electric field at any point within a material layer is given by Equations (1) and (2).

$$E(z) = E(z_j) \cos(\varphi) - iH(z_j) \sin(\varphi) / Y(j), \quad (1)$$

$$H(z) = H(z_i) \cos(\varphi) - iE(z_i) \sin(\varphi) / Y(i), \quad (2)$$

where $E(z_j)$ and $H(z_j)$ are electric and magnetic fields at layer interface between layers j and $j - 1$. $Y(j)$ is the optical admittance of the layer and the phase is given by Equation (3). The intensity profile is generated for the device and the photogeneration rate is given by Equation (4).

$$\varphi = \frac{2\pi n \cos(\theta) (z - z_j)}{\lambda}, \quad (3)$$

$$G(z) = \frac{\lambda}{hc} \alpha \frac{|E(z)|^2}{2\eta}. \quad (4)$$

3 | RESULTS AND DISCUSSION

3.1 | Sub-cell simulations

Initially, the CZTS cell comprises of Al/AZO/i-ZnO/CdS/CZTS/Mo layers and silicon solar cell comprises of Al/silicon/MgZnO/AZO layers are designed in accordance with the experimental structures reported in Reference 17 and sample C¹⁸ of respectively. Silicon/MgZnO is chosen for this study as it forms a better heterojunction with silicon when compared to zinc oxide (ZnO) thin film

material.¹⁹ The material, defect, and recombination parameters used in the modeling of both sub-cells are listed in Table 1. Each of the materials in the sub-cells are modeled by providing the refractive index (n) and extinction coefficient (k) data^{23,27-30} spanning over the wavelength from 300 nm to 1200 nm. Both the sub-cells are illuminated with AM 1.5 radiation with intensity of 100 mW/cm².

The electron affinity of CZTS material is tailored in accordance with the experimental conduction band offset (ΔE_c) of 0.41 eV¹⁷ at the CZTS/CdS interface. The CZTS acceptor concentration which is approximately 10^{16} cm⁻³ is raised to 3.5×10^{16} cm⁻³ and interface recombination velocity (IRV) value of 5×10^6 cm/s are considered as fitting parameters, and the simulated solar cell parameters are in close agreement with experimental results (Table 2). For the Si/MgZnO solar cell design, the optimized composition of Mg in MgZnO ternary compound semiconductor is assumed to be 20% according to²⁵ and the band gap is obtained using Vegard's law¹⁹ with bowing parameter $b = 2.05$ is considered in accordance to the MgZnO wurtzite structure.³¹ The model is validated by comparison with experiment in Table 2.

3.2 | Dual-junction simulations and identification of loss mechanisms

Indium tin oxide (ITO) material is introduced between the top and bottom modules to enable electrical coupling between the sub-cells and to pass the near infra-red light to the bottom absorber by minimizing the parasitic absorption.³² ITO material is defined as conducting material with resistivity value of 540 $\mu\text{ohm-cm}$, and the absorption data are obtained from.³³ The possibility of creating CZTS/ITO and ITO/AZO interfaces is experimentally realized in References 34 and 35, and the proposed tandem structure shown in Figure 2A can be experimentally fabricated. The tandem structure is illuminated with AM 1.5 radiation with intensity of 100 mW/cm². The tandem configuration yields poor efficiency of 3.18% when compared to individual sub-cells as clearly evident from Figure 3.

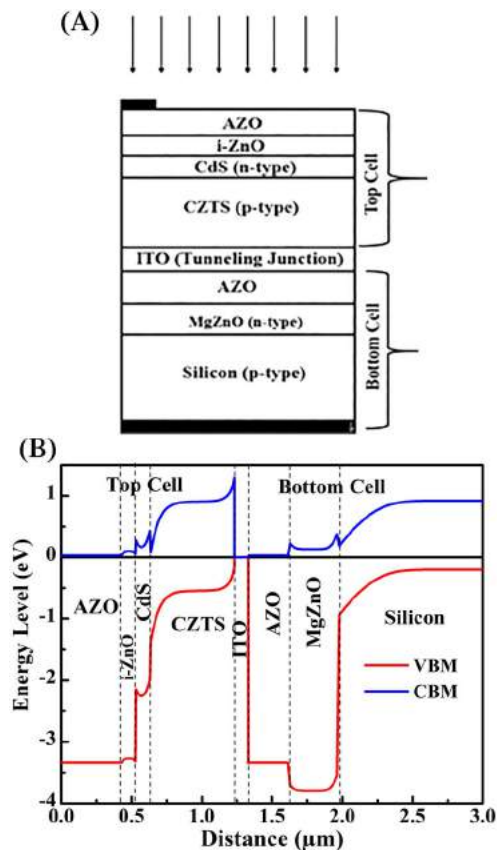
The degradation in performance is attributed to the current mismatch between top and bottom cells which is clearly evident from Figure 4A. The current generated in the top module is much greater than the bottom module, and the current is limited by the lowest current of these modules as they are connected in series configuration. Most of the light is absorbed by the top cell leaving behind less amount of photons for the bottom cell as seen clearly from Figure 4B. The power absorbed by both the top and bottom cells should be equal in order to obtain

TABLE 1 Material parameters used in the modeling of individual solar cells and tandem structure

Parameters	CZTS	CdS	ZnS	i-ZnO	AZO	Si	MgZnO
Band gap (eV)	1.45 ¹⁷	2.42 ²⁰	3.58 ²⁰	3.37 ²⁰	3.37 ²⁰	1.12 ²¹	3.93
Permittivity	7 ²⁰	10 ²⁰	9 ²⁰	9 ²⁰	9 ²⁰	11.9 ²¹	8.49 ¹⁵
Electron affinity (eV)	4.16	3.75 ²⁰	3.8 ²⁰	4.0 ²⁰	4.0 ²⁰	4.05 ²²	3.75
Conduction band DOS	1.91 × 10 ¹⁸ 22	1.8 × 10 ¹⁹ 22	6.35 × 10 ¹⁸ 23,24	2.2 × 10 ¹⁸ 15,22	2.2 × 10 ¹⁸ 15,22	2.8 × 10 ¹⁹ 22	4.42 × 10 ¹⁸ 25
Valence band DOS	1.5 × 10 ¹⁹ 22	2.4 × 10 ¹⁸ 22	6.03 × 10 ¹⁹ 15,24	1.8 × 10 ¹⁹ 15,22	1.8 × 10 ¹⁹ 15,22	1.04 × 10 ¹⁹ 21	1.76 × 10 ¹⁹ 25
Donor concentration (cm ⁻³)	-	1.1 × 10 ¹⁷	1.1 × 10 ¹⁷	1.5 × 10 ¹⁷ 20	1 × 10 ¹⁸	-	1 × 10 ¹⁷
Acceptor concentration (cm ⁻³)	3.5 × 10 ¹⁶	-	-	-	-	4.31 × 10 ¹⁵ 18	-
Electron mobility (cm ² /Vs)	100 ²⁰	160 ²⁰	230 ²⁰	100	50 ²⁰	990 ²⁵	16 ²⁵
Hole mobility (cm ² /Vs)	25 ²⁰	15 ²⁰	40 ²⁰	20	5 ²⁰	269 ¹⁸	4 ²⁵
Thickness (μm)	0.6 ¹⁷	0.1 ¹⁷	0.1 ¹⁷	0.08 ¹⁷	0.45/0.3 (TC/BC) ^{17,18}	180 ¹⁸	0.35 ¹⁸
<i>Defect parameters</i>							
Density of deep states (cm ⁻³ /eV)	1.2 × 10 ¹⁷ (D)	1 × 10 ¹⁶ (A)	1 × 10 ¹⁶ (A)	1 × 10 ¹⁷ (A)	1 × 10 ¹⁷ (A)	1 × 10 ¹¹ (D)	1 × 10 ¹⁷ (A)
Peak energy (eV)	0.725	1.21	1.79	1.685	1.685	0.56	1.965
Characteristic decay energy (eV)	0.1	0.1	0.1	0.1	0.1	0.1	0.1
Density of shallow states (cm ⁻³ /eV)	3 × 10 ¹⁹ (D)	8 × 10 ¹⁷ (A)	8 × 10 ¹⁷ (A)	6 × 10 ¹⁸ (A)	6 × 10 ¹⁸ (A)	1 × 10 ¹⁴ (D)	6 × 10 ¹⁸ (A)
Decay energy (eV)	0.1	0.1	0.1	0.1	0.1	0.1	0.1
<i>Recombination parameters</i>							
SRH lifetime (s)	7.8 × 10 ⁻⁹ 17	7.5 × 10 ⁻¹⁰ 20	5.5 × 10 ⁻¹⁰ 20	2.1 × 10 ⁻⁹ 26	1 × 10 ⁻⁹	2.5 × 10 ⁻³ 21	9 × 10 ⁻⁹ 25
Radiative recombination rate	1.04 × 10 ⁻¹⁰ 20	1.02 × 10 ⁻¹⁰ 20	1.5 × 10 ⁻¹⁰ 20	1.1 × 10 ⁻⁸ 15	1.1 × 10 ⁻⁸ 15	-	1.1 × 10 ⁻⁸ 15
Auger recombination	1 × 10 ⁻²⁹	-	-	-	-	2.8 × 10 ⁻³¹ (electrons) 9.9 × 10 ⁻³² (holes)	-
Interface recombination velocity	CZTS/CdS	2 × 10 ⁶ cm/s	CZTS/ZnS	10 ³ cm/s ¹⁶	Si/MgZnO	10 ⁶ cm/s	-

TABLE 2 Comparison of individual top cell and bottom cell parameters with Experiment

Module	J_{sc} (mA cm ⁻²)	V_{oc} (V)	FF (%)	η (%)
<i>Top cell</i>				
Experimental ¹⁷	19.5	0.661	65.8	8.4
Simulation	19.11	0.698	63.55	8.47
<i>Bottom cell</i>				
Experimental ¹⁸	32	0.470	69	10.5
Simulation	30.38	0.499	68.59	10.39

**FIGURE 2** A, Silicon CZTS tandem cell structure and B, energy band diagram of silicon CZTS tandem solar cell [Colour figure can be viewed at wileyonlinelibrary.com]

current matching between the top cell and bottom cells.²⁰ The open circuit voltage of the tandem structure is approximately equal to the sum of the open circuit voltage of top and bottom cells as expected.

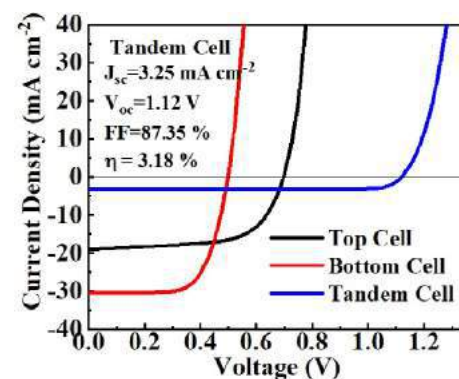
3.3 | Toward obtaining current matching

Current mismatch occurs because of the unequal amount of current generated by the top and bottom modules. One of the main causes for the unequal amount of current

generation is the unequal amount of photon absorption by the top and bottom modules apart from several other factors. The photon absorption/current generation by top and bottom modules is optimized by careful tuning of CZTS material band gap, and thickness of top and bottom cell absorber materials are discussed in the following sections.

3.3.1 | CZTS absorber band gap

The CZTS absorber band gap might vary depending on the process conditions during the fabrication process as well as the stoichiometry changes.³⁶ For the CZTS absorber tunable band gap analysis, the same absorption data are used owing to the unavailability of concrete data in literature. Electrically, the raise in the band gap widens the quasi-fermi levels which is used to describe the nonequilibrium conditions, and it represents the number of carriers available, and they can recombine up to a certain distance, and, as a result, the probability of recombination reduces,^{37,38} resulting in the linear increase in V_{oc} of the top module and thus the tandem configuration in Figure 5A. The fill factor is also

**FIGURE 3** Comparison of J-V curves of tandem cell with the individual sub-cells [Colour figure can be viewed at wileyonlinelibrary.com]

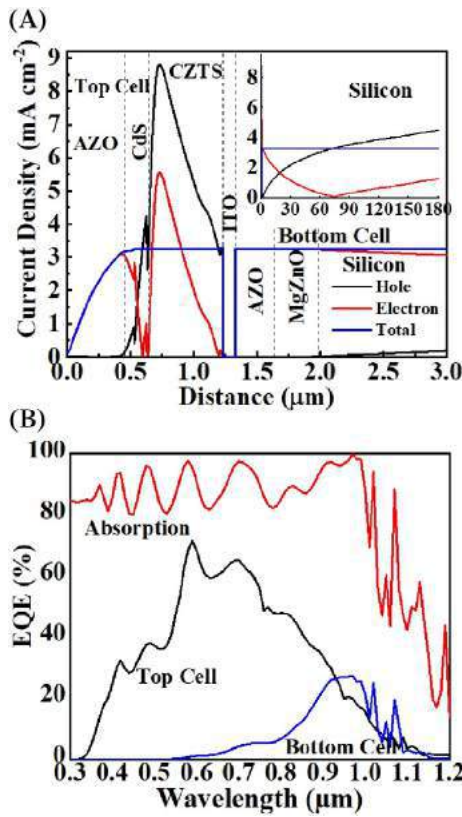


FIGURE 4 A, Electron and hole current density components in tandem cell and B, EQE of top and bottom cells and absorption in tandem structure [Colour figure can be viewed at wileyonlinelibrary.com]

dependent on open circuit voltage apart from the series and shunt resistance which is given by

$$FF_0 = \frac{v_{oc} - \ln(v_{oc} + 0.72)}{v_{oc} + 1}, \quad (5)$$

where $v_{oc} = \frac{q}{nKT} V_{oc}$ ³⁹ and hence the increase in fill factor is observed in Figure 5B. The efficiency shows a linear increase with the increase in band gap of the CZTS absorber material owing to the slight increase in J_{sc} , almost linear rise in V_{oc} and fill factor of the device. From Figure 5, it is revealed that the solar cell shows better performance for CZTS band gap value of 1.7 eV, and this optimized value is used for further analysis.

3.3.2 | CZTS absorber thickness

More amount of light is absorbed by the top module (Figure 4B) which leaves behind less amount of photons for the bottom module, and hence the thickness of CZTS absorber material is reduced step by step (100 nm in each step) from the original 0.6 μm to 0.1 μm as an attempt to

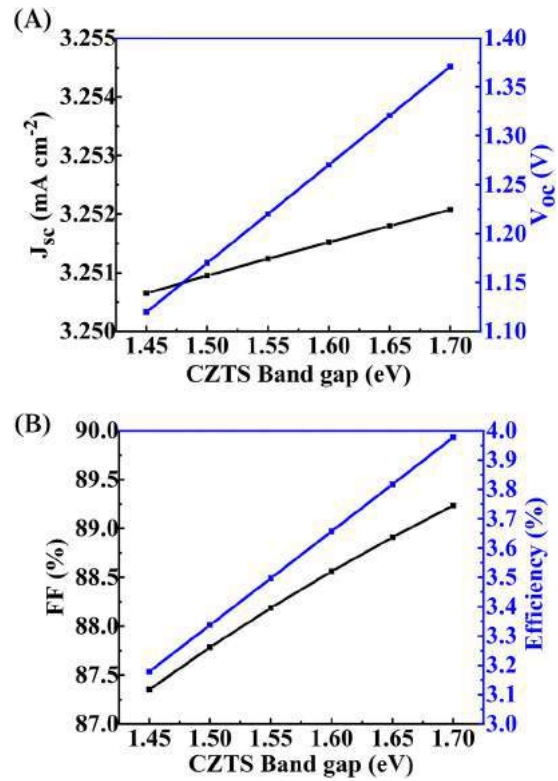


FIGURE 5 Dependency of solar cell parameters with CZTS band gap [Colour figure can be viewed at wileyonlinelibrary.com]

equalize the power absorption of top cell and bottom cells. Also, additional amount of current will be lost due to resistive heating²⁰ owing to this mismatch in J_{sc} as the short circuit current follows the bottom cell with lower J_{sc} in our tandem configuration (Figure 4A). For wavelength range < 520 nm, most of the light is absorbed by the AZO and CdS material layers and hence remains almost unaffected by the CZTS thickness variation as revealed from Figure 6. On reducing the thickness of CZTS material, photon absorption beyond 520 nm till the absorption edge (above band gap absorption) reduces along with the parasitic absorption allowing more number of photons to the bottom cell to enhance the effective light absorption in the tandem structure and the efficiency has increased from 3.98% to 13.03% as clearly evident from EQE graph of Figure 6.

3.3.3 | Silicon absorber thickness

From the nature of contour graphs in Figure 7, it is inferred that slight variation in CZTS thin film thickness has a more significant variation in the solar cell parameters than the silicon wafer thickness. J_{sc} , V_{oc} , and η parameters increase with the reduction in the CZTS thickness and increase in silicon thickness owing to the

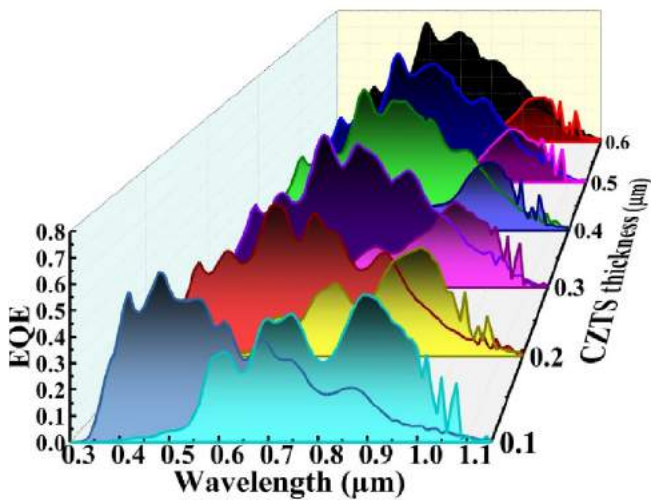
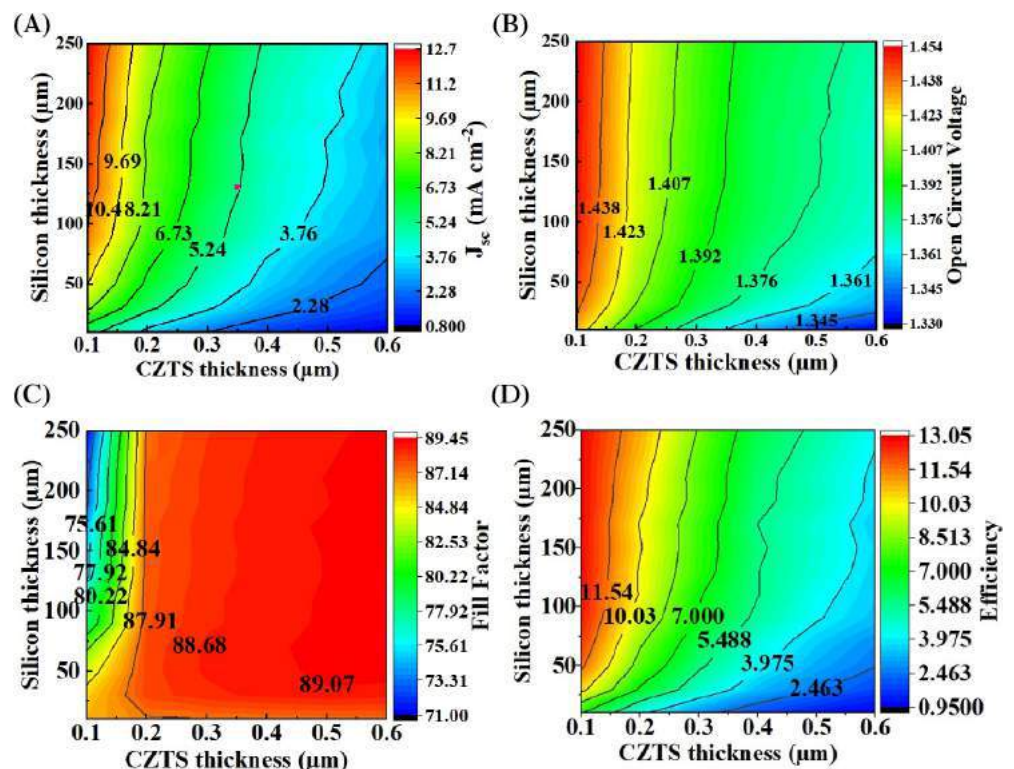


FIGURE 6 EQE of top and bottom cells in tandem configuration for varying thickness of a CZTS absorber [Colour figure can be viewed at wileyonlinelibrary.com]

reduction in the current losses with the improved current matching between the top and bottom cells. However, with the reduction in CZTS absorber thickness, the fill factor gradually decreases till CZTS thickness of 150 nm, and it drastically reduces beyond 150 nm as evident from Figure 7C owing to the fact that the fill factor reduces because the J-V curve is predominantly affected near the open circuit voltage with the increase in series resistance.⁴⁰ Therefore, considering all the solar cell parameters, the

FIGURE 7 Dependency of solar cell parameters on the thickness of both CZTS and Si absorber layers A, J_{sc} , B, V_{oc} , C, fill factor, and D, efficiency [Colour figure can be viewed at wileyonlinelibrary.com]



tandem configuration shows enhanced performance for CZTS thickness of 150 nm and silicon thickness of 250 μm .

3.4 | Minimize parasitic absorption

The steps used for mitigating the photon losses in of top and bottom modules are listed out sequentially in Table 3 and the corresponding photon absorption rate in Figure 8A. Figure 8B shows the magnified graph of the circled section of Figure 8A depicting the changes in the photon absorption profile for each case mentioned in Table 3. To reduce the parasitic absorption loss, the CdS buffer is replaced by ZnS, and the material parameters are listed in Table 1, and the absorption data are obtained from.⁴¹ ZnS possesses lower extinction coefficient (higher band gap) than CdS buffer, and the minority carrier mobility of ZnS is greater than CdS material, promoting the collection of minority carriers.²⁰ With the replacement of buffer layer in the top module, the photon losses are reduced (case “b” of Figure 8B), and the amount of photons reaching the CZTS absorber changes thereby influencing the current owing to which the current matching is disturbed. The thickness of CZTS layer is reduced to 100 nm (case “c” of Figure 8B) to obtain current matching with the bottom cell after the replacement of buffer layer. The optimized thickness of ZnS layer is considered as 30 nm¹⁶ for minimizing the photon losses, and the current density is increased (case “d” of Figure 8B). Further, to minimize the parasitic absorption,

TABLE 3 Top cell and bottom cell optimization design steps for minimizing photon losses due to parasitic absorption

Case	Design steps	Value	J_{sc} (mA cm ⁻²)	V_{oc} (V)	FF (%)	Eff (%)
a)	After band gap and thickness optimization		10.61	1.44	85.56	13.03
<i>Top cell optimization</i>						
b)	Replacement of CdS by ZnS buffer	-	8.98	1.44	88.20	11.44
c)	Optimized CZTS thickness	100 nm	11.17	1.46	86.37	14.10
d)	Optimized ZnS thickness	30 nm	13.15	1.47	85.15	16.42
e)	Optimized AZO thickness	300 nm	13.70	1.47	84.84	17.07
<i>Bottom cell optimization</i>						
f)	Removal of AZO layer		13.96	1.47	84.53	17.33
	Optimized ITO thickness	25 nm	15.26	1.47	82.44	18.52

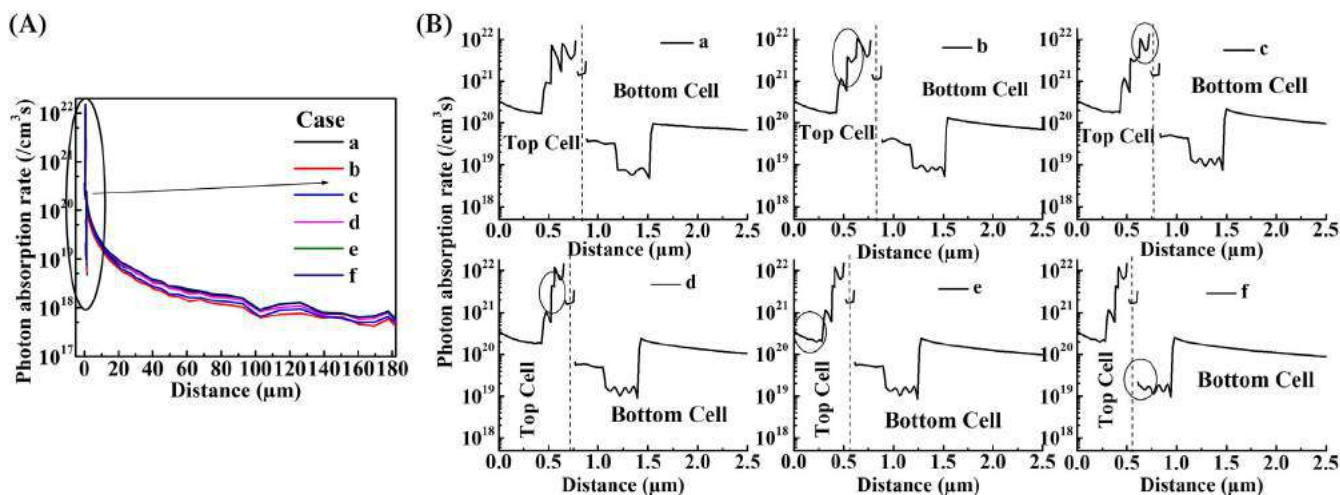


FIGURE 8 Photon absorption profile for various cases from “a” to “f” in Table 4; A, silicon region in bottom cell and B, changes in the photon absorption profile in the top and bottom cells are indicated by circle marks [Colour figure can be viewed at wileyonlinelibrary.com]

the window layer thickness is reduced slightly to 300 nm in case “e.” Owing to the presence of ITO layer which itself can act as a window layer for the bottom cell, the AZO window layer is eliminated from the design in case “f” resulting in more efficient absorption by top and bottom absorbers (case “e” and “f” of Figure 8B), and the current matching is not disturbed with an increase in current density.

From the spectral response in Figure 9, it is observed that the top module utilizes the spectrum more efficiently in the lower wavelength range from 400 nm to 520 nm with the replacement of ZnS buffer (case “b”). The above band gap absorption in CZTS absorber reduces and silicon increases in case “c” and “d” which is reflected in EQE graphs. The above band gap absorption increases for both CZTS and silicon absorbers and hence the increase in EQE for both top and bottom modules for cases “e” and “f,” minimizing the photon losses in the tandem device.

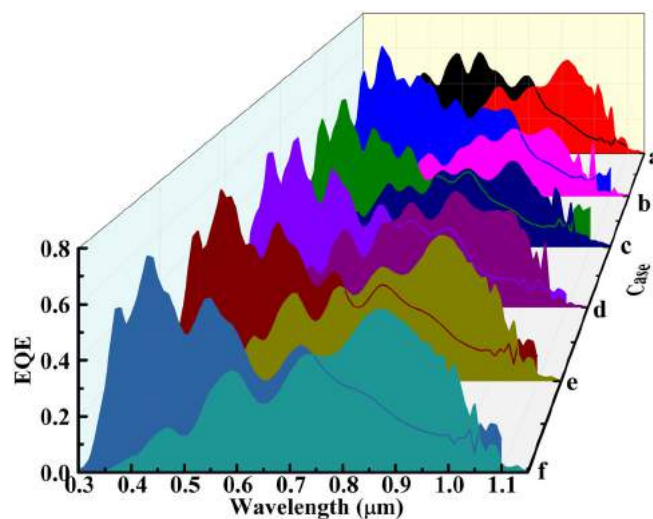
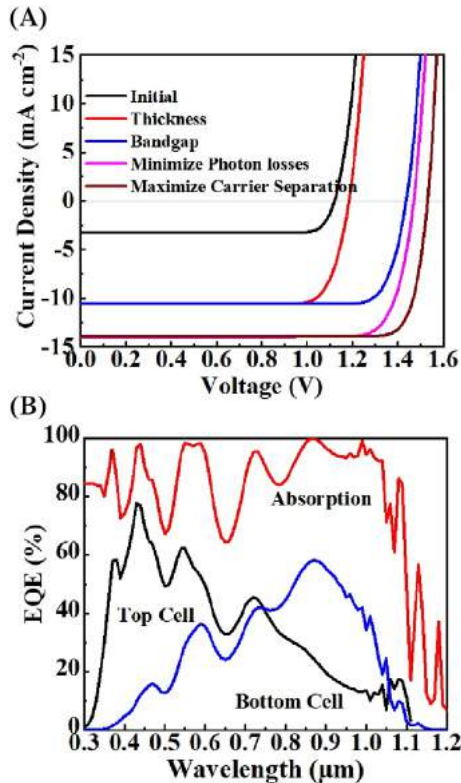


FIGURE 9 EQE graphs of top and bottom modules for minimizing parasitic absorption for different cases listed in Table 4 [Colour figure can be viewed at wileyonlinelibrary.com]

TABLE 4 Effect of solar cell parameters on the carrier concentration in top and bottom cells

Material parameters	Values	J_{sc} (mA cm ⁻²)	V_{oc} (V)	FF (%)	η (%)
CZTS acceptor concentration	10 ¹⁶ cm ⁻³	15.26	1.47	83.80	18.75
MgZnO donor concentration	10 ¹⁹ cm ⁻³	15.23	1.51	84.53	19.48
CZTS deep states	10 ¹⁶	15.23	1.53	86.41	20.17

**FIGURE 10** A, J-V curves for the various levels of optimization and B, EQE and Absorption graphs of the optimized device [Colour figure can be viewed at wileyonlinelibrary.com]

3.5 | Device optimization through modeling improvements

The efficiency can be further enhanced by minimizing the recombination losses in top cell and improving the electric field strength in bottom cell as follows. CZTS acceptor density may vary from 10¹⁶ to 10¹⁷ cm⁻³, and the optimized CZTS concentration is found to be 10¹⁶ cm⁻³. The optimal achievable value of CZTS deep states is found to be 10¹⁶ cm⁻³/eV. The top cell is optimized for acceptor density and deep states in the CZTS absorber. The optimized concentration of Mg-doped ZnO material for Si/MgZnO design is 10¹⁹ cm⁻³.¹⁹ Hence, the bottom cell is optimized for MgZnO concentration, and favorable performance is observed in terms of V_{oc} and FF values owing to the development of stronger field sweeping more carriers across the heterojunction. The solar cell parameters are

extracted, and efficiency has been increased to 20.17% as evident from Table 4 and Figure 10.


4 | CONCLUSION

The present work proposes a framework for the design and optimization of Si-CZTS tandem structure using an ATLAS simulator. The tandem structure initially yields very low efficiency of 3.18%. From the spectral analysis, the photon losses due to parasitic absorption in the front layers and the unequal absorption of light by top and bottom modules are identified as the major causes for the low efficiency, and the current is limited by the lowest among the currents in top and bottom modules. As most of the power is absorbed by the top cell, the thickness of CZTS absorber is reduced and bottom absorber is increased and current matching is obtained for optimized thickness values of 150 nm and 250 nm thicknesses, respectively. The parasitic absorption is minimized in the lower wavelength region by the replacement of CdS buffer by ZnS buffer, and the overall absorption is increased through careful optimization of window and buffer layers. The optimum thickness of AZO, ZnS buffer, and CZTS absorber is found to be 300 nm, 30 nm, and 100 nm for minimizing the photon and current losses and obtain current matching. Upon optimizing other material parameters such as CZTS acceptor density, deep defect states, and MgZnO donor concentration within experimentally achievable values, maximum attainable efficiency of 20.17% is obtained. The efficiency can be enhanced further by employing four-terminal configurations which eliminates the need for current matching resulting in the improvement of short circuit current density and hence the efficiency of the tandem solar cell.

DATA AVAILABILITY STATEMENT

The data that support the findings of this study are available from the corresponding author upon reasonable request.

ORCID

Vallisree Sivathanu  <https://orcid.org/0000-0002-2170-9612>

REFERENCES

- Blanker AJ, Berendsen P, Phung N, Vroon ZEAP, Zeman M, Smets AHM. Advanced light management techniques for two-terminal hybrid tandem solar cells. *Sol Energy Mater Sol Cells*. 2018;181:77-82. <https://doi.org/10.1016/j.solmat.2018.02.017>.
- Zhou C, Chung H, Wang X, Bermel P. Design of CdZnTe and crystalline silicon tandem junction solar cells. *IEEE J Photovolt*. 2016;6(1):301-308. <https://doi.org/10.1109/JPHOTOV.2015.2481598>.
- Enam FMT, Rahman KS, Kamaruzzaman MI, et al. Design prospects of cadmium telluride/silicon (CdTe/Si) tandem solar cells from numerical simulation. *Optik (Stuttg)*. 2017;139:397-406. <https://doi.org/10.1016/j.ijleo.2017.03.106>.
- Ferhati H, Djefal F. An efficient analytical model for tandem solar cells. *Mater Res Express*. 2019;6(7):076424. <https://doi.org/10.1088/2053-1591/ab1596>.
- Bin Qasim U, Imran H, Kamran M, Faryad M, Butt NZ. Computational study of stack/terminal topologies for perovskite based bifacial tandem solar cells. *Sol Energy*. 2020;203:1-9. <https://doi.org/10.1016/j.solener.2020.03.078>.
- Cherif FE, Sammouda H. Strategies for high performance perovskite/c-Si tandem solar cells: effects of bandgap engineering, solar concentration and device temperature. *Opt Mater (Amst)*. 2020;106:109935. <https://doi.org/10.1016/j.optmat.2020.109935>.
- Ferhati H, Djefal F, Drissi BL. Performance improvement of Perovskite/CZTS tandem solar cell using low-cost ZnS/Ag/ITO multilayer spectrum splitter. *Superlattice Microst*. 2020;148:106727. <https://doi.org/10.1016/j.spmi.2020.106727>.
- Al-Ashouri A, Köhnen E, Li B. Monolithic perovskite/silicon tandem solar cell with >29% efficiency by enhanced hole extraction. *Science*. 2020;370(6522):1300-1309. <https://doi.org/10.1126/science.abd4016>.
- Zhao D, Chen C, Wang C, et al. Efficient two-terminal all-perovskite tandem solar cells enabled by high-quality low-bandgap absorber layers. *Nat Energy*. 2018;3(12):1093-1100. <https://doi.org/10.1038/s41560-018-0278-x>.
- Zhao D, Ding L. All-perovskite tandem structures shed light on thin-film photovoltaics. *Sci Bull*. 2020;65(14):1144-1146. <https://doi.org/10.1016/j.scib.2020.04.013>.
- Mailoa JP, Bailie CD, Johlin EC, et al. A 2-terminal perovskite/silicon multijunction solar cell enabled by a silicon tunnel junction. *Appl Phys Lett*. 2015;106(12):121105. <https://doi.org/10.1063/1.4914179>.
- Dhakal TP, Peng CY, Reid Tobias R, Dasharathy R, Westgate CR. Characterization of a CZTS thin film solar cell grown by sputtering method. *Sol Energy*. 2014;100:23-30. <https://doi.org/10.1016/j.solener.2013.11.035>.
- Tang D, Wang Q, Liu F, et al. An alternative route towards low-cost Cu₂ZnSnS₄ thin film solar cells. *Surf Coat Technol*. 2013;232:53-59. <https://doi.org/10.1016/j.surfcoat.2013.04.052>.
- Vallisree S, Sharma A, Thangavel R, Lenka TR. Investigations of carrier transport mechanism and junction formation in Si/CZTS dual absorber solar cell technology. *Appl Phys A Mater Sci Process*. 2020;126:163. <https://doi.org/10.1007/s00339-020-3343-9>.
- Silvaco Inc. Atlas User's Manual - Device Simulation Software. 2010.
- Vallisree S, Thangavel R, Lenka TR. Theoretical investigations on enhancement of photovoltaic efficiency of nanostructured CZTS/ZnS/ZnO based solar cell device. *J Mater Sci Mater Electron*. 2018;29(9):7262-7272. <https://doi.org/10.1007/s10854-018-8715-y>.
- Shin B, Gunawan O, Zhu Y, Bojarczuk NA, Chey SJ, Guha S. Thin film solar cell with 8.4% power conversion efficiency using an earth-abundant Cu₂ZnSnS₄ absorber. *Prog Photovolt Res Appl*. 2013;21(1):72-76. <https://doi.org/10.1002/pip.1174>.
- Pietruszka R, Witkowski BS, Zielony E, Gwozdz K, Placzek-Popko E, Godlewski M. ZnO/Si heterojunction solar cell fabricated by atomic layer deposition and hydrothermal methods. *Sol Energy*. 2017;155:1282-1288. <https://doi.org/10.1016/j.solener.2017.07.071>.
- Vallisree S, Thangavel R, Lenka TR. 2018. Modelling, simulation, optimization of Si/ZnO and Si/ZnMgO heterojunction solar cells. *iopscience.iop.org*. [Online]. Available: <https://iopscience.iop.org/article/10.1088/2053-1591/aaf023/meta>.
- Saha U, Alam MK. Proposition and computational analysis of a kesterite/kesterite tandem solar cell with enhanced efficiency. *RSC Adv*. 2017;7(8):4806-4814. <https://doi.org/10.1039/C6RA25704F>.
- Fahrner WR. Amorphous Silicon / Crystalline Silicon Heterojunction Solar Cells. 2013, pp. 1-97.
- Courel M, Andrade-Arvizu JA, Vigil-Galán O. The role of buffer/kesterite interface recombination and minority carrier lifetime on kesterite thin film solar cells. *Mater Res Express*. 2016;3(9):1-14. <https://doi.org/10.1088/2053-1591/3/9/095501>.
- ElAnzeery H, el Daif O, Buffière M, et al. Refractive index extraction and thickness optimization of Cu₂ZnSnSe₄ thin film solar cells. *Phys Status Solidi Appl Mater Sci*. 2015;212(9):1984-1990. <https://doi.org/10.1002/pssa.201431807>.
- Sivathanu V, Rajalingam T, Lenka TR. Modelling of CZTS/ZnS/AZO solar cell for efficiency enhancement. *IEEE Xplore*. 2018, pp. 1-2, doi: <https://doi.org/10.1109/ICMAP.2018.8354643>.
- Knutsen KE, Schifano R, Marstein ES, Svensson BG, Kuznetsov AY. Prediction of high efficiency ZnMgO/Si solar cells suppressing carrier recombination by conduction band engineering. *Phys Status Solidi Appl Mater Sci*. 2013;210(3):585-588. <https://doi.org/10.1002/pssa.201228527>.
- Layek A, Manna B, Chowdhury A. Carrier recombination dynamics through defect states of ZnO nanocrystals: from nanoparticles to nanorods. *Chem Phys Lett*. 2012;539-540:133-138. <https://doi.org/10.1016/j.cplett.2012.05.028>.
- Adachi S. *Earth-Abundant Materials for Solar Cells Cu₂-II-IV-VI₂ Semiconductors*. Chichester, England: Wiley; 2015.
- Green MA. Self-consistent optical parameters of intrinsic silicon at 300 K including temperature coefficients. *Sol Energy Mater Sol Cells*. 2008;92(11):1305-1310. <https://doi.org/10.1016/j.solmat.2008.06.009>.
- Yang S, Liu Y, Zhang Y, Mo D. Spectroscopic ellipsometry studies of mg-doped ZnO thin films prepared by the sol-gel method. *Phys Status Solidi Appl Mater Sci*. 2009;206(7):1488-1493. <https://doi.org/10.1002/pssa.200824481>.
- Lisco F, Kaminski PM, Abbas A, et al. The structural properties of CdS deposited by chemical bath deposition and pulsed direct current magnetron sputtering. *Thin Solid Films*. 2015;582:323-327. <https://doi.org/10.1016/j.tsf.2014.11.062>.
- Wang X, Saito K, Tanaka T, et al. Energy band bowing parameter in MgZnO alloys. *Appl Phys Lett*. 2015;107(2):022111. <https://doi.org/10.1063/1.4926980>.

32. Todorov T, Gershon T, Gunawan O, Sturdevant C, Guha S. Perovskite-kesterite monolithic tandem solar cells with high open-circuit voltage. *Appl Phys Lett*. 2014;105(17):173902. <https://doi.org/10.1063/1.4899275>.
33. Sopra SA. Optical Data from Sopra SA. <http://www.spectra.com/sopra.html>.
34. Ge J, Chu J, Jiang J, Yan Y, Yang P. Characteristics of in-substituted CZTS thin film and bifacial solar cell. *ACS Appl Mater Interfaces*. 2014;6(23):21118–21130. <https://doi.org/10.1021/am505980n>.
35. Rezaie MN, Manavizadeh N, Abadi EMN, Nadimi E, Boroumand FA. Comparison study of transparent RF-sputtered ITO/AZO and ITO/ZnO bilayers for near UV-OLED applications. *Appl Surf Sci*. 2017;392:549–556. <https://doi.org/10.1016/j.apsusc.2016.09.080>.
36. Malerba C, Biccari F, Azanza Ricardo CL, et al. CZTS stoichiometry effects on the band gap energy. *J Alloys Compd*. 2014; 582:528–534. <https://doi.org/10.1016/j.jallcom.2013.07.199>.
37. Redinger A, Unold T. High surface recombination velocity limits quasi-Fermi level splitting in kesterite absorbers. *Sci Rep*. 2018;8(1):1–9. <https://doi.org/10.1038/s41598-018-19798-w>.
38. Bauer GH, Brüggemann R, Tardon S, Vignoli S, Kniese R. Quasi-Fermi level splitting and identification of recombination losses from room temperature luminescence in $\text{Cu}(\text{In}_{1-x}\text{Ga}_x)\text{Se}_2$ thin films versus optical band gap. *Thin Solid Films*. 2005; 480–481:410–414. <https://doi.org/10.1016/j.tsf.2004.11.061>.
39. Green MA. Solar cell fill factors: general graph and empirical expressions. *Solid State Electron*. 1981;24(8):788–789. [https://doi.org/10.1016/0038-1101\(81\)90062-9](https://doi.org/10.1016/0038-1101(81)90062-9).
40. Boccard M, Ballif C. Influence of the subcell properties on the fill factor of two-terminal Perovskite-silicon tandem solar cells. *ACS Energy Lett*. 2020;5(4):1077–1082. <https://doi.org/10.1021/acseenergylett.0c00156>.
41. Cheng J, Fan D, Wang H, Liu B, Zhang Y, Yan H. Chemical bath deposition of crystalline ZnS thin films. *Semicond Sci Technol*. 2003;18(7):676–679. <https://doi.org/10.1088/0268-1242/18/7/313>.

How to cite this article: Sivathanu V, R T, Lenka TR. Modeling and performance optimization of two-terminal $\text{Cu}_2\text{ZnSnS}_4$ -silicon tandem solar cells. *Int J Energy Res*. 2021;1–11. <https://doi.org/10.1002/er.6540>



AUTOMATIC IDENTIFICATION OF BRAIN TUMOUR USING MATLAB BY FUZZYC MEANS CLUSTERING

B. Ramu

Assistant Professor, Geethanjali College of Engineering and Technology, Hyderabad India

M. Anand

Assistant Professor, Geethanjali College of Engineering and Technology, Hyderabad India

V. Praneeth

Student, Geethanjali College of Engineering and Technology, Hyderabad India

S. Shreedha

Student, Geethanjali College of Engineering and Technology, Hyderabad India

ABSTRACT

Image process is one in the entire foremost tough and discontinuous inflicting strange emotions and behaviour and distinguished field within the gift day. This paper describes the additionally loss of consciousness.

propounded strategy to sight & extract from the pictures of the Magnetic Resonance Imaging (MRI) could be a sophisticated brain. This technique adopts some noise removal provision, medical imaging technique accustomed turn out top of the range segmentation and morphological tasks that are the basic ideas of pictures of the components contained inside the body magnetic image process. Detection and extraction of tumour type magnetic resonance imaging is typically used once treating brain tumours, resonance imaging pictures of the brain is finished by the MATLAB ankle, and foot. From these high-resolution pictures, we are code.

Automatic defects detection in MR images is extremely important in many diagnostic and therapeutic applications. Due to high quantity data in MR images and blurred boundaries, tumour segmentation and categorization is enormously tough. These efforts have introduced one mechanical brain tumor detection method to expand the accurateness and give way and decrease the diagnosis time. The ambition be classify the tissues to 3 module of normal, begin and malignant. . In MR images, the quantity of knowledge is just too much for manual interpretation and analysis. Throughout precedent few years, brain tumour segmentation in resonance imaging (MRI) has turn out to be an rising research area within the field of medical imaging system. Exact finding of size and site of brain tumour plays an significantrole within the diagnosis of

tumor. The diagnosis method consists of 4 stages, pre-processing of MR images, feature extraction, and classification. After histogram equalization of image, the features are extracted supported Dual-Tree Complex wavelet transformation (DTCWT). within the last stage, Back Propagation Neural Network (BPN) are employed to classify the traditional and abnormal brain. An efficient algorithm is proposed for tumor detection supported the Spatial Fuzzy C- Means Clustering.

Key words: C-means clustering, magnetic resonance imaging, segmentation, Tumor Detection.

Cite this Article: B. Ramu, M. Anand, V. Praneeth and S. Shreedha, Automatic Identification of Brain Tumour Using MATLAB by Fuzzy C means Clustering, *International Journal of Advanced Research in Engineering and Technology (IJARET)*, 12(2), 2021, pp. 652-656.

<http://iaeme.com/Home/issue/IJARET?Volume=12&Issue=2>

1. INTRODUCTION

The tumour is caused by abnormal growth of the tissue. brain tumour is that the excess fully grown tissue during which cells grow and multiply quicker on the face of it unmonitored by the mechanisms that management traditional cells.

Epilepsy could be a disorder occurring in brain which ends up in formation in clusters of nerve cells and signal abnormally. chemical science pulses generated by neurons act on neighbour neurons and muscles to provide thoughts, feelings and actions. During this quite disorder, the somatic cell activity is going to derive elaborated anatomical data to appear at human brain development and establish abnormalities.

Pre-processing of magnetic resonance imaging pictures is that the first step in image analysis that perform image sweetening and noise- reduction techniques that are accustomed enhance the image quality, then some morphological operations are applied to sight the neoplasm inside the image.

2. REQUIRED SOFTWARE TOOL(S)

2.1 Windows Operating System

Microsoft introduced an operating system environment named Windows on November 20, 1985, as a graphical operating system shell for MS-DOS in response to the growing interest in graphical user interfaces (GUIs). Microsoft Windows came to dominate the world's personal computer (PC) market with over 90% market share, overtaking Mac OS, which had been introduced in 1984. In 2015 Microsoft released MS 10, which comes by means of Crotona, a digital individual helper like Apple's Siri, and the Web browser Microsoft Edge, which replace Internet Explorer. Microsoft also announced that Windows 10 would be the previous edition of Windows, meaning that users would receive regular updates to the OS but that no more large-scale revisions would be completed.

2.2 MATLAB

Matlab is a more paradigm numerical computing environment and proprietary programming language developed by Math Works. MATLAB allow matrix manipulations, intrigues of functions plus data, completion of algorithms, formation of user interfaces, and interfacing by program on paper in other languages. As of 2020, MATLAB has more than 4 million users worldwide. MATLAB users come from various backgrounds of engineering, science, and economics.

3. PROPOSED METHODS

3.1 DWT for Segmentation

A. Steps to be followed:

Step A: Input MRI image

Step B: Convert it into greyscale Step C: noise removal

Step D: enhancement Step E: DWT

Step F: feature extraction

Step G: NN based classification Step H: Validation

4. PROCESS

4.1 Input Image

- Input: MRI image of brain
- Output: it is stored in array format in order to resize the image, because the image is of larger size, it required additional time used for segmentation and picture value is reduced. Therefore, the image can be re-sized to 256*256.

4.2 Preprocessing

- Input: stored input image
- Output: analyzed image
- The main purpose of pre-processing to analyze the image in different formats like conversions, resizing.

4.3 Median Filter

- Input: analyzed image
- Output: filtered image
- Then it improved the standard a picture. Close by no fall in contrast. We want it just for noised images and therefore the image once passed through this filter needn't be applied to the identical filter again.

4.4 Segmentation Process

- Input: filtered image
- Output: segmented image using DWT
- DWT used to identify the tumor in brain (MRI) and lung CT images. Here both algorithms are used to segmentation the tumor from brain plus lung images. The image can be segmented carefully and lastly obtain the image into segments.
- GLCM for feature extraction
- NN Network for classification
- Fuzzy clustering for tumour detection and structural

4.5 Feature Extraction

- Input: edge detected(segmented) image
- Output: estimating features of image

- The feature extraction may be a most important process in detection application plus classifications, the feature-based feature extraction goes on during in this effort, usually quite a few texture-based feature extraction classifications are readily on hand persons are GLCM.
- In features extracted are:
Tumour level, Intensity, Contrast, Entropy, Sensitivity, Correlation & Energy

5. CLASSIFICATION

- Input: trained dataset(features)
- Output: classified as normal or abnormal image
- Usually the categorization is employed to classify to the image is normal or abnormal. Neural Network is one form of classifier, the features and values of the tumour precious image and non-tumour image is already located in database, the strength is additionally having in tumour affected image, the classifier compares the given image within the database but the tumour is identified as compared the every pixels, it show the message box the tumour is affected, after completing the NN training.

6. RESULT

Input

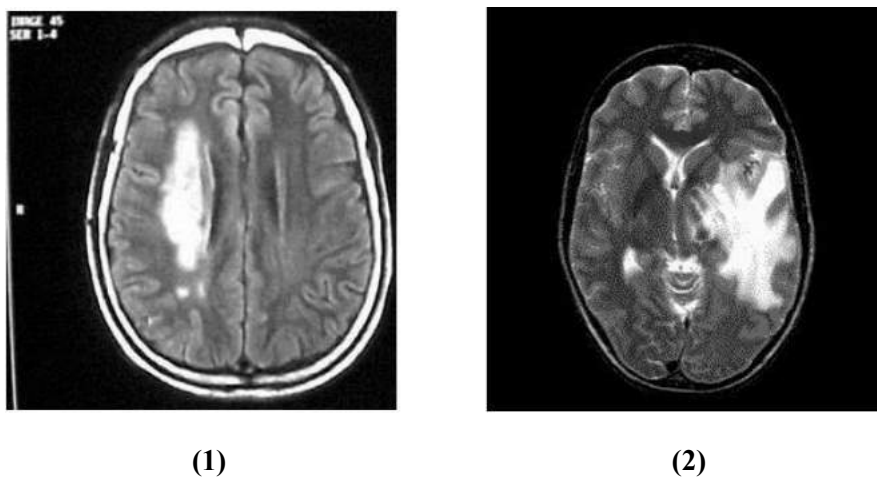


Figure 1

Output

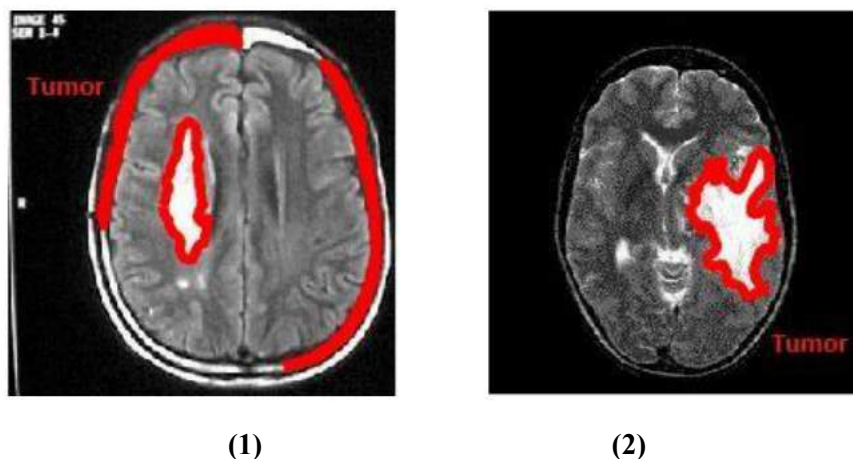


Figure 2

7. CONCLUSION

The project “Automatic Identification of Brain Tumour Using MATLAB by Fuzzy C means Clusterin” has been successfully designed and tested. It has been developed by integrating features of all the software used. Presence of every module has been reasoned out and placed carefully thus contributing to the best working of the unit

REFERENCES

- [1] Ardizzone.E, Pirrone.R, and Orazio.O.G, "Fuzzy C-Means Segmentation on Brain MR Slices Corrupted by RF-Inhomogeneity," In Proc. The 7th international workshop on Fuzzy Logic and Applications: Applications of Fuzzy Sets Theory, WILF '07, Springer- Verlag, pp: 378-384, 2007.
- [2] Bianrgi.P.M, Ashtiyani.M, and Asadi.S, "MRI Segmentation Using Fuzzy C- means Clustering Algorithm Basis Neural Network," In Proc. ICTT A 3rdInternationai Conference on Information and Communication Technologies: From Theory to Applications, pp: 1-5, 2008.
- [3] Sikka.K, Sinha.N, Singh.P.K, and "A fully automated algorithm under modified FCM framework for improved brain MR image segmentation," Magn. Reson. Imag, vol. 27, pp. 994-1004, Jul. 2009.
- [4] Xiao.K, Ho.S.H, and Bargiela.B, "Automatic Brain MRI Segmentation Scheme Based on Feature Weighting Factors Selection on Fuzzy C means Clustering Aigorithms with Gaussian Smoothing," International Journal of Computational Intelligence in Bioinformatics and Systems Biology1(3):316- 331,2009.3

AUTHORS PROFILE

B. Ramu, Assistant Professor, Geethnajali College of Engineering and Technology

M. Anand, Geethanjali College of Engineering and Technology

V Praneeth and S. Shreedha, Student, Geethanjali College of Engineering and Technology



DESIGN OF AN AREA EFFICIENT 16-BIT LOGARITHMIC MULTIPLIER

R. Odaiah

Associate Professor, Department of Electronics and Communication Engineering,
Geethanjali College of Engineering and Technology, Hyderabad, India

M. Krishna

Assistant Professor, Department of Electronics and Communication Engineering,
Geethanjali College of Engineering and Technology, Hyderabad, India

T. Sai Ganesh, A. Vineeth, M. Bhaskar Yadav

Department of Electronics and Communication Engineering,
Geethanjali College of Engineering and Technology, Hyderabad, India

ABSTRACT

Digital signal processing applications often use major mathematical operations such as multiplication, which consume more power and time. Operations like Fast Fourier Transform, Convolution and correlation depends heavily on a large number of multiplications. There are many techniques available to perform multiplications. One such technique is logarithmic multiplication. Logarithmic multiplication is achieved by adding the binary logarithms of two numbers and deriving the antilog of the result. In this paper, an efficient algorithm for logarithmic multiplication is presented with the use of adders, decoders, multiplexers and a few combinational circuits that effectively reduce the power and area of the multiplier.

Key words: Logarithmic number system, Digital Signal Processing, logarithmic multiplication, Verilog HDL, Multiplexer.

Cite this Article: R. Odaiah, M. Krishna, T. Sai Ganesh, A. Vineeth and M. Bhaskar Yadav, Design of an Area Efficient 16-bit Logarithmic Multiplier, *International Journal of Advanced Research in Engineering and Technology (IJARET)*, 12(2), 2021, pp. 743-748.

<http://iaeme.com/Home/issue/IJARET?Volume=12&Issue=2>

1. INTRODUCTION

Multipliers play an important role in today's digital signal processing and various other applications. With advances in technology, many researchers have tried and are trying to design multipliers which offer either of the following design targets– high speed, low power consumption, regularity of layout and hence less area or even combination of them in one

multiplier thus making them suitable for various high speed, low power and compact VLSI implementation. The common multiplication method is “add and shift” algorithm.

In order to reduce the error generated by the Logarithmic Number System, techniques such as iterative and non-iterative methods are used.

Mitchell algorithm (MA) is one of the non- iterative multiplication methods are used. In MA, $\log(1+m)$ is approximated as m to reduce the complexity of logarithms. Here m represents the mantissa of a number. But MA is proved to be generating nearly 11% error in the product as stated.

To overcome such errors, an iterative algorithm similar to Mitchell algorithm was proposed. In this method, the product is given by the sum of the approximate product and error. The error here refers to the residues that are discarded in the process. These residues are again fed into the algorithm and the products are added to get result with the least possible error. In our presented architecture, we optimized the performance of the algorithm by redesigning the shifter and leading one detector.

A Logarithmic number system is introduced to simplify multiplication, especially in cases when the accuracy requirements are not rigorous. As shown in figure 1. general blockdiagram of logarithmicnumber system. In LNS two operands are multiplied by finding their logarithms, adding them, and after that looking for the antilogarithm of the sum.

The logarithm of the product is: $\text{Log}_2(N1. N2) = K_1 + K_2 + \log_2(1+X_1) + \log_2(1+X_2)$

where K_1 and K_2 represents the places of the most significant operands’ bits with the value of ‘1’ For 16-bit numbers the range is from 0 to 15. The fractions X_1 and X_2 are in range(0,1).

2. LOGARITHMIC MULTIPLIER

In this section, Mitchell’s algorithm based logarithmic multiplier is explained. Mitchell’s Algorithm based Logarithmic multiplier is shown in fig 2

2.1 Steps

- Inputs $N1, N2$ are n -bit binary numbers to be multiplied, Output P_{approx} is product of that two numbers with $2n$ -bits.
- $N1, N2$ are taken as inputs to the Leading One Detectors (LODs), outputs of LODs will be 2^{x1} and 2^{x2} . Where $x1$ and $x2$ are the leading one positions of $N1$ and $N2$.
- With inputs as 2^{x1} and 2^{x2} , encoders calculate the values of $x1$ and $x2$.
- $(N1 - 2^{x1})$ and $(N2 - 2^{x2})$ are the outputs of the two XOR banks, where the operands and output of LODs are given as input.
- By using Barrel Shifters, $(N1 - 2^{x1})$ is left-shifted by $x2$ bits and $(N2 - 2^{x2})$ is left-shifted by $x1$ bits then the obtained result is $(N1 - 2^{x1})2^{x2}$ and $(N2 - 2^{x2})2^{x1}$.
- The above result is added using 32-bit adder to obtain the resultant sum as:
- $(N1 - 2^{x1})2^{x2} + (N2 - 2^{x2})2^{x1}$.
- The values of $x1$ and $x2$ obtained in step-3 are added and the result is given as an input to the Decoder which gives the output as 2^{x1+x2} .
- The results obtained in the step 6 and step 7 are added to give output as 2^{x1+x2}
- $+ (N1 - 2^{x1})2^{x2} + (N2 - 2^{x2})2^{x1}$.
- The outputs of XOR banks are taken as error operands and repeat the above same procedure, the accurate product can be achieved at some iteration.

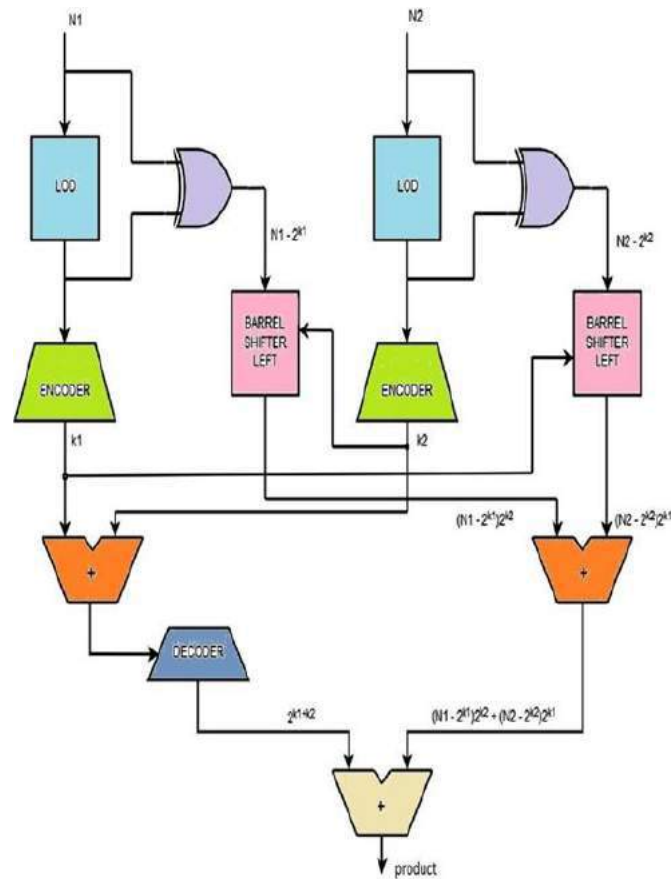


Figure 1 Mitchell's algorithm based logarithmic multiplier

3. BRAUN ARRAY MULTIPLIER

Array Multiplier is well known due to its regular structure as shown in the fig- 2b. Multiplier circuit is based on add and shift algorithm. Each partial product is generated by the multiplication of the multiplicand with one multiplier bit.

The partial product are shifted according to their bit orders and then added. The addition can be performed with normal carry propagate adder. N-1 adders are required where n is the multiplier length.

Although the method is simple as it can be seen from the below example shown in the fig 2a. Example of 4- bit multiplication. The addition is done serially as well as in parallel. To improve on the delay and area the CRAs are replaced with Carry Save Adders, in which every carry and sum signal is passed to the adders of the next stage. Final product is obtained in a final adder by any fast adder (usually carry ripple adder). In array multiplication we need to add, as many partial products as there are multiplier bits

Although the method is simple as it can be seen from the below example shown in the fig 2a. Example of 4- bit multiplication. The addition is done serially as well as in parallel. To improve on the delay and area the CRAs are replaced with Carry Save Adders, in which every carry and sum signal is passed to the adders of the next stage. Final product is obtained in a final adder by any fast adder (usually carry ripple adder). In array multiplication we need to add, as many partial products as there are multiplier bits.

Design of an Area Efficient 16-bit Logarithmic Multiplier

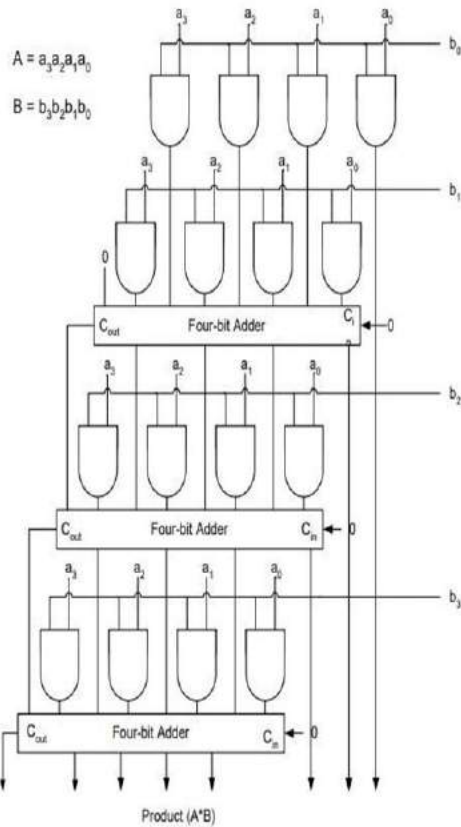


Figure 2a Example of 4bit multiplication

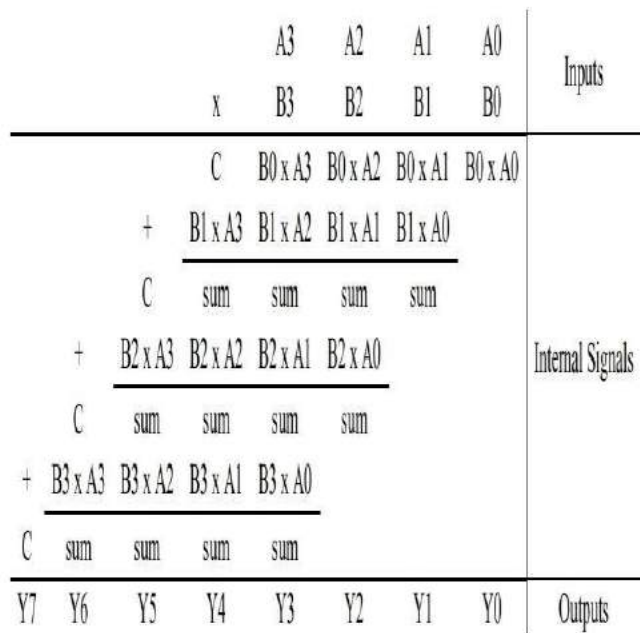


Figure 2b Structure of array multiplier

4. SIMULATION RESULTS

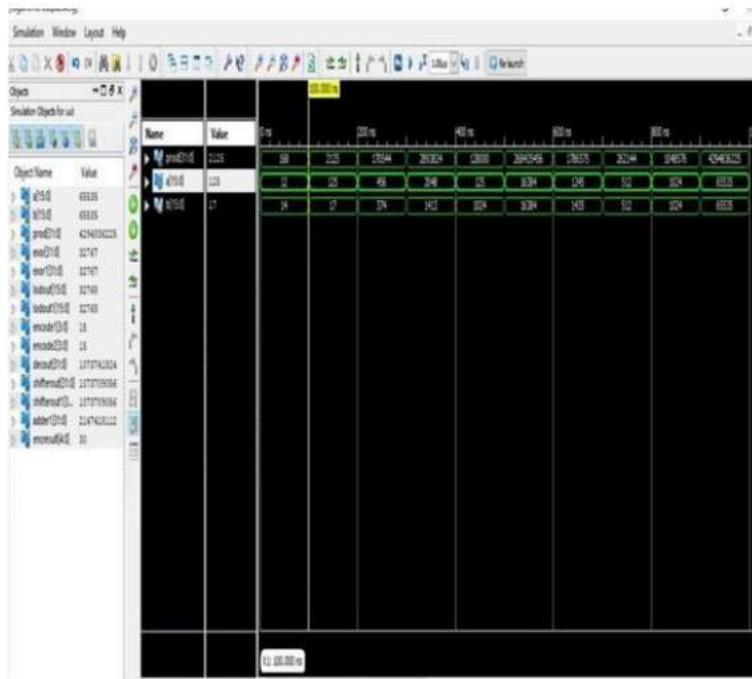


Figure 3 Logarithmic multiplier output

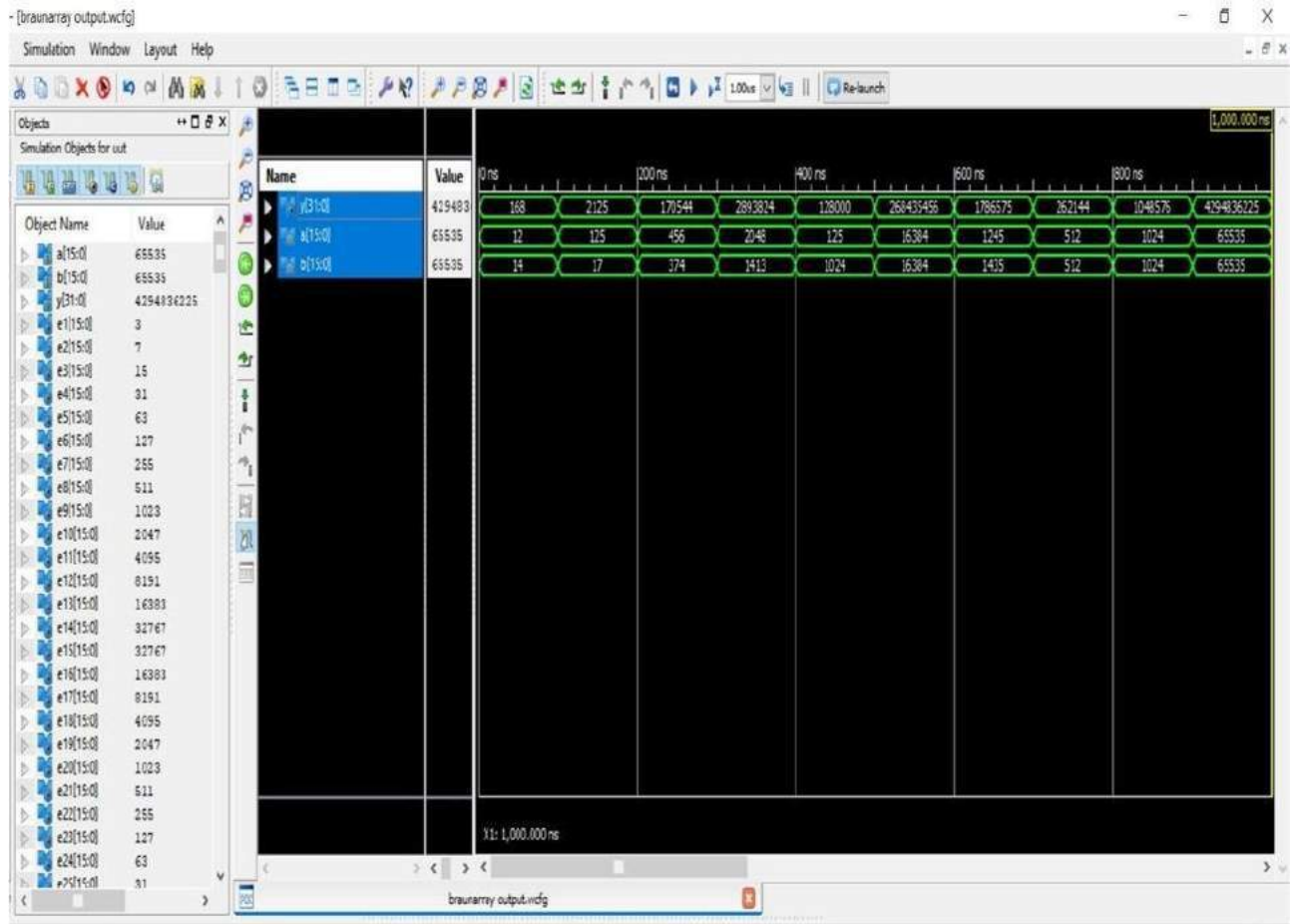


Figure 4 Braun array multiplier output

5. COMPARISON

Table 1

Parameter	Logarithmic multiplier	Braun array multiplier
Delay	24.637ns	417.779ns
Levels of logic	45	392
Total Gates count	2,773	23,313
AND gate count	1,636	12,398
OR gate count	381	4,612
NOT gate count	692	6,303
XOR Gate count	64	--

6. CONCLUSIONS

From the above parameters compared in the table comparison of various parameters, we can come to a conclusion that all factors like Delay, gate count and Levels of Logic are very less for the Logarithmic Multiplier designed using Mitchell’s algorithm than that of Braun Array Multiplier. Hence, the logarithmic multipliers can be used in the Signal processing applications so that the area can be reduced and more efficient output can be observed.

REFERENCES

- [1] Babić, Z., Avramović, A. and Bulić, P. (2011). "An iterative logarithmic multiplier", *Microprocessors and Microsystems*, 35(1), pp.23-33.
- [2] Weiqiang Liu, Danye Wang, Jiahua Xu, Chenghua Wang, Fabrizio Lombardi, and Paolo Montuschi. "Design and Evaluation of Approximate Logarithmic Multipliers for Low Power Error-Tolerant Applications", *IEEE Transactions on Circuits and Systems I: Regular Papers*, 65(9), pp.2856-2868.
- [3] Aleksej Avramovk, Zdenka babi, Patrido Bulic, "A simple pipelined logarithmic multiplier," 2010 IEEE International Conference on Computer Design, 2010.
- [4] S. Ahmed and M. Srinivas, "An Improved Logarithmic Multiplier for Media Processing", *Journal of Signal Processing Systems*, 2018. Available: 10.1007/s11265-018-1350-2.
- [5] R. K. Agrawal and H. M. Kittur, "ASIC based logarithmic multiplier using iterative pipelined architecture," 2013 IEEE Conference on Information And Communication Technologies, 2013.
- [6] Hoefflinger, F. Warkowski, and B. M. Selzer, "Digital logarithmic CMOS multiplier for very-high-speed signal processing," *Proceedings of the IEEE 1991 Custom Integrated Circuits Conference*.
- [7] Ch. Achuth Reddy, Alen Anurag Pandit, Dr. Gautam Narayan, "Design and Simulation of 16×16 bit Iterative Logarithmic Multiplier for Accurate Results," 2018 Second International Conference on Electronics, Communication and Aerospace Technology (ICECA), 2018.
- [8] Raymond E. Siferd, Khalid H. Abed, "VLSI Implementations of Low Power Leading-One Detector Circuits," *Proceedings of the IEEE SoutheastCon 2006*.

AUTOMATIC CLASSIFICATION OF MAMMOGRAMS USING 2D-DISCRETE WAVELET TRANSFORM AND FEATURE SELECTION METHODS

SPANDANA PARAMKUSHAM , GREESHMA KALSHAM

Department of Electronics and Communication
Geethanjali college of Engineering and Technology, Cheeryala, Hyderabad, Telangana, India
Email: spandana.ece@gcet.edu.in Email:greeshmakalsham@gmail.com

Abstract: Breast cancer is the most common cancer among women. The survival rate due to breast cancer increases if detected in early stages. In this paper, we proposed an efficient method to classify abnormal and normal mammograms. The method uses 2D-discrete wavelet transform (2D-DWT) to extract texture features and further different feature selection methods such as neighborhood component analysis and relief-f algorithms has been used to select significant features which contain qualitative information for classification of mammograms into normal and abnormal. The method was tested on mammogram images taken from Image retrieval for medical applications (IRMA) database. The proposed method was validated with different classifiers and achieved accuracy of 98%.

Keywords: *Breast Cancer, Mammogram, Feature Extraction, Feature Selection, Classification..*

1. INTRODUCTION

Breast Cancer is one of the second most common cancer among women. It affects almost 2.1 million in the world. Nearly 627,000 women have died due to breast cancer In 2018 [1]. Early detection of breast cancer is very important to increase survival rate. A vast research has been done in the field of image processing to detect breast cancer in early stages.

Digital mammography is an efficient screening tool that is used to detect breast cancer. Radiologists diagnose breast cancer in early stages by looking into abnormalities such as masses and microcalcifications in the mammogram. Masses and fibroglandular tissue are adjacent and have high density hence, it is very difficult to identify shape of the mass. In order, to detect abnormalities in breast radiologists go for computer aided diagnosis (CAD) system. CAD utilizes several image processing and machine learning techniques. Feature extraction is a prominent step in CAD system, to identify the prominent features from image. In this work, features are extracted using multiresolution analysis which is based on 2D-discrete wavelet transform (DWT) and feature selection methods. Feature selection method is used to select important features from the DWT features. In this context, several methods have been proposed to classify mammograms into normal and abnormal. Adaptive orthogonal transformation was proposed to classify masses into benign and malignant in mammogram images [2]. Fractal texture analysis and fast correlation based filter are used for feature extraction and feature selection to classify mammograms into normal and abnormal [3]. 2D-DWT and statistical features are utilized for classification of abnormalities [4]. Spherical wavelet transform is applied to extract features for distinguishing normal, benign and malignant mammograms in [5]. Transfer learning technique [6] is applied for automatic classification of breast masses. Local binary pattern and local ternary pattern [7] methods are used to extract features from mammograms. 2D-DWT [8] is applied on mammograms for segmentation and classification of mammograms,

From the above literature, we can observe that many feature extraction methods were proposed to obtain information from mammograms. However, the extracted features are huge in number due to which the computational complexity and time taken increases to classify mammograms. Hence, it is very much important to propose efficient method to extract features and select significant features to increase the classifier performance for normal and abnormal classification. In this paper features are extracted using multi resolution analysis based on 2D-DWT from regions of interest (ROIs) of mammograms. Further, neighborhood component analysis and Relief-f algorithms has been used to select important features from feature vector obtained from 2D-DWT. Figure.3 shows block diagram of the proposed model.

2. METHODOLOGY

2.1 Data Sets

Our proposed method is evaluated by considering ROIs taken from IRMA database. It consists of normal, benign and malignant mammogram ROIs. The proposed method is tested on 58ROIs out of which 29 are normal and 29 are

abnormal mammogram ROIs.

2.2 Preprocessing

Mammogram requires initial pre-processing to remove noise. In this work, Contrast Limited Adaptive Histogram Equalization (CLAHE) method is used for removal of noise from ROIs. The objective of histogram equalization (HE) is to enhance the global contrast of the original image with uniform histogram. Histogram of the digital image of size M*N with intensity values in the range 0 to L-1 is given by the equation (1)

$$h(r_k) = n_k \tag{1}$$

Where r_k is the k^{th} intensity value and n_k is the number of pixels in the image with intensity r_k [9]. A normalized histogram is given by equation (2)

$$p_r(r_k) = \frac{n_k}{MN} \quad k = 0,1,2,3 \dots L - 1 \tag{2}$$

The histogram equalization is obtained by the following equation (3)

$$s_k = (L - 1) \sum_{j=0}^k p_r(r_j) \quad k = 0,1,2, \dots \dots L - 1 \tag{3}$$

where s_k is the cumulative distribution function (CDF). Histogram equalization method cannot resolve the problem of global change in pixel values when the grayscale distribution is highly localized. Hence, Adaptive histogram equalization (AHE) method was derived by transforming each pixel with a transformation function derived from neighborhood. Contrast Limited Adaptive Histogram Equalization (CLAHE) was proposed to overcome the problem of noise amplification in AHE. In CLAHE, the histogram is clipped by a predefined factor known as clip limit before computing CDF in the neighborhood region of the pixel. This clip limit depends on the normalized histogram and size of the neighborhood region and it is given in equation (4).

$$\beta = \frac{MN}{L} (1 + \frac{\alpha}{100} (s_{max} - 1)) \tag{4}$$

Where α is a clip factor (ranges from 0 to 1) and s_{max} is the max slope. Finally, CDF of the resultant histograms of all blocks is obtained for mapping pixel values. Figures. 1a&b shows original ROI and preprocessed ROI of mammogram. Figures 2a &b shows histograms of original and preprocessed ROI.

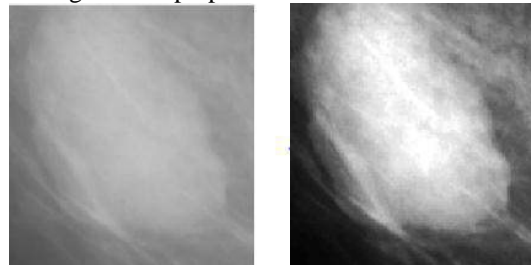


Fig 1a) Original Image b) Pre-processed Image

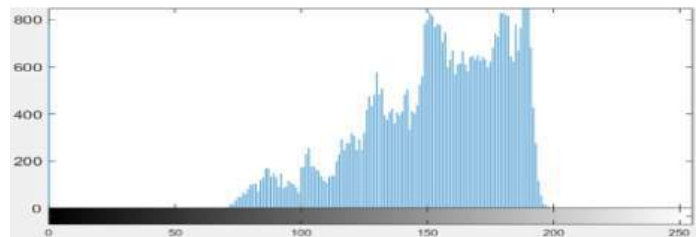
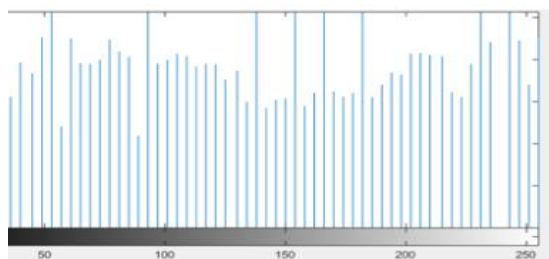


Fig.2. a) Histogram of ROI



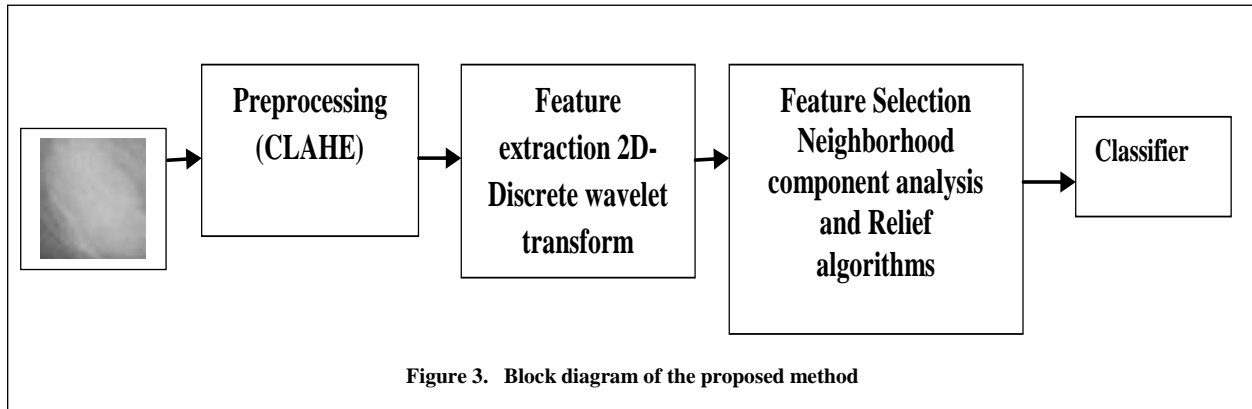


Figure 3. Block diagram of the proposed method

2.3 Multiresolution analysis using 2D wavelets for feature extraction

The decomposition of mammographic images was done using two-dimensional discrete wavelet transform (2D-DWT). The result gives two types of coefficients: approximation coefficients and detail coefficients [10]. Approximation coefficients are obtained by low pass filtering the image followed by down sampling. Detail coefficients are obtained by high pass filtering the image followed by down sampling. The resolution of images varies with each decomposition level. The resolution decreases with the increase in a number of decomposition levels. DWT decomposes mammogram into LL, LH, HL and HH components. This property of wavelet helps to extract edges, noise and separate bright and low contrast regions from a mammogram. This region gives texture information and highlights important details of image. The wavelet coefficients are extracted from all components to form a feature vector for each ROI. Further, subset of this feature vector is selected as significant feature vector using feature selection process discussed in next section

2.4 Feature Selection

Feature Selection plays key role in many pattern recognition problems such as image classification. Too many features do not always lead to a better classification performance [11]. Feature selection process selects a compact and relevant reduced feature subset to improve accuracy and decrease time. Two algorithms have been proposed for feature selection. One is neighborhood component analysis and other is relief-f. Brief explanation of these algorithms is given in next section

2.4.1 NCA Feature Selection

Neighborhood component analysis estimates weight vector w such that it helps to select optimized feature set from high dimensional feature vector using nearest neighborhood classification. Training samples $T= \{ (x_1,y_1), (x_2,y_2), \dots, (x_N, y_N) \}$ are considered to compute weight vector. In order to compute weight vector the distance between two samples is calculated and it is given by

$$D_w(x_i, y_j) = \sum_{l=1}^d w_l^2 |x_{il} - x_{jl}|.$$

where w_l is weight of l^{th} vector

The weight vector w is calculated using gradient descent approach. Based on the values of weights to each features, optimized features are selected and given to classifier for further validation

2.4.2 Relief-F Algorithm

Relief-F [12] is a simple yet efficient procedure to estimate the quality of feature in problems with strong dependencies between attributes. In practice, relief-f is usually applied in data pre-processing for selecting a feature subset. The key idea of the relief-f is to estimate the quality of feature according to how well their values distinguish between instances that are near to each other. Relief-F algorithm randomly selects an instance R_i from its class, and then searches for K of its nearest neighbors from the same class, called nearest hits H , and also K nearest neighbors from each of the different classes, namely nearest misses M . Then it updates the quality measure W_i for feature i according to values for R_i , hits H and misses M . If instance R_i and those in H have different quality estimation on feature i , then the estimation W_i is decreased. Meanwhile, if instance R_i and those in M have different values on feature i , the estimation W_i will be increased. The process is repeated n times. Here, n is usually set by users and for

most purposes it can be safely set to 10. According to the mentioned discussion, the quality measure W_i can be updated as follows:

$$W_i = W_i \frac{\sum_{k=1}^k D_H(k)}{n.k} + \sum_{c=1}^{c-1} p_c \cdot \frac{\sum_{k=1}^k D_M(k)}{n.k} \dots\dots\dots (13)$$

where $D_H(k)$ (or $D_M(k)$) is the sum of distance between the selected instance and its k th nearest neighbor in H (or M), p_c is the prior probability of class c .

2.5 Classification

Image classification is a necessary step in pattern recognition, the efficiency and accuracy mainly depends on the classification. Classification performance can be measured by evaluation parameter such as accuracy, sensitivity and specificity. To test our method we have used different classifiers to find accuracy, sensitivity and specificity of our proposed method. These evaluation parameters can be calculated by using following parameters

True positives (TP) are cases in which we predicted yes (they have the disease), and they do have the disease.

True negatives (TN) are the cases we predicted no, and they don't have the disease.

False positives (FP) are the cases we predicted yes, but they don't actually have the disease.

False negatives (FN) are the cases we predicted no, but they actually do have the disease

$$\text{Accuracy} = \frac{TP+TN}{TP+TN+FP+FN}$$

$$\text{Sensitivity} = \frac{TP}{TP+FN}$$

$$\text{Specificity} = \frac{TN}{TN+FP}$$

3 EXPERIMENT RESULTS

Our proposed method was tested on 58 ROIs. In these ROIs, 29 are normal and other 29 are abnormal ROIs. The results are simulated using MATLAB 2018a. The images are of size 128X128 spatial resolution. The proposed scheme utilizes 2D-DWT for extraction of features from image and neighborhood component analysis and Relief algorithms for selecting significant feature vector. To evaluate our optimized feature vector, it is given to classifier. In this method, support vector machine(SVM), K-nearest neighborhood (KNN), Fine tree and linear discriminant classifiers [13] was used to distinguish normal and abnormal mammograms. For classification, ten-fold cross validation technique was used for different classifiers. Table.1 gives the length of feature vector before and after feature selection.

Table.1. Number of features before and after feature selection

	2D-DWT	NCA	Relief-F
Number of features	4226	124	51

The number of features obtained using 2D-DWT is 4226 but after feature selection it got reduced to 124 or 51 feature as shown in Table.1. The classification performance obtained before feature selection process is shown in Table.2. From the table.2 we can observe that SVM and linear discriminant classifier obtained highest accuracy of 94.8%, sensitivity of 89.6% and specificity of 100%.

Table .2. Evaluation Parameters Using 2D-DWT features

Classifier	Accuracy	Sensitivity	Specificity
Linear SVM	94.8%	89.6%	100%
Cosine KNN	86.2%	72.4%	100%
Fine Tree	86.2%	86.2%	86.2%
Linear Discriminant	94.8%	89.6%	100%

Further, the subset of features is selected from 2D-DWT features using NCA and Relief-F algorithms. This subset of features is given to classifiers for validation of proposed method. Table.2 gives comparison of accuracy, sensitivity and specificity using different feature selection methods. Among all the classifiers, Fine tree classifier gave accuracy

of 98.6%, sensitivity of 97.6% and specificity of 95.2% using Relief-F feature selection algorithm. From Table.3 we can conclude that feature selection process does not affect the performance of the classifier.

Table.3. Calculation of Parameters Using 2D-DWT+Feature Selection

Classifier		Accuracy	Sensitivity	Specificity
Linear SVM	dwt+NCA	89.7%	89.6%	89.6%
	dwt+relief-f	94.8%	89.6%	100%
Cosine KNN	dwt+NCA	91.4%	89.6%	93.1%
	dwt+relief-f	89.7%	79.3%	100%
Fine Tree	dwt+NCA	89.7%	89.6%	89.6%
	dwt+relief-f	98%	97.6%	95.2%
Linear Discriminant	dwt+NCA	87.9%	96.5%	79.3%
	dwt+relief-f	94.8%	89.6%	100%

Table.4. Classification Time Comparison Table For Different Approaches

Classifier	Time taken for dwt	Time taken for NCA	Time taken for Relief-F
Linear SVM	23.6sec	0.74sec	5.3sec
Cosine KNN	15.3sec	0.78sec	2.58sec
Fine Tree	8.5sec	0.90sec	2.30sec
Linear Discriminant	20.6sec	0.77sec	3.16sec

4 CONCLUSION

In this paper, a scheme is proposed to delineate the normal or abnormal regions in mammogram. Our method extracts features using 2D-DWT from the mammograms. Further, these abnormal features are given to feature selection methods such as Relief-F and NCA to get more efficient features from 2D-DWT features. The feature subset is given to different classifiers to validate performance of our proposed scheme. The proposed method achieved highest accuracy of 98% with computation time less than 1sec with linear discriminant classifier and Relief-F method. The proposed scheme achieved better performance and less computation time with combination of feature selection and feature extraction approaches.

REFERENCES

[1] <https://www.who.int/cancer/prevention/diagnosis-screening/breast-cancer/en/>

[2] El Fahssi, Khalid, et al. "Novel approach to classification of Abnormalities in the mammogram image." *International Journal Of Biology And Biomedical Engineering* vol 10 (2016).

[3]. Beura, Shradhananda, BanshidharMajhi, and Ratnakar Dash. "Automatic characterization of mammograms using fractal texture analysis and fast correlation based filter method." *Proceedings of the 2nd International Conference on Perception and Machine Intelligence*. 2015.

[4]. Reyad, Yasser A., Mohamed A. Berbar, and Muhammad Hussain. "Comparison of statistical, LBP, and multi-resolution analysis features for breast mass classification." *Journal of medical systems* 38.9 (2014): 100.

[5] Patel, BhagwatiCharan, and G. R. Sinha. "Abnormality detection and classification in computer-aided diagnosis (CAD) of breast cancer images." *Journal of Medical Imaging and Health Informatics* 4.6 (2014): 881-885.

[6] Jiang, Fan, Hui Liu, Shaode Yu, and YaoqinXie. "Breast mass lesion classification in mammograms by transfer learning." *In Proceedings of the 5th international conference on bioinformatics and computational biology*, pp. 59-62. 2017.

[7] Paramkusham, Spandana, K. M. M. Rao, and BVVSN Prabhakar Rao. "Novel technique for the detection of abnormalities in Mammograms using texture and geometric features." *2015 International Conference on Microwave, Optical and Communication Engineering (ICMOCE)*. IEEE, 2015.

- [8] Zebari, Dilovan Asaad, et al. "Enhance the Mammogram Images for Both Segmentation and Feature Extraction Using Wavelet Transform." 2019 International Conference on Advanced Science and Engineering (ICOASE).IEEE, 2019.
- [9] C. Gonzalez and E. Woods, *Digital Image Processing*, Third edition
- [10] Merry, R. J. E. (2005). *Wavelet theory and applications: a literature study*. (DCT rapporten; Vol. 2005.053).Eindhoven: Technische Universiteit, Eindhoven.
- [11] Kumar, Vipin, and Sonajharia Minz. "Feature selection: a literature review." *SmartCR* 4.3 (2014): 211-229.
- [12] Zhou, Xuan. "Feature selection for image classification based on a new ranking criterion." *Journal of Computer and Communications* 3.03 (2015): 74.
- [13]. Kamavisdar, Pooja, Sonam Saluja, and Sonu Agrawal. "A survey on image classification approaches and techniques." *International Journal of Advanced Research in Computer and Communication Engineering* 2.1 (2013): 1005-1009.

Hybrid Power Gating Technique In FinFET Based Memory for High Speed Applications

Dr. S. Suryanarayana¹, B. Mamatha², S. Vishnu Teja³

¹Professor, Dept of ECE, Geethanjali College of Engineering and Technology, Keesara, Hyderabad

²Asst Prof., Dept of ECE, Geethanjali College of Engineering and Technology, Keesara, Hyderabad

³B-Tech 4th year student, ECE, Geethanjali College of Engineering and Technology, Keesara, Hyderabad

Abstract

ICs have been through for four generations, i.e., Small Scale Integration (SSI), Medium Scale Integration (MSI), Large Scale Integration (LSI) and Very Large-Scale Integration (VLSI). Over past several years, CMOS technology has become dominant for relatively high performance and cost-effective VLSI circuits. ICs are used in high-speed applications like satellite imaging, future generation ubiquitous computing and etc. To attain high speed and to reduce the power consumption, high speed/low power techniques are introduced like Sleep technique, Stack technique, Sleepy Keeper technique, Leakage Control Transistor technique and etc. In this paper it is proposed to introduced an SRAM cell, using FinFET (Fin Field Effect Transistor) and applying novel high speed/low power technique, namely, Sleepy Keeper Leakage Control Transistor (SK-LCT), to increase the speed of the SRAM circuit, as it is a widely used memory element in many computers. This paper presents the performance analysis and efficiency of FinFET technology. The simulations are done using Cadence Virtuoso tool, in 14nm technology (FinFET) and the results obtained show a significant improvement in terms of speed.

Key words: SRAM, FinFET, SK-LCT, Sleepy Stack, LECTOR.

I. Introduction

Invention of transistor by William B. Shockly, Walter H. Brattiam and John Bardeen made a momentous change in electronics industry and paved way for development of IC (Integrated Circuits) technology. The electronic technology node is scaled down to increase the performance without disturbing the functionality. In the course of advancement, FinFET is a newly emerged technology having less propagation delay when compared with CMOS (Complementary Metal Oxide Semiconductor). FinFET itself has less propagation delay and if we apply low power high speed techniques to this FinFET circuits, the speed is further increased and area is reduced.

With advancement in technology the demand for large storage of data is increasing. Concurrently, the accessing speed has also become a major obstacle. SRAM (Static Random-Access Memory) is very essential component in most of the VLSI based circuits. During standby mode SRAM has low power consumption and high speed when compared to other memories [1]. The accessing speed of SRAM can be further increased by using FinFETs.

Many power gating techniques available in the literature such as sleep technique, stack technique, sleepy stack technique, sleepy keeper technique, Leakage control transistor technique for high speed and leakage power reduction. In this paper, it is proposed to design a high-speed SRAM cell by applying a novel high speed-low power technique, Sleepy Keeper Leakage Control Transistor (SK-LCT) technique, which is the combination of both Sleepy Keeper and LCT techniques, using FinFETs and compare its performance with the above-mentioned methods.

II. FinFET Structure

Fin Field Effect Transistor is a non-planar device in which the conducting channel is warped by thin silicon called "Fin", hence the name, FinFET. It was invented by Dr. Chenming Hu, who has been called "Father of 3D Transistor". Regarding its structure [7], a thin and vertical fin is laid down between the drain and source (fig.1). The orientation of gate is about right angled to the fin. The gate is warped along the fin interfacing the three sides of channel. This type of structure ensures more electrical control over channel and reduces short channel effects, if any. The main advantage of FinFET is its supply voltage is just 0.8V for 14nm structure.

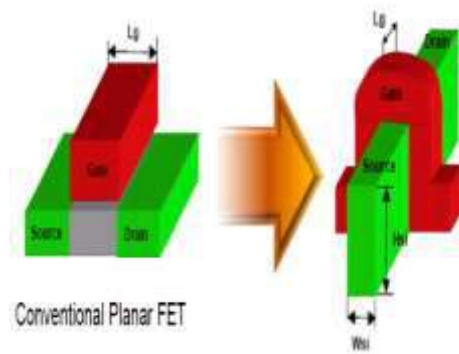


Fig. 1: structural comparison between planar MOSFET and FinFET

FinFET can be used in two different modes [7] namely, Shorted Gate (SG) mode and Independent Gate (IG) mode. In SG-FinFET, both the gates are physically blended whereas in IG-FinFET the gates are set apart. Both of these modes have their own advantages and disadvantages.

III. Low power - high speed techniques

A. Sleep, Stack, Sleepy Stack, Sleepy Keeper and LECTOR techniques:

Low power – high speed techniques are frequently used in IC design to increase the speed and also to reduce the leakage power. A variety of techniques are there to lessen the propagation delay, in literature.

Firstly, in sleep technique, a pMOS is placed in between pull-up and supply and an nMOS is positioned between pull-down and ground, as shown in Fig:2. It works in sleep and active modes. In sleep mode a direct path is established between input and output by shutting down unnecessary transistors. This increases the speed and decreases the leakage power [2]. Disadvantage of this technique is it does not hold the state and gives floating output.

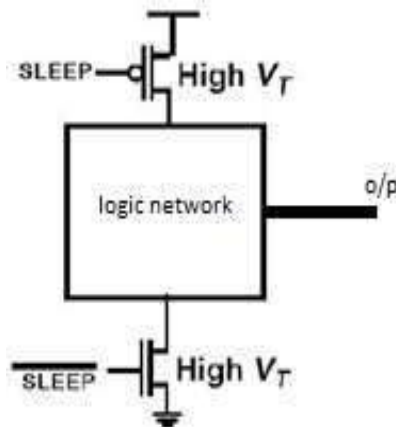


Fig. 2: Sleep Transistor technique

Stack technique is state upkeep technique which chops off the leakage current but increases delay and area [3]. The sleepy stack technique, shown in Fig: 3, decreases the power but drastically increases the delay [4].

To overcome the disadvantage of sleep technique, an nMOS is kept parallel to pMOS in pull up and vice versa to maintain the output is both active and sleep modes. This technique is called as Sleepy Keeper technique. In LECTOR technique, two high voltage transistors (pMOS & nMOS) are inserted between pull-up and pulldown networks. It is observed that it has delay penalty but low leakage power.

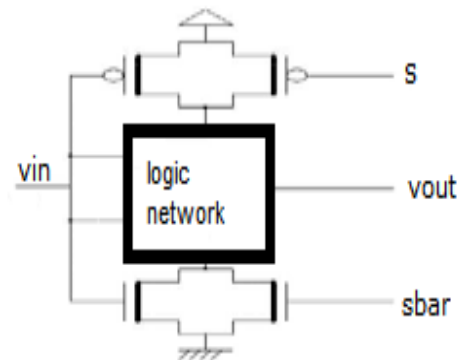


Fig. 3: Sleepy Stack technique

So, there is a need of new techniques to decrease the propagation delay.

B. Proposed Method

The proposed hybrid technique, namely, Sleepy Keeper Leakage Control Transistor technique (SK-LCT) is a combination of both Sleepy Keeper technique and LECTOR technique (fig: 4). The delay is significantly reduced and also the data retention be maintained using this proposed method.

In this technique, two leakage control transistors, LCT-pMOS and LCT-nMOS, are inserted between pull up and pull-down networks. The gate of LCT-pMOS is tied to drain of pull-down network and gate of LCT-nMOS is connected to drain of pull up network. Parallel connected pMOS and nMOS are connected between pull up and supply connections and vice versa. In this type of connection, parallel connected nMOS between pull up and supply and parallel connected pMOS between pull down and ground is the path. In this technique, both the available techniques are completely involved. This proposed technique increases the speed as well as reduces the leakage power.

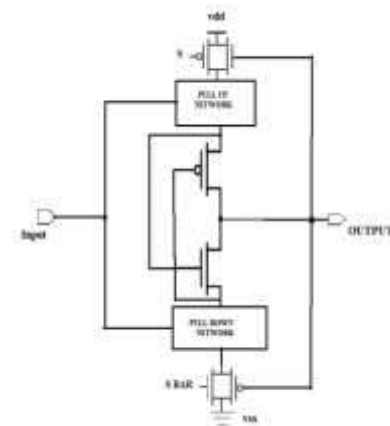


Fig.4: SK-LCT technique

IV. Design of the Proposed Method

Fig: 5 shows design of proposed SRAM cell using FinFET, applying SK-LCT technique.

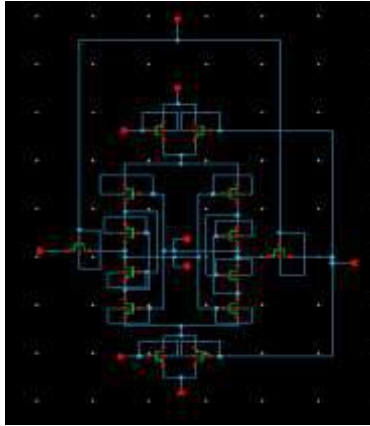


Fig 5: SRAM Cell using FinFET in SG mode with SK-LCT

V. Simulation Results

Technique used	FinFET technology	
	Avg. power (uW)	Delay (nS)
Normal	14.25	10.53
Sleepy Keeper	18	8.1
LECTOR	3.13	14
Proposed (SK-LCT)	18	5.8

Table 1: Simulation Results

VI. Conclusion

It is to be concluded that, while using the proposed hybrid method with FinFET, it is superior, in terms of speed. When average power is main constraint, then the same FinFET can be used by applying LECTOR technique, alone. Hence for high speed applications, FinFET circuit with proposed hybrid method is suitable.

References

- [1] M. Adisheshaiah, D. sharath Babu Rao and V. Venkateswara Reddy, "Implementation and Design of 6T SRAM with Read and write Assist circuits, IJREAS, Volume2, Issue 5 (May 2012), 2249-3905.
- [2] Tripathi Mehta, "A Comparative Study of Low Power Consumption Techniques in a VLSI Circuit", IJERA, ISSN: 2248-9622, Vol. 5, Issue 7, (Part - 2) July 2015, pp.30-33.
- [3] Anu Tonk and Shilpa Goyal, "A literature review on Leakage and Power reduction Techniques in CMOS VLSI Design", IJARCCCE, Vlo.3, Issue.2, pp.554-558.
- [4] J. Park, "Sleepy Stack: A new Approach to Low power VLSI and Memory", Ph.D. Dissertation. May 2014.

The proposed design is simulated using Cadence Virtuoso tool for Sleepy Keeper, LECTOR and proposed (SK-LCT) techniques. The performance of the design is analyzed in terms of power consumption and delay. The simulation results are presented in table:1.

The delay for SRAM without using any high speed-low power technique is 10.53 nS for FinFET. When high speed-low power techniques are used, FinFET circuit outperforms in terms of delay. But it is to be observed that average power consumption increased. With LECTOR method, FinFET circuit exhibits significantly very less power consumption with a great delay, in comparison with its counterparts.

In FinFET technology using proposed method, the delay is considerably reduced to 5.8 nS against other two methods. But the power consumption is increased.

For the proposed method, even though average power consumption is high, the delay is reduced by 41.4% for proposed method compared to LECTOR technique. Hence, there is a significant increment in the speed of the circuit using proposed method. So, the FinFET SRAM may be used for high speed applications, with proposed (SK-LCT) technique.

[5] Rajani H. P and Srimannarayan Kulkarni, "Novel Sleep Transistor techniques for Low Leakage Power Peripheral Circuits", IJVLISCS, Vol.3, No.4, August 2012.

[6] Shreya R. Patel, K. R. Bhatt and Rachna Jani, "Leakage current reduction techniques in SRAM", IJERT, ISSN: 2278-0181, Vol. 2 Issue 1, Jan-2013.

[7] Debajit Bhattacharya and Niraj K. Jha, "Review article FinFETs: From Device to Architectures", HPCA, Vol. 2014, Article Id: 364689, 21 pages.

Performance analysis of MIMO System capacity with various Receiver Architectures

R V Durga^{1,2}, A McLauchlin¹

¹Department of Electronics and Communication Engineering, University of Hertfordshire, College Ln, Hatfield AL10 9AB, UK.

²Geethanjali College of Engineering and Technology (Autonomous), Cheeryal (V), Keesara (M), Medchal Dist., Telangana - 501 301, India.

Abstract

Progress is aspired by the present-day technologies. Due to such progressions various researches are performed in substantial improvement areas. In the wireless spectrum, end-users' amount is increasing day by day that leads to the requirement of enhanced BER values and bandwidth usage. Furthermore, in these modern times, new technologies are proved as research's crucial point that increases the wireless systems' capacities. A comparison of their BER performance charts is used to evaluate different combinations of multiple user receivers for determining performance under normal working conditions. In order to use the increased capacity rates, which can be achieved using a MIMO (multiple input and multiple output) configuration, MIMO systems are combined into system. MIMO with technology's complete dissemination through key attributes and components' investigation regarding single user communications. Various MIMO receivers' BER (Bit Error Rate) performance is also investigated. Adding SIC (Successive Interference Cancellation) to the MMSE (Minimum Mean square error) as well as ZF (Zero Forcing) MIMO receiver gives some changes to enhancements of BER value, but such minor change is important while ordering is performed with SIC. This particular paper provides a typical MIMO system. Compared to above-developed user systems, modern systems adopt a multi-user scenario. The present requirement for higher data rates resulted in the various techniques use like OFDM by the industry and the additional use of MIMO capabilities in WIFI (Wireless fidelity) and CDMA (Code Division Multiple Access).

Keywords- Successive Interference Cancellation (SIC), Minimum Mean square error (MMSE) Zero Forcing (ZF).

1. Introduction

The word "MIMO" is utilized to characterize system which utilize many antennas both at transmitters and at receivers to boost efficiency with the achievement of increased BERs. Smart antennas are used by this technology [1]. This is considered as the key innovations in wireless networking infrastructure of the third century and is studied globally. The signals are distributed over many pathways such that spatial variation is imposed on the data stream of the system. It is doubtful that all tracks will suffer from extreme fading, allowing the MIMO system to boost signal obligations in a wireless natural world. MIMO networks have been desirable developments in WiMAX (IEEE 802.16), WCDMA and, wireless LAN (IEEE 802.11n). This has been primarily because of the large improvement in data link range and data throughput, without either requiring increasing system bandwidth or transmitting power.

2. Implementation

The various transmission antennas on the transmitter relay separate sources of the data into the tube. The streams transmitted are assisted by a transmission channel consisting of a matrix

representation created by several antennas at both transmitting as well as receiving ends [2]. Many signal vectors obtained to retrieve the data stream are decoded by the receiver. Depending on the design purpose in question, the MIMO system's total performance as well as capability are described. MIMO systems are usually used for one or more of the following strategies, depending on the appropriate scenario.

2.1 MIMO Transmitter

2.1.1 MIMO with Pre-Coding

For modifying the beam forming [3] for supporting MIMO multi-layer transmissions pre-coding method is utilized. Beam shaping is a mechanism in which each antenna transmits the same signal with the correct weighting of the corresponding power and stage to optimize the signal power at the recipient antenna. Factors such as line of sight and location influence this particular setting and therefore it must be tailored to the MIMO scenario. Multiple antennas are possessed by MIMO receivers so that single layer beam formation at all the receiving antennas is not adequate to simultaneously achieve maximum received signal levels. This is achieved by pre-coding for this multilayer level configuration layout of the MIMO to improve overall system performance. In such system in which pre-coding is utilized, multiple streams with separate weighting per antenna of the intended transmission signal(s) are modulated to the source. This would improve the necessary data efficiency in the processing of the receiver. It necessitates earlier information on the state of channel, and CSI must be used effectively on the transmitter.

2.1.2 MIMO with Spatial Multiplexing

Normally, a signal with higher data rate is distributed by separating it into many low-rate data sources. In the same frequency band, each current is then transmitted from another antenna. At the source, the flux is divided into parallel channels, providing distinct spatial signatures arrive at the source antenna. With or without CSI information, this multiplexing approach can be applied.

2.1.3 MIMO with Diversity Coding

Diversity coding strategies are used to improve device efficiency in a standard MIMO communication situation in which the CSI is not identified. A single stream from each antenna is transmitted using different coding methods, for example space-time coding that uses selective or complete orthogonal coding. According to modern wireless communication networks, a route from sender to receiver via a viewing line is typically not very simple, thus diverse systems use the means to make the best possible approximation for the transmitted stream of the various paths generated by the transmitted signal's interaction with the atmosphere (that are mountains, tree, buildings and so on) Space time encryption is used to use the signal received at the source. Owing to the multi-path situation, the signal transmitted typically undergoes multiple degradations, time delays, and phase changes because of scenarios of multi-path. At the source, no CSI expertise is required. There are various diversity coding systems, but the final selection of the scheme, or MIMO implementation, typically relies on device specifications. Figure1 gives an example of a MIMO uplink device.

For evaluating the MIMO systems, its associated signals' linear representation is needed. Supposing a system which comprising of M receive as well as N transmit antenna, in which n_n represents the noise, h_{mn} represents the channel matrix, H's related entry and x_n presents the transmitted signal; therefore, y_m received signal is presented as:

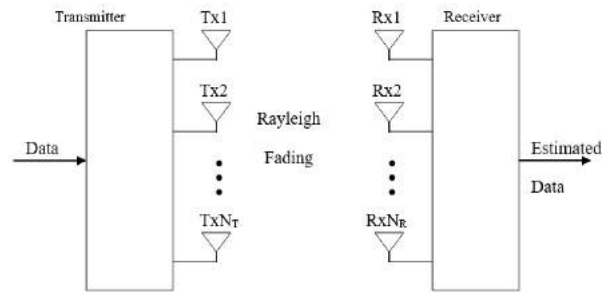


Figure 1: A Standard MIMO System

$$y_m = \sum_{n=1}^N h_{mn} x_n + n_n \quad m = 1, 2, \dots, M \quad (1)$$

The multiple receives and transmit antennas produce coefficients of channel which are comprehended in an $M \times N$ channel matrix form represented as.

$$H = \begin{bmatrix} h_{11} & h_{12} & \dots & h_{1N} \\ h_{21} & h_{22} & \dots & h_{2N} \\ \vdots & \vdots & \ddots & \vdots \\ h_{M1} & h_{M2} & \dots & h_{MN} \end{bmatrix} \quad (2)$$

Thus; the received signal at any given time, t , is stated as:

$$y(t) = Hx(t) + n(t) \quad (3)$$

Where, noise is presented by $n(t)$ with σ variance. MIMO systems' advantages can be understood by its throughput that is capacity of MIMO system.

2.2 MIMO System Capacity

[3] is included with derived as well as documented MIMO capacities equations. Various assumptions are included for deriving these equations that are:

- During the data burst there exists narrowband Rayleigh channel
- Irrespective of the transmit antennas' number total transmitted power and additive white Gaussian noise found to be constant
- Receiver channel knowledge.

As per the abovementioned assumptions; following equations are utilized for calculating the overall channel capacity is given [4], [5], [6], [7].

$$C = \log_2 \det [I_m + (\rho/n) HH^H] \text{ b/s/Hz} \quad (4)$$

$$C = \log_2 \det \left[I_m + \frac{\rho}{n} R \right] \text{ b/s/Hz} \quad (5)$$

Where, R presents the normalized channel correlation matrix, ρ presents the average SNR exhibited at every receiving antenna. I_m presents an identity matrix. and C presents capacity of system. A "water filling" algorithm

$$C = \sum_1^k \log_2 \det \left[1 + \frac{\rho}{n} \lambda_i \right] \text{ b/s/Hz} \quad (6)$$

the single value decomposition theory [7]. It resulted in famous equation as given:

(6)

Where, k represented the matrix rank as well as λ_i represents the HH^H matrix's i^{th} eigen mode. Such equations allow a MIMO channel's visualization to be parallel SISO, *single-input single-output*, pipes that possesses the gains equivalent to their eigenvalues respectively. Thus, in case of transmitter known channels, for increasing their capacities only “**good channels**” are used that means those channels under an unequal power distribution exhibits greatest gain. Because of this (7) is transformed from (6) as:

$$C = \sum_1^k \log_2 \det \left[1 + \frac{P_i}{\sigma^2} \lambda_i \right] \text{ b/s/Hz} \quad (7)$$

Where, p_i represents the i^{th} pipe power.

The water-filling method previously described can be used to quantify this amount. The functionality of a single MIMO user system varies from multi-user applications.

2.3 MIMO Detectors

Few detectors are possible but most are non-linear and/or linear detectors' combinations. VBLAST, OSIC, MMSE and ZF devices are the primary detectors. New technology like Sphere Detectors have arisen that have Bit Error Rate with lower device complexity similar to ML approximation. These detectors are measured using various modulation and antenna setups. There are several different MIMO setups, but the approach followed and the observations taken in this study are seen as.

2.3.1 Zero Forcing (ZF) Detector

It is among the easiest available algorithm. This acts like a regular equalizer as the opposite of output of the frequency of channel is used in the received signal. In principle, such effective, however this is very susceptible for noise in realistic conditions since the opposite of the noise received to the signal is also true, as the response of channel involves a noise (3). Thus, for unnoisable signals, the ZF algorithm proves to be very successful, because ISI (Inter-Symbol Interference) can be removed through it but not suitable for a noisy signal because receiver's noise is increased by it [8].

Clearly, channel knowledge is important to use this algorithm on the receiver that enhances the system's complexity. The calculation, y of the obtained signal can therefore be written in respect of MIMO systems as:

$$\bar{y}_{ZF} = (H^H H)^{-1} H^H y = H^+ y \quad (8)$$

Where Moore-Penrose inverse is represented by H^+ that effectively is H matrix's pseudo-inverse.

Further analysis of the MIMO mechanism is possible (3). The data received by the two recipients was precisely generated by signals from both transmitter antennas. The obtained data from the first slot are y_1 and y_2 , where antennas are collected

$$y_1 = h_{1,1}x_1 + h_{1,2}x_2 + n_1 ; \quad y_1 = [h_{1,1}, h_{1,2}] \begin{pmatrix} x_1 \\ x_2 \end{pmatrix} + n_1 \quad (9)$$

$$y_2 = h_{2,1}x_1 + h_{2,2}x_2 + n_2 ; \quad y_2 = [h_{2,1}, h_{2,2}] \begin{pmatrix} x_1 \\ x_2 \end{pmatrix} + n_2 \quad (10)$$

$$\begin{bmatrix} y_1 \\ y_2 \end{bmatrix} = \begin{bmatrix} h_{1,1} & h_{1,2} \\ h_{2,1} & h_{2,2} \end{bmatrix} \begin{bmatrix} x_1 \\ x_2 \end{bmatrix} + \begin{bmatrix} n_1 \\ n_2 \end{bmatrix} \quad (11)$$

- x_1 : First antenna's transmitted symbol
- x_2 : Second antenna's transmitted symbol
- y_1 : First transmitter's evident received signal
- y_2 : Second transmitter's evident received signal
- $h_{1,1}$: Channel to first receive antenna from first transmitting antenna
- $h_{1,2}$: Channel to first receiving antenna from second transmitting antenna
- $h_{2,1}$: Channel to second receiving antenna from first transmitting antenna
- $h_{2,2}$: Channel to second receiving antenna from second transmitting antenna
- n_1 : First receiver noticed noise
- n_2 : Second receiver noticed noise

The (11) H matrix represents the matrix and H^+ its corresponding matrix is presented in (12).

$$H^+ = (H^H H)^{-1} H^H = \begin{bmatrix} \bar{h}_{1,1} & \bar{h}_{2,1} \\ \bar{h}_{1,2} & \bar{h}_{2,2} \end{bmatrix} \begin{bmatrix} h_{1,1} & h_{1,2} \\ h_{2,1} & h_{2,2} \end{bmatrix} \quad (12)$$

$$H^+ = \begin{bmatrix} h_{1,1}^2 + h_{2,1}^2 & \bar{h}_{1,1}h_{1,2} + \bar{h}_{2,1}h_{2,2} \\ \bar{h}_{1,2}h_{1,1} + \bar{h}_{2,2}h_{2,1} & h_{1,2}^2 + h_{2,2}^2 \end{bmatrix}^{-1} H^H$$

For higher antenna configuration adjustment of the solution means more work as well as makes the system more complex. For example, solving the opposite matrix of a 4x4 MIMA system where a similar procedure as the above can be shown below.

$$\text{For } H = \begin{bmatrix} h_{1,1} & h_{1,2} & h_{1,3} & h_{1,4} \\ h_{2,1} & h_{2,2} & h_{2,3} & h_{2,4} \\ h_{3,1} & h_{3,2} & h_{3,3} & h_{3,4} \\ h_{4,1} & h_{4,2} & h_{4,3} & h_{4,4} \end{bmatrix} \quad (13)$$

Because of four receive antennas' presence, receiver receives antenna signatures of four distinct types shown as

$$y_3 = [h_{3,1} \ h_{3,2} \ h_{3,3} \ h_{3,4}] \begin{pmatrix} x_1 \\ x_2 \\ x_3 \\ x_4 \end{pmatrix} + n_3 \quad y_4 = [h_{4,1} \ h_{4,2} \ h_{4,3} \ h_{4,4}] \begin{pmatrix} x_1 \\ x_2 \\ x_3 \\ x_4 \end{pmatrix} + n_4$$

$$y_1 = [h_{1,1} \ h_{1,2} \ h_{1,3} \ h_{1,4}] \begin{pmatrix} x_1 \\ x_2 \\ x_3 \\ x_4 \end{pmatrix} + n_1 \quad y_2 = [h_{2,1} \ h_{2,2} \ h_{2,3} \ h_{2,4}] \begin{pmatrix} x_1 \\ x_2 \\ x_3 \\ x_4 \end{pmatrix} + n_2$$

(14)

Therefore:

$$y = \begin{pmatrix} y_1 \\ y_2 \\ y_3 \\ y_4 \end{pmatrix} = \begin{bmatrix} h_{1,1} & h_{1,2} & h_{1,3} & h_{1,4} \\ h_{2,1} & h_{2,2} & h_{2,3} & h_{2,4} \\ h_{3,1} & h_{3,2} & h_{3,3} & h_{3,4} \\ h_{4,1} & h_{4,2} & h_{4,3} & h_{4,4} \end{bmatrix} \begin{pmatrix} x_1 \\ x_2 \\ x_3 \\ x_4 \end{pmatrix} + n_1$$

(15)

$$H^+ = (H^H H)^{-1} H^H$$

(16)

The reverse of a 4x4 matrix is important for a warning (13). To measure its inverse, new matrix's elements generated through H^+ , the determinant values are required. Normally, the reverse of a matrix is achieved for co-factors. This technology makes the framework in the H^+ matrix's higher order more complicated and redundant.

2.3.2 MMSE (Minimum Mean Squared Error) Detector

It's a better algorithm in comparison to the ZF under harsh situations. However, it does not remove ISI as well as the ZF algorithm; this lowers considerably overall power of noise of the user [4].

$$\bar{y}_{MMSE} = (H^H H + (\sigma_n / \sigma_s)^2 I)^{-1} H^H y$$

(17)

where σ_s and σ_n represents the received signal power and noise power respectively and identity matrix is represented by I . The estimates of ZF and MMSE are found to be equal when $\sigma_s \gg \sigma_n$. Hence, it should be noted that when; the MMSE estimate equates to the ZF estimate. Thus, with the inclusion of a scaling factor, the 2x2 and 4x4 (17) figures can be seen as similar to their ZF equivalents.

2.3.3 Successive Interference Cancellation

This algorithm initially detects, deletes and removes largest individual from the receivable signal. You should do so in two ways. Next, the soft information may be extracted from the obtained signal; it induces little to no error propagation, but for vulnerable users obtains a combined noise effect. Secondly, hard information may be extracted from the received signal which results in little to no noise but potential mistakes. Successive cancellation may be implemented in a circular fashion, at low convergence's cost and therefore higher complexity. MAI is decreased and the problem has evolved almost / far. The most effective and the most accurate cancellation is the cancellation of the best signal [9]. The SIC algorithm will then most likely suffer from error propagation, since the most effective cancellation is possible. The channel estimation at the recipient is also necessary [9]. The ZF or MMSE

detector usually is used as pre-filtering for general SIC systems. For the pre-coding, detector utilizing ZF algorithm is investigated as given.

Initial estimates for efficient performance of SIC systems are required. The initial calculations are derived from the ZF detector output. For the 2x2 scenario, the transmitted symbols x_1 as well as x_2 and for the 4x4 scenario, x_2 , x_3 and x_4 are estimated depending on number of antennas. This is then taken by the SIC detector and deducted from actual data stream. The total iterations number depends once more on used antennas numbers. Only one estimate is necessary, in a 2x2 scenario, whereas three estimates are needed in the 4x4 scenario. The estimates of a 2x2 and a 4x4 MIMO system may, as illustrated below, be expressed by using a ZF detector.

$$\begin{bmatrix} \tilde{x}_1 \\ \tilde{x}_2 \end{bmatrix} = H^+ \begin{bmatrix} y_1 \\ y_2 \end{bmatrix} \quad (18)$$

$$\begin{bmatrix} \tilde{x}_1 \\ \tilde{x}_2 \\ \tilde{x}_3 \\ \tilde{x}_4 \end{bmatrix} = H^+ \begin{bmatrix} y_1 \\ y_2 \\ y_3 \\ y_4 \end{bmatrix} \quad (19)$$

The incident signal received at the first antenna, y_1 has been seen underneath when a 2x2 MIMO system is adopted to make it easy.

$$y_1 = h_{1,1}x_1 + h_{1,2}x_2 + n_1 = [h_{1,1} \ h_{1,2}] \begin{bmatrix} x_1 \\ x_2 \end{bmatrix} + n_1 \quad (20)$$

Therefore, at the second receiver, the received signal matches with y_2 below.

$$y_2 = h_{2,1}x_1 + h_{2,2}x_2 + n_2 = [h_{2,1} \ h_{2,2}] \begin{bmatrix} x_1 \\ x_2 \end{bmatrix} + n_2 \quad (21)$$

Utilizing (1) where

$$y_m = \sum_{n=1}^N h_{mn} x_n + n_n \quad m=1,2,\dots,M \quad (22)$$

$$y = Hx + n$$

The ZF approach is used for simple purposes because the ZF and MMSE counterparts can be considered to be substantially similar via a weighing factor. Input signal estimates are decoded by using a ZF algorithm to meet a limit below in which H^+ is a matrix with the parent matrix 'size, H which shows the ratio shown in (23).

$$H^H H = I \quad (23)$$

Identity matrix is represented by I and utilizing an identity matrix's convenient properties [8], the H^+ matrix, is represented as:

$$H^+ = (H^H H)^{-1} H^H \quad (24)$$

The received estimates can be represented as seen in (25), by means of the relation in (22) for solving the estimates received.

$$\begin{bmatrix} \tilde{x}_1 \\ \tilde{x}_2 \end{bmatrix} = H^+ \begin{bmatrix} y_1 \\ y_2 \end{bmatrix} \quad (25)$$

$$\begin{bmatrix} \bar{x}_1 \\ \bar{x}_2 \end{bmatrix} = (H^H H)^{-1} H^H \begin{bmatrix} y_1 \\ y_2 \end{bmatrix} \quad (26)$$

It has been supposed that in (26) estimates have been provided that are to be subtracted as first estimates, furthermore, received signal consists of \tilde{x}_1 , that is remaining estimate only as provided in (27).

$$\begin{bmatrix} r_1 \\ r_2 \end{bmatrix} = \begin{bmatrix} h_{1,1} \\ h_{2,1} \end{bmatrix} x_1 + \begin{bmatrix} n_1 \\ n_2 \end{bmatrix} \quad (27)$$

It can be seen from (27); because, after one iteration, at the receiver the incident signal comprises of a particular symbol, but further iterations are necessary in cases with a larger number of transmission antennas, and the composition of that signal is a mixture of other transmitted signal components. The first prototype for a 4x4 MIMO device can be seen from the descriptor of the obtained signal.

$$\begin{bmatrix} r_1 \\ r_2 \\ r_3 \\ r_4 \end{bmatrix} = \begin{bmatrix} h_{1,1} & h_{1,2} & h_{1,3} & h_{1,4} \\ 0 & 0 & 0 & 0 \\ h_{3,1} & h_{3,2} & h_{3,3} & h_{3,4} \\ h_{4,1} & h_{4,2} & h_{4,3} & h_{4,4} \end{bmatrix} \begin{bmatrix} x_1 \\ 0 \\ x_3 \\ x_4 \end{bmatrix} + \begin{bmatrix} n_1 \\ 0 \\ n_3 \\ n_4 \end{bmatrix} \quad (28)$$

The new values for the H matrix are modified according to every iteration, that is the h values for the preceding value are adjusted to zero as well as the iteration is repeated for the r new value before all the symbols are decoded.

2.3.4 OSIC (Ordered Successive Interference Cancellation) Algorithm

The detection algorithm used in this project is a non-linear equalization method. Co-Antenna Interference, CAI, is the key limitation in MIMO systems. The OSIC algorithm is readily used to prevent this disability. The incoming sub streams i.e., layers are identified by this algorithm recursively. It can identify the strongest layer first, that is to say, the highest SNS sub line, as well as after that delete it from the actual signal obtained so that the CAI can be correctly extracted. The process continues the procedure for layers afterwards; the signal intensity is used for detecting and extracting from the initial signal all of the sub-streams / layers available [10].

The successive interference cancellation approach requires ordering as the mistakes connected with previously observed layers will be continuously related to the detection system. Therefore, layers with lower probability of error must first be observed before other layers are observed. In the following three key steps the ordering process and the OSIC algorithm can be shown.

2.3.4.1 Interference Cancellation

The interruption of the transmitter will occur when the mark is sensed. This interruption is extracted from the initial signal obtained as seen in the mathematical expression.

$$y' = y - h_1 \bar{y}_1 - \dots - h_{i-1} \bar{y}_{i-1} \quad (29)$$

where within the matrix H, respective i_{th} column is represented by h_i , y the received signal's estimated hard decisions are represented by y_i .

2.3.4.2 Interference Nulling

This method is very critical and typically takes a linear equalizer. This is a very important technique. This is performed using MMSE or ZF in existing systems [10]. The MMSE algorithm was utilized by this project.

2.3.4.3 Optimal Ordering

The design of the detection pattern of SIC systems is a significant source of error propagation. This will impair the overall BER output if sub-streams with high probability of error are observed and eliminated in the early stages of the detection from the reception system. This will allow the acquired error to propagate across the entire chain of identification. This error propagation is avoided by optimum ordering by allowing the line to be identified earlier in the obtained signal vector with the maximum SNR post detection. Therefore, immediately after the interruption zero's occurrence inside the OSIC decoder there is an optimum ordering mechanism.

3. Simulations and Results

In the case that a $m \times m$ MIMO channel is available, the data will be sent in a single antenna-scenario chain, $x = [x_1, x_2, x_3, x_4 \dots, x_n]$, normally and data will require data slots for transmitting the data-stream. Here the " $m \times m$ MIMO detector" in which " m " antennas are available, data for regular transmission can be transmitted at " m " times the actual data rate. The " m " symbols can be included now with any system. This occurs. In a 2×2 scenario, for example, x_1, x_2 are sent to the first timepiece with x_3 from both transmit antennas, x_4 in the second timepiece and the like. The data rate is quadrupled in the case of 4×4 MIMO when four symbols are sent in any time frame. The other key theories that are used are:

- Flat Rayleigh fading is experienced by the channel
- At the receiver, from (2), the channel matrix, H is received

3.1 MIMO System's Capacity

The abovementioned potential in (7) were achieved by utilizing value decomposition theory [41] as well as tested for various transmitter and recipient combinations. A pattern in terms of the observed ability increase in a growing antennas number, as represented in Fig. 3-7, is automatically recognized.

3.2 Implementation Utilizing Various Receiver Configuration

OSIC, MMSE and ZF varieties were tested. ZF-OSIC, MMSE-OSIC, MMSE and ZF are tested for receiver variants. A comparison message of n to 1×10^5 bits sent by a fading channel Flat Rayleigh. The modulated signals transmitted were divided in right streams that are antenna suitable. For example, the signal should be broken up in 4 different data streams with a 4×4 system, as well as a 2×2 system would need 2 stream, and so on. The BER output of two separate receptor combinations as seen in Fig. 3-8 as well as 3-9 respectively.

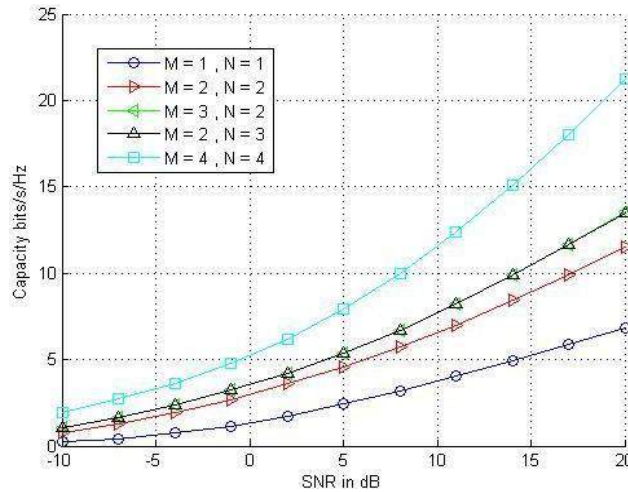


Figure7: Various MIMO Configurations' Capacities

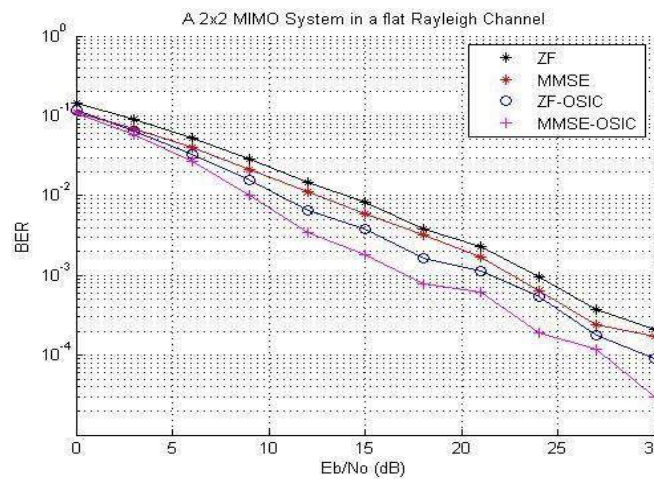


Figure8: 2x2 MIMO with different Receive Architectures

4. Conclusion and Summary

As overall antennas number seen in Figure3 thus grows the power of a standard MIMO device. The capabilities of an N-familial MIMO systems are similar as those of M-familiar MIMO systems.

Adding SIC to the MMSE as well as ZF MIMO receiver gives some changes to enhancements of BER value, but such minor change is important while ordering is performed with SIC according to fig. 3–8 as well as 3–9. It is noticed that the output BER images for MMSE-OSIC to ZF-OSIC are now comparable in Fig. 3-10, while 16PSK is being used, although BER values are still higher in MMSE-OSIC. Figure10 indicates the achievable BER values by including an optimum ML decoder, which needs even more device complexities, is also used in an ML decoder.

A 2x2MIMO system, based on the simple ZF detector, was studied as represented Fig. 3-11. As total symbols transmitted per second increases, the total errors also increases as well as thus, there exists requirement for higher SNR values. Figure11 also shows the need for higher SNRs to be used for greater order modulation.

The particular paper provides a typical MIMO system's brief introduction. Compared to above-developed user systems, modern modern systems adopt a multi-user scenario. The present requirement

for higher data rates resulted in the various techniques use like OFDM by the industry and the additional use of MIMO capabilities in WIFIs and CDMA. The next paper examines the integration of multi-user MIMO with receiving architectures.

References

- [1] F. B. Gross, *Smart Antennas for Wireless Communications with Matlab*, McGraw- Hill, 2005
- [2] B. M. Hochwald and S. Brink, "Achieving near capacity on a multiple-antenna channel", *IEEE Trans. Comm.*, vol. 51, no. 3, pp. 389-399, 2003.
- [3] G. J. Foschini and Michael. J. Gans, "On limits of wireless communications in a fading environment when using multiple antennas". *Wireless Personal Communications*. January 1998.
- [4] S. Lokya and A. Kouki, "New compound upper bound on MIMO channel capacity", *IEEE Communication Letters*, vol. 6, No. 3, 2002, pp 96-98.
- [5] S. Lokya, "Channel capacity of MIMO architecture using the exponential correlation matrix", *IEEE Communication Letters*, vol. 5, No 9, 2001. pp 369-371.
- [6] M. F. Demirkol, M. A. Ingram, Z. Yun, "Feasibility of closed loop operation for MIMO links with MIMO interference," *Proc. of the IEEE Int'l Symp. on Antennas and Prop.*, Jun. 2004.
- [7] E. J. Ientilucci, "Using the Singular Value Decomposition", *Chester F. Carlson Centre for Imaging Science, Rochester Institute of Technology*, May 29, 2003.
- [8] A. Paulraj, R. Nabar and D. Gore, *Introduction to Space-Time Wireless Communications*, 2003, ISBN: 0-521-82615-2
- [9] R. Sinha, A. Yener, R.D. Yates; "Non-coherent Multi-user Communications: Multistage Detection and Selective Filtering", *EU RASIP Journal on Applied Signal Processing* 2002:12, 1415–1426
- [10] P. Wolniansky, G. J. Foschini, G. D. Golden, and R. A. Valenzuela, "VBLAST: An architecture for realizing very high data rates over the rich scattering wireless channel," *URSI International Symposium on Signals, Systems, and Electronics*, ISSUE 98, 1998.

The MIMO System Capacity Analysis with Various Detectors and Different Modulation Schemes

R V Durga^{1,2}, A McLauchlin¹

¹Department of Electronics and Communication Engineering, University of Hertfordshire, College Ln, Hatfield AL10 9AB, UK.

²Geethanjali College of Engineering and Technology (Autonomous), Cheeryal (V), Keesara (M), Medchal Dist., Telangana - 501 301, India.

Abstract

Progress is aspired by the present-day technologies. Due to such progressions various researches are performed in substantial improvement areas. In the wireless spectrum, end-users' amount is increasing day by day that leads to the requirement of enhanced BER values and bandwidth usage. Furthermore, in these modern times, new technologies are proved as research's crucial point that increases the wireless systems' capacities. A comparison of their BER performance charts is used to evaluate different combinations of multiple user receivers for determining performance under normal working conditions. In order to use the increased capacity rates, which can be achieved using a MIMO (multiple input and multiple output) configuration, MIMO systems are combined into system. MIMO with technology's complete dissemination through key attributes and components' investigation regarding single user communications. Various MIMO receivers' BER performance is also investigated. In terms of the required transmission factors, the modulation scheme is chosen depending on the situation. For example, 16QAM as well as 16PSK send more as compared to BPSK and QPSK symbols. A 2x2MIMO system, based on the simple ZF detector, As total symbols transmitted per second increases, the total errors also increases as well as thus, there exists requirement for higher SNR values. the need for higher SNRs to be used for greater order modulation is shown.

This particular paper provides a typical MIMO system. Compared to above-developed user systems, modern systems adopt a multi-user scenario. The present requirement for higher data rates resulted in the various techniques use like OFDM by the industry and the additional use of MIMO capabilities in WIFIs and CDMA.

Keywords- Successive Interference Cancellation (SIC), Minimum Mean square error (MMSE) Zero Forcing (ZF).

1. Introduction

The word "MIMO" is utilized to characterize system which utilize many antennas both at transmitters and at receivers to boost efficiency with the achievement of increased BERs. Smart antennas are used by this technology [1]. This is considered as the key innovations in wireless networking infrastructure of the third century and is studied globally. The signals are distributed over many pathways such that spatial variation is imposed on the data stream of the system. It is doubtful that all tracks will suffer from extreme fading, allowing the MIMO system to boost signal obligations in a wireless natural world. MIMO networks have been desirable developments in WiMAX (IEEE 802.16), WCDMA and, wireless LAN (IEEE 802.11n). This has been primarily because of the large improvement in data link range and data throughput, without either requiring increasing system bandwidth or transmitting power.

2. Implementation

2.1 MIMO System Capacity

In case of transmitter known channels, for increasing their capacities only “good channels” are used that means those channels under an unequal power distribution exhibits greatest gain.

$$C = \sum_1^k \log_2 \det \left[1 + \frac{P_i}{\sigma^2} \lambda_i \right] \text{ b/s/Hz} \quad (1)$$

Where, p_i represents the i^{th} pipe power.

2.2 MIMO Detectors

Few detectors are possible but most are non-linear and/or linear detectors' combinations. VBLAST, OSIC, MMSE and ZF devices are the primary detectors. New technology like Sphere Detectors have arisen that have Bit Error Rate with lower device complexity similar to ML approximation. These detectors are measured using various modulation and antenna setups. There are several different MIMO setups, but the approach followed and the observations taken in this study are seen as.

2.2.1 Zero Forcing (ZF) Detector

It is among the easiest available algorithm. This acts like a regular equalizer as the opposite of output of the frequency of channel is used in the received signal. In principle, such effective, however this is very susceptible for noise in realistic conditions since the opposite of the noise received to the signal is also true, as the response of channel involves a noise (3). Thus, for unnoisable signals, the ZF algorithm proves to be very successful, because ISI (Inter-Symbol Interference) can be removed through it but not suitable for a noisy signal because receiver's noise is increased by it [2].

Clearly, channel knowledge is important to use this algorithm on the receiver that enhances the system's complexity. The calculation, y of the obtained signal can therefore be written in respect of MIMO systems as:

$$\bar{y}_{ZF} = (H^H H)^{-1} H^H y = H^+ y \quad (2)$$

Where Moore-Penrose inverse is represented by H^+ that effectively is H matrix's pseudo-inverse.

Further analysis of the MIMO mechanism is possible (3). The data received by the two recipients was precisely generated by signals from both transmitter antennas. The obtained data from the first slot are y_1 and y_2 , where antennas are collected

$$y_1 = h_{1,1}x_1 + h_{1,2}x_2 + n_1 ; \quad y_1 = [h_{1,1}, h_{1,2}] \begin{pmatrix} x_1 \\ x_2 \end{pmatrix} + n_1 \quad (3)$$

$$y_2 = h_{2,1}x_1 + h_{2,2}x_2 + n_2 ; \quad y_2 = [h_{2,1}, h_{2,2}] \begin{pmatrix} x_1 \\ x_2 \end{pmatrix} + n_2 \quad (4)$$

$$\begin{bmatrix} y_1 \\ y_2 \end{bmatrix} = \begin{bmatrix} h_{1,1} & h_{1,2} \\ h_{2,1} & h_{2,2} \end{bmatrix} \begin{bmatrix} x_1 \\ x_2 \end{bmatrix} + \begin{bmatrix} n_1 \\ n_2 \end{bmatrix} \quad (5)$$

- x_1 : First antenna's transmitted symbol
- x_2 : Second antenna's transmitted symbol
- y_1 : First transmitter's evident received signal
- y_2 : Second transmitter's evident received signal
- $h_{1,1}$: Channel to first receive antenna from first transmitting antenna
- $h_{1,2}$: Channel to first receiving antenna from second transmitting antenna
- $h_{2,1}$: Channel to second receiving antenna from first transmitting antenna
- $h_{2,2}$: Channel to second receiving antenna from second transmitting antenna
- n_1 : First receiver noticed noise
- n_2 : Second receiver noticed noise

2.2.2 MMSE (Minimum Mean Squared Error) Detector

It's a better algorithm in comparison to the ZF under harsh situations. However, it does not remove ISI as well as the ZF algorithm; the MMSE estimate of the user [3].

$$\bar{y}_{MMSE} = (H^H H + (\sigma_n / \sigma_s)^2 I)^{-1} H^H y \quad (6)$$

where σ_s and σ_n represents the received signal power and noise power respectively and identity matrix is represented by I . The estimates of ZF and MMSE are found to be equal when $\sigma_s \gg \sigma_n$. Hence, it should be noted that when; the MMSE estimate equates to the ZF estimate. Thus, with the inclusion of a scaling factor, the 2x2 and 4x4 (17) Figures can be seen as similar to their ZF equivalents.

2.2.3 Successive Interference Cancellation

This algorithm initially detects, deletes and removes largest individual from the receivable signal. You should do so in two ways. Next, the soft information may be extracted from the obtained signal; it induces little to no error propagation, but for vulnerable users obtains a combined noise effect. Secondly, hard information may be extracted from the received signal which results in little to no noise but potential mistakes. Successive cancellation may be implemented in a circular fashion, at low convergence's cost and therefore higher complexity. MAI is decreased and the problem has evolved almost / far. The most effective and the most accurate cancellation is the cancellation of the best signal [4]. The SIC algorithm will then most likely suffer from error propagation, since the most effective cancellation is possible. The channel estimation at the recipient is also necessary [4]. The ZF or MMSE detector usually is used as pre-filtering for general SIC systems. For the pre-coding, detector utilizing ZF algorithm is investigated a iteration, that is the h values repeated for the r new value b

$$\begin{bmatrix} r_1 \\ r_2 \\ r_3 \\ r_4 \end{bmatrix} = \begin{bmatrix} h_{1,1} & h_{1,2} & h_{1,3} & h_{1,4} \\ 0 & 0 & 0 & 0 \\ h_{3,1} & h_{3,2} & h_{3,3} & h_{3,4} \\ h_{4,1} & h_{4,2} & h_{4,3} & h_{4,4} \end{bmatrix} \begin{bmatrix} x_1 \\ 0 \\ x_3 \\ x_4 \end{bmatrix} + \begin{bmatrix} n_1 \\ 0 \\ n_3 \\ n_4 \end{bmatrix}$$

2.2.4 OSIC (Ordered Successive Interference Cancellation) Algorithm

The detection algorithm used in this project is a non-linear equalization method. Co-Antenna Interference, CAI, is the key limitation in MIMO systems. The OSIC algorithm is readily used to prevent this disability. The incoming sub streams i.e., layers are identified by this algorithm recursively. It can identify the strongest layer first, that is to say, the highest SNS sub line, as well as after that delete it from the actual signal obtained so that the CAI can be correctly extracted. The process continues the

procedure for layers afterwards; the signal intensity is used for detecting and extracting from the initial signal all of the sub-streams / layers available [5].

2.2.3.1 Interference Cancellation

The interruption of the transmitter will occur when the mark is sensed. This interruption is extracted from the initial signal obtained as seen in the mathematical expression.

$$y' = y - h_1 \bar{y}_1 - \dots - h_{i-1} \bar{y}_{i-1} \quad (8)$$

where within the matrix H, respective i_{th} column is represented by h_i , y the received signal's estimated hard decisions are represented by y_i .

2.2.3.2 Interference Nulling

This method is very critical and typically takes a linear equalizer. This is a very important technique. This is performed using MMSE or ZF in existing systems [5]. The MMSE algorithm was utilized by this project.

2.2.3.3 Optimal Ordering

The design of the detection pattern of SIC systems is a significant source of error propagation. This will impair the overall BER output if sub-streams with high probability of error are observed and eliminated in the early stages of the detection from the reception system. This will allow the acquired error to propagate across the entire chain of identification. This error propagation is avoided by optimum ordering by allowing the line to be identified earlier in the obtained signal vector with the maximum SNR post detection. Therefore, immediately after the interruption zero's occurrence inside the OSIC decoder there is an optimum ordering mechanism.

The Benchmark for Space Time Systems is the OSIC algorithm of detection. This was originally developed by Bell Labs and is generally called BLAST [5]. The following is the various BLAST systems' forms divulgation.

2.3 BLAST Techniques in MIMO

Continuous need for increased capability, high data speeds as well as service efficiency have led QoS to realize the potential performance benefits that MIMO systems will offer. Many experiments have been carried out from MIMO's arrival in the mid-90s to now. This has culminated in the introduction of various MIMO systems. This project uses Bell Labs Layered Space-Time Structure (BLAST) [5], an early, acclaimed and revered MIMO high-quality architecture. The multiplexing design of the MIMO systems is used for this reason. Many single output inputs (SISO) channels are created in a rich dispersion setting. This is because of the logic that the decay of each of the space-multiplexed pathways is distinct. The BLAST architecture would then increase its capability in line with the amount of multiplexed spatial trails it creates. In various setups, the BLAST mechanism can be used. The mostly famous ones are: **TURBO-BLAST**; "vertical, **V-BLAST**; horizontal, **H-BLAST**; and diagonal, **D-BLAST**". Figure 2 represents a typical BLAST configuration as below.

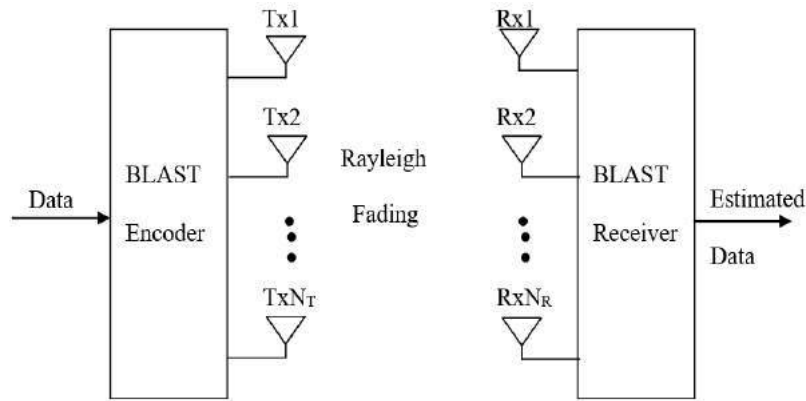


Figure 2: A Typical BLAST Architecture

Because of its features with substantially high spectral efficiencies, in 1995 Gerard J. Foschini developed the original BLAST system which became very attractive to telecommunications. By benefiting from the multiplexing nature of MIMO systems, it substantially increases the transmission capacity of the system. D-BLAST was the first BLAST design. It uses multiple elements of antenna both for transmission and reception of ends and a diagonally layered coding structure which spreads the coded blocks in space. This codec structure increases its power linearly with the number of antenna elements in a rich Rayleigh dispersing environment, which could increase to up to 90% of the theoretical capability limit of Shannon [5]. The architecture on the chip provides considerably high difficulty considering the appealing qualities of the D-BLAST. Consequently, various BLAST architectural designs have arisen. The big disparity in the way data is distributed is between these BLAST architectures. Next also mentioned some of these various architectures.

2.3.3 D-BLAST

It is very original proposed BLAST system as well as is now a benchmark on which BLAST systems are designed. Therefore, it is necessary to establish this architecture [5]. While the wireless MIMO communications systems are widely respected due to its large capacity; due to the high difficulty involved in their deployment there is a significant downside.

2. 1.1 D-BLAST Transmitter

Initially, data from a serial data source is de-multiplied into a parallel streams' set. After that the encoding as well as translation of these individual parallel streams is performed into specific signals. These sub-streams' resulting symbols are therefore diagonally distributed over time around the arrays of antenna. As seen in Figure 3, the spatial inter-leaver block can be used for courtesy of this task.

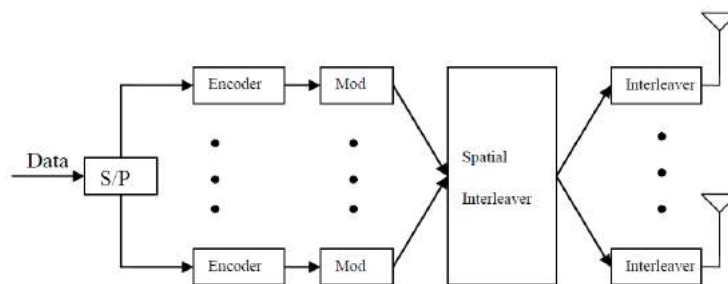


Figure 3: D-BLAST Transmitter

As defined in Figure 4, the symbols can be distributed over many antennas, thus showing

diversity of transmissions. It should be stressed that there are many more symbols for the transmitted frame than the numbers of antennas that will cause the frame to be very long and contribute to a serious loss of space time [5]. The encoding design of the receiver is responsible for this wastage. One device with four transmission antennas is defined in Fig. 3-4.

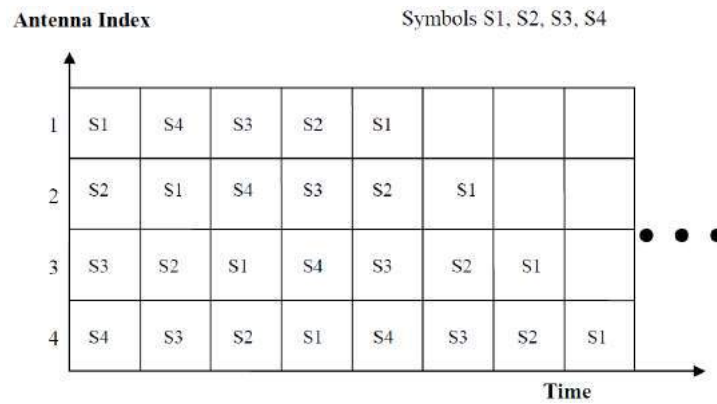


Figure 4: D-BLAST Diagonal Layering

The D-BLAST layer structure in Figure 4 is clearly shown. Figure 4 in the unoccupied time areas in the diagram, the resulting loss of time induced by its configuration is shown.

2.3.1.2 D-BLAST Receiver

It is performed by layer-by-layer detection of the incoming data which means initially, first layer is detected, which is discarded, then second one is detected, again it is discarded and thus the loop goes on with the following layers. This detection aspect adds to the loss of space time, when any layer must be first detected before the next layer. Figure 5 gives an example.

The first symbol of a sheet is always demodulated and observed, since it is always transmitted alone, with a great probability of close to zero errors. After that the following symbol is also demodulated and observed; the original layer observed would interfere with this symbol. We should then term it an interferer pain. The next symbol is demodulated and observed, but the two previous signals will interfere. We would then call it a symbol suffering from two interferers. The method continues for more symbols up to demodulation and identification for the whole layer [5]. The sub-stream of this layer will then be decoded after identification of the whole layer. The coding of channel linked with stream needs to basically lengthy to increase resistance to errors. Finally, it can be deleted from the obtained data after the whole layer has been decoded. In other words, the received data can be stripped off so that the next layer to be observed can be revealed. Then the process is repeated as shown above.

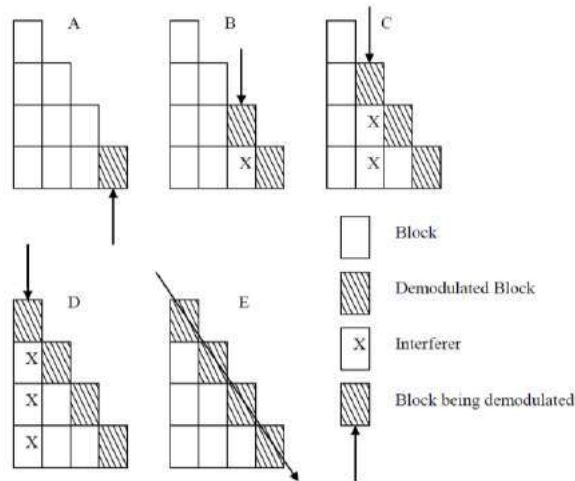


Figure 5: Decoding Process of D-BLAST

2.3.2 H-BLAST

The architecture is BLAST and was created as the solution to the D-BLAST architecture was found. The D-BLAST variant is simple and helps to reduce the D-BLAST architecture's computing complexity. This current strategy has a negative impact in terms to its predecessor's lack to transmission diversity. This is because the data is stored in a horizontal manner. While the H-BLAST systems suffer from this downside, the original D-BLAST system explicitly avoids the space-time waste problem.

The key variations in the BLAST architecture can be seen from the block diagrams demonstrating the system's re-organization. Figure 6 represents an H-BLAST transmitter. The D-BLAST transmitter's noticed Space Inter-leaver blocks are removed by the H-BLAST. Every sub-stream is then transmitted independently after they are encoded from one another. This ensures that a specific sub stream's channel coding is conveniently accessible and can also be delivered using the same antenna to remove the loss of space time problem faced by the previous D-BLAST design.

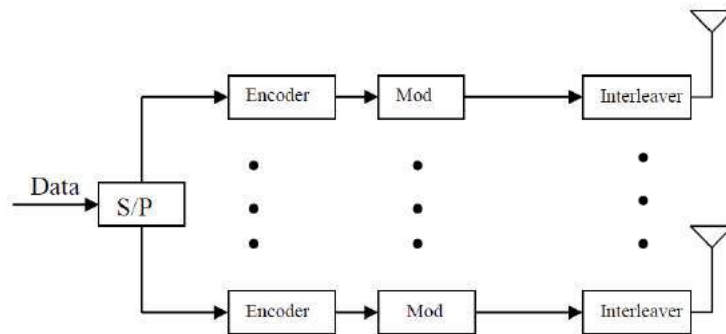


Figure 6: H-BLAST Transmitter

A traditional one-dimensional device may be the decoder, since the observed streams originate from the similar antennas.

2.3.3 Architecture of V-BLAST

The DataStream is separated in several sub-streams and the parallel sub-streams are distributed using a series of antennas. Both sub-streams are broadcast on the same frequency band that makes very effective use of the spectrum. With the exception of the type of encode used [5] the V-BLAST is identical to the H-BLAST. Because of the low complexity in comparison to other architectures types of

BLAST this recipient has been selected for the focal recipient used in this project. Paper 4 allows for optimal diffusion of VBLAST architecture.

2.3.4 Turbo-BLAST Architecture

It is considered as D-BLAST technique's version developed to reduce its complexities. In the transmitter structure this variant is the same as D-BLAST but varies in terms of the encoding used. The high spectral potential of the D-BLAST system was using a special series of codes without undue loss of space-time. The machine sophistication increases however, which defies the overall goal of making the D-BLAST machine easier to achieve.

2.3.5 BLAST Receivers

Compared to other MIMO systems, including Space Time Trellis Protocols, their complexity increases exponentially as many transmitting antennas are the primary appeal of using BLAST architectures. This renders these devices inefficient, which is why the BLAST architectures are advantageous [6]. In relation to the degree of sophistication involved in the operation, the various BLAST receivers often vary. The Maximum Likelihood (ML) approach is the best possible means of detection for optimum results, but this strategy is dynamic and therefore uses sub-optimal approaches. This involves primarily linear techniques of equalization as discussed in the last Paper. A modern method, called **Sphere Decoding** [8], has emerged in this modern century. Compared to the methods discussed above, this method achieves the highest results with much lower difficulty. Paper 5 explains this algorithm.

3 Simulations and Results

In the case that a $m \times m$ MIMO channel is available, the data will be sent in a single antenna-scenario chain, $x = [x_1, x_2, x_3, x_4 \dots, x_n]$, normally and data will require data slots for transmitting the data-stream. Here the " $m \times m$ MIMO detector" in which " m " antennas are available, data for regular transmission can be transmitted at " m " time the actual data rate. The " m " symbols can be included now with any system. This occurs. In a 2×2 scenario, for example, x_1, x_2 are sent to the first timepiece with x_3 from both transmit antennas, x_4 in the second timepiece and the like. The data rate is quadrupled in the case of 4×4 MIMO when four symbols are sent in any time frame. The other key theories that are used are:

- Flat Rayleigh fading is experienced by the channel
- At the receiver, from (2), the channel matrix, H is received

3.1 MIMO System's Capacity

The abovementioned potential in (7) were achieved by utilizing value decomposition theory [10] as well as tested for various transmitter and recipient combinations. A pattern in terms of the observed ability increase in a growing antennas number, as represented in Fig. 3-7, is automatically recognized.

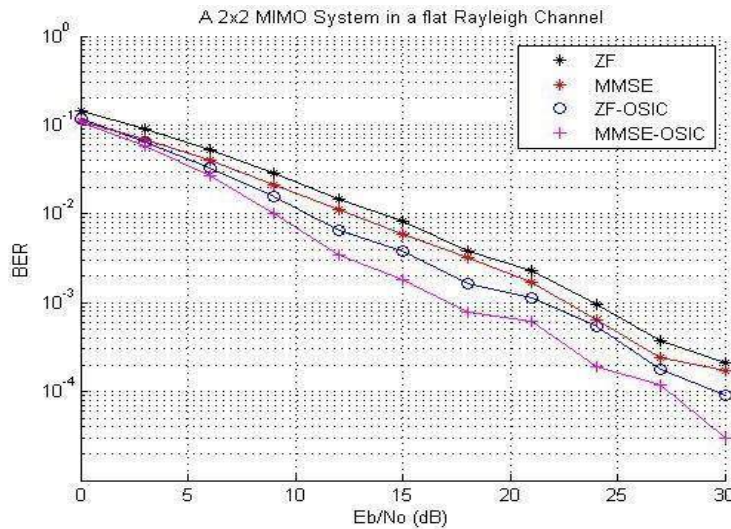


Figure 7: Various MIMO Configurations' Capacities

3.1.1 Implementation Utilizing Various Receiver Configuration

OSIC, MMSE and ZF varieties were tested. ZF-OSIC, MMSE-OSIC, MMSE and ZF are tested for receiver variants. A comparison message of n to 1×10^5 bits sent by a fading channel Flat Rayleigh. The modulated signals transmitted were divided in right streams that are antenna suitable. For example, the signal should be broken up in 4 different data streams with a 4×4 system, as well as a 2×2 system would need to stream, and so on. The BER output of two separate receptor combinations as seen in Fig. 3-8 as well as 3-9 respectively.

A spatial-multiplexing open-loop system [8] will be used for the incoming QPSK data signal [9] which refers to the assumption which receiver has "full channel information" without input to the transmitter. As a way of comparing output limits shown in Figure 10, a detector based on the highest probability algorithm is used to compare each detector combination with a 4×4 device. A zero-phase offset is believed to be the broadcast signal and the transmitter is used for grey scale coding. There was no need of spatial coding.

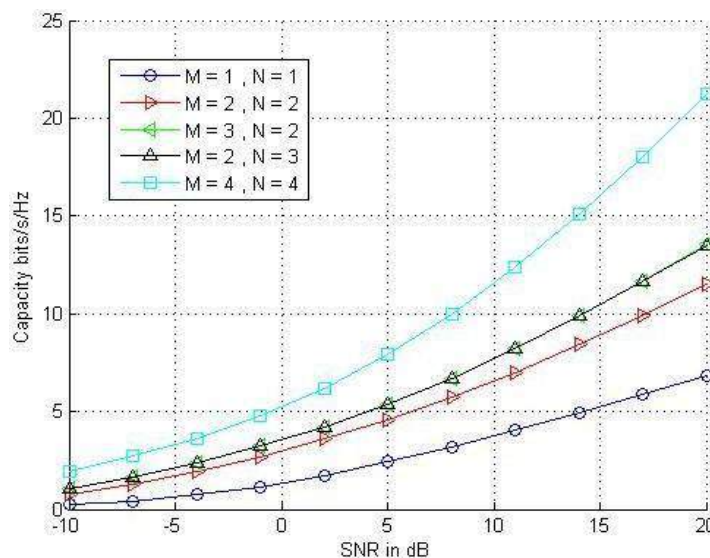


Figure 8: 2x2 MIMO with different Receive Architectures

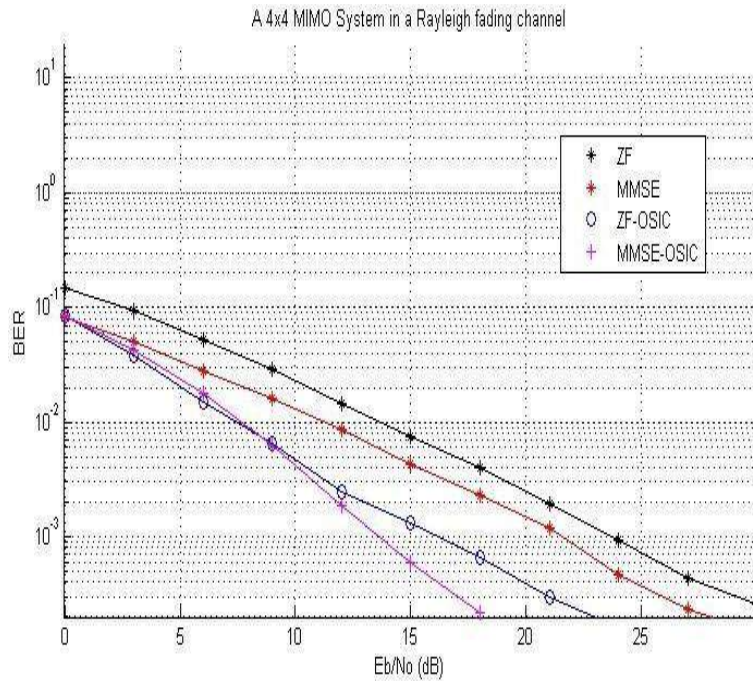


Figure 9: 4x4 MIMO with various Architecture of Receiver

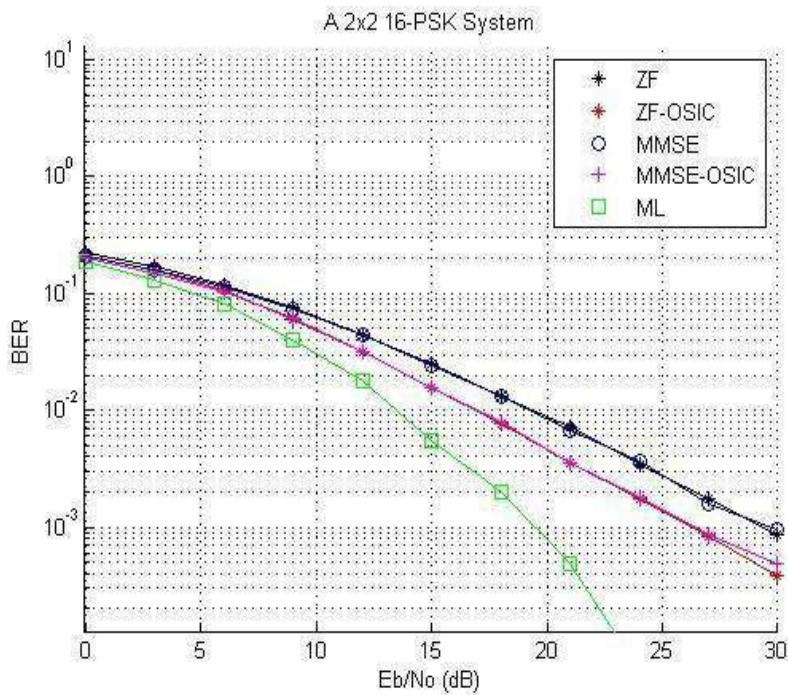


Figure 10: 16-PSK modulation in a 2x2 MIMO System

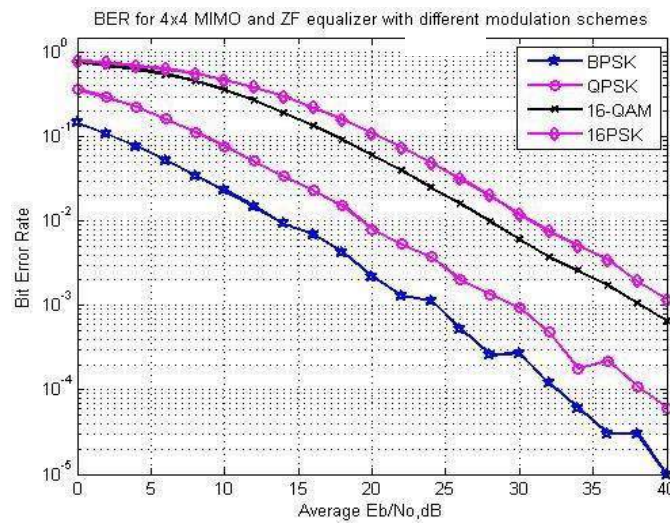


Figure 11: Various Modulation Scheme in A 4x4 MIMO

3.2 Utilizing various modulation scheme

Using a basic digital modulation application from QPSK the first MIMO system was introduced. The results of multiple modulation systems with the MIMO system have to be understood. In Figure 11, for a ZF receiver, the system was compared with the most commonly modulation systems like BPSK, QPSK, 16-PSK and 16-QAM.

4. Conclusion and Summary

As overall antennas number seen in Figure 3 thus grows the power of a standard MIMO device. The capabilities of an N-familial MIMO systems are similar as those of M-familiar MIMO systems.

Adding SIC to the MMSE as well as ZF MIMO receiver gives some changes to enhancements of BER value, but such minor change is important while ordering is performed with SIC according to fig. 3–8 as well as 3–9. It is noticed that the output BER images for MMSE-OSIC to ZF-OSIC are now comparable in Fig. 3-10, while 16PSK is being used, although BER values are still higher in MMSE-OSIC. Figure 10 indicates the achievable BER values by including an optimum ML decoder, which needs even more device complexities, is also used in an ML decoder. In terms of the required transmission factors, the modulation scheme is chosen depending on the situation. For example, 16QAM as well as 16PSK send more as compared to BPSK and QPSK symbols. A 2x2MIMO system, based on the simple ZF detector, was studied as represented Fig. 3-11. As total symbols transmitted per second increases, the total errors also increase as well as thus, there exists requirement for higher SNR values. Figure 11 also shows the need for higher SNRs to be used for greater order modulation.

The particular Paper provides a typical MIMO system’s brief introduction. Compared to above-developed user systems, modern modern systems adopt a multi-user scenario. The present requirement for higher data rates resulted in the various techniques use like OFDM by the industry and the additional use of MIMO capabilities in WIFIs and CDMA. The next Paper examines the integration of multi-user MIMO with receiving architectures.

References

- [1] F. B. Gross, *Smart Antennas for Wireless Communications with Matlab*, McGraw- Hill, 2005
- [2] A. Paulraj, R. Nabar and D. Gore, *Introduction to Space-Time Wireless Communications*, 2003, ISBN: 0-521-82615-2
- [3] S. Verdu, "Minimum Probability of Error for Asynchronous Gaussian Multiple Access Channels," *IEEE Trans. Info. Theory*, vol. IT-32, no.1, pp 85 -96, 1986.
- [4] R. Sinha, A. Yener, R.D. Yates; "Non-coherent Multi-user Communications: Multistage Detection and Selective Filtering", *EU RASIP Journal on Applied Signal Processing* 2002:12, 1415–1426
- [5] P. Wolniansky, G. J. Foschini, G. D. Golden, and R. A. Valenzuela, "VBLAST: An architecture for realizing very high data rates over the rich scattering wireless channel," *URSI International Symposium on Signals, Systems, and Electronics*, ISSUE 98, 1998.
- [6] T. Ito, X.Wang, Y. Kakura, M. Madihian and A. Ushirokawa, "Performance comparison of MF and MMSE combined iterative soft interference canceller and V- BLAST technique in MIMO/OFDM systems," in *Proc. IEEE Veh. Technol. Conf.*, 2003, vol. 1, pp. 488–492.
- [7] L. Brunel, "Optimum and sub-optimum multiuser detection based on sphere decoding for Multi-Carrier Code Division Multiple Access systems," *ICC'02*, New York, April 2002.
- [8] G. J. Foschini and Michael. J. Gans, "On limits of wireless communications in a fading environment when using multiple antennas". *Wireless Personal Communications*. January 1998.
- [9] M. F. Demirkol, M. A. Ingram, Z. Yun, "Feasibility of closed loop operation for MIMO links with MIMO interference," *Proc. of the IEEE Int'l Symp. on Antennas and Prop.*, Jun. 2004.
- [10] W. Abediseid and M.O. Damen, "On the Computational Complexity of Sphere Decoder for Lattice Space-Time Coded MIMO Channel", Department of Elect. & Comp. Engineering, University of Waterloo. March 2011.

MRI BRAIN TUMOR SEGMENTATION WITH SLIC AND CONVOLUTIONAL NEURAL NETWORKS

Panditi Sai Pavan¹, Yepuganti Karuna², Saladi Saritha³

^{1,2}School of Electronics and Communication Engineering, Vellore Institute of Technology, Vellore,

³Geethanjali College of Engineering and technology, Hyderabad, Telangana.

E-mail: saipavan.panditi@gmail.com¹, karun@vit.ac.in², saritha.saladi3188@gmail.com³

Received: May 2020 Revised and Accepted: August 2020

ABSTRACT: Brain tumor segmentation of MRI imagery is very essential in detecting and analyzing brain tumors. But it's a herculean task due to the presence of noise and intensity inhomogeneity in the MRI imagery. The main motive of this paper is to develop a useful and potent methodology for automatic brain tumor segmentation of MRI images that will aid the radiologists for better diagnosis. The proposed methodology involves two processes, first process is pre-segmentation of the MRI image using SLIC superpixel algorithm and second segmentation process is based on CNN. The proposed method is validated for both real-time datasets obtained from a radiologist and datasets from an online database. The results are shown in terms of the Dice index (DICE) and the Jaccard index (JACCARD). The evaluation of performance of the proposed methodology shows that it achieves higher average values of DICE and JACCARD, which indicates good segmentation performance and better accuracy compared to existing methods.

KEYWORDS: Brain tumor, CNN, MRI, Pre-segmentation, Region of Interest (ROI), Simple Linear Iterative Clustering (SLIC)

I. INTRODUCTION

Day-by-day there is a huge increase in the cases of brain tumors being reported around the globe. They have a very high mortality rate [1]. The growth rate of the brain tumor can vary significantly. So measuring the growth rate and identification of location of the brain tumor determines the affect it has on the brain and the central nervous system. Imaging tests offer useful details such as type, location, size and stage of the tumor, which helps doctor evaluate the brain tumor and plan treatment. There are many medical imaging tests but Magnetic resonance imaging (MRI) is the most widely used imaging test to provide images of brain cancer and help diagnose brain tumors [2].

MRI provides thorough images of the body with the help of radio waves and magnetic fields. MR imaging is the most preferred because of satisfactory soft tissue contrast and wide availability. Accurate brain tumor segmentation of MR imagery is very much essential for surgical scheduling, and treatment evaluation. Manual brain tumor segmentation of MR imagery by a radiologist is strenuous and prone to human errors. Manual segmentation also restricts the usage of accurate quantitative measures in medical practice. Therefore, it is very difficult for radiologists to consolidate the related information about brain tumor acquired from MRI imagery. So automatic segmentation methods, which offer precise and consistent measurements of the tumors, are required [3]. There exist different preprocessing methods in MRI brain images like enhancement [4], denoising [5] and with wavelets and PCA [6]. Precise automatic brain tumor segmentation is very essential for assessment of brain tissues.

Over the years, several research works have been conducted on segmentation of brain tumor in MR imagery. Wang, J, et. al. [7] and Anjali, W, et. al [8] has given a summary of works for segmentation of brain tumor in MR imagery. They found that the major challenges would be the accuracy and requirement of great computing power. There are also various different automatic segmentation approaches [9-14]. Automatic approaches using fuzzy c-means have been examined for segmentation of brain tumor [15-19]. Automatic approaches are broadly divided as supervised and unsupervised approaches. Supervised learning approaches for segmentation of brain tumor are examined [20, 21]. C. Ouchicha, et. al. [22] and B. Srinivas, et. al. [23] provides a detailed overview of unsupervised approaches for segmentation of brain tumors. Over the years, owing to the swift evolution of computing performance, numerous deep learning techniques for segmentation of brain tumors have been examined [24,33]. They have shown success in segmentation of brain tumors. These methods obtain complicated and intricate features directly from the data. Amongst the deep learning methodologies, the methodologies based on CNN have attained superior performance for brain tumor segmentation [25]. In the recent years, CNN has made huge progress in the field of computer vision [26]. This paper, motivated by the

recent developments on CNN, is our attempt to develop a useful and potent methodology for automatic segmentation of brain tumors, which will aid the radiologists. We propose a method using CNN with high segmentation performance and great memory efficiency. The proposed method is implemented with real time datasets of MR imagery provided by a consultant radiologist. The proposed methodology comprises of two processes. The first process is pre-segmentation of the image using SLIC superpixel algorithm [27]. The second process is the actual segmentation method which is to further segment the outcome of pre-segmentation based on CNN [28]. Hence, final result is generated.

This paper is arranged as follows. In Section 2, proposed methodology is shown. Results and discussion are presented in Section 3. In Section 4, the conclusion is described.

II. METHODOLOGY

The proposed methodology contains two key processes. They are: 1) Pre-segmentation using SLIC super-pixel algorithm for brain tumor segmentation and 2) Segmentation: classification via CNN algorithm. The process flow of proposed methodology is presented in figure 1.

2.1. Pre-Segmentation

Brain tumors are generally found in varying sizes and uneven shapes, and are very complicated to differentiate from other brain tissues. Also directly using CNN to segment the MRI images is very complex to evaluate. Due to these factors, the pre-segmentation step is performed to make the MRI images suitable for segmentation and to increase the segmentation performance. This way the segmentation range is also constricted.

SLIC superpixel algorithm is used in the pre-segmentation of MRI images [27]. At first the input image is partitioned into several equal sized blocks. Then, computation and segmentation of superpixels are performed. At last, the size of the image is scaled down to Region of Interest (ROI) which is smaller than the original image. Due to the identification of ROI, the non-tumorous part in the given image is eliminated from the process of tumor segmentation and tumor part is obtained.

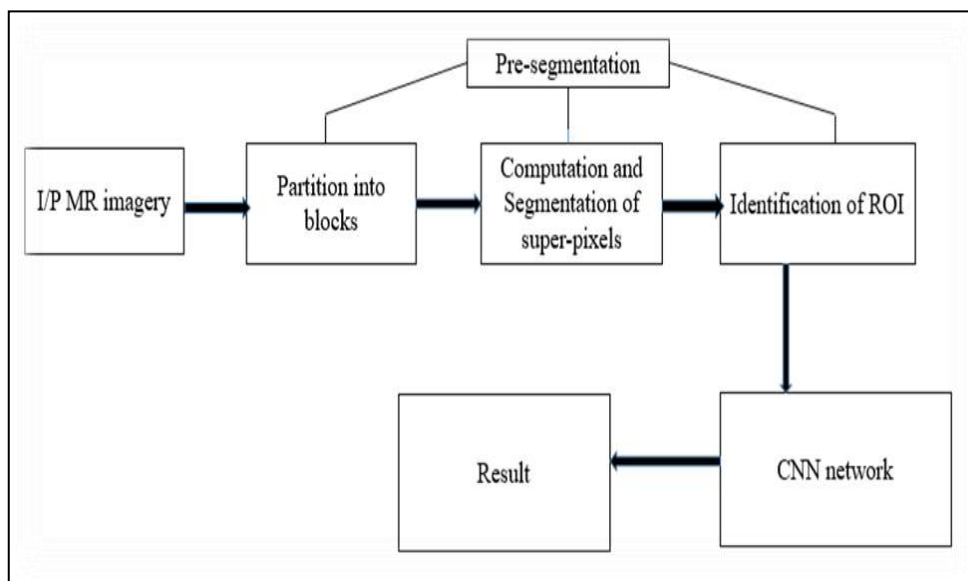


Figure 1. Process Flow of Proposed Methodology

2.2. Convolutional Neural Network

CNN obtains the image features of various different layers by convolution operation [28]. The important features of CNN are that the weights of the convolutional kernels are shared and connection is thinly scattered. This way, CNN is easier to train and more resistant to over-fitting. Figure 2 presents the process flow in the CNN. The following are the important steps in the CNN.

1) Initialization and pooling: It is used to obtain convergence. In pooling, the nearby spatial features in the feature maps are integrated. Convolution is performed in this step.

$$S(x, y) = J(x, y) * K(x, y) \tag{1}$$

here, J represents the input image and K represents convolution kernel.

2) Activation Function: It is used for non-linear transformation of data.

$$f(x) = \max(0, x) \quad (2)$$

3) Regularization: In this step, the over-fitting problem is diminished using dropout in the convolutional layers.

4) Data Enhancement: This step is used to restore the original features of the input image such as size and resolution.

5) Training: The input images are trained using Alexnet to transform into models acceptable for brain tumor segmentation.

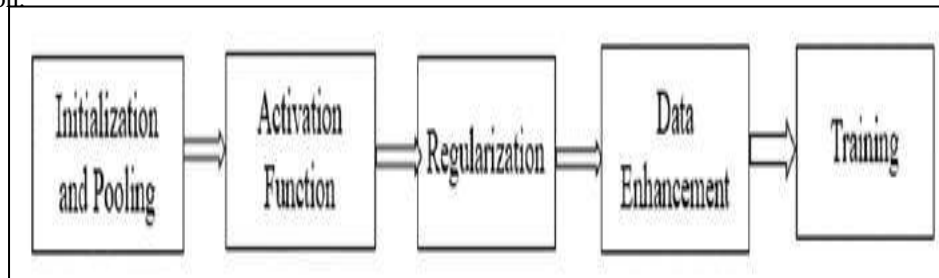


Figure 2. Process Flow of CNN

III. RESULTS AND DISCUSSION

The real time MRI datasets of three patients are obtained from a consultant radiologist at Kanta's Sanjeevini Psychiatry and Rehabilitation Center, Guntur. The segmentation consists of two stages: pre-segmentation using SLIC superpixel algorithm and classification based on CNN. The efficiency of the proposed methodology is measured in terms of two metrics, Dice index [30] and Jaccard index [31].

3.1. Performance Metrics

The efficiency of the proposed methodology is measured in terms two performance metrics, Dice index and Jaccard index.

A) Dice index is a mathematical tool which is used to calculate the similarity between two sets of data.

$$D(K, L) = 2 * (|K \cap L|) / (|K| + |L|) \quad (3)$$

here, K and L represent two images.

B) Jaccard index is also a mathematical tool used to measure the similarity between two sets of data.

$$J(K, L) = |K \cap L| / |K \cup L| \quad (4)$$

here, K and L represent two images.

3.2. Results

Results of the proposed methodology are showcased in this section. The proposed methodology is validated on two different datasets, A) Datasets of five patients from Radiopaedia [32] and B) Real time datasets of three patients from a consultant radiologist.

A) The experimental results of the proposed method for datasets of five patients are demonstrated in this section. In figure 3, all the steps involved in the proposed method for five different datasets are presented [32]. First column in figure 3 shows the step 1 where MRI image is taken input. Column 2 shows the input image is partitioned into a number of equal sized blocks. Column 3 represents ROI which is identified and non-tumorous part is eliminated. Column 4 is the final result of the proposed method is shown after further segmentation using CNN. The ground truth images are obtained with the help of radiologist shown in column 5 in figure 3, shown for datasets I, II, III, IV and V respectively.

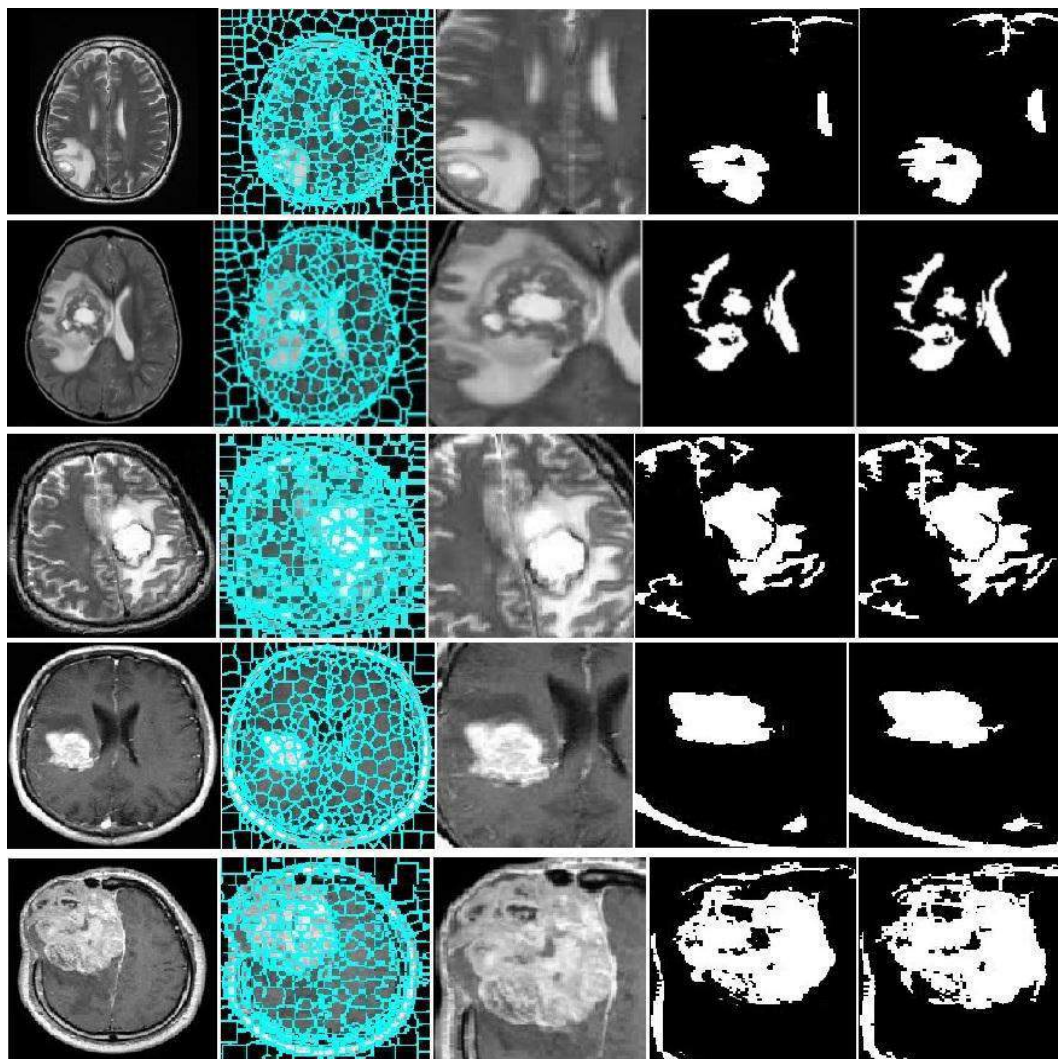


Figure 3. Segmentation Results of the Online Datasets of 5 Input Images from Radiopaedia. Column 1: Input MRI Image, Column 2: Block Partition, Column 3: Region of Interest, Column 4: Results Obtained with the Proposed Method, Column 5: Ground Truth Images.

- B) In this section, results of the proposed method for real time datasets of three patients are presented. In figure 4, row 1 demonstrates all the steps involved in the proposed method for patient A. Column 1 in figure 4 shows the step 1 where input MRI image is taken. Column 2 represents the input image that is partitioned into a number of equal sized blocks. Column 3 represents the ROI that is identified and non-tumorous part is eliminated. The final result of the proposed method after further segmentation using CNN is shown in column 4 in figure 4. The ground truth images obtained from the consultant radiologist are shown in column 5 in figure 4. Similar process is demonstrated in row 2 and row 3 in figure 4 respectively.

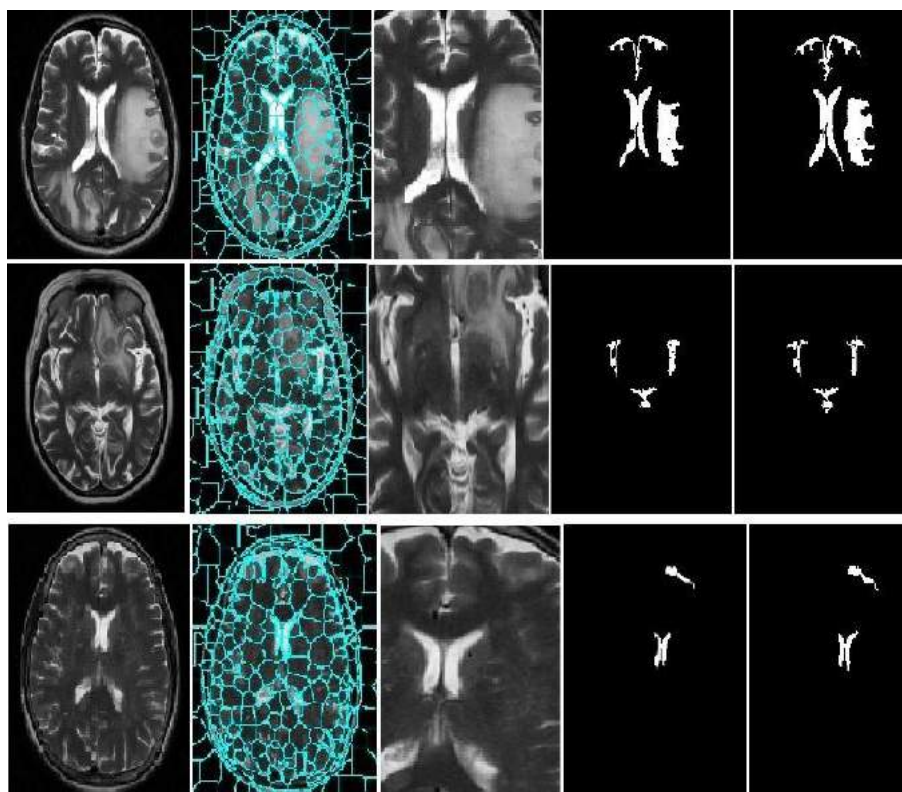


Figure 4. Segmentation Results of Real Time Data Obtained from Radiologist. Column 1: Input MRI Image, Column 2: Block Partition, Column 3: Region of Interest, Column 4: Results Obtained with the Proposed Method, Column 5: Ground Truth Images.

3.3. Evaluation and Comparison of Performance

In this section, performance evaluation of the proposed methodology using metrics DICE and JACCARD is presented. Performance comparison of the proposed methodology with existing brain tumor segmentation methodology [29] is shown in Table 1 and Table 2.

Numerical results of performance evaluation of proposed methodology for datasets of five patients are shown in Table 1. From table 1, it can be observed that for the proposed method the segmentation performance using DICE and JACCARD are in a ranging of 89% - 96% and 91% - 97%, respectively and the average values of segmentation performance using DICE and JACCARD are 93% and 94%, respectively. As shown in table 1, for the existing methodology the segmentation performance is in a ranging of 78% - 87% and 80% - 86% using DICE and JACCARD, respectively. From table 1, the average values of segmentation performance using DICE and JACCARD are 83% and 82%, respectively for the existing methodology.

Table 1. Evaluation of Performance of the Proposed Methodology for Datasets from Online Database Using DICE and JACCARD index.

DATASET	DICE		JACCARD	
	PROPOSED	EXISTING	PROPOSED	EXISTING
I	0.93	0.84	0.94	0.82
II	0.92	0.78	0.93	0.80
III	0.89	0.82	0.91	0.82

IV	0.96	0.85	0.97	0.86
V	0.95	0.87	0.92	0.84

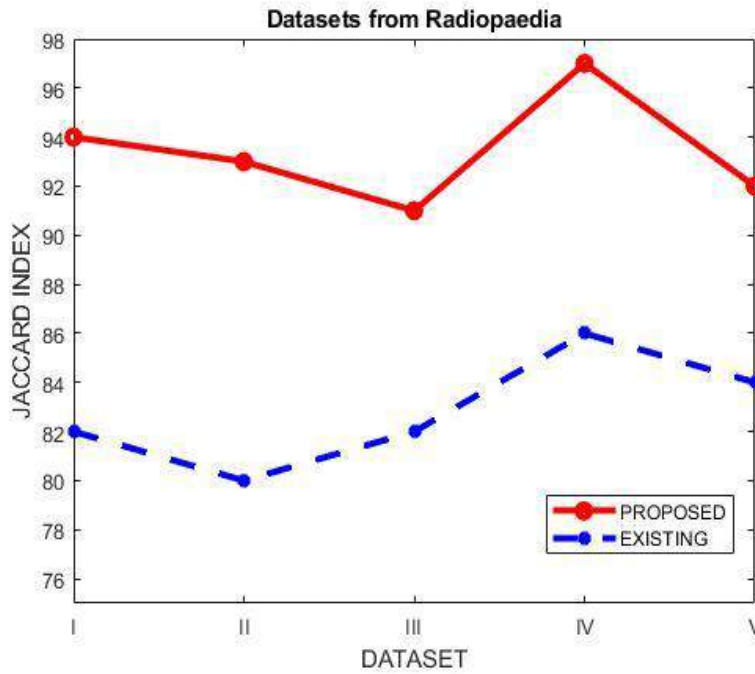


Figure 5. Performance Comparison of Jaccard Index of images from online database.

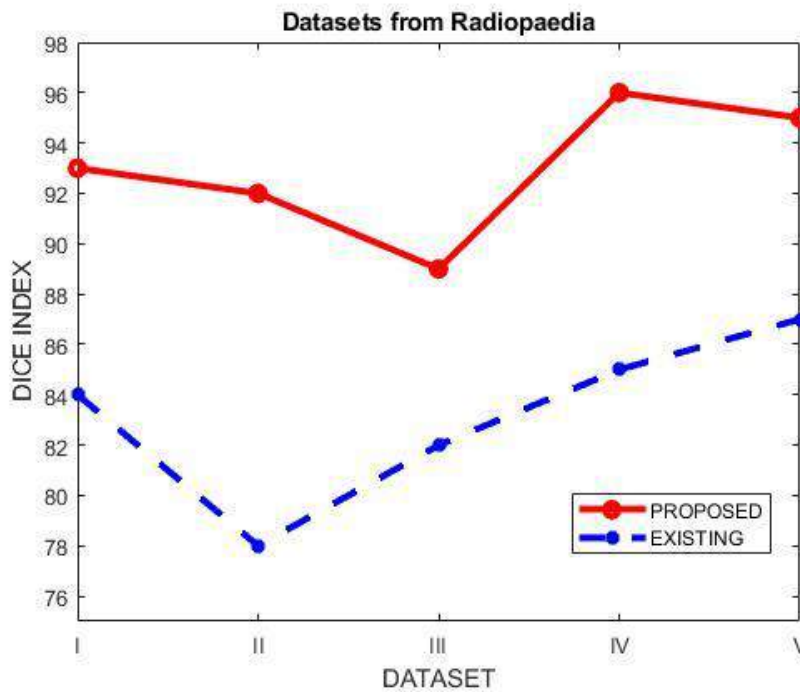


Figure 6. Performance Comparison of Dice Index of images from online database.

Numerical results of segmentation performance of proposed methodology for real time datasets of three patients are presented in table 2. As shown in table 2, the segmentation performance using DICE and JACCARD for proposed methodology is in a ranging of 90% -94 and 91% - 95%, respectively and for the existing method is in

a ranging of 82% - 85% and 82% - 86%, respectively. The average values of segmentation performance using JACCARD and DICE are 93% and 92%, respectively for the proposed methodology and 85% and 84%, respectively for the existing methodology as shown in figure 7 and figure 8.

Table 2. Evaluation of Performance of the Proposed Methodology for Real Time Datasets of Three Patients Using DICE and JACCARD index.

PATIENT	DICE		JACCARD	
	PROPOSED	EXISTING	PROPOSED	EXISTING
A	0.91	0.85	0.93	0.86
B	0.94	0.84	0.91	0.82
C	0.90	0.82	0.95	0.86

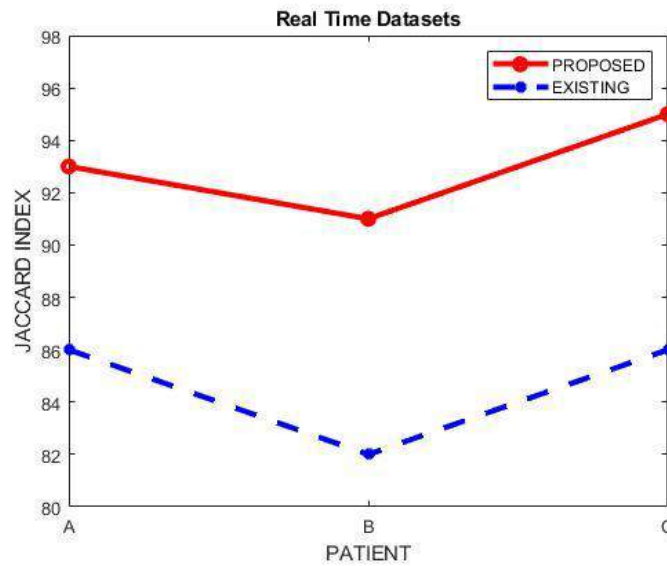


Figure 7. Performance Comparison of Jaccard Index of Real Time image Datasets from a Radiologist.

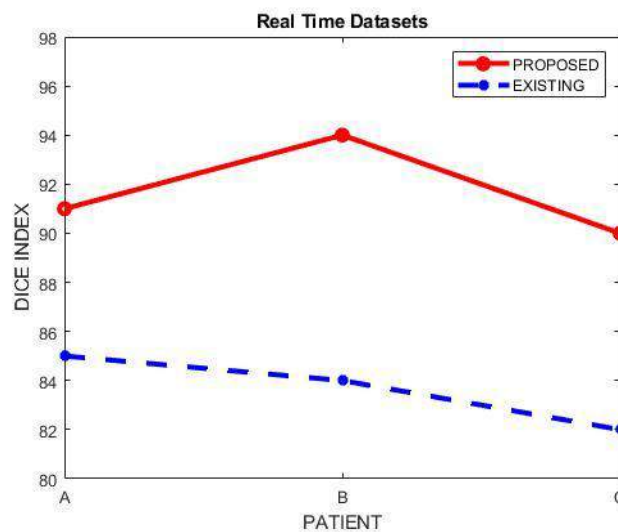


Figure 8. Performance Comparison of Dice Index of Real Time image Datasets from a Radiologist.

IV. CONCLUSION

The main motive is to develop a useful methodology for automatic segmentation of brain tumors, which assists radiologists in a better way for diagnosis. The proposed methodology comprises of two stages. First stage is pre-segmentation of the MRI image based on SLIC superpixel algorithm and second stage is to further segment the MRI image based on CNN. The evaluation of performance of the proposed methodology indicates that it has an impressive segmentation performance and good accuracy with DICE and JACCARD being 92% and 93% respectively for real time datasets obtained from a consultant radiologist. This helps the radiologist in diagnosis of the disease in short span of time to save the life a human.

Acknowledgments

We thank Dr.Rajya Lakshmi Marisetty MDRD, consultant radiologist, Guntur for providing real time MRI imagery and valuable suggestions to improve the results with more accuracy.

V. REFERENCES

- [1]. Simpson, Victoria. "Cancers with the Highest Mortality Rates." WorldAtlas, May. 18, 2020, worldatlas.com/articles/cancers-with-the-highest-mortality-rates.html.
- [2]. Saritha, Saladi. "Development of Hybrid Algorithms for Tissue and Tumor Segmentation of Magnetic Resonance Brain Images." (2018).
- [3]. Saritha, Saladi, and N. Amutha Prabha. "A comprehensive review: Segmentation of MRI images—brain tumor." *International Journal of Imaging Systems and Technology* 26, no. 4 (2016): 295-304.
- [4]. Suryavamsi, R. V., L. Sai Thejaswin Reddy, Saritha Saladi, and Yepuganti Karuna. "Comparative Analysis of Various Enhancement Methods for Astrocytoma MRI Images." In 2018 International Conference on Communication and Signal Processing (ICCSP), pp. 0812-0816. IEEE, 2018.
- [5]. Saladi, Saritha, and N. Amutha Prabha. "Analysis of denoising filters on MRI brain images." *International Journal of Imaging Systems and Technology* 27, no. 3 (2017): 201-208.
- [6]. Shridhar, Sameera, Yepuganti Karuna, Saritha Saladi, and Ramachandra Reddy. "Denoising of ECG signals using wavelet transform and principal component analysis." Available at SSRN 3356368 (2019).
- [7]. Wang, J., Liu, T.: A survey of MRI-based brain tumor segmentation methods. *Tsinghua Sci. Technol.* 19(6), 578–595 (2014).
- [8]. Anjali Wadhwa, Anuj Bhardwaj, Vivek Singh Verma, A review on brain tumor segmentation of MRI images, *Magnetic Resonance Imaging*, Volume 61, 2019, Pages 247-259, ISSN 0730-725X.
- A. Monalisa, D. Swathi, Y. Karuna and S. Saladi, "Robust Intuitionistic Fuzzy c-Means Clustering Algorithm for Brain Image Segmentation," 2018 International Conference on Communication and Signal Processing (ICCSP), Chennai, 2018, pp. 0781-0785.
- [9]. V. Zeljkovic et al., "Automatic brain tumor detection and segmentation in MR images," 2014 Pan American Health Care Exchanges (PAHCE), Brasilia, 2014, pp. 1-1.
- [10]. Agrawal, Ankur, Varun Kumar Kouda, Yepuganti Karuna, and Saladi Saritha. "Automated Classification of Brain Images Using DWT and Biogeography-Based Optimisation." In 2018 2nd International Conference on Trends in Electronics and Informatics (ICOEI), pp. 204-209. IEEE, 2018.
- [11]. Raghavendra, RV Sai, Yepuganti Karuna, and Saritha Saladi. "MS Lesion Segmentation for Single and Multichannel MRI Images Using MICO Technique." In 2018 International Conference on Communication and Signal Processing (ICCSP), pp. 0807-0811. IEEE, 2018.
- [12]. Karuna, Yepuganti, Saritha Saladi, and Budhaditya Bhattacharyya. "Brain Tissue Classification using PCA with Hybrid Clustering Algorithms." *International Journal of Engineering & Technology* 7, no. 2.24 (2018): 536-540.
- [13]. Krishna, Garrepally Gopi, S. Ashwin, Yepuganti Karuna, and Saritha Saladi. "Brain MR Image Classification Using DWT and Random Forest with AdaBoostM1 Classifier." In 2018 International Conference on Communication and Signal Processing (ICCSP), pp. 0820-0824. IEEE, 2018.
- [14]. C. P. S. Raj and R. Shreeja, "Automatic brain tumor tissue detection in T-1 weighted MRI," 2017 International Conference on Innovations in Information, Embedded and Communication Systems (ICIIECS), Coimbatore, 2017, pp. 1-4.
- [15]. Karuna, Yepuganti, Saritha Saladi, Pramodh Konduru, and G. Ramachandra Reddy. "Magnetic Resonance Brain Images Individual Recognition with PCA." *International Journal of Innovative Technology and Exploring Engineering (IJITEE)*, Volume-8, Issue-4S February, 2019:157-161.
- [16]. Saladi, Saritha, and N. Amutha Prabha. "MRI brain segmentation in combination of clustering methods with Markov random field." *International Journal of Imaging Systems and Technology* 28, no. 3 (2018): 207-216.

- [17]. Karuna, Yepuganti, Saritha Saladi, and Budhaditya Bhattacharyya. "Brain Tissue Classification using PCA with Hybrid Clustering Algorithms." *International Journal of Engineering & Technology* 7, no. 2.24 (2018): 536-540.
- [18]. Saladi Saritha, N. Amutha Prabha, "A Novel Fuzzy Factor for MRI Brain Image Segmentation using Intuitionistic Fuzzy Kernel Clustering Approach." *Journal of Advanced Research in Dynamical and Control Systems* 2018:10-Special Issue-02:639-652.
- [19]. M. Goetz et al., "DALSA: Domain Adaptation for Supervised Learning From Sparsely Annotated MR Images," in *IEEE Transactions on Medical Imaging*, vol. 35, no. 1, pp. 184-196, Jan. 2016.
- [20]. S. Pavlov, A. Artemov, M. Sharaev, A. Bernstein and E. Burnaev, "Weakly Supervised Fine Tuning Approach for Brain Tumor Segmentation Problem," 2019 18th IEEE International Conference On Machine Learning And Applications (ICMLA), Boca Raton, FL, USA, 2019, pp. 1600-1605.
- [21]. C. Ouchicha, O. Ammor and M. Meknassi, "Unsupervised Brain Tumor Segmentation from Magnetic Resonance Images," 2019 International Conference on Wireless Networks and Mobile Communications (WINCOM), Fez, Morocco, 2019, pp. 1-5.
- [22]. B. Srinivas and G. S. Rao, "Unsupervised learning algorithms for MRI brain tumor segmentation," 2018 Conference on Signal Processing and Communication Engineering Systems (SPACES), Vijayawada, 2018, pp. 181-184.
- [23]. S. Somasundaram and R. Gobinath, "Current Trends on Deep Learning Models for Brain Tumor Segmentation and Detection – A Review," 2019 International Conference on Machine Learning, Big Data, Cloud and Parallel Computing (COMITCon), Faridabad, India, 2019, pp. 217-221.
- [24]. Jose Dolz, Christian Desrosiers, Li Wang, Jing Yuan, Dinggang Shen, Ismail Ben Ayed, Deep CNN ensembles and suggestive annotations for infant brain MRI segmentation, *Computerized Medical Imaging and Graphics*, Volume 79, 2020, 101660, ISSN 0895-6111, (<http://www.sciencedirect.com/science/article/pii/S0895611119300771>).
- [25]. T. Nishio and T. Nishida, "Specific Object Recognition and Tracking by Cascade Connection of Different Types of CNNs and a Time-series Filter," 2018 International Symposium on Intelligent Signal Processing and Communication Systems (ISPACS), Ishigaki, Okinawa, Japan, 2018, pp. 7-11.
- [26]. L. Zhang, C. Han and Y. Cheng, "Improved SLIC superpixel generation algorithm and its application in polarimetric SAR images classification," 2017 IEEE International Geoscience and Remote Sensing Symposium (IGARSS), Fort Worth, TX, 2017, pp. 4578-4581.
- [27]. R. M. Prakash and R. S. S. Kumari, "Classification of MR Brain Images for Detection of Tumor with Transfer Learning from Pre-trained CNN Models," 2019 International Conference on Wireless Communications Signal Processing and Networking (WiSPNET), Chennai, India, 2019, pp. 508-511.
- [28]. Silvana Castillo L, Alexandra Daza L, Carlos Rivera L, et al. Volumetric multimodality neural network for brain tumor segmentation[C]// Society of Photo-optical Instrumentation Engineers. 2017.
- [29]. C. Stephanie and R. Sarno, "Detecting Business Process Anomaly Using Graph Similarity Based on Dice Coefficient, Vertex Ranking and Spearman Method," 2018 International Seminar on Application for Technology of Information and Communication, Semarang, 2018, pp. 171-176.
- [30]. Y. Wang and Y. Li, "Deep Web Entity Identification Method Based on Improved Jaccard Coefficients," 2009 International Conference on Research Challenges in Computer Science, Shanghai, 2009, pp. 112-115.
- [31]. <https://radiopaedia.org/>
- [32]. Yepuganti, Karuna, Saritha Saladi, and C. V. Narasimhulu. "Segmentation of tumor using PCA based modified fuzzy C means algorithms on MR brain images." *International Journal of Imaging Systems and Technology* (2020).

Segmentation of tumor using PCA based modified fuzzy C means algorithms on MR brain images

Karuna Yepuganti¹  | Saritha Saladi²  | C. V. Narasimhulu²

¹School of Electronics Engineering,
Vellore Institute of Technology, Vellore,
India

²Geethanjali College of Engineering and
Technology, Hyderabad, Telangana, India

Correspondence

Email: saritha.saladi3188@gmail.com

Abstract

In the field of medical sciences, automatic detection of tumor using magnetic resonance (MR) brain images is a major research area. The goal of the proposed work is to identify the tumors in MR images using segmentation methods and to locate the affected regions of the brain more accurately. Medical images have vast information but they are difficult to examine with lesser computational time. An innovative process is proposed to extract tumor cells using the discrete wavelet transform (DWT). After extracting features with DWT feature reduction is carried out with the principal component analysis (PCA). Modified fuzzy C means (MFCM) technique is used for segmenting the tumor cells. The efficiency of the proposed method to identify different abnormalities in real MR images for intracranial neoplasm detection, tuberculoma, and bilateral thalamic fungal granulomas identification is tested. The results obtained are shown in-terms of Accuracy, Dice Similarity Index (DSI), and Jaccard Index (JI) measures. The performance of the proposed method is tested in terms of performance measures like Accuracy, DSI, and JI. These results are compared with the conventional fuzzy C means (FCM) method.

KEYWORDS

brain tumor, DWT, feature extraction, fuzzy C means and MRI

1 | INTRODUCTION

The objective of the medical image processing techniques is to identify images or objects with tranquil visually. Medical images are used as an evidence for the physical attributes. MRI images are used to identify tumors in brain. The most significant aspect is segmenting the tumors to locate the actual position and regions of the abnormal tissues in MRI images. The tumors can have variability in shape, size, and can appear at any position in brain with diverse intensities. They are classified into two categories:

- Benign tumors are consistent compositions that do not enclose cancer cells. They are simple to monitor by

radiological apparatus. These tumors may eternally develop back again.

- Malignant tumors are inconsistent compositions and they comprise of cancer cells. They have to be treated by the combination of radiotherapy and chemotherapy. They are life frightening.

In this article, we have concentrated on three types of diseases:

1. *The intracranial neoplasm disease*: It is formed when abnormal cells mount up in the interior lobe of the brain, formally named as a tumor. These cells reproduce in an abandoned way and destruct the brain tissues.

2. *The bilateral thalamic fungal granulomas*: This results from *Mycobacterium tuberculosis* as a focal mass and considered as form of morphological tuberculosis disorder.
3. *Tuberculoma*: It is the generally found tumor as blood clot in the brain.

Extraction of the tumor region involves the segmentation of brain into normal cells and tumor cells. The proposed classification uses the feature extraction, segmentation and feature reduction method to determine the tumor part in the MR images. MR imaging is a low risk imaging technique that provides anatomical structure of the brain. Radio waves and magnetic field are employed to get high quality images. The magnetization and radio waves used in MRI scanners are not harmful as compared to X-rays which use ionized radiation. MRI gives clear image of soft brain tissues like gray matter, white matter, and cerebro spinal fluid. There are many other modalities like Positron Emission Tomography scan, Computed Tomography scan, Single-Photon Emission Computed Tomography scan, and Nuclear Magnetic Resonance (NMR) scan. But MRI provides superior contrast of brain tissues. Earlier numerous manual methods were used for diagnosis which are time consuming and are not accurate enough because of large imaging datasets.

Every year, the expected number of brain tumor cases in India is around 64 349 where malignant affected people are 23 828 and people affected with benign tumor are 40 521 and children are about 5782. The estimated deaths recognized are merely 18 124. The mean of deaths per year in India is 58 963 computed between 2008 and 2018. Many approaches are developed to identify the tumor using segmentation and detection methods.¹ In References 2, 3 the thresholding method is proposed using cluster organization from the histograms. The knowledge-based FCM approach for MR images is proposed to detect glioma.⁴ The multi-featured clustering and confirmation theory on multimodal tumor segmentation is proposed in Reference 5. The two-phase FCM is pooled with knowledge based process for detection of tumors in low contrast images is discussed in Reference 6 Effective tumor segmentation is proposed with watershed along with thresholding and the morphological operators are used to locate the tumor in brain images.⁷ The adaptive local thresholding is used with kernel fuzzy clustering to overcome the limitations in conventional FCM for unequal sized clusters in images.⁸ The article is organized as follows. The general tumor extraction methods are discussed in Section 2. The proposed methodology is described in Section 3. Section 4 presents the results and discussion. The conclusion part is presented in Section 5.

2 | MATERIALS AND METHODS

This section presents the techniques to extract tumor cells in the MRI images.

2.1 | Feature extraction with wavelets

To extract features from MRI brain images, wavelet transform (WT) is used. The Discrete WT is extensively utilized to extract features where dissimilar frequencies are observed with dissimilar determinations.⁹ In this method, DWT is employed to extract tumor features from MRI brain images. These features are identified in the form of DWT coefficients.^{10,11} Approximation coefficients are low frequency components and many researchers work with low frequency components with smaller datasets. The level-2 Haar 2D DWT is used for the extraction of features and to form a feature matrix. MRI brain images are applied to series of low pass filters (LPFs) and high pass filters (HPFs). The output of HPF and LPF belongs to detail and approximation coefficients, respectively.^{12,13} DWT is used as a denoising filter to eliminate noise in images.¹⁴ The two-level decomposition with DWT is described in Figure 1. where A , approximation; V , vertical; H , horizontal; and D , diagonal coefficients of the input image. The advantage of WT's is the detentions of frequency information in the image and provides most valuable data for classification.¹⁵

2.2 | Feature reduction using principle component analysis

The PCA is well known technique to project the input features into a lower dimension feature space using the principal eigenvectors of the correlation matrix. PCA is

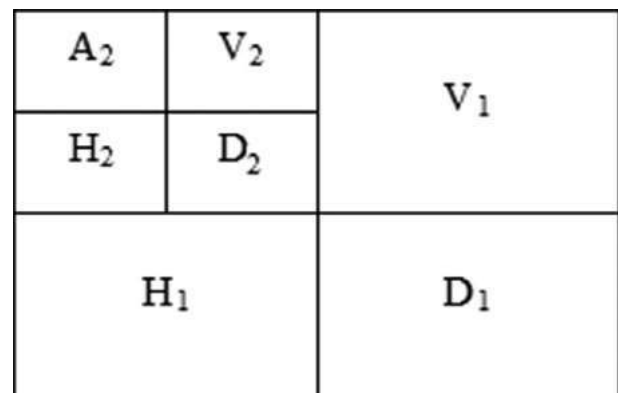


FIGURE 1 Two-level decomposition using DWT

one of the common and best multivariate methods for data reduction in image analysis, pattern recognition, and statistical learning.¹⁶ The concept behind using PCA is to decrease the dimensionality of WT coefficients that result in efficient classification.^{17,18} This method projects multivariate high dimensional data onto low-dimensional subspace, while retaining as much information as possible.¹⁹ It is notable that the size of the matrix obtained after feature normalization is quite large and it is necessary to reduce the dimension of the matrix. The data points present in the original orthogonal space are known as the principle components. In this proposed method the size of each Principal Feature (PF) is $32 \times 32 = 1024$ which leads to high computational complexity. For dimensionality reduction, the different PF (axes) is found incrementally. The PCA is computationally very efficient method and one of the most common forms of factor analysis.^{20,21} It is a linear projection method employed to decrease the number of parameters by transferring a set of correlated variables into uncorrelated variables.

2.2.1 | Dimension reduction process

An image is represented as a group of pixels arranged in the form of 2D matrix. The statistical approach to find the principal features of a distributed dataset is based on the total variance. Thus PCA finds the maximum variations of the original dataset. The dimensionality reduction steps are as follows:

- 1 Image normalization.
- 2 Determination of covariance matrix.
- 3 Calculation of the Eigen vector and Eigen values from the covariance matrix.
- 4 Transformation of image data into new basis.

2.3 | Fuzzy C means

FCM is one of the most effective procedures in data clustering. FCM is an unsupervised method associated with a wide range of issues including feature analysis, clustering, and classification. It has wide range of application in horticultural designing, astronomy, science, geography, image investigation, therapeutic determination, boundary detection, and target recognition. FCM has good ability in handling the partial volume effect (PVE) and segment the data into two or more clusters. It considers only intensity of the segmented image and it is an iterative method. Therefore, this method has negative aspect when confronted with noisy images. Clustering process is typically employed on a set of objects,

$$A = \{a_1, a_2, \dots, a_m\}, \forall a_j \in A \quad (1)$$

where A —set of data points. Segmentation of the brain image using FCM has turned out to be an effective research area and its steps are:

$$X_y = \sum_{i=1}^n \sum_{j=1}^m v_{ij}^y d(a_j, t_i) \quad (2)$$

$$d(a_j, t_i) = \|a_j - t_i\|^2 \quad (3)$$

where y is degree of fuzziness in clustering (in general $y = 2$), v is membership function of fuzzy data a_j to t_i , t is center of the cluster, d —distance between a_j data and cluster center t_i . The v must satisfy the conditions,

$$\sum_{i=1}^n v_{ij} = 1, 0 < \sum_{j=1}^m v_{ij} < m, \text{ and } v_{ij} \in [0, 1]; \quad (4)$$

The v and t_i are obtained as,

$$t_i = \frac{\sum_{j=1}^m v_{ij}^y \cdot a_j}{\sum_{j=1}^m v_{ij}^y} \quad (5)$$

$$v_{ij} = \frac{1}{\sum_{k=1}^m \left(\frac{d(a_j, t_i)}{d(a_j, t_k)} \right)^{\frac{2}{y-1}}} \quad (6)$$

The t_j iterations end at,

$$\max \left\{ \left| v_{ij}^b - v_{ij}^{(b-1)} \right| \right\} \leq \varepsilon \quad (7)$$

where ε —is termination that lies between 0 and 1, b —number of iteration steps.²² The conventional FCM technique is inefficient to take into account the spatial correlation between the neighboring pixels/voxels, inhomogeneities of intensity and noise sensitivity. In brain segmentation, FCM is considered as an iterative method and consumes more time for execution^{23,24}

3 | PROPOSED MODIFIED FUZZY C MEANS ALGORITHM

Segmentation of the MRI images is implemented by combining feature extraction and feature reduction along with modified fuzzy C means algorithm (MFCM). Figure 2 presents the block diagram of the proposed technique to extract tumor from the MRI brain images. An important

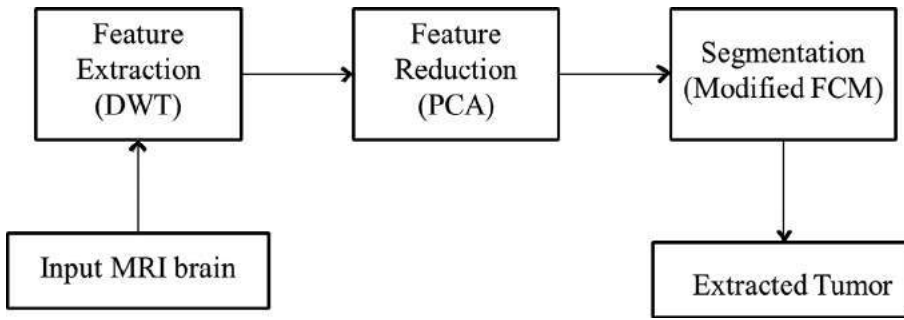


FIGURE 2 Block diagram of the proposed method (DWT, modified FCM, and PCA)

aspect in MRI images is the neighboring pixels/voxels have similar feature values. To obtain the spatial information of the pixels perfectly, membership function is modified. It is now defined as,

$$v'_{ij} = \frac{v_{ij}^y \cdot s_{ij}^m}{\sum_{k=1}^n v_{kj}^y \cdot s_{kj}^m} \quad (8)$$

$$s_{ij} = \sum_{k \in N(a_j)} v_{ik} \quad (9)$$

where s_{ij} —spatial function presenting the probability of pixel/voxel a_j belonging to the i th cluster. $N(a_j)$ is the square window centered on pixel/voxel a_j in spatial domain and y, m are parameters of the window. The spatial function improves the inventive membership value, and the clustering results in residues unaffected.²⁵⁻²⁷ MFCM Algorithm steps are:

Let $A = \{a_1, a_2, a_3, \dots, a_m\}$ be the set of data points and $t = \{t_1, t_2, t_3, \dots, t_c\}$ be the set of centers:

- Step 1: Set the number of clusters c and the parameter y .
- Step 2: Compute membership matrix $V^b = [v_{ij}^b]$ using Equation (8),
- Step 3: Compute t_j using Equation (5),
- Step 4: Repeat steps 2 and 3 until the resulting termination condition is satisfied: $|V^b - V^{(b-1)}| < \epsilon$, where b —number of iteration steps ($b = 0, 1, 2, \dots$).

Thus, the MFCM algorithm improves the performance by combing the other clustering methods with a minimum number of iterations.

4 | RESULTS AND DISCUSSIONS

The performance analysis of the proposed algorithm is checked on real time images of tumor and nontumor subjects along with the case studies obtained from Vijaya Diagnostic Center, Hyderabad, Telangana, India. To evaluate the efficiency of the proposed hybrid method,

the results of it in combination with DWT, PCA, and MFCM are compared with conventional FCM scheme. To estimate the performance of the proposed hybrid method, three different real time MRI images are taken for identifying abnormalities of Intracranial neoplasm: 32 years female with $146 \times 218 \times 28$ image dimensions, tuberculoma: 3 years male child $186 \times 220 \times 48$ image dimensions, and bilateral thalamic fungalgranulomas: 40 years male $220 \times 236 \times 32$ image dimensions. The metrics used are Dice Similarity Index (DSI), Accuracy, and Jaccard Index (JI). Ground Truth (GT) image, which is prepared with the help of medical specialist, is used to compute the metrics.

Figure 3A represents the axial view of T1W MRI image. Figure 3B corresponds to the GT of Figure 3A, Figure 3C is the obtained MRI image using conventional FCM method, and Figure 3D is the output obtained by the proposed method. Figure 4A and Figure 5A correspond to coronal and sagittal T1W MRI images of Figure 3A. Figure 4B corresponds to the GT of Figure 4A, Figure 4C is the obtained MRI image using conventional FCM method, and Figure 4D is the output obtained by the proposed method. Similarly, Figure 5B corresponds to the GT of Figure 5A, Figure 5C is the obtained MRI image using conventional FCM method, and Figure 5D is the output obtained by the proposed method.

Figure 6A represents the axial T1W image. Figure 6B corresponds to the GT of Figure 6A, Figure 6C is the obtained MRI image using conventional FCM method, and Figure 6D is output acquired by the proposed MFCM method. Figure 7 corresponds to the coronal T1 weighted MRI image of Figure 6A. Figure 7B corresponds to the GT of Figure 7A, Figure 7C is the obtained MRI image using conventional FCM method, and Figure 7D is output attained by the proposed MFCM method.

Figure 8A represents the axial TW image. Figure 8B corresponds to the GT of Figure 8A, Figure 8C is the obtained MRI image using conventional FCM method, and Figure 8D is output with the MFCM method.

The proposed MFCM technique considers spatial information for processing images that are affected by artifacts like noise and intensity inhomogeneties.

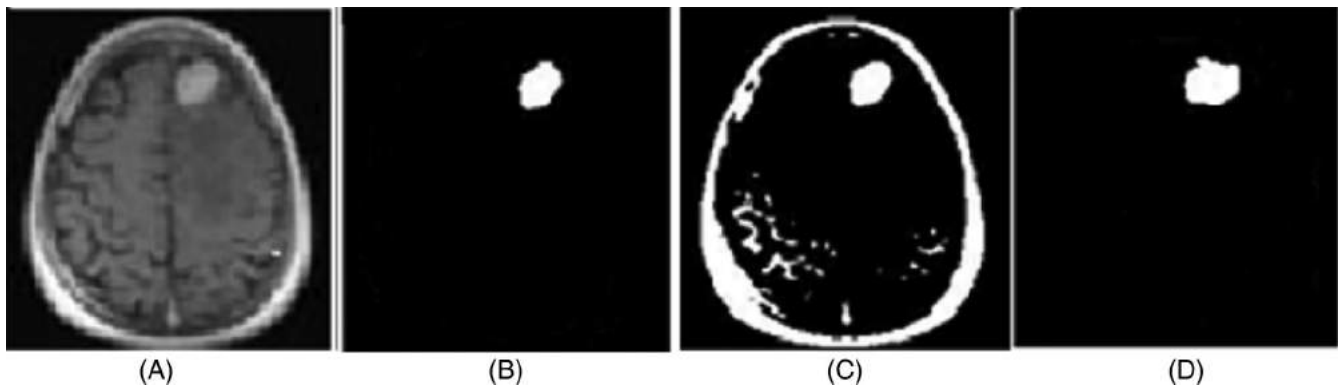


FIGURE 3 Intracranial tuberculoma axial view. A, original image, B, GT, C, FCM, and D, proposed MFCM

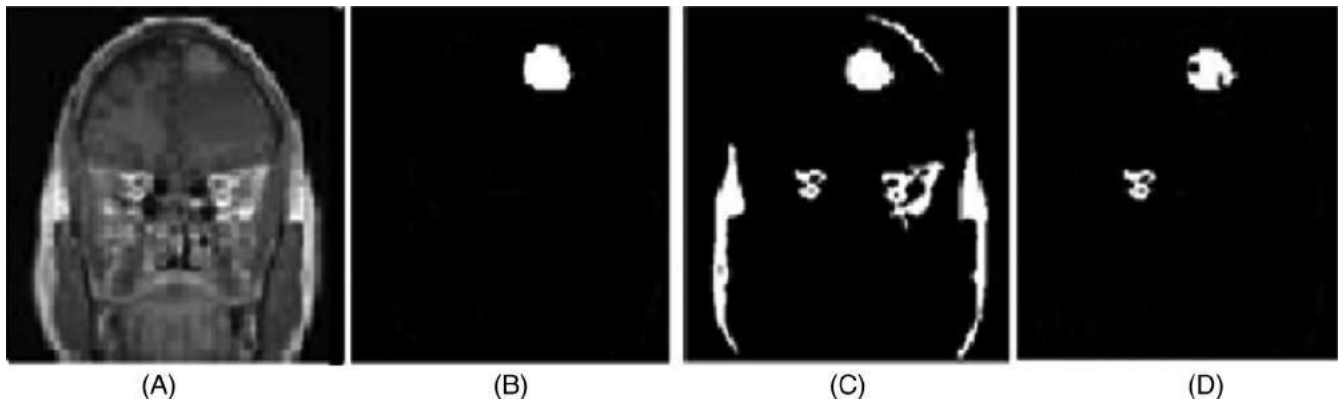


FIGURE 4 Intracranial tuberculoma coronal view. A, original image, B, GT, C, FCM, and D, proposed MFCM

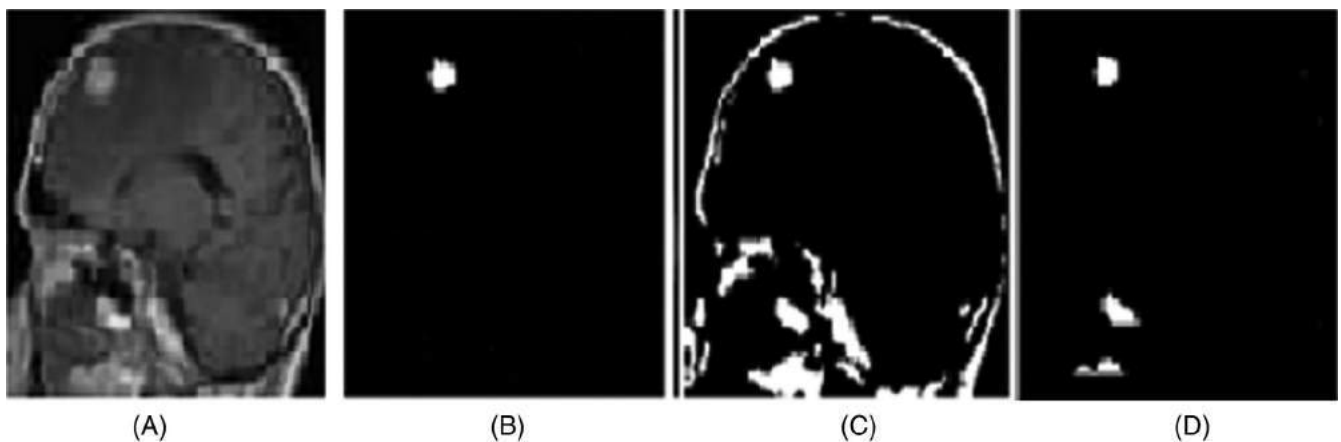


FIGURE 5 Intracranial tuberculoma sagittal view. A, original image, B, GT, C, FCM, and D, proposed MFCM

Hence, this procedure includes the effect of neighborhood pixels/voxels. Thus, it is capable to extract the boundaries in a proper manner as compared to conventional FCM technique. It is witnessed that the proposed method is able to classify the effects of shielding and

bright variations. Therefore, in brief, the main advantages of proposed method are its robustness to noise and shielding effect. The metrics of Accuracy, DSI, and JI,²⁸ are computed between the segmented and GT images.

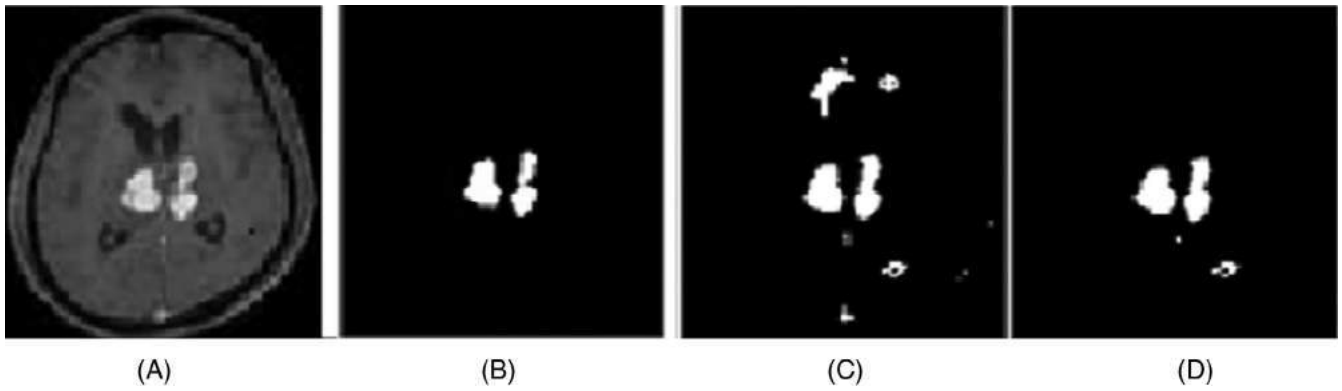


FIGURE 6 Bilateral thalamic fungal granulomas axial view. A, original image, B, ground truth, C, FCM, and D, proposed method

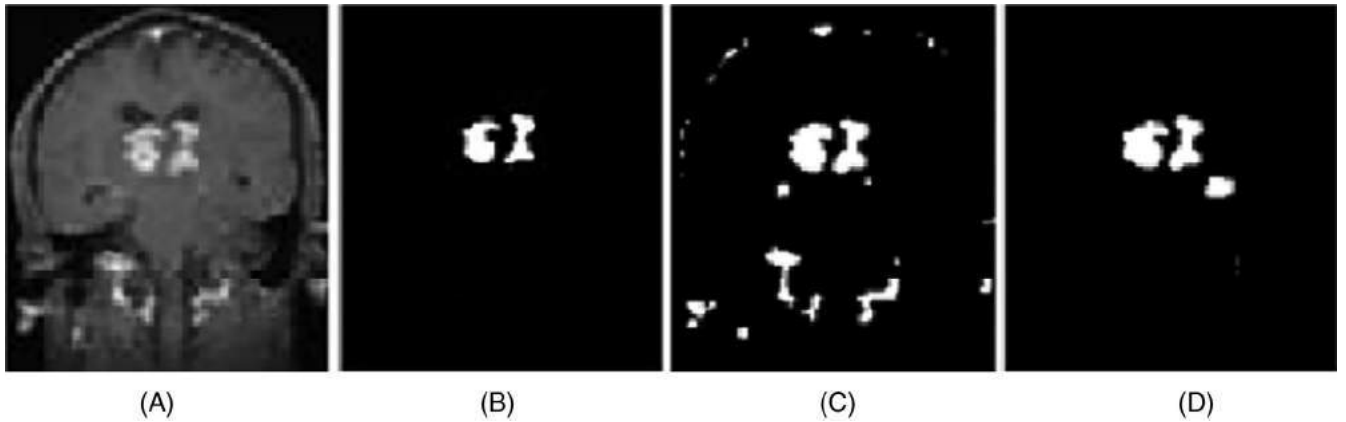


FIGURE 7 Bilateral thalamic fungal granulomas coronal view. A, original image, B, ground truth, C, FCM, and D, proposed method

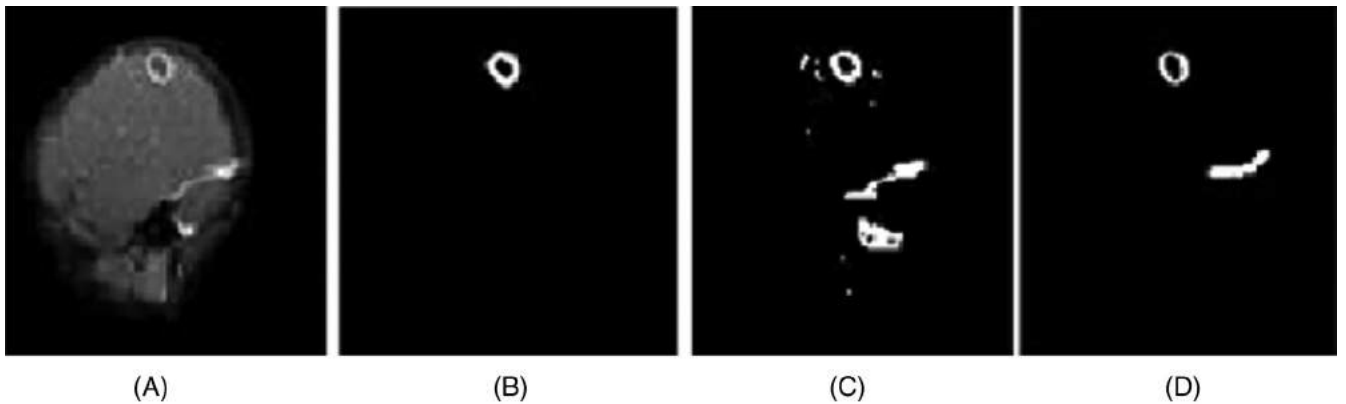


FIGURE 8 Tuberculoma A, original image, B, ground truth, C, FCM, and D, proposed method

$$\text{Accuracy} = \frac{tp + tn}{tp + fp + tn + fn} \quad (10)$$

$$\text{Dice Index} = \frac{2|A_i \cap B_i|}{|A_i| + |B_i|} \quad (11)$$

$$\text{Jaccard Index} = \frac{|A_i \cap B_i|}{|A_i \cup B_i|} \quad (12)$$

where A_i is GT image and B_i is the processed image. If JI is above 70%, the segmentation results are supposed to be good. The DSI value should be near to 1.

tp (true positives): correctly categorized positive cases.
 tn (true negative): correctly categorized negative cases.
 fp (false positives): wrongly categorized negative cases.
 fn (false negative): wrongly categorized positive cases.

The proposed MFCM algorithm is providing better results after 15 iterations, whereas conventional FCM method is taking 50 iterations for similar results. The evaluation of the experimental results are computed using the tp; tn; fp; and fn values which are obtained with the help of confusion matrix. The correctly classified positive values are appreciably acceptable when compared with the GT images. The conventional FCM method is failing to locate the tumor regions, whereas the proposed method is giving acceptable results even in the presence of artifacts in MRI images.

The results are tabulated to show the effectiveness of the conventional FCM and proposed MFCM method.

TABLE 1 Dice Similarity Index (%) comparison of the proposed method with FCM

Diseases		FCM	Proposed
Intracranial neoplasm	Axial	64.12	98.86
	Coronal	78.59	98.54
	Sagittal	68.24	97.39
Bilateral thalamic fungal granulomas	Axial	82.31	97.42
	Coronal	76.47	99.12
Tuberculoma	Axial	85.89	98.92

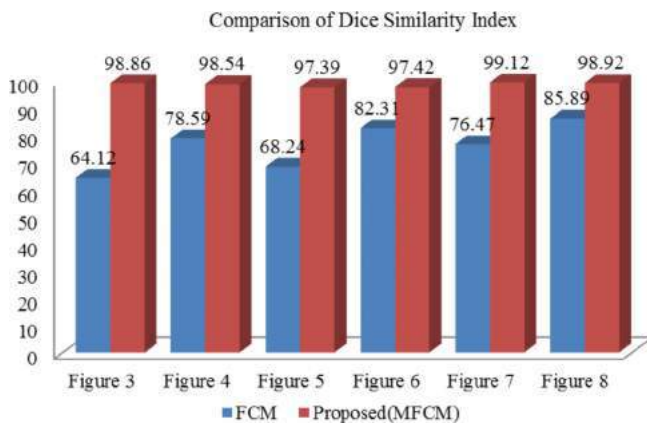


FIGURE 9 Graphical representation of the Dice Similarity Index [Color figure can be viewed at wileyonlinelibrary.com]

TABLE 2 Accuracy (%) comparison of the proposed MFCM with FCM

Diseases		FCM	Proposed
Intracranial neoplasm	Axial	88.04	98.78
	Coronal	84.75	99.56
	Sagittal	87.32	98.61
Bilateral thalamic fungal granulomas	Axial	85.29	99.39
	Coronal	89.16	99.42
Tuberculoma	Axial	86.61	99.35

Performance is evaluated in terms of DSI, Accuracy, and JI. In Table 1 the DSI metric is compared and its graphical representation is shown in Figure 9. In Table 2 the measure “Accuracy” is compared between FCM and proposed method. Pictorial presentation is provided in Figure 10. In Table 3 the JI values are tabulated with their graphical representation shown in Figure 11. From the tabulations, it can be seen that the proposed method

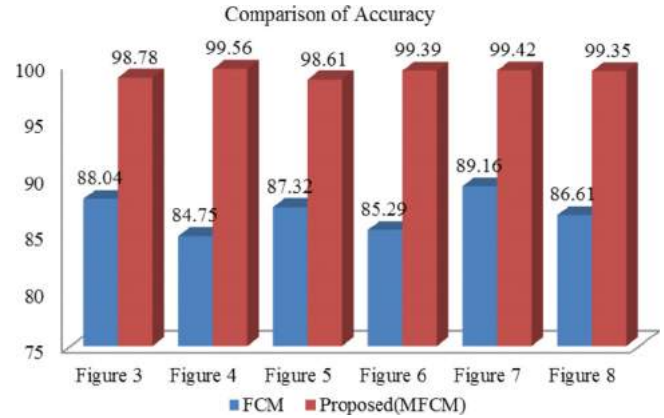


FIGURE 10 Graphical representation of Accuracy metric [Color figure can be viewed at wileyonlinelibrary.com]

TABLE 3 Jaccard Index (%) comparison of the proposed method with FCM

Diseases		FCM	Proposed
Intracranial neoplasm	Axial	88.04	98.78
	Coronal	84.75	99.56
	Sagittal	87.32	98.61
Bilateral thalamic fungal granulomas	Axial	85.29	99.39
	Coronal	89.16	99.42
Tuberculoma	Axial	86.61	99.35

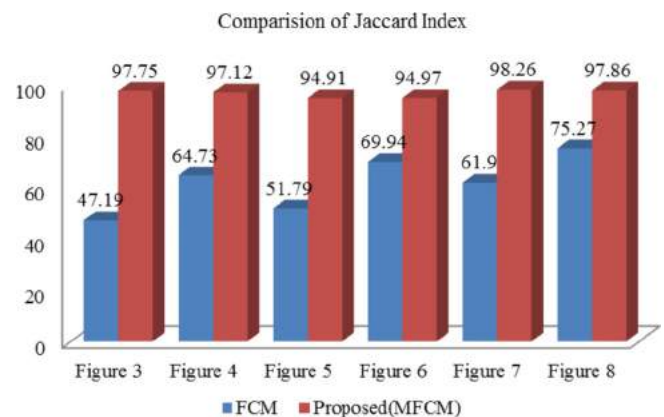


FIGURE 11 Graphical representation of Jaccard Index [Color figure can be viewed at wileyonlinelibrary.com]

outperforms the conventional FCM with an improvement of Accuracy, DSI, and JI by a factor of 99:18, 98:37, and 96:86%, respectively.

5 | CONCLUSIONS

To evaluate the efficiency of the proposed method, the results of the proposed hybrid. A new segmentation methodology in combination with DWT, PCA, and MFCM is proposed to deal with tumor MRI images. The results of the proposed algorithm are compared with the conventional FCM technique in terms of DSI, Accuracy, and JI measures. The proposed hybrid method is tested on three different MRI brain images for classifying various abnormalities (intracranial neoplasm, tuberculoma, and bilateral thalamic fungal granulomas) and for segmenting the tumor parts. The proposed hybrid method has provided efficient and robust results when compared to FCM technique by a factor of 99.18% of Accuracy, 98.37% of DSI, and 96.68% of JI. The algorithm can help the physician to check the presence of abnormality in MRIs in various parts of the brain. The proposed modified FCM method has proved to be robust to noise, able to take care of shielding effects and correctly locating the tumor in affected regions.

ACKNOWLEDGMENT

The authors would like to thank Dr. Anusha. D, a radiologist, Vijaya Diagnostic Center, Hyderabad, Telangana for the evaluation of the results and valuable suggestions to improve the standard of the article.

ORCID

Karuna Yepuganti  <https://orcid.org/0000-0003-4203-5554>

Saritha Saladi  <https://orcid.org/0000-0002-7044-6783>

REFERENCES

- Saladi S, Amutha Prabha N. A comprehensive review: segmentation of MRI images—brain tumor. *Int J Imaging Syst Technol*. 2016;26(4):295-304.
- Arifin AZ, Asano A. Image segmentation by histogram thresholding using hierarchical cluster analysis. *Pattern Recogn Lett*. 2006;27(13):1515-1521.
- Suryavamsi RV, Sai Thejaswin Reddy L, Saladi S, Yepuganti K. Comparative analysis of various enhancement methods for astrocytoma MRI images. Paper presented at: International Conference on Communication and Signal Processing (ICCSP). 2018. IEEE; pp. 0812-0816.
- Emblem KE, Nedregard B, Hald JK, Nome T, Due-Tonnessen P, Bjornerud A. Automatic glioma characterization from dynamic susceptibility contrast imaging: brain tumor segmentation using knowledge-based fuzzy clustering. *J Magn Reson Imaging*. 2009;30(1):1-10.
- Wafa M, Zagrouba E. Tumor extraction from multimodal MRI. *Computer Recognition Systems 3. Advances in Intelligent and Soft Computing*, Vol. 57. Springer: Berlin, Heidelberg; 2009. https://link.springer.com/chapter/10.1007/978-3-540-93905-4_49.
- Fletcher-Heath LM, Hall LO, Goldgof DB, Murtagh FR. Automatic segmentation of non-enhancing brain tumors in magnetic resonance images. *Artif Intell Med*. 2001;21(1-3):43-63.
- Mustaqeem A, Javed A, Fatima T. An efficient brain tumor detection algorithm using watershed and thresholding based segmentation. *Int J Image Graphics Signal Process*. 2012;4(10):34-39.
- Sivanand S. Adaptive local threshold algorithm and kernel fuzzy c-means clustering method for image segmentation. *Int J Latest Trends Eng Technol (IJLTET)*. 2013;2:261-265.
- Karibasappa K, Patnaik S. Face recognition by ANN using wavelet transform coefficients. *Inst. of Eng. (India) J: Comp. Eng*. 2004;85:17-23.
- Sarwinda D, Arymurthy AM. Feature selection using kernel PCA for Alzheimer's disease detection with 3D MR images of brain. Paper presented at: International Conference on Advanced Computer Science and Information Systems (ICACSIS), 2013. IEEE, pp. 329-333.
- Shridhar S, Karuna Y, Saladi S, Reddy R. Denoising of ECG signals using wavelet transform and principal component analysis. *SSRN Electronic Journal*. <http://dx.doi.org/10.2139/ssrn.3356368>.
- Mallat S. *A Wavelet Tour of Signal Processing*. 3rd ed. London: Elsevier; 2009.
- Agrawal A, Varun Kumar K, Yepuganti K, Saladi S. Automated classification of brain images using DWT and biogeography-based optimisation. Paper presented at: 2nd International Conference on Trends in Electronics and Informatics (ICOEI). 2018; IEEE. pp. 204-209.
- Saladi S, AmuthaPrabha N. Analysis of denoising filters on MRI brain images. *Int J Imag Syst Technol*. 2017;27(3):201-208.
- Kong J, Wang J, Lu Y, Zhang J, Li Y, Zhang B. A novel approach for segmentation of MRI brain images. *Electrotechnical Conference. ELECON 2006. IEEE Mediterranean*. 2006. IEEE. pp. 525-528.
- Lu J, Plataniotis KN, Venetsanopoulos AN, Li SZ. Ensemble-based discriminant learning with boosting for face recognition. *IEEE Trans Neural Netw*. 2006;17(1):166-178.
- Jain AK, Duin RP. Statistical pattern recognition: a review. *IEEE Trans Pattern Anal Mach Intell*. 2000;22(1):4-37.
- Sengur A. An expert system based on principal component analysis, artificial immune system and fuzzy k-nn for diagnosis of valvular heart diseases. *Comput Biol Med*. 2008;38(3):329-338.
- Diamantaras KI, Kung SY. *Principal Component Neural Networks: Theory and Applications*. 5th ed. New York: Wiley; 1996.
- Krishna GG, Ashwin S, Karuna Y, Saritha S. Brain MR image classification using DWT and random forest with AdaBoostM1 classifier. Paper presented at: International Conference on Communication and Signal Processing (ICCSP); April, 2018. IEEE; pp. 0820-0824.
- Yepuganti K, Saladi S, Bhattacharyya B. Brain tissue classification using PCA with hybrid clustering algorithms. *Int J Eng & Technol*. 2018;7(2.24):536-540.

22. Kannan S, Ramathilagam S, Sathya A, Pandiyarajan R. Effective fuzzy c-means based kernel function in segmenting medical images. *Comp Biol Med.* 2010;40(6):572-579.
23. Kumar NTJP, Achalla S, Yepuganti K, Saritha S. An improved type 2 fuzzy C means clustering for MR brain image segmentation based on possibilistic approach and rough set theory. Paper presented at: International Conference on Communication and Signal Processing (ICCSP). 2018. IEEE. pp. 0786-0790.
24. Monalisa A, Dasari S, Yepuganti K, Saritha S. Robust intuitionistic fuzzy c-means clustering algorithm for brain image segmentation. Paper presented at: International Conference on Communication and Signal Processing (ICCSP). 2018. IEEE. pp. 0781-0785.
25. Wang J, Kong J, Lu Y, Qi M, Zhang B. A modified FCM algorithm for MRI brain image segmentation using both local and non-local spatial constraints. *Computerized Medical Imaging and Graphics.* 2008;32(8):685-698. <http://dx.doi.org/10.1016/j.compmedimag.2008.08.004>.
26. Saladi S, AmuthaPrabha N. A novel fuzzy factor for MRI brain image segmentation with intuitionistic fuzzy kernel clustering approach. *J Adv Res Dyn Control Syst.* 2018;10(02):639-652.
27. Saladi S, AmuthaPrabha N. MRI brain segmentation in combination of clustering methods with Markov random field. *Int J Imaging Syst Technol.* 2018;28(3):207-216.
28. Taha AA, Hanbury A. Metrics for evaluating 3D medical image segmentation: analysis, selection, and tool. *BMC Med Imaging.* 2015;15(1):15-29.

How to cite this article: Yepuganti K, Saladi S, Narasimhulu CV. Segmentation of tumor using PCA based modified fuzzy C means algorithms on MR brain images. *Int J Imaging Syst Technol.* 2020; 1-9. <https://doi.org/10.1002/ima.22451>

Modified Euler Frobenius Halfband Polynomial Filter based Dual-Tree Complex Wavelet Transform and Metaheuristic Optimization Algorithms for Image Denoising along with Artificial Neural Networks

P.Venkata Lavanya^{1*}, C.Venkata Narasimhulu², K. Satya Prasad³

^{1*} *Research Scholar, ECE Department, Jawaharlal Nehru Technological University Kakinada, Kakinada, Andhra Pradesh, India.*

² *Department of ECE, Geethanjali College of Engineering and Technology, Hyderabad, Telangana, India.*

³ *Vignan's Foundation for Science, Technology and Research, Guntur, Andhra Pradesh, India.*

pvlavanya999@gmail.com^{1}, narasimhulucv@gmail.com², prasad_kodati@yahoo.co.in³*

Abstract

In recent years Dual Tree Complex Wavelet Transform (DT-CWT) has been applied to heterogeneous image denoising problems. The quality of reconstructed images depends on low pass and high pass filter coefficients of the transform. The design of bi-orthogonal low pass filters and selection of an optimal set of filter coefficients is therefore necessary for effective image restoration. Hence the main contribution of our paper is a DT-CWT based image denoising model, where low pass filters are designed using Modified Euler Frobenius Half Band Polynomial (MEFHBP) and filter coefficients are optimized by hybrid meta heuristic algorithms termed Earth Worm based Grey Wolf (EWGW) optimization. In the proposed de-noising process, DT-CWT of noisy image is initially found by employing appropriate MEFBP based filters. The coefficients of filters are then optimized by EWGW algorithm, objective function being maximization of Peak Signal to Noise Ratio (PSNR). With optimized set of filter coefficients, final DT-CWT is performed resulting in denoised image. As an extension, ability of EWGW algorithm in optimizing weights of Artificial Neural Network (ANN) is also studied by means of classification model. In classification stage, noisy images first undergo multi-level thresholding based segmentation. Noise Power Spectrum and Bark frequency features are then extracted from the image and are fed to ANN whose weights are optimized by EWGW. Experiments are conducted on texture, medical and satellite image datasets. The performance of the algorithm is measured by means of various performance metrics and is compared with other optimization techniques. Finally statistical analysis is done to substantiate experimental results. The analysis shows that MEFHBP-EWGW outperforms many optimization techniques and results in better denoised images. It is also able to optimize ANN weights in a subtle manner.

Keywords: *Image Denoising, Dual Tree Complex Wavelet Transform, Euler Frobenius Polynomial, Filter Coefficients, Grey Wolf based Earth Worm Optimization.*

1. Introduction

De-noising is an operation performed on noisy images aimed at reconstructing original images. It is usually done by manipulating the degradation element which corrupted the image. This element which corrupts the image is termed as noise [1]. Noise is caused by various factors like quality of camera used, position from which photograph is taken, environmental situations and skill of photographer. The amount to which an image is filled with noise also depends on above factors. Human brains can classify these images without much difficulty even when image is filled with higher amount of noise, due to its inherent capacity. But this is not the case of computers where classification accuracy

drops with increase in amount of noise. Hence, noise need to be removed preliminarily before carrying out any classification related tasks. Even though numerous de-noising algorithms are available, Dual Tree Complex Wavelet Transform (DT-CWT) is mostly sought by researchers as it addresses problems of its predecessors such as lack of shift invariance, improper de-noising of edges and computational expenses [2]. In conventional DT-CWT, input noisy image is taken by both trees (real & imaginary) of the transform. The trees are composed of low pass and high pass filters characterised by their filter coefficients. But the fact is that design of these filters are quite challenging. [3] Showed that for perfect reconstruction analyticity property must be satisfied. This satisfaction comes only from designing filters that satisfy Hilbert pair criteria. Hilbert pair criteria specify Vanishing Moments (VMs) and Half Sample Delay (HSD) constraints as minimum requirements. Since normal filters are unable to satisfy Hilbert criteria, FIR bi-orthogonal filters are used. Most of the bi-orthogonal filter design techniques are based on odd/even design or common factor technique. They work by selecting one filter bank and designing other filter bank based on the preselected filter bank. Such type of filter design based on matching has restricted amplitude and frequency responses which affect reconstruction. A possible extension is iterative matching i.e., after selecting a filter bank, design another filter bank based on preselected one and then redesign preselected one based on new one and continue the process iteratively. Though generalized polynomial factorization methods are available they possess low degrees of freedom, hindering effective reconstruction. Further 2D DT-CWT produces six high pass bands and 2 low pass bands at each level of decomposition. Applying sum and difference operators, six wavelet coefficients are obtained from six high pass bands and two approximation coefficients are obtained from low pass bands. These output coefficients are adjusted normally by thresholding such that those below a particular threshold are set to zero. Finally, inverse DT-CWT is performed with modified output coefficients to reconstruct original image. However thresholding always neglects output coefficients below particular thresholds which undermine significance of those coefficients [4]. Hence alternative ways to obtain reconstructed images, which consider significance of output coefficients to maximum possible extent, need to be devised. One way is to manipulate filter coefficients. But applying thresholding to filter coefficients will result in low quality images as it will make filter coefficients to become zero at some instances. Hence the most appropriate option is to optimize filter coefficients. Most de-noising approaches are iteration based and optimized values continuously changes in each iteration. But optimized filter coefficients at each level might become significant at a later stage of de-noising process. So an optimization approach which remembers previously obtained solutions is of interest in this context. Numerous optimization techniques are found in literature with a majority of them falling under the category of Genetic Algorithms (GA). Though proven good they suffer from complexity and premature convergence. Additionally, quality of remembrance of previous best solutions is not guaranteed by GAs. Experiments proved that Grey Wolf Optimization (GWO) could be an effective solution in this case, but its low solving precision, slow convergence and bad local searching ability affects final optimized value of filter coefficients. Hence our objective is to develop a better DT-CWT based de-noising approach by designing bi-orthogonal filters that has unrestricted frequency response for better reconstruction and to optimize filter coefficients with reduced computation time. Thus our main contribution is a Modified Euler Frobenius Half band Polynomial (MEFHBP) based filter design and an Earth Worm - Grey Wolf (EWGW) algorithm based optimization oriented Dual Tree Complex Wavelet Transform (DT-CWT) de-noising model, which reduces computation time and complexity in addition to solving optimization issues. EWGW is a hybrid version of two nature inspired Meta heuristic algorithms, GWO [5] and Earth Worm Optimization (EWA) [6]. It overcomes limitations of GAs and other heuristic methods. Initially, DT-CWT is performed on noisy image using MEFHBP filters and filter coefficients are optimized by EWGW. These optimized DT-CWT coefficients are trained in Artificial Neural Network (hereafter referred as first ANN) with extracted features Noise Power

Spectrum (NPS) and Bark frequency from classification model which is discussed in the following paragraph. As an extension, capability of EWGW in optimizing weights of normal ANN is tested by means of classification model. Initially, noisy image is fed to multilevel thresholding based segmentation block. Next Noise Power Spectrum (NPS) and bark frequency features are extracted from resultant image and are trained in another Artificial Neural Network (ANN) (hereafter referred as second ANN) with respect to type of image (natural, medical, satellite). The weights of ANN are optimized using EWGW optimization algorithm. Training is carried out for 70% of images from data set. Both de-noising as well as classification process runs simultaneously. Consequently when a test image is applied, 1st ANN predicts optimized coefficients and 2nd ANN classifies image. Based on these optimized coefficients DT-CWT is carried out resulting in de-noised image. Finally, current approach is compared with traditional models like Genetic Algorithm-Bayesian Regularization (GA-BR) [32], Levenberg—Marquardt-Neural Network (LM-NN) [33], Particle Swarm Optimization-Neural Network (PSO-NN) [34], Grey Wolf Optimization-Neural Network (GWO-NN) [35], and Earth Worm Optimization-Neural Network (EWA-NN) [36] in terms of Peak Signal to Noise Ratio (PSNR), Mean Absolute Error (MAE), Second Derivative like Measure of Enhancement (SDME), Mean Squared Error (MSE), Structural Similarity Index (SSIM), Root Mean Square Error (RMSE), Pearson Coefficient (PC), Symmetric Mean Absolute Percentage Error (SMAPE) and computation time. Analysis shows dominance of proposed method over state of the art methods. The rest of the paper is organized as follows. Section 2 describes related work. Section 3 focuses on mathematical preliminaries. Section 4 describes proposed de-noising architecture. Section 5 discusses obtained results. Section 6 concludes the paper.

2. Literature Review

An image de-noising technique should be chosen such that in resultant image flat areas are smooth, textures are preserved, edges are not blurred and new artifacts are not created. Image de-noising techniques can be broadly classified into spatial domain methods and transform domain methods. In spatial domain methods image is de-noised using grey scale value of each pixel. This value is calculated by considering the correlation between pixels of noisy images [7]. Spatial methods can be further classified into spatial domain filtering and variational de-noising. The former one uses both linear and non-linear filters for de-noising. Linear filtering fails in preserving textures. Mean filtering was adapted to overcome this, but does not work out in the case of images with high noise resulting in over smoothness [8]. As an advancement wiener filtering was suggested which lead to blurred edges [9]. Hence applicability of non-linear filters for de-noising was explored. Bilateral filter is one such non-linear filter which preserves edges and curbs the over smoothing effects. It works by replacing pixel intensity with average of neighbourhood intensity values. Efficiency and larger computation time question its suitability for real life applications [10]. All spatial domain methods assume that noise occupies a higher region of frequency spectrum. Also de-noising is performed at the expense of blurring sharp edges. Hence, variational de-noising was suggested as an alternative option. In variational de-noising initially an error function is estimated from the noisy image. It is assumed that minimizing this error function leads to noise free image and hence steps are implemented to minimize it. Tikhonov regularization is one of its sub types which minimize error function using L2 norm. But it also suffers from over-smoothness [11] that leads to proposal of anisotropic diffusion methods [12]. However results showed blurred edges. To solve such issues Total Variation Regularization (TVR) was proposed. It is based on gradient of noisy image. Even though it retained sharp edges, over smoothness and contrast issues limited its use [13]. To overcome smoothness issues fast gradient method was proposed by [14]. Although Peak Signal to Noise Ratio (PSNR) values got improved, only local characteristics of image were taken into account. Such local methods though produce low time complexities have performance limitations when noise is high. To address local problems, Non-Local Means (NLM) approaches were put forward. It

estimates pixel value by comparing weighted average of pixels similar to it. Numerous acceleration and performance enhancements were then proposed as an extension to NLM. At present, research is shifting from local to nonlocal means and their hybrids. Nevertheless structural information is not preserved by these methods which degrade visual quality. Recent techniques use sparsity prior of natural images for de-noising. It works on the principle of K Singular Value decomposition (K-SVD) where a dictionary is learned from noisy image and shows better flexibility and bit rates. Here too the algorithm is local which results in inefficient de-noising when noise is high [15]. Another variational de-noising approach is low rank minimization model. Unlike sparse representation it formats similar patches as a matrix. By manipulating low rank matrix priors effective noise reduction is assured [16], limitations being necessity of an input rank. A lower rank will lead to loss of details and higher rank will lead to preservation of noise. De-noising methods gradually developed from spatial domain methods to transform based methods. Transform based methods started with Fourier transform and continues through cosine transform and wavelet transform. As the name implies, transform based de-noising methods includes transformation of an image from one domain to another. The noise and image characteristics are different in transformed domain. De-noising is performed on this transformed domain and is based on the principle that larger coefficients denote significant parts of image whereas smaller coefficients denote noise. According to basis transform functions transform based methods can be either data adaptive or non-data adaptive. Independent Component Analysis (ICA) is a data adaptive method which works well for non-Gaussian data. Since it uses sliding windows, their computation cost is very high. Also it requires a sample of noise free data. Non-adaptive type can be further subdivided into spatial frequency domain and wavelet domain. Spatial domain filtering works on the principle of low pass filtering. After being transformed by low pass filters like Fourier transform, noise occupies higher frequencies whereas image details occupies lower frequencies. By designing a frequency domain filter that passes low frequency and attenuates higher frequencies, de-noised image can be obtained. However they are time consuming and are dependent on cut off frequency [17]. On the other hand Discrete Cosine Transform (DCT) represents image in a sparse fashion [18]. Alike Fourier transform, it also fails in representing all image details leading to development of wavelet based de-noising methods. Wavelet transforms is an area which gathered interest recently due to its wide de-noising scope such as sparseness and multi-scale capabilities. The wavelet transform changes input image into a scale-space representation. Irrespective of frequency content, wavelets are proven to remove noise while preserving image details. A Discrete Wavelet Transform (DWT) was proposed by [19] for still image de-noising. Problems concerning diversity undermined its performance. The performance of diversity enhanced DWT was studied by [20]. Here, diversity was increased by computing wavelet transform with different parameters. Though it improved diversity, lack of shift invariance and directional selectivity issues were not addressed. All these limitations pointed towards the need of a new wavelet based de-noising technique. Dual Tree Complex Wavelet Transform (DT-CWT) was suggested in this context by [21]. DT-CWT works by employing two DWTs which is the reason for the name dual tree. The first DWT gives real parts of transformed image, whereas second DWT gives its imaginary part. This transformation is facilitated by high pass and low pass filters of DT-CWT. These filters have filter coefficients on which wavelet transform heavily relies. Reconstruction is effective only when filters satisfy Hilbert pair criteria. Odd even design filter approach is able to satisfy HSD constraints whereas common factor technique is able to satisfy VM constraints. An alternative is to use a general polynomial based spectral factorization approach that satisfies VM as well as HSD constraints. However they have restricted frequency response. Euler Frobenius polynomials are handy in this situation as their coefficients are computed recursively. Though these coefficients are desirable in spline theory, they are not suitable in sub band coding due to their limited compact filter support. Hence in this approach we propose a Modified Euler Frobenius Half band

Polynomial (MEFHBP) by using an independent variable, and combining VMs. On output coefficients thresholding is done prior to inverse DT-CWT resulting in de-noised image. However if an inappropriate selection of threshold value is made de-noising effect will be poor [22]. Research has been more in the area of manipulating output coefficients, but low in the area of optimizing filter coefficients. Meta heuristic algorithms have been proposed to estimate threshold values of output coefficients for wavelet transforms but not for filter coefficients [23]. [24] Proposed Hybrid Genetic Algorithm (HGA) in combination with anisotropic diffusion and weiner filtering but not with wavelet transform. [25] employed Artificial Bee Colony algorithm for optimizing threshold value of DT-CWT. [26] used Genetic Algorithm (GA) for optimizing threshold value of wavelet transform but optimization of filter coefficients were not considered. Hence Meta heuristic algorithms can be utilized for optimizing filter coefficients too due to their simplicity, flexibility and local optima avoidance capability. Meta heuristic algorithms can be sub divided into single solution based and population based algorithms. Single solution based algorithms starts with single solution and improves the solution over the course of the iteration [27] whereas population based ones starts with multiple solutions and are enhanced over course of the iteration. The advantage of population based algorithms is that it shares information about search space with each other and assists each other in avoiding local optima. Swarm Intelligence (SI) is a type of population based algorithm which mimics collective behaviour of organisms in nature. SI algorithms are often chosen as they have fewer parameters and operators and are easy to implement. It also memorizes the best solution obtained so far. PSO is an important SI algorithm in which particle moves considering its best solution as well as best solution of swarm. Yet it is prone to local optima [28]. If an algorithm prone to local optima is used for de-noising, de-noised image will be of low quality compared to an algorithm which avoids local optima as the search space is large. Ant Colony Optimization (ACO) is another Meta heuristic algorithm which imitates social behaviour of ants [29]. It takes more time to converge which would result in increased de-noising time. Similar is the case of Bat algorithm. Hence a meta-heuristic algorithm which is suitable for larger search spaces as well as that keep track of previously obtained best solutions is suitable in DT-CWT based optimization context. GWO addresses the above needs to a certain extent as it memorizes three best solutions obtained so far. However its search space, though higher than other SI algorithms need to be improved further so that more exploration is possible. This can be done by using a cross over operator. Another meta-heuristic algorithm named Earth Worm Optimization (EWA) could be used to perform it. Hence in our approach hybrid version of GWO and EWA referred as EWGW is employed. EWGW optimizes initial filter coefficients of DT-CWT of noisy image and stores them in a library. The calculation of optimized filter coefficients for large sets of noisy images consumes a lot of time. Hence optimized filter coefficients need to be trained. For this purpose we employ ANN so that when a new image comes, trained ANN can predict optimal filter coefficients without implementing EWGW algorithm again. ANN is preferred over BR to tackle over fitting and limited data handling capacity [32]. As mentioned in previous section, our subsidiary contribution is an image classification model to assess performance of EWGW in optimizing ANN weights. Though all classification models employ de-noising process prior to performing any classification operations, here we attempt to classify images with noise as our aim is just to verify EWGW optimization capability. Hence when de-noising is skipped, segmentation becomes the first step of classification model. It results in partitioning of images in to foreground and background regions. Segmentation techniques are broadly classified into similarity based and discontinuity based ones. Thresholding, region growing, splitting and merging comes under similarity based category whereas line, point and edge detection techniques come under discontinuity based ones. Considering robustness, simplicity and accuracy thresholding is highly recommended [30]. Thresholding partitions an image into two regions using pixel grey values. But in real world, images are multimodal which necessitates multilevel thresholding. Among proposed methods, Otsu's method based on class variance [31] and Kapur's method based

on entropy [37] are proven to be best ones. We chose Otsu’s method as it is the simplest one. Studies have been less concentrated on extracting features from noisy images which underwent thresholding. [38] Proposed feature extraction technique for pulmonary node detection after multilevel thresholding using shape and intensity oriented features which is appropriate for de-noised medical images. Scale Invariant Feature Transformation (SIFT), Speeded-Up Robust Features (SURF) and Histogram of Oriented Gradient (HOG), though termed feature extraction techniques were actually used to reconstruct images [39]. Hence in our approach we extracted Noise Power Spectrum (NPS) and Bark Frequency (BF) as features. Though the former was used to extract features in clinical CT scanners, its application for other image types like satellite, nature etc., are not explored [40]. NPS is a thorough noise pixel descriptor compared to pixel standard deviation. Bark frequency is a bark scale representation of Hertz frequency which also is a good descriptor of noise. Based on related studies, in this paper a new de-noising approach found on MEFHBP based bi-orthogonal filter design and optimization of DT-CWT filter coefficients using EWGW and ANN is proposed. Detailed description on theoretical, mathematical and implementation concepts are provided in later sections.

3. Proposed System

We extracted Noise Power Spectrum (NPS) and Bark Frequency (BF) as features. Though the former was used to extract features in clinical CT scanners, its application for other image types like satellite, nature etc., are not explored [40]. NPS is a thorough noise pixel descriptor compared to pixel standard deviation. Bark frequency is a bark scale representation of Hertz frequency which also is a good descriptor of noise. Based on related studies, in this paper a new de-noising approach found on MEFHBP based bi-orthogonal filter design and optimization of DT-CWT filter coefficients using EWGW and ANN is proposed. Detailed description on theoretical, mathematical and implementation concepts are provided in later sections.

4. Methodology

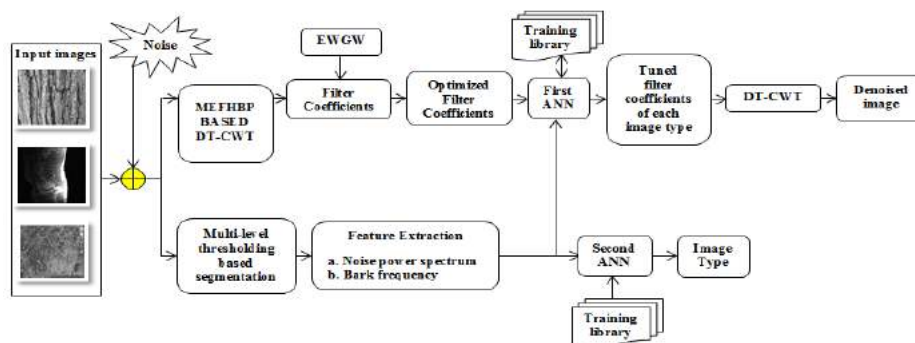


Figure 1: Proposed De-Noising Architecture

In this section, mathematical preliminaries of all techniques used in current approach are discussed. Figure 1 shows proposed de-noising architecture. The input image type belongs to texture, medical and satellite classes. While training, each image undergoes DT-CWT and optimization by EWGW simultaneously with multilevel thresholding based segmentation followed by feature extraction. Let us discuss processes in de-noising and classification stage separately.

4.1 Dual Tree Complex Wavelet Transform (DT-CWT)

As DT-CWT is an extension of Discrete Wavelet Transform (DWT), first mathematical model of DWT is dealt. DWT employs series of High Pass (HP) and Low Pass (LP) filters for separating frequency bands. To be precise, when image $x[n]$ is given to DWT block, it is initially passed through half band HP and LP filter $h[n]$ and $l[n]$ respectively. The HP filter passes samples above half band and LP filter passes samples below half band. The output of LP filter constitutes frequencies from 0 to $p/2$ radians/s and output of HP filter constitutes frequencies from $p/2$ to p radians/s. Hence according to

Nyquist rule half of the samples can be eliminated as highest frequency in both the filters is $\pi/2$ rad/s. Therefore sub sampling is performed by a factor of 2. The process can be expressed mathematically as shown in equation (1) and (2).

$$y_{high}(k) = \sum x[n].h[2k - n] \quad (1)$$

$$y_{low}(k) = \sum_n x[n].l[2k - n] \quad (2)$$

Where $y_{high}(k)$ and $y_{low}(k)$ are outputs of HP and LP filters after sub sampling by 2. This completes first level decomposition and output of HP filter corresponds to first level DWT coefficients. The process, also called sub band coding is repeated for output of LP filters and is continued until two samples are left. The output of HP filters at each level corresponds to DWT coefficients of that particular level. HP and LP filters in the decomposition stage are collectively called analysis filters and are not independent of each other. They are related as in equation (3)

$$h[L - 1 - n] = (-1)^n.l[n] \quad (3)$$

Where L is filter length? Thus DWT coefficients corresponding to all levels are obtained. A plot of DWT coefficients starting from last level (two samples) against amplitude gives frequency domain representation of input image. Reversing same process by replacing sub sampling with up sampling and using synthesis filters (HP and LP filters in reconstruction stage are called synthesis filters) results in original image. This reconstruction process is called inverse DWT. The coefficients of synthesis filters are transposes of analysis filter coefficients. DT-CWT is a combination of two DWT's. It is to be noted that in DT-CWT, output of both DWT's are not same. This is due to the fact that filter settings of two DWT's are different. The output of one DWT corresponds to real coefficients and other corresponds to imaginary coefficients. Equations (1) and (2) are written in terms of real and imaginary parts of LP and HP filters, as given in equations (4), (5), (6) and (7).

$$y_{high_{real}}(k) = \sum x[n].h_{real}[2k - n] \quad (4)$$

$$y_{low_{real}}(k) = \sum_n x[n].l_{real}[2k - n] \quad (5)$$

$$y_{high_{im}}(k) = \sum x[n].h_{im}[2k - n] \quad (6)$$

$$y_{low_{im}}(k) = \sum_n x[n].l_{im}[2k - n] \quad (7)$$

The total of real and imaginary coefficients is given in equations (8) and (9).

$$y_{real}(k) = y_{high_{real}}(k) + y_{low_{real}}(k) \quad (8)$$

$$y_{im}(k) = y_{high_{im}}(k) + y_{low_{im}}(k) \quad (9)$$

Sub band coding and reconstruction are carried out similar to DWT resulting in reconstructed image. Let $\phi_h(t)$ and $\Psi_h(t)$ be the scaling and wavelet functions corresponding to synthesis section of tree 1 and $\phi_g(t)$ and $\Psi_g(t)$ be the scaling and wavelet functions corresponding to synthesis section of tree 2. Similarly $\widetilde{\phi}_h(t), \widetilde{\phi}_g(t), \widetilde{\Psi}_h(t), \widetilde{\Psi}_g(t)$ correspond to scaling and wavelet functions of analysis section of tree 1 and tree 2. For effecting reconstruction these functions should satisfy Hilbert Pair criteria i.e., synthesis wavelet function of tree 2 should be the Hilbert transform of synthesis wavelet function of tree 1. For analysis section too same criteria follows. The wavelet functions are dependent on scaling functions which in turn is dependent on LP filters. Hence for efficient DT-CWT reconstruction LP filters must be designed such that they satisfy Half Sample Delay (HSD) constraint $g_0(n) \approx h_0(n - 0.5)$, where $g_0(n)$ is LP filter satisfying HSD and $h_0(n)$ is random LP filter. This can be expressed in Fourier domain as in equation (10)

$$G_0(\omega) \approx e^{-\frac{j\omega}{2}} H_0(\omega) \quad (10)$$

Where $G_0(\omega)$ and $H_0(\omega)$ are Fourier Transforms of $g_0(n)$ and $h_0(n)$ respectively. The magnitude and phase responses are given as follows

$$|G_0(\omega)| = |H_0(\omega)| \quad (11)$$

$$\angle G_0(\omega) = -\frac{\omega}{2} + \angle H_0(\omega) \quad (12)$$

However any methods can satisfy only one of the above two conditions whereas the other condition need to be approximated. Odd even design approach comes under HSD (P) in which equation (12) is satisfied and equation (11) is approximated. In conventional odd even approach Cohen-Daubechies-Feauveau (CDF 9/7) filters selected from Triplet Half band Filter Bank (THFB) are used in tree1. Tree 2 filters are designed such that their amplitude response matches with that of tree 1 thereby satisfying phase response. In our approach we employ Modified Euler Frobenius Half band Polynomials (MEFHBP) to design tree 2 filters the details of which are described in section 4. However DT-CWT operation can be improved by manipulating the filter coefficients of MEFHBP filters. This is the area of focus in our research and in this paper we optimize filter coefficients by EWGW algorithm. Since in our paper optimization of filter coefficients is performed by EWGW algorithm, mathematical model of normal Gray Wolf and Earth Worm Optimization algorithms is given in following sections. In later sections actual optimization process using hybrid version of above algorithms is discussed.

4.2 Grey Wolf Optimization (GWO)

GWO is an optimization technique founded on behaviour of Grey Wolves in hunting preys. A typical grey wolf pack consists of approximately 5-12 members. These wolves are categorized in to 4 groups namely alpha (α), beta (β), delta (δ) and omega (ω). α Wolves are leaders of the pack. It comprises of a male and a female wolf. The decision of α wolves is followed by entire pack. α Wolves are responsible for decisions like time to wake up; walking, hunting, time and place to sleep etc., β wolves are subordinate wolves that assist α wolves in decision making. They advise α wolves but command other wolves, and are responsible for carrying out decision of α wolves in entire pack. They replace α wolves if any of the α wolves become old or passes away. ω Are lowest ranking wolves and obeys all other wolves. If any of the wolves do not belongs to α , β or ω categories, they are called δ wolves. They submit to α and β wolves but dominate ω wolves. δ wolves are subdivided in to scouts; which are responsible for watching boundaries and issue warning in case of danger, sentinels; which guard the pack, hunters; which assist α and β in hunting, elders; which were previously α or β wolves, and caretakers; which are responsible for taking care of old, ill and wounded wolves. The mathematical modelling of hunting behaviour of Grey Wolves is described as follows. As stated previously, hierarchy of dominance starts from α and ends at ω . For mathematical simplicity we consider that there are only one α , β and δ wolf in the pack and infinite number of ω wolves. Consider that there is a prey at position \vec{X} in search space. It is assumed that α has best knowledge of prey position, followed by β and then δ . ω Wolves follow all these wolves. The initial position of α , β and δ wolves is labelled \vec{X}_α , \vec{X}_β and \vec{X}_δ respectively. Now ω wolves change their positions according to position of α , β and δ wolves. It is expressed mathematically in equation (13).

$$\vec{X}(t+1) = \frac{\vec{X}_1 + \vec{X}_2 + \vec{X}_3}{3} \quad (13)$$

Where $\vec{X}(t+1)$ is updated position of ω wolves,
 $\vec{X}_1 = \vec{X}_\alpha - A_1 \cdot (D_\alpha)$, $\vec{X}_2 = \vec{X}_\beta - A_2 \cdot (D_\beta)$, $\vec{X}_3 = \vec{X}_\delta - A_3 \cdot (D_\delta)$ and
 $\vec{A} = 2\vec{a} \cdot \vec{r}_1 - \vec{a}$, $\vec{D}_\alpha = |\vec{C}_1 \cdot \vec{X}_\alpha - \vec{X}|$, $\vec{D}_\beta = |\vec{C}_2 \cdot \vec{X}_\beta - \vec{X}|$, $\vec{D}_\delta = |\vec{C}_3 \cdot \vec{X}_\delta - \vec{X}|$ and $\vec{C} = 2 \cdot \vec{r}_2$

Here t denotes iteration (hunting steps) and for initial case its value is 0. \vec{r}_1 and \vec{r}_2 are random vectors in the range [0 1]. The components of \vec{a} are linearly decreased from 2 to 0

in the course of iteration as distance between prey and wolves minimizes in each step. When equation (13) is substituted with values it becomes evident that ω wolves occupy positions within a circular region with respect to positions of α , β and δ values. The arrow mark above symbols represent vectors as movement includes both magnitude and direction. It is to be noted that linear decrease of \vec{a} along with random number \vec{r}_1 result in a range of \vec{A} values. The effect of this is that, when $|\vec{A}| > 1$, ω wolves position $\vec{X}(t + 1)$ diverges from prey and when $|\vec{A}| < 1$ it converges towards prey. With random numbers of \vec{r}_2 , value of \vec{C} falls in range $[0, 2]$. This is modelled to represent obstacles in path which wolves may experience in real situations. Each time α , β and δ wolves advances towards prey, ω wolves update their positions and finally all wolves jointly attack the prey and eventually consume it. From the model it is clear that hunting works purely based on position of α , β and δ wolves and objective function is minimisation of distance between wolves and prey. However one of the main aspect of hunting process i.e., advise of β to α wolves is not considered, as the model concentrates only on the position of ω wolves with respect to other dominant wolves. When we apply this process to optimization problems α , β and δ correspond to first, second and third best solutions respectively, satisfying objective functions of that particular optimization problem. In our case α , β and δ are first, second and third best groups of filter coefficients that maximizes PSNR (our objective function) of reconstructed image. It is to be noted that in our approach only first group of filter coefficients is significant as it is the group which provides maximum PSNR from so far concluded iterations. But as stated earlier second best solution β should also be considered so that first best solution can be improved. Hence a technique to obtain final best solution by incorporating best characteristics of both α and β solutions is necessary. This is done by means of EWA algorithm which is described in following section.

4.3 Earth Worm Optimization (EWA)

EWA is an optimization technique founded on the reproduction behaviour of earth worms. The characteristics of EWA is mentioned as follows: 1) Earth worm produces next generation by means of only two kinds of reproduction viz Reproduction 1 and Reproduction 2. 2) The genes of parent and child earth worms are of same lengths. 3) If a parent is better than child, it is carried to next generation without change. Earth worms are hermaphrodites, i.e., it has both male and female sex organs. So production of new off springs from a single parent comes under reproduction 1. In reproduction 2, two off springs are produced from two parents and they undergo cross over to obtain the final generated earthworm. As it is clear from previous section, our aim is to fuse both α and β solutions and obtain a probably better final solution. Hence we deal with reproduction 2.

Let P_1 and P_2 are two parents which produces off springs u_{12} and u_{22} . A random value in $[0, 1]$ range is taken to compare the parents and off springs as shown in equation (14).

$$\begin{cases} u_{12} = P_1 \text{ if } rand > 0.5; \text{ otherwise } u_{12} = u_{12} \\ u_{22} = P_2 \text{ if } rand > 0.5; \text{ otherwise } u_{22} = u_{22} \end{cases} \quad (14)$$

The final generated earthworm is given by equation (15)

$$\begin{cases} u_2 = u_{12} \text{ if } rand < 0.5 \text{ else} \\ u_2 = u_{22} \end{cases} \quad (15)$$

When applied to our de-noising approach, generated earthworm in (15) will be the final optimized filter coefficients

4.4 Multi-level Thresholding based Segmentation

The pixels of a grey level image can be represented as $[1, 2, \dots, L]$. In thresholding, image is divided into different levels and the number of pixels in each level is n_i . Hence total number of pixels is given as $N = n_1 + n_2 + n_3 + \dots + n_L$. The probability of number of pixels is given by equation (16).

$$p_i = \frac{n_i}{N} \quad (16)$$

$$\sum_{i=1}^L p_i = 1, \text{ where } p_i \geq 0 \quad (17)$$

Let us consider a single level thresholding process. Here image is divided into two classes, C_0 and C_1 with threshold k . C_0 and C_1 constitute pixels with levels $[1 \ 2 \ \dots \ k]$ and $[k + 1, \dots, L]$ respectively. The probabilities of class occurrence and class mean levels are given by equations (15) and (16)

$$\phi_0 = Pr(C_0) = \sum_{i=1}^k p_i = \phi(k) \quad (18)$$

$$\phi_1 = Pr(C_1) = \sum_{i=k+1}^L p_i = 1 - \phi(k) \quad (19)$$

And

$$\mu_0 = \sum_{i=1}^k iPr(i|C_0) = \sum_{i=1}^k ip_i/\phi_0 = \mu(k)/\phi(k) \quad (20)$$

$$\mu_1 = \sum_{i=k+1}^L iPr(i|C_1) = \sum_{i=k+1}^L \frac{ip_i}{\phi_1} = \frac{\mu_T - \mu_k}{1 - \phi(k)} \quad (21)$$

Where $\mu(k) = \sum_{i=1}^k ip_i$, $\mu_k = \sum_{i=1}^k ip_i$ and $\mu_T = \mu(L) = \sum_{i=1}^L ip_i$ are zeroth order cumulative moment of histogram up to k^{th} level, first order cumulative moment of histogram up to k^{th} level and total mean of original picture respectively. The class variances are given as follows

$$\sigma_0^2 = \sum_{i=1}^k (i - \mu_0)^2 Pr(i|C_0) = \sum_{i=1}^k (i - \mu_0)^2 p_i/\phi_0 \quad (22)$$

$$\sigma_1^2 = \sum_{i=k+1}^L (i - \mu_1)^2 Pr(i|C_1) = \sum_{i=k+1}^L (i - \mu_1)^2 p_i/\phi_1 \quad (23)$$

For analysing goodness of threshold at level k , discriminate criterion measures λ , K and η are introduced

$$\lambda = \frac{\sigma_B^2}{\sigma_W^2} \quad (24)$$

$$K = \frac{\sigma_T^2}{\sigma_W^2} \quad (25)$$

$$\eta = \frac{\sigma_B^2}{\sigma_T^2} \quad (26)$$

Where $\sigma_W^2 = \phi_0 \sigma_0^2 + \phi_1 \sigma_1^2$, $\sigma_B^2 = \phi_0 \phi_1 (\mu_1 - \mu_0)^2$ and $\sigma_T^2 = \sum_{i=1}^L (i - \mu_T)^2 p_i$ are within class variance, between class variance and total variance. Since σ_T^2 is independent of k and σ_B^2 is dependent on class means η is taken as a suitable measure. Therefore $\eta(k) = \frac{\sigma_B^2(k)}{\sigma_T^2}$ and $\sigma_B^2(k) = \frac{[\mu_T \phi(k) - \mu(k)]^2}{\phi(k)[1 - \phi(k)]}$. Optimal threshold k^* is the value which maximizes $\sigma_B^2(k)$. Hence,

$$\sigma_B^2(k^*) = \max_{1 \leq k < L} \sigma_B^2(k) \quad (27)$$

For multi-level thresholding processes like in our case the number of thresholds is increased, and optimal threshold is selected by the following formula

$$\sigma_B^2(k_1^*, k_2^*, \dots, k_n^*) = \max_{1 \leq k < L} \sigma_B^2(k_1^*, k_2^*, \dots, k_n^*) \quad (28)$$

Where $k_1^*, k_2^*, \dots, k_n^*$ are the thresholding levels? After multilevel thresholding, feature extraction is carried out, the mathematical preliminaries of which are discussed below. Based on above discussed mathematical derivations, proposed de-noising and subsidiary classification architecture is discussed in following section.

4.5 Noise Power Spectrum (NPS) and Bark Frequency based Feature Extraction

NPS

The NPS is obtained by applying Fourier transform to multilevel thresholded image as given in equation (29).

$$F_1 = K(f_a, f_b) = \lim_{\Delta a, \Delta b \rightarrow \infty} \frac{1}{\Delta a \Delta b} \left| \int w(a, b) \exp[-2\pi i(bf_b + af_a)] da db \right|^2 \quad (29)$$

Where F_1 NPS is feature, $K(f_a, f_b)$ correspond to pixels of transformed image, $w(a, b)$ are pixels of original image and $\Delta a, \Delta b$ denote t area over which integration is performed which ideally tends to infinity. For 2D images, F_1 is 2D image in frequency domain.

Bark Frequency

From frequency domain image obtained using NPS, Bark frequency is obtained by following formula

$$F_2 = B_f[f_e] = 13 \arctan[0.00076f_e] + 3.5 \arctan\left(\left[\frac{f_e}{7500}\right]^2\right) \quad (30)$$

Where F_2 is Bark frequency feature, B_f is frequency in Bark scale and f_e is frequency in Hertz scale. Based on above discussed mathematical derivations, proposed de-noising and subsidiary classification architecture is discussed in following section.

Since the method is carried out via two stages viz., training and testing, the steps in each stage is discussed separately as follows.

4.6 Proposed DTCWT filter design using Euler Frobenius Half band Polynomials (EFHBP)

The LP filter in THFB for non-causal forms is given as follows

$$H_0(z) = \frac{1+P}{2} + \frac{1}{2}T_1(z)(1-pT_0(z)) \quad (31)$$

$$G_0(z) = 1 + \frac{pT_0(z)}{1+p} + \frac{1-p}{1+p}T_2(z)\left\{\frac{1+p}{2} - \frac{1}{2}T_1(z)(1+pT_0(z))\right\} \quad (32)$$

Where $T_0(z), T_1(z)$ and $T_2(z)$ are kernels obtained from lagrange interpolation formula and p is parameter in the range [0 1] for shaping appropriate frequency response of filters. When $P=0$ THBP reduces to Half Band Pair Filter Bank (HPFB), which shows restrictions in frequency response. However in THBP at $\omega = \frac{\pi}{2}$ desired frequency response can be generated by adjusting the value of p .

The EFHBP can be expressed as follows

$$E(z) = \sum_{i=0}^N e(i+1)z^{-i} \quad (33)$$

Where N is polynomial order, whose coefficients are

$$e(i+1) = \sum_{k=0}^i (-1)^k \binom{N+2}{k} (i+1-k)^{N+1} \quad (34)$$

A sample even length polynomial thus obtained is given as follows

$$1 + 120z + 1191z^2 + 2416z^3 + 1191z^4 + 120z^5 + z^6 \quad (35)$$

This EFHBP is used to design desired HBP in our approach. Odd length EFHBP (orders 1, 3, 5 etc) are combined with Vanishing Moments (VMs) and an independent variable α_i to convert them into half band polynomials. The MEFHBP is expressed as follows.

$$P(z) = (1 + z^{-1})^M E(z) \sum_{i=0}^L a_i z^{-i} \quad (36)$$

Where M corresponds to number of vanishing moments and $E(z)$ is n^{th} order EF polynomial. Thus different half bands can be obtained by varying VMs and EFHBP. The final low pass synthesis and analysis filters are obtained by equations (31) and (32). The resulting filter thus contains two degrees of freedom.

4.7 Implementation Concept: Training Stage

Initially an image that belongs to any of the classes under study (texture, medical or satellite) is fed to the proposed system. Pre-processing steps such as greyscale conversion and resizing is done and then image is mixed with any of the desired noise type (Gaussian or Speckle). One copy of noisy image is fed to multi-level thresholding based segmentation block and another copy is fed to MEFHBP based DT-CWT block. Before beginning DT-CWT, PSNR of noisy image is calculated. As mentioned earlier, DT-CWT has a set of filter coefficients in each stage of sub band coding. In our approach, 2 stage DT-CWT is considered, as including multiple stages increase overall computation time. Consequently there are three sets of filter coefficients in 2 stages DT-CWT: one in first stage HP filter, one in second stages HP filters and one in second stage LP filter. The diagrammatic representation is given in figure 2.

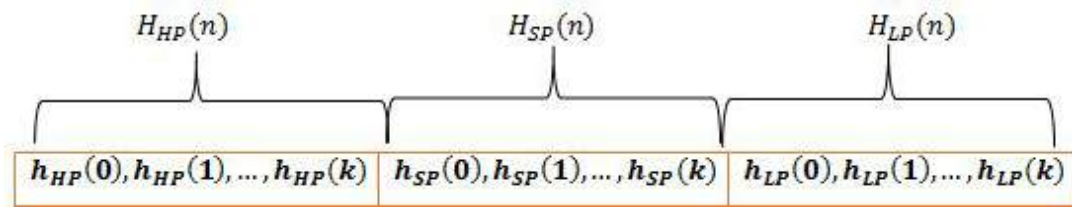


Figure 2: Filter Coefficients

The first stage HP filter coefficients are denoted as $[h_{HP}(0), \dots, h_{HP}(k)]$, second stage HP filter coefficients are denoted as $[h_{SP}(0), \dots, h_{SP}(k)]$ and second stage LP filter coefficients are denoted as $[h_{LP}(0), \dots, h_{LP}(k)]$. These filter coefficients are collectively denoted as $H_{HP}(n)$, $H_{SP}(n)$ and $H_{LP}(n)$. Now minimum and maximum value of each category of filter coefficients is identified. Let us assume that minimum and maximum values of $H_{HP}(n)$, $H_{SP}(n)$ and $H_{LP}(n)$ are $[a \ b]$, $[c \ d]$ and $[e \ f]$. From the range, new values are assigned to filter coefficients randomly. With new set of filter coefficients DT-CWT is performed. For reconstructed image PSNR is calculated. If current PSNR value is higher than PSNR value of noisy original image then current set of filter coefficients are labelled \vec{X}_α and earlier set of filter coefficients are labelled \vec{X}_β . Otherwise current ones are labelled \vec{X}_β and older ones are labelled \vec{X}_α . From new \vec{X}_α values, again random value assignment using minimum and maximum values is carried out. This makes sure that only \vec{X}_α values have dominance in predicting next set of filter coefficients. The newly obtained filter coefficients are given as input to inverse DT-CWT and from reconstructed image PSNR is calculated. By comparing PSNR of \vec{X}_α , \vec{X}_β and newly obtained image, filter coefficients with highest PSNR is labelled as \vec{X}_α , second highest is assigned \vec{X}_β and third highest is assigned \vec{X}_δ . Based on the values of \vec{X}_α , \vec{X}_β and \vec{X}_δ , another set of filter coefficients \vec{X}_ω is deduced using equation (13). PSNR is calculated for reconstructed image using \vec{X}_ω too and labelling of highest PSNR among the four as \vec{X}_α , second as \vec{X}_β , third as \vec{X}_δ and fourth as \vec{X}_ω is performed. Once all four values are obtained iteration 1 is begun. The first best solution \vec{X}_α and second best solution \vec{X}_β are given as input to EWA algorithm. They correspond to parents in EWA algorithm. The filter coefficients are randomly changed in the same manner mentioned above and two new set of filter coefficients each for \vec{X}_α and \vec{X}_β are generated. They are referred as u_{12} and u_{22} . These new sets of filter coefficients are termed off springs. PSNR is calculated again for

these off springs and if they are lesser than the corresponding parents they are discarded and their parents are kept as shown in equation (28)

$$\begin{cases} u_{12} = \vec{X}_\alpha \text{ if } PSNR\{\vec{X}_\alpha\} > PSNR\{u_{12}\}; \text{ otherwise } u_{12} = u_{12} \\ u_{22} = \vec{X}_\beta \text{ if } PSNR\{\vec{X}_\beta\} > PSNR\{u_{22}\}; \text{ otherwise } u_{22} = u_{22} \end{cases} \quad (37)$$

From the generated off springs, the final earthworm or best solution is produced by

$$\begin{cases} u_2 = u_{12} \text{ if } PSNR\{u_{12}\} > PSNR\{u_{22}\} \text{ else} \\ u_2 = u_{22} \end{cases} \quad (38)$$

\vec{X}_α , \vec{X}_β and \vec{X}_δ are replaced with first, second and third best solutions obtained so far. This completes iteration 1. It is to be noted that \vec{X}_β becomes significant only when offspring of \vec{X}_β shows a better solution compared to \vec{X}_α or offspring of \vec{X}_α . The procedure is repeated for fixed number of iterations and thus optimized filter coefficients which result in noise-free image is obtained. In our approach any of the solutions can become best solution \vec{X}_α at any iteration unlike normal GWO algorithm where only \vec{X}_β is permitted to replace \vec{X}_α . This solves local optimization problems to a little extent. Further in normal GWO algorithm, only α wolves are considered dominant whereas β and δ wolves are used to update position of ω wolves. This does not take into account advice of β wolves to α wolves in a social hierarchy. Integrating GWO with EWA solves this problem as coefficients of \vec{X}_β is also taken into account. The proposed EWGW algorithm is given below.

Algorithm 1: EWGW Optimization Algorithm
Initialize the population of the grey wolves
Initialize A, D and IT ^(max) (no of iterations)
Each search agent's fitness value is evaluated
Assign X_α and X_β as the first and second-best search agents
Assign X_α and X_β as the first and second parent
While (i<IT ^(max))
For each of the search agents
The parents X_α and X_β are combined using Eq. (28 & 29)
to form the child (updated solution)
End for
Update A and D
Calculate the fitness function of each search agent
Update the vectors X_α , X_β
i=i+1
End While
Return best solution

The optimized filter coefficients obtained after a fixed number of iterations need to be trained in ANN. So now the question is how to train these filter coefficients or to be more precise, with respect what parameter should we train optimized filter coefficients? The answer is the features NPS and Bark frequency extracted from the multi-level thresholded image. So let us shift our attention towards the classification stage from which the required features are extracted. The second part of the de-noising training process can be dealt after describing training process of classification stage. As previously discussed, one copy of noisy image is taken as input by multi-level thresholding based segmentation block. In our thresholding approach we consider only two thresholds and therefore there are three levels in thresholded image. Two thresholds are chosen as an increase in number of thresholds lead to decreased credibility of threshold levels. This is because equation (28) loses its meaning as well as get complicated with increased number of classes. Further two thresholds cover almost all practical applications. Now Fourier transform is

calculated for this multilevel thresholded image using equation (26). These NPS values forms the first feature set f_1 . From NPS value frequencies in Hertz scale is converted to bark scale using equation (30) which results in second feature set f_2 . Now these features are fed to two ANN (1stANN in de-noising and 2nd ANN in classification as discussed in introduction), the parameters of which are given in table 1.

TABLE 1: ANN PARAMETERS

Sl . No	Parameter	Value
1	Number of neurons in the Input Layer	PxQx2
2	Number of neurons in the hidden layer	(2/3* PxQx2)+R
3	Number of neurons in the output layer	R
4	Learning Rate	0.3
5	Momentum	0.9
6	Training type	Training by minimum error
7	Epochs	50
8	Minimum Error	0.01

Where PxQ is size of input image and R is number of object classes. In 2nd ANN feature values are multiplied with random weights so that we obtain a final value. The 2nd ANN maps this value to input image type. Now 2nd ANN is of the view that, any input image which produces same final value as that of first image, belongs to category of first image. Next an image type from another category is fed as an input. It also undergoes multi-level thresholding based segmentation and feature extraction and corresponding features produce a final value. If it is the same value as that of previous one then 2nd ANN groups it in the same class, to which it actually does not belong to. This is a problem of concern in our study because, as we took features from multi-level thresholding based segmented image, there are chances that images of different category might produce same values. Even though NPS and bark frequency curbs it to a commendable extent, in other cases weights need to be changed such that both images produce different values. This changing of weights is normally done by Back Propagation (BP) algorithms. But BP algorithms have a problem that they catastrophically forget earlier set of weights which might become useful in future training process. Therefore an algorithm which also considers previous weights needs to be used here. EWGW algorithm used in de-noising stage satisfies this requirement as they store first, second and third best solutions in \vec{X}_α , \vec{X}_β and \vec{X}_δ respectively. So EWGW is used to optimize weights. It works in similar manner as in de-noising stage with the only difference being objective function. Here objective function is minimization of classification error. The process is repeated for different images of three different categories resulting in optimized weights. Since we use only three types of images viz texture, medical and satellite in our approach, production of different values by all images is not feasible. This will lead to formulation of N values for N images leading to computational complexity. Therefore weights are optimized by EWGW in such a way that texture images produces a particular value, medical images produces a particular value and satellite images produce a particular value. A diagrammatic representation of optimized weights $[O_1, O_2, \dots, O_N]$ is shown in figure 3.

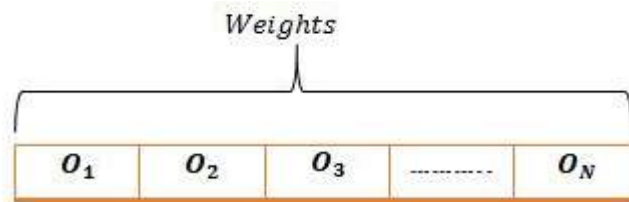


Figure 3: Ann Weights

Now second stage of de-noising can be explained. The optimized filter coefficients of first image as well as extracted features of 1st image are fed to 1st ANN. Here a one-one mapping of features f_1 and f_2 as well as optimized filter coefficients is performed.

We can summarize the training process as follows. When an image is fed to the model, it is mixed with noise and a copy is fed to multilevel thresholding based segmentation block and another copy is fed to the DT-CWT. After multilevel thresholding, NPS and Bark frequency features are extracted and fed to 1st and 2nd ANN. Meanwhile optimized filter coefficients are calculated by EWGW and is fed to the 1st ANN. 1st ANN trains optimized filter coefficients with respect to extracted features and objective function is given in equation (39). The second ANN trains extracted features with respect to image type using EWGW and objective function is given in equation (40). Training is repeated for 70% of images in the data set.

$$OF_1 = \text{Max}[PSNR] \quad (39)$$

$$OF_2 = \text{Min}[ER] \quad (40)$$

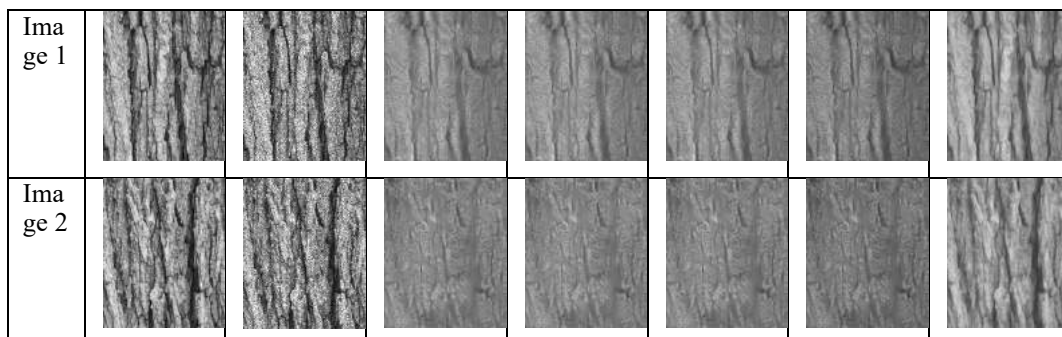
Next testing is done, the details of which are explained as follows.

4.8 Implementation Concept: Testing Stage

For testing process, remaining 30% of images from the data set are taken. These images are fed one by one to the system model. Like training process, image first undergoes multilevel thresholding based segmentation and DT-CWT. After segmentation NPS and Bark frequency features are extracted which are send to 2ndANN. The ANN based on optimized weights from training stage, calculates final value of image and based on the value classifies image to texture, satellite or medical classes. Meanwhile extracted features are fed to 1stANN which based on training library produces optimized filter coefficients, best suited for image features. With these optimized filter coefficients DT-CWT is performed resulting in final de-noised image. The results obtained for three images belonging to three different classes are taken for analysis. The following section discusses results obtained.

5. RESULTS AND DISCUSSION

The experiments are carried out in MATLAB R2018a. The images were taken from texture, medical and satellite data sets. Speckle noise with zero mean is considered as noise which corrupts image. The de-noised image for a sample image from texture class with noise variance of 0.02is shown in figure 4.



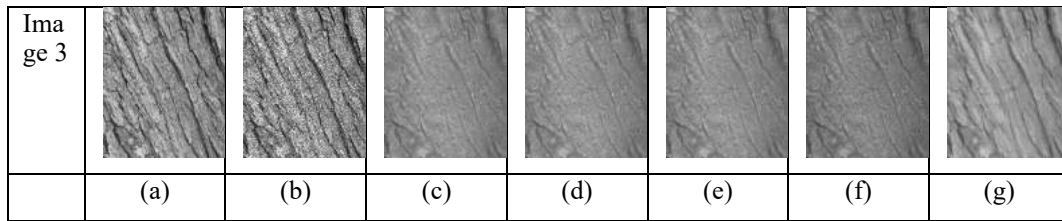


Figure 4: Experimental results using texture images for proposed Denoising model over the conventional models for (a) Original image (b) Noisy Image (c) LM-NN (d) PSO-NN (e) GWO-NN (f) EWA-NN (g) Proposed EWGW-NN

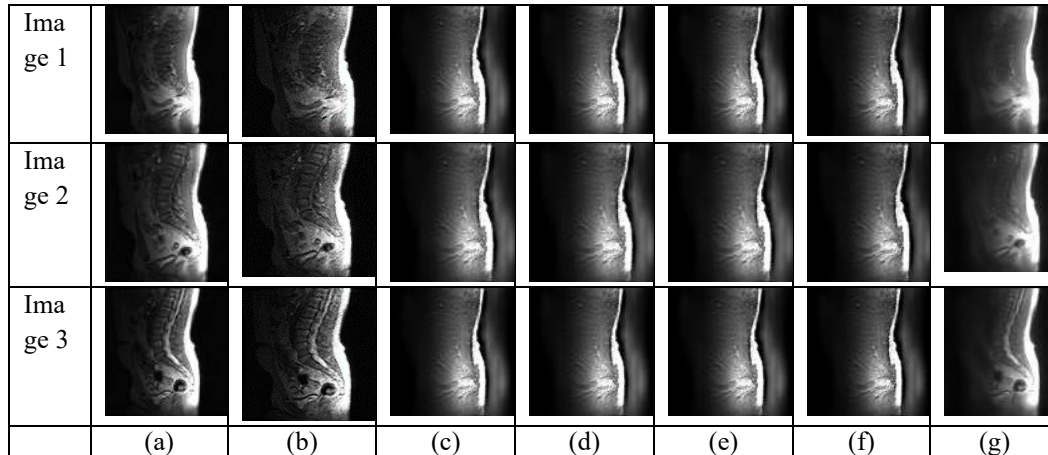


Figure 5: Experimental results using Medical images for proposed Denoising model over the conventional models for (a) Original image (b) Noisy Image (c) LM-NN (d) PSO-NN (e) GWO-NN (f) EWA-NN (g) Proposed EWGW-NN

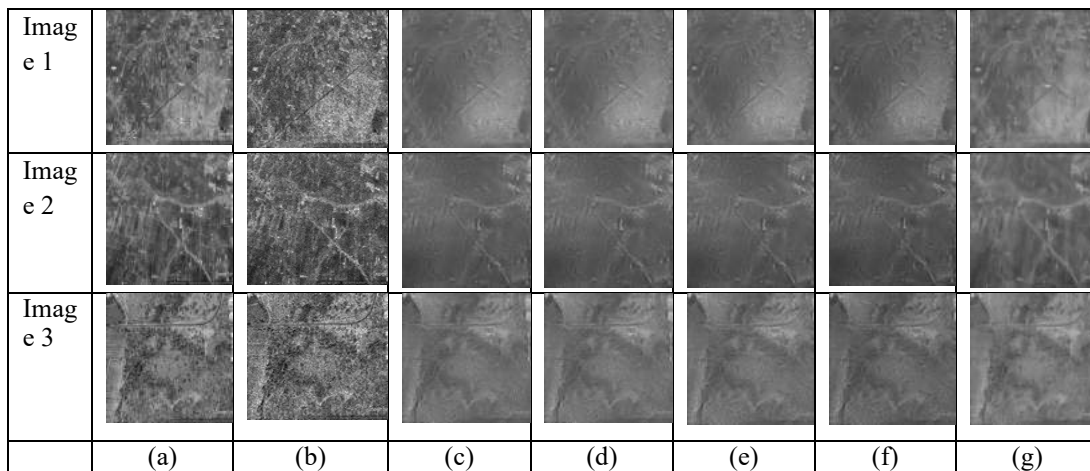


Figure 6: Experimental results using satellite images for proposed Denoising model over the conventional models for (a) Original image (b) Noisy Image (c) LM-NN (d) PSO-NN (e) GWO-NN (f) EWA-NN (g) Proposed EWGW-NN

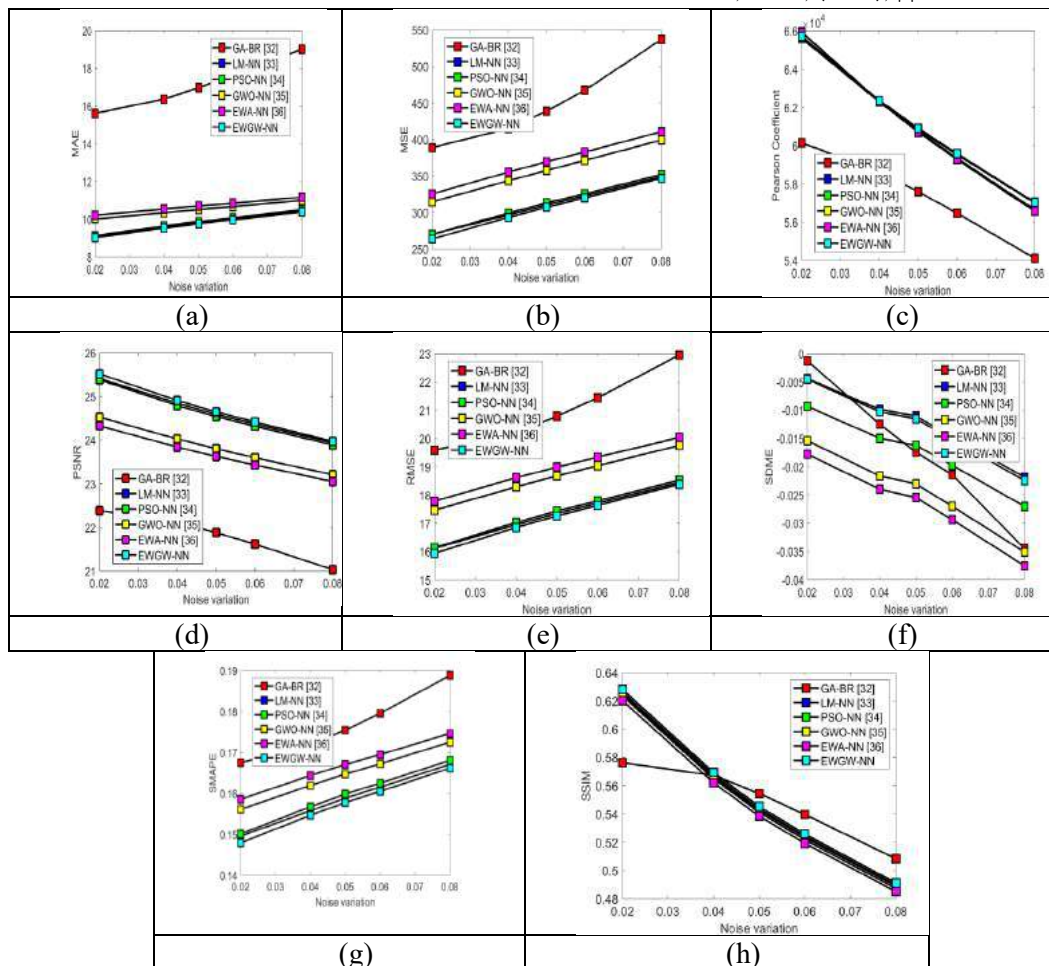


FIGURE 7: Analysis on proposed Denoising model over the conventional models for texture images showing error measures like (a) MAE (b) MSE (c) PC (d) PSNR (e) RMSE (f) SDME (g) SMAPE and (h) SSIM

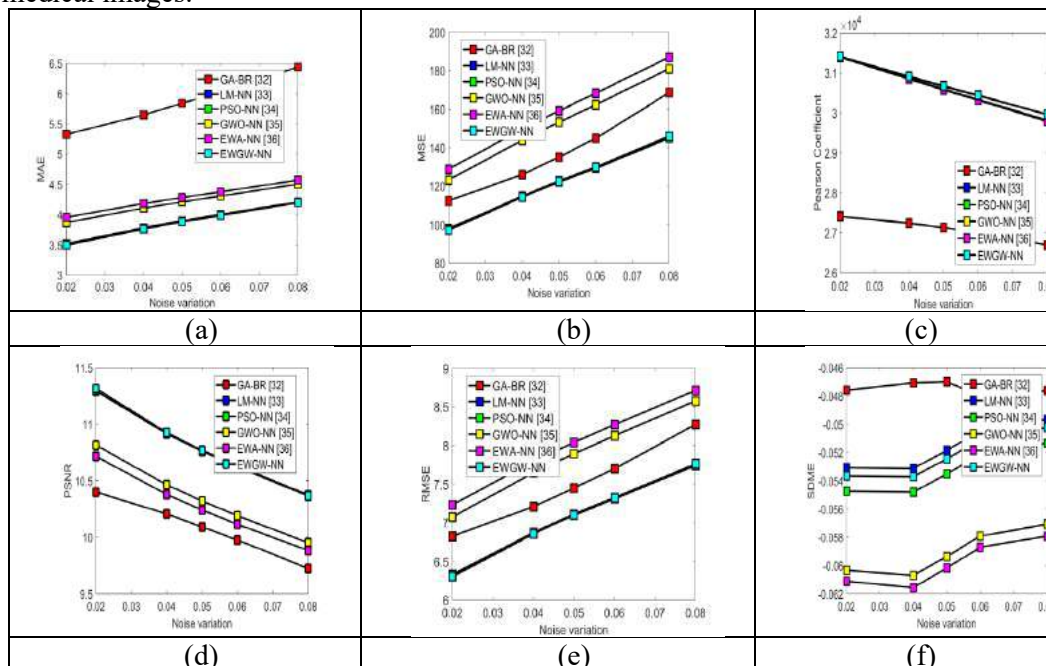
5.1 Texture Image Performance Parameter Analysis

Figure 7 depicts behaviour of the algorithms in terms of performance parameters for texture images. It is clear from the graphs that as noise is increased, MAE increases for all algorithms. This is due to the fact that ratio of image size to noise density decreases with increase in noise. Hence output image is less de-noised which lead to rise in MAE. This points out that MAE increases with increased levels of noise irrespective of algorithm used, and effective de-noising is also dependent on amount of noise present in image. The GA-BR algorithm shows highest MAE values compared to other algorithms studied. This can be attributed to the fact that GA is sensitive to initial population used. Moreover BR network does not define how to select a prior and hence require skills to translate subjective prior beliefs to mathematical prior. Without caution, results can be inaccurate which is evident from changes in MAE. Thus an algorithm which is dependent on initial conditions and priors produces lesser de-noised images. Exploration of search space and exploitation of same space resulted in plotted MAE values of EWA-NN. GWO-NN possesses low solving precision which ended in MAE values slightly lower than EWA-NN. PSO is unable to address problem of scattering especially for texture images. Premature convergence and lack of techniques to deal with scattering, lead to inefficient de-noising as seen from MAE values of PSO-NN. When EWA is combined with GWO, exploitation space is enlarged showing lower most MAE values for proposed EWGW algorithm. From graph of MSE and RMSE, it is found that GA-BR has highest values. However gap between EWA and GWO as well as PSO and EWGW is a little widened. This is because, MSE and RMSE assigns higher weight to large errors. For de-noising applications, RMSE is a preferred metric as large errors are undesirable. As noise

increases, correlation between input image and de-noised image decreases which is evident from PC graph. The lowest correlation exists for GA-BR algorithm and highest correlation is shown for proposed EWGW algorithm. As mentioned in case of MAE, amount of input noise has a profound impact on de-noised image. It can be noted that difference between algorithms becomes less and less and is the lowest at the point of large noise. If noise is increased further, at a point all algorithms will converge, producing identical outputs for noisy images. This can be best described by convergence phenomena of heuristic algorithms as best solutions become almost equal for all algorithms when image is filled with large amount of noise. For lowest noise value, EWA has better PC value compared to EWGW. This is mainly due to initial search space of EWA. As search space gets widened for EW, EWGW outperforms EW exhibiting better performance owing to enhanced exploitation. PSNR being a function of noise also shows decrement in values with noise. But unlike PC, PSNR values of all algorithms maintain almost constant distance between each other. This is because; both PSNR and SMAPE are calculated as function of MSE. Further from the graph it is clear that proposed EWGW algorithm has high PSNR values compared to others. From these values and perception of resultant images in figures 8, 9 and 10, improvement in edge sharpness and edge contrast compared to other methods is evident. The fitness value of GA algorithm is its SDME. Since GA-BR algorithm is dependent on initial population, its SDME value is high for lowest noise. But as noise increases, SDME value stoops drastically. This shows inability of fitness function to restore original image. LM algorithm shows best SDME results as SDME being a second order function are naturally dependent on LM update rules. However proposed method also shows results much closer to LM-NN despite its first order inclination. This is due to inclusion of cross over operation in EWGW algorithm. The EWA and GWO algorithms in their standalone versions produce negligible results due to its limited exploration space and bad local searching ability. Further LM-NN cannot be used to train large scale ANNs due to complexity issues. PSO shows SDME results in a medium scale as it converges prematurely and gets trapped into local minimum. SSIM considers that pixels of an image have strong interdependencies when they are close. So, when the SSIM is high, it means that closeness of de-noised image to actual image is more in terms of structure. However for texture images, GA-BR algorithm produces high SSIM than proposed algorithm, which is an area requiring further research.

5.2 Medical Image Performance Parameter Analysis

Figure 8 depicts behaviour of the algorithms in terms of performance parameters for medical images.



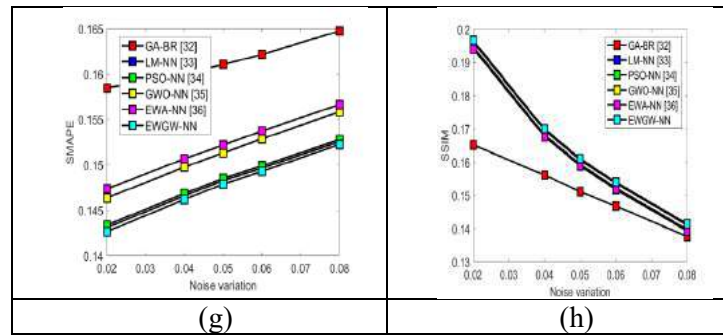


Figure 8: Analysis on proposed Denoising model over the conventional models for Medical images showing error measures like (a) MAE (b) MSE (c) PC (d) PSNR (e) RMSE (f) SDME (g) SMAPE and (h) SSIM

It is clear from graphs that as intensity of speckle noise is increased, MAE increases for all algorithms. The rise in MAE shows that image is less de-noised. However MAE values are significantly less for medical images compared to texture images. This can be attributed to the fact that medical images itself are of low contrast. The GA-BR algorithm shows highest MAE values compared to other algorithms studied. This is due to presence of big stochastic component in GA. Further BR produces different results unless same random seed is used. Thus an algorithm which has stochastic components and is dependent on a single random seed produces lesser de-noised images. Exploration of search space and exploitation of same space resulted in plotted MAE values of EWA-NN. GWO-NN possesses slow convergence which ended in MAE values slightly lower than EWA-NN. In PSO, first particle evaluated is redundant for some time and hence gives slow feedback. Thus de-noising with PSO is not effective as is evident from MAE values of PSO-NN. When EWA is combined with GWO, exploitation space is broadened showing lower most MAE values. However number of off springs generated is set to 2 in our approach and development of general frame work for any number of off springs is under research. From the graph of MSE and RMSE, it is found that GA-BR has highest values. However gap between EWA and GWO as well as PSO and EWGW is little widened. This is because, MSE and RMSE magnifies error values. The PC can be interpreted in the same way as in the case of texture images. PSNR is found to decrease with noise. However, PSNR values of all algorithms maintain steady distance between them as it calculated as a function of MSE. Same is the case of SMAPE. Since uniformity exists to an extent in the pixel values of medical images barring the region of interests, GA algorithm which is dependent on initial population gives more accurate results for de-noising in terms of SDME. It can be seen that as noise increases, SDME gets increased and is higher for large noises. This can be viewed as an effect of second order derivatives on studied algorithms. The GA-BR when it comes to medical images fails in case of SSIM and proposed algorithm overtakes it which can be explained as an effect of strong inter pixel dependencies.

5.3 Satellite Image Performance Parameter Analysis

Figure 9 shows behaviour of studied algorithms in terms of performance parameters for satellite images. In satellite images also, as noise factor is increased, MAE increases for all algorithms. But its MAE values are the lowest compared to medical and texture images. This can be attributed to spatial, temporal, spectral and radiometric characteristics of satellite images. As population size is small, GA-BR algorithm shows highest MAE values compared to other algorithms studied. Thus population size is a major factor affecting the de-noising of images. Exploration of search space and exploitation of same space resulted in plotted MAE values of EWA-NN. The MAE values of PSO and EWGW almost coincides with each other as PSO only has few inherent parameters to adjust. MSE, RMSE and SMAPE assign higher weights for small errors resulting in higher graph values. PC and PSNR values follow same description as in the case of texture and medical images. SDME shows stooping values initially and then rises for all algorithms in the case of satellite images. This is due to inherent second order derivatives. GA-BR fails when it

comes to SSIM of satellite images because in BR the posterior quantities vary due to random number generator.

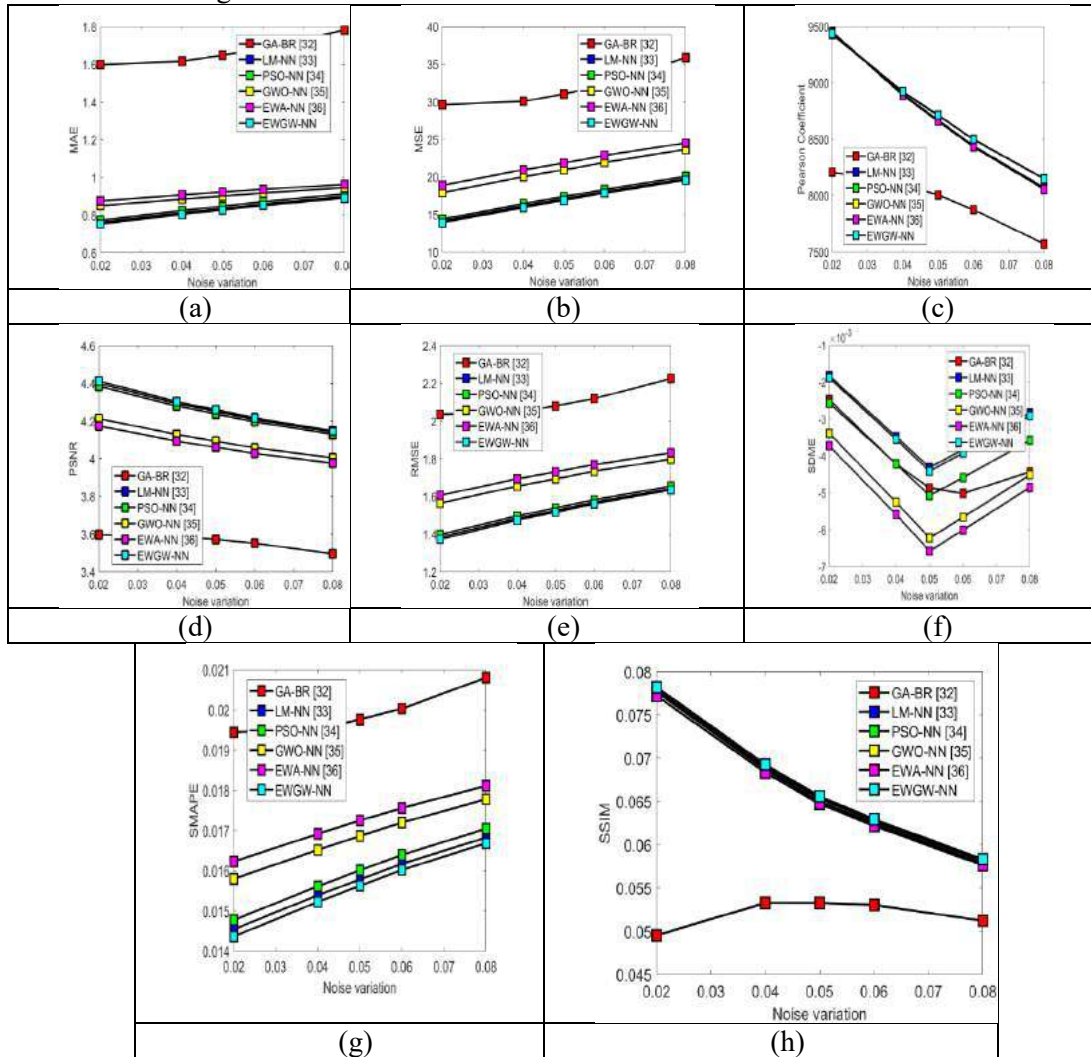


Figure 9: Analysis on proposed Denoising model over the conventional models for Satellite images showing error measures like (a) MAE (b) MSE (c) PC (d) PSNR (e) RMSE (f) SDME (g) SMAPE and (h) SSIM

5.4 Computational Efficiency

Figure 10 shows computation time comparison between proposed model and other algorithms.

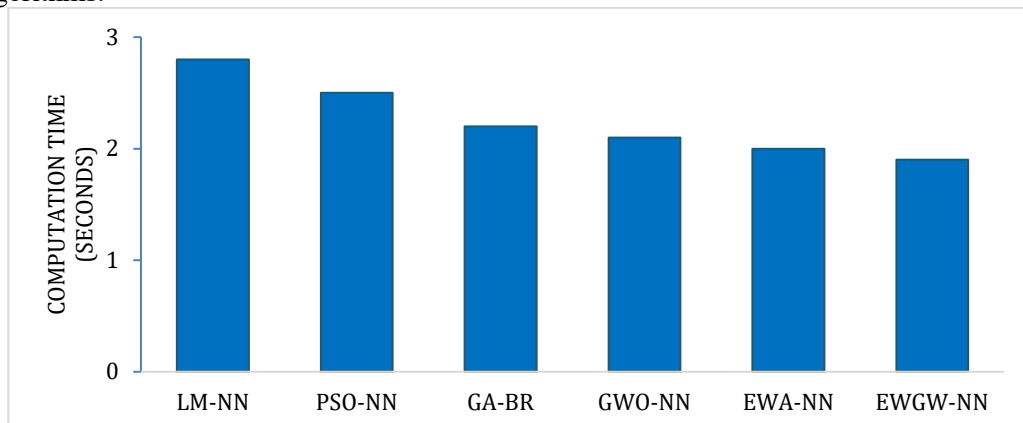


Figure 10: Computation Time Comparison of Proposed Method with Other Methods

From the graphs it is clear that computational efficiency of proposed scheme is 14.28% better than GA-BR, 40% better than LM-NN, 20% better than PSO-NN, 10% better than GWO-NN and 5% better than EWA-NN algorithms. This substantiates the view that EWGW is efficient in optimizing ANN weights with a lower computation time. Thus, computational efficiency of proposed model has been validated. From results of de-noised images as well as analysis of parametric values including computation time, optimization of DT-CWT filter coefficients by hybrid EWGW is found to perform better in the context of image de-noising.

6. CONCLUSION

The efficiency of DT-CWT has made it popular for image de-noising applications. However design of filters and optimization of filters is required for better de-noising. In this method an effort has been made to put forward a de-noising approach by designing a bi-orthogonal filter using Modified Euler Frobenius Polynomial and optimizing filter coefficients by a nature inspired Meta heuristic hybrid Earth Worm based Grey Wolf optimization (EWGW) algorithm. The algorithm is implemented on three different data sets and performance is compared based on different performance metrics. PSNR, SDME, SSIM, MSE, RMSE, MAE, PC SMAPE and computation time are the performance metrics used. To obtain better de-noised images, PSNR values should be high. The performance of EWGW is compared against GA-BR, LM-NN, PSO-NN, GWO-NN and EWA-NN based methods. The results validate that EWGW approach performs better than other approaches. The proposed filter design approach improved frequency response of analysis and synthesis filters in addition to improving linear phase properties, which is evident from quality of reconstructed denoised images.

References

- [1] A.Awad, Denoising images corrupted with impulse, Gaussian, or a mixture of impulse and Gaussian noise, *Engineering Science and Technology, an International Journal*, Volume 22, Issue 3, June 2019, Pages 746-753.
- [2] H.Naimi, A.B.H.A.Mitiche, L.Mitiche, Medical image denoising using dual tree complex thresholding wavelet transform and Wiener filter, *Journal of King Saud University - Computer and Information Sciences*, Volume 27, Issue 1, January 2015, Pages 40-45.
- [3] S.S.Gajbhar , M.V.Joshi, Image denoising using tight-frame dual tree complex wavelet transform, *Machine Intelligence and Signal Analysis-Advances in Intelligent Systems and Computing*, 748, Springer Nature, 2019.
- [4] U.Bal, Dual tree complex wavelet transform based denoising of optical microscopy images, *Biomedical Optics Express*, Volume 3, Issue 12, November 2012, Pages 3231-3239.
- [5] S.Mirjalili, S.M.Mirjalili, A.Lewis, Grey wolf optimizer, *Advances in Engineering Software*, Volume 69, January 2014, Pages 46-61.
- [6] G.G.Wang, S.Deb, L.Coelho, Earthworm optimization algorithm: a bio-inspired metaheuristic algorithm for global optimization problems, *International Journal of Bio-Inspired Computation*, Volume 12, Issue 1, January 2018, Pages 1-22.
- [7] X.Li, Y.Hu, X.Gao, D.Tao, B.Ning, A multi-frame image super-resolution method, *Signal Processing*, Volume 90, Issue 2, February 2010, Pages 405-414.
- [8] Z.Al-Ameen, S.Al-Ameen, G Sulong, Latest methods of image enhancement and restoration for computed tomography: a concise review, *Applied Medical Informatics*, Volume 36, Issue 1, March 2015, Pages 1-12.
- [9] J.Benesty, J.Chen, Y.Huang, Study of the widely linear wiener filter for noise reduction, In: *IEEE International Conference on Acoustics, Speech and Signal Processing*, Dallas, TX, USA, March 2010, Pages 205-208.
- [10] C.Tomasi, R.Manduchi, Bilateral filtering for gray and color images, In: *IEEE International Conference on Computer vision*, Bombay, India, January 1998, Pages 839-846.
- [11] M.Nikolova, Local strong homogeneity of a regularized estimator, *SIAM Journal on Applied Mathematics*, Volume 61, Issue 2, July 2006, Pages 633-658.
- [12] S. Esedoglu, S.J.Osher, Decomposition of images by the anisotropic rudin-osher-fatemi model, *Communications on Pure and Applied Mathematics*, Volume 57, Issue 12, December 2004, Pages 1609-1626.
- [13] A.Chambolle, T.Pock, A first-order primal-dual algorithm for convex problems with applications to imaging, *Journal of Mathematical Imaging and Vision*, Volume 40, Issue 1, May 2011, Pages 120-145.
- [14] A.Beck, M.Teboulle, Fast gradient-based algorithms for constrained total variation image denoising and deblurring problems, *IEEE Transactions on Image Processing*, Volume 18, Issue 11, July 2009, Pages 2419-2434.

- [15] M.Aharon, M.Elad, A.Bruckstein, K-SVD: an algorithm for designing overcomplete dictionaries for sparse representation, *IEEE Transactions on Signal Processing*, Volume 54, Issue 11, October 2006, Pages 4311-4322.
- [16] I.Markovskiy, *Low rank approximation: algorithms, implementation, applications*, Springer-Verlag London, 1 Edition, 2012.
- [17] L.Zhang, W.S.Dong, D.Zhang, G.M.Shi, Two-stage image denoising by principal component analysis with local pixel grouping, *Pattern recognition*, Volume 43, Issue 4, April 2010, Pages 1531-1549.
- [18] R.C. Gonzalez, R.E. Woods, *Digital Image Processing*, Pearson, 4 Edition, 2017.
- [19] H.Hassan, A.Saparon, Still image denoising based on discrete wavelet transform, In: *IEEE International Conference on System Engineering and Technology*, Shah Alam, Malaysia, June 2011, Pages 188-191.
- [20] V.Nigam, S.Bhatnagar, S.Luthra, Image denoising using wavelet transform and wavelet transform with enhanced diversity, *Advanced Materials Research*, Volume 403-408, 2012, Pages 866-870.
- [21] I.W.Selesnick, R.G.Baraniuk, N.G.Kingsbury, The dual-tree complex wavelet transform, *IEEE Signal Processing Magazine*, Volume 22, Issue 6, December 2005, Pages 123-151.
- [22] R.D.da Silva, R.Minetto, W.R.Schwartz, H.Pedrini, Adaptive edge-preserving image denoising using wavelet transforms, *Pattern Analysis and Applications*, Volume 16, Issue 4, November 2013, Pages 567-580.
- [23] L.Y.Hsu, S.J.Horng, P.Fan, H.H.Chou, X.Wang, M.Guo, Adaptive non-local means for image denoising using turbulent PSO with no-reference measures, In: *IEEE International Symposium on Biometrics and Security Technologies*, Chengdu, China, July 2013, pp. 251–258.
- [24] J.L.DePaiva, C.F.Toledo, H.Pedrini, An approach based on hybrid genetic algorithm applied to image denoising problem, *Applied Soft Computing*, Volume 46, September 2016, Pages 778-791.
- [25] Y.Dasari, S.K.Nayak, Image de-noising with the aid of dual tree wavelet transform and artificial bee colony optimization algorithm, *i-manager's Journal on Image Processing*, Volume 3, Issue 4, January 2016, Pages 9-18.
- [26] S.P.Zhao, X.W.Lei, J.H.Xing, Y.W.Ye, Wavelet image denoising by threshold optimization based on genetic algorithm, *Advanced Materials Research*, Volume 186, 2011, Pages 337-341.
- [27] S.Kirkpatrick, C.D.Gelatt Jr, M.P.Vecchi, Optimization by simulated annealing. *Science*, Volume 220, Issue 4598, May 1983, Pages 671-680.
- [28] J.Kennedy, R.Eberhart, Particle swarm optimization, *Proceedings of ICNN'95-International Conference on Neural Networks*, Perth, WA, Australia, December 1995, Pages 1942-1948.
- [29] M.Dorigo, M.Birattari, T.Stutzle, Ant colony optimization, *IEEE Computational Intelligence Magazine*, Volume 1, Issue 4, November 2006, Pages 28-39.
- [30] K.P.B.Resma, M.S.Nair, Multilevel thresholding for image segmentation using krill herd optimization algorithm, *Journal of King Saud University - Computer and Information Sciences*, April 2018, Pages 1-14.
- [31] N.Otsu, A threshold selection method from gray-level histograms, *IEEE Transactions on System, Man and Cybernetics*, Volume SMC 9, Issue 1, January 1979, Pages 62-66.
- [32] P.Venkata Lavanya, C.Venkata Narasimhulu, K.Satya Prasad, Dual stage Bayesian Network with Dual - Tree Complex Wavelet Transformation for Image Denoising, *Journal of Engineering Research*, Volume 8, Issue 1, Pages 154-178 March 2020.
- [33] S.Basterrech, S.Mohammed, G.Rubino et al, Levenberg—Marquardt training algorithms for random neural networks, *The Computer Journal*, Volume 54, Issue 1, January 2011, Pages 125-135.
- [34] M.R.Tanweer, S.Suresh, N.Sundararajan, Self regulating particle swarm optimization algorithm, *Information Sciences*, Volume 294, February 2015, Pages 182-202.
- [35] C.Lu, L.Gao, J.Yi, Grey wolf optimizer with cellular topological structure, *Expert Systems with Applications*, Volume 107, October 2018, Pages 89-114.
- [36] M.Ali, S.Abid, A.Ghafar et al, Earth worm optimization for home energy management system in smart grid, In: Barolli L., Xhafa F., Conesa J. (eds) *Advances on Broad-Band Wireless Computing, Communication and Applications. BWCCA 2017. Lecture Notes on Data Engineering and Communications Technologies*, Volume 12, Springer, Cham.
- [37] J.N.Kapur, P.K.Sahoo, A.K.C.Wong, A new method for gray level picture thresholding using the entropy of the histogram, *Volume 29, Issue 3, March 1985, Pages 273-285.*
- [38] J.John, M.G.Mini, Multilevel thresholding based segmentation and feature extraction for pulmonary nodule detection, *Procedia Technology*, Volume 24, 2016, Pages 957-963.
- [39] S.Routray, A.K.Ray, C.Mishra, Analysis of various image feature extraction methods against noisy image: SIFT, SURF and HOG, In: *Second International Conference on Electrical, Computer and Communication Technologies*, Coimbatore, India, February 2017, Pages 1-5.
- [40] S.Dolly, H.C.Chen, M.Anastasio et al, Practical considerations for noise power spectra estimation for clinical CT scanners, *Journal of applied clinical medical physics*, Volume 17, Issue 3, May 2016, Pages 392-407.

SUMULTI CODES- A Binary Forward Error Correcting Scheme

Dr.P.Sri Hari.*

Department of Electronics and Communication Engineering
GEETHANJALI COLLEGE OF ENGINEERING&TECHNOLOGY, Hyderabad, India
Email: mail2pshari@yahoo.com

Abstract

Forward Error correction, also referred to as Channel Encoding plays a vital role in providing error free or reliable information transmission/reception. A linear Block Code specified as (n, k) code encodes 'k' bit data into 'n' bit code word, by appending $r = n - k$ redundant bits, which are also referred to as parity bits.. The (n, k) Block Code is with a code efficiency or code rate of $R = \frac{k}{n}$, expressed as percentage. The provision of parity bits enables the code to address the influence of the additive noise in the channel on the message transmitted. The errors occurred in the data received can be Random errors, Burst Errors, and Random-Burst-type errors. The present discussion proposes two Channel encoding schemes namely "DATA INVERTING CODES" and "SUMULTI CODES", which are capable of correcting the channel errors.

Key words: Code efficiency, Parity word, Data Inverting Code, Sumulti code, Random and Burst errors, Constituent code, Error Vector

1.Introduction:

In a linear Block code represented as (n, k) code, each data word represented by a k-tuple as $D = [d_1 \ d_2 \ \dots \ d_k]$ is transformed independently into a code word represented as an n-tuple $C = [c_1 \ c_2 \ \dots \ c_n]$. In a Binary Block Code, the code elements are selected from binary alphabets 0 and 1, and hence the code is Binary Code.

In a systematic block code, each code word contains the original 'k' symbol(bit) data block unaltered, and the redundant bits are expressed in terms of data bits. These expressions are code specific. In the present paper, "SUMULTI CODES", with the ability of correcting various types of channel errors are proposed and each code word of SUMULTI code is 2- Dimensional, which is constructed using a 1-Dimensional (n, k) Data Inverting code (Weight Based Code) which is the constituent code for the specified SUMULTI code. In this 1-Dimensional code, in some of the code words, the inverted data word is the parity word and hence the name. The encoding of a data word is depending on the number of Non-Zero elements that are present in it i.e. its Weight. Hence, is the name Weight Based Code. All these constituent codes are 50% efficient. The code word of A SUMULTI code is a two dimensional $(8, k)$ code array and thus contains $8 \times k$ elements.

2. (n, k) Data Inverting Codes:

These codes can also be named as "Codes with Unequal Parity Bit Structure", since all the data words are not of the same weight. All the proposed Data Inverting codes (which are the constituent codes for SUMULTI codes) are systematic codes and are capable of correcting single error.

Dr.P.Srihari
mail2pshari@yahoo.com

2.1.Code word generation:

The code word of a Data Inverting code is expressed as $C = [d_1 \ d_2 \ \dots \ d_k \ p_1 \ p_2 \ \dots \ p_k]$ where $D = [d_1 \ d_2 \ \dots \ d_k]$ is the 'k' bit data word and $P = [p_1 \ p_2 \ \dots \ p_k]$ is the parity word of length $(n - k)$ with $n = 2k$.

In the code word C

- ❖ For the data word with zero/even weight → parity word is same as data word .
- ❖ For the data word with odd weight → parity word is the negated data word.

2.2.Decoding:

Let the code word at the receiver be $R = [d_1 \ d_2 \ \dots \ d_k \ p_1 \ p_2 \ \dots \ p_k]$

(R may not be equal to C)

Under the reception with no error, each R satisfies the following conditions:

In the received code word,

Condition1:

- If parity word is same as the data word, $\sum_i(d_i + p_i) = 0$, i bounded from 1 to k
- If the parity word is the negated data word, $\sum_i(d_i + p_i) = 1$, i bounded from 1 to k

Condition2:

- If the parity bits are same as the data bits, there will be $2k$ summations, where all result in a 0.
- Each sum consists of k terms.
- In each sum, the difference between number of data bits and parity bits will have a value form the set of integers $\{0,1,2,\dots,k\}$.

For Ex., in a (6, 3) Data inverting code, the summations are,

$$d_1 + d_2 + d_3 = 0; d_2 + d_3 + p_1 = 0; d_3 + p_1 + p_2 = 0; p_1 + p_2 + p_3 = 0;$$

$$p_2 + p_3 + d_1 = 0; p_3 + d_1 + d_2 = 0;$$

- If the parity bits are the inverted data bits, the above $2k$ summations result in alternate 1/0

For the received code word, if Condition-1 and condition-2 deviate from the results under error free communication, it indicates the reception is not error free.

2.2.1. Error Detection and Correction:

The difference between the received(R) and the transmitted (C) code vectors is referred to as Error Vector E. This is expressed as $E = R + C$. Under error free reception, $E = [0 \ 0 \ 0 \ \dots \ 0]_{1 \times n}$. If the reception is with error/s, E is a non zero vector.

For a given R, computation of E depends on the structure of the parity word and error location in R.

2.2.1.1. Identifying the structure of the parity word :

The structure of the parity word in R can be identified based on the Modulo-2 sum (length k) of D and P of R i.e. $D + P$.

In R,

- if the parity word is same as the data word,
 - ✓ $D + P = [0 \ 0 \ \dots \ 0]_{1 \times k}$, under error free R

- ✓ $D + P$ consists of $(k - 1)$ number of 0s, under R with error
- If the parity word is the negated data word,
 - ✓ $D + P = [1\ 1\ \dots\ 1]_{1 \times k}$ under error free R
 - ✓ If the reception is with error, $D + P$ consists of $(k - 1)$ number of 1s , under R with error

2.2.1.2. Estimating the Error Location:

Error location in R can be estimated using Condition-1. Deviation of any of the ' k ' summations of R with reference to the error free condition is an indication of either d_i or p_i of that summation is in error.

3.2.1.2.1. Locating the Error :

Error in R can be located using the **Condition-2**. The ' $2k$ ' summations of Condition-2 are partitioned into two equal halves, such that if k summations in one of the partitions contain d_i , then the summations of other partitions contain p_i or vice versa. The k summations of which partition differ from the error free conditions is considered to contain the error and the error will be either d_i or p_i that is available in all the k summations of that partition.

2.2.1.2.2. Error Correction:

The corresponding E consists of $(n - 1)$ zeros and a single 1. The position of 1 in E corresponds to the position of the located error in R. The corrected Code word is $C = R + E$.

3. SUMULTI CODES:

Using the proposed single error correcting Data Inverting code as the constituent code, the code word of the SUMULTI code can be generated. SUMULTI code stands for SUM-MULTIPLICATION code. The code word of the code is 2-dimensional. There are two stages of encoding. In the first stage, the 2-Dimensional code array is constructed using the specific Data Inverting code being the constituent code. In the final stage, all the columns of the array are encoded using an (8,4) Data Inverting code, column wise. The total number of elements in the code word of the SUMULTI code is $8Xk$.

3.1. Code word Generation:

In the first stage of encoding, the k bit data word is encoded using the respective Data inverting code. The k bit data word and the k bit parity word of the above data inverting code form the first and second rows respectively in the code array of the code word of a SUMULTI code. The third row and fourth rows of the array are respectively the Modulo-2 sum and the AND product (element wise) of the first and second rows.

In the second stage of encoding, each of the ' k ' columns of the code array will be encoded using (8, 4) Data Inverting Code, there by forming an $(8, k)$ code word of the SUMULTI Code.

3.2. Locating and correcting the Error/s:

The code word will be sent through Block interleaving, i.e. row wise with $(8Xk)^{th}$ element in the last row of the array as the first and first element of the first row as the last.

At the receiver, is arranged back in the same order as an array.

The process of locating and correcting the error/s is implemented on the received on column by column basis.

4. Illustration:

Let the received code array be

$$\begin{matrix} 1 & 0 & 1 \\ 0 & 0 & 1 \\ 1 & 1 & 1 \\ 0 & 0 & 0 \\ 1 & 0 & 0 \\ 0 & 1 & 1 \\ 1 & 1 & 1 \\ 0 & 0 & 0 \end{matrix}$$

(6,3) Data Inverting code is the constituent code, as the first row of the array which is the actual data word is of length 3.

Column-1 of the received code array is

$$\begin{matrix} a & b & c & d & e & f & g & h \\ 1 & 0 & 1 & 0 & 1 & 0 & 1 & 0 \end{matrix}$$

** a, b, c, \dots , represent the bit positions.

The Modulo-2 sum of bits in the positions e, f, g, h and the bits in the positions a, b, c, d is 0000 , indicating that the column-1 of the received array is encoded using the Data Inverting code $(8, 4)$, where the parity bits of this code word are same as the first four bits, **and is received without error. The corresponding Error Vector is $E=00000000$.**

Similar Modulo-2 additions for column-2 of the code array results in 0100 indicating that column-2 is also encoded similar to column-1, and there is a single error in the received.

Its location can be estimated as either the position b or f of the 2nd column.

To locate the error, the summations of Condition-2 are partitioned into two halves such that summations in Partition-1 contains the bit in position b and summations in Partition-2 contains the bit in position f .

Under Error Free reception, this partitioning will be

Table1. Partitioning under error free reception

Partition-1	Partition-2
$a + b + c + d = 0$	$c + d + e + f = 0$
$b + c + d + e = 0$	$d + e + f + g = 0$
$g + h + a + b = 0$	$e + f + g + h = 0$
$h + a + b + c = 0$	$f + g + h + a = 0$

The summations are for the bits in the positions indicated.

These summations for column-2 of the received result in

Table2. Partitioning in the case of received

Partition-1	Partition-2
$a + b + c + d = 1$	$c + d + e + f = 0$
$b + c + d + e = 1$	$d + e + f + g = 0$
$g + h + a + b = 1$	$e + f + g + h = 0$
$h + a + b + c = 1$	$f + g + h + a = 0$

Since, the summations in Partition-1 are differing from the results under error free conditions, and all the summations are having b in common, it can be decided that the bit in that position of column-2 of the array is in error. The respective Error Vector is $E = 0 1 0 0 0 0 0$. Thus, the error free column -2 of the received array will be $E + \text{Column-2 of the received}$, which results in $0 1 1 0 0 1 1 0$.

Similar process for column-3 of the received array indicates the presence of error in position a of the column-3. The respective Error Vector is $E = 1 0 0 0 0 0 0 0$. Thus, the error free column -3 of the received array will be $E + \text{Column-3 of the received}$, which results in $0 1 1 0 0 1 1 0$

Thus, the error free code array is

$$\begin{matrix} 1 & 0 & 0 \\ 0 & 1 & 1 \\ 1 & 1 & 1 \\ 0 & 0 & 0 \\ 1 & 0 & 0 \\ 0 & 1 & 1 \\ 1 & 1 & 1 \\ 0 & 0 & 0 \end{matrix}$$

5. Probability of Undetected Error:

If the presence of the error is not detected, such error becomes an Undetected error. With reference to a Binary Symmetric Channel, if the code used for only error detection, the probability with which the detector misses the error i.e. probability with which the error is undetected is $p(e)$.

The probability for the receiver for not detecting the error $p(e) =$

$(1 - p)^L \cdot [W\left(\frac{p}{1-p}\right) - 1]$, where, $W\left(\frac{p}{1-p}\right) = W(\alpha)|_{\alpha=\frac{p}{1-p}}$, where $W(\alpha) = \sum_{i=0}^n W_i \cdot \alpha^i$ is the weight enumerator of the code, and W_i gives the number of code words of the SUMULTI codes having weight ' i '. ' p ' is the transition probability i.e. $p(0/1)$ or $p(1/0)$ and ' L ' is the length of the code word.

The set of weight distributions of the SUMULTI code, with (6,3) Data Inverting constituent code is $\{W_0, W_{12}\} = \{1, 7\}$, i.e. the code is having 1 code word with a zero weight and 7 code words with weight Twelve. Thus, the corresponding (24,3) SUMULTI code has a weight enumerator $W(\alpha) = 1 + 7\alpha^{12}$.

The Probability of for the receiver for missing the error detection is $p(e) =$

$$(1 - p)^{24} \left[1 + 7 \left(\frac{p}{1-p} \right)^{12} - 1 \right].$$

For a transition probability of 10^{-1} , $p(e)$ is found to be 1.97×10^{-12} . This can be interpreted as: if there are 10^{12} code digits present at the detector, on average 2 incorrect digits will be undetected.

6. Conclusion:

The Proposed Data Inverting Code corrects single error present in the code word. SUMULTI code is a Two dimensional code used to correct multiple number of errors, both random and Burst errors. The proposed SUMULTI code words will be obtained from the corresponding Data Inverting Code as a constituent code.

The proposed SUMULTI codes has the capacity of correcting burst errors of burst length ' k ' (appearing along a row of the code array), in addition to having the capacity of correcting random errors.

7. References:

1. Abraham Lempel, & Shmuel Winograd (July 1977). - "A New Approach to Error Correcting Codes" - IEEE Trans. Inform. Theory, vol. IT-23, No. 4, pp. 505-508.
2. Andrew J. Viterbi, & Jim K. Omura (1979). - "Principles of Digital Communication and Coding" - McGraw-Hill International Edition
3. F. J. MacWilliams & N. J. A. Sloane (1977). - "The Theory of Error-Correcting Codes" - North Holland Publishing Company
4. Richard E. Blahut (Nov. 1977). - "Composition Bounds for Channel Block Codes", IEEE Trans. Inform. Theory, Vol. IT-23, No. 6, pp. 656-674.
5. Shu Lin, Daniel & J. Costello, JR (1983). - "Error Control Coding - Fundamentals and Applications" Prentice-Hall, Inc. Englewood Cliffs, New Jersey 07632
6. P. Sri Hari & Dr. B. C. Jinaga (2007). - "DATA INVERTING CODES" - Ph.D Thesis, Jawaharlal Nehru Technological University, Hyderabad, India.
7. N. SHRIBALA, Dr. P. SRIHARI and Dr. B. C. JINAGA. - "Data Negation Codes - A Binary Channel Coding Scheme" - 2013 IEEE INDICON held at Indian Institute of Technology, Bombay, India, during 13-15 Dec, 2013
8. Dr. P. SRIHARI. - "Multiple Error Correcting Binary Channel Coding Schemes and their error Performance" - International Journal of Innovative Research in Computer and Communication Engg. - Vol. 2 Issue 2, February, 2014.
9. Dr. P. SRIHARI. - "Sum Codes - A Binary Channel Coding Scheme" - International Journal of Computer Science and Technology - Vol. 5 Issue Spl 1, January - March, 2014, p. No. 60-64.
10. Dr. P. SRIHARI. - "Multiplication Codes - A Multiple Error correcting Binary Channel Coding Scheme" - International Journal of Applied Engineering Research, Vol. No. 9, Pg. Nos. 8857-8873 August 2014

Authors



Name: Dr. P. Srihari

Profile:

Dr. P. Srihari obtained his Ph.D from Jawaharlal Nehru Technological University, Hyderabad, India. He is having 30 years of Teaching experience. His areas of interest are Communication Engineering and Signal processing. He is the author of Text Books in the area of Digital Communication, Random Variables and Random Processes.

Dual Stage Bayesian Network with Dual-Tree Complex Wavelet Transformation for Image Denoising

P.Venkata Lavanya*, C.Venkata Narasimhulu** and K.Satya Prasad***

*Research Scholar, Department of ECE, Jawaharlal Nehru Technological University, Kakinada, Kakinada, Andhra Pradesh, India

**Department of ECE, Geethanjali College of Engineering and Technology, Hyderabad, Telangana, India

***Vignans Foundation for Science, Technology and Research, Guntur, Andhra Pradesh, India

*Corresponding Author: pvlavanya999@gmail.com

ABSTRACT

Image denoising always plays a vital role in various engineering bids. Moreover, in image processing technology, image denoising statistics is persisted as a substantial dispute. Over the past decades, certain denoising methods have reached incredible accomplishments. Since there is no much contribution on image denoising considering multimodal and heterogeneous images, this paper motivates us to extend it with the aid of intelligent approach. Dual-tree Complex Wavelet Transform (DT-CWT) is exploited for image transformation for which the wavelet coefficients are estimated using Bayesian Regularization (BR). To ensure the denoising performance for heterogeneous images, the statistical and wavelet features are extracted. Subsequently, the image characteristics are combined with noise spectrum to develop BR model, which estimates the wavelet coefficients for effective denoising. Hence, the proposed denoising algorithm exploits two stages of BR. The first stage predicts the image type, whereas the second stage estimates appropriate wavelet coefficients to DT-CWT for denoising. As a main contribution, the filter coefficients of DT-CWT are optimized by Genetic Algorithm (GA). The performance of the proposed model is analysed in terms of Peak Signal to Noise Ratio (PSNR), Second derivative Measure of Enhancement (SDME), Structural Similarity (SSIM), Mean Squared Error (MSE), Root Mean Square Error (RMSE), Mean Absolute Error (MAE), Pearson Coefficient (PC), and Symmetric Mean Absolute Percentage Error (SMAPE), respectively. The proposed model is compared to the conventional models, and the significance of the developed model is clearly described. From the analysis, it is observed that the PSNR of the developed model is 69.97%, 5.85%, 76.91%, 33.38%, 46.40%, and 46.44% better than 2D SMCWT, DT-CWT, DT-CDWT, DT-RDWT, W-ST, and W-HT, respectively. Similarly, for SSIM measure, the proposed model has great deviation over conventional methods, and the model is 19.17%, 83.66%, 24.65%, 72.99%, and 73.15% better than DT-CWT, DT-CDWT, DT-RDWT, W-ST, and W-HT, respectively.

Keywords: Bayesian Regularization; DT-CWT; Genetic Algorithm.; Image Denoising; Filter coefficient.

INTRODUCTION

Image noise removal is a necessary pre-processing function in diverse optical engineering applications (Liu & Fang, 2015; Wang & Kai Fu, 2010; Nasri & Nezamabadi-pour, 2009; Jin, 2013; Liu *et al.*, 2009; AM Wagh & Todmal, 2015; Sable & Jondhale, 2010). The multiple noises occurred from the image acquisition, and transmission process destroys the image quality. In the domain of image processing, image denoising has been persisted as a significant issue (Guo *et al.*, 2017; Hou *et al.*, 2011; Wang *et al.*, 2013; Ghorai, 2013; Xin & Jiangtao, 2011). As a challenge to this issue, numerous researchers have developed several noise reduction techniques for the removal of noise from the image. The development of new sensors and the improvement of image denoising models have eventually brought the remote sensing community to consider the use of satellite images acquired under heterogeneous conditions (Wei *et al.*, 2017; Maoguo *et al.*, 2016; Zhun-ga *et al.*, 2017; Luigi *et al.*, 2017). This has led to methods based on heterogeneous sources of data (Wei *et al.*, 2017; Puzhao *et al.*, 2016; Zhun-ga *et al.*, 2017; G. Mercier *et al.*, 2008; Jorge *et al.*, 2015; Zhunga *et al.*, 2018), also referred to as multi-source (Maoguo *et al.*, 2016; Devis *et al.*, 2016), multi-modal

(Redha et al., 2018), multi-sensor or cross-sensor (Bard et al., 2009; Michele et al., 2015; Redha et al., 2018), and information unbalanced data (Linzi et al., 2017). Among those techniques, more conventional algorithms execute image denoising process in the pixel domain. Over the past decades, some denoising techniques based on transform domain have revealed incredible achievements (Rabbani, 2009; Shang et al., 2012; Yang et al., 2012; Wong et al., 2011; Luo & Zhu, 2012; Decker et al., 2010). In fact, the transform-based denoising characteristically approximates the true signal by a linear grouping of some basic features (Liu et al., 2008), which specifies the signal in the form of transform domain. Thus this technique transfers the true signal energy by conserving some transform coefficients with high magnitude and destroys the uncertainty due to noise, leading to estimate the true signal in an effective manner. Moreover, the properties of transform, as well as true signal, provide the sparsity of overall representation.

In fact, a number of standard models are there for denoising the noisy image, which has the capability of performing distinct filtering process that minimizes the level of noise. However, the image comes under the blur condition or under over smoothed since it loses its edges. Noise minimization is utilized to eliminate the noise even without losing any details present in the images. Some of the spatial filters, such as mean as well as median, are utilized to eliminate the noise from the corresponding image. However, a drawback of the spatial filter is that while smoothing the image, the edges become blurred. Thus, the wavelet transform is very efficient to preserve the image's edges. It is considered as one of the powerful tools of signal processing because of its multi-resolution possibilities. Wavelets also produce the effective performance in denoising the image with its precious properties like sparsity as well as multi-resolution structure. Moreover, wavelet transform (Li et al., 2016) has already shown its effectiveness in removal of noise, also minimizes the complexity of the computations, and facilitates best noise minimization performance.

The wavelet transform achieves effective sparsity for localized details including edges and singularities. Basically, those details are typically very high in natural images and also convey the particular portion the data embedded in, and the wavelet transform is represented as the distinct application for denoising of image (Wang et al., 2010). More advanced denoising models are developed based on wavelet transforms (Beck & Teboulle, 2009; Luisier et al., 2007; Pizurica & Philips, 2006; Portilla et al., 2003; Yan et al., 2008). For some particular natural images, the wavelet coefficients comprise small magnitudes, but present some large magnitude also, which is considered as the vital high-frequency features of image including edges. Between all wavelet coefficients, the white noise is distributed evenly, but while eliminating small wavelet coefficients, minimizing the noise energy at the time of preservation. The problem of image noise suppression remains an open challenge, especially in situations where the images are acquired under poor conditions where the noise level is very high. To denoise an image, wavelet transform is adopted because it gives coefficients with respect to the functions. Once the coefficients are obtained, they can be used for any purpose. With that coefficient, one can reconstruct, denoise, compress the image, etc.

This paper contributes an intelligent image denoising model. The proposed denoising algorithm exploits two stages of BR. The first stage categorizes the image types, whereas the second stage estimates appropriate wavelet coefficients to DT-CWT for denoising. The paper intends to exploit BR since it explores advantages like easier implementation, good result obtainment in most of the cases, and also it necessitates a smaller amount of training data to estimate parameters (Aggarwal et al., 2005). Further, the filter coefficient parameter of DT-CWT is optimally selected using Genetic Algorithm (GA), which is chosen because it can find fit solutions in much less time. Moreover, it is intrinsically parallel and gives chances for getting more optimal solutions. In addition, DT-CWT parameters solve the problems of shift variance and low directional selectivity in two and higher dimensions found with the commonly used Discrete Wavelet Transform. Since the Bayesian Network has been used for both image classification and image denoising, the process is termed as Dual-stage network. The proposed model is compared to conventional methods like 2D Scale Mixing CWT (2D SMCWT), DT-CWT, Dual-Tree Complex DWT (DT-CDWT), Dual-tree Real DWT (DT-RDWT), Wavelet Soft Thresholding (W-ST), and Wavelet Hard Thresholding (W-HT). The rest of the paper is organized as follows: Section II reviews the literature work. Section III describes the developed image classification model. Section IV explains the weight optimization based image denoising strategy. Section V discusses the results obtained, and Section VI concludes the paper.

LITERATURE REVIEW

In 2017, Guo *et al.* have presented the image denoising model, which was on the basis of ‘Stationary Wavelet Transform (SWT)’ along light noise. SWT based denoising procedure was offered after the analysis of light noise. With the use of this denoise algorithm, the developed model was established conforming to granting accurate DIC measurements even in the light noise scenario. Further, the developed method was compared with the existing models, and the real-time experimentation was also carried out to ensure the performance of the model. From the results, it was evident that the developed denoising model could be applied for the full-field strain measurement in light interference with more accuracy and stability, respectively.

In 2016, Li *et al.* have developed a ‘Wavelet-based Contour let transform (WBCT)’ model to achieve an Adaptive Optics image denoising. This model was implemented via ‘Bayes Shrink’ theory for the assessment of the threshold. Then they also contributed to the enhancement of the adaptive model for threshold choosing by which they have attained optimal threshold. Here, the denoising of image was achieved by choosing the adaptive optimal threshold by using the WBCT transform coefficients of varied decomposition scale and directions. The algorithm was evaluated with the aid of ‘DTCWT-BayesShrink algorithm’, ‘DWT-NA Bayes Shrink algorithm’, and ‘CbATD algorithm’. The developed model was examined using real AO images and simulated images. From the analysis, they have attained better performance in terms of ‘peak signal-to-noise ratio (PSNR)’ and visual quality as well.

In 2014, Remenyi *et al.* have developed an image denoising model, which was on the basis of ‘2D scale-mixing complex-valued wavelet transform’. To attain this, they have used both unitary (minimal) and maximal (redundant) versions. By this, they have established the covariance structure of a noise, namely, white noise in wavelet domain. The model assessment was achieved through empirical Bayesian modalities that include the preserved versions of the complex-valued wavelet coefficients. Hence, the new procedure has displayed the perfect quantitative performance as well as visual performance through simulation.

In 2015, Jesus *et al.* have established a model for high resolution small animal 3D PET data. This has been aimed for the minimization of noise and for providing the detailed pervasiveness. This was on the basis of assessment of the non-sampled Haar wavelet coefficients with the aid of linear estimator. The model was applied to the images like volumetric images, which were reconstructed without alteration influences (reconstruction). The simulation results have shown the pervasiveness of the developed model, and also the method has ultimately minimized the noise presented in the image.

In 2014, Sun *et al.* have presented a novel image denoising model with the use of linear Bayesian ‘Maximum a Posteriori (MAP)’ assessment on the basis of sparse demonstration classic. In the preliminary step, the probability dissemination was constructed in representation vector. They have also constructed the ‘linear Bayesian MAP estimator’ for obtaining the probabilistic observation. This was adopted for solving the problem, named inverse problem. Moreover, they have also attained the solution for closed-form solution and hence, they have achieved better image denoising strategy. They have also classified them to various sub-groups with their patterns and performed the training process of various dictionaries with the aid of ‘K-SVD algorithm.’ The denoised image was acquired by smearing the denoising to each subgroups, which was on the basis of estimator and also by doing mean of the two outputs. The proposed model was compared to the existing models. The simulation results have shown the competitive performance of the developed denoising model in terms of both visual quality and PSNR value.

In 2016, Song *et al.* have developed a deblurring model, which was based on ‘Gradient Histogram Preserving (GHP)’. In the methods used for the development, they were parameterized with Hyper-Laplacian dissemination. With the consideration of blurring complexity, a Bayesian model named Gaussian processes reversion was used for assessing the parameters of the histogram. The experimentation was carried out for the developed model, and the results have viewed the efficiency of the parameter assessment. Moreover, the quality of the image was highly enhanced, and the restoration of the image was well performed.

In 2015, Naimi *et al.* have developed a denoising model, which was on the basis of DTCWT with wiener filtering model. The experimentation was carried out for the proposed image and from the results, it was proved that the denoised images with DTCWT have more balancing power among smoothness as well as the accuracy, whereas the remaining models like SWT (Stationary Wavelet Transform) have less accuracy. They have also utilized the SSIM (Structural Similarity Index Measure) with PSNR as well as SSIM map for the assessment of the image quality.

In 2013, Zhang *et al.* have established the model of the combination of 2D discrete wavelet transform and bilateral denoising. Initially, they have adopted the wavelet transform for doing the image decomposition in which the component of low frequency persisted unaffected. Later, the image is reconstructed by treating the bilateral filtering. The developed model was compared to the existing models and from the results, it was proved that the combinations of wavelet transform and bilateral filtering could attain the betterments in retaining the details of the image. Moreover, it was also achieved the efficient visual effect. The model was identified as the efficient one while comparing with the bilateral filtering alone and wavelet transform alone.

One of the primary challenges in the field of image processing is image denoising, where the underlying goal is to estimate the original image by suppressing noise from a noise-contaminated version of the image. Image noise may be caused by diverse intrinsic and extrinsic conditions, which are often not possible to avoid in practical situations. Several researchers are undoing research on image denoising concept, where they have proposed diverse algorithms for the purpose of image denoising. The detailed review papers on image denoising by wavelet transform is shown in Table 1. The different wavelet transforms adopted in the literature include Stationary wavelet transform (Guo *et al.*, 2017), Contourlet transform (Li *et al.*, 2016), Complex wavelet transform (Remenyi *et al.*, 2014), Haar wavelet transform (Jesus *et al.*, 2015), Bayesian MAP estimation (Sun *et al.*, 2014), Gradient histogram (Song *et al.*, 2016), DT-CWT (Naimi *et al.*, 2015), and 2D-DWT (Zhang, 2013). Image denoising using Stationary wavelet transform (Guo *et al.*, 2017) provides high accuracy and high stability; yet there is a presence of very large redundancy, and the computational complexity is increased. Next, better restoration quality and high PSNR is attained by the Contour let transform (Li *et al.*, 2016), whereas it requires more calculation time and its basic images are localized in the frequency domain. Moreover, the Complex wavelet transform (Remenyi *et al.*, 2014) offers excellent quantitative and visual performance and it is conceptually simple and practically efficient algorithm, but it fails to perform the threshold limit selection based on statistical models of wavelet coefficients. The noise of the image is drastically reduced by the Haar wavelet transform (Jesus *et al.*, 2015); yet, it is continuous and therefore non-differentiable and cannot compress the energy of the original signal into a few high-energy values. The Bayesian MAP estimation (Sun *et al.*, 2014) is an effective method to remove noise that is possible to obtain sharp edges and clear textures and high quality. However, the information is theoretically infeasible, and the process is not automatic and computationally infeasible. In addition, the restoration of image texture is easy in gradient histogram (Song *et al.*, 2016), and it exhibits improved image quality, but the robustness and the detection speed are very low. Moreover, DT-CWT (Naimi *et al.*, 2015) provides high efficiency in denoising, less redundant and easy computation, whereas it takes a long time as the process is too long. Furthermore, 2D-DWT (Zhang, 2013) can retain all the required details from the image and suppress the image noise. However, the complexity is high and it is theoretically difficult to understand and interpret the results.

In recent years, wavelet transform has attracted significant attention in scientific research and engineering applications since it is very powerful for analyzing transient signals/images for its capability of multiresolution analysis with localization in both time and frequency domains. The wavelet-based multiresolution analysis is very efficient in pattern recognition, image compression, and image denoising, but there is no guarantee for all these denoising techniques that edges can be preserved well when high PSNR is achieved for the denoised image. Motivated by the above mentioned points, this paper develops an effective optimized wavelet-based denoising approach.

Table 1. Review on Image Denoising by Wavelet Transform.

Author [Citation]	Adopted Methodology	Features	Challenges
Xiang <i>et al.</i> (2017)	Stationary wavelet transform	<ul style="list-style-type: none"> ❖ High accuracy ❖ High stability 	<ul style="list-style-type: none"> ❖ Presence of redundancy ❖ Increased computational complexity
Li <i>et al.</i> (2016)	Contourlet transform	<ul style="list-style-type: none"> ❖ Better restoration quality ❖ High PSNR value 	<ul style="list-style-type: none"> ❖ Requires more calculation time ❖ Its basic images are localized in the frequency domain
Remenyi <i>et al.</i> (2014)	Complex wavelet transform	<ul style="list-style-type: none"> ❖ Excellent quantitative and visual performance ❖ Conceptually simple and practically efficient algorithm 	<ul style="list-style-type: none"> ❖ Failed to perform threshold limit selection based on statistical models of wavelet coefficients
Jesus <i>et al.</i> (2015)	Haar wavelet transform	<ul style="list-style-type: none"> ❖ Drastically reduces the noise ❖ Improved variance stabilization 	<ul style="list-style-type: none"> ❖ It is continuous and therefore non-differentiable ❖ It can't compress the energy of the original signal into a few high-energy values
Sun <i>et al.</i> (2014)	Bayesian MAP estimation	<ul style="list-style-type: none"> ❖ Effective method to remove noise ❖ Possible to obtain sharp edges and clear textures ❖ High quality 	<ul style="list-style-type: none"> ❖ Information acquired is theoretically infeasible ❖ Not automatic and computationally infeasible
Song <i>et al.</i> (2016)	Gradient histogram	<ul style="list-style-type: none"> ❖ Can easily restore the image textures ❖ Improved image quality 	<ul style="list-style-type: none"> ❖ Less robustness ❖ Low detection speed
Naimi <i>et al.</i> (2015)	DT-CWT	<ul style="list-style-type: none"> ❖ High efficiency in denoising ❖ Less redundant and easy computation 	<ul style="list-style-type: none"> ❖ Long process leads take a long time
Zhang <i>et al.</i> (2013)	2D-DWT	<ul style="list-style-type: none"> ❖ Can better retain the required details from the image ❖ Suppress the image noises 	<ul style="list-style-type: none"> ❖ Greater complexity ❖ Difficulties in data interpretation

BACKGROUND

Feature Extraction

Image denoising procedure is carried out for five sets of images like texture, nature, medical, satellite, and other images. In order to extract features from each image, this paper uses Noise power spectra (NPS) and bark frequency after adding noise to the images, which are described as follows.

NPS: In general, NPS (Hanson, 1998) is also termed as Wiener spectrum, which is modeled as Fourier Transform of noise images that are given in Eq. (1) as a mathematical form, where (x, y) indicates the position and $v(x, y)$ specifies the noise image. The bracket $\langle \rangle$ denotes mean over an infinite ensemble of noise images. Over the area $\Delta x \Delta y$, integration

is provided that extends to infinity. If the image is in 2-dimension frequency domain, NPS of an image is naturally in 2-dimension format. If the noise is Gaussian distributed regarding a zero mean value and stationary, the NPS can be termed as a method that provides effective characterization of the noise. Therefore, the covariance is independent of position in the image.

$$N(f_x, f_y) = \lim_{\Delta x, \Delta y \rightarrow \infty} \frac{1}{\Delta x \Delta y} \left\langle \left| \int v(x, y) \exp[-2\pi(yf_y + xf_x)] dx dy \right|^2 \right\rangle \quad (1)$$

The average of the power of Fourier transform of noisy image samples obtained from a single noisy image or multiple images is the estimation pattern of NPS. Through this method, gradual alternation in the image intensity is eliminated, and samples are windowed before taking the Fourier transform. However, it is a complex task to work with frequency region of NPS and its analysis. Let M be the averaged samples, and relative rms deviation in the power in each 2-dimentional frequency bin is almost $[M]^{-1/2}$. Even though the method is complex, it generates the outcome with outright normalization that admits various laboratories.

In the spatial domain, the convolution of two images is proportionate to multiplication in the frequency domain Fourier transforms. Thus, the NPS of a noisy image is improved by convolving a noisy image with a by a factor of $|A|^2$, where a denotes the convolution kernel and A refers to the Fourier Transform of a . As the total power in the frequency domain is equal to the spatial domain, Eq. (2) determines the variance of convolved image.

$$\sigma_a^2 = \int |A|^2 N(f_x, f_y) df_x df_y \quad (2)$$

In the case of discretely sampled images, $-f_M$ to f_M are the ranges of integration for both f_x and f_y , where f_M indicates the Nyquist frequency. The term f_M is determined using Eq. (3), where l denotes the pixel spacing in both x and y directions.

$$f_M = [2l]^{-1} \quad (3)$$

The modified equation of Eq. (2) is provided in Eq. (4), where K_a indicates the normalization constant and the bracket $\langle \rangle$ refers to an average function of the power spectrum of a , which is weighted by $|A|^2$.

$$\langle N \rangle_{|A|^2} = \sigma_a^2 l^2 K_a \quad (4)$$

The reciprocal of total power of kernel defines K_a , which is given in Eq. (5), where the elements of the convolution kernel for discretely sampled images are denoted as $a_{i,j}$.

$$K_a^{-1} = \int |A|^2 df_x df_y = \sum_{i,j} a_{i,j}^2 \quad (5)$$

Therefore, NPS F_1 of the image at concerned spatial frequencies is estimated by properly choosing not only the convolution kernel but also the variance in the convolved noise image.

Bark frequency: It is defined as “a frequency scale on which equal distances correspond with perpetually equal distances” (Chung *et al.*, 2017). In fact, the critical band can be termed as bark scale, a perpetual measure that is associated with image frequency to the perpetual resolution, which is non-linear. Here, one critical band is covered by one bark. Eq. (6) specifies the logical expression of the mapping function from \hat{f} frequency to B bark frequency.

$$F_2 = B[\hat{f}] = 13 \arctan [0.76 \hat{f}] + 3.5 \arctan \left(\left[\hat{f} / 7.5 \right]^2 \right) \quad (6)$$

Classification

Before denoising the image, it is essential to analyze the type of the image. Here, BR classifier is used to classify the type of the image. BR is selected since it has been proven to have better predictive capability to reveal relationship

between data of different data distributions (Aggarwal et al., 2005). The extracted features F_1 and F_2 are given as the input to BR classifier, which results in the respective type of image. The BR classifier model is explained in the below section.

Optimization Of Filter Coefficients

In this paper, the filter coefficient parameter of DT-CWT is optimally selected using GA algorithm (Call, 2005). The algorithm consists of six major steps. (i) Crossover, (ii) Mutation, (iii) Genotype-Phenotype Mapping, (iv) Fitness, (v) Selection, and (vi) Termination.

Crossover: This is an operator, which allows the permutation of the genetic factual of two or more solutions. Naturally, most species comprise two parents. Moreover, in some exceptional cases, there are no different sexes and thus they have only one parent. This operator implements an application, which combines the genetic factual of the parents. A famed one for bit string demonstration is c point crossover. It splits into two solutions at c positions and consecutively gathers them into one. The formulation for crossover is defined in Eq. (7) and Eq. (8), where i indicates i^{th} gene, C_p indicates the crossover point, and C_r indicates the crossover rate and L indicates the length of chromosome.

$$x^{\text{child}}(i) = \begin{cases} x_1(i) & \text{if } i < C_p \\ x_2(i) & \text{else} \end{cases} \quad (7)$$

$$C_p = [C_r \times L] \quad (8)$$

Mutation: This is the second step, in which the mutation operator alters the solutions by distributing them. Mutation works on the basis of random changes. The strength of this disruption is known as the mutation rate. Three major desires are there in the mutation operator. The initial condition is reachability. Every point in the solution space must be accessible or reachable from the random point in the solution space. The second condition is unbiasedness. The operator should not persuade a point of the exploration to a specific direction. The third condition or principle of this operator is scalability. Each mutation operator must grant the degree of freedom that its strength is adjustable. The formulation for mutation is in eq. (9), where $j \in (R^{1 \times N_g})$, $(R^{1 \times N_g})$ indicates the real number with dimension N_g .

$$x(j) = \text{rand}(x_i) \quad (9)$$

Genotype-Phenotype Mapping: The new offspring population has been estimated after the evaluation of crossover and mutation operators. The mapping of the chromosome (genotype) depends on the representation, named as phenotype. This type of genotype-phenotype mapping must avoid the bias introduction.

Fitness: In this step, the phenotype of solution is formulated on fitness model. This function measures the solution's quality, which is generated by this algorithm. Further, it is a part of modeling process of the entire optimization model. The performance of GA in problem-solving is measured in correspondence with the count of required fitness function assessments till the optimal is found.

Selection: The selection is a process that chooses the parents of the new generation, which is termed as survival selection. This operator defines which operator must survive and which operator must die. This perception directly implements the 'Darwin's Principle of survival'. However, the developed survival operator can be employed for mating selection, which is the part of the crossover operators. Moreover, mating strategy is a vital part, where it decides which parents should join in the crossover progression.

Termination: This condition defines when the major evolutionary loop terminates. GA often runs in the predefined count of generations. The time and cost of the fitness model estimation often restrict the length of the optimization procedure.

The pseudo code of the GA algorithm is given in Algorithm 1 and the flow chart is illustrated in Fig. 1.

Algorithm 1: GA-based Filter Coefficient optimization
Initialize the random C population
Formulate the fitness $Fit(p)$ of each p chromosome in the population
Repeat
Choose the ‘best’ entities that are to be utilized by the genetic operators
Generation of new entities using crossover and mutation operators.
Fitness evaluation of new entities
‘Worst’ entities are replaced by ‘best’ entities
Until it reaches the ‘best’ solution

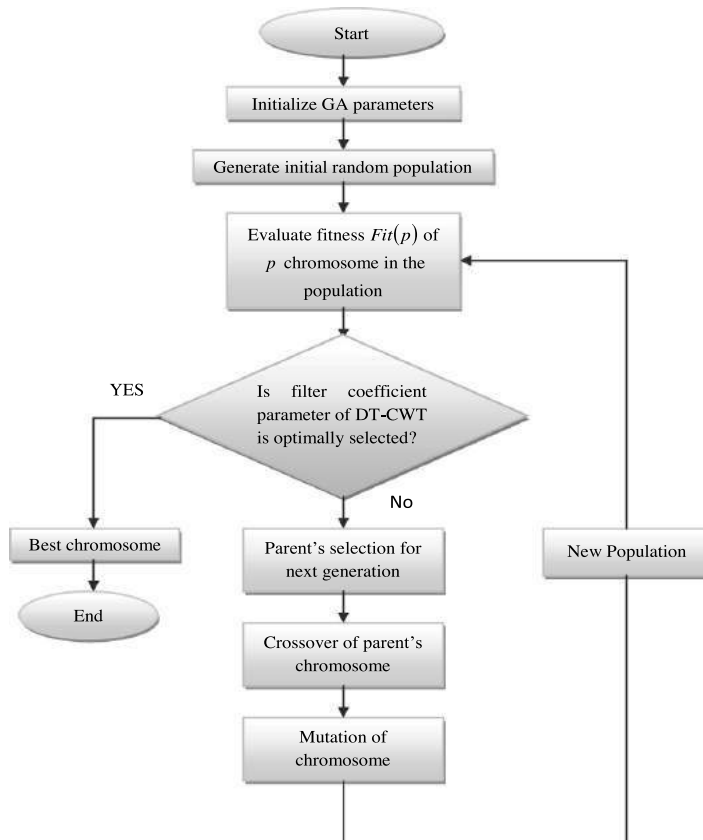


Fig. 1. Flow chart for GA- based filter coefficient optimization.

Bayesian Regularization

BR is a regularization technique that has the capability of obtaining the lower mean squared errors. The framework for neural network is on the basis of probabilistic interpretation of the parameters of the network and involves a probability distribution of network weights. In the BR network, the regularization adds subordinate term and objective function to penalize large weights for attaining better smoother mapping. The objective function as given in Eq. (11) is minimized using gradient-based optimization algorithm.

$$O = \beta M_s(I|W, NN) + \alpha S_s(W|NN) \tag{11}$$

where $S_s(W|NN)$ is $S_s = \frac{1}{p} \sum_{k=1}^p W_k^2$, the sum of squares of network weights W , α and β are the hyperparameters, M_s denotes the mean sum of squares of the network error, $I = \{F_1, F_2\}$ specifies the input target features, NN refers to the neural network architecture, which comprises the specification of count of layers, count of unit in every layer, and the activation function type, $\alpha S_s(W|NN)$ is known as weight decay, and α is also termed as decay rate. If $\alpha \ll \beta$, then the algorithm minimizes the error, and the training of algorithm reduces the weight size if $\alpha \gg \beta$. The posterior P_D distribution of weight is updated using Bayes' rule, which is defined in Eq. (12), where $P_D(W|\alpha, NN)$ denotes the prior distribution of weight, and $P_D(I|W, \beta, NN)$ denotes the likelihood function.

$$P_D(W|I, \alpha, \beta, NN) = \frac{P_D(I|W, \beta, NN) P_D(W|\alpha, NN)}{P_D(I|\alpha, \beta, NN)} \tag{12}$$

The optimized weight maximizes the posterior probability of W , which is equivalent to reducing the regularized objective function $O = \beta M_s + \alpha S_s$. The joint posterior density is defined as given in Eq. (13).

$$P_D(\alpha, \beta|I, NN) = \frac{P_D(I|\alpha, \beta, NN) P_D(\alpha, \beta|NN)}{P_D(I|NN)} \tag{13}$$

According to Mackay, Eq. (12) is determined as given in Eq. (13), where p and q specify the count of observation as well as the total count of parameters of network, respectively. Eq. (14) (Laplace approximation) grants Eq. (15), where H^{MAP} denotes the Hessian matrix of the objective function and MAP stands for 'Maximum A Posteriori.'

$$\begin{aligned} P_D(I|\alpha, \beta, NN) &= \frac{P_D(I|W, \beta, NN) P_D(W|\alpha, NN)}{P_D(W|I, \alpha, \beta, NN)} \\ &= \frac{Z_o(\alpha, \beta)}{(\pi/\beta)^{p/2} (\pi/\alpha)^{q/2}} \end{aligned} \tag{14}$$

$$Z_o(\alpha, \beta) = \infty | H^{MAP} |^{-\frac{1}{2}} \exp(-O(W^{MAP})) \tag{15}$$

The parameter at t iteration is updated as given in Eq. (16), where μ refers to the Levenberg damping factor, and J denotes the jacobian matrix, which comprises the first derivative of the network errors in terms of network parameters. Further, μ is adjustable for all iterations, which leads to optimization.

$$W^{t+1} = W^t - [J^T J + \mu I]^{-1} J^T e \tag{16}$$

Therefore, BR classifier automatically predicts the filter coefficient that to be given to DT-CWT for denoising each image.

To analyze the performance of the proposed model, the performance metrics such as PSNR, SDME, SSIM, MSE, RMSE, MAE, PC, and SMAPE are used, where the mathematical formulation is given in Table 2 (Srivastava, 2014).

Table 2. Performance metrics utilized for analysis.

Performance Measures	Formulas
PSNR	$20 \log_{10} \left[\frac{255}{RMSE} \right]$
SDME	$-\frac{1}{\hat{K}_1 \hat{K}_2} 20 \ln \frac{\hat{I}_{\max:\hat{k},\hat{l}} - 2\hat{I}_{\text{centrw}:\hat{k},\hat{l}} + \hat{I}_{\min:\hat{k},\hat{l}}}{\hat{I}_{\max:\hat{k},\hat{l}} + 2\hat{I}_{\text{centrw}:\hat{k},\hat{l}} + \hat{I}_{\min:\hat{k},\hat{l}}}$
SSIM	$\frac{(2\mu_{\hat{X}}\mu_{\hat{Y}} + C_1)(2\sigma_{\hat{X}\hat{Y}} + C_2)}{(\mu_{\hat{X}}^2 + \mu_{\hat{Y}}^2 + C_1)(\sigma_{\hat{X}}^2 + \sigma_{\hat{Y}}^2 + C_1)}$
MSE	$\frac{1}{\hat{N}} \sum_{i,j} (\hat{X}_{i,j} - \hat{Y}_{i,j})^2$
RMSE	$\sqrt{\frac{1}{\hat{N}} \sum_{i,j} (\hat{X}_{i,j} - \hat{Y}_{i,j})^2}$
MAE	$\frac{1}{\hat{N}} \sum_{i,j} \hat{X}_{i,j} - \hat{Y}_{i,j} $
PC	$\frac{\sum_{i,j=1} (\hat{X}_{i,j} - \bar{\hat{X}}_{i,j})(\hat{Y}_{i,j} - \bar{\hat{Y}}_{i,j})}{\sqrt{\sum_{i=1}^N (\hat{X}_{i,j} - \bar{\hat{X}}_{i,j})^2} \sqrt{\sum_{j=1}^N (\hat{Y}_{i,j} - \bar{\hat{Y}}_{i,j})^2}}$
SMAPE	$\frac{1}{\hat{N}} \sum_{i,j} \frac{ \hat{X}_{i,j} - \hat{Y}_{i,j} }{ \hat{X}_{i,j} + \hat{Y}_{i,j} }$

PROPOSED METHODOLOGY

Proposed Architecture

Fig. 2 illustrates the block representation of the proposed DT-CWT based image denoising model. This model intends to denoise the input image, and the procedure is as follows: the preliminary process is adding noise to the input image, by which the effective denoising of image can be achieved. This work mainly contributes two tasks: (i) classification of image type using BR and (ii) denoising the image by estimating the optimal wavelet coefficient to DT-CWT using GA. In the first contribution, the extracted F_1 and F_2 features are given as the input to BR classify the corresponding image.

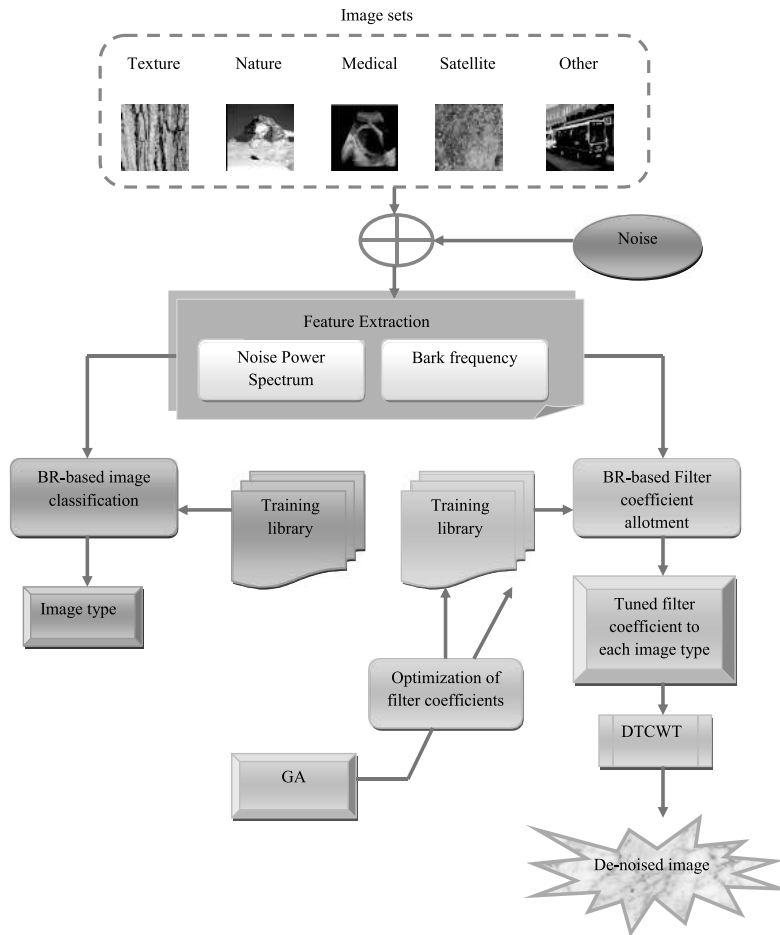


Fig. 2. Block diagram of proposed image denoising model.

On the other hand, the contribution is made in solving the problem of determining the optimal ‘filter coefficient’ to increase the PSNR value. Here, GA algorithm is used to identify the apt filter coefficient. The objective function of the proposed model is defined in Eq. (17).

$$D = \text{Max}\{PSNR\} \tag{17}$$

DT-CWT Model

DT-CWT (YueSi *et al.*, 2016; Selesnick *et al.*, 2005; Mohan *et al.*, 2016; Sunil *et al.*, 2016) is one of the effective models for the application of analytic wavelet transform. This model consists of two real DWTs: the first DWT grants the real part of transform, whereas the second grants the imaginary part. Further, the model grants perfect reconstruction and directional discernment and is independent of count of scales. The diagrammatic representation of DT-CWT is illustrated in Fig 3, where $L_0(n)$ and $L_1(n)$ refer to the low pass/high pass filter pair for upper Filter Bank (FB) and $H_0(n)$ and $H_1(n)$ denotes the low pass/ high pass filter pair for lower FB, respectively.

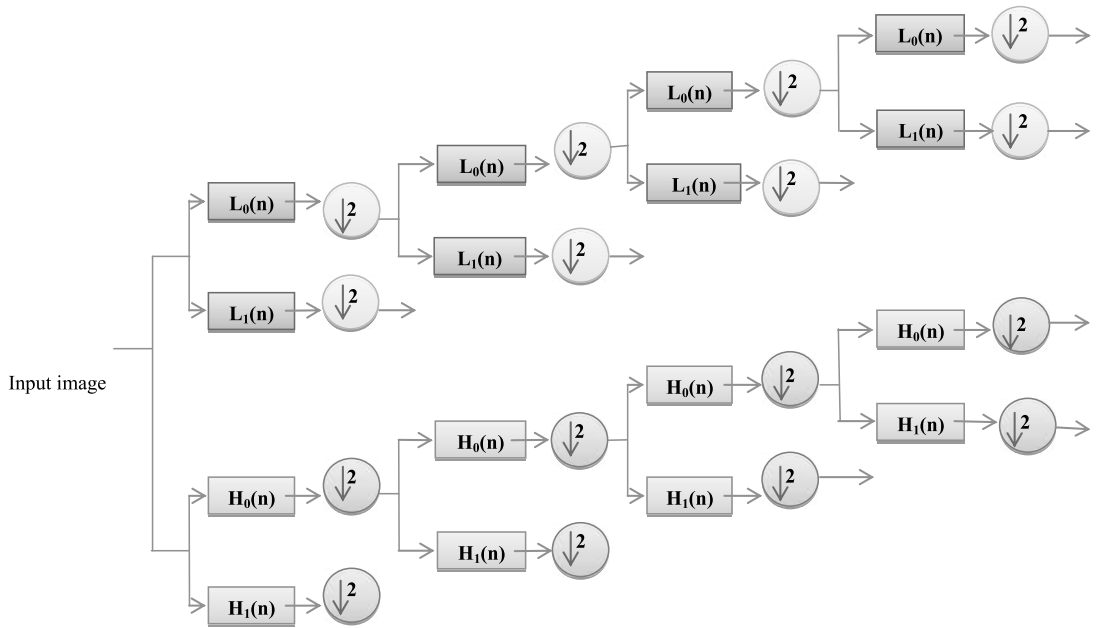


Fig. 3. Diagrammatic representation of DT-CWT model.

Consistent with wavelet theory, both wavelet coefficients $w_i^{real}(K)$ and scaling coefficients $s_j^{real}(K)$ of the real part transform are attained through inner products, which are defined in Eq. (18) and Eq. (19), where i refers to the scale factor, j denotes the decomposition level, and ω_h and ϕ_h denote the wavelet functions of real part transform. Further, the coefficients of the imaginary part transform can be formulated as defined in Eq. (20) and (21).

$$w_i^{real}(K) = 2^{i/2} \int_{-\infty}^{+\infty} Y(u) \omega_h(2^i u - K) du \quad i = 1, \dots, j \tag{18}$$

$$s_j^{real}(K) = 2^{j/2} \int_{-\infty}^{+\infty} Y(u) \phi_h(2^j u - K) du \tag{19}$$

$$w_i^{imaginary}(K) = 2^{i/2} \int_{-\infty}^{+\infty} Y(u) \omega_g(2^i u - K) du \quad i = 1, \dots, j \tag{20}$$

$$s_j^{imaginary}(K) = 2^{j/2} \int_{-\infty}^{+\infty} Y(u) \phi_g(2^j u - K) du \tag{21}$$

Hence, the wavelet as well as the scaling coefficients of DT-CWT are acquired as defined in Eq. (22) and (23), respectively. Then the wavelet or scaling coefficients are reconstructed as defined in Eq. (24) and (25), respectively.

$$w_i^s(K) = w_i^{real}(K) + j w_i^{imaginary}(K) \quad i = 1, \dots, j \tag{22}$$

$$s_j^s(K) = s_j^{real}(K) + j s_j^{imaginary}(K) \tag{23}$$

$$w_i(u) = 2^{(i-1)/2} \left[\sum_n w_i^{real}(K) \omega_h(2^i u - n) + \sum_m w_i^{imaginary}(K) \omega_g(2^i u - m) \right] \tag{24}$$

$i = 1, \dots, j$

$$s_j(u) = 2^{(j-1)/2} \left[\sum_n s_j^{real}(K) \phi_h(2^j u - n) + \sum_m s_j^{imaginary}(K) \phi_g(2^j u - m) \right] \tag{25}$$

DT-CWT decomposes the vibration signal $Y(u)$, which is defined as given in Eq. (26), where $w_i(u) i = 1,2,\dots,j$ and $s_j(u)$ denotes the sub-band signals that are organized from high to low frequency.

$$Y(u) = s_j(u) + \sum_{i=1}^j w_i(u) \tag{26}$$

The application of 2D DT-CWT comprises two major steps: Initially, the input image is decomposed up to certain levels via two 2D- DWT branches, a and b . At each level, six high pass sub-bands are engendered like $HL_a, LH_a, HH_a, HL_b, LH_b$ and HH_b . Next to this, the respective sub-bands that have same pass bands are combined linearly through averaging or differencing. As a result of this, the sub-bands of 2D DT-CWT at all levels are generated as defined in Eq. (27)

$$\begin{aligned} & (LH_a + LH_b)/\sqrt{2}, (LH_a - LH_b)/\sqrt{2}, (HL_a + HL_b)/\sqrt{2} \\ & (HL_a - HL_b)/\sqrt{2}, (HH_a + HH_b)/\sqrt{2}, (HH_a - HH_b)/\sqrt{2} \end{aligned} \tag{27}$$

The six wavelets defined here have sum or difference operation, which is orthonormal. Further, the 2D DT-DWT has same basis function and real part, and the structure has the extension of conjugate filtering.

Among the analysis filter, the low pass $H_L(n)$ and high $H_H(n)$ pass filters of first level coefficients and low pass $H_S(n)$ of second level coefficients are given as solutions for optimization since the mentioned coefficients give more informative details about the image. The solution encoding is diagrammatically illustrated in Fig. 4, where $n = 1, \dots, N_s$, N_s denotes the number of samples.

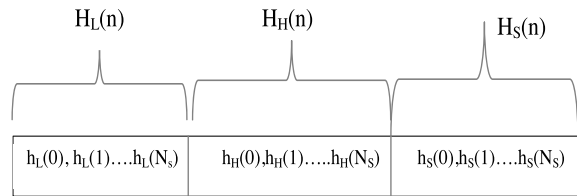
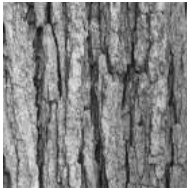




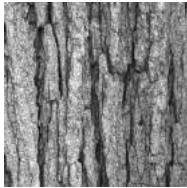


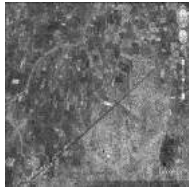

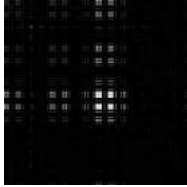
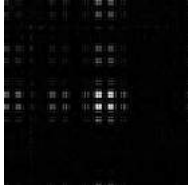

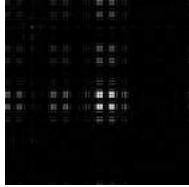



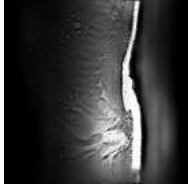


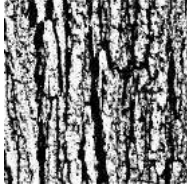


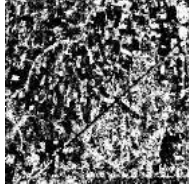

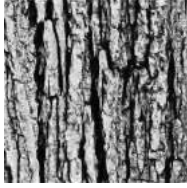

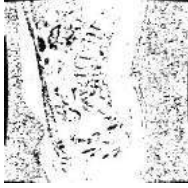
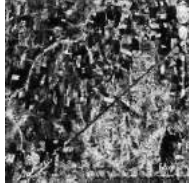

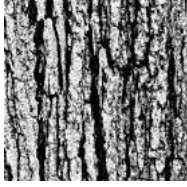

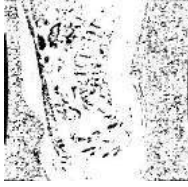
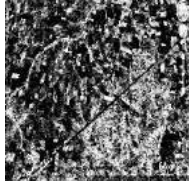



Fig. 4. Representation of solution encoding.

RESULTS AND DISCUSSIONS

Simulation Setup

The developed intelligent image classification was carried out in MATLAB 2015a. Five image sets were chosen, namely, Texture image set, Nature image set, Medical image set, Satellite image set, and Miscellaneous image set. The texture images were downloaded from (http://www-cvr.ai.uiuc.edu/ponce_grp/data/: access data 2019-02-15), medical images were downloaded from (<http://www.ultrasoundcases.info/case-list.aspx?cat=26>: access date 2019-02-15), satellite images were manually collected, natural images were downloaded from (http://www-cvr.ai.uiuc.edu/ponce_grp/data/: access data 2019-02-15), and miscellaneous images were downloaded from two links (<http://vismod.media.mit.edu/pub/VisTex/>, <https://sites.google.com/site/dctresearch/Home/content-based-image-retrieval>: access data 2019-02-15). The images Features like NPS and Bark frequency were extracted from the image. The classification was done using BR classifier. Moreover, the classifier was trained using the renowned GA algorithm, where the optimized filter coefficients of DT-CWT were generated. The performance of the proposed model was analyzed in terms of measures like PSNR, SDME, SSIM, MSE, RMSE, MAE, PC, and SMAPE, respectively. Further, the developed model was compared to some of the conventional models like 2D SMCWT, DT-CWT, DT-CDWT, DT-RDWT, W-ST, and W-HT in terms of efficient image denoising. Fig 5 illustrates the experimental results for five image sets using proposed and conventional models.

Models	Image sets				
	Texture Image	Nature image	Medical image	Satellite image	Miscellaneous image
(a)					
(b)					
(c)					
(d)					
(e)					
(f)					
(g)					

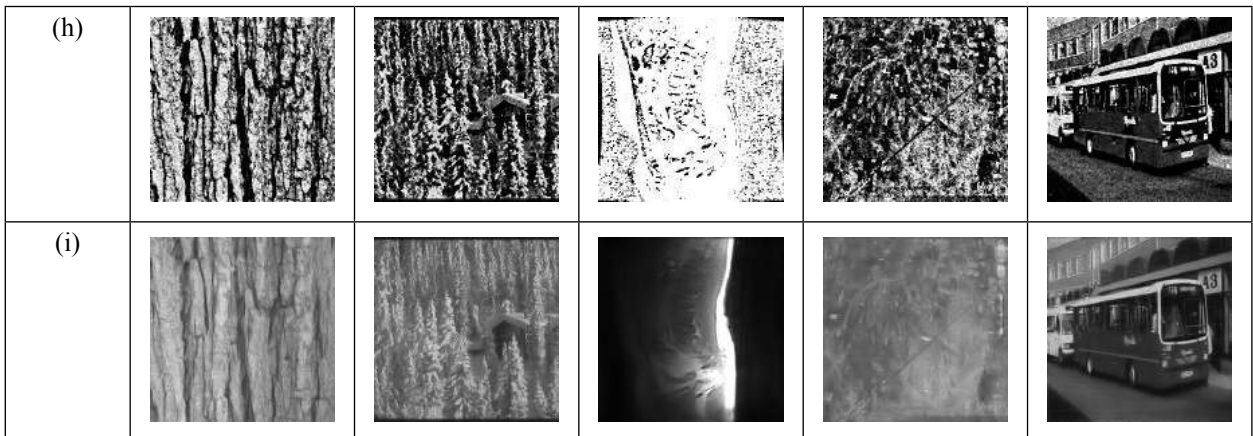


Fig. 5. Experimental results using five image sets for proposed Denoising model over the conventional models for a) Original image, b) Noisy image, c) 2D SMCWT-based denoising, d) DT-CWT-based denoising, e) DT-CDWT-based denoising, f) DT-RDWT-based denoising, g) W-ST-based denoising, h) W-HT-based denoising, and i) Proposed image denoising.

Qualitative Assesment

Table 3 shows the performance analysis of proposed model over conventional methods in terms of various analytical measures. The analysis has been made for all the five image sets. From Table 3, it is observed that, for texture image, the proposed model has attained promising results. PSNR of the developed model is 69.97%, 5.85%, 76.91%, 33.38%, 46.40%, and 46.44% better than 2D SMCWT, DT-CWT, DT-CDWT, DT-RDWT, W-ST, and W-HT, respectively. The SDME of the proposed model is 97.42%, 41.26%, 98.64%, 89.66%, 93.88%, and 93.89% superior to 2D SMCWT, DT-CWT, DT-CDWT, DT-RDWT, W-ST, and W-HT, respectively. Similarly, for SSIM measure, the proposed model has great deviation over conventional methods, and the model is 19.17%, 83.66%, 24.65%, 72.99%, and 73.15% better than DT-CWT, DT-CDWT, DT-RDWT, W-ST, and W-HT, respectively. The MSE of the proposed model is 97.05%, 27.31%, 97.83%, 81.30%, 90.11%, and 90.12% better than 2D SMCWT, DT-CWT, DT-CDWT, DT-RDWT, W-ST, and W-HT, respectively. The MAE of the model is 12.33%, 86.39%, 57.68%, 70.13%, and 70.16% better than DT-CWT, DT-CDWT, DT-RDWT, W-ST, and W-HT, respectively. The PC of the proposed model is 98.24%, 11.73%, 22.51%, 10.99%, 17.51%, and 17.53% superior to 2D SMCWT, DT-CWT, DT-CDWT, DT-RDWT, W-ST, and W-HT, respectively. For SMAPE measure, the proposed model is 90.50%, 10.11%, 84.61%, 65.46%, 79.40%, and 79.43% superior to 2D SMCWT, DT-CWT, DT-CDWT, DT-RDWT, W-ST, and W-HT, respectively. For nature image set, it is observed that the PSNR of the proposed model is 67.16% and 12.71% better than 2D SMCWT and DTCWT, respectively. The same analysis is made for all the other image sets and it is clearly tabulated in Table 3. Altogether, it is reviewed that the performance of the proposed model is more efficient than that of the conventional methods by denoising the images more precisely.

Table 3. Performance Of Proposed Model Versus Conventional Methods In Terms Of Various Analytical Measures.

Texture images								
Methods	PSNR	SDME	SSIM	MSE	RMSE	MAE	PC	SMAPE
W-HT	11.679	-0.285	0.3172	4551.4	67.093	57.35	47326	0.858
W-ST	11.686	-0.285	0.317	4543.9	67.037	57.31	47336	0.857
DT-RDWT	14.526	-0.168	0.4406	2403.2	48.549	40.45	51081	0.511
DT-CDWT	5.0333	-1.288	0.089	20784.9	143.79	125.80	44469	1.148
DT-CWT	20.530	-0.029	0.460	618.2	24.466	19.52	50655	0.196
2D-SMCWT	6.5477	-0.675	-0.000	15246.1	122.01	114.6	1009.4	1.860
Proposed	21.806	-0.017	0.549	449.37	20.996	17.11	57391	0.176
Natural images								
W-HT	-1.804	-0.155	0.072	6524	2940	1850.3	21722	0.1528
W-ST	-1.801	-0.155	0.072	65249	2940	1850.3	21726	0.1525
DT-RDWT	-0.950	-0.124	0.098	65193	2933.8	1845.5	23300	0.0946
DT-CDWT	-4.067	-0.359	0.0210	1.34 × 10 ⁸	4231.3	2655.1	18633	0.2069
DT-CWT	8.4888	-0.069	0.1502	402.69	12.170	8.8928	2405	0.0344
2D-SMCWT	3.1950	-0.284	-0.0005	6177.4	49.188	40.98	51.835	0.3533
Proposed	9.731	-0.042	0.161	171.89	8.333	6.2906	26271	0.0320
Medical images								
W-HT	6.55642	-0.11516	0.127394	940.8481	19.47514	14.13926	22840.94	0.068702
W-ST	6.560875	-0.11507	0.127369	938.7568	19.45269	14.12093	22848.89	0.068547
DT-RDWT	8.140015	-0.08393	0.149509	424.1882	12.89597	9.224428	25148.3	0.041373
DT-CDWT	3.602328	-0.25176	0.027016	4367.145	42.48501	32.72749	19773.04	0.103215
DT-CWT	8.916861	-0.07111	0.136066	255.6865	10.22897	7.852905	25485.98	0.023244
2D-SMCWT	3.493316	-0.28554	-0.00025	5573.821	45.89287	38.69709	352.3181	0.205667
Proposed	10.07988	-0.04745	0.151369	137.3159	7.489622	5.85446	27093.47	0.019075
Satellite images								
W-HT	1.662	-0.037	0.025	659.64	9.645	8.165	5820.7	0.119
W-ST	1.663	-0.037	0.025	658.44	9.636	8.157	5822.6	0.119
DT-RDWT	2.120	-0.024	0.039	319.16	6.6905	5.513	6482.01	0.067
DT-CDWT	0.751	-0.135	0.007	2847.8	20.066	17.112	5356.5	0.165
DT-CWT	3.548	-0.006	0.055	34.10	2.152	1.644	7237.9	0.018
2D-SMCWT	1.304	-0.094	-0.0001	1249	13.085	12.52	48.319	0.258
Proposed	3.561	-0.004	0.052	31.76	2.101	1.666	7953.7	0.019
Miscellaneous images								
W-HT	4.916	-0.41	0.216	9316	3678.7	2017.3	47149.2	0.3490
W-ST	4.923	-0.409	0.216	9316	3678.7	2017.3	47161.7	0.3474
DT-RDWT	7.420	-0.341	0.317	9310	3666.8	2008.1	50708.8	0.1606
DT-CDWT	-0.44	-0.831	0.036	1.78E+08	5112.5	2912.8	40409.4	0.5231
DT-CWT	15.267	-0.191	0.285	4879.1	42.60	31.891	50612.3	0.1544
2D-SMCWT	5.323	-0.543	-0.001	57069.3	152.35	107.94	434.49	0.8337
Proposed	17.987	-0.168	0.3532	2461.4	29.72	22.35	54235.7	0.1289

Adaptiveness in DT-CWT

Table 4 shows the comparison of proposed model over the conventional DT-CWT method by varying noise levels as 0.02, 0.04, 0.05, 0.06, and 0.08, respectively. The analysis is made in terms of various measures like PSNR, SDME, SSIM, MSE, RMSE, MAE, PC, and SMAPE, respectively; its formula is provided in table 2. For texture image set, it is observed that the proposed model has attained better PSNR at noise variance 0.02, which is 69.19% superior to DT-CWT, respectively. At 0.04 noise variance, the proposed model is 68.38% better than DT-CWT, respectively. Similarly, for 0.05, 0.06, and 0.08 noise variance, the proposed model is 68.03%, 67.71%, and 67.06% superior to DT-CWT, respectively. For nature image set, the PSNR of proposed model for noise variance 0.02, 0.04, 0.05, 0.06, and 0.08 is 63.88%, 62.70%, 62.33%, 61.84%, and 61.00% superior to DT-CWT, respectively. For medical image set, the PSNR of proposed model for noise variance 0.02, 0.04, 0.05, 0.06, and 0.08 is 62.71%, 61.35%, 60.74%, 60.20%, and 59.13% better than conventional DT-CWT, respectively. For satellite image set, the PSNR of proposed model for noise variance 0.02, 0.04, 0.05, 0.06, and 0.08 is 64.67%, 63.68%, 63.27%, 62.85%, and 62.20% better than conventional DT-CWT, respectively. For miscellaneous image sets, the PSNR of proposed model for noise variance 0.02, 0.04, 0.05, 0.06, and 0.08 is 66.81%, 65.61%, 65.04%, 64.50%, and 63.53% better than conventional DT-CWT, respectively. The investigation is made for all the remaining measures by varying noise levels, and from the results it is observed that the proposed image denoising model is more efficient than the conventional DT-CWT.

Table 4. Performance Of Proposed Versus Conventional DT-CWT In Image Denoising By Varying Noise.

Texture images																
Noise variance	PSNR		SDME		SSIM		MSE		RMSE		MAE		PC		SMAPE	
	Proposed	DT-CWT	Proposed	DT-CWT	Proposed	DT-CWT $\times 10^3$	Proposed	DT-CWT	Proposed	DT-CWT	Proposed	DT-CWT	Proposed	DT-CWT	Proposed	DT-CWT
0.02	21.26	6.55	-0.02	-0.68	0.53	-0.25	527.12	15241.62	22.53885	122.0009	18.09	114.64	54753.43	1016.23	0.18	1.87
0.04	20.72	6.55	-0.03	-0.68	0.48	-0.24	590.43	15244.79	23.92084	122.014	19.10	114.64	51752.87	1009.98	0.19	1.86
0.05	20.49	6.55	-0.03	-0.68	0.46	-0.24	620.24	15246.14	24.54043	122.0194	19.57	114.64	50448.08	1006.39	0.20	1.86
0.06	20.29	6.55	-0.03	-0.67	0.44	-0.24	647.68	15247.36	25.10048	122.0245	19.99	114.64	49280.9	1006.52	0.20	1.86
0.08	19.89	6.55	-0.04	-0.67	0.41	-0.25	705.62	15250.81	26.23163	122.0387	20.88	114.64	47042.65	1007.97	0.21	1.85
Nature images																
0.02	8.86	3.20	-0.06	-0.28	0.18	-0.57	338.92	6176.43	11.09566	49.18246	8.24	40.98	25017.99	53.56	0.03	0.37
0.04	8.58	3.20	-0.07	-0.29	0.16	-0.53	382.43	6176.77	11.86273	49.18499	8.70	40.98	24343.78	54.82	0.04	0.37
0.05	8.47	3.19	-0.07	-0.28	0.15	-0.55	403.76	6177.66	12.21283	49.18861	8.91	40.98	24023.21	49.11	0.03	0.34
0.06	8.36	3.19	-0.07	-0.28	0.14	-0.58	424.28	6177.90	12.54011	49.19018	9.12	40.99	23728.36	48.53	0.03	0.34
0.08	8.18	3.19	-0.07	-0.29	0.13	-0.54	464.05	6178.70	13.14225	49.19393	9.49	40.99	23172.14	53.16	0.04	0.34
Medical images																
0.02	9.36	3.49	-0.07	-0.29	0.16	-0.23	200.91	5572.76	9.069204	45.88684	7.08	38.68	26147.92	350.59	0.02	0.20
0.04	9.03	3.49	-0.07	-0.28	0.14	-0.25	238.76	5573.29	9.908618	45.89021	7.64	38.69	25698.37	351.51	0.02	0.21
0.05	8.89	3.49	-0.07	-0.29	0.13	-0.24	256.55	5573.72	10.27418	45.89236	7.89	38.70	25480.5	349.43	0.02	0.21
0.06	8.77	3.49	-0.07	-0.29	0.13	-0.26	273.31	5574.07	10.61344	45.89452	8.11	38.70	25268.58	353.75	0.02	0.21
0.08	8.54	3.49	-0.06	-0.28	0.12	-0.26	308.90	5575.26	11.2794	45.90044	8.55	38.71	24834.53	356.31	0.02	0.20
Satellite images																
0.02	3.68	1.30	-0.004	-0.09	0.07	-0.15	27.83	1248.75	1.943528	13.08382	1.50	12.53	7857.40	48.92	0.02	0.25
0.04	3.58	1.30	-0.006	-0.09	0.06	-0.14	32.22	1248.91	2.095634	13.08481	1.60	12.53	7395.54	47.94	0.02	0.27
0.05	3.54	1.30	-0.007	-0.10	0.05	-0.15	34.24	1249.07	2.161179	13.08556	1.65	12.53	7206.77	48.96	0.02	0.24
0.06	3.50	1.30	-0.006	-0.09	0.05	-0.14	36.28	1249.20	2.225776	13.08616	1.70	12.53	7019.21	47.11	0.02	0.27
0.08	3.44	1.30	-0.005	-0.09	0.05	-0.14	39.96	1249.42	2.335946	13.08741	1.78	12.53	6710.90	48.67	0.02	0.27
Miscellaneous images																
0.02	16.06	5.33	-0.18	-0.55	0.33	-1.23	3876.75	57047.2	38.18263	152.3231	29.33	107.83	51957.58	435.78	0.13	0.81
0.04	15.47	5.32	-0.19	-0.54	0.29	-1.23	4548.27	57063.06	41.29973	152.3418	31.08	107.91	51027.08	430.90	0.16	0.86
0.05	15.22	5.32	-0.19	-0.55	0.28	-1.22	4876.63	57067.23	42.71521	152.3477	31.94	107.95	50589.7	441.38	0.17	0.85
0.06	14.99	5.32	-0.196	-0.54	0.27	-1.21	5221.81	57078.69	44.12461	152.3612	32.78	107.98	50152.76	428.84	0.16	0.80
0.08	14.59	5.32	-0.20	-0.54	0.25	-1.22	5872.17	57090.44	46.69325	152.3771	34.32	108.07	49334.8	435.55	0.16	0.85

Fig 6 shows the performance of the proposed model for texture image set over the conventional methods by varying noise levels from 0.02 to 0.08. From Fig 6, it is observed that the PSNR of the proposed model for noise level 0.02 is 68.96%, 10.77%, 74.56%, 31.89%, and 43.53% superior to 2D-SMCWT, DT-CWT, DT-CDWT, DT-RDWT, and W-ST, respectively. Similarly, SDME of the proposed model is 44.44%, 82.75%, 28.57%, and 16.66% better than 2D-SMCWT, DT-CDWT, DT-RDWT, and W-ST, respectively. The analysis is also made for all the remaining measures. From the analysis, it is observed that the proposed model has attained high SSIM and PC when compared to the conventional methods. Further, the model has attained low MSE, RMSE, MAE, and SMAPE, which shows the betterment of the proposed model.

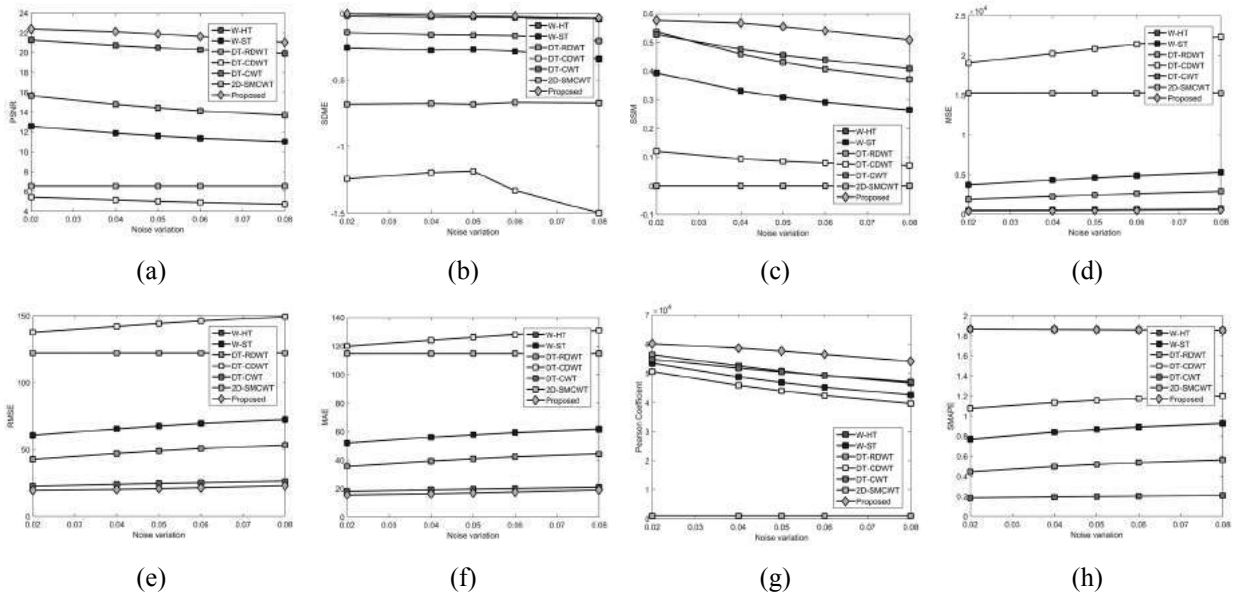
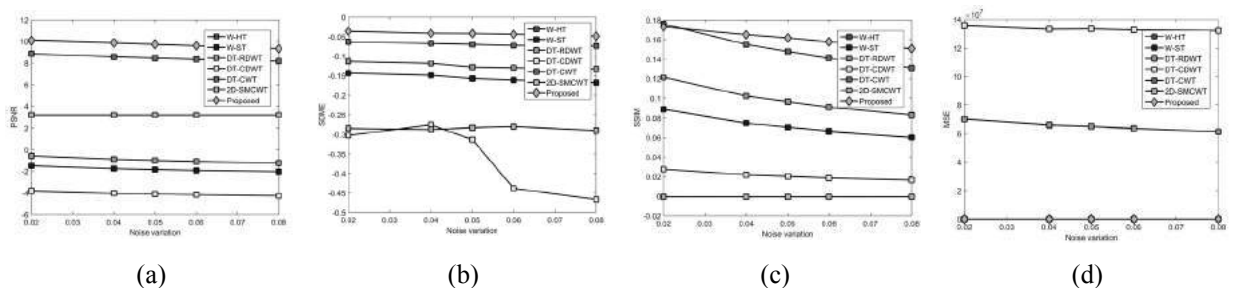


Fig. 6. Performance analysis of proposed image denoising model for Texture image set by varying noise in terms of (a) PSNR, (b) SDME, (c)SSIM, (d) MSE, (e) RMSE, (f) MAE, (g) PC, and (h) SMAPE.

Fig 7 shows the performance of the proposed model for nature image set over conventional methods by varying noise levels from 0.02 to 0.08. From the figure, it is detected that the PSNR of the proposed model is 65.14% and 16.53% better than 2D-SMCWT and DT-CWT, respectively. The SDME of the proposed model is 89.28% and 90% superior to 2D-SMCWT and DT-CDWT, respectively. Similarly, the same analysis is made for all measures, and the superiority of the proposed model is proved from the attained results.



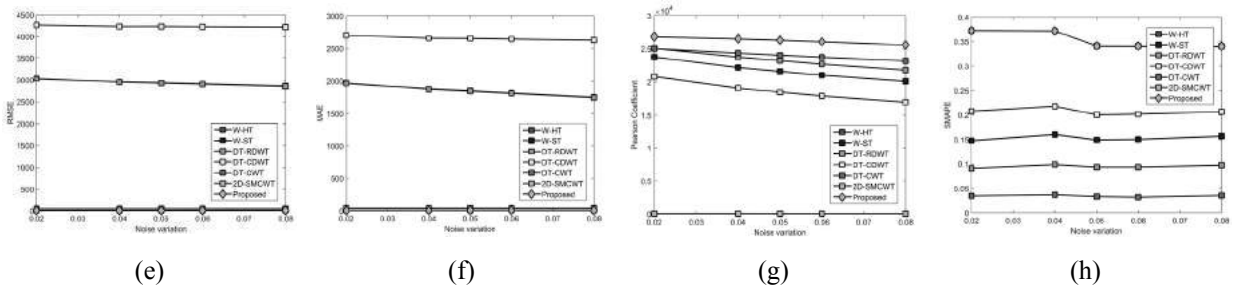


Fig. 7. Performance analysis of the proposed denoising model for Nature image set by varying noise in terms of (a) PSNR, (b) SDME, (c)SSIM, (d) MSE, (e) RMSE, (f) MAE, (g) PC, and (h) SMAPE.

Fig 8 illustrates the performance of the proposed model for medical image set over conventional methods by varying noise levels from 0.02 to 0.08. It is evident that the PSNR of the proposed model is 65.82%, 9.96%, 58.78%, 12.01%, and 41.24% superior to 2D-SMCWT, DT-CWT, DT-CDWT, DT-RDWT, and W-ST, respectively. The SDME of the proposed model is 82.14%, 37.5%, 44.445, and 58.3% better than 2D-SMCWT, DT-CWT, DT-RDWT, and W-ST, respectively.

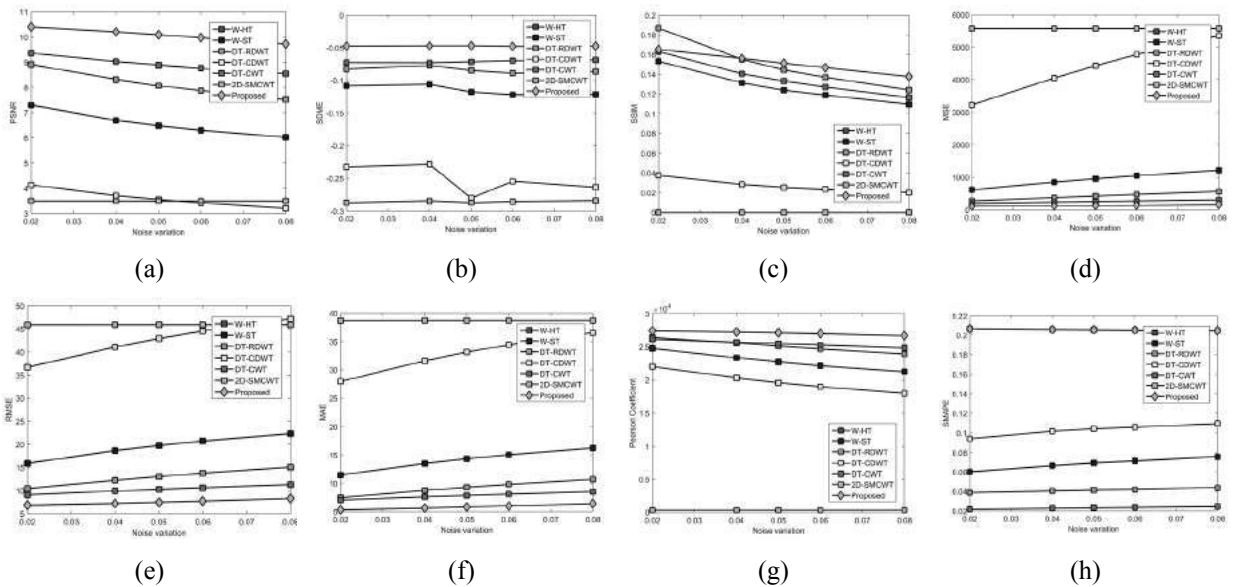


Fig. 8. Performance analysis of the proposed image denoising model for Medical image set by varying noise in terms of (a) PSNR, (b) SDME, (c)SSIM, (d) MSE, (e) RMSE, (f) MAE, (g) PC, and (h) SMAPE.

Fig 9 shows the performance of the proposed model for satellite image set over conventional methods by varying noise levels from 0.02 to 0.08. It is observed that the PSNR of the proposed model is 61.93%, 34.095, and 51.13% superior to 2D-SMCWT, DT-RDWT, and W-ST, respectively. Fig 10 shows the performance of the proposed model for miscellaneous image set over conventional methods by varying noise levels from 0.02 to 0.08. From the figure, it is observed that the PSNR of the proposed model is 17.67%, 99.9%, 55.6%, and 67.02% superior to DT-CWT, DT-CDWT, DT-RDWT, and W-ST, respectively. Similarly, the performance analysis of the proposed model for both satellite and miscellaneous image set is analyzed in terms of SDME, SSIM, MSE, RMSE, MAE, PC, and SMAPE, respectively. From the observed results, it is evident that the proposed model is superior to the conventional methods in terms of performance.

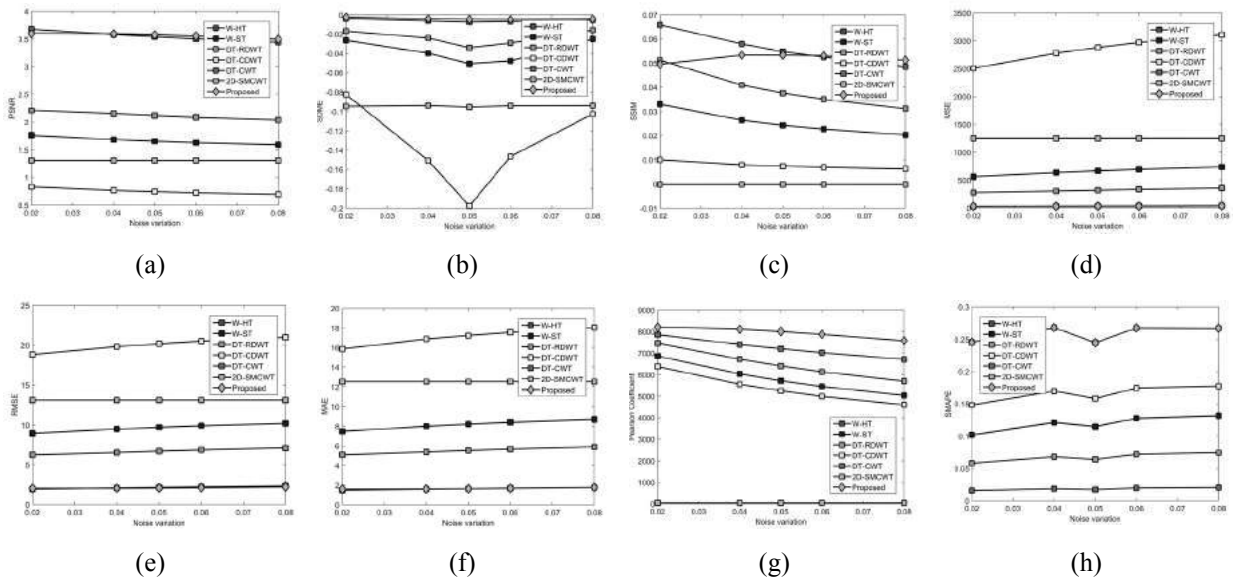


Fig. 9. Performance analysis of the proposed model for Satellite image set by varying noise in terms of (a) PSNR, (b) SDME, (c)SSIM, (d) MSE, (e) RMSE, (f) MAE, (g) PC, and (h) SMAPE.

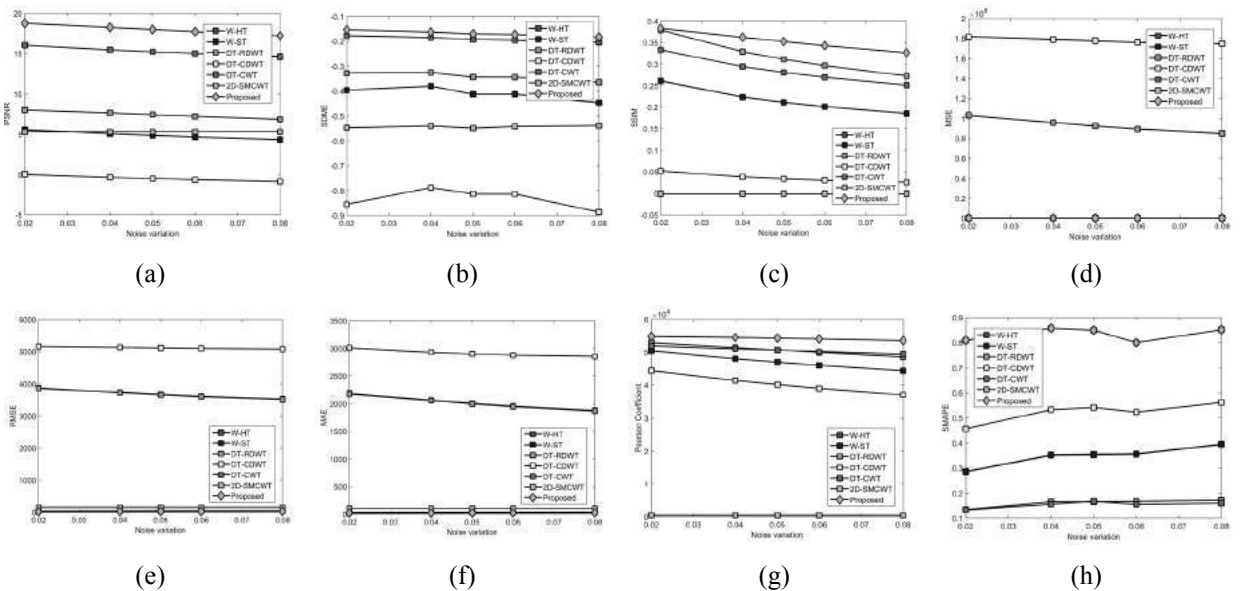


Fig. 10. Performance analysis of the proposed model for Miscilleneous image set by varying noise in terms of (a) PSNR, (b) SDME, (c)SSIM, (d) MSE, (e) RMSE, (f) MAE, (g) PC, and (h) SMAPE.

Computing Complexity

A model should be considered as an efficient model only if it incurs less computation complexity. Fig 11 shows the observed computational time of the proposed model. From Fig 11 it is detected that the proposed model falls on the second place with computing time 0.15sec. Even though it is in the second place, while analyzing the performance of developed model, it is proved that the proposed model is more efficient than the other conventional methods.

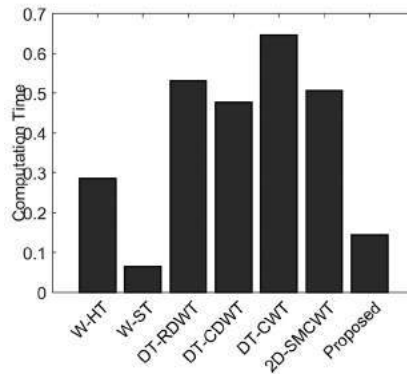


Fig. 11. Computational complexity of the proposed over conventional image denoising model.

CONCLUSION

This paper has developed a denoising algorithm for multi-modal images. Here, DT-CWT was exploited for image transformation for which the wavelet coefficients were estimated using BR classifier. The performance of denoising model was ensured by extracting the statistical and wavelet features. Consequently, the image characteristics were combined with noise spectrum for the development of BR model that has estimated the wavelet coefficients for effective denoising. Thus, the proposed denoising algorithm has exploited two stages of BR. The first stage has predicted the type of image, whereas the second stage has estimated optimal wavelet filter coefficients to DT-CWT for denoising. The performance of the proposed model was analyzed in terms of certain measures like PSNR, SDME, SSIM, MSE, RMSE, MAE, PC, and SMAPE, respectively, by comparing the developed model with other conventional models. From the results, it was observed that, for Texture image, the proposed model had attained promising results. The PSNR, SDME, SSIM, MSE, MAE, PC, and SMAPE of the developed model showed approximately 46.49%, 85.79%, 54.72%, 80.62%, 59.33%, 29.75%, and 68.25% superior to 2D SMCWT, DT-CWT, DT-CDWT, DT-RDWT, W-ST, and W-HT, respectively.

REFERENCES

- Aggarwal, K.K., Singh, Y., Chandra, P. & Puri, M. (2005).** Bayesian Regularization in a Neural Network Model to Estimate Lines of Code Using Function Points, *Journal of Computer Sciences*, **1**(4): 505-509.
- Beck, A. & Teboulle, M. (2009).** A fast iterative shrinkage-thresholding algorithm for linear inverse problems, *SIAM Journal of Imaging Sciences*, **2**(1): 183–202.
- Call, J.M. (2005).** Genetic algorithms for modelling and optimisation, *Journal of Computational and Applied Mathematics*, **184**(1): 205-222.
- Chung, H., Plourde, E. & Champagne, B. (2017).** Regularized non-negative matrix factorization with Gaussian mixtures and masking model for speech enhancement, *Speech Communication*, **87**: 18-30.
- Decker, A.D., Lee, J.A. & Verleysen, M. (2010).** A principled approach to image denoising with similarity kernels involving patches, *Neurocomputing*, **73**(7–9):1199-1209.
- Ghorai, S.K. (2013).** A novel blind source separation technique using fractional Fourier transform for denoising medical images, *Optik - International Journal for Light and Electron Optics*, **124**(3): 265-271.
- Gong, M., Zhang, P., Su, L & Liu, J. (2016).** Cou-pled dictionary learning for change detection from multisourcedata,” *IEEE Transactions on Geoscience and Remote Sensing*, **54**(12): 7077–7091.
- Guo, X., Li, Y., Suo, T. & Liang, J. (2017).** Denoising of digital image correlation based on stationary wavelet transform, *Optics and Lasers in Engineering*, **90**: 161-172.

- Hanson, K.M. (1998).** A simplified method of estimating noise power spectra, *Physics of Medical Imaging*, pp. 243-250.
- Hou, R., Wang, Z., Diamond, J.J., Zheng, Z., Zhu, J., Wang, Z. & Chu, B. (2011).** A quantitative evaluation model of denoising methods for surface plasmon resonance imaging signal, *Sensors and Actuators B: Chemical*, **160**(1): 951-956.
- Jesus, H., Domínguez, O., Máynez, L.O., Villegas, O.O.V., Mederos, B., Mejía, J.M. & Sanchez, V.G.C. (2015).** Denoising of high resolution small animal 3DPET data using the non-sub sampled Haar wavelet transform, *Nuclear Instruments and Methods in Physics Research*, **784**: 581–584.
- Jin, W.U. (2013).** Wavelet domain denoising method based on multistage median filtering, *The Journal of China Universities of Posts and Telecommunications*, **20**(2): 113-119.
- Li, D., Zhang, L., Yang, J. & Su, W. (2016).** Research on wavelet-based contourlet transform algorithm for adaptive optics image denoising, *Optik - International Journal for Light and Electron Optics*, **127**(12): 5029-5034.
- Liu, C., Szeliski, R. & Kang, S.B. (2008).** Automatic estimation and removal of noise from a single image, *IEEE Transactions on Pattern Analysis and Machine Intelligence*, **30**(2): 299–314.
- Liu, T.C.K., Dong, X. & Lu, W.S. (2009).** Multiresolution wavelet denoising for ultra-wideband time-of-arrival estimation with regularized least squares, *Physical Communication*, **2**(4): 285-295.
- Liu, X. & Fang, S. (2015).** A convenient and robust edge detection method based on ant colony optimization, *Optics Communications*, **353**: 147–157.
- Liu, Z., Li, G., Mercier, G., He, Y & Pan, Q. (2018).** Change detection in heterogenous remote sensing images via homogeneous pixel transformation,” *IEEE Transactions on Image Processing*, **27**(4): 1822–1834.
- Liu, Z., Zhang, L., Li, G & He, Y. (2017).** Change detection in heterogeneous remote sensing images based on the fusion of pixel transformation,” *Information Fusion (Fusion)*, 2017 20th International Conference on. IEEE, 1–6.
- Luisier, F., Blu, T. & Unser, M. (2007).** A new SURE approach to image denoising: Interscale orthonormal wavelet thresholding, *IEEE Transactions on Image Processing*, **16**(3): 593–606.
- Luo, J. & Zhu, Y. (2012).** Denoising of medical images using a reconstruction-average mechanism, *Digital Signal Processing*, **22**(2): 337-347.
- Luppino, L.T., Anfinsen, S.N., Moser, G., Jenssen, R., Bianchi, F.M., Serpico, S & Mercier, G. (2017).** A clustering approach to heterogeneous change detection,” in *Scandinavian Conference on Image Analysis*. Springer, 181–192.
- Mercier, G., Moser, G & Serpico, S.B. (2008).** Conditional copulas for change detection in heterogeneous remote sensing images,” *IEEE Transactions on Geoscience and Remote Sensing*, **46**(5): 1428–1441.
- Mohan, Y., Chee, S.S., Xin, D.K.P. & Foong, L.P. (2016).** Artificial neural network for classification of depressive and normal in EEG, *2016 IEEE EMBS Conference on Biomedical Engineering and Sciences (IECBES)*, Kuala Lumpur, pp. 286-290.
- Naimi, H., Houda, A.B., Mitiche, A. & Mitiche, L. (2015).** Medical image denoising using dual-tree complex thresholding wavelet transform and Wiener filter, *Journal of King Saud University - Computer and Information Sciences*, **27**(1): 40-45.
- Nasri, M. & Nezamabadi-pour, H. (2009).** Image denoising in the wavelet domain using a new adaptive thresholding function, *Neurocomputing*, **72**(4–6): 1012-1025.
- Pizurica, A. & Philips, W. (2006).** Estimating the probability of the presence of a signal of interest in multiresolution single-and multiband image denoising, *IEEE Transactions on Image Process*, **15**(3): 645–665.
- Portilla, J., Strela, V., Wainwright, M.J. & Simoncelli, E.P. (2003).** Image denoising using scale mixtures of Gaussians in the wavelet domain, *IEEE Transactions on Image Process*, **12**(11): 1338–1351.
- Prendes, J., Chabert, M., Pascal, F., Giros, A & Tourneret, J. (2015).** A new multivariate statistical model for change detection in images acquired by homogeneous and heterogeneous sensors,” *IEEE Transactions on Image Processing*, **24**(3): 799–812.
- Rabbani, H. (2009).** Image denoising in steerable pyramid domain based on a local Laplace prior, *Pattern Recognition*, **42**(9): 2181–2193.
- Remenyi, N., Nicolis, O., Nason, G. & Vidakovic, B. (2014).** Image Denoising With 2D Scale-Mixing Complex Wavelet Transforms, *IEEE Transactions on Image Processing*, **23**(12): 5165-5174.

- Sable, A.H & Jondhale, K.C. (2010). Modified Double Bilateral Filter for Sharpness Enhancement and Noise Removal.
- Selesnick, I.W., Baraniuk, R.G. & Kingsbury, N.G. (2005). The Dual-Tree Complex Wavelet Transform, *IEEE SIGNAL PROCESSING MAGAZINE*, pp. 123-150.
- Shang, L., Su, P. and Liu, T. (2012). Denoising MMW image using the combination method of contourlet and KSC shrinkage, *Neurocomputing*, **83**: 229-233.
- Song, C., Deng, H., Gao, H., Zhang, H. & Zuob, W. (2016). Bayesian non-parametric gradient histogram estimation for texture-enhanced image deblurring, *Neurocomputing*, **197**: 95–112.
- Srivastava, R. (2014). Performance measurement of image processing algorithms. Professor, Department of Computer Science & Engineering, IIT BHU, India.
- Storvik, B., Storvik, G & Fjortoft, R. (2009). On the combination of multisensor data using meta-gaussian distributions,”*IEEE Transactions on Geoscience and Remote Sensing*, **47**(7): 2372–2379.
- Su, L., Gong, M., Zhang, P., Zhang, M., Liu, J & Yang, H. (2017). Deep learning and mapping based ternary change detection for information unbalanced images,”*Pattern Recognition*, **66**: 213–228.
- Sun, D., Gao, Q., Lu, Y., Huang, Z. & Li, T. (2014). A novel image denoising algorithm using linear Bayesian MAP estimation based on sparse representation, *Signal Processing*, **100**: 132–145.
- Sunil, B.S., Manjunath, A.S., Christopher, S. & Menon, R.L. (2016). Motion-compensated adaptive dual tree complex wavelet transform coding for scalable color video compression using SPIHT, **9**: 47-57.
- SunilKumar, B.S., Manjunath, A.S., Christopher, S. & Menon, R. (2016). Enhanced Scalable Video Coding Technique with an Adaptive Dual- Tree Complex Wavelet Transform, *Procedia Computer Science*, **85**: 70-77.
- Touati, R & Mignotte, M. (2018). An energy-based model encoding nonlocal pairwise pixel interactions for multisensor change detection,” *IEEE Transactions on Geoscience and Remote Sensing*, **56**(2): 1046–1058.
- Tuia, D., Marcos & G., Camps-Valls. (2016). Multi-temporal and multi-source remote sensing image classification by nonlinear relative normalization,” *ISPRS Journal of Photogrammetry and Remote Sensing*, **120**: 1–12.
- Volpi, M., Camps-Valls, G & Tuia, D. (2015). Spectral alignment of multi-temporal cross-sensor images with automated kernel canonical correlation analysis,” *ISPRS Journal of Photogrammetry and Remote Sensing*, **107**: 50–63.
- Wagh & Todmal. (2015). Eyelids, Eyelashes Detection Algorithm and Hough Transform Method for Noise Removal in Iris Recognition”, *International Journal of Computer Applications*, **112**(3).
- Wang, X.Y. & Kai Fu, Z. (2010). A wavelet-based image denoising using least squares support vector machine, *Engineering Applications of Artificial Intelligence*, **23**(6): 862-871.
- Wang, X.Y., Yang, H.Y. & Kai Fu, Z. (2010). A New Wavelet-based image denoising using undecimated discrete wavelet transform and least squares support vector machine, *Expert Systems with Applications*, **37**: 7040–7049.
- Wang, X.Y., Yang, H.Y., Zhang, Y. & Kai Fu, Z. (2013). Image denoising using SVM classification in nonsubsampled contourlet transform domain, *Information Sciences*, **246**: 155-176.
- Wong, A., Mishra, A., Zhang, W., Fieguth, P. & Clausi, D.A. (2011). Stochastic image denoising based on Markov-chain Monte Carlo sampling, *Signal Processing*, **91**(8): 2112-2120.
- Xin, Z. & Jiangtao, Q. (2011). De-noising of GIS UHF Partial Discharge Monitoring based on Wavelet Method, *Procedia Environmental Sciences*, **11**: 1302-1307.
- Yan, F., Cheng, L. & Peng, S. (2008). A new interscale and intrascale orthonormal wavelet thresholding for SURE-based image denoising, *IEEE Transactions on Signal Processing Letters*, **15**: 139–142.
- Yang, H.Y., Wang, X.Y. & Kai Fu, Z. (2012). A new image denoising scheme using support vector machine classification in shiftable complex directional pyramid domain, *Applied Soft Computing*, **12**(2): 872-886.
- YueSi, Zhang, Z., Wang, H. & Yuan, F. (2016). Mono modal feature extraction for bonding quality detection of explosive clad structure with optimized dual-tree complex wavelet transform, *Journal of Sound and Vibration*.
- Zhang, P., Gong, M., Su, L., Liu, J & Li, Z. (2016). Change detection based on deep feature representation and mapping

transformation for multi-spatial-resolution re-mote sensing images,” *ISPRS Journal of Photogrammetry and Remote Sensing*, **116**: 24–41.

Zhang, W. (2013). Image denoising algorithm of refuge chamber by combining wavelet transform and bilateral filtering, *International Journal of Mining Science and Technology*, **23**(2): 221-225.

Zhao, W., Wang, Z., Gong, M & Liu, J. (2017). Discriminative feature learning for unsupervised change detection in heterogeneous images based on a coupled neural network,” *IEEE Transactions on Geoscience and Remote Sensing*.

Submitted: 28/12/2017

Revised: 01/05/2019

Accepted: 02/05/2019

استخدام شبكة بايزي ثنائية المرحلة مع التحويل المويجي المعقد ذي الشجرة الثنائية لتقليل تشويش الصور

*فينكاتا لافانيا، **فينكاتا ناراسيمهولو و***ساتيا براساد

*قسم اللجنة الاقتصادية لأوروبا، جامعة جواهر لال نهرو التكنولوجية بكينادا، أندرا براديش، الهند

**قسم اللجنة الاقتصادية لأوروبا، كلية جيتانجال للهندسة والتكنولوجيا، حيدر أباد، تيلانجانا، الهند

***مؤسسة فيجن للعلوم والتكنولوجيا والبحث، جونتور، أندرا براديش، الهند

الخلاصة

إزالة التشويش من الصور تلعب دوراً حيوياً في العروض الهندسية المختلفة. وكذلك في تكنولوجيا معالجة الصور، ظل الخلاف حول إحصاءات إزالة التشويش من الصورة قائماً. على مدى العقود الماضية، كشفت بعض الطرق لإزالة التشويش عن إنجازات لا تصدق. ونظراً لعدم وجود مساهمات كبيرة في إزالة التشويش من الصور متعددة الوسائط وغير المتجانسة، فإن هذا البحث يعرض نهج ذكي لذلك. تم استخدام التحويل المويجي المعقد ذي الشجرة الثنائية (DT-CWT) لتحويل الصور التي يتم تقدير معالمها مويجاتها باستخدام تنظيم بايزي (BR). ولضمان تنفيذ عملية إزالة التشويش من الصور غير المتجانسة، تم استخراج الخصائص الإحصائية والمويجية. بعد ذلك، تم دمج خصائص الصورة مع طيف التشويش لتطوير نموذج BR، والذي يقدر معاملات المويجات لإزالة التشويش بشكل فعال. وبالتالي، فإن خوارزمية إزالة التشويش المقترحة تستخدم مرحلتين من BR. تتوقع المرحلة الأولى نوع الصورة، في حين أن المرحلة الثانية تقدر معاملات المويجات المناسبة للتحويل المويجي المعقد ذي الشجرة الثنائية لإزالة التشويش. كمساهمة رئيسية، تم تحسين معاملات فلتر DT-CWT بواسطة الخوارزمية الجينية (GA). تم تحليل أداء النموذج المقترح بواسطة مقياس نسبة قمة الإشارة إلى التشويش (PSNR)، الاشتقاق الثاني لمقياس التحسين (SDME)، التشابه الهيكلية (SSIM)، خطأ التربيع المتوسط (MSE)، خطأ الجذر التربيعي (RMSE)، خطأ المتوسط المطلق (MAE)، ومعامل بيرسون (PC)، وخطأ النسبة المئوية المطلقة لمتوسط متشابه (SMAPE) على التوالي. وتم مقارنة النموذج المقترح بالنماذج التقليدية، وتم توضيح أهمية النموذج المطور بوضوح. ولوحظ من التحليل أن PSNR للنموذج المطور هو 69.97%، 5.85%، 76.91%، 33.38%، 46.40% و 46.44% أفضل من DT-CDWT، DT-CWT، 2D SMCWT، DT-CDWT، DT-CWT، RDWT و W-ST و W-HT، على التوالي. وبالمثل بالنسبة لمقياس SSIM، فإن النموذج المقترح له انحراف كبير على الطرق التقليدية، وهو 19.17%، 83.66%، 24.65%، 72.99% و 73.15% أفضل من DT-CDWT، DT-CWT، DT-RDWT، W-ST و W-HT، على التوالي.



Design and implementation of low complexity circularly symmetric 2D FIR filter architectures

Venkata Krishna Odugu¹ · C. Venkata Narasimhulu² · K. Satya Prasad³

Received: 29 September 2019 / Revised: 19 February 2020 / Accepted: 24 February 2020
© Springer Science+Business Media, LLC, part of Springer Nature 2020

Abstract

This paper presents a low complexity two dimensional (2D) circular symmetric Finite Impulse Response (FIR) filter design and implementation of architecture. The optimized circular symmetric 2D FIR filter is designed using a modified Park–McClellan transformation method and filter coefficients are quantized using a canonical signed digit (CSD) binary number format. The CSD encoded coefficients are optimized to reduce the number of adder/subtractors using common subexpression elimination (CSE) algorithms. Based on the modified filter coefficients, the two structures fully direct form and hybrid-II form 2D FIR filter architectures are implemented using CSD and CSD with Horizontal CSE and Vertical CSE techniques. The proposed architectures compared with the conventional symmetry 2D filters and state-of-the-art architectures in terms of area, power, and speed.

Keywords 2D FIR filter · McClellan transformation · Canonical signed digit (CSD) · Multiple constant multiplication (MCM) · Common sub-expression elimination (CSE) · Low power

1 Introduction

The two-dimensional (2D) linear phase filters are frequently used in image and video processing applications. The efficient and low complexity Finite Impulse Response (FIR) filters often need for image restoration, image enhancement, and denoising applications, etc. The design and implementation of low power and low complexity with high-speed digital filter architecture is a challenging task. The optimization is required for 2D FIR filters to meet the coveted filter specifications. The pruning of hardware complexity with low power consumption is desired for the Very Large Scale Integration (VLSI) implementation of any filter architecture.

✉ Venkata Krishna Odugu
venkatakrishna.odugu@gmail.com

¹ JNTUK, Kakinada, India

² Geethanjali College of Engineering and Technology, Hyderabad, India

³ Vignan's Foundation for Science, Technology and Research, Guntur, India

Many optimization algorithms are proposed for designing the 2D FIR filters, such as Genetic Algorithm, Particle Swarm and Differential Evolution, ABC algorithm, etc. (Chandra and Chattopadhyay 2016). The above methods suffer from the large execution time and premature convergence. The optimization is carried out to meet the filter frequency domain specifications, passband ripple, and stopband ripple. The McClellan transformation method is the best technique for the design of 2D FIR filters for an efficient hardware structure implementation. McClellan transformation based method results in a low complexity 2D FIR architecture using a transformation approach. The circularly symmetric, fan type and elliptic filters are designed by kth-McClellan transformation technique with remarkable results. The transformation approach is most valuable for linear phase filters and they should be in the symmetry of quadrant. This algorithm is fast and it gives a moderate degree and good implementation. Here, the one dimensional (1-D) FIR filter is designed and mapped to 2D FIR Filter using McClellan transform (Das et al. 2019). The kth-McClellan transform is added by a new term which is used to get circular shape at all frequencies is called as T1 transformation. The T1 transformation is modified into to approximate the constants to avoid the squarish shape at the center of the low pass filter is T2 transformation. The T2 is changed to P2 transformation to achieve circularity for wideband frequencies in 2D FIR filters (Bindima et al. 2016).

Recently, Bindima and Elias (2016, 2017, 2019) proposed low complexity circular and fan type 2D FIR filter design methods using tunable Farrow structure. This work focused on the design of higher-order filters using P2 transformation with Parks McClellan transformation. The design required a huge number of multipliers for the implementation of the hardware architecture. In Baboji and Sridevi (2019), Frequency Response Masking (FRM) approach is proposed for the multiplierless design of 1-D FIR filters with low complexity in terms of hardware. The Signed Sum of Powers of Two (SOPOT) form is used to approximate the filter coefficients with less run time. The Modified Artificial Bee-Colony algorithm (MABC) is proposed in Dwivedi et al. (2016), to optimize the coefficients of circular symmetric 2D FIR filters. This design is validated and synthesized to reduce the power consumption, passband ripple, and stopband ripple. Many authors have proposed 2D FIR filter design concepts and optimization techniques to reduce the complexity and power (Odugu et al. 2019). Here, the optimization is carried by many transformations in the design level only and no exploration in architecture level for 2D FIR filters.

The designed filter implementation in hardware with necessary optimization schemes is a challenging task. Many efficient multipliers are available for low complexity implementation of FIR filters. But, the full flexibility is not required for the multiplication process in filters and multiplier is a power-hungry circuit in the filter architecture. To multiply the inputs and delay version of inputs with fixed filter coefficient constants, Multiple Constant Multiplication (MCM) technique and multiplierless filter operations can be used.

Many systolic 2D filter architectures are proposed with less number of computations by symmetry property. Mohanty et al. (2013) proposed, the memory-efficient 2D FIR filters inseparable and non-separable structures with medium critical path and medium computations. But in this work, multipliers are complex blocks and occupies more area and consumes large power.

The symmetry property in the frequency response of the filter reduces the number of multipliers or computations. In the papers (Chen et al. 2010, 2013), area and power-efficient 2D filter structures with various symmetry properties are suggested with complex multipliers. Due to the symmetry number of multipliers are reduced but, these multipliers are power-consuming blocks in the filter. Aksoy et al. (2014) have been introduced efficient multiplierless designs with the minimum number of adders/subtractors for only one dimen-

sional FIR filters using exact and approximated models. Recently, a Distributed Arithmetic (DA) block-based 2D FIR filter in a systolic structure style is proposed using pipelining and parallel processing to reduce the complexity of hardware (Kumar et al. 2018, 2019).

Many researchers are focused on 2D filter architectures with no exploration of design issues. Whereas designers are only concentrated on the design concepts and optimization in filter specifications and no exploration for the hardware structures.

In this paper, at the design level, the filter coefficients are optimized and hardware architectures are implemented using appropriate optimizing algorithms. The design of 2D FIR filter using T2 and P2 transformations in kth-McClellan transform gives circularity in the contour of low pass filter. The efficient approach for the implementation of designed coefficients of 2D FIR filter is canonical signed digit (CSD) encoding method under multiplierless filter implementation. The CSD format consists of less number of non zero digits and causes to reduce the number of adders/subtractors. The CSD coefficients of the filter will be implemented using add and shift operations only.

In this paper, the 2D FIR filter is designed with circular symmetry using kth-Park McClellan transform using T2 and P2 transformations for desired specifications and different VLSI architectures are suggested with low complexity. The optimized 1-D FIR filter is designed and transformed to 2D filter using a transformation approach. Next, the designed filter coefficients are optimized using CSD, CSD with horizontal common subexpression elimination (HCSE) and CSD with vertical common subexpression elimination (VCSE) techniques. Based on the optimized coefficients, the hardware architectures are implemented in the form of fully direct type and hybrid-II type filters.

The paper is organized as follows: Sect. 2 presents the design of circular symmetry 2D FIR filter using T2 and P2 transformations with CSD space. The word length and number of Signed Power (SPT) terms are restricted without any deviation from given specifications. Section 3 provides the 2D FIR filter architectures in fully direct form and hybrid-II form architectures for continuous coefficients, CSD coefficients and optimized CSD coefficients using HCSE and VCSE. Experimental results and comparison of hardware complexity of different architectures styles are presented in Sect. 4. The work conclusion is summarized in Sect. 5.

2 Design of 2D circularly symmetric FIR filter

The McClellan transform is used to transform the zero phase 1-D FIR filter into zero phase 2D FIR filter. This transformation mostly applied for odd length one-dimensional filters. The length of the 1-D filter with zero phase is $2N + 1$ and it should be symmetric. The frequency response of the 1-DFIR filter is given in Eq. 1.

$$H(e^{j\omega}) = h(0) + \sum_{n=1}^N h(n)[e^{-j\omega n} + e^{j\omega n}] \tag{1}$$

$$= h(0) + \sum_{n=1}^N 2h(n)\cos\omega n \tag{2}$$

where $h(n)$ is an impulse response. Then 1-D zero-phase filter frequency response is converted into 2D filter response with zero phase and is denoted by Eq. 2. The McClellan transforma-

tion generally transforms the 1-D to 2D filter using the substitution of some variables. The substitution term is given by Eqs. 3 and 4.

$$H(e^{j\omega_1}, e^{j\omega_2}) = \sum_{m=0}^{M1} \sum_{n=0}^{M2} a(m, n) \cos m\omega_1 \cos n\omega_2 \tag{3}$$

$$\cos \omega = \sum_{p=0}^P \sum_{q=0}^Q t(p, q) \cos p\omega_1 \cos q\omega_2 \tag{4}$$

Finally, the relation of 2D impulse response $h(m, n)$ and 1-D filter impulse response $h(n)$ is can be written as Eq. 5,

$$H(e^{j\omega}) = \sum_{n=0}^N b(n) [\cos \omega]^n \tag{5}$$

According to the Chebyshev polynomial recurrence formula, the overall response of 2D FIR filter is written in the form of Eq. 2 with filter sizes $(2NP + 1) \times (2NQ + 1)$ expressed in Eq. 6.

$$H(e^{j\omega_1}, e^{j\omega_2}) = \sum_{n=0}^N b(n) \left[\sum_{p=0}^P \sum_{q=0}^Q t(p, q) \cos p\omega_1 \cos q\omega_2 \right]^n \tag{6}$$

Here, the McClellan transform considered for the case of $P = 1$ and $Q = 1$ only. The shape of the 2D filter contours depends on the parameter values of $t(p, q)$, where $0 < p < P$, and $0 < q < Q$. The frequency response of the 2D FIR filter is controlled by the impulse response of 1-D filter $h(n)$. First, a 1-D prototype FIR filter is designed for the desired specifications and transformed into a 2D FIR filter using McClellan. In this paper, a circular symmetric filter is considered with parameter values of $P = 1$ and $Q = 1$, then $-t(0, 0) = t(1, 0) = t(0, 1) = t(1, 1) = 1/2$.

By appropriately selecting the $t(p, q)$ values different shapes of filters can be designed. Such as circular, elliptical, diamond and fan shapes, etc. This original McClellan transformation gives circular contour for small radii values and it nearly becomes square-shaped at higher radii frequencies of ω . For low pass filter, it gives square shape at the center of the contour as shown in the Fig. 1. The contour has to be approximated using appropriate transformation parameters $t(p, q)$ to achieve exact circular shape at the center of the low pass filter. The contours are produced by the transformation by approximating the constants in the passband and stopband of the low pass filter (Liu and Tai 2010; Shyu et al. 2008). For approximation consider kth-McClellan transform as given in Eqs. 7 and 8.

$$\cos \omega = F(\omega_1, \omega_2) \tag{7}$$

$$F(\omega_1, \omega_2) = \sum_{p=0}^P \sum_{q=0}^Q t(p, q) \cos p\omega_1 \cos q\omega_2 \tag{8}$$

The original kth-McClellan transform can be written as Eq. 9 using basic trigonometric series.

$$\cos(\Omega) = f(\omega_1, \omega_2) = 2 \left[\cos\left(\frac{\omega_1}{2}\right) \cos\left(\frac{\omega_2}{2}\right) \right]^2 - 1 \tag{9}$$

$$\cos(\Omega) = g(\omega_1, \omega_2) = 2 \left[\cos\left(\frac{\omega_1}{2}\right) \cos\left(\frac{\omega_2}{2}\right) \right]^{2k} - 1 \tag{10}$$

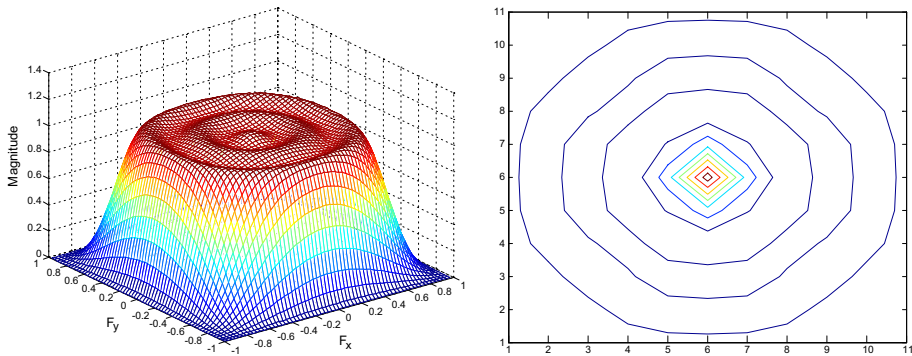


Fig. 1 Frequency response and contour of Low Pass Filter using McClellan transform

where k is integer constant i.e. $k \geq 1$. It is nothing but k th-McClellan transform. If k value is 1, then the above Eq. 10 becomes an original McClellan transform. The frequency response of the low pass filter using k th-McClellan transform is shown in Fig. 1.

The squarish effect at the center of the low pass filter, and for higher frequencies on (ω_1, ω_2) plane can be observed from the Fig. 1. This is overcome by introducing the additional terms for the k th-McClellan transform equation and the modified equations are called T1 transformation as given by Eq. 11 and T2 transformation is given by Eq. 12.

$$\cos(\Omega) = 2 \left[\cos\left(\frac{\omega_1}{2}\right) \cos\left(\frac{\omega_2}{2}\right) \right]^{2k} \times \left[1 - \sin^2\left(\frac{\omega_1}{2}\right) \sin^2\left(\frac{\omega_2}{2}\right) \right] - 1 \quad (11)$$

$$\cos(\Omega) = 2 \left[\cos\left(\frac{\omega_1}{2}\right) \cos\left(\frac{\omega_2}{2}\right) \right]^{2k} \times \left[\cos^2\left(\frac{\omega_1}{2}\right) + \cos^2\left(\frac{\omega_2}{2}\right) \right] - 1 \quad (12)$$

Further, another modified term is introduced in the T2 transformation to improve the circularity at the higher frequency for wideband filters Bindima and Elias (2019). i. e $P(\omega_1, \omega_2) = 0.5[\cos^2(\frac{\omega_1}{2}) + \cos^2(\frac{\omega_2}{2})]$ is called as P2 transformation is given by (13). The frequency response and contour of the circular symmetric 2D FIR filter using P2 transformation in k th-McClellan transform is shown in the Fig. 2.

$$\cos(\Omega) = 2 \left[\cos\left(\frac{\omega_1}{2}\right) \cos\left(\frac{\omega_2}{2}\right) \right]^{2k} \times P(\omega_1, \omega_2) - 1 \quad (13)$$

The smaller order filters are more preferable for image enhancement applications than higher-order filters. Hence to achieve low power and better optimization in hardware complexity, lower-order filters are designed in this work. To obtain a lower order, the following specifications are considered. The proposed 2D FIR filter design is applied for the Low pass filter with specifications of, band edges in Hz = [1500 2000], desired magnitude values in each band is [1 0], the ripple in each band is [0.0559 0.01] and the sampling frequency is 4000 Hz. This specified 2D FIR filter is designed using P2 transformation in the k th-McClellan transform and the order of the filter is obtained as 9×9 with Stop Band (SB) attenuation of 32 dB and Pass Band (PB) ripple 5.8 dB.

The continuous coefficient filter design result in SB attenuation of 32 dB and PB ripple of 5.8 dB. If the filter coefficients are quantized using 18-bit CSD number representation with the precision of 7 SPT terms then it results in an SB attenuation of 30.7 dB and a PB ripple of 6.017 dB. To reduce the number of non-zero bits in CSD, the word length is decreased to 16-bits with SPT terms of 6. It gives the SB attenuation of 29.93 dB and PB ripple of 6.016 dB.

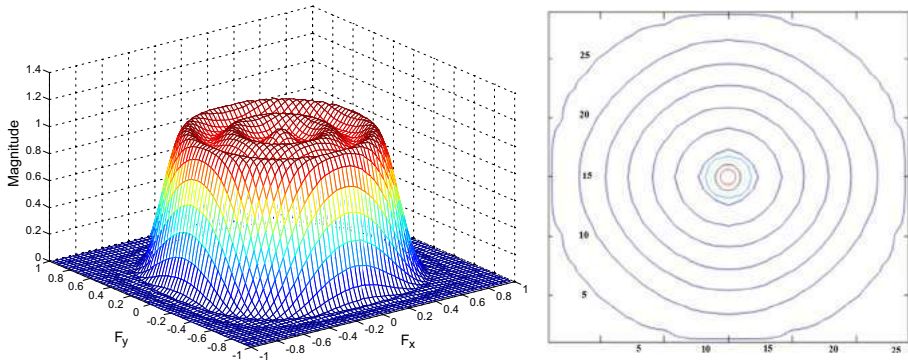


Fig. 2 Frequency response and contour of Low Pass Filter using P2 transformation in kth McClellan transform

Table 1 SB attenuation & PB ripple values for 2D FIR filter for different word lengths and SPT terms

Word length (bits)	No. of SPT terms	Stop band attenuation (dB)	Pass band ripple (dB)
Continuous Coefficient	–	32	5.8
18	7	30.7	6.017
16	6	29.93	6.016
15	6	29.28	6.00
14	5	29.12	6.47
12	5	28.72	6.53

Further, when the coefficients are quantized with less number of SPT terms by decreasing of word length to 12-bits, the SB attenuation is 28.72 dB and PB ripple is 6.53 dB. Table 1 shows the different word lengths and SPT terms with SB and PB results of the designed 2D FIR filter. If the word length is decreased beyond 12-bits with restricted number SPT terms then the performance of the filter is degraded. Hence, a 12-bit CSD coefficient quantization coding is used to reduce the hardware complexity without any diversion of filter parameters. The resultant filter parameters, SB attenuation, and PB ripple are acceptable in range.

The frequency response of the 2D FIR filter with CSD encoding with a word length of 12-bits and 5 SPT terms has not deviated from the magnitude response of the continuous coefficients magnitude response. Hence, the decreasing in word length bits and SPT terms can reduce the number of adders required for the implementation of filter architecture.

3 Implementation of 2D FIR filter architectures

In this section, the 2D FIR filter circular symmetric architecture is implemented in hardware using continuous coefficients with MCM, multiplierless multiplication scheme using CSD. The filter coefficients obtained from the design of the circular symmetric 2D FIR filter using MATLAB for the given specifications are considered for the hardware implementation. The multiple constant multiplications are different concerning the type of architectures. The MCM operation is preferred for the transpose form type filter and Constant Array Vector Multiplication (CAVM) technique is used for the implementation of direct form filters. 2D FIR filters can be implemented in 4 different types of architectures are, (1) fully direct form,

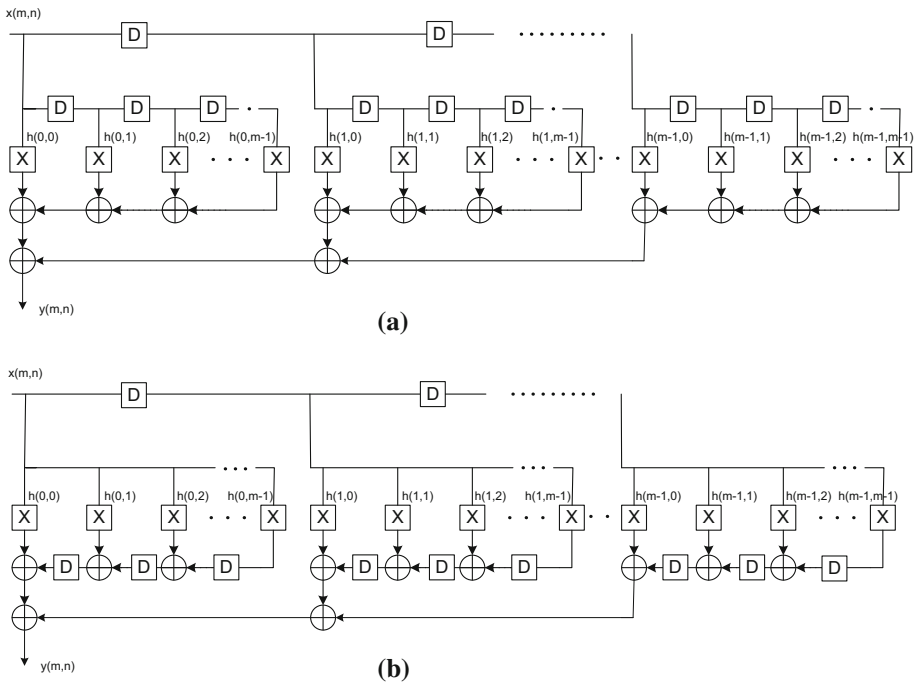


Fig. 3 General Architectures of 2D FIR filters. **a** Fully Direct form **b** Hybrid-II form

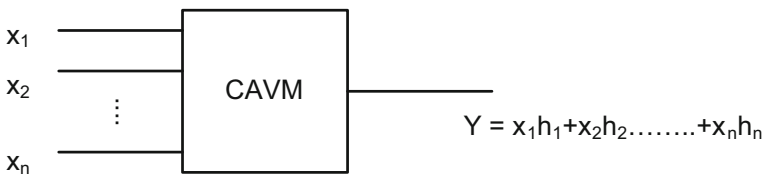


Fig. 4 Basic CAVM technique

(2) fully transpose form, (3) transpose-direct form (hybrid-I) and (4) direct-transpose form (hybrid-II) structures. In this work, fully direct form and hybrid-II structures are implemented with circular symmetry. The symmetrical filters itself reduces some hardware complexity. The general structure of fully direct form and hybrid-II type (direct-transposed type) 2D FIR filters without symmetry is shown in the Fig. 3a, b.

In CAVM, the current input and time-shifted inputs are considered as a vector. The input vector is multiplied with an array of constant coefficients as shown in Fig. 4. The symmetrical 2D FIR filter architectures in fully direct form and hybrid-II form are shown in Fig. 5a, b with CAVM and MCM multiplication techniques respectively.

In the hybrid-II type architecture, the current input sample is multiplied with all coefficients as same as MCM technique. Here, at the input level, the registers will give the delayed inputs for each row filter and internal row filter is implemented in transposed form. The overall filter is in direct form type hence, it is treated as hybrid-II (direct-transpose form) filter.

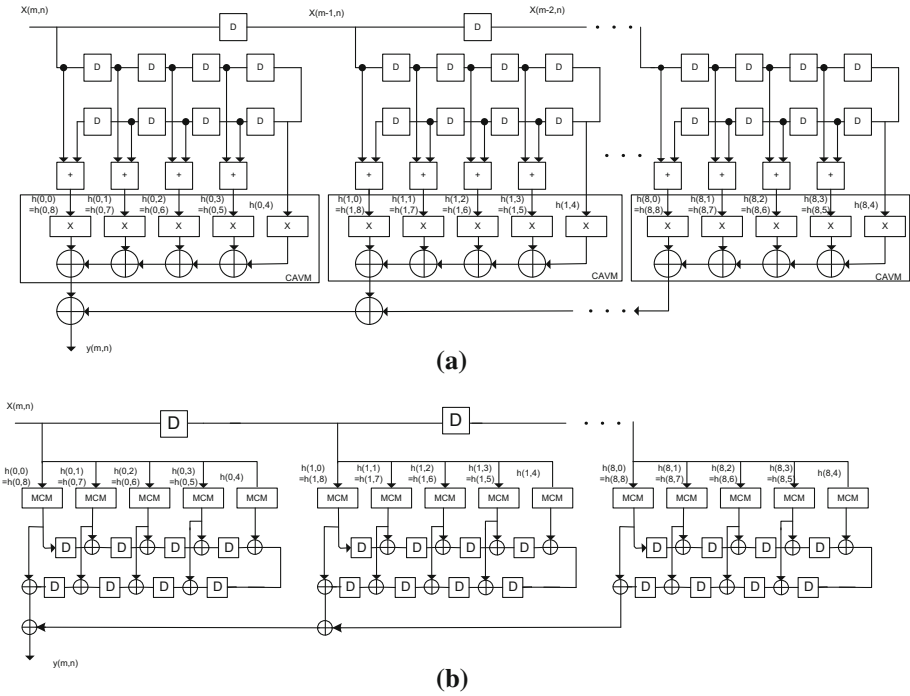


Fig. 5 **a** Fully direct form 2D FIR Filter architecture for continuous coefficients with symmetry using CAVM operation **b** Hybrid-II 2D FIR filter using MCM technique with symmetry of coefficients

3.1 Multiplierless 2D FIR filter architecture implementation using CSD

In multiplierless filter operation, the filter coefficients are denoted by an optimized binary encoding number format for pruning the number of adders/subtractors. The constant-coefficient multiplication scheme is optimized using the CSD representation of coefficients of the filter. The number of adders is reduced to less than the non-zero bits of the coefficient. This representation is used to reduce the area and power consumption of the filter by encoding the coefficients in the fewest number of non-zero elements. This representation is most preferable for high-level synthesis. A coefficient or any number is considered as $C = c_{w-1}, c_{w-2}, \dots, c_1, c_0$. Where each number $c_i (P - 1 \geq i \geq 0)$ is in the set of $\{-1, 0, 1\}$ is a ternary number system. CSD representation is a special case and unique number representation, which consist of no two consecutive bits in the number are non-zero. It is possible minimum non-zero number representation is called canonic. The CSD number representation contains about 33% of fewer non zero bits comparatively conventional 2^s complement number (Parhi 1999). The iterative algorithm represents the computation of CSD format for the p-bit number.

$$\begin{aligned}
 \bar{c}_{-1} &= 0 \\
 \alpha - 1 &= 0 \\
 \bar{c}_p &= \bar{c}_{p-1} \\
 &\text{for } (i = 0 \text{ to } p - 1) \\
 \{\beta_i &= \bar{c}_i \oplus \bar{c}_{i-1} // \oplus \text{denotes the XOR operation} \\
 \alpha_i &= \overline{\alpha_{i-1}} \beta_i \\
 c_i &= (1 - 2\bar{c}_{i+1})\alpha_i \}
 \end{aligned}$$

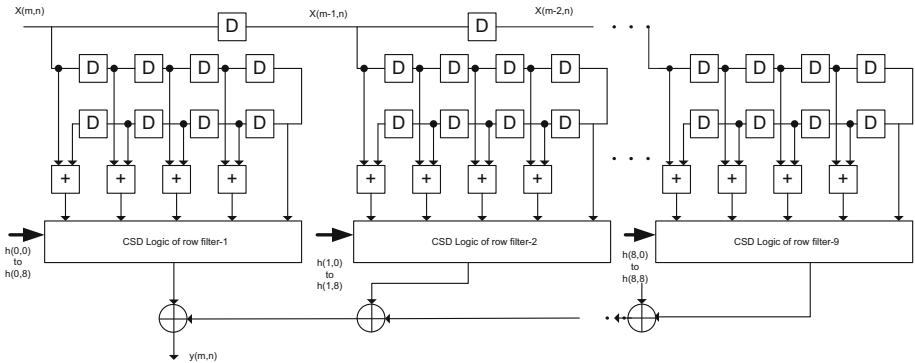


Fig. 6 The architecture of 2D FIR filter in the fully direct form using CSD coefficients

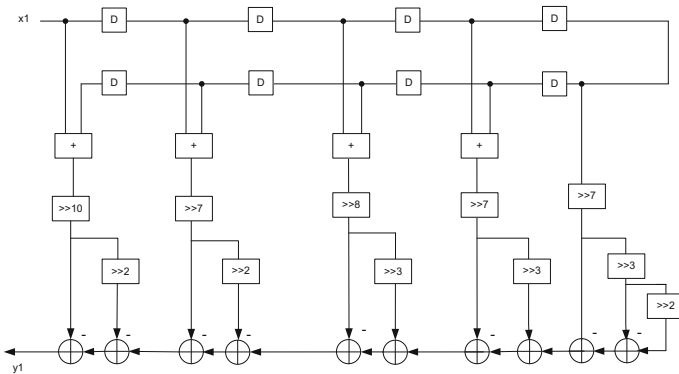


Fig. 7 CSD logic of row filter-1 for fully direct type 2D FIR filter

The constant multiplication is generally carried out by adding or subtracting the number of partial products corresponding to the non-zero elements of the constant multiplier. The CSD representation of the coefficient consists of least number of non-zero bits and hence the number of subtractors and adders to compute the multiplication of input and coefficients are decreased. A 12-bit CSD encoding process has been used for the 2D FIR filter with circular symmetry and CSD coefficients are implemented in fully direct type 2D FIR architecture as shown in Fig. 6. Each row of the two-dimensional coefficients matrix is considered as a sub-filter named as row filter. Each row filter is designed and implemented using CSD format and all the row filters are integrated as direct-form 2D FIR filter structure. The internal hardware structure using CSD logic for row filter-1 is shown in Fig. 7 and the corresponding equation is given in Eq. 14. The CSD format is used to represent the filter coefficients to avoid the multipliers and to reduce the number of adder/subtractors in the filter. Here, the multiplier is completely replaced with add and shift operations only. In this architecture, the row filter structure is implemented using adders, subtractors, and right shifters. According to CSD format, the shifting and adding operations are performed in the applied input signal.

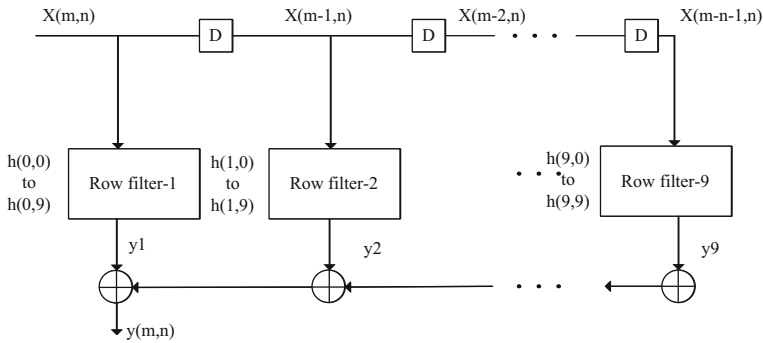


Fig. 8 The architecture of 2D FIR filter in hybrid-II form using CSD coefficients

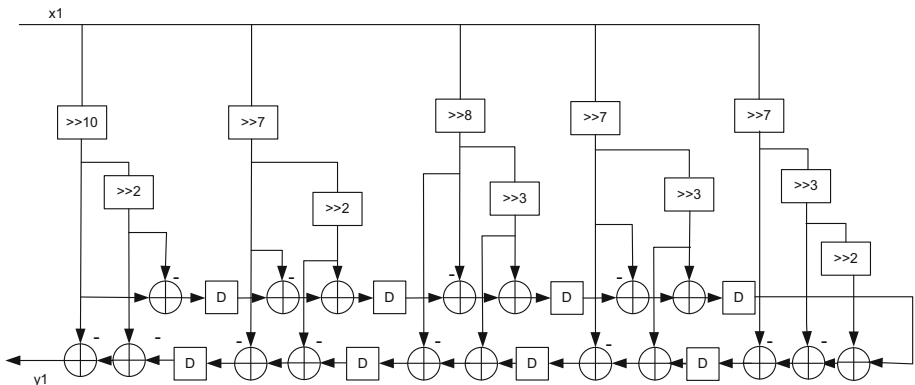


Fig. 9 CSD logic for row filter-1 for hybrid-II type filter

The remaining design equations for 9×9 2D FIR filter with symmetrical row filters are given by Eqs. 15–18.

$$\begin{aligned}
 y_1 = y_9 = & -[x + (x - 8)] \ggg 10 - [x + (x - 8)] \ggg 12 - [(x - 1) + (x - 7)] \ggg 7 \\
 & - [(x - 1) + (x - 7)] \ggg 9 - [(x - 2) + (x - 6)] \ggg 8 + [(x - 2) + (x - 6)] \ggg 11 \\
 & - [(x - 3) + (x - 5)] \ggg 7 + [(x - 3) + (x - 5)] \\
 & \ggg 10 - (x - 4) \ggg 7 - (x - 4) \ggg 10 + (x - 4) \ggg 12
 \end{aligned}
 \tag{14}$$

The hybrid-II filter is a combination of direct form and transposed form, which is shown in Fig. 8. Here the registers are placed on the input signal side for overall filter and, inside the row filter the registers are placed on the output side as transposed form. The Fig. 9 represents the internal structure of CSD logic for row filter-1 used in hybrid-II filter architecture.

The output of the row filter-2 and row filter-8 is same and given by Eq. 15.

$$\begin{aligned}
 y_2 = y_8 = & -[x + (x - 8)] \ggg 7 - [x + (x - 8)] \ggg 9 - [(x - 1) + (x - 7)] \ggg 8 \\
 & - [(x - 2) + (x - 6)] \ggg 10 - [(x - 2) + (x - 6)] \ggg 12 + [(x - 3) + (x - 5)] \ggg 10 \\
 & - [(x - 3) + (x - 5)] \ggg 12 + (x - 4) \ggg 7 - (x - 4) \ggg 9
 \end{aligned}
 \tag{15}$$

The output of the row filter-3 and row filter-7 are equal and given by Eq. 16.

$$\begin{aligned}
 y_3 = y_7 = & -[x + (x - 8)] \gg 8 + [x + (x - 8)] \gg 11 - [(x - 1) + (x - 7)] \gg 8 \\
 & - [(x - 1) + (x - 7)] \gg 10 - [(x - 1) + (x - 7)] \gg 12 + [(x - 2) + (x - 6)] \gg 6 \\
 & - [(x - 2) + (x - 6)] \gg 8 - [(x - 2) + (x - 6)] \gg 10 - [(x - 2) + (x - 6)] \gg 12 \\
 & + [(x - 3) + (x - 5)] \gg 5 + [(x - 3) + (x - 5)] \gg 9 - [(x - 3) + (x - 5)] \gg 11 \\
 & + (x - 4) \gg 5 + (x - 4) \gg 7 + (x - 4) \gg 9 + (x - 4) \gg 11 \tag{16}
 \end{aligned}$$

The output of the row filter-4 and row filter-6 are equal and given by Eq. 17.

$$\begin{aligned}
 y_4 = y_6 = & -[x + (x - 8)] \gg 7 + [x + (x - 8)] \gg 10 + [(x - 1) + (x - 7)] \gg 7 \\
 & + [(x - 1) + (x - 7)] \gg 9 - [(x - 1) + (x - 7)] \gg 12 + [(x - 2) + (x - 6)] \gg 5 \\
 & + [(x - 2) + (x - 6)] \gg 9 - [(x - 2) + (x - 6)] \gg 11 + [(x - 3) + (x - 5)] \gg 4 \\
 & + [(x - 3) + (x - 5)] \gg 6 + [(x - 3) + (x - 5)] \gg 8 + [(x - 3) + (x - 5)] \gg 10 \\
 & + [(x - 3) + (x - 5)] \gg 12 + (x - 4) \gg 3 - (x - 4) \gg 5 + (x - 4) \gg 9 \tag{17}
 \end{aligned}$$

The output of the row filter-5 is given by Eq. 18.

$$\begin{aligned}
 y_5 = & -[x + (x - 8)] \gg 7 - [x + (x - 8)] \gg 10 + [x + (x - 8)] \gg 12 \\
 & + [(x - 1) + (x - 7)] \gg 7 + [(x - 1) + (x - 7)] \gg 9 + [(x - 2) + (x - 6)] \gg 5 \\
 & + [(x - 2) + (x - 6)] \gg 7 + [(x - 2) + (x - 6)] \gg 9 + [(x - 2) + (x - 6)] \gg 11 \\
 & + [(x - 3) + (x - 5)] \gg 3 - [(x - 3) + (x - 5)] \gg 5 + [(x - 3) + (x - 5)] \gg 9 \\
 & + (x - 4) \gg 3 - (x - 4) \gg 7 + (x - 4) \gg 12 \tag{18}
 \end{aligned}$$

We can observe that, the row filter equations are symmetrical and the multiplication operation is carried out using only adders/subtractors and right shifts operations. Table 2 shows the row filter-1 coefficients in decimal and CSD number with total number of adders 14 and 18 for fully direct form and hybrid-II form filters respectively.

Table 3 presents the number of adders/subtractors required for the implementation of each row filter and the total number of the adders obtained as 151 in fully direct form filter. 66 adders are ignored by symmetric structure then adders are reduced to 85. Table 4 shows the total of 206 adders is required for the entire filter implementation using CSD in hybrid-II form architecture. Here, due to symmetrical, the 206 is reduced to 116, whereas 90 adders are due to the symmetrical operation. The 2D fully direct form filter has 26% of adder saving than the hybrid-II type filter.

3.2 The 2D FIR filter architecture using CSD with common subexpression elimination

The number of adders/subtractors required for each row filter implementation can be further reduced by common subexpression elimination (CSE) technique. The repeated sub-patterns of non-zero bits in one filter coefficient in CSD format can be used for the process of another coefficient. This process will decrease the number of adders required for filter operation (Hsiao et al. 2013). The CSE techniques are two types, Horizontal CSE (HCSE) and Vertical CSE (VCSE).

3.2.1 Horizontal CSE

The common subexpressions are pre-computed and used for the required coefficients. Here, the common non-zero element patterns are identified in the horizontal direction for the entire

Table 2 Comparison of adder complexity for Row filter-1

Row filter-1 coefficients	Decimal value of coefficients	CSD representation	SPT terms	Word length	(Fully direct) No. of adders	(Hybrid-II) no. of adders
$h(0, 0)$	- 0.0012	0.000000000 - 10 - 1	5	12	14	18
$h(0, 1)$	- 0.0098	0.000000 - 10 - 1000				
$h(0, 2)$	- 0.0034	0.0000000 - 100 + 10				
$h(0, 3)$	- 0.0068	0.000000 - 100 + 100				
$h(0, 4)$	- 0.0085	0.000000 - 100 - 10 + 1				
$h(0, 5)$	- 0.0068	0.000000 - 100 + 100				
$h(0, 6)$	- 0.0034	0.0000000 - 100 + 10				
$h(0, 7)$	- 0.0098	0.000000 - 10 - 1000				
$h(0, 8)$	- 0.0012	0.000000000 - 10 - 1				

Table 3 The number of adder/subtractors for all row filters in 2D FIR filter in the fully direct form

Row filter number	No. of adders/subtractors
Row filter-1	14
Row filter-2	12
Row filter-3	20
Row filter-4	20
Row filter-5	19
Row filter-6	20
Row filter-7	20
Row filter-8	12
Row filter-9	14
Total no. of adders	151

row filter as shown in Table 5. The HCSE patterns of row filter-1 and the corresponding internal structure of row filter-1 are shown in the Fig. 10. The Eqs. 19–23 represents the all row filters outputs in 2D FIR filter using HCSE in CSD format. The $h(0, 0)$ coefficient consists of pattern of binary bits (- 1, 0, - 1) and same pattern is repeated in coefficients $h(0, 1)$, $h(0, 7)$ and $h(0, 8)$ which are highlighted in Table 4. Similarly, the pattern (- 1, 0, 0, + 1) bits in $h(0, 2)$ also repeated in $h(0, 3)$, $h(0, 5)$ and $h(0, 6)$ coefficients.

The row filter-1 and row filter-9 are symmetrical concerning hardware as shown in the Eq. 19.

The common subexpressions from Table 5 are assumed as x_2 and x_3 are given by,

Table 4 Number of adder/subtractors for all row filters in 2D FIR filter in hybrid-II form

Row filter number	No. of adders/subtractors
Row filter-1	18
Row filter-2	17
Row filter-3	27
Row filter-4	28
Row filter-5	26
Row filter-6	28
Row filter-7	27
Row filter-8	17
Row filter-9	18
Total no. of adders	206

Table 5 Row filter-1 with 12-bit CSD coefficients using HCSE

Coefficients	CSD representation	1	2	3	4	5	6	7	8	9	10	11	12
$h(0, 0)$	0.00000000 - 10 - 1	0	0	0	0	0	0	0	0	0	-1	0	-1
$h(0, 1)$	0.000000 - 10 - 1000	0	0	0	0	0	0	-1	0	-1	0	0	0
$h(0, 2)$	0.0000000 - 100 + 10	0	0	0	0	0	0	0	-1	0	0	+1	0
$h(0, 3)$	0.000000 - 100 + 100	0	0	0	0	0	0	-1	0	0	+1	0	0
$h(0, 4)$	0.000000 - 100 - 10 + 1	0	0	0	0	0	0	-1	0	0	-1	0	+1
$h(0, 5)$	0.000000 - 100 + 100	0	0	0	0	0	0	-1	0	0	+1	0	0
$h(0, 6)$	0.0000000 - 100 + 10	0	0	0	0	0	0	0	-1	0	0	+1	0
$h(0, 7)$	0.000000 - 10 - 1000	0	0	0	0	0	0	-1	0	-1	0	0	0
$h(0, 8)$	0.00000000 - 10 - 1	0	0	0	0	0	0	0	0	0	-1	0	-1

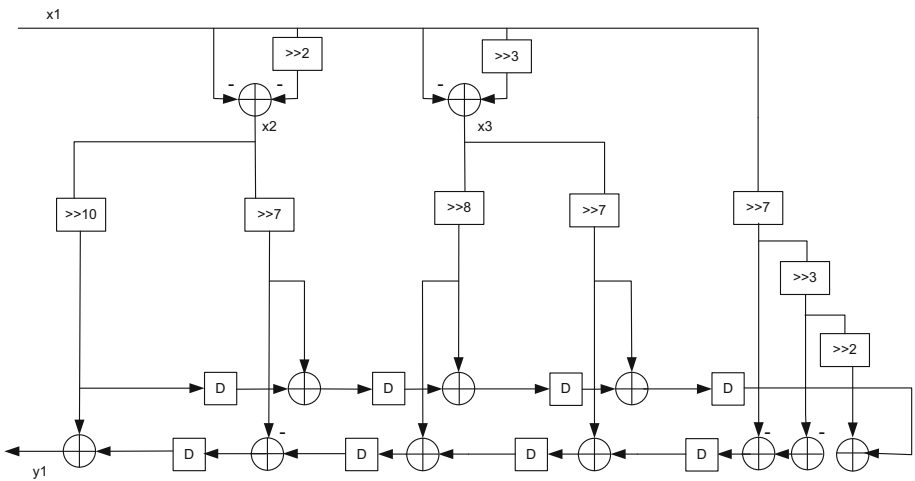


Fig. 10 Hardware structure of row filter-1 using HCSE

Assume $x_2 = -x_1 - x_1 \gg 2$ and $x_3 = -x_1 + x_1 \gg 3$.

$$y_1 = y_9 = [x_2 + (x_2 - 8)] \gg 10 + [(x_2 - 1) + (x_2 - 7)] \gg 7 + [(x_3 - 2) + (x_3 - 6)] \gg 8 + [(x_3 - 3) + (x_3 - 5)] \gg 7 - (x_1 - 4) \gg 7 - (x_1 - 4) \gg 10 + (x_1 - 4) \gg 12 \quad (19)$$

Assume $x_2 = -x_1 - x_1 \gg 2$ and $x_3 = x_1 - x_1 \gg 2$, then the output of the row filter-2 is same as row filter-8 is given by,

$$y_2 = y_8 = [x_2 + (x_2 - 8)] \gg 7 - [(x_1 - 1) + (x_1 - 7)] \gg 8 - [(x_1 - 2) + (x_1 - 6)] \gg 8 + [(x_2 - 2) + (x_2 - 6)] \gg 10 + [(x_3 - 3) + (x_3 - 5)] \gg 10 - (x_3 - 4) \gg 7 \quad (20)$$

Assume $x_2 = -x_1 - x_1 \gg 2$ and $x_3 = x_1 + x_1 \gg 2$, then the row filter-3 and row filter-7 output is same and is given by,

$$y_3 = y_7 = -[x_1 + (x_1 - 8)] \gg 8 + [x_1 + (x_1 - 8)] \gg 11 + [x_2 + (x_2 - 7)] \gg 8 + [(x_1 - 2) + (x_1 - 6)] \gg 6 + [(x_2 - 2) + (x_2 - 6)] \gg 8 + [(x_1 - 3) + (x_1 - 5)] \gg 5 + [(x_1 - 3) + (x_1 - 5)] \gg 9 - [(x_1 - 3) + (x_1 - 5)] \gg 11 + (x_3 - 4) \gg 5 + (x_3 - 4) \gg 9 \quad (21)$$

Assume $x_2 = -x_1 + x_1 \gg 3$ and $x_3 = x_1 - x_1 \gg 2$ then the row filter-4 output is same as row filter-6 is same is given by,

$$y_4 = y_6 = [x_2 + (x_2 - 8)] \gg 7 + [(x_1 - 1) + (x_1 - 7)] \gg 7 - [(x_2 - 1) + (x_2 - 7)] \gg 9 + [(x_1 - 2) + (x_1 - 6)] \gg 5 + [(x_3 - 2) + (x_3 - 6)] \gg 9 + [(x_1 - 3) + (x_1 - 5)] \gg 4 + [(x_3 - 3) + (x_3 - 5)] \gg 6 + [(x_1 - 3) + (x_1 - 5)] \gg 10 + [(x_1 - 3) + (x_1 - 5)] \gg 12 + (x_3 - 4) \gg 3 + (x_1 - 4) \gg 9 \quad (22)$$

Assume $x_2 = -x_1 + x_1 \gg 2$ and $x_3 = x_1 + x_1 \gg 2$ then the row filter-5 output is,

$$y_5 = -[x + (x - 8)] \gg 7 + [(x_2 + (x_2 - 8)] \gg 10 - [(x_2 - 1) + (x_2 - 7)] \gg 7 + [(x_3 - 2) + (x_3 - 6)] \gg 5 + [(x_3 - 2) + (x_3 - 6)] \gg 9 - [(x_2 - 3) + (x_2 - 5)] \gg 3 + [(x - 3) + (x - 5)] \gg 9 + (x - 4) \gg 3 - (x - 4) \gg 7 + (x - 4) \gg 12 \quad (23)$$

The coefficient implementation of row filter-1 in CSD required 17 adder/subtractors, whereas in CSD with HCSE required only 12 adders. HCSE has been reduced by 5 adders for single row filter. The total number of adders for the 2D FIR filter using HCSE in CSD format is 146 as shown in Table 6. Due to symmetry, 64 are adders are subtracted from the total number of adders, then the resultant adder number is 82 only. The original CSD architecture required a total of 116 adders/subtractors for hybrid-II architecture and whereas CSD with HCSE required only 82 adder/subtractors. Hence, 29% of adder/subtractors are saved by HCSE in CSD architecture.

3.2.2 Vertical CSE

VCSE also can be used for the further reduction of adders in coefficient implementation instead of horizontal CSE. It may not continue the linear phase filter symmetry. It is suitable for the hybrid-II filter structure. Sometimes, particularly in a few row filters, the number of adders may be maintained as same as HCSE or more than.

The row filter-4 is considered to understand the technique of VCSE in CSD as shown in Table 7. The vertical common patterns are highlighted and used to derive the design Eq. 24. The row filter-4 consumes 19 adders and whereas in CSD with HCSE, 21 adders are required

Table 6 Number of adders/subtractors for all row filters in 2D FIR architecture using CSD-HCSE

Row filter number	HCSE No. of adders/subtractors
Row filter-1	12
Row filter-2	12
Row filter-3	19
Row filter-4	21
Row filter-5	18
Row filter-6	21
Row filter-7	19
Row filter-8	12
Row filter-9	12
Total no. of adders	146

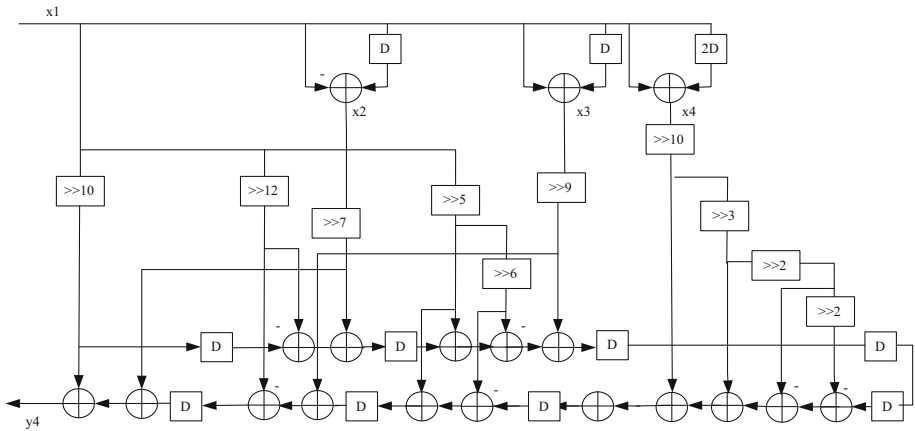


Fig. 11 Logic structure for row filter-4 using CSD with VCSE

to implementation of row filter-4. The hardware structure of row filter-4 using CSD-VCSE is shown in Fig. 11.

From the Table 7, the common sub expressions are assumed as follows:

$$x2 = -x1 + (x1 - 1),$$

$$x3 = x1 + (x1 - 1),$$

$$x4 = x1 + (x1 - 2)$$

Then the output equation of row filter-4 is,

$$y4 = [x1 + (x1 - 8)] \ggg 10 - [(x1 - 1) + (x1 - 7)] \ggg 12 + [(x1 - 2) + (x1 - 6)] \ggg 5 - [(x1 - 2) + (x1 - 6)] \ggg 11 + [x2 - (x2 - 7)] \ggg 7 + [(x3 - 1) + (x3 - 6)] \ggg 9 + (x4 - 3) \ggg 4 + (x4 - 3) \ggg 8 - (x4 - 3) \ggg 10 - (x4 - 3) \ggg 12 \tag{24}$$

All the 9 row filters implemented using VCSE in CSD technique. Table 8 represents the total number of adders for the implementation of 2D FIR filter using CSD with VCSE is 153 and symmetry reduce the 67 adders. Therefore the net number of adders is 86. Where

Table 7 Row filter-4 with 12-bit CSD coefficients using VCSE

Coefficients	CSD representation	1	2	3	4	5	6	7	8	9	10	11	12
$h(0, 0)$	0.000000 - 100 + 100	0	0	0	0	0	0	-1	0	0	+1	0	0
$h(0, 1)$	0.000000 + 10 + 100 - 1	0	0	0	0	0	0	+1	0	+1	0	0	-1
$h(0, 2)$	0.0000 + 1000 + 10 - 10	0	0	0	0	+1	0	0	0	+1	0	-1	0
$h(0, 3)$	0.000 + 10 + 10 - 10 - 10 - 1	0	0	0	+1	0	+1	0	-1	0	-1	0	-1
$h(0, 4)$	0.00 + 10 - 1000 + 1000	0	0	+1	0	-1	0	0	0	+1	0	0	0
$h(0, 5)$	0.000 + 10 + 10 - 10 - 10 - 1	0	0	0	+1	0	+1	0	-1	0	-1	0	-1
$h(0, 6)$	0.0000 + 1000 + 10 - 10	0	0	0	0	+1	0	0	0	+1	0	-1	0
$h(0, 7)$	0.000000 + 10 + 100 - 1	0	0	0	0	0	0	+1	0	+1	0	0	-1
$h(0, 8)$	0.000000 - 100 + 100	0	0	0	0	0	0	-1	0	0	+1	0	0

Table 8 Number of adders/subtractors for all row filters in 2D FIR architecture in VCSE

Row filter number	VCSE no. of adders/subtractors
Row filter-1	16
Row filter-2	13
Row filter-3	20
Row filter-4	18
Row filter-5	19
Row filter-6	18
Row filter-7	20
Row filter-8	13
Row filter-9	16
Total no. of adders	153

HCSE in CSD space requires 82 only and CSD requires 116 respectively. VCSE reduce the 25% adders/subtractors comparatively CSD architecture. Some significant saving in adders achieved using HCSE as well as VCSE in CSD format of filter architectures.

4 Experimental results

The circular symmetric 2D FIR filter is designed using kth-McClellan transform with T2 and P2 transformations in MATLAB. The fully direct form and hybrid-II form architectures are implemented using generic multipliers for the continuous coefficients with CAVM and MCM techniques respectively in Hardware Description Language (HDL). The continuous coefficients are converted into CSD number format to implement multiplierless architectures. The optimization is introduced in CSD using CSE algorithms to reduce the complexity in hardware.

The reconfigurable designs are implemented using Xilinx ISE tool with Verilog HDL and the custom designs are implemented in TSMC 45 nm CMOS generic library using RTL encounter from CADENCE tools. The fully direct and hybrid-II filter architectures are proposed to meet the desired specifications in multiplierless multiplication technique.

For reconfigurable applications, Vertex-6 FPGA is considered as target device and both the architectures of 2D FIR filters are implemented. For comparison purpose, architectures are also implemented for continuous coefficients using generic multipliers with MCM and CAVM schemes. The hardware complexity comparison concerning target device is FPGA is presented in Table 9. The continuous coefficients design requires DSP48 slices for the computation of the multiplier. For the multiplierless design, no DSP48 slices were used and these resources may be used for the other computations in the application. The multiplierless design is applied for the two architectures fully direct form and hybrid-II form. The fully direct filter requires less number of slices and (Look-Up-Table) LUTs comparatively hybrid-II filter. Next, the CSD and CSD with CSE decreases the number of adders/subtractors and registers also. The power dissipation and delay of both architectures is directly decreased. The different input bit widths are considered for the filter with multipliers and multiplierless 2D filter architectures. The input bit width is reduced from 16 to 8 for the continuous coefficient 2D filter, then the output bit width also reduced. This can prune the complexity of the filter in terms of area, power, and delay. This is because the input bit width affects the size of the adder/subtractors, multipliers, and registers.

Table 9 Comparison of complexity and parameters of 2D FIR filter in different architectures with target device of FPGA

Type of coefficients	Type of architecture	8-bit filter input				16-bit filter input			
		LUTs	FFs	Slice Registers	DSP48Es	LUTs	FFs	Slice Registers	DSP48Es
Continuous coefficients	Fully Direct	2048	387	416	90	2549	481	562	90
	Hybrid-II	2056	598	578	90	2688	715	688	90
CSD	Fully Direct	624	325	398	0	2549	987	1002	0
	Hybrid-II	651	373	416	0	2691	1010	1097	0
CSD with HCSE	Fully Direct	560	321	335	0	2002	866	897	0
	Hybrid-II	563	365	379	0	2013	895	989	0
CSD with VCSE	Fully Direct	588	332	397	0	2022	864	872	0
	Hybrid-II	681	381	412	0	2076	912	897	0

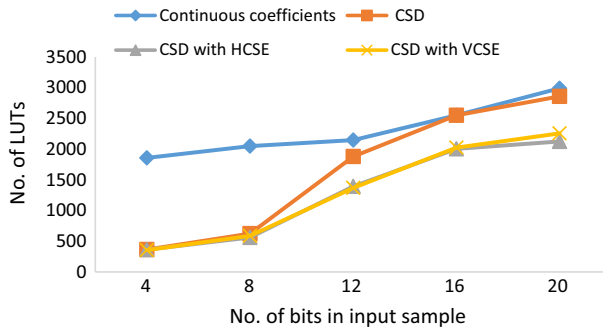


Fig. 12 Comparison of number of LUTs required for different coefficient representations

Figure 12 describes the comparison of number of LUTs required for the implementation of fully direct architecture for different input widths, such as 4, 8, 12, 16 and 20 bits. The number of LUTs required for CSD with HCSE almost same as CSD with VCSE. But less number of LUTs when compared with conventional CSD and continuous coefficients architectures.

4.1 Custom design results

The (Application Specific Integrated Circuit) ASIC or Custom design of the multiplierless filters both fully direct and hybrid-II form 2D filter architectures leads to savings in the area and power to the continuous coefficient 2D FIR filter. The complexity of the fully direct form filter is less than the hybrid-II filter. The reason for this, the size of the registers in the hybrid form is increasing after multiplication process, whereas in the direct form filter, the bit width and the corresponding number of registers are same at the input and output sides. For the implementation of each row filter of direct form required less number of adders than the transposed form. The delay of the continuous coefficient implementation with generic multipliers is less than the shift-add designs due to more operations are required and connected in series in the multiplierless design. To reduce this delay to some extent Carry Save adders are used for filter structural adders.

Table 10 presents the four different coefficient types and two forms of architectures for 2D filters comparison in terms of area, power and delay with different input bit widths. The both proposed 2D circular symmetric FIR filters in CSD with HCSE has given best results for desired filter specifications. The multiplierless design of fully direct form 2D FIR filter with CSD-HCSE given 90% power reduction when compared with continuous filter coefficients with multipliers. The delay is reduced by 8% using CSD, CSD with HCSE and CSD with VCSE architectures when compared to continuous coefficient filter architecture. More than 80% area saving is obtained by multiplierless designs using CSD, CSD-HCSE, and CSD-VCSE than the conventional continuous coefficient filter.

The Figs. 13 and 14 represents the line graph comparison of power consumption and area of CSD filter, conventional continuous coefficients, CSD-HCSE and CSD-VCSE with respect to different number of bits per input sample respectively on ASIC platform. From the observations, CSD architectures power consumption and area are very much less as compared with continuous coefficients structure.

In Table 11, the proposed circular symmetric 2D FIR filter architectures are compared with the existing 2D FIR filter architectures with the nearest length of the filter in terms of VLSI

Table 10 Comparison of complexity and parameters of 2D FIR filter in different architectures in Custom design or ASIC platform

Type of coefficients	Type of architecture	8-bit filter input				16-bit filter input			
		Cells	Area (μm^2)	Power (mW)	Delay (ns)	Cells	Area (μm^2)	Power (mW)	Delay (ns)
Continuous Coefficients	Fully Direct	7899	89,010	34.8	905	16,980	18,9543	51.002	1800
	Hybrid-II	7299	90,134	35.60	905	16,188	188,319	50.84	1809
CSD	Fully Direct	872	3109	2.1803	628	5347	16,239	5.1358	1656
	Hybrid-II	951	3305	2.3041	611	5920	18,049	5.3304	1523
CSD with HCSE	Fully Direct	824	2429	2.309	623	5009	16,105	5.1204	1640
	Hybrid-II	876	2921	2.3234	598	5437	17,809	5.2432	1500
CSD with VCSE	Fully Direct	799	2571	2.7898	635	5231	16,111	5.7538	1650
	Hybrid-II	822	2989	2.9001	605	5333	17,635	5.8390	1512

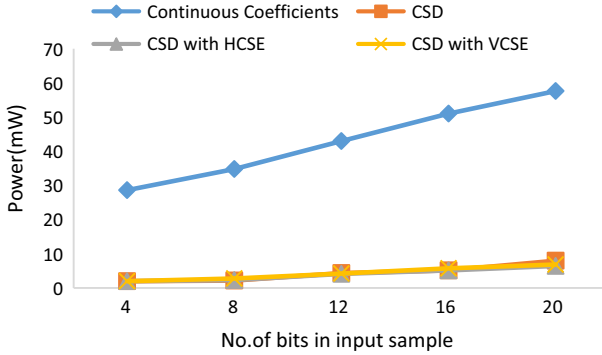


Fig. 13 Comparison of power consumption of different coefficient representations

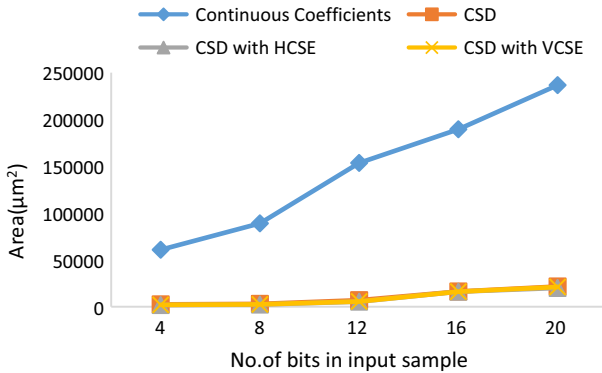


Fig. 14 Comparison of area occupancy of different coefficient representations of 2D FIR filters

Table 11 Comparison of synthesis results of proposed 2D FIR filters with state-of-art works

Architectures	N (Order of the filter)	Area (μm^2)	Power (mW)	Delay (ns)	ADP (μm^2 ms)
Kumar et al. (2018)	8	651,615	20.1069	6.53	0.531880
Mohanty et al. (2013)	8	1,720,962	50.0106	11.79	25.375558
Khoo et al. (2010)	8	356,293	9.3807	13.1	4.636084
Chen et al. (2010)	9	22,359	9.356	19.23	0.429963
Proposed 1 (Fully Direct)	9	17,199	5.1204	16.52	0.284127
Proposed 2 (Hybrid-II)	9	17,809	5.2432	16.56	0.294917

N is order of the filter, ADP= Area Delay Product

parameters. Total 75% and 85% of power saving is obtained by proposed filter architectures when compared with 2D FIR filter architecture proposed in Kumar et al. (2018) and Mohanty et al. (2013) respectively. More than 45% of power saving is obtained using the proposed-1 2D FIR filter than Khoo et al. (2010) and Chen et al. (2010) for fixed desired coefficients. This power saving achieved by replacing the power hunger multiplier blocks with shift-add technique using CSD representation of coefficients in 2D filters.

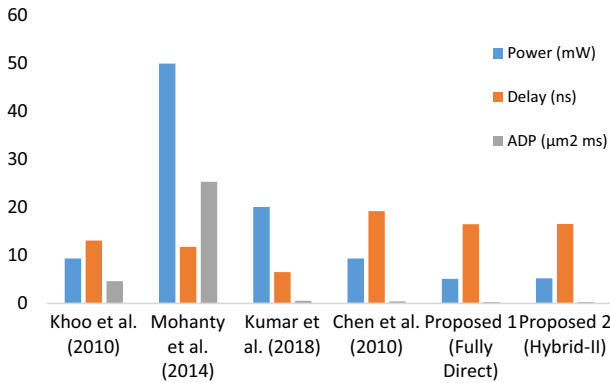


Fig. 15 Comparison of proposed architectures with existing works in terms of delay, power and ADP for N=8

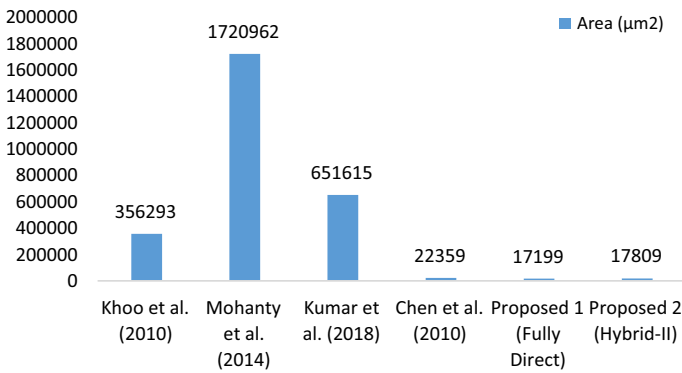


Fig. 16 Comparison of proposed architecture area with existing works for N=8

Drastic reduction in area is achieved by proposed filters when comparing with 2D FIR filter architectures of Kumar et al. (2018), Mohanty et al. (2013) and Khoo et al. (2010). The 47% and 39% of ADP is reduced when compared with ADP results of Kumar et al. (2018) and Chen et al. (2010) respectively.

The ADP values of Mohanty et al. (2013) and Khoo et al. (2010) are huge when compared to proposed architectures.

The two proposed 8th order filter architectures are compared with four different state-of-art works in terms of power, delay and Area Delay Product (ADP) values using bar graphs in Fig. 15. It may be noted that the power and ADP of proposed architectures are very much less than when compared with existing filter architectures. Figure 16 depicts the area comparison of existing and proposed filter structures.

The proposed CSD-HCSE and CSD-VCSE filter architectures are also implemented for N=16 and the detailed comparison results of filter architectures are presented in Table 12. The Fig. 17 depicts the comparison of power, delay and ADP of proposed filters with existing filters for N=16. From Table 12, it can be observed that Fully direct architecture with N=16 are more efficient in terms of power and ADP by 89% and 52% respectively, when compared with DA based block structure Kumar et al.(2018). The huge power reduction and ADP reduction is achieved in proposed methods when compared with Mohanty et al. (2013), Meher and Park (2011) and Guo and DeBrunner (2011). This is due to the optimization using CSE in

Table 12 Comparison of synthesis results of existing and proposed 2D FIR filters for N=16

Architectures	N (Order of the filter)	Area (μm^2)	Power (mW)	Delay (ns)	ADP (μm^2 ms)
Kumar et al. (2018)	16	4,936,081	102.3432	6.91	2.131770
Mohanty et al. (2013)	16	12,661,783	181.165	13.33	10.550431
Meher and Park (2011)	16	59,244	12.08	24.38	1.444368
Guo and DeBrunner (2011)	16	40,187	21.16	12.92	0.519216
Khoo et al. (2010)	16	1,154,123	26.9941	14.65	16.907903
Proposed 1 (Fully Direct)	16	54,321	10.2354	18.98	1.031012
Proposed 2 (Hybrid-II)	16	56,243	10.5689	19.06	1.071991

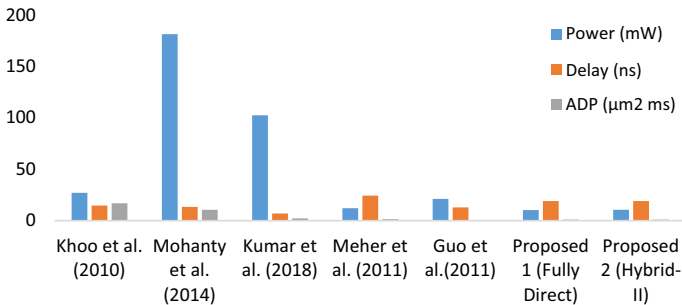


Fig. 17 Comparison of ADP, delay and power for filter length N=16

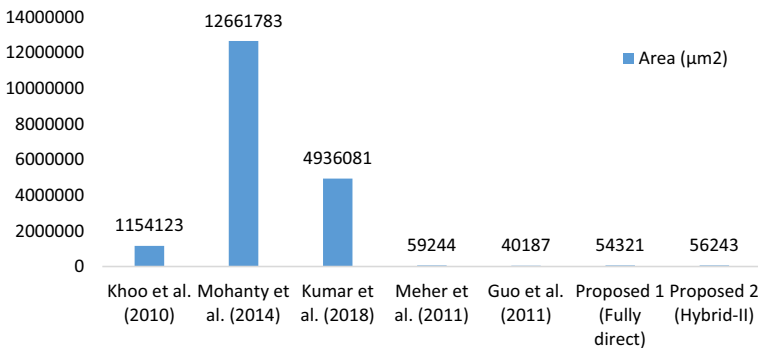


Fig. 18 Comparison of area for proposed architecture with existing works (N=16)

CSD technique. It may be observed that from Fig. 18 the significant area saving is obtained than other state-of-art architectures.

Figure 19 shows the power comparison of proposed architectures with architectures available in the literature for the filter order of N = 8 and N = 16. It is observed that the power is proportionally increasing with respect to order of the filter in existing architectures. But in the proposed filter architectures less power variations are observed with increase in order of

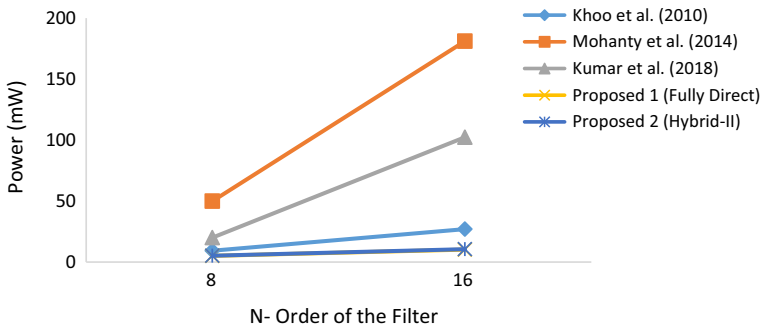


Fig. 19 Comparison of power consumption for various filter architectures for $N = 8$ and $N = 6$

the filter. The propose filter 1(Fully Direct form) and proposed 2 filter (Hybrid-II) consumes almost same power.

5 Conclusion

In this paper, the prominent architectures are designed and implemented using multiplierless constant multiplications and described in fully direct form and hybrid-II form architectures of 2D FIR filter. The filter coefficients are generated for the desired specifications to achieve circular symmetry using kth-Park's McClellan transformation, T2 and P2 transformation techniques. The continuous coefficients are optimized using a CSD number format to reduce the number of adder/subtractors. Further, the optimization of filter coefficients is carried out by CSE algorithms. Horizontal and Vertical CSE techniques have been used to reduce the hardware complexity of CSD. A low complexity circular symmetric 2D FIR filter is proposed, which has been designed in MATLAB and implemented in TSMC 45 nm CMOS technology using the generic library. High-level synthesis is carried out for the continuous filter with generic multipliers and multiplierless designs with CSD, CSD-HCSE, and CSD-VCSE.

For area-efficient applications, the fully direct form is the best architecture to implement symmetric 2D FIR filters in custom designs and FPGA designs. For high-speed applications, the hybrid-II form is the best architecture on Custom designs and reconfigurable design platform. For low power applications, the algorithms to optimize hardware complexity is better to implement the filter in a fully direct form in ASIC platform. The experimental results indicate that high-level synthesis algorithms have a significant impact on the multiplierless design of 2D FIR filters in terms of complexity, power, and performance using both architectures. The complexity comparison and analysis is carried out for two different filter orders such as $N=8$ and $N=16$. The limitation of the filter design is fixed coefficients are considered for certain specifications only.

Compliance with ethical standards

Conflict of interest The authors declare that they have no conflict of interest.

References

- Aksoy, L., Flores, P., & Monteiro, J. (2014). A tutorial on multiplierless design of FIR filters: Algorithms and architectures. *Circuits, Systems, and Signal Processing*, 33(6), 1689–1719.
- Baboji, K., & Sridevi, S. (2019). Optimal design of multiplier-less non-uniform channel filters with successive approximation of vectors. *Circuits, Systems, and Signal Processing*, 1–24.
- Bindima, T., & Elias, E. (2016). Design of efficient circularly symmetric two-dimensional variable digital FIR filters. *Journal of Advanced Research*, 7(3), 336–347.
- Bindima, T., & Elias, E. (2017). Design and implementation of low complexity 2-D variable digital FIR filters using single-parameter-tunable 2-D farrow structure. *IEEE Transactions on Circuits and Systems I: Regular Papers*, 65(2), 618–627.
- Bindima, T., & Elias, E. (2019). Low-complexity 2-D digital FIR filters using polyphase decomposition and farrow structure. *IEEE Transactions on Circuits and Systems I: Regular Papers*, 66(6), 2298–2308.
- Bindima, T., Manuel, M., & Elias, E. (2016). An efficient transformation for two dimensional circularly symmetric wideband FIR filters. *2016 IEEE Region 10 Conference (TENCON)*. IEEE.
- Chandra, A., & Chattopadhyay, S. (2016). A new strategy of image denoising using multiplier-less FIR filter designed with the aid of the differential evolution algorithm. *Multimedia Tools and Applications*, 75(2), 1079–1098.
- Chen, P. Y., Van, L. D., Khoo, I. H., Reddy, H. C., & Lin, C. T. (2010). Power-efficient and cost-effective 2-D symmetry filter architectures. *IEEE Transactions on Circuits and Systems I: Regular Papers*, 58(1), 112–125.
- Chen, P. Y., Van, L. D., Reddy, H. C., & Khoo, I. H. (2013). Area-efficient 2-D digital filter architectures possessing diagonal and four-fold rotational symmetries. In: *2013 9th International Conference on Information, Communications & Signal Processing (ICISAP)* (pp. 1–5).
- Das, P., Naskar, S. K., & Narayan Patra, S. (2019). Fast converging cuckoo search algorithm to design symmetric FIR filters. *International Journal of Computers and Applications*, 1–19.
- Dwivedi, A. K., Ghosh, S., & Londhe, N. D. (2016). Low power 2D finite impulse response filter design using modified artificial bee colony algorithm with experimental validation using field-programmable gate array. *IET Science, Measurement and Technology*, 10(6), 671–678.
- Guo, R., & DeBrunner, L. S. (2011). Two high-performance adaptive filter implementation schemes using distributed arithmetic. *IEEE Transactions on Circuits and Systems II: Express Briefs*, 58(9), 600–604.
- Hsiao, S.-F., Jian, J.-H. Z., & Chen, M.-C. (2013). Low-cost FIR filter designs based on faithfully rounded truncated multiple constant multiplication/accumulation. *IEEE Transactions on Circuits and Systems II: Express Briefs*, 60(5), 287–291.
- Khoo, I. H., Reddy, H. C., Van, L. D., & Lin, C. T. (2010). Generalized formulation of 2-D filter structures without global broadcast for VLSI implementation. In: *2010 53rd IEEE international Midwest symposium on circuits and systems* (pp. 426–429). IEEE.
- Kumar, P., Shrivastava, P. C., Tiwari, M., & Dhawan, A. (2018). ASIC Implementation of area-efficient, high-throughput 2-D IIR filter using distributed arithmetic. *Circuits, Systems, and Signal Processing*, 37(7), 2934–2957.
- Kumar, P., Shrivastava, P. C., Tiwari, M., & Mishra, G. R. (2019). High-throughput, area-efficient architecture of 2-D block FIR filter using distributed arithmetic algorithm. *Circuits, Systems, and Signal Processing*, 38(3), 1099–1113.
- Liu, J.-C., & Tai, Y.-L. (2010). Design of 2-D wideband circularly symmetric FIR filters by multiplierless high-order transformation. *IEEE Transactions on Circuits and Systems I: Regular Papers*, 58(4), 746–754.
- Meher, P. K., & Park, S. Y. (2011). High-throughput pipelined realization of adaptive FIR filter based on distributed arithmetic. *VLSI Symp. Tech. Dig.*, 428–433.
- Mohanty, B. K., Meher, P. K., Al-Maadeed, S., & Amira, A. (2013). Memory footprint reduction for power-efficient realization of 2-D finite impulse response filters. *IEEE Transactions on Circuits and Systems I: Regular Papers*, 61(1), 120–133.
- Odugu, V. K., Venkata Narasimhulu, C., & Prasad, K. S. (2019). Implementation of low power and memory efficient 2D FIR filter architecture. *International Journal of Recent Technology and Engineering*, 8(1), 927–935.
- Parhi, K. K. (1999). *VLSI digital signal processing systems*. New York, USA: Wiley.
- Shyu, J.-J., Pei, S.-C., & Huang, Y.-D. (2008). Design of variable two-dimensional FIR digital filters by McClellan transformation. *IEEE Transactions on Circuits and Systems I: Regular Papers*, 56(3), 574–582.



Mr. Venkata Krishna Odugu received B.Tech. degree in Electronics and Communication Engineering from Acharya Nagarjuna University, 2004 and Master of Technology with specialization VLSI System Design from JNTU Hyderabad in 2009 and pursuing Ph.D. from JNTU Kakinada in the area of VLSI Signal Processing. Interested areas are VLSI Design and VLSI Signal Processing etc.



Dr. C. Venkata Narasimhulu received B.Tech. degree in Electronics and Communication Engineering from S V University, Tirupathi in 1995 and Master of Technology in Instrumentation and Control Systems from REC, Calicut in 2000 and Ph.D. from JNTU, Kakinada in 2013 in the area of signal Processing. He has published more than 25 technical papers in national and international Journals and Conferences. His interested areas are Signal Processing, Image processing and medical image processing etc.



Dr. K. Satya Prasad received B.Tech. degree in Electronics and Communication Engineering from JNTU college of Engineering, Anantapur, in 1977 and M.E. degree in Communication Systems from Guindy College of Engineering, Madras University, in 1979 and Ph.D. from Indian Institute of Technology, Madras in 1989. He has published more than 139 technical papers in different National and International conferences and Journals and Authored one Text book. His areas of Research include Communications Signal Processing, Image Processing, Speech Processing, Neural Networks and Ad-hoc wireless networks etc.

Denoising Images by Dual–Tree Complex Wavelet Transform Combined With Meta Heuristic Optimization Algorithms

P. Venkata Lavanya, C. Venkata Narasimhulu, K. Satya Prasad

Abstract: Denoising is a prime objective technique for processing images. Image denoising techniques removes the noises present in an image without interrupting its features and contents. The image gets interrupted by channel or processing noise depending on the applications. Thus, the contaminated noises produce degradable image qualities with respect to subjective and objective approach. To overcome this, image denoising approaches were suggested. In the present research, Dual–Tree Complex Wavelet transform (DTCWT) is utilized to achieve image denoising since they perform multi resolution decomposition by two DWT trees. Soft and hard thresholding methods are used to threshold wavelet coefficients. The present research proposes a novel technique to denoise images which gives image information clearly by thresholding and optimization technique. The optimization is carried through different Meta-heuristic optimization Algorithms Genetic Algorithm (GA) and Grey-wolf optimization (GWO) algorithm. Optimization of threshold value is performed after Bayesian method and the observed output produces better results when compared to other techniques involving Visu shrink, Sure shrink and Bayes shrink based on peak signal to noise ratio (PSNR) and visual qualities.

Keywords: Image denoising approach, Dual-Tree Complex wavelet transform, Genetic algorithm, Bayesian shrinkages, Grey-wolf optimization algorithm, PSNR, MSE.

I. INTRODUCTION

Noises gets interrupted with images while transmitting and receiving images from the storage medium. The present trends in processing images leads to the need of 2 principles given as: modification of pictorial representation for easily understandable to humans; and efficient image processing to store, transmit and represent image processing[1]. The transformation method is used in different applications because it possesses fine resolution details to improve the efficiency. This process mainly aims at transforming an object from a suitable domain to other for the purpose of providing implicit information for image recognition. Additive white Gaussian noises easily corrupt the images as it comprises environmental ambient noises and transmission

noises while passing through the equipment. Hence it is necessary to suppress the noises from images to add further effectiveness in diagnosing medical images. Consider $g(t)$ and $h(t)$ as the input image and white Gaussian noises present in the images respectively. The output noisy image $f(t)$ with zero mean is dictated as presented in (1):

$$f(t)=g(t)+ h(t) \quad (1)$$

Where σ_n represents the noise variance and $h(t)$ follows normal distribution belonging to $N(0,1)$ and is said to be distributed independently and identically known as (i.i.d.). A novel method is presented in this research to remove noises through DTCWT.

The discrete wavelet transforms (DWT) plays significant role in solving limitations that occurs while processing signals [2]. Wavelet denoising methods does not limits its advantage within noise removal but also involved in conserving signal characteristic irrespective of its frequency contents. This type of denoising technique seems to be efficient in removing noises from natural images as it possesses improved tendency in capturing signal energies at fewer transform value. However, in many applications, it reaches its limitations, such as singular oscillations of the coefficients, limited directional selectivity factor particularly at high dimensions, aliasing effect and subsequent shift variance.

In order to overcome the said disadvantages[3], DTCWT is used. The dual tree approach uses 2 real wavelet filter to acquire the real as well as imaginary part of respective transform and the combined filters are referred as an analytic filter. The sub-band signal enabled by the upper (Tree A) and lower (Tree B) DWT is dictated as the real and imaginary transform respectively. A proper selection of threshold leads to higher denoising performance [4]. Denoising technique normally uses two thresholding technique [5,6] named as the soft and hard thresholding. Although, various researchers indicates the utilization of this denoising technique, some other different shrinkage methods also available for more efficient denoising. Thresholding of the wavelet coefficients is performed by various techniques like Visu shrink, Sure shrink and Bayes shrink. The observed output indicate that the Bayes shrink produces improved output than that of Visushrink and Sure shrink with respect to mean squared error. Maximum PSNR can be obtained by optimizing threshold value. Hence in the presented research, Meta-heuristic optimization techniques: Genetic Algorithm and Grey Wolf Optimization algorithm is used as an extension of Bayesian threshold to determine accurate threshold values.

Revised Manuscript Received on February 06, 2020.

* Correspondence Author

P. Venkata Lavanya*, Research Scholar, Department of ECE Jawaharlal Nehru Technological University Kakinada, Kakinada, Andhra Pradesh, India. Email: pvlavanya999@gmail.com

C. Venkata Narasimhulu, Department of ECE, Geethanjali College of Engineering and Technology, Hyderabad, Telangana, India. Email: cvnarasimhulu@gmail.com

K. Satya Prasad, Vignam's Foundation for Science, Technology and Research, Guntur, Andhra Pradesh, India. Email: prasad_kodati@yahoo.co.in

Experimental output indicates better performance while removing noises based on visual quality, PSNR and MSE.

II. DUAL TREE COMPLEX WAVELET TRANSFORM

The compact energy enabled by wavelet transform serves great enhancement in denoising images. Energy compactness signifies that the larger energy portions are presented in a limited amount of larger wavelet coefficients and smaller energy portions are distributed in larger smaller wavelet coefficients. Wavelet coefficients represents the detailed information and higher frequency noises. Achievement of image denoising with preservation of final structural images is done by thresholding wavelet coefficients [7]. The properties involved in denoising images using wavelet transform include sparseness, clustering, and correlation between neighboring wavelet coefficients.

The two-dimensional (2D) wavelet transform predicts to be an extended version of one dimensional (1D) wavelet transform. For achieving this, initially one-dimensional transform is applied along every rows and columns at every structural decomposition level. This generates 4 different coefficient sets known as: LL as the average, LH, HL and HH indicates the detailed data in respective information in horizontal, vertical and diagonal directions. Additional denoising technique that produces improved denoising results involves translation invariant (TIWT), complex wavelet transform etc. In TIWT, the original and the shifted coefficients are filtered through multi resolution analysis in every decomposition level. Such transform varies with time hence known as shift invariant (time invariant). It also has the ability to produce wavelet coefficients with varied properties enabling from similar sources which further leads to improved performance. Recent developments lead to the introduction of CWT and the limitation existing in traditional methods is overcome in CWT.

- *Oscillations* enabled by every pixel value while achieving zero crossing.
- *Shift variance*, the effective output result is dominated with respect to smaller input variations
- *Aliasing*, exists because of the sampling technique adopted at the time of filtering.
- *Lack of directional selectivity*, involves the signification changes in direction eg. The variation in +15 and -15 oriented degrees cannot be explained.

The 2D DT-CWT possesses the capacity to select discriminate features that belongs to different orientations. The critically decimated 2D DWT selects three sub-bands which conveys the information related to the features of an image with an orientation angle of 90° , $\pm 45^\circ$, and 0° respectively whereas in case of 2D DT-CWT, six directional sub bands are produced for revealing the detailed images with orientation angle of $\pm 15^\circ$, $\pm 45^\circ$ and $\pm 75^\circ$ directions including 4:1 redundancy. 2-D DTCWT is implemented in 2 steps and is described as follows. First, decomposition of input images into different 2D DWT branches (branch *a* and *b*) at desired levels takes place in which the filters are designed mainly to satisfy the needed requirements of Hilbert pair transform. Further the decomposed branches generate 6 high-pass sub bands (HL_a, LH_a, HH_a, HL_b, LH_b and HH_b) and 2 low-pass sub bands respectively [8]. Next, linear combination of correspondent two sub-bands having similar pass-bands takes place through

averaging or differentiation process. Thus, the obtained sub-bands at every level of 2D DT-CWT is given below

$$(LH_a + LH_b)/\sqrt{2}, (LH_a - LH_b)/\sqrt{2}, (HL_a + HL_b)/\sqrt{2}, (HL_a - HL_b)/\sqrt{2}, (HH_a + HH_b)/\sqrt{2}, (HH_a - HH_b)/\sqrt{2}$$

These 6 wavelet sub bands with different orientations possess orthonormal sum/difference operation meaning that the reconstruction wavelet transform is accurate. The basis function of both the real and imaginary part is similar. Use of identical filters at upper and lower trees degrades the performance hence the sub bands belonging to upper tree is designated as real part of CWT while the other sub band is considered as the imaginary part of lower CWT tree.

III. WAVELET BASED DENOISING

Denoising wavelet coefficients eliminates the noises from the images. In addition to this, it preserves the characteristics of images irrespective of its frequency content.

A general framework to denoise images based on wavelet transform is described as

- Step 1: The corrupted noisy image is considered as an input.
 - Step 2: Apply Forward 2D Dual Tree CWT to determine sub band wavelet Coefficients.
 - Step 3: Evaluate variance of noise from the input
 - Step 4: Determine threshold value by applying non-linear shrinkage function.
 - Step 5: Adopt soft /hard thresholding technique based on the obtained threshold value.
 - Step 6: Finally use inverse 2D Dual Tree CWT on the thresholded coefficients for image restoration.
 - Step 7: Obtain the denoised image.
 - Step 8: Determine quality of the output image.
- Illustrate 'x' as an input image with corrupted 'z' Gaussian noise. The output 'n' noisy image is represented in (2).

$$n = x + z \tag{2}$$

The Gaussian noise follows i.i.d distribution and then DWT shown as W is applied to perform image decomposition process that results in producing different coefficients and is dictated in (3):

$$N = W(n) \tag{3}$$

CWT partitions the images to different sub bands, labeled as HL_k, LH_k, HH_k, HL_b, LH_b and HH_b, where *k* = 1, 2... *m* indicates the decomposition level and *m*, the largest decomposition level. These six directional sub bands per level gives the details of an image in $\pm 15^\circ$, $\pm 45^\circ$ and $\pm 75^\circ$ directions. Low pass sub bands are further decomposed recursively. On determining the value of threshold, wavelet coefficients produce significant and dependent relation shrinkage function S, and can be expressed in (4) as:

$$F = S(N) \tag{4}$$

After performing the shrinkage rule, inverse transformation is applied on the denoised wavelet coefficients as represented in (5) as:

$$f' = W^{-1}(F) \tag{5}$$



Denoising can be achieved by 2 thresholding approach known as hard and soft thresholding. Processing of wavelet coefficients that are obtained after performing decomposition is filtered in which the threshold value is selected within a limited user constraint or based on restricted contents.

IV. THRESHOLD ESTIMATION

a) Hard Thresholding Method

It operates based on the logic principles involving hard decisions and is found to be fixed in a limited value or produces 0 as the condition is satisfied. When the absolute value of X coefficients is greater than or equal to the threshold value λ , it produces the similar coefficient whereas in other cases it outputs 0 and is expressed in mathematical equation in (6) as [9]:

$$\hat{M} = \begin{cases} X, & \text{if } |X| \geq \lambda \\ 0, & \text{otherwise} \end{cases} \quad (6)$$

X dictates noise coefficients, \hat{M} indicate evaluated output coefficients with threshold λ

b) Soft Thresholding Method

It functions discontinuously resulting in producing ringing / Gibbs impact. For resolving such limitation, soft thresholding is implemented. Mathematically, the soft thresholding technique varies based on the shrinkage threshold factor λ and is represented in (7) as [9]:

$$\hat{M} = \begin{cases} X - \lambda, & \text{if } X \geq \lambda \\ X + \lambda, & \text{if } X < -\lambda \\ 0, & \text{otherwise} \end{cases} \quad (7)$$

The discontinuities present in an image can be removed and it also suppresses different coefficients leading to blurred images. Based on the impact caused by the noises, the usage of thresholding approach varies. Due to the practical impact caused by dynamic noises, the usages of fixed threshold are avoided and thus derive the optimal threshold analyzed in analytic manner with the consideration of effective noises and its variance for exploring its relation in terms of selecting threshold.

The optimal threshold selection process serves a vital role in denoising images. Larger values of threshold fail to eliminate the noises but for smaller threshold values, the noises are removed along with the detailed image features that may results in overly smoothed images. The inefficient threshold may affect the detailed information of the image edges which lead to visual quality degradation. Thus, the threshold must to be selected carefully.

Various approach to estimate threshold involves (i)Visu Shrink, (ii) Sure Shrink, (iii) Bayes Shrink. The methods varies based on selecting threshold λ and the strategy employed in applying the threshold operator.

A. Visu Shrink

Donoho and Johnstone introduces Visu Shrink, the common threshold technique meant to adopt universally and its threshold value is given in (8) :

$$T = \sigma * \sqrt{(2 * \log M)} \quad (8)$$

In which M dictates the no of pixel present in an image and σ represents the noisy standard deviation accomplished by images. This may also produce smoothed images because of its dependent relation with M.

B. Sure Shrink

The hybrid combination of Visu and SURE threshold is designated as SURE SHRINK and its aim is to minimize the unbiased Stein risk estimator [10]. This method operates better when compared to visu shrink. The threshold is estimated in (9) as:

$$T = \text{arg } m \geq 0 \min SU(m, X) \quad (9)$$

In which SURE dictates the unbiased Stein's risk estimator and the minimization of this factor is given in (10) as:

$$\text{SURE}(m, X) = d - 2 \{ \sum_{i: |X_i| \leq m} |X_i| + \sum_{i=1}^d \min(|X_i|, m) \}^2 \quad (10)$$

X indicates the sub band coefficients and d, the no of sub band coefficients.

C. Bayes Shrink

In statistics, after the invention by Donoho and Johnstone, research progresses to determine the threshold factor of non-parametric estimation. Bayes Shrink selects the adaptive sub-bands to evaluate threshold where wavelet coefficients are specified as a Generalized Gaussian Distribution (GGD) for every sub bands [11]. Obtained threshold value is expressed in (11) as well as (12):

$$T = (\sigma_{noise}^2 / \sigma_{signal}) \quad (11)$$

$$\sigma_{signal} = \sqrt{(\max(\sigma_y^2 - \sigma_{noise}^2, 0))} \quad (12)$$

Where $\sigma_y^2 = \frac{1}{d} \sum_{i=1}^d X_i^2$ and d represents the no of wavelet coefficients that belong to Y_i .sub-band. At every sub bands, the signal to noise ratio is predicted in which the noise variance of the wavelet coefficients is chosen to be the median absolute value. The noise variance is expressed in (13) as:

$$\sigma_{noise} = (\text{median}(|Y_{i,j}|)) / 0.6745 \quad (13)$$

Where Y_i belongs to sub band HH and $Y_{i,j}$ predicts the HH sub band coefficients that indicates the advanced decomposition level. The mean squared error is minimized to a greater restricted value that adds further advantage to the method.

V. PROPOSED DENOISING ALGORITHM

Denoising wavelet coefficients predicts to implement successfully in different application when suitable factors like decomposition level, wavelet function and threshold value is evaluated accurately. Further optimizing such parameters results in producing improved restoration output. Such existing drawbacks can be avoided through adopting randomized search algorithm in the present technique. Bayes shrink produces better restoration result in which tuning can be performed perfectly using optimization parameters such as threshold and decomposition level and its performance seems to be better than that of sub band adaptive thresholding method. Along with Bayes shrink, GA-GWO algorithm is used for providing an accurate threshold value. Fig.1 presents the schematic diagram of proposed technique.



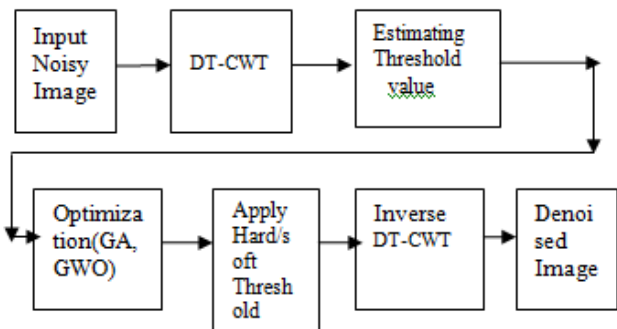


Figure 1: Schematic flow diagram of optimized DT-CWT

VI. GA BASED OPTIMIZATION TECHNIQUE

GA follows the behavior of randomly searching Meta-heuristic optimization technique that inspires the characteristics of naturally operating genetic system and operates based on the principles of biological evolution method. Encoding of individual's initial population of takes place in random manner and then fitness values of every individual is computed. Among the individual, the fittest solution is preferred to perform reproduction, crossover and mutation process and this progresses till it obtains an appropriate result. The individual population is encoded in random manner so that the GA determines the perfect Bayesian threshold value and decomposition level. Minimization of mean squared error with maximization of its PSNR is the major role. Its fitness function is given in (14).

$$f = PSNR() = 10 * \log_{10} (255^2 / MSE) \quad (14)$$

The mean square error is given in (15) .

$$MSE = \frac{1}{M*N} \sum_{m,n} [I_{1\ m,n} - I_{2\ m,n}]^2 \quad (15)$$

In which m and n dictates the input image dimensions. I₁ and I₂ are the original and filtered images. Fig. 3 presents the schematic flow diagram of GA. Binary tournament selection (BTS) [12][13] technique is used for selecting the fittest individual chromosomes for the purpose of making mating pool with similar size of the population. Selection of two chromosomes appropriately and then the best solution is stored in the mating pool of successive generations and this continues till the pool becomes empty. Similarities in the selection technique can be resolved. Crossover operation is performed among 2 certain chromosomes with high probabilistic ratio at every time. In this, the Uniform crossover technique is adopted and is performed at n/2 size with pool size n in iteratively. Initially only 2 chromosomes are chosen among the pool as in [14]. As crossover operation gets completed, each offspring performs mutation operator which is also known as operation. Mutation refers to the process of bit swapping in which the bits are swapped from 0 to 1 or vice-versa with lower probabilities.

The white additive Gaussian noise is eliminated by GA filtering technique that finally results in minimized mean squared error.

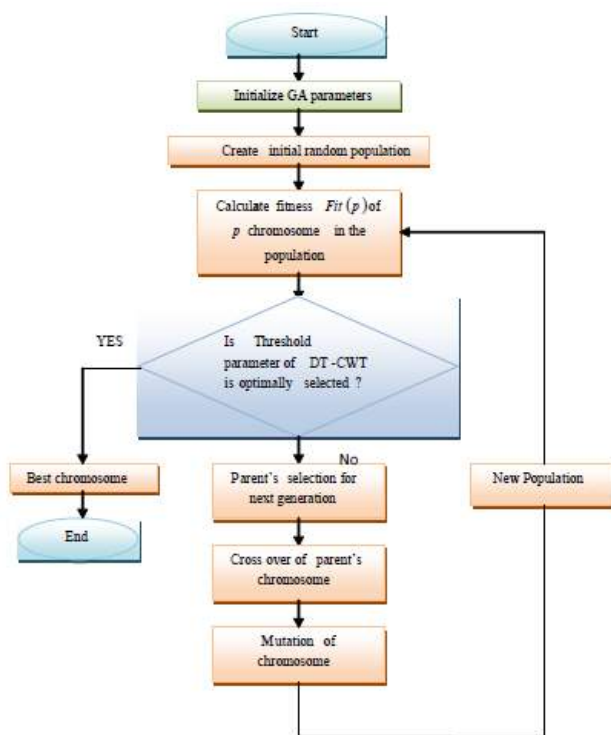


Figure 2:Flowchart of genetic algorithm

VII. GREY WOLF OPTIMIZATION TECHNIQUE

GWO [15] is a swarm intelligence algorithm developed by Mirjalili imitating the natural characteristics shown by grey wolf. The grey wolves survives as groups and are categorized into four groups: α (alpha), the highest authority that is responsible for taking decisions, β (beta) that support in taking decisions, ω (omega) that submit to all other wolves and δ that dominate ω and report to α and β .

A. Mathematical Model of GWO

(i) **Search for prey:** Each wolf searches for their prey individually. α , β and δ represents 1st, 2nd and 3rd fit solutions.

(ii) **Encircling the prey:** This is represented in Eq. (16) and Eq. (17)

$$M = |N \cdot Y_q(i) - Y(i)| \quad (16)$$

$$Y(i + 1) = Y_q(i) - G \cdot M \quad (17)$$

where i correspond to the present correspondent iteration, G and N indicate vector coefficient, Y illustrate grey wolf location, Y_q indicates the respective location of prey and M indicates best fit solution.

The value of G and N are calculated using Eq. (18) and Eq. (19).

$$G = 2 \cdot g \cdot x_1 - g \quad (18)$$

$$N = 2 \cdot x_2 \quad (19)$$

where x_1 and x_2 are random values and the value of vector g gradually decreases from 2 to 0.

(iii) **Hunting:** In the search space, there is no location based information about the prey. α , β and δ has the ability to locate them. The formula for modelling the hunting nature of wolves is given from Eq. (20) to Eq. (26)



$$M_{\alpha} = |N \cdot Y_{\alpha} - Y| \quad (20)$$

$$Y_1 = Y_{\alpha} - G_1(M_{\alpha}) \quad (21)$$

$$M_{\beta} = |N \cdot Y_{\beta} - Y| \quad (22)$$

$$Y_2 = Y_{\beta} - G_2(M_{\beta}) \quad (23)$$

$$M_{\delta} = |N \cdot Y_{\delta} - Y| \quad (24)$$

$$Y_3 = Y_{\delta} - G_3(M_{\delta}) \quad (25)$$

$$Y(i+1) = \frac{Y_1 + Y_2 + Y_3}{3} \quad (26)$$

where M_{α} , M_{β} and M_{δ} are the first three best solutions.

(iv) Attacking the prey: This is the final stage of hunting, and it takes place only when the prey is stationary.

```

Initialize the grey wolf population  $X_i(i=1,2,\dots,n)$ 
Parameter initialization a, A and C
Compute search agent's fitness value
 $X_{\alpha}$ -fittest better search agent
 $X_{\beta}$ -second fittest search agent
 $X_{\delta}$ - third fittest search agent
While ( $t <$  Maximum no of iterations)
For every search agent
Position of the current search agent is updated in relevance
To equation 26
End
Parametric factor a, A and C are updated
Compute its fitness values
Then update the computed parameters  $X_{\alpha}$ ,  $X_{\beta}$  and  $X_{\delta}$ 
 $t = t + 1$ 
end while
return to the updated  $X_{\alpha}$ 
    
```

Figure 3: Pseudo code of the GWO algorithm

VIII. RESULT AND DISCUSSION

Quantitative and qualitative analysis is performed on the filter operating based on GA to determine its performance through MATLAB software. Different denoising technique like Visu shrink, Sure shrink, Integrated GA based Bayes shrink, GWO dependent Bayes shrink technique is adopted. Input X-ray images are utilized to make denoising technique so easier and are compared with different techniques. Table I shows the independent results of GA and GWO based optimization method which is compared with different filtering technique for X – ray images and in Table II for Barbara image. X-ray images, Barbara images are interrupted by additive white Gaussian noise with $\sigma=30$ and proposed GA algorithm, proposed GWO algorithms are performed on it. The observed results produce accurate output when compared to traditional denoising method. The image restoration output is presented in Fig.4 and Fig.5.

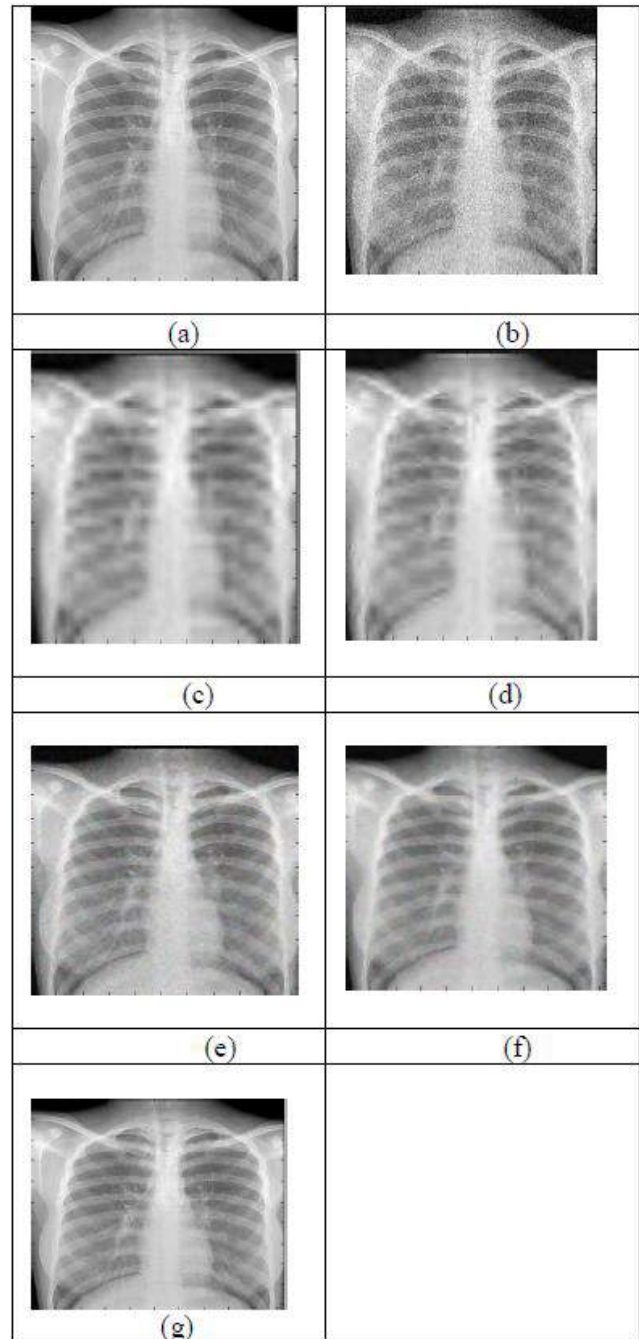


Figure 4. (a) Input X-ray image. (b) Noise image. (c) Visu shrink based denoising image output (d) Sure shrink. (e) Bayes shrink (f)Image output of proposed GA dependent denoising technique(g) Proposed GWO based denoised image.

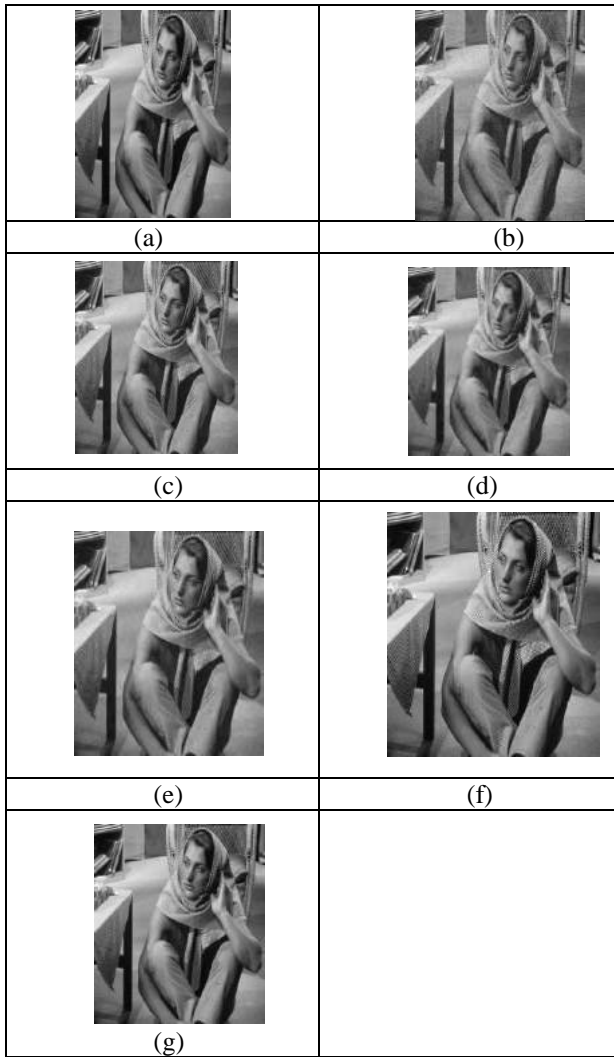


Figure 5. (a) Input Barbara image. (b) Noise image. (c) Visu shrink based denosing image output (d) Sure shrink. (e) Bayes shrink(f) Image output of proposed GA dependent denosing technique(g) Proposed GWO based denoised image.

Table .I Comparison ofPSNR, MSE possessed by various denosing technique in related to the proposed algorithm particularly on X-ray image of 256x256 with Gaussian noise variance $\sigma =10$ and 30.

Filter	$\sigma =10$		$\sigma =30$	
	PSNR	MSE	PSNR	MSE
Visu shrink	29.82	280.45	27.33	292.34
Sure shrink	31.32	141.32	27.95	152.20
Bayes shrink	33.25	92.25	28.71	94.055
Proposed GA Algorithm	34.51	90.36	29.80	93.56
Proposed GWO Algorithm	35.62	75.25	26.90	84.23

Table .II Comparison of PSNR,MSE values for various denosing techniques methods in relation to the proposed algorithm on Barbara image of 256x256 with Gaussian noise variance $\sigma =10$ and 30.

Filter	$\sigma =10$		$\sigma =30$	
	PSNR	MSE	PSNR	MSE
Visu shrink	26.1371	158.2579	22.33	192.34
Sure shrink	30.629	56.2548	27.25	142.20
Bayes shrink	28.4809	72.2548	22.71	94.055
Proposed GA Algorithm	36.21	80.66	25.70	93.56
Proposed GWO Algorithm	38.52	65.45	28.20	84.23

IX. CONCLUSION

This research has been proposed a novel technique in denosing different images that are corrupted by Gaussian noises to improve the effectiveness of DTCWT along with optimization. For denosing wavelet coefficients, threshold technique was applied either on entire images or on every image sub bands after getting optimized Threshold value. The optimization of the Bayesian threshold is done by Genetic Algorithm and Grey wolf optimization algorithms for every independent sub bands. Different image denosing techniques such as Visu shrink, Sure shrink, Bayes shrink, proposed GA as well as GWO relevant thresholding method were adopted to prove the effectiveness of the research. The proposed denosing technique implementation results shows improved results when compared to other technique with respect to PSNR and MSE.

REFERENCES

- Gonzalez, R.C., and Woods, R. E., *Digital Image Processing (2nd Ed*, University of Tennessee, Prentice Hall Inc., 2002).
- P.Venkata Lavanya, C.Venkata Narasimhulu, K.Satya Prasad, "Transformations Analysis for Image Denosing Using Complex Wavelet Transform" 2017 International Conference on Innovations in Information, Embedded and Communication Systems (ICIIECS).
- I.W.Selesnick, R.G.Baraniuk, N.C.Kingsbury, " The dual Tree complex wavelet Transform", IEEE Signal processing Magazine, volume 22, Issue 6, Nov 2005, DOI: [10.1109/MSP.2005.1550194](https://doi.org/10.1109/MSP.2005.1550194)
- Ling wang, Jianming Lu, Yeqiu Li and Takashi Yahagi, "A Method of Image Denosing in the Complex Wavelet Domain", IEEE, 2008.
- Varsha.A and PreethaBasu , "An Improved Dual Tree Complex Wavelet Transform based Image denosing using GCV Thresholding", 2014 First International Conference on Computational Systems and Communications (ICCSC), IEEE, 2014.
- LaheceneMitiche and AmelBahaHouda Adamou-Mitiche , and HilalNaimi, "Medical image denosing using Dual Tree Complex Thresholding Wavelet Transform", Jordan Conference on Applied Electrical Engineering and Computing Technologies (AEECT), IEEE, 2013.
- Qingwu Li, Chunyuan He, "A new thresholding method in wavelet packet analysis," in proc. conf. Mechatronics and Automation, 2006, pp. 2074 – 2078.
- N.G.KINGSBURY. The dual-tree complex wavelet transform: a new technique for shift invariance and directional filters.,In Proceedings of the IEEE Digital Signal Processing workshop, 1998.
- S. Grace chang, Bin Yu, Martin Vetterli, "Adaptive wavelet thresholding for image denosing and compression", IEEE transactions on image processing, pp.1532- 1546, 2000



10. F. Luisier, T. Blu, and M. Unser, "A new SURE approach to image denoising: Inter-scale orthonormal wavelet thresholding", IEEE Trans. Image Process., vol. 16, no. 3, pp. 593–606, Mar.1998
11. H.Chipman, E. Kolaczyk, R. McCulloch, "Adaptive bayesian wavelet shrinkage", J Am Stat Assoc 440 (92), 1413–1421,1997
12. K.F.Man, K.S.Tang, S.Kwong, "Genetic algorithms: concepts and applications", IEEE Transaction on Industrial Electronics volume 43,Issue 5, oct 1996, DOI:10.1109/41.538609
13. S. Mukhopadhyay, J. K. Mandal, "Wavelet based medical image denoising using sub band adaptive thresholding techniques through genetic algorithm",Procedia technology 10, pp.680-689,2013.
14. Zhang Fang,Li Na,Li Jinhui , "Application Research of the Genetic Algorithm on the Intelligent Test paper composition of Examination Database", ICAIC 2011: Applied Informatics and Communication pp 443-448
15. Lu, C., Gao, L., Yi, J.: 'Grey wolf optimizer with cellular topological structure', Expert Systems with Applications, 2018, 107, pp. 89-114

AUTHORS PROFILE



P. Venkata Lavanya working as an Associate Professor in TKR college of Engineering & Technology, ECE Department, Hyderabad, Telangana, India. She is currently Research Scholar of JNTUK, A.P, India. She has 15 years of Teaching experience. She is speciliased in the subjects of Digital Image processing and

Microprocessors & Microcontrollers. She published papers in 2 National and 3 International Journals and conferences. One paper is included in IEEE Digital Library also.She is in charge for MPMC Lab, Mini and Major projects. She organized FDPs, various workshops. Her research interests include the Bayesian modeling in the wavelet domain, Image denosing.



C. Venkata Narasimhulu is currently Professor in ECE Dept, Geethanjali College of Engg&Technology,Telangana, India. He received M.Tech from REC, CALICUT. He received Ph.D in signal and Image processing from JNTUK, Kakinada, A.P, India. He has twenty years of teaching experience in various reputed engineering colleges. He worked in various administrative

positions such as HOD, Dean academics and Principal. He involves actively in various co-curricular and extra-curricular activities to enhance the students overall development. He published several research papers in International Journals and Conferences. He is life member in ISTE, IE and IETE. He is the member of selection committee for recruiting faculty for various engineering colleges under JNTUH. He delivered several lectures for under graduate programs in reputed engineering colleges.He is sincere, dynamic, honest, highly motivated, inspiring, outcome oriented person. He has great skills in organizing things from scratch to shine. He works for the betterment of the student community round the clock and always engaged in helping the needy. He is actively involved in preparing manuscripts for NBA, NAAC, UGC-Autonomous, AICTE and JNTUH.



K. Satya Prasad is currently Rector in vignan's Foundation for science, Technology &Research, Guntur, A.P, India. He had 38 years of Teaching experience and 28 years of Research, Administrative experience. Worked as Examiner for UPSC, New Delhi, Different Universities in A.P. & Bangalore University, BITS Ranchi, GOA University etc., He is Reviewer of Research Papers for IEEE Transactions

on Circuits and Systems, IEEE International symposium on Circuits and systems and Elsevier Journal on Signal Processing. He received Ph.D in Digital signal Processing from Indian Institute of Technology, Madras. He published Textbooks of Electronic Devices, Network Analysis, Signals & Systems and Microwave Engineering. He Guided more than 30 research scholars. He published more than 147 papers in International Journals and conferences. He published more than 70 papers in National Journals .Life Member, Indian Society for Technical Education, New Delhi. (Member of Executive council from Jan'93 to Dec'94) .Fellow in Institute of Engineers (INDIA) (F-1071846) .Fellow in Institute of Electronics & Telecommunication Engineering (F-1837852). He got STATEBEST TEACHER Award by AP State Govt. in 2009,Best PRINCIPALAward by IIE&Min 2010,SIKSHA RATAN Puraskar by IIFS in 2010 ,BEST CITIZEN OF INDIA Award by International Publishing House.





Investigations of carrier transport mechanism and junction formation in Si/CZTS dual absorber solar cell technology

S. Vallisree¹ · Akash Sharma¹ · R. Thangavel¹ · T. R. Lenka²

Received: 4 December 2019 / Accepted: 26 January 2020
© Springer-Verlag GmbH Germany, part of Springer Nature 2020

Abstract

We report on dual absorber n-silicon/p-Cu₂ZnSnS₄ (Si/CZTS) solar cell model with CZTS as top absorber, silicon as bottom absorber and ITO acting as transparent conducting oxide layer on top of CZTS material in order to exploit the advantages of well-established silicon technology and low-cost earth abundant CZTS materials. The valence band edge develops a triangular potential at the Si/CZTS interface, and hence, the drift–diffusion and thermionic carrier transport mechanisms are investigated using Silvaco ATLAS 2D simulator. The thermionic emission current component is suggested to improve the fill factor at the cost of short circuit current and open circuit voltage. The band discontinuities, built-in potential developed across the heterojunction, generation–recombination profile, electron and hole current densities are carefully examined to understand the transport phenomena of Si/CZTS structure for varying thickness, acceptor concentration, electron affinity and optical band gap of top CZTS absorber materials. Synthesis and deposition of CZTS thin films were carried out via sol-gel spin coating process with different preheating temperature range between 250 and 350 °C for 10 min, and absorption data obtained from experiment is used to explore the benefits of tunable band gap properties of CZTS absorbers in the Si/CZTS heterojunction solar cell device. The increased band gap for 350 °C preheated sample has minimized the electrical recombination losses and improved the infrared light absorption resulting in efficiency enhancement. Then the CZTS physical parameters are optimized for the Si/CZTS solar cell model and the conversion efficiency is improved from 8.97 to 14.74% by minimizing the electrical and optical losses of the materials.

Keywords Heterojunction · Silicon · CZTS · TCAD · Solar cell modeling · Thermionic Emission · Triangular Potential

1 Introduction

In the past decades, crystalline and polycrystalline solar cells dominated the photovoltaic market. In order to improve the efficiency of the device, the solar cells were either textured [1] in a highly corrosive environment [2] which involves expensive manufacturing processes or by utilizing light trapping structures [3] to reduce the reflection losses [4]. Therefore, another alternative approach to enhance the efficiency of the device is by designing tandem structures with

silicon as bottom cell absorber. Chao Zhou [5] has reported the design of tandem structure with CdZnTe as top cell absorber and silicon as bottom cell absorber. Photovoltaic properties are studied for the tandem structure with CdTe as top absorber and silicon as bottom cell absorber layers in [6]. Two terminal tandem configurations with CIGS and hydrogenated amorphous silicon absorber layers were studied and reported [7]. Thomas P. White [8] explored the design requirements of top cells with absorber materials such as CuInS₂, CZTS, hydrogenated amorphous silicon, Sb₂S₃ and c-Si material as bottom cell absorber. Out of all the thin-film absorbers, kesterite-based CZTS material has gained increased attention owing to the abundance of zinc and tin, low-cost, tunable band gap and absorption coefficient > 10⁴ cm⁻¹ [9, 10]. However, the performance of kesterite-based solar cells is bounded by the open circuit voltage deficit and less efficiency [11]. Ashok Chaudhari et al. have reported the possibility of creating a smooth interface between silicon and CZTS experimentally in [12].

✉ R. Thangavel
rthangavel@iitism.ac.in

¹ Condensed Matter Physics Laboratory, Department of Physics, Indian Institute of Technology (ISM), Dhanbad, Jharkhand 826004, India

² Department of Electronics and Communication Engineering, National Institute of Technology Silchar, Cachar, Assam 788010, India

Epitaxial CZTS films are deposited on silicon (100) [13] and (001) [14] substrates by thermal evaporation. Also, Ning Song et al. deposited CZTS epitaxial films over the silicon (111) substrate [15]. Polycrystalline non-epitaxial CZTS/Si heterojunction formations for photovoltaic applications are investigated by few researchers [16–18]. CZTS films were deposited on Si wafers using pulsed laser deposition and reported efficiency of 1.1% ($J_{sc} = 26 \text{ mA/cm}^2$, $V_{oc} = 0.140$, $FF = 31\%$) [19]. To the best of our knowledge, there is no report on the study of optical and electrical properties of the Si/CZTS/ITO heterojunction solar cell with CZTS layer acting as top absorber and silicon substrate acting as bottom absorber.

As both the CZTS and silicon are good absorbers and can form a p–n junction, the power conversion efficiency can be improved significantly by careful design of the material parameters. Moreover, it is necessary to elucidate the free carrier absorption, carrier transport mechanism and influence of Si/CZTS interface offset band alignment on the cell performance which is carried out in the present study. Also, the effect of CZTS thickness, acceptor carrier density and interface recombination on the device performance has been analyzed. The tunable band gap properties of CZTS materials which is synthesized using sol–gel spin coating method by varying preheating temperatures is utilized in the Si/CZTS heterojunction solar cell model in order to study and minimize the optical losses. The experimental part of the preparation of CZTS material sample is discussed in Sect. 2. The simulation methodology used for the modeling of Si/CZTS solar cell is elaborated in Sect. 3, and device optimization by varying the parameters of CZTS material within experimentally achievable ranges is covered in Sect. 4.

2 Experiment

In order to extract the optical properties of the CZTS material, a cost-effective, solution-based approach was adopted for the fabrication of the CZTS thin films as earlier reported in [20]. Briefly, all the metal chlorides (Cu, Zn and Sn) precursors along with thiourea were dissolved in a 2-methoxyethanol solvent along with few drops of monoethanolamine (MEA) by simply stirring for certain duration. The mixture so obtained was further kept in rigorous stirring for about 1 h at 60 °C. The Cu/Zn/Sn/S molar ratio was maintained as 2:1:1:10. An excess amount of sulfur precursor was used in order to compensate for the loss of the same during annealing. A transparent yellow solution was obtained after filtration and aged for 24 h. The CZTS thin films were fabricated by spin coating the aged solution on the cleaned soda lime glass (SLG) substrates at 1500 rpm for 30 s. After each coating, the films were dried at 150 °C for 10 min followed by immediate heating at 250 °C for 10 min. The coating–drying

process was carried out twice to ensure proper thickness of the film. Another sample was prepared by varying the later drying condition to 350 °C for 10 min. Figure 1a represents the absorbance data recorded by a UV–Vis–NIR double beam spectrophotometer (Agilent Cary Model) within the wavelength range of 300 to 1200 nm. The band gap of the material was estimated from the Tauc's plot as shown in Fig. 1b. This absorption data and the extracted band gap values are utilized for the tunable CZTS band gap analysis of Si/CZTS solar cell in Sect. 4.3.

3 Simulation methodology

The n-Si/p-CZTS heterojunction solar cell has been modeled using ATLAS simulator as shown in Fig. 2a. ITO serves the purpose of transmitting most of the visible light to the absorber layers and acts as conducting electrode as well which is defined as a conductor with resistivity of 540 $\mu\Omega$ cm in the simulator. The ITO material forms a good ohmic contact with CZTS material according to the literature [21]. The initial material parameters used in the modeling of Si/CZTS solar cell device are elaborated in Table 1. The refractive index and extinction coefficient spanning over the visible spectrum of light for Si, CZTS and ITO materials are obtained from the standard literatures [22–24]. According to Anderson's rule, heterojunction is formed between Si and CZTS material with conduction band offset $\Delta E_C = -0.05 \text{ eV}$ and valence band offset $\Delta E_V = 0.43 \text{ eV}$ which are obtained using $\chi_1 - \chi_2$ and $(E_{g2} - E_{g1}) - \Delta E_C$, respectively, where χ_1, χ_2 refers to the electron affinity of Si and CZTS, respectively. E_{g1}, E_{g2} corresponds to the band gap of Si and CZTS materials, respectively [25]. The valence band offset forms a peak [26] at the junction between the silicon and CZTS material as shown in Fig. 2b.

The potential is calculated at each and every mesh point with the use of Poisson's equation which relates the electrostatic potential to the space charge density

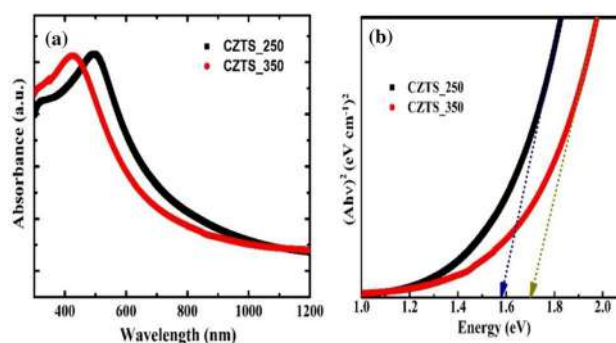


Fig. 1 **a** Absorbance data and **b** Tauc's plot of CZTS samples prepared by varying baking temperatures during the fabrication process

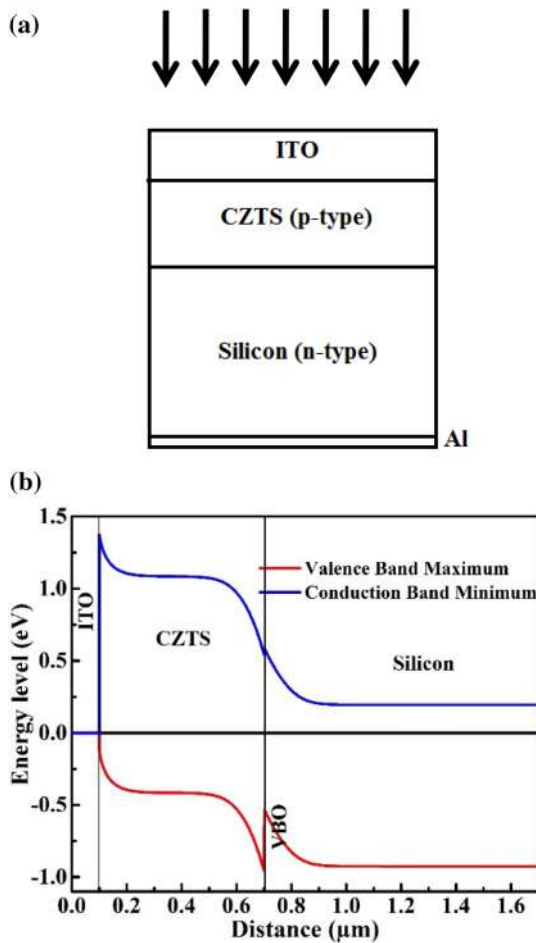


Fig. 2 a Schematic of silicon/CZTS solar cell and b energy band diagram extracted at the middle of the structure from the top to bottom

$\text{div}(\epsilon \nabla \psi) = q(n - p - N_D^+ + N_A^-) - Q_T$ and carrier continuity equations [34]. The last term Q_T in the space charge density accounts for the charges induced due to trap and defect states. The recombination velocity at the Si/CZTS interface is assumed to be 10^6 cm/s. The recombination statistics is modeled using Shockley–Read–Hall (SRH) recombination theory which incorporates the recombination which occurs due to defects and traps. Radiative recombination is dominant in CZTS direct band gap material and auger recombination is included for both silicon and CZTS materials. The standard AM 1.5 G spectrum with intensity of 100 mW/cm^2 is used to illuminate the device. The real part of refractive index is used to obtain the optical intensity at each and every grid point and the carriers which are photogenerated by light absorption are obtained from the extinction coefficient. The photon generation rate is obtained from the internal quantum efficiency η_0 and ray intensity factor P using $G = \eta_0 \left(\frac{P\lambda}{hc} \right) \alpha e^{-\alpha y}$, where α is the absorption coefficient and the ray intensity factor incorporates the collective effect of

reflection, transmission and absorption losses on the ray path.

3.1 Thermionic emission and tunneling

Apart from drift–diffusion (D–D) carrier transport mechanism, thermionic emission (TE) and tunneling phenomenon may occur across abrupt heterojunctions [35] where majority carriers acquiring more energy overcome the barrier, and at high carrier concentrations, tunneling of carriers can occur through the narrow valence band barrier at the heterojunction. This thermionic emission-dominated current density is applied for the node points along the interface in the ATLAS 2D device simulator [34] using the below expressions.

$$\vec{J}_n = q(1 + \delta) \left(v_{n+} n^+ - v_{n-} n^- \exp \left(\frac{-Q\Delta E_c}{KT_L} \right) \right) \quad (1)$$

$$\vec{J}_p = -q(1 + \delta) \left(v_{p+} p^+ - v_{p-} p^- \exp \left(\frac{-Q\Delta E_v}{KT_L} \right) \right) \quad (2)$$

where v_{n-} – v_{n+} are the electron thermal velocities in the “–” and “+” regions, v_{p-} – v_{p+} are the hole thermal velocities in the “–” and “+” regions, δ is the tunneling factor.

$$\delta = \frac{1}{KT} \int_{E_{\min}}^{E_c^+} \exp \left(\frac{E_c^+ - E_x}{KT} \right) \exp \left(\frac{-4\pi}{h} \int_0^{x_E} [2m_n^*(E_c - E_x)]^{0.5} dx \right) dE_x \quad (3)$$

where E_x is the energy component in the x direction. The solar cell parameters pertaining to different carrier transport mechanisms are carefully examined and the details are elaborated in Table 2. The photon absorption is maximum at the ITO/CZTS interface resulting in maximum hole current density, and it decreases exponentially toward the CZTS/Si interface in Fig. 3a. However, the hole current increases and the electron current decreases at the CZTS/Si interface for the thermionic emission case owing to the movement of majority carriers overcoming the barrier potential by thermionic emission. The increase in the forward current due to thermionic emission is the possible cause for the reduction in the short circuit current density and open circuit voltage as shown in Table 2. However, the fill factor shows improvement due to the thermionic transport of carriers across the interface as evident from Table 2 and Fig. 3b. As evident from Table 2, thermionic transport of carriers plays a major role in the transport of carriers across the abrupt heterojunctions, and hence, both the drift diffusion and thermionic transport mechanisms are taken into consideration for the entire analysis.

Table 1 Initial material parameters used in the Si/CZTS solar cell model

Material parameters	CZTS	c-Si (n)
Band gap (eV)	1.5 [27]	1.12 [28]
Permittivity	7 [11]	11.9 [28]
Affinity (eV)	4.1 [11]	4.05 [28]
Electron mobility (cm ² /Vs)	100 [11]	1111 [29]
Hole mobility (cm ² /Vs)	25 [11]	421.6 [29]
Thickness (μm)	0.6	180
Conduction band density of states	1.91 × 10 ¹⁸ [27]	2.8 × 10 ¹⁹ [28]
Valence band density of states	2.58 × 10 ¹⁸ [27]	1.04 × 10 ¹⁹ [28]
Acceptor concentration (cm ⁻³)	2 × 10 ¹⁶ [30]	–
Donor concentration (cm ⁻³)	–	1.5 × 10 ¹⁶ [29]
<i>Recombination parameters</i>		
Carrier lifetime (s) (SRH)	7.8 × 10 ⁻⁹ [31]	0.5 × 10 ⁻³ [32]
Radiative recombination rate (/cm ³ s)	5 × 10 ⁻⁹ [33]	–
Auger recombination rate (/cm ³ s)	1 × 10 ⁻²⁹	2.8 × 10 ⁻³¹ (electrons) 9.9 × 10 ⁻³² (holes) [34]
<i>Defect parameters</i>		
Density of Gaussian deep states (cm ⁻³ /eV)	1 × 10 ¹⁶	1 × 10 ¹⁰
Decay energy for deep states (eV)	0.1	0.1
Peak energy for deep states (eV)	0.75	0.56
Density of tail states (cm ⁻³ /eV)	1 × 10 ¹⁹	1 × 10 ¹⁴
Decay energy for tail states (eV)	0.1	0.1

Table 2 Dependency of solar cell parameters on the carrier transport mechanism

Carrier transport mechanism	J_{sc} (mA cm ⁻²)	V_{oc} (V)	FF (%)	η (%)
Drift–diffusion model (D–D)	18.26	0.781	62.93	8.98
D–D + thermionic emission (TE)	17.02	0.769	68.53	8.97
D–D + TE + tunneling	17.01	0.769	68.51	8.96

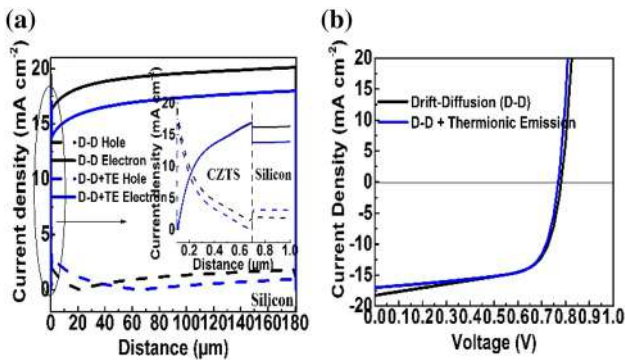


Fig. 3 **a** Electron and hole (dotted lines) current densities for the drift–diffusion (D–D) transport model and after inclusion of the thermionic transport (TE) of carriers at the interface. **b** J–V curves before and after inclusion of thermionic transport phenomenon

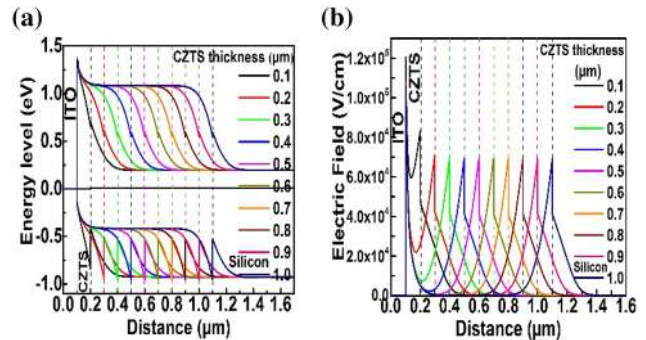


Fig. 4 **a** Energy band diagram and **b** electric field for varying thickness of CZTS absorber layer (Si/CZTS interface is shown by dotted line for varying thickness of CZTS absorber)

4 Device optimization

4.1 Dependence of CZTS thickness on the device performance

The band offset configurations for varying thickness of CZTS layer (t_{CZTS}) is shown in Fig. 4a. Initially, the slope of the band edges changes with the ultra-thin layer of CZTS has 300 nm thickness, and hence, the initial

reduction in electric field as shown in Fig. 4b. After 0.3 μm thickness, the conduction band offset and valence band offset are almost unaffected by the varying t_{CZTS} and hence the electric field strength.

As the top-layer ITO itself acts as an absorber layer, the photon absorption has reached maximum at the ITO/CZTS interface as clearly depicted in the inset of Fig. 5a and decreases exponentially toward the Si/CZTS interface. However, the overall above band gap absorption of CZTS material increases with the increase in t_{CZTS} resulting in decreased absorption at the Si/CZTS interface and in the silicon region as clearly evident from inset of Fig. 5a. The net recombination profile through the entire device is illustrated in Fig. 5b. The SRH interface recombination of carriers reduces at the Si/CZTS heterojunction because of the reduction in photon absorption (Fig. 5a) with the increase in t_{CZTS} as illustrated in Fig. 5c. The probability of radiative and SRH recombination rate of CZTS material increases on moving away from the Si/CZTS interface toward ITO as shown in Fig. 5c and d owing to its finite carrier diffusion length [27] and carriers traveling longer path with the increase in t_{CZTS} . The radiative recombination at the vicinity of the interface in the CZTS material shows a decreasing trend with the increase in t_{CZTS} (Fig. 5d) because of the reduced photon absorption. The results indicate that

radiative recombination is predominant for higher values of t_{CZTS} and SRH recombination is prominent at the interface for lower values of t_{CZTS} . The presence of defects and finite diffusion length of minority carriers (i.e., electrons) leads to the increased SRH recombination [36] with the increase in t_{CZTS} on moving away from the junction in the CZTS material. The photogenerated carrier in the silicon layer reduces and hence the SRH recombination with the increase in t_{CZTS} as illustrated in Fig. 5b and c.

To clearly understand the portion of light absorbed in the absorber layers and the carrier collection efficiency, EQE graph is extracted as shown in Fig. 6. With the increase in CZTS absorber thickness, the CZTS above band gap absorption increases; hence, J_{sc} and EQE show increasing trend till 400 nm. However, the decreasing trend beyond 400 nm is because of the finite diffusion length of carriers which has resulted in increased recombination losses. The reduction of absorption in silicon with the increase in CZTS absorber thickness is indicated by the increased dip levels in the 900–1000 nm range in Fig. 6. The above band gap absorption increases for CZTS and the photoconversion efficiency attains maximum for CZTS thickness of 0.4 μm. Beyond 0.4 thicknesses, the amount of light absorption by the silicon absorber reduces and the net recombination in the CZTS material increases with the increase in the t_{CZTS} .

With the increase in t_{CZTS} beyond 0.4 μm, even though the absorption increases, there is a raise in probability of overall recombination owing to its fixed diffusion length [31] affecting the carrier collection efficiency in Fig. 7a. Hence beyond 0.4 μm, there is a reduction in photocurrent density. For 0.1 μm thickness, the photon absorption is insufficient; however, all the generated carriers are swept by the stronger field. With the increase in t_{CZTS} , for 0.2 μm, the photoabsorption increases and the electric field is sufficient enough to sweep the carriers and the recombination increases owing to finite diffusion length of carriers beyond 0.2 μm thickness resulting in the degradation of V_{oc} . The fill factor (without considering the series and shunt resistance) is related to the

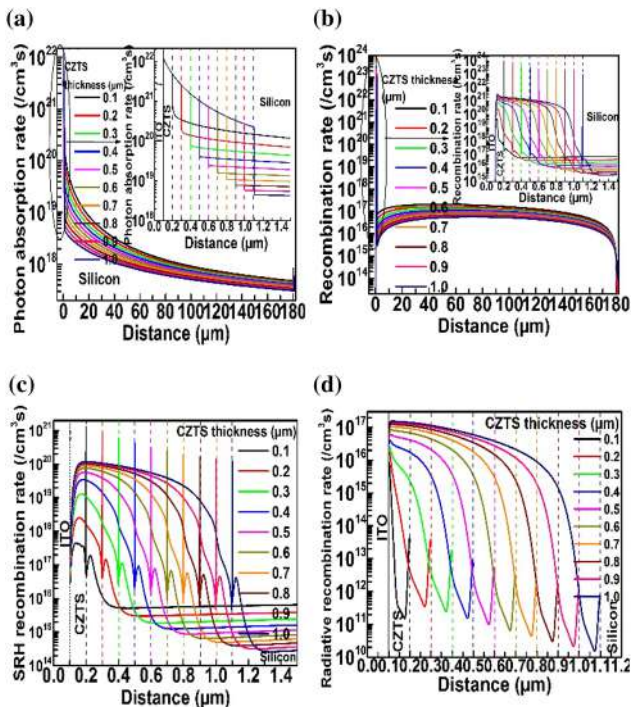


Fig. 5 a Photon absorption profile and b net recombination profile with the insets showing the absorption/recombination rate in the CZTS absorber and the Si/CZTS interface c SRH and d radiative recombination rate in the CZTS material for varying t_{CZTS}

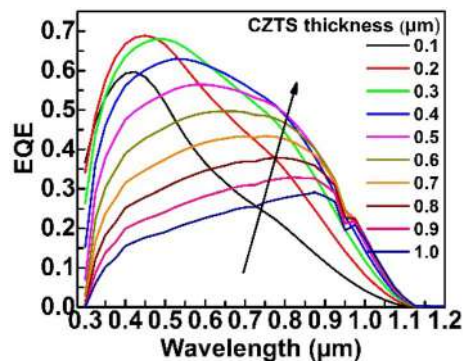


Fig. 6 External QE graph with the CZTS absorber thickness

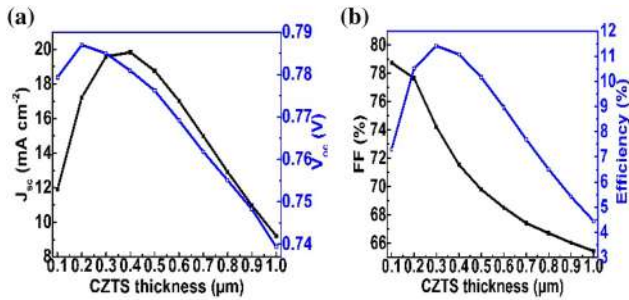


Fig. 7 Dependency of solar cell parameters on the t_{CZTS} a J_{sc} and V_{oc} b Fill Factor and Efficiency

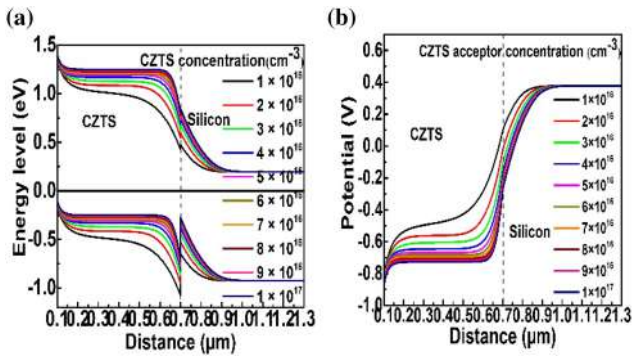


Fig. 8 a Energy band profile and b built-in potential of the ITO/CZTS/Si device under equilibrium conditions

open circuit voltage as per relation $FF_0 = \frac{v_{oc} - \ln(v_{oc} + 0.72)}{v_{oc} + 1}$ [37] where $v_{oc} = \frac{q}{nKT} V_{oc}$ and hence the reduction in fill factor in Fig. 7b. The efficiency attains maximum at 0.3 μm for the optimized generation–recombination profile (Fig. 5a, b) and decreases beyond it.

4.2 Dependence of CZTS acceptor density on the device performance

The acceptor concentration of CZTS material is varied from 10^{16} to 10^{17} cm^{-3} , and the evolution of the band edges is shown in Fig. 8. With the increase in hole carrier density in CZTS layer, more number of holes at the vicinity of the CZTS/Si junction tend to recombine with more number of electrons in n-silicon resulting in the narrowing of depletion region in p-CZTS and widening of depletion region in n-silicon as shown in Fig. 8b. The increased recombination has raised the potential difference (Fig. 8b) resulting in stronger built-in electric field at the Si/CZTS interface. Owing to this, there is a slight reduction in the SRH interface recombination with the increase in acceptor concentration. The radiative and SRH recombination increases in the entire CZTS region due to the increased

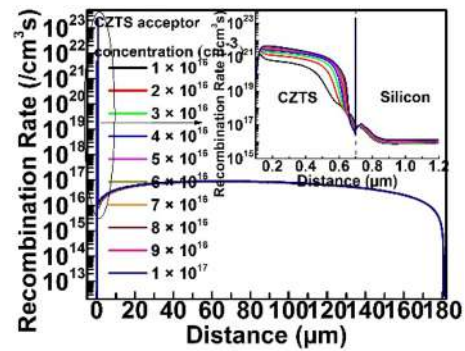


Fig. 9 Recombination profile for varying CZTS concentration in the solar cell device under light illumination

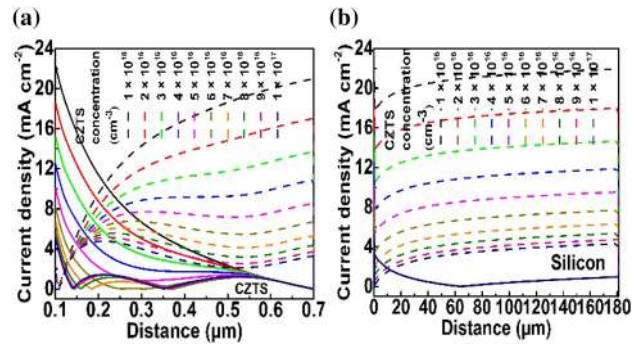


Fig. 10 Electron (dotted line) and hole current densities for varying CZTS acceptor concentration in the a CZTS material b silicon material

availability of holes for recombination on moving away from the junction as shown in Fig. 9.

With the increase in acceptor concentration, the availability of more number of holes has increased the probability of recombination and hence the reduction in the hole current and the electron current as shown in Fig. 10a. There is a raise in hole current and decrease in electron current observed at the interface owing to the thermionic emission of charge carriers. The electron current increases further in the silicon region owing to its increased mobility and silicon acts as electron transport layer for the CZTS photogenerated minority carriers and CZTS acts as hole transport layer thereby promoting the carrier separation process as clearly evident from Fig. 10a and b, respectively. As CZTS plays a dominant role in photon absorption, J_{sc} follows the hole current density (Fig. 11a) attaining maximum for $1 \times 10^{16} \text{ cm}^{-3}$ and then decreases beyond it. In spite of the development of stronger electric field at the Si/CZTS interface, the photogenerated carriers are maximum at the ITO/CZTS interface and the carriers generated at the Si/CZTS undergo increased recombination [27] with the increase in CZTS acceptor carrier

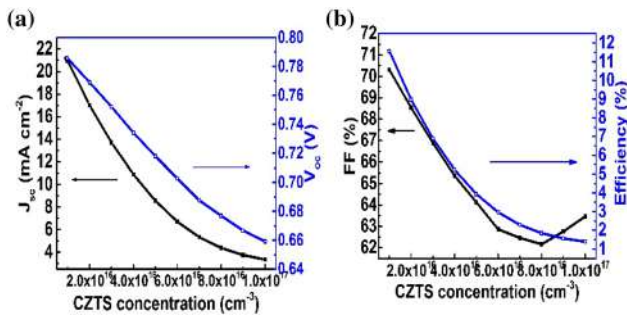


Fig. 11 Solar cell parameters as a function of CZTS acceptor concentration **a** J_{sc} and V_{oc} **b** fill factor and efficiency

concentration and hence the decreasing nature of V_{oc} and fill factor.

4.3 Dependence of CZTS band gap on the device performance

The absorption data and band gap obtained from sol-gel method of deposition discussed in Sect. 2.1 are fed as input into the simulator. The band gap obtained from Tauc's plot is 1.58 and 1.7 eV for the two samples. The photon absorption and the valence band offset are two of the main parameters impacted by the change in the absorption profile and absorber band gap. The valence band offset ΔV_c has increased from 0.43 to 0.63 eV with the increase in CZTS band gap as depicted in Fig. 12a. The increase in CZTS band gap has increased the negative potential in the CZTS material and hence the potential difference/built-in electric field as seen clearly from Fig. 12b.

With the increase in band gap of the experimentally obtained samples, the photon absorption is greater in the CZTS material toward the Si/CZTS interface (inset of Fig. 13) and significant increase is observed in the silicon substrate near the heterojunction resulting in more efficient utilization of the solar spectrum (Fig. 13b). Moreover, the

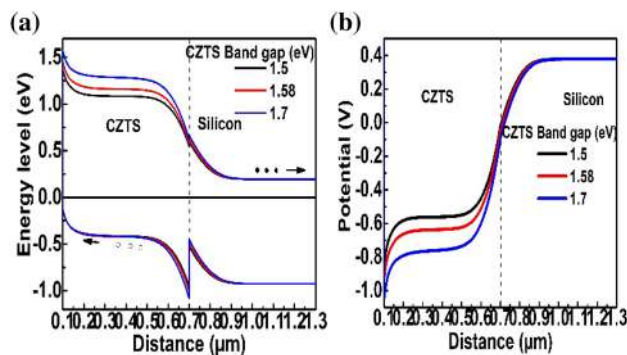


Fig. 12 **a** Energy band profile and **b** potential of Si/CZTS structure for different values of CZTS band gap

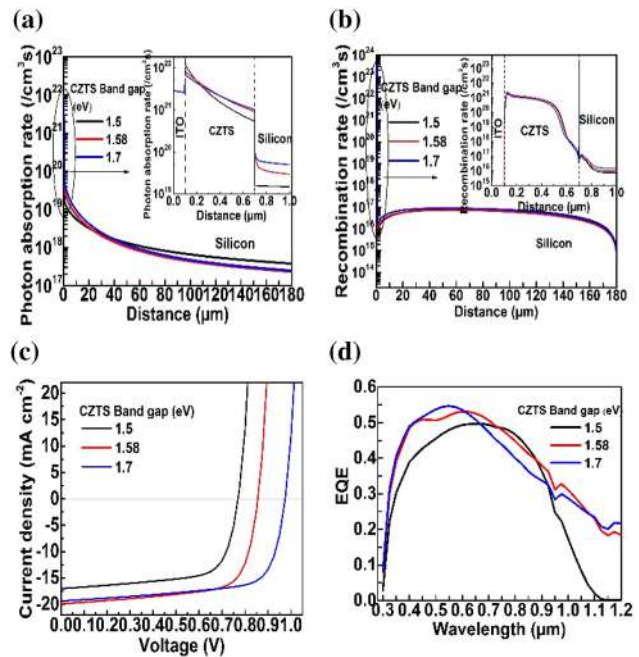


Fig. 13 **a** Photon absorption profile **b** net recombination profile **c** J–V curves and **d** external quantum efficiency as a function of CZTS band gap

infrared absorption in the silicon region has improved for the experimentally prepared CZTS samples as evident from Fig. 13d. The net recombination slightly reduces in the CZTS layer owing to the increase in band gap, and it meagerly increases in the silicon region in spite of the drastic increase in photogenerated carriers owing to the inherent advantages of silicon such as increased mobility and carrier lifetime. Also, the large band offset at the minority carrier band seems to favor the carrier separation process. The simulation results indicate that the increase in the CZTS material band gap is also suggested to favor the V_{oc} and fill factor of the device as shown in Fig. 13c.

4.4 Effect of CZTS affinity on the device performance

The affinity of CZTS layer χ_{CZTS} varies from 3.8 to 4.5 eV reported in the literature [11, 27, 38]. With the increase in χ_{CZTS} , both the conduction and valence band edges form abrupt heterojunctions with ΔE_c varied from 0.25 to -0.3 eV and ΔE_v from 0.13 to 0.68 eV. For $\Delta E_c > 0$ (i.e., $\chi_{CZTS} < 4.05$), the band alignment formed at the Si/CZTS heterojunction is type I and for $\Delta E_c < 0$ (i.e., $\chi_{CZTS} > 4.05$), type II band alignment is formed at the heterojunction and the transformation in band alignment from type I to type II at the heterojunction is clearly evident from Fig. 14a. The potential difference at the heterojunction increases owing to the increased negative potential in the

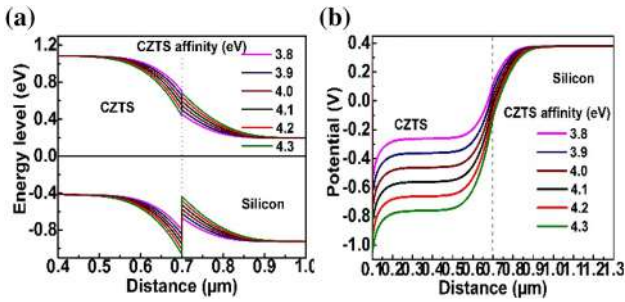


Fig. 14 Energy band profile and **b** potential at the Si/CZTS interface as a function of χ_{CZTS}

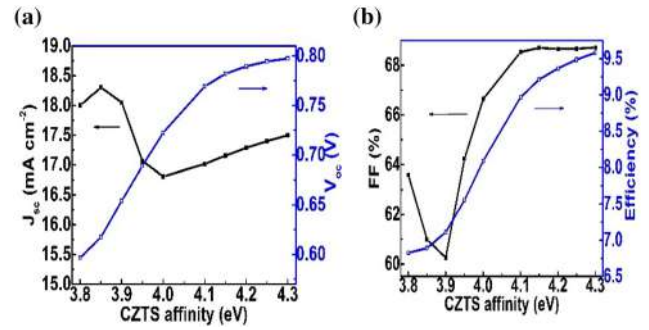


Fig. 16 Different solar cell parameters as a function of χ_{CZTS} **a** J_{sc} and V_{oc} **b** FF and η

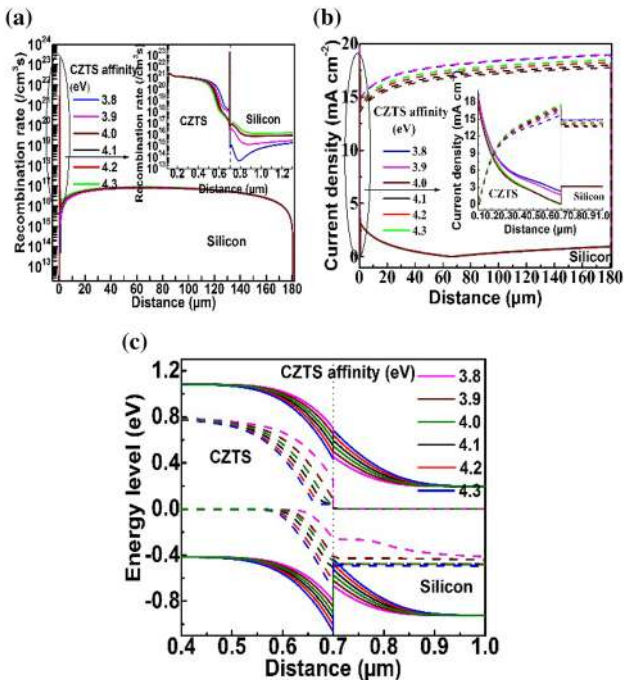


Fig. 15 Recombination profile **b** electron (dotted line) and hole current densities and **c** change in the quasi-Fermi potential as a function of χ_{CZTS} under light illumination

CZTS material with the raise in valence band discontinuities as shown in Fig. 14b. Beyond 4.35 eV, the obtained VB discontinuity becomes so large and newton algorithm has not reached convergence. The hole and electron currents become complicated with the increase in χ_{CZTS} owing to the added barrier which acts as a bottleneck for the movement of charge carriers over the junction [26]. The photon generation rate remains unaffected for different values of affinity, and the carrier collection efficiency depends on the electric field at the interface, thermionic emission current and the rate of recombination probability.

The overall recombination rate has reduced in CZTS layer (Fig. 15a) with the increase in χ_{CZTS} and hence the increase

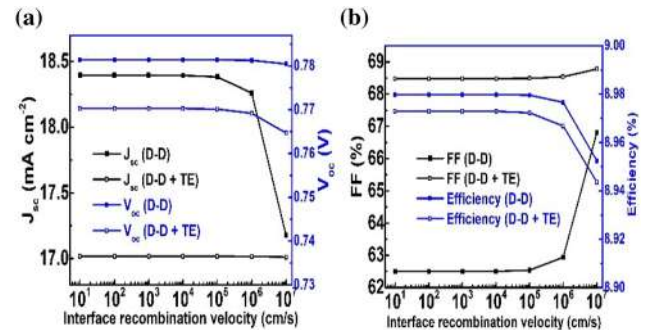


Fig. 17 Solar cell parameters **a** J_{sc} and V_{oc} **b** FF and η as a function of Si/CZTS interface recombination velocity

in J_{sc} as shown in Fig. 16a. Moreover, the photogenerated carriers are more easily swept across by the stronger built-in potential/electric field developed with the increase in χ_{CZTS} . The increase in the difference between electron and hole quasi-Fermi potentials with the χ_{CZTS} (Fig. 15c) favors the V_{oc} [27] and fill factor as shown in Fig. 16a and b.

4.5 Effect of recombination velocity on the device performance

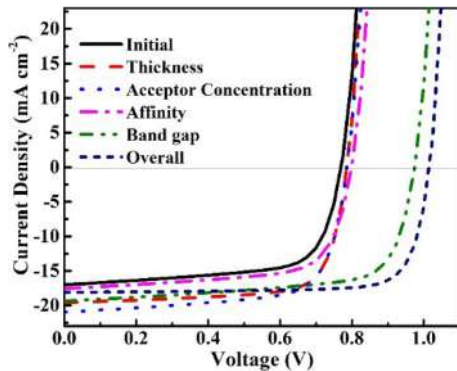
The interface recombination velocity is varied from 10^1 to 10^7 cm/s, and the dependency of solar cell parameters is studied for the drift–diffusion and thermionic carrier transport mechanism. J_{sc} starts reducing beyond recombination velocity of 10^5 cm/s, and fill factor attains maximum for 10^7 cm/s. Thermionic emission of carriers across the discontinuities of hetero interface suppresses the effect of interface recombination, and the solar cell parameters has undergone a meager variation which is clearly evident from Fig. 17.

4.6 Efficiency enhancement

From the above analysis, by considering the drift diffusion and thermionic emission transport mechanisms, the

Table 3 Solar cell parameters before and after optimization of CZTS parameters

Solar cell parameters	J_{sc} (mA cm ⁻²)	V_{oc} (V)	FF (%)	η (%)
Initial model	17.02	0.769	68.54	8.97
CZTS thickness	19.58	0.785	74.22	11.41
CZTS affinity	17.58	0.799	68.80	9.66
CZTS acceptor density	20.96	0.786	70.31	11.58
CZTS band gap	19.37	0.974	70.04	13.21
Overall optimization	18.11	1.01	80.31	14.74

**Fig. 18** J–V curves before and after optimization for Si/CZTS solar cell

optimized values of CZTS thickness, acceptor concentration, band gap and affinity values are found to be 300 nm, 10^{16} cm⁻³, 1.7 eV and 4.35 eV, respectively. The variation of solar cell parameters for individual parameter optimization and overall optimization are listed in Table 3. J–V curves obtained for each individual parameter optimization are shown in Fig. 18. With the optimized CZTS parameters, the efficiency has improved from 8.97 to 14.74% which is the maximum predicted efficiency of the Si/CZTS solar cell.

5 Conclusions

Si/CZTS heterojunction solar cell has been modeled and optimized for CZTS layer parameters such as thickness, acceptor density, affinity and band gap. The simulation results revealed that the electrical losses (recombination) are minimized by reducing the acceptor density in CZTS layer. Contradicting to the conventional solar cell, the photon absorption is maximum at the ITO/CZTS interface and the short circuit current has improved significantly for optimized CZTS material parameters such as thickness, acceptor density and band gap. The increase in CZTS band gap for 350° C preheated sample has suggested to minimize both the electrical recombination losses and optical losses (enhance

infrared absorption) and contribute significantly to the raise in J_{sc} and V_{oc} values. The increase in band discontinuities favors the carrier separation; however, the short circuit current slightly reduces owing to the thermionic emission of carriers. Also, the simulation results indicate that the thermionic emission of carriers across abrupt heterojunction has suppressed the effect of recombination at the interface. The CZTS layer affinity beyond 4.35 eV imposes limitation in the carrier transport across the heterojunction, and the tunable band gap favors the device performance. Hence, the simulation reveals that CZTS layer absorber with the optimized material parameters are found to be suitable candidate for the Si/CZTS heterojunction solar cell fabrication with anticipated conversion efficiency reached up to 14.74%.

References

1. F. Chen, L. Wang, Light trapping design in silicon-based solar cells, in *Solar Cells—Silicon Wafer-Based Technologies*, ed: www.intechopen.com, (2011)
2. R. Pietruszka, B.S. Witkowski, E. Zielony, K. Gwozdz, E. Placzek-Popko, M. Godlewski, ZnO/Si heterojunction solar cell fabricated by atomic layer deposition and hydrothermal methods. *Sol. Energy* **155**, 1282–1288 (2017)
3. N.-N. Feng, J. Michel, L. Zeng, J. Liu, C.-Y. Hong, L.C. Kimerling et al., Design of highly efficient light-trapping structures for thin-film crystalline silicon solar cells. *IEEE Trans. Electron Devices* **54**, 1926–1933 (2007)
4. S. Zhong, B. Liu, Y. Xia, J. Liu, J. Liu, Z. Shen et al., Influence of the texturing structure on the properties of black silicon solar cell. *Sol. Energy Mater. Sol. Cells* **108**, 200–204 (2013)
5. C. Zhou, H. Chung, X. Wang, P. Bermel, Design of CdZnTe and crystalline silicon tandem junction solar cells. *IEEE J. Photovolt.* **6**(1), 301–308 (2016)
6. F.M.T. Enam, K.S. Rahman, M.I. Kamaruzzaman, K. Sobayel, P. Chelvanathan, B. Bais et al., Design prospects of cadmium telluride/silicon (CdTe/Si) tandem solar cells from numerical simulation. *Optik* **139**, 397–406 (2017)
7. A.J. Blanker, P. Berendsen, N. Phung, Z.E.A.P. Vroon, M. Zeman, A.H.M. Smets, Advanced light management techniques for two-terminal hybrid tandem solar cells. *Sol. Energy Mater. Solar Cells* **181**, 77–82 (2018)
8. T.P. White, N.N. Lal, K.R. Catchpole, Tandem solar cells based on high-efficiency c-Si bottom cells: Top cell requirements for > 30% efficiency. *IEEE J. Photovolt.* **4**(1), 208–214 (2014)
9. T.P. Dhakal, C.Y. Peng, R.R. Tobias, R. Dasharathy, C.R. Westgate, Characterization of a CZTS thin film solar cell grown by sputtering method. *Sol. Energy* **100**, 23–30 (2014)
10. D. Tang, Q. Wang, F. Liu, L. Zhao, Z. Han, K. Sun et al., An alternative route towards low-cost Cu₂ZnSnS₄ thin film solar cells. *Surf. Coat. Technol.* **232**, 53–59 (2013)
11. U. Saha, M.K. Alam, Proposition and computational analysis of a kesterite/kesterite tandem solar cell with enhanced efficiency. *RSC Adv.* **7**, 4806–4814 (2017)
12. A. Chaudhari, Method of making a CZTS Silicon thin film tandem solar cell, US Patent, 2016
13. K. Oishi, G. Saito, K. Ebina, M. Nagahashi, K. Jimbo, W.S. Maw et al., Growth of Cu₂ZnSnS₄ thin films on Si (100) substrates by multisource evaporation. *Thin Solid Films* **517**, 1449–1452 (2008)

14. B. Shin, Y. Zhu, T. Gershon, N.A. Bojarczuk, S. Guha, Epitaxial growth of kesterite $\text{Cu}_2\text{ZnSnS}_4$ on a Si(001) substrate by thermal co-evaporation. *Thin Solid Films* **556**, 9–12 (2014)
15. N. Song, M. Young, F. Liu, P. Erslev, S. Wilson, S.P. Harvey et al., Epitaxial $\text{Cu}_2\text{ZnSnS}_4$ thin film on Si (111) 4° substrate. *Appl. Phys. Lett.* **106**, 252102 (2015)
16. G. Turgut, E.F. Keskenler, S. Aydın, S. Dogan, S. Duman, S. Özçelik et al., Fabrication and characterization of Al/ $\text{Cu}_2\text{ZnSnS}_4$ /n-Si/Al heterojunction photodiodes. *Phys. Status Solidi A* **211**, 580–586 (2014)
17. X. Sheng, L. Wang, Y. Tian, Y. Luo, L. Chang, D. Yang, Low-cost fabrication of $\text{Cu}_2\text{ZnSnS}_4$ thin films for solar cell absorber layers. *J. Mater. Sci.: Mater. Electron.* **24**, 548–552 (2013)
18. F. Jiang, H. Shen, W. Wang, L. Zhang, Preparation and properties of $\text{Cu}_2\text{ZnSnS}_4$ absorber and $\text{Cu}_2\text{ZnSnS}_4$ /amorphous silicon thin-film solar cell. *Appl. Phys. Express* **4**, 074101 (2011)
19. Z.O. Elhmaidi, R. Pandiyan, M. Abd-Lefdil, M.A.E. Khakani, Pulsed laser deposition of CZTS thin films, their thermal annealing and integration into n-SiCZTS photovoltaic devices, in *International Renewable and Sustainable Energy Conference (IRSEC)* (2016)
20. A. Ghosh, R. Thangavel, A. Gupta, Solution-processed Cd free kesterite $\text{Cu}_2\text{ZnSnS}_4$ thin film solar cells with vertically aligned ZnO nanorod arrays. *J. Alloys Compd.* **694**, 394–400 (2017)
21. J. Tao, J. Liu, J. He, K. Zhang, J. Jiang, L. Sun et al., Synthesis and characterization of $\text{Cu}_2\text{ZnSnS}_4$ thin films by the sulfurization of co-electrodeposited $\text{Cu}_2\text{ZnSnS}_4$ precursor layers for solar cell applications. *RSC Adv.* **4**, 23977–23984 (2014)
22. S. Adachi, *Earth-Abundant Materials for Solar Cells Cu2-II-IV-VI4 Semiconductors* (Wiley, Hoboken, 2015)
23. S. Adachi, *Optical Constants of Crystalline and Amorphous Semiconductors Numerical Data and Graphical Information* (1999)
24. S.S.A. Software for the design and manufacture of optical thin film coatings [Online]. <http://www.sspectra.com>
25. R.L. Anderson, Experiments on Ge-GaAs Heterojunction. *Solid-State Electron.* **5**, 341–351 (1962)
26. S.M. Sze, K.K. Ng, *Physics of Semiconductor Devices* (Wiley, Hoboken, 2006)
27. S.R. Meher, L. Balakrishnan, Z.C. Alex, Analysis of $\text{Cu}_2\text{ZnSnS}_4/\text{CdS}$ based photovoltaic cell: a numerical simulation approach. *Superlattices and Microstruct.* **100**, 703–722 (2016)
28. W.R. Fahrner, *Amorphous Silicon/Crystalline Silicon Heterojunction Solar Cells* (2011)
29. L. Shen, F. Meng, Z. Liu, Roles-of-the-Fermi-level-of-doped-a-Si-H-and-band-offsets-at-a-SiHc-Si interfaces in n-type HIT solar cells. *Sol. Energy* **97**, 168–175 (2013)
30. I. Bouchama, S. Ali-Saoucha, Effect of wide band-gap TCO properties on the bifacial CZTS thin-films solar cells performances. *Optik* **144**, 370–377 (2017)
31. M. Courel, J.A. Andrade-Arvizu, O. Vigil-Galán, Towards a $\text{CdSCu}_2\text{ZnSnS}_4$ solar cell efficiency improvement: a theoretical approach. *Appl. Phys. Lett.* **105**, 1–5 (2014)
32. K.E. Knutsen, R. Schifano, E.S. Marstein, B.G. Svensson, A.Y. Kuznetsov, Prediction of high efficiency ZnMgO/Si solar cells suppressing carrier recombination by conduction band engineering. *Phys. Status Solidi A* **210**, 585–588 (2013)
33. S. Vallisree, R. Thangavel, T.R. Lenka, Theoretical investigations on enhancement of photovoltaic efficiency of nanostructured CZTS/ZnS/ZnO based solar cell device. *J. Mater. Sci.: Mater. Electron.* **29**, 7262–7272 (2018)
34. Silvaco, *Atlas User's Manual—Device Simulation Software* (2010)
35. K. Yang, J.R. East, G.I. Haddad, Numerical modeling of abrupt heterojunctions using a thermionic-field emission boundary condition. *Solid-State Electron.* **36**, 321–330 (1993)
36. S. Vallisree, R. Thangavel, T.R. Lenka, Modelling, simulation, optimization of Si/ZnO and Si/ZnMgO heterojunction solar cells. *Mater. Res. Exp.* **6**, 025910 (2018)
37. M.A. Green, Solar cell fill factors: general graph and empirical expressions. *Solid-State Electron.* **24**, 788–789 (1981)
38. A.D. Adewoyin, M.A. Olopade, M. Chendo, Enhancement of the conversion efficiency of $\text{Cu}_2\text{ZnSnS}_4$ thin film solar cell through the optimization of some device parameters. *Optik Int. J. Light Electron Opt.* **133**, 122–131 (2017)

Publisher's Note Springer Nature remains neutral with regard to jurisdictional claims in published maps and institutional affiliations.

Border Guard Spy Robot

B. Ramu¹, M. Anand², S. Jyothirmaye³

Assistant Professor^{1,2} Associate Professor³- Dept of ECE,
Geethanjali college of Engineering and Technology, Hyderabad, India

Article Info

Volume 81

Page Number: 5177 - 5180

Publication Issue:

November-December 2019

Article History

Article Received: 5 March 2019

Revised: 18 May 2019

Accepted: 24 September 2019

Publication: 24 December 2019

Abstract

What is a Robot? It is a multifunctional, reprogrammable device which is principally designed to work like humans. It is expected to interpret the works such as surveillance, aerospace, loading and unloading, industrial, health care, pick & place of goods. Spy Robots can perform the most hazardous activities and with more accuracy to increase the productivity as it can work for 24 by 7 without rest. This paper explains the architectural design and controlling of automated vehicle kind robot which can move in desired track, capturing pictures and videos of required locations and immediate transmission of data. The main controlling device of the intact system is Arduino micro-controller. When the user turns on the robot, the robot moves within predefined path. SR04 and 5 laser guns are interfaced to the Arduino micro-controller. In this paper we present an android application developed by use of MIT App inventor and Wi-Fi communication is established which interfaces with micro-controller to control its direction and speed. Major work in this paper is to design a motion controlled robot using Wi-Fi of an Android device.

Keywords: Android OS, Microcontroller, laser, Wi-Fi module

1. Introduction

The major controlling device in the entire system is Arduino micro-controller. When the user turns on the robot, it moves on predefined path. 5 laser guns and SR04 are connected to the Arduino microcontroller. When motion is detected by SR04 sensor this data is fed to the Arduino. The Arduino gets on the laser guns for shooting automatically. We can check the IP camera video in mobile phone. To complete this immediate task, a program is written in embedded-C language and loaded in microcontroller. These robots consist of ultrasonic sensor to detect the motion and 5 laser guns represent shooting indication. The advent of latest high-speed machinery provides realistic prospect for robot controls and recognition of innovative methods for controlling it. This scheme describes a new economical solution of robot control systems. The robot control system presented in this paper can be used for different and

complicated robotic applications. In current applications the International border area surveillance is a critical task. The most important work is done by border guarding forces that continuously do patrolling of border but to survey the border at each and every instance is difficult. An essential requirement for this duty can be done by evolving a robot which automatically detects gatecrasher in the border without human intervention and report it to nearby border security. Now a day many of the military departments utilize the robots to carry out unsafe jobs that cannot be done by the soldiers which keeps their lives in danger. In this work spy robot based on Arduino system, which will save human lives, and also reduces manual fault and protect the nation from enemies. Surveillance system using spy robot described in this paper can also be modified as per the application for various fields.

2. System Architecture:

2.1 Arduino Uno-Board

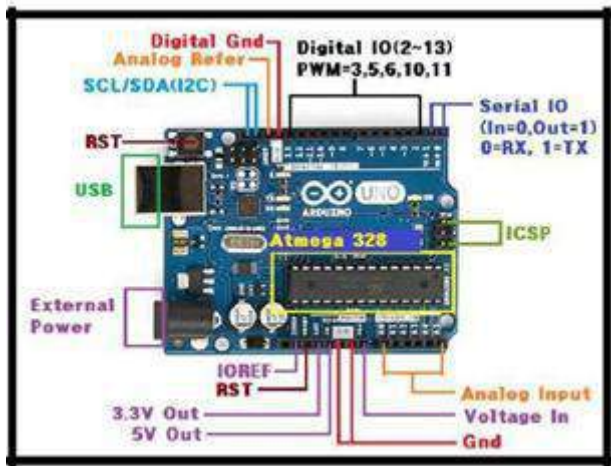


Fig.-1: Board Design of Arduino Uno R3

The Arduino Board is as shown in fig 1. This is the brain of Wi-Fi interfaced Spy robot loaded with a program written in embedded C language specifying various operations to do the necessary functioning. Here the motor drivers are used to make the system work as necessary. The Arduino is an open source electronics platform which gives easy-to-use embedded hardware-software. Arduino uses a range of microcontrollers equipped with set of digital and analog input/output (I/O) pins that possibly be interfaced to various expansion boards or breadboards and other circuits.

2.2. Architecture of Proposed systems

This robot consists of ultrasonic sensor SR04 and 5 laser guns to detect the motion and represent the indication of execution. The main controlling device of the entire system is Arduino microcontroller. When the user turns on the robot, the robot moves on predefined path. 5 laser guns are interfaced to the Arduino microcontroller, when the motion is detected by SR04 sensor, this data is fed to the Arduino. The Arduino gets on the laser guns for shooting automatically. We can check the IP camera video in mobile phone. The Block Diagram shown in fig 2 provides information about proposed system architecture.

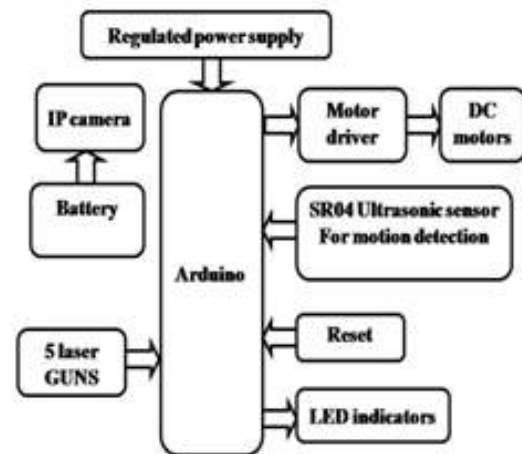


Fig.2 Block Diagram

DC Motor:

Any electric motor operates based on concept of electromagnetism. A current carrying conductor generates a magnetic field and when this conductor is placed in an external magnetic field, it will experience a force proportional to the current in the conductor. The external magnetic field is produced by using High-strength permanent magnet.

D.C. motor is an electrical component controlled by DC voltage. It can move in left and right, forward and backward directions according to the polarity of applied voltage. Every DC motor has six major parts -axle, rotor (armature), field magnets, commutator, stator and brushes. All typically mechanical movements which robots need to perform are accomplished by the use of electric motor, which are means of converting electrical energy into mechanical energy and are best suited as power device.

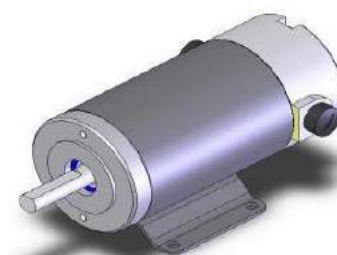


Fig: 3 DC motor

Ultrasonic sensor:

It is also known as Transceiver when it sends signals as well as receives. It works on a correlated principle to radar or sonar by estimating attributes of an object by taking the echoes from sound or radio waves correspondingly. It can be used to generate high frequency sound waves. Mainly sensors compute the time interval between transporting the signal and getting the echo back to determine the distance of an object. This technology can be used for measuring: direction and speed.

IP or Web Camera:

A webcam is a camera that can feed its captured image in real time to a computer or computer network. IP camera is shown in fig 4. A webcam is not like an IP camera which uses a direct

connection using Ethernet or Wi-Fi, it is generally connected by a FireWire cable, USB cable, or similar cable.



Fig:4 IPCamera

3. SYSTEM ARCHITECTURE

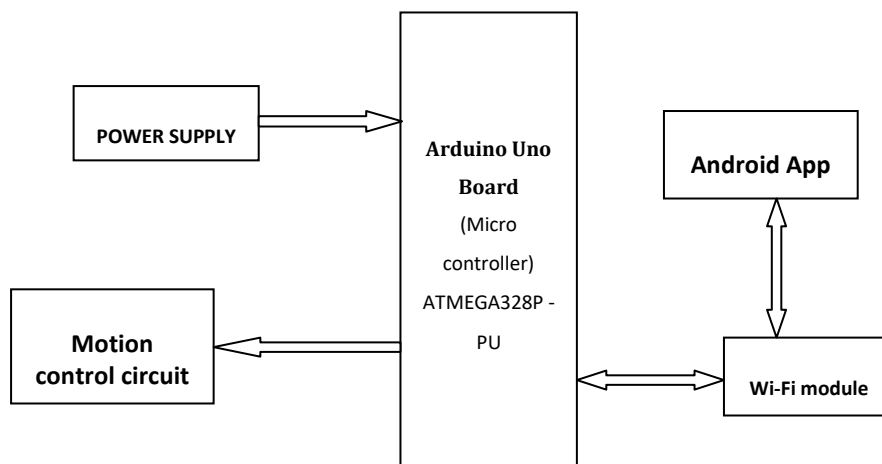


Fig. 5: System Architecture of proposed design

3.1 Border guard Detection system

The Arduino Atmega328 microcontroller is used in this project. In this Arduino controller we use 4 digital pins 8, 9, 10 and 11. 8 and 9 pins to move in forward directions and pin number 10 and 11 to move in backward directions. Motor driver is used to detect the path which mechanically moves in forward and backward directions. Here

ultrasonic sensor is used to intellect the obstacles. The complete live streaming is seen in IP camera which rotates 360 degrees. The use of DC motor is for the wheels rotation of spy robot.

4. Results

SpyRobot presented in this project is the android application based design, made through App Inventor. The major task of this application is to

control the robot. This robot has special buttons integrated to it with each button having different function. These robots consist of ultrasonic sensor to detect the motion and 5 laser guns represent shooting indication. Laser gun attached to it works when any undesirable condition happens or robot is being attacked by any person. Fig 6 and 7 shows outputs of the project.



Fig: 6 Spy Robot

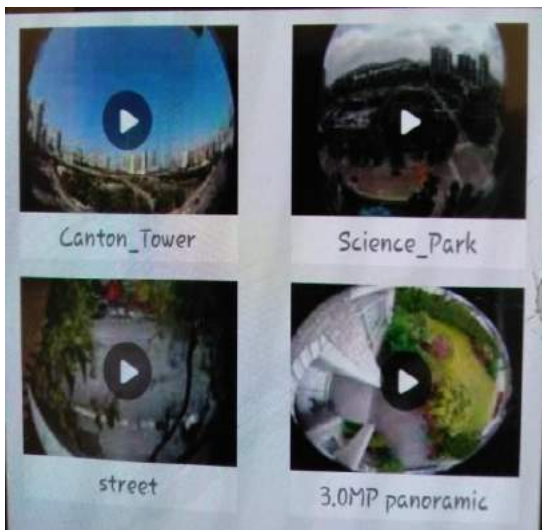


Fig:7 Live Streaming

5. Conclusion

The proposed Robot in this paper shows how it can be used for spy & rescuing purpose. Smartphone with latest Android version operating system, is used to develop effective remote controlling program which also uses Wi-Fi wireless network, making it simple and suitable to control the robot.

It establishes a two-way communication connection between the Android phone and robot which would allow a non-expert to interact with and fine-tune the functionality of a system. Atmega 328 controller is projected to make the purpose of interactive objects or environments more reliable. The border surveillance has always been a relatively sensitive task which includes countless risks. This robot can do this job instead of people, by controlling the robots efficiently. This can provide better results. This proposed system is a reliable solution for secure surveillance in military areas.

REFERENCES

- [1] "Wireless Indoor Surveillance Robot" Hou-Tsan Lee, Wei-Chuan Lin, Ching-Hsiang Huang, Yu-Jhih Huang, SICE Annual Conference 2011, Waseda University, Tokyo, Japan, September 13-18, 2011.
- [2] "Intelligent Surveillance & Security Robot Systems", Kyunghoon Kim, Soonil Bae, and Kwanghak Huh 978-1-4244-9123-0/1 ©2010 IEEE.
- [3] "Image-Based 3D Surveillance in Man-Robot-Cooperation", Jorg Krieger, Bertram Nickday, Oliver Schulz 0-7803-8513 6/4/2004 IEEE.

Design and Research of Rectangular, Circular and Triangular Microstrip Patch Antenna

S.Krishna Priya, Jugal Kishore Bhandari, M.Krishna Chaitanya

Abstract—Modern Wireless communication Systems need high gain, light-weight and straightforward structure antennas to assure high potency, quality and additional dependableness. A patch antenna is incredibly easy in building, employing the fabrication techniques of standard Microstrip. It consists of a blotch of metal on a grounded dielectric substrate which forms a light-weight antenna best suited for mobile and aerospace applications. Patch antennas have developed significantly throughout preceding years and plenty of their limitations are overcome by changes in its design and fabrication techniques. The conducting patch may well be of any form however rectangular patterned configuration is used foremost. In this study we tend to have an interest not solely in rectangular however comparison of it with circular and triangular patch antenna styles. The objective here is to analyze the results of various patches.

Keywords: HFSS tool, patch antenna.

I. INTRODUCTION

Antenna is like Eye and Ear of any radio system. A system with no antenna won't have ability to transmit or receive to its full facility. Antenna is the system which receives the radio signal and converts it into lower voltage and when transmitting it converts voltage into radio signal which is electromagnetic wave. An Antenna is a reciprocal device i.e. it can work on a frequency in both directions. Antenna plays a vital role for success of a radio system. Such a lot rests on antenna. Antenna is the component which provides direction to the signal if required. [1]

A Microstrip Antenna (MSA) in its simplest kind consists of a divergent patch on one aspect of a substrate and a ground plane on the other aspect. MSAs are also named as "patch antennas" or "printed antennas" or "planar antennas". Microstrip or patch antennas have become more and more helpful as a result of they are low (paper-thin) profile, planar configuration and conformal structured, robust and light weight. There is ease of fabrication using printed-circuit technology, both Linear and circular (right or left -handed) polarizations is possible (useful for frequency - reuse), they are compatible with modular designs. Hence solid state components can be added directly into the microstrip antenna substrate, which are easily integrable with the circuits; feed lines and matching networks. It is easy to achieve dual-frequency performance and arrays can be easily created to increase directivity. They can be easily mount on satellites, space vehicles and missiles without major alteration and also compatible with MMIC designs.

Revised Manuscript Received on September 14, 2019.

S.Krishna Priya, Associate Professor, Geethanjali college of Engineering and Technology, Hyderabad, Telangana, India.

Jugal Kishore Bhandari, Assistant Professor, Geethanjali college of Engineering and Technology, Hyderabad, Telangana, India.

M.Krishna Chaitanya, -Department of ECE, Geethanjali college of Engineering and Technology, Hyderabad, Telangana, India.

Every element has some limitations so does MSAs have, which are: Low radiation efficiency, small bandwidth, practical limitations on the maximum gain, poor polarization purity, low power handling capability, poor isolation between the feed and also the diverging component, chance of excitation of surface waves, spurious radiation from feeds, junctions and surface waves, high performance arrays need complicated feed systems[2].

Microstrip patch antenna has many applications. a number of these applications are: Mobile and satellite communication application, Global Positioning System applications, Worldwide ability for Microwave Access (WiMax), measuring device Application, Rectenna Application, Telemedicine Application, medicative applications of patch. [3]

To fabricate an antenna, first we select the frequency of operation, the substrate used and thickness of the substrate. The shape of the antenna is determined and then from these the dimensions of the substrate and patch are calculated. The antenna is designed and simulated in software. After obtaining the desired results, the actual fabrication process starts. Here HFSS software is used for simulation. Different shapes of the patch are designed for obtaining the best results and the same is concluded.

II. EXPERIMENTAL

A. DESIGN OF MICROSTRIP PATCH ANTENNA:

Design of Microstrip Patch Antenna involves the idea of dimensions of the patch from the knowledge of resonant frequency in Hz.

Firstly we have taken length of patch as 32mm, breadth as 30mm and then its area is equated to area of circle and corresponding radius is calculated. Radius is calculated as 17.4mm.

The simulation is accomplished on HFSS (High frequency structure simulator) software. HFSS is high performance electromagnetic field simulator with 3D volumetric view of passive device modeling that gives advantages accustomed with Microsoft Windows GUI. It integrates solid modeling, visualization, simulation, automation with easy to learn environment. Typical uses of HFSS are: designing, simulation and package modeling of EMC/EMI, connectors, waveguide, antennas for mobile communications, PCB board modeling and filters. HFSS uses finite element method a numerical technique and is a procedural simulator. In this a structure is subdivided into various smaller subsections called as finite elements such as tetrahedral and complete collection of tetrahedral called as

mesh. For these finite elements Solution is found for the fields within the finite element. And these solutions are interrelated so that Maxwell's equations are satisfied across the inter elements, which can yield a field solution for the entire inventive structure. Once the field solution is establish the s-matrix solution is determined. [4]

B. SIMULATIONS:

- After designing the single band linearly Polarized Micro Strip antenna the simulations are performed.
- First Validation check is performed to observe warnings and errors if any in the design.
- Next the setup is assigned to the antenna, which includes operating frequency band 2.60-2.85 GHz sweep in the range 1-4 GHz with 0.01 GHz step.
- Results for return loss, VSWR, gain and other parameters of antenna are obtained from the generate report section of HFSS tool.

Boundaries and excitations of the Microstrip antenna:
 Perfect E: Patch, Ground
 Radiating only: Air (except bottom face)
 Excitation: Wave port (port 1)

C. FORMULAE FOR DIMENSIONS OF RECTANGULAR PATCH ANTENNA:

Calculation of W (Width):

$$W = \frac{c}{2fo\sqrt{\frac{\epsilon_r+1}{2}}}$$

The above equation gives the width of the micro strip patch antenna.

On substituting, $c = 3 \times 10^{11}$ mm/sec; $f_0 = 2.72$ GHz, $\epsilon_r = 2.94$; so $W = 30$ mm..

Calculation of L_{eff} (Effective Length):

$$L_{eff} = \frac{c}{2fo\sqrt{\epsilon_{reff}}}$$

The above equation gives the effective length of the micro strip patch antenna.

On substituting, $c = 3 \times 10^{11}$ mm/sec; $f_0 = 2.72$ GHz, $\epsilon_{reff} = 2.60$; so $L_{eff} = 34$ mm.

D. FORMULA FOR RADIUS OF CIRCULAR PATCH ANTENNA:

$$r = \frac{1.8412}{2\pi f \sqrt{\epsilon_r \mu_0 \epsilon_0}}$$

Where, $f = 2.72$ GHz, $\epsilon_r = 2.94$, $\mu_0 = 1.25 \times 10^{-6}$, $\epsilon_0 = 8.85 \times 10^{-12}$, so $r = 18.8$ mm.

E. FORMULA FOR SIDE LENGTH OF TRIANGULAR PATCH ANTENNA:

The equilateral triangular patch has a substrate of thickness 'h' with side length 'S' on with relative dielectric constant ' ϵ_r '.

The below equation gives the resonant frequency of ETMA with side length S

$$f_{mn} = \frac{2c\sqrt{m^2 + n^2 + mn}}{3S_e\sqrt{\epsilon_0}}$$

Where, S_e is the effective side length given by,

$$S_e = S + \frac{h}{\sqrt{\epsilon_e}}$$

Where, ϵ_e is the effective dielectric constant given by,

$$\epsilon_e = \frac{\epsilon_r + 1}{2} + \frac{\epsilon_r - 1}{2} \left[1 + \frac{10h}{S} \right]^{-1/2}$$

Where, h is the height of the dielectric substrate and ϵ_r is the dielectric constant.

Therefore, we obtain the side as 45mm.

III. SIMULATION RESULTS

A. SIMULATION RESULTS OF RECTANGULAR PATCH ANTENNA

The figure below gives the shape, VSWR, gain, return loss, and other parameters of the rectangular Microstrip patch antenna.

Values of parameters are,

Return loss	=	-13.48 dB
VSWR	=	1.53
Gain	=	2.3
Radiation efficiency	=	99%

The dimensions used in tool to design the patch antenna are approximate values and are almost near to the calculated values.

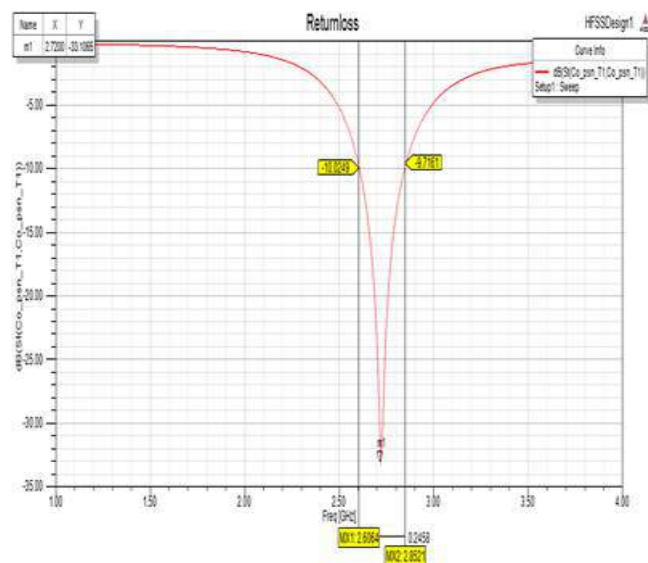


Fig 1: S₁₁ Graph for designed rectangular patch antenna



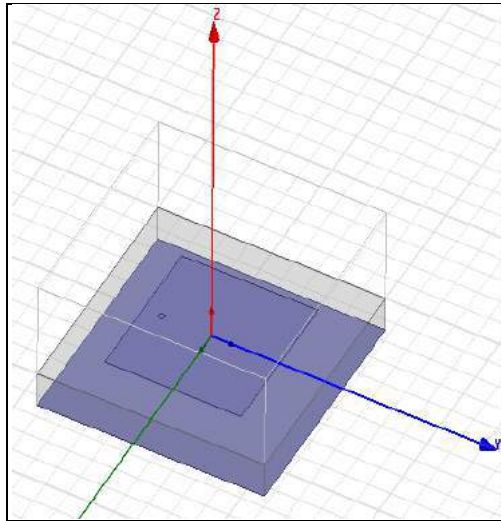


Fig 2: Rectangular patch antenna

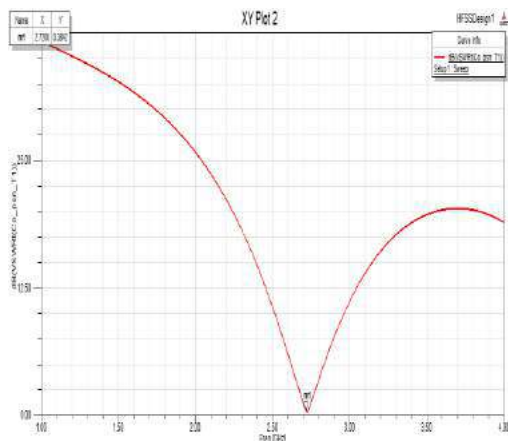


Fig3: VSWR graph for designed rectangular patch antenna

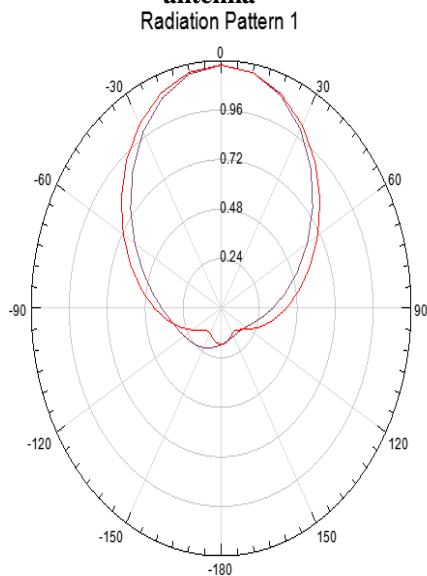


Fig 4: Radiation pattern of designed rectangular patch antenna

$$\begin{aligned} \text{VSWR} &= 0.38 \\ \text{Gain} &= 2.38 \end{aligned}$$

Inputs

Setup Name:	Infinite Sphere1	OK
Solution:	LastAdaptive	Export
Array Setup:	None	Export Fields
Intrinsic Variation:	Freq='2.72GHz'	
Design Variation:	brea='32mm' bread='30mm' fi	

Antenna Parameters:

Quantity	Value	Units
Max U	0.0018403	W/sr
Peak Directivity	2.4107	
Peak Gain	2.3882	
Peak Realized Gain	2.2856	
Radiated Power	0.0095934	W
Accepted Power	0.0096837	W
Incident Power	0.010118	W
Radiation Efficiency	0.99067	
Front to Back Ratio	44.838	
Decay Factor	0	

Fig 5: Parameters of designed rectangular patch antenna

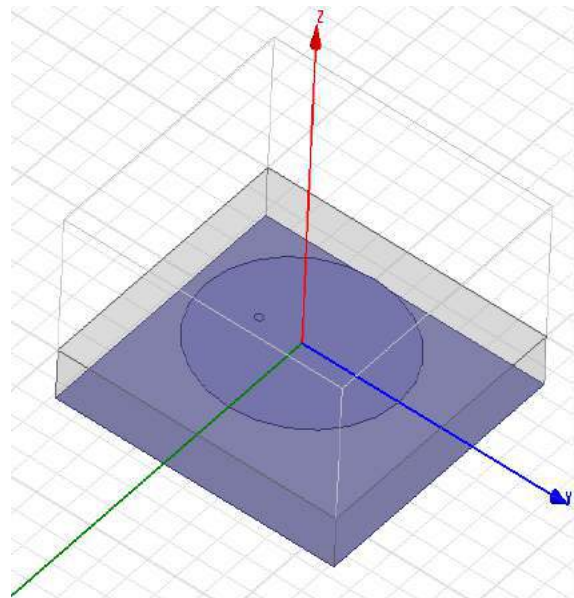


Fig 6: Circular Patch Antenna

B. SIMULATION RESULTS OF CIRCULAR PATCH ANTENNA:

The figures 5.6 - 5.10 give the shape, return loss, VSWR, gain, various parameters of the rectangular Microstrip antenna. Values of parameters are given below.

$$\text{Return loss} = -33.1 \text{ dB}$$

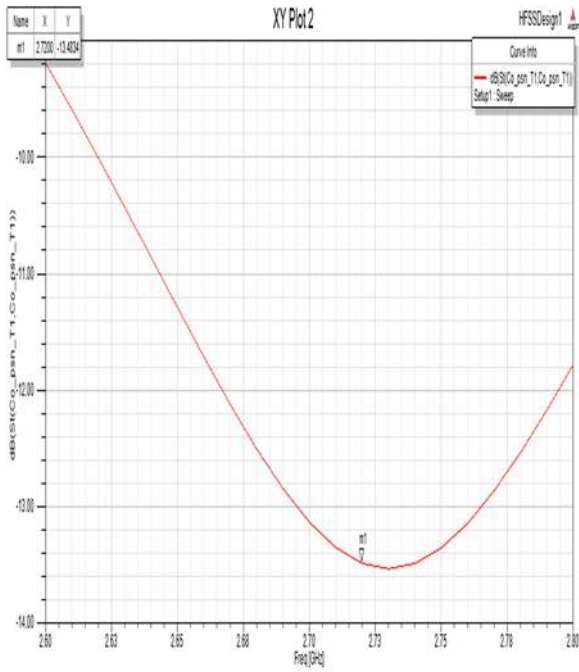


Fig 7: S_{11} Graph for designed circular patch antenna

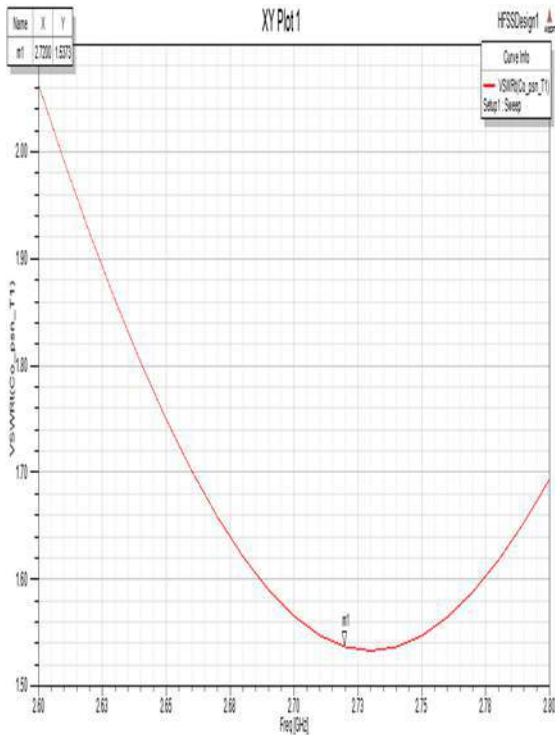


Fig 8: VSWR graph for circular patch antenna

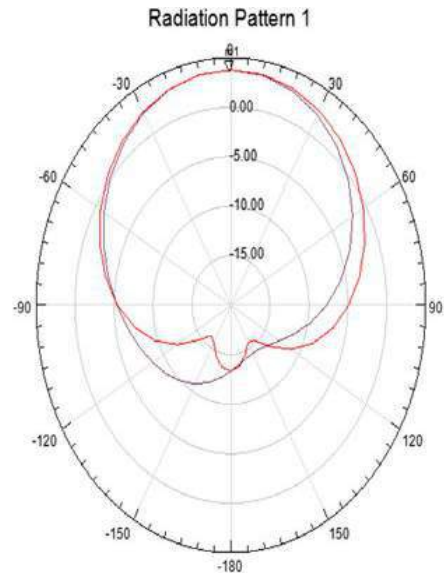


Fig 9: Radiation Pattern of designed circular patch antenna

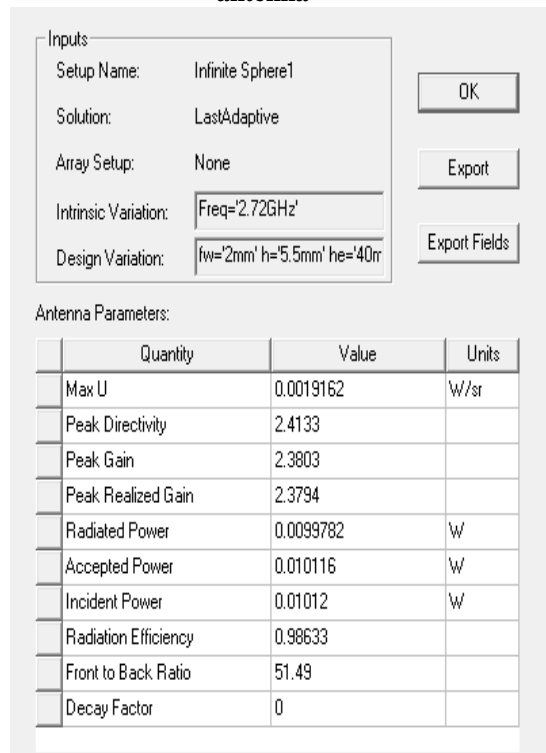


Fig 10: Parameters of designed circular patch antenna

C. SIMULATION RESULTS OF TRIANGULAR PATCH ANTENNA:

The figures give the shape; return loss, VSWR, gain, various parameters of the rectangular microstrip antenna. Values of parameters are given below.

Return loss = -33.1 dB
 VSWR = 1.35
 Gain = 2.38

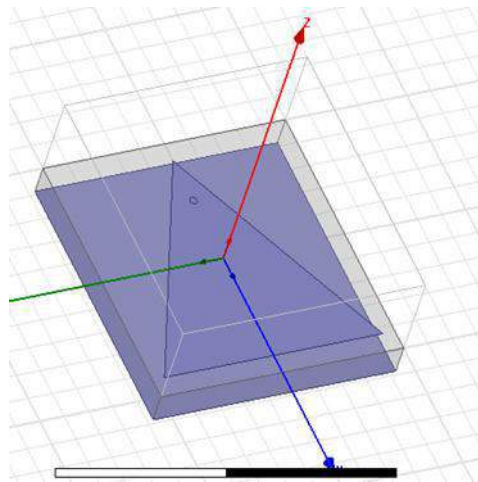


Fig 11: Triangular Patch Antenna

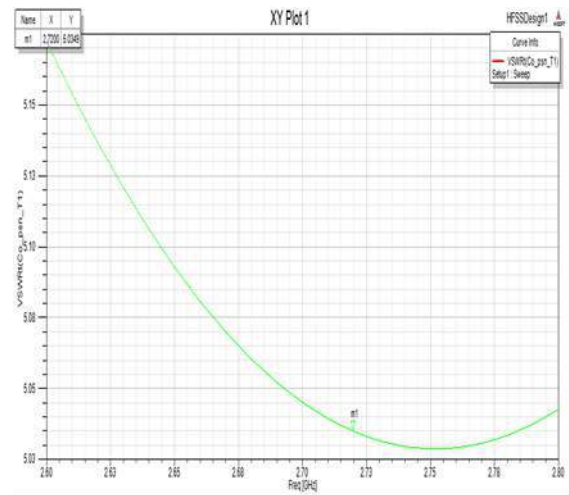


Fig 14: VSWR graph for triangular patch antenna

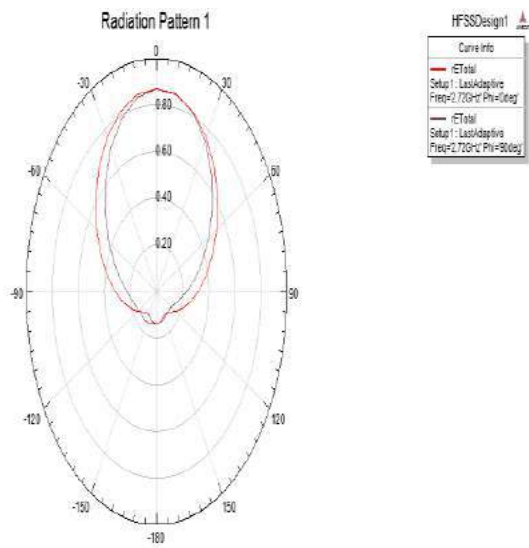


Fig 12: Radiation Pattern of designed triangular patch antenna

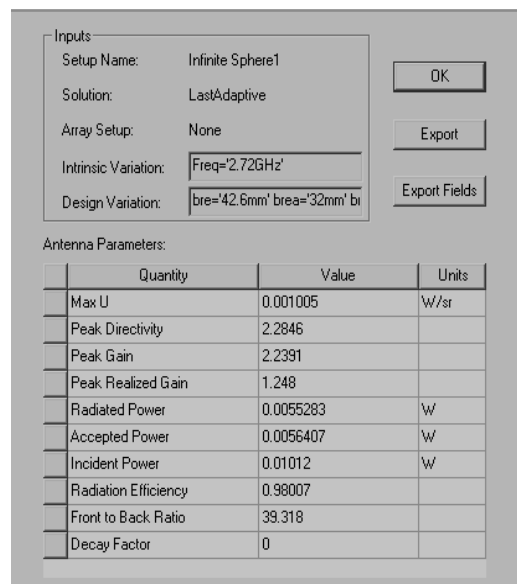


Fig 15: Parameters of designed triangular patch antenna

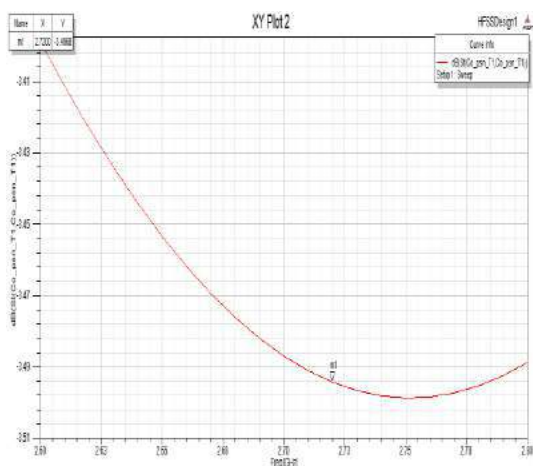


Fig 13: S_{11} Graph for designed triangular patch antenna

IV. ANALYSIS AND COMPARISON

First microstrip antenna with rectangular shape has been considered and simulated. This is done by calculating length and breadth of the antenna using specified formulae. The performance of the antenna has been evaluated using results. After this, circular shape antenna has been designed. Approximate radius of circular patch antenna is calculated by using the specified equation. The simulation is done for the circular patch and results are obtained. Next, triangular shape antenna has been designed. Approximate side length of triangular patch antenna is calculated by applying the specified equation. The simulation is done for the triangular patch and results of three antennas are compared. Finally conclusion may be given as circular patch is more appropriate in terms of optimized parameters. The table gives the comparison of rectangular, circular and triangular patch antennas.

V. CONCLUSION

This paper offers the design, Simulation and performance comparison of circular, triangular and rectangular patch antennas. These designed antennas are of better directivity, high gain and improved impedance. These parameters are attained with improved less increase in the wideness of the antenna structure. The considerable enhancement in the directivity, High Power Beam width is the main achievement of the projected work. This designed antenna may attest to be a useful structure in recent wireless satellite communication systems, where circular polarized radiations which provide higher axial ratio bandwidth are preferred. In simulation frequency of 2.72GHz for calculation of desired parameters of circular, triangular and rectangular patches.

Parameter	Rectangular Mm	Circular Mm	Triangle Mm
Dimensions (mm)	L=32, B=30	R=17.4	B=45, H=42.6
S11 (dB)	-13.5	-33	-3.49
VSWR(dB)	1.52	0.70	5.03
Feed Position (mm)	0,-11,0	0,- 7.74,0	0,-12.6,- 5.5
Directivity (dB)	2.4	2.4	2.28
Gain (dB)	2.38	2.38	2.23

Table 1: Comparison of various parameters of designed rectangular, circular and triangular patch antenna

From the above table we conclude that circular patch antenna is the most efficient patch design than rectangular and triangular patch antennas in comparing the parameters such as VSWR, directivity and radiation pattern. For far better results the value of dielectric constant should be lowered. Circular patch has wide applications and is always of use where compact antennas are required and as well as desired patch antenna for several wireless and satellite applications.

VI. FUTURE SCOPE

Manual calculations of parameter are complex for all types of patch antennas. The GUI can be used to analyze the influence of the Changes in input parameters on radiation pattern and also gives Ease in Calculations. Due to changes in the material of the patch, physical parameters of the Microstrip Patch changes (mentioned in results). This could help the designer in determining the antenna performance and make necessary adjustment before fabricating the antenna structure. There are many antenna design simulators. One of them is MATLAB which is very challenging as it uses very complex programming to achieve the desired results and requires more time for simulations. But, this can be effortlessly solved by use of software tools

available for RF simulation. Some of them are Zealand IE3D and HFSS. Further work on design and simulation can be carried out by use of such advanced software’s with additional 3D volumetric view options.

Calculation of directivity, gain, High Power Beam width, characteristic Impedance, is done. A further study can be done on designing of UHF frequency operating microstrip patch antenna, further improving directive or gain to meet the demand for long distance communications providing a fixed beam of specified shape (beam shape) or a beam that scans in response to system stimulus.

REFERENCES

1. <https://www.quora.com/What-is-the-importance-of-antenna>
2. <https://www.quora.com/What-is-a-microstrip-patch-antenna-What-are-its-applications>
3. Indrasen Singh, Dr. V.S. Tripathi , Micro strip Patch Antenna and its Applications: a Survey, Vol 2 (5), 1595-1599
4. <https://www.quora.com/What-is-HFSS>
5. <https://www.hindawi.com/journals/ijap/si>
6. C.A. Balanis, “Antenna Theory, Analysis and Design” John Wiley & Sons, New York, 1997.

Implementation of MAC Protocol for Analysis of Traffic in Smart Cities

Appala Raju. Uppala, Research Scholar, Department of ECE, JNTUK, Kakinada, India.

E-mail: raju.mdl@gmail.com

C. Venkata Narasimhulu, Department of ECE, Geethanjali College of Engineering and Technology, Hyderabad, India. E-mail: narasimhulucv@gmail.com

K. Satya Prasad, Rector, VIGNAN'S Foundation for Science, Technology and Research, Guntur, India.

E-mail: prasad_kodati@yahoo.co.in

Abstract--- Human beings made Smart Transportation system as an essential need in their daily activity in the present era. For avoiding the road accidents in the present busy lives, it is necessary to create an application which is capable of transferring the emergency information between the vehicle and roadside units. This paper explains such network. The betterment of safety and no safety message delivery will be done by the MAC protocol. Threats occurring with 802.11p MAC protocol will be observed here. Hybrid MAC is capable of accessing two channels simultaneously, so that it can provide better performance during increased traffic load. MAC layer protocol is a challenging architecture for the vehicular network system. It is because of frequent changes in the topology of the vehicular network, huge quality of service requirements, infrastructure inadequacy, and automobile nodes during high speed. If the position of the vehicle is nearer to the network then the operation of the algorithm begins. New vehicles generate the request for sending the message. If there is any availability of the channel, then the channel is allocated and initiates the communication. If it is an old vehicle then it directly goes to the communication monitoring. The vehicle will be in a queue position if there is no availability of channels. When the channel becomes free then it gives first priority to the vehicles which are in the queue. The main aim of the Hybrid MAC protocol is to ensure that all vehicles get a proper channel accessing for conveying their message. Hybrid MAC is capable of reducing the loss of packet, delay in overall function, and collision reduction.

I. Introduction

The advanced achievements of wireless communication technology in last few years, made the users to have a superfluity of new networking [1] research fields concentrating at enlarging connectivity to the atmosphere where the wired connections are not possible. Under these circumstances, VANETS has become one of the most fascinating and reassuring for analysts and automotive industries. The public government has given its assurance with the proviso of safer roads and smooth driving. VANET's are not only limited for road safety but also capable of controlling the vehicle traffic [2] in traffic like bottleneck flow control route inflation for commercial applications like sharing of files, accessing the internet and reporting about parking location.

This paper explains the perception of vehicular networks by demonstrating various types of communication and the important concepts involving these networks. If observed at worldwide present projects they are committed to the exaltation of VANETs. The last part explains the types of network architectures [3] proposed for supporting the VANETs. Due to accidents occurring in present-day traffic man is trying for making his journey safer and acceptable. Even the government also needs a journey with better road safety for technical and cultural evolutions. Since, last decenniums public force and automobile industries are targeting at the development of transportation systems safety by lowering the result of fast approaching accidents and lessening the amount of injuries happening on road.

Although, all these precautionary scopes are capable of providing only restricted securities because they will focus only on stage post accidents. Types of equipment like airbags and seat belts are capable of reducing the accidents but not for complete prevention. This identification of the shortage of passive measures made the developers to work in the direction to completely avoid accidents instead of trying to reduce the damage. Automobile manufacturers have taken a drastic step of enhancing the drivers for the range of awareness. If the destruction cannot be avoided, then the automobile industries are productively preparing the vehicles for reducing the injuries. For example, the sensor [4] gives the early warnings to the drivers about the accidents' and condition of the vehicles.

The above all problems can be overcome with the help of the network VANETs. These secured networks are influencing the developers to make a great research in the development of vehicular networks with the help of communication networks. This processing will be mainly between the vehicles that mean exchanging the messages from one vehicle node to the other vehicle node, through this process information will be shared by one vehicle to the other. With the help of this framework of data and telematics horizon given to drivers [5], safety measures can be planned and exercised before the actual incident happens. These unique capabilities of smart vehicles and their result have a great impact about safety on road and awareness for the driver, developer's attention while designing the car, the government will be with merit.

The VANETs are used for conveying applications such as communicating with multi hop broadcast method which propagates a message from a source to specific destination point. This helps in informing the surrounding drivers about the emergency situation occurred and also to the people about to arrive. Under practical situations, this crucial information has to be forwarded through multi hop broadcast method. This forwarded information will be helpful to provide navigation, obstacle detection and this providing safety. So for VANET services, vehicle discovery and broadcasting are taken into the consideration. A lot of dissipation methods are taken into consideration for the operation VANETs. Many scenarios turn out to be challenging in the present conditions. It requires better network performances for efficient vehicular safety schemes. Considering the theoretically based evolution some mathematical aspects are also been studied.

One of the major problems in vehicular networks is the distribution of the traffic information from one to the other. While comparing with the routing technique [6], which is frequently mentioned in the unicast information conveyance from source to the definite destination point, gridlock data in VANETs has a broadcast-oriented nature. Thus, the information will be delivered to all the nodes within a certain specific region. The information has to be propagated with a network through the multi-hop relaying technique [7] for reaching to the specific zone. The major advantage of this particular broadcasting technique is that it is independent of the destination IP address or the destination nodes path.

This paper presents a MAC protocol scheme for the vehicles to be connected to the nearest server at the junctions for the exchange of information. The primary purpose of such a connection is to facilitate traffic information exchange to facilitate smooth driving to the users.

The vehicles are considered as nodes and each node has to be quickly connected to the Wi-Fi network with minimum delay. The paper addresses the concepts of node entry and exit, node connectivity procedure and exhaustion of network channels. The paper is organized in the following manner. The first section contains the introduction. The literature depicting the various research works in this domain is presented in section 2. Section 3 presents the proposed algorithm. Section 4 presents the results.

II. Literature

A. *Mac Protocols for VANET*

A Medium Access Control (MAC) protocol determines the structure where the nodes are being shared by the channel. Plenty of issues arise by the MAC when using for VANET [8]. Some of them are the prioritized approach, unreliable acknowledgment, and accuracy. These all necessary as because the device is using for the safety applications. Because of the hidden terminal and exposed node problems, it will be difficult to provide the loyal broadcast communication in wireless networks. While vehicles are traveling in the high velocity there will be a huge change in the network topology, which has become a major threat of VANET. The main focus of the VANET MAC protocols [9] is to have a frequent observation of hasty topology changes, when it is using for safety applications, the main aim is to reduce the medium access delay.

B. *Contention-based Protocols*

Here, the nodes which want to communicate will challenge with each other for channel access, and the winning node uses the shared medium for an agreed time. These protocols will be not capable of delivering the messages in the real-time as because there will be no boundless delay. These protocols are applicable at burst network traffic where the effective utilization of bandwidth is feasible. Multimedia applications and real-time traffic applications are not suitable for this method.

The best example for such protocol is CSMA (Carrier Sense Multiple Access). In CSMA [10], before transmitting the information the transmitting device first communicates with the network for avoiding destructions. Collisions will be more in this protocol.

The unbounded delay will occur in packets because of the collision or destruction. For increasing the accessibility the contention based MACS are highly applicable for a vehicle to infrastructure applications. For roadside medium communications MAC protocol is projected. This will perform on the basis of IEEE 802.11. For effective node speed, the DCF will be adjusted in this scheme. If the contention window of each vehicle is increased then there will be a fair access to shared medium. The limitation is that it is not capable of vehicle-to-vehicle communication.

The contact time is very less in this type of communication. The speed of other nodes will not be determined continuously in this type of communication. IEEE 802.11e is capable of providing the various priority levels which are capable of allowing the high priority packets accessing first and the lower priority next. The main disadvantage of this protocol is that if the count of the vehicles increases then the efficiency of the protocol will be reduced. Distribute coordinate function (DCF) and Enhanced Distributed Channel Access (EDCA) is some of the forthcoming standards [11] as MAC. These standards play a major role in future inter-vehicular communications.

C. Contention-Free Protocol

These are also named as controlled access protocols. The medium accessing is preallocated with the help of the access techniques like TDMA (Time Division Multiplexing Access) and FDMA (Frequency Division Multiplexing Access). If the nodes are not competing for the channel accessibility then they are said to be contention free MAC protocols. Each TDMA protocol uses a particular method for assigning the time slots. Definitive allocation of time slot suffers from underutilization of bandwidth. With this explicit allocation of time slot, MAC is capable of providing effective Quality of Service (QoS) [12]. One of the major disadvantages is that this protocol needs a central entity for giving the lawful distribution of channel resources between the nodes.

The user first explains how to make the clusters, based on the direction of the vehicles that means all the vehicles moving in one direction comes under the part of one cluster. In every cluster, one node is preferred as a Cluster Head (CH) and the other all are mentioned as Clustered Members (CM) who can communicate directly with cluster head CH. If any CM identifies about an accident then it directly informs the CH. The CH centralizes all the texts coming from the CM's and then transmits the information to all the members. The acceptance of the message will be documented by the acknowledgment. Every cluster member who is receiving the information makes the acknowledgment and that ACK in its next frame.

If any of the members is not receiving the message, then other member nodes who have received the message can work as a potential helper and preserve the list of nodes that haven't received the messages and gives that information to the CH. By this process, the achievement of safety messages reliability will be high. This process mainly works with the help of the spread spectrum technique [13] which is capable of simultaneously sending the information over a single channel communication.

D. Hybrid MAC Protocols

Multichannel Token protocol (MCTRP) is one of the hybrid MAC protocol. The main objective of this protocol is to decrease the delay while sending the messages. This happens when the nodes are organized independently into the passing rings of the token. If the type of token passing mechanism is from the TDMA basis it has a capability of controlling the medium access during the intra ring transmissions. CSMA/CA will be used as a control medium for inter ring transmission.

There are many drawbacks to MCTRP. If the leader node is unreachable in topology then the functioning of the complete ring gets collapsed. It has to be reinitiated for the ring association. This technique is most suitable for the vehicles which are moving on a platoon form. Here, the data transformation will be done through TDMA whereas the token passing takes place from CSMA. If there is a presence of heavy loads, it can lead to an unbounded delay for the safety messages.

For the location information and external timing purpose, the device needs GPS. There will be an inefficient transmission as because the information is not being transmitted from the node, as per the vehicle two radios will be maintained in this protocol and a complete transmission slot will be allocated for the individual radio. The clustering based multichannel MAC is having the similarities from the MCTRP proposed by Su et al.

E. Applications of VANET

- Safety applications
 - ✓ Hazardous location warning
 - ✓ Vehicle to vehicle cooperative awareness

- ✓ Sign extension
- Traffic-related applications
- ✓ Intelligent traffic flow control
- ✓ Vehicle to vehicle merging assistance

III. Broadcasting Scheme

The directional antennas with broadcasting technique [14] are used for dispersing the information to the required destination in development of R-EBDR (Reliable EBDR). The main target of it is to concentrate on the transmission range adjustment of vehicles.

A. Transmission Range Adjustment Vehicles

Here each node transmission range is adjusted by multiplying the authentic value with a coefficient named as adjustment coefficient. The adjustment coefficient will be similar for all the nodes of the vehicles. The alert message will be originated from the sender, from this the coefficient gets computed, then the relay nodes helps in the performance of the broadcast operation. The parameters which are used for calculating the transmission [15] range are as below:

Considering the first node (as the creator of the information), the message is broadcasted with an angle θ and a radius x_1 , later it becomes a fixed parameter. The distance from the source to the destination points is considered as z_1 . Then the equation for adjustment coefficient is taken as:

$$C = \frac{x_1}{z_1} \dots \dots \dots (1)$$

The node_i transmission range is adjusted and is considered as x_i , the calculation is done by a rule as

$$x_i = C * z_i$$

when the vehicle comes nearer to the destination node z_i , then the transmission range goes on reducing by using the above equation, it comes to zero approximately. It makes the propagation of the message to be easily blocked. Due to this issue, the other participating nodes gets unreachable, cant able to propagate the required information to the destination point.

For overcoming this issue, the minimum value of the transmission range x_{min} is considered as a least possible threshold value, so that all the nodes are capable of maintaining a greater or equal transmission radius to this value. The minimum transmission node value x_{min} is confided in the local density of nodes δ_i which is calculated by each relaying *node*_i in the network. The *node*_i local density is expressed as:

$$\delta_i = \frac{C_{connectivity}^i}{\pi * x_i^2}$$

$C_{connectivity}^i$ = the number of direct neighbors

By using the beaconing mechanism the above equation can easily be modified as

$$(x_{min}^i)^2 * \frac{\theta}{2} * \delta_i \approx 1$$

By substituting the $x_{min}^i \approx q\theta * \frac{2}{\delta_i}$ then equation above can be rewritten as

$$x_i = \max(x_{min}^i * C * d_i)$$

The above-obtained equation gives a perfect non-zero dynamic transmission range for the communicating nodes of the vehicles.

Initially, the performance of the proposed transmission range adjustment technique is examined with a vehicular network. Then the value obtained is again compared with a previous EBDR value. Then the Matlab based simulation tool is developed for performing the simulation [16] in real time application.

This will mainly concentrate on the bandwidth and the power utilization. This reduces the interferences and makes the average number of implicated nodes as less as possible, so that makes an efficient end-to-end reachability.

B. Technique in Real Vehicular Road Network

The investigation process happens by taking a real-time road-based network simulation [17]. For making this simulation process the following assumptions are taken into consideration:

1. An idea MAC layer with the absence of conflict and destruction are to be assumed.
2. The initial transmission nodes of all nodes should be equal and its value is considered to 200m.
3. The limitation of the vehicles ranges from 250 to 1000.
4. The beam forming angle is varied between 22.5 to 135 degrees.

The simulation configuration values are taken as below

Parameter	Value
Number of vehicles	from 250 to 1000
Beamforming angle θ	from 11.25° to 120°
Initial distance z_1	1500m
Initial transmission range x_1	200m
Coefficient C	0.13

Simulation Configurations

The two main scenarios which are taken into consideration are Fixed and Dynamic transmission ranges [18] used for beam forming broadcasting process. The initial transmission range should be equal to the fixed radius of the fixed technique.

IV. Proposed Algorithm

To establish communication between the inter vehicle and vehicle to the server it needs a channel. To access a channel following procedure is followed.

Step 1: Declare the vehicle model and channels.

Step 2: For each vehicle, generate the model parameters:

- Speed
- Mode
- Initial pos
- Inout
- Assigned channel

Step 3: For each second Check if the vehicle is not yet reached the network or inside the network.

Step 4: update the position of the vehicles for every second.

Step 5: When vehicle position is in between 900 to 1100.

Step 6: If the vehicle is already online it goes to communication monitoring. Comm_monitoring is a function what we want to communicate.

Step 7: Else, Send_Req to send is a function assigned to Clear to Send.

Step 8: if channels are available to establish a communication channel

Step 9: Else, Vehicle is kept in a queue variable in which it stores the vehicle number.

Step 10: when vehicle position is greater than 1100, this indicates the vehicle exits the network.

Step 11: Channel occupancy count decremented by one.

Step 12: the free channel is a variable which stores the assigned channel number

Establish communication to the first vehicle in the queue.

A. Flow Chart

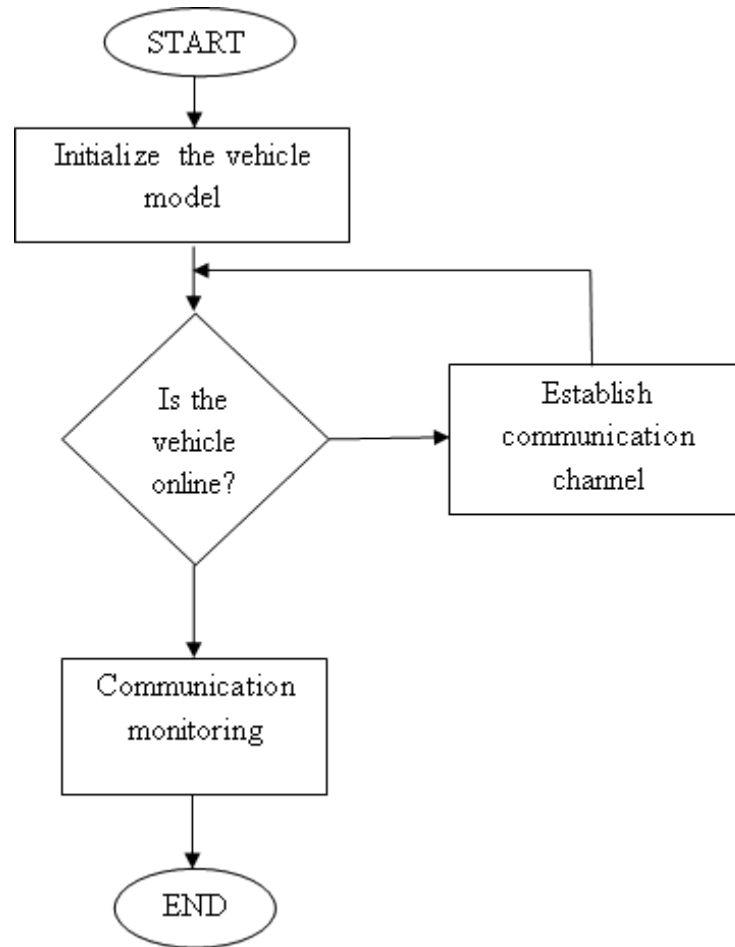


Figure 1: Flowchart of the Proposed Model

B. Description of Flow Chart

- Declare vehicle model and channels
- For each vehicle, generate the model parameters:
 - speed
 - mode
 - initial_position
 - inout
 - assigned_channel
- For each second
- Check if the vehicle is not yet reached the network or inside the network
- update the position of the vehicle for every second
- When vehicle position is in between 900 to 1100
- If the vehicle is already online it goes to communication monitoring. Communication is a function what we want to communicate.
- Else
- Send_Request To Send is a function assigned to Clear To Send
- if channels are available
- establish a communication channel

- Else
- The vehicle is kept in a queue variable in which it stores the vehicle number
- when vehicle position is greater than 1100, This indicates the vehicle exist in the network.
- Channel occupancy count decremented by one
- The free channel is a variable which stores the assigned channel number.

Establish communication to the first vehicle in the queue.

C. Advantage

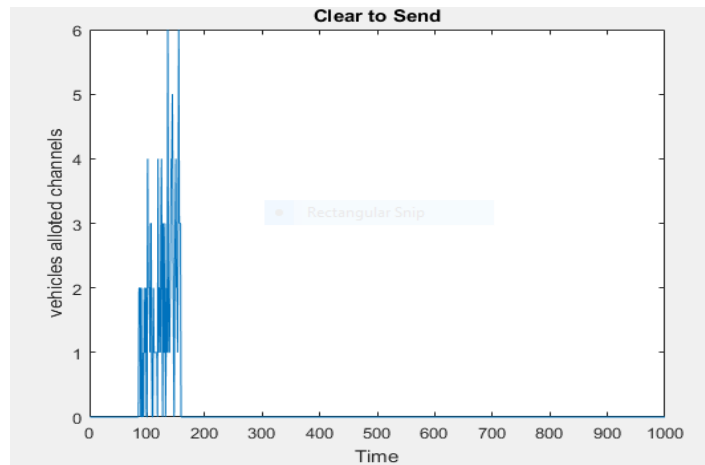
- We can avoid a collision.
- We can track the stolen vehicle.
- The Government will have total information about the vehicles.
- Will have the information about traffic density in a particular network.
- We can secure data by proper encryption technique.

D. Disadvantages

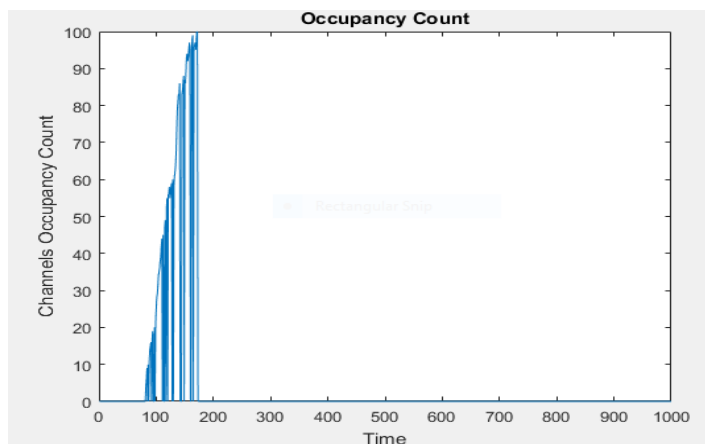
If there is no vacant channel then the vehicle has to wait for some time.

V. Results

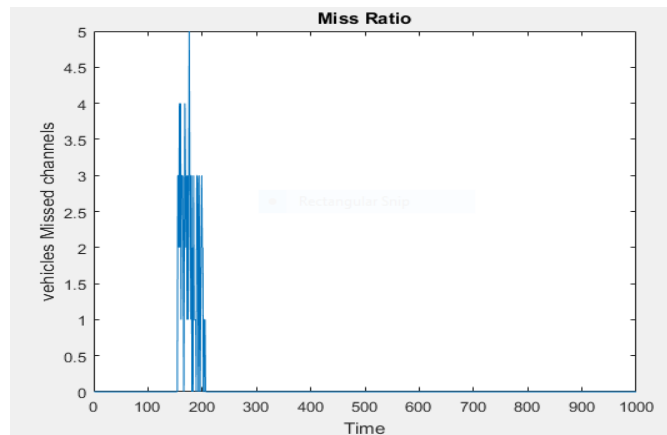
Time vs. Vehicles allowed channels: When the vehicle enters the network it request a channel to establish a communication if all the channels are free then the server will show Clear to Send. Below figure shows a Time vs. Vehicle allowed.



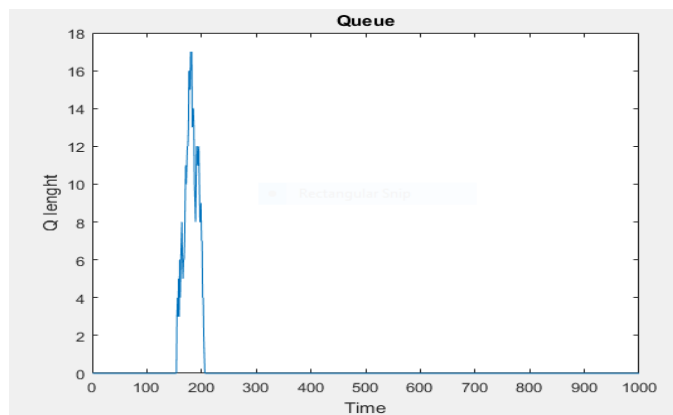
Time vs. Channel Occupancy Count: Below figure shows Channels Occupancy Count. As the number of vehicles increases the channel occupancy count increases.



Time vs. Vehicles Missed Channels: When the vehicle enters the network it sends a request to the server then it checks all the channels. If all the channels are busy and the vehicle does not get any channels when it is in the network then we consider it as Miss Ratio. Below figure shows Time vs Vehicle vs Missed Channels.



Time vs. Queue Length: When the vehicle enters the network it sends a request to the server then it checks all the channels. If all the channels are busy then vehicle number goes to queue. When another vehicle exit the network then the channel of that vehicle will be assigned to the vehicle which is stayed in the queue. Assigning the channel will be done as the priority level. Below figure shows Time vs. Queue Length.



VI. Conclusion

The architecture of MAC layer protocol in a vehicular network is comparatively challenging because of its continuous variations in topology, vehicle nodes at high-speed movement, infrastructure deficiency, and various quality of service requirements. If the position of the vehicle is in the network range then the functioning of the algorithm begins. The request will be generated from the new vehicle for sending the information or message. If there is any channel availability, channel allocation and communication is initiated. The vehicle will directly go to communication monitoring if it is already online. If there is no availability of the channel then the vehicle will be kept in a queue where the vehicle number and other parameters will be stored. When the channel becomes free, then it communicates with the vehicle which is in a queue first then the others. The main aim of the hybrid protocol is to give fair channel accessibility for transferring the message. It reduces the collision, overall delay and loss of packets.

References

- [1] L. Cao, J. Tian and D. Zhang, “Networked Remote Meter Reading System based on Wireless Communication Technology”, proc. of IEEE International Conference on Information Acquisition, China, August 2006.
- [2] R. Sugumar, A. Rengarajan, and C. Jayakumar, “Trust based authentication technique for cluster based vehicular ad hoc networks (VANET),” Wireless Netw., pp. 1–10, 2016.

- [3] C. Prehofer and C. Bettstetter, "Self-organization in communication networks: principles and design paradigms," *Communications Magazine*, IEEE, vol. 43, no. 7, pp. 78 – 85, July 2005.
- [4] S Cheng, Z Cai, J Li, H Gao, Extracting kernel dataset from big sensory data in wireless sensor networks. *IEEE Trans. Knowl. Data Eng.* 29(4), 813–827 (2017)
- [5] L. Moreira-Matias, J. Gama, M. Ferreira, J. Mendes-Moreira, and L. Damas, "Predicting taxi-passenger demand using streaming data," *IEEE Trans. Intell. Transp. Syst.*, vol. 14, no. 3, pp. 1393–1402, Sep. 2013.
- [6] J.N. Al-Karaki, A.E. Kamal, Routing techniques in wireless sensor networks: a survey, *IEEE Wireless Commun.* 11 (6) (2004) 6–28
- [7] X. Chen, D. W. K. Ng, W. Gerstaecker, and H-H. Chen, "A survey on multiple-antenna techniques for physical layer security," *IEEE Commun. Surveys Tuts.*, doi: 10.1109/COMST.2016.2633387.
- [8] H. Omar, W. Zhuang, and L. Li, "VeMAC: A TDMA-based MAC protocol for reliable broadcast inVANETs," *IEEE Trans. Mobile Comput.*, vol. 12, no. 9, pp. 1724–1736, Sep. 2012.
- [9] F. Lyu, H. Zhu, H. Zhou, W. Xu, N. Zhang, M. Li, and X. Shen, "Ss-mac: A novel time slot-sharing mac for safety messages broadcasting in vanets," *IEEE Transactions on Vehicular Technology*, vol. PP, no. 99, pp. 1–1, 2017.
- [10] J.P. Monks, V. Bharghavan and W.M.W. Hwu, A power controlled multiple access protocol for wireless packet networks, in: *Proc. INFOCOM 2001* (April 2001)
- [11] Z. Tao and S. Panwar, "Throughput and delay analysis for the IEEE 802.11e enhanced distribute channel access," *IEEE Trans. Commun.*, vol. 54, no.8, pp. 596-603, Apr. 2006.
- [12] W. Liu, W. Lou, X. Chen, and Y. Fang, "A QoS-enabled MAC architecture for prioritized service in IEEE 802.11 WLANs", *Proc. IEEE GLOBECOM'03*, Vol.7, pp.3802-3807, Dec. 2003.
- [13] M.Z. Win, R.A. Scholtz, Ultra-wide bandwidth time hopping spread-spectrum impulse radio for wireless multiple-access communication, *IEEE Trans. Commun.* 48 (4) (2000) 679–689.
- [14] A. Nasipuri, S. Ye, and R.E. Hiromoto, "A MAC Protocol for Mobile Ad Hoc Networks Using Directional Antennas," *Proceedings of the IEEE Wireless Communications and Networking Conference (WCNC)*, 2000
- [15] R. Perez P´erez, C. Luque, A. Cervantes, P. Isasi, ´ Multi-objective Algorithms to Optimize Broadcasting Parameters in Mobile Ad-hoc Networks, *IEEE CEC*, pp. 3142-3149 , 2007.
- [16] W. Wang, D. Zhao, J. Xi, and W. Han, "A learning-based approach for lane departure warning systems with a personalized driver model," *arXiv preprint arXiv: 1702.01228*, 2017.
- [17] J. Nzouonta, N. Rajgure, G. Wang, and C. Borcea, "VANET Routing on City Roads using Real-Time Vehicular Traffic Information" *IEEE Transactions on Vehicular Traffic Information*, in press, 2009.
- [18] W.-P. Chen, J. Hou, and L. Sha, B Dynamic clustering for acoustic target tracking in wireless sensor networks, [*IEEE Trans. Mobile Comput.*, vol. 3, no. 3, pp. 258–271, Jul.-Aug. 2004.

Implementation of Low Power and Memory Efficient 2D FIR Filter Architecture

Venkata Krishna Odugu, C Venkata Narasimhulu, K Satya Prasad

Abstract: A memory efficient design is analyzed to derive a low power-area-delay two dimensional (2D) Finite Impulse Response (FIR) filter architecture. The parallel processing concept is introduced in the fully direct-form 2D FIR filter. Due to this, memory reuse is carried out, and it reduces the overall storage memory of the FIR filter. The non-separable 2D FIR filter structure is designed and implemented with block size L and filter length N . The high speed and power efficient multipliers and optimized Carry Look Ahead (CLA) adders are used in the arithmetic module of the FIR filter and a pipelined adder unit is used for the final computation of the filter output. The switch level modification in the logic gates is proposed to reduce the area, power and delay of the adders. This proposed architecture is represented in HDL code and validation is carried out in CADENCE environment using NC Simulator and RTL Compiler synthesis tool. The area, power and delay reports are generated and compared with existing memory efficient 2D FIR filter hardware structures. The power is reduced to 44% and delay is reduced by 20% using Modified CLA (MCLA) adders and pipelining in the design.

Index Terms: 2D-FIR, low power Multiplier, Parallel prefix adder, CLA, and memory reuse.

I. INTRODUCTION

In the two-dimensional signal processing such as image, video processing applications and for bio-medical signal processing [1], 2D digital filters are most frequently used. In the biometric systems, for feature extraction [2] and face recognition purpose [3] 2D filters are desired. The two-dimensional concept can be applied for both FIR and Infinite Impulse Response (IIR) filters, but 2D FIR filters are more popular than IIR filters in terms of stability and simplicity of the design.

A. Related Work

To implement a memory efficient and less hardware complexity 2D FIR architecture, some investigations are carried out on existing structures. The symmetry 2D filters are discussed in [4]. The hardware metrics analysis and VLSI (Very Large Scale Integration) architectures for several symmetrical IIR and FIR filters are presented. Here, the un-symmetry frequency response is decomposed into sub components after that desired symmetry is obtained. This research paper provides four-fold symmetry IIR and FIR filters with less number of multipliers. In [5], the generalized formulas are defined to derive the new 2D VLSI filter

architectures using sub filter blocks with local interconnection framework without any global broadcasting. In this work, FIR filter with quadrant symmetry and IIR filters with separable denominators are realized with the advantage of less number of multipliers. Many systolic architectures are implemented for 2D FIR filters to achieve optimization in an area, power, and delay. Few papers are considered to examine the concept of 2D Filters. In [6], the new systolic transformation technique and modified reordering schemes are accomplished to implement 2D systolic FIR and IIR filters. Due to the combinations of these two techniques, lower quantization error, local broadcast, zero latency, and satisfactory critical paths are achieved. Another systolic transformation based on reordering of delay elements and summations, a new VLSI systolic array FIR and IIR filter structures [7] are realized. In this, a detailed logic gate level structure is presented with low latency, local broadcast with an accepted number of multipliers and delay elements. A bit level VLSI architectures for one dimensional and 2D filter are discussed in [8]. These structures are regular, modular and also compatible with other dedicated systems. In this work, hardware utilization and throughputs are improved with less latency. These structures are good enough for optimization due to structure modularity and simplicity. These existing structures consist of many delay or storage elements in the data path to overcome the global signal broadcast. Memory complexity is a major issue in existing structures. The memory complexity affects the area occupancy and power consumption of the structure [9]. A memory-centric 2D FIR filter in non-separable and separable models are proposed in [10] with some penalty of power and delay. In this structure, through-put increased L - times when compared with previous works, but the hardware modules also increased to L times. The high number of hardware modules increases the area and power consumption. In this paper, a memory efficient 2D FIR filter with low power-area, and low delay architecture is proposed. In the proposed work, block based input processing is used for the reduction of memory storage and to achieve memory reuse in the fully direct-form 2D FIR filter. In the fully direct-form structure, the registers are placed in an input data path only, whereas in fully transpose-form the registers are placed in the intermediate signal level [10]. The fully direct-form structure is converted into an optimized block-based architecture with memory reuse. The architecture consists of the arithmetic module and memory modules. The arithmetic module consists of a functional unit (FU) and adder block. In the FU, the important module is a multiplier which consumes more power and requires more hardware resources.

Revised Manuscript Received on May 22, 2019

Venkata Krishna Odugu, Electronics & Communication Engineering Department, Research Scholar JNTUK, Kakinada, India.

C. Venkata Narasimhulu, Electronics & Communication Engineering Department, Geethanjali College of Engineering and Technology, Hyderabad, India.

K. Satya Prasad, Rector, Vignans Foundation for Science, technology & Research, Guntur, India

Implementation of Low Power and Memory Efficient 2D FIR Filter Architecture

In this paper, the optimization is carried out in order to prune the power consumption, delay, and area of the multiplier. Always a compromise is required between the power consumption and speed of the multiplier. In the VLSI design, dynamic power is the major part of the total power consumption. The dynamic power is reduced in the multiplier by the reduction of the switching activities.

In this work, a new multiplier is used named as Bypass Zero Feed Multiplicand Directly (BZ-FMD) multiplier to reduce the power and to improve the speed of the structure. This multiplier is modified version of Bypass Zero, Feed A Directly (BZ-FAD) multiplier [11]. The switching activities and hardware blocks are reduced in this existing multiplier. Due to this multiplier, the total dynamic power of the proposed FIR filter is reduced.

The performance of the multiplier is further improved using a parallel prefix adder for the fast addition of partial products. This fast parallel prefix adder is based on the high-speed adder logic of CLA. A modification is taken place in the conventional CLA to optimize the addition process with respect to speed, area, and power. These Modified CLA (MCLA) are also used for the final addition of the filter.

The optimized MCLA adders are used instead of normal Ripple Carry Adders (RCA) in the FU and adder block to improve the speed and power reduction of the FIR filter. The pipelined addition process is carried out using MCLAs for the computation of the final addition of the FIR filter. The MCLA adders and pipelining concepts are reducing the power consumption and delay of the entire filter structure.

The Transmission Gate Logic (TGL) is proposed to implement the all logic gates required for the implementation of adders. TGL can reduce the number of transistors each gate and improves the speed of the circuit.

The designing of a non-separable 2D FIR filter to avoid the redundancy in computations of the filter is presented in section II. Section III describes the proposed architecture of block based 2D FIR non-separable filter and sub modules implementation. Synthesis results and conclusions are explained in section V and section VI respectively.

B. Background Work

The 2D FIR filters can be represented and implemented in two ways, such as separable and non-separable. The general equations (1) and (2) represents 2D FIR separable and non-separable filters respectively:

$$H(z_1, z_2) = \sum_{l=0}^{N-1} \sum_{k=0}^{N-1} h(l, k) z_1^{-l} z_2^{-k} \quad (1)$$

$$H(z_1, z_2) = \sum_{l=0}^{N-1} \sum_{j=0}^{N-1} h_1(i).h_2(j).z_1^{-i}z_2^{-j} \quad (2)$$

Where, $h(l, k)$ is the coefficient matrix of the non-separable FIR filter and $h(i), h(j)$ are one-dimensional impulse responses of a separable FIR filter.

The basic separable and non-separable 2D FIR filter block diagrams are represented in Fig.1. Memory complexity and hardware logic blocks such as adders and multipliers required for the conventional design of the non-separable filter is high. From (1) the non-separable 2D FIR filter with a size of $(N \times N)$ requires $(N - 1)$ shift registers, each shift register size

is $M, (N - 1)^2$ registers for the processing of a column of the input image $(M \times M)$. The hardware blocks, N^2-1 adders, and N^2 multipliers are required. In this paper, the conventional structure is modified to reduce the complexity.

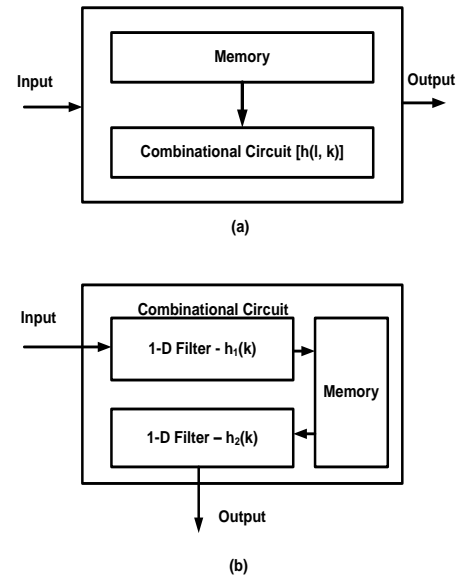


Fig. 1. Conventional (a) separable and (b) non-separable 2D FIR filters.

II. DESIGN OF NON-SEPARABLE 2D FIR FILTER

The basic equation (1) of a non-separable FIR filter can be rewritten as follows:

$$H(z_1, z_2) = \sum_{l=0}^{N-1} z_1^{-l} H_l(z_2) \quad (3)$$

$$H_l(z_2) = \sum_{k=0}^{N-1} h(l, k).z_2^{-k} \quad (4)$$

The above equations (3) and (4) of 2D FIR non-separable filters can be implemented in a fully direct form structure or fully transpose form structures as shown in Fig. 2. The fully direct form of the 2D FIR filter requires less number of memory elements. The memory of a fully direct-form 2D FIR filter is independent of intermediate signal width bits. All delay elements are placed in the input path of architecture only. This is a useful feature to reduce memory [10]. The fully transform-structure memory depends on intermediate signal widths. The intermediate signal width is more than the input signal width. The same number of delay elements and arithmetic components are required for these two structures. The word length of the input and intermediate signals are different, so the overall memory of the two structures is different in terms of bits. The Table I shows the estimated memory of two structures, with a filter length of $N = 8$, the input image size is 512×512 , the input signal width $b = 8$, and an intermediate signal width $d = 16$. The fully direct structure requires less memory as per Table I.

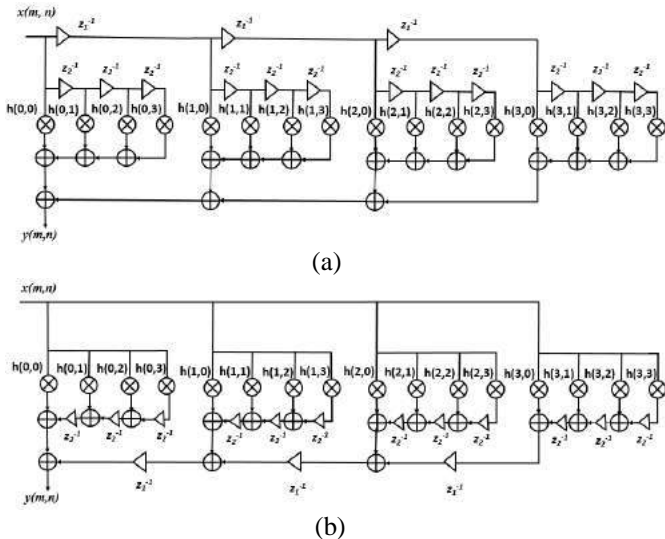


Fig. 2. (a) Fully Direct form structure and (b) Fully Transpose form structure.

Table.I Comparison of Memory requirement for fully-direct and fully transpose forms

Name of the structure	Shift Register-Words		Total Memory Bits	Memory Bits
	Input signal memory	Intermediate signal memory		M=512, b=8, N=8, d=16
Fully- direct form structure	(M+N)(N-1)	0	(M+N)(N-1)b	29120
Fully-transpose form structure	0	(M+N)(N-1)	(M+N)(N-1)d	58240

A. Memory Reuse

The fully direct-form structure is considered for the design of proposed 2D FIR filter architecture. The input data flow of the direct-form structure is analyzed to explore the reusing of memory in the FIR filter. For understanding the memory reuse concept, the redundancy of input samples for the filter length N = 4 as shown in Fig.3. If the mth row output computation is considered, then the outputs are {y(m,n), y(m,n+1), y(m,n+2), y(m,n+3)}. For the 4 x 4 filter, 16 input samples are required with respect to 4 columns and 4 rows of 2D input as shown in Fig.3. The shift registers and Serial-In-Parallel-Out (SIPO) Shift Register Blocks (SRB) are used to give past samples of rows and columns respectively.

The data flow of a fully direct structure represents, the 28 samples out of 64 samples are different and the remaining 36 samples are redundant. These redundant samples corresponding to the outputs {y(m,n), y(m,n+1), y(m,n+2), y(m,n+3)} are highlighted in the Fig.3. The parallel computation or using block-based structure the redundancy can be avoided in direct form structure. For the determination of the particular output, past sample values are required. These past samples can be retrieved from the SRBs in every clock cycle [10].

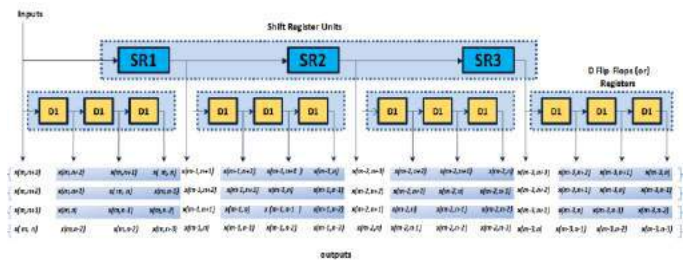


Fig.3. Data flow in the fully direct form structure for N=4 with four outputs { y(m,n), y(m,n+1), y(m,n+2), y(m,n+3)}, [10].

B. Block formulation of the Non-separable 2D FIRFilter

In this section, the block-based non-separable filter design equations are derived. The block size L, input samples are processed and generate the L output samples in every clock cycle. The output equation of non-separable FIR filter for mth row is given by,

$$y_{m,k} = \sum_{i=0}^{N-1} V_{i,k} \tag{5}$$

Where y_{m,k} is the final output the filter represented by,

$$y_{m,k} = [y(m, kL) \ y(m, kL - 1) \ \dots \ y(m, kL - L + 1)]^T \tag{6}$$

and V_{i,k} is an intermediate vector defined as,

$$V_{i,k} = [v(i, kL) \ v(i, kL - 1) \ \dots \ v(i, kL - L + 1)]^T \tag{7}$$

V_{i,k} is the product of an impulse response matrix with input matrix A_k^{m-i} as given by,

$$V_{i,k} = A_k^{m-i} \cdot h_i \tag{8}$$

Where, A_k^{m-i} is part of the input matrix is given by (9), from (m-i)th row of the image matrix of size 512 x 512.

$$A_k^{m-i} = \begin{bmatrix} x(m-i, k) & x(m-i, kL-1) & \dots & x(m-i, kL-N+1) \\ x(m-i, kL-1) & x(m-i, kL-2) & \dots & x(m-i, kL-N) \\ \vdots & \vdots & \ddots & \vdots \\ x(m-i, kL-L+1) & x(m-i, kL-L) & \dots & x(m-i, kL-N-L+2) \end{bmatrix} \tag{9}$$

The impulse response matrix is given by equation (10),

$$h_i = [h(i, 0) \ h(i, 1) \ \dots \ h(i, N-1)]^T \tag{10}$$

The internal vectors of matrix V_{i,k} are the inner product of impulse response h_i and S_{k,l}^{m-i} is the l-th row of A_k^{m-i} is given by equation (11),

$$v(i, kL-1) = S_{k,l}^{m-i} \cdot h_i \tag{11}$$

III. IMPLEMENTATION OF PROPOSED 2D FIR FILTER ARCHITECTURE

The proposed block-based FIR filter is implemented in a systematic architecture to avoid the redundancy in the data flow of the filter. To avoid redundancy samples, memory reuse concept is carried out and it reduces the overall storage memory with respect to the input data path. The architecture is designed with a block of $L = 4$ and length of the filter $N = 8$.

The non-separable block-based 2D FIR filter architecture is presented in the Fig.4. The equations (5) and (8) are converted into a fully direct-form structure with $L = 4$ parallel inputs. This architecture is comprised of two main modules, such as memory module and the arithmetic module.

Memory module consists of an array of 28 shift registers of $P = 128$ words and 8 input register units (IRU), where $P = M/L = 512/4 = 128$. From 28 shift registers, every 4 registers are grouped and named as SRB. For this architecture, 7-SRBs are required i.e. SRB1, SRB2, ...,SRB7.

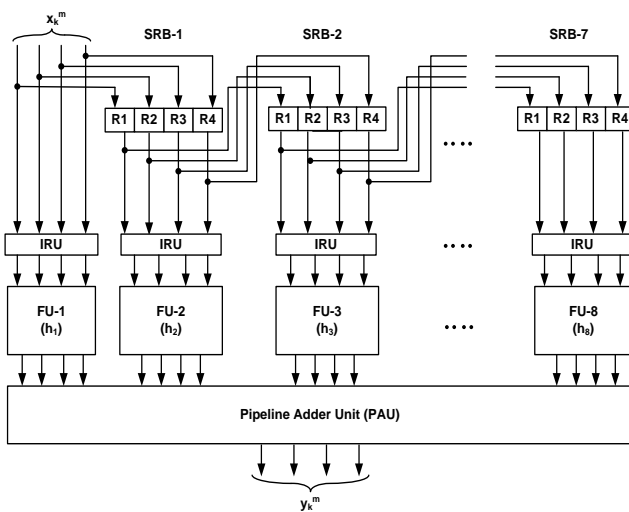


Fig. 4. Block-based non-separable 2D FIR filter architecture.

The block of 4 inputs are applied to the filter and it computes 4 outputs in every clock cycle. Like this, all the inputs from the input image matrix of 512×512 are applied block by block in serial order and generate corresponding outputs [15]. Due to the block based concept, the entire image can be completed in $MP = 512 \times 128$ clock cycles instead of 512×512 cycles. The delay is reduced and throughput increased. In every clock cycle, $N - 1 = 7$ input blocks are corresponding to $N - 1 = 7$ consecutive input rows are obtained from the SRB unit.

The 7-past input blocks and current input block samples are applied to 8-IRUs. The internal register arrangement corresponding of redundancy avoiding logic is shown in Fig.5 for $L = 4$ and $N = 8$. It consists of $(N - 1) = 7$ registers or D-Flip Flops to produce 8-point input vectors. The 8-point input vector is a combination of past and current input samples.

The 8 - IRUs generate the matrix of $[A_k]$ is shown in (9) of size 4×8 because $L= 4$ and $N = 8$; The first IRU receives the input samples from the current block and generates the 4×8 matrix, which is applied to the Functional Unit (FU). Similarly, 7 IRUs generates the 4×8 matrices and passed to the corresponding 7-FUs.

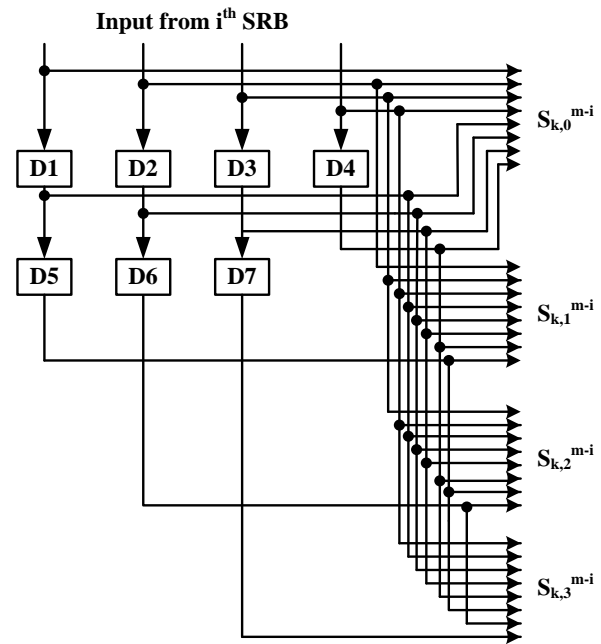


Fig. 5. The internal structure of IRU.

A. Arithmetic module

The first important block in the arithmetic module is FU. Here, $N = 8$ FUs are required to multiply the input vectors and the filter coefficients $[h_i]$. FU receives 4 input vectors from each of 8 IRUs. The $(i + 1)^{th}$ FU receives from $(i + 1)^{th}$ IRU and computes the inner product of the input vector and $(i + 1)^{th}$ row of impulse response matrix. The output matrix of FUs is called as $[V_i]$.

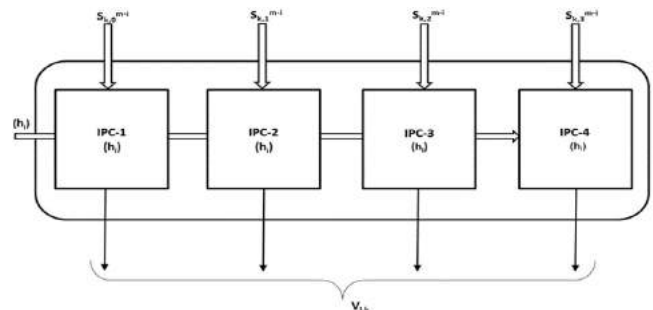


Fig. 6. The Internal block diagram of FU.

The internal structure of FU is shown in Fig.6. FU comprises 4 inner product cells (IPC). IPC is used to multiply the input vectors and corresponding elements of the impulse response matrix. The internal combinational logic of IPC is shown in Fig.7. It produces an 8-point inner product and adds 8 partial products together using an adder circuit.

B. Multiplier Implementation

Each IPC requires N multipliers and $N-1$ adders to produce the product of input samples and coefficients of the filter. The optimized multiplier and adder circuits are described in this section.



The basic multiplication operation consists of two steps, partial product generation and addition of partial products. The dynamic power consumption of multiplier or any circuit depends on the switching activities. Equation (12) represents the general dynamic power in the VLSI circuits.

$$P_{Dynamic} = \alpha \cdot C_L \cdot f_{clk} V_{DD}^2 \quad (12)$$

Where C_L is Load capacitance, f_{clk} is clock frequency, V_{DD} is the power supply and α represents switching activity. The number of switching activities represents the power consumption of the circuit.

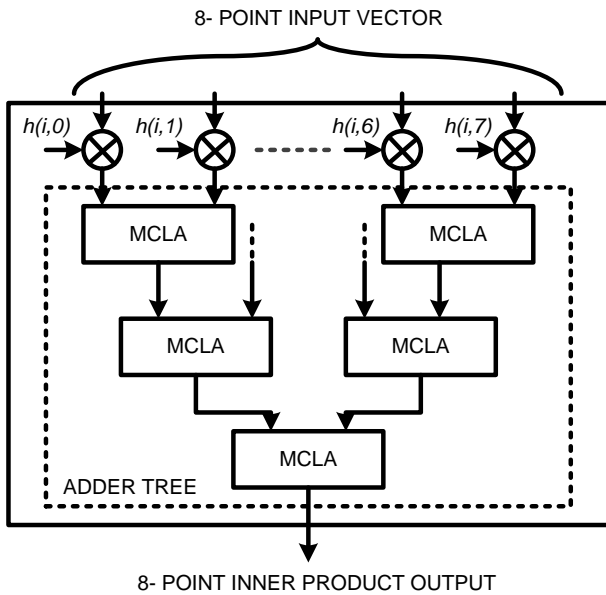


Fig. 7. Internal combinational logic diagram of IPC.

The conventional shift-add multiplier is modified and a new multiplier is developed based on Bypass Zero, Feed A Directly (BZ-FAD) is proposed in [11]. The BZ-FAD multiplier switching activities depends on (i) shifting the bits of multiplier (ii) switching of partial product bits (iii) adder switching activities and (iv) multiplexer switching activities for final addition. For further reduction in delay and to reduce the number of hardware blocks, the BZ-FAD is modified as Bypass Zero, Feed Multiplicand Directly (BZ-FMD) [12].

BZ-FMD multiplier architecture is shown in Fig. 8. It consists of an adder, multiplexer, product register, feed-register, and a controller. In order to reduce delay and area, some components are removed in the BZ-FAD multiplier. Ring counter is replaced with binary counter to reduce the complexity and are placed in the control block.

Initially, the controller checks the multiplier 0th position bit to '0' or '1'. The controller consists of a synchronous binary counter instead of the ring counter, which increments for every clock cycle and selects each bit and checks. The adder, multiplexer, and feed register blocks are completely controlled by the controlling block. The control block controls the feed register data which feeds to adder block or multiplexer.

The multiplier bit decides the output of the multiplexer either it should be feeder register value of a previous partial

product or adder output. The adder processing is skipped for the multiplier bit as '0' and feeder register feeds the previous partial product value directly to the MUX. Otherwise, the sum of multiplicand value and the previous partial product is directly given to MUX. The switching activity required for the zero bit addition is eliminated and directly the multiplicand fed to MUX.

The switching activities regarding shifting of the partial product is also reduced in this multiplier structure. In this multiplier, the higher half partial product bits only shifted right after processing and lower half partial product bits are remained and stored directly in the product register. Conventionally, the entire partial product is shifted right, whereas in proposed multiplier only half of the product bits are shifted. The switching activities for partial product shifting are reduced to 50% in the proposed multiplier.

In the designed multiplier, the switching activities corresponding to shifting of multiplier bits, addition and shifting of partial products are reduced. The reduction in switching activities decreases the major part of the dynamic power consumption. An 8-bit multiplier is implemented in this paper for the multiplication of filter coefficients and input samples.

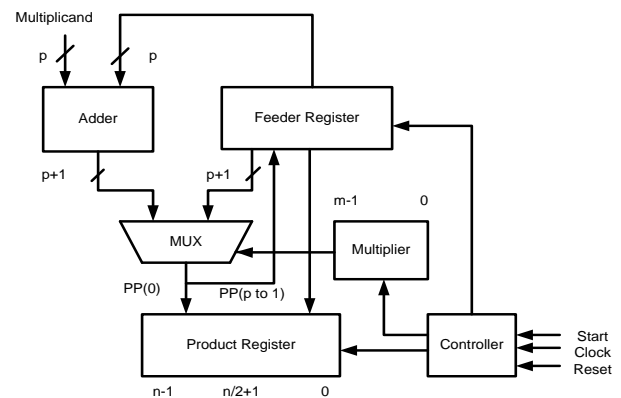


Fig.8. Architecture of multiplier

C. Parallel Prefix adder based on Modified CLA (MCLA)

The multiplication process is a combination of shifting and summation. Many adders are required for higher bit multiplication. Hence, the performance of the multiplier depends on adder also. For the N-tap filter implementation, N number of adders required for the summing of individual tap outputs and to get final filter output. In order to reduce power consumption and delay, the adder optimization is needed. In this section, a high-speed Carry Look Ahead (CLA) adder with necessary modification is described. The CLA equation is modified for the saving of the hardware and further to improve the performance and power saving. In this paper, the 8-bit and 16-bit parallel prefix MCLA adders are presented. The 8-bit MCLAs are used for the addition of partial products in the multiplier and 16-bit MCLA adders are used in adder tree.

Implementation of Low Power and Memory Efficient 2D FIR Filter Architecture

In this Modified CLA (MCLA), a modified carry M_i is determined in the place of conventional carry c_i . After the calculation of propagating and generate terms, a parallel prefix addition concept is used to reduce the time [13].

The modified carry M_i and sum S_i of the MCLA is given by equations (13) and (14) respectively.

$$M_i = g_i + g_{i-1} + p_{i-1} \cdot g_{i-2} + p_{i-1} \cdot p_{i-2} \cdot g_{i-3} + \dots + p_{i-1} \cdot p_{i-2} \cdot \dots \cdot p_1 \cdot g_0 \quad (13)$$

Where g_i and p_i are generating and propagate terms in equation (13). This equation is modified to improve the efficiency of the adder. The real carry is given by equation

$$c_i = M_i \cdot p_i \quad (14)$$

The modified carry for even and odd bit positions are different. The M_i for even and M_{i+1} for odd given by equations (15) & (16),

$$M_i = (G_i^*, P_{i-1}^*) \odot (G_{i-2}^*, P_{i-3}^*) \odot \dots \odot (G_0^*, P_{-1}^*) \quad (15)$$

$$M_{i+1} = (G_{i+1}^*, P_i^*) \odot (G_{i-1}^*, P_{i-2}^*) \odot \dots \odot (G_1^*, P_0^*) \quad (16)$$

After the computation of above-modified carries for even and odd bit positions, the real carry is determined. Using an equation (14). The sum is calculated using the equation (17).

$$S_i = d_i \oplus (p_{i-1} \cdot M_{i-1}) \quad (17)$$

The above carry calculation methods are only used for the lower half of the bits. The upper half of the bits carry is parallel computed as follows. In this method, the modified carry determined using intermediate propagate term and intermediate generate term as given in the equation (18).

$$c_i = (G_{i:k} + P_{i-1:k-1} \cdot G_{k-1:j+1}) \cdot p_i \quad (18)$$

If we consider 16-bit adder, then the carry of the 8th bit is defined as equation (19)

$$M_8 = (G_{8:7}, P_{7:6}) \odot (G_{6:3}, P_{5:2}) \odot (G_{2:-1}, P_{1:-2}) \\ = (G_{8:7} + P_{7:6} \cdot G_{6:-1}, P_{7:6} \cdot P_{5:-2}) \quad (19)$$

The remaining upper half bits carries are determined using the equations from (20) to equation (27).

$$c_8 = (G_{9:8} + P_{7:6} \cdot G_{6:-1}) \cdot p_8 \quad (20)$$

$$c_9 = (G_{9:8} + P_{8:7} \cdot G_{7:0}) \cdot p_9 \quad (21)$$

$$c_{10} = (G_{10:7} + P_{9:6} \cdot G_{6:-1}) \cdot p_{10} \quad (22)$$

$$c_{11} = (G_{11:8} + P_{10:7} \cdot G_{7:0}) \cdot p_{11} \quad (23)$$

$$c_{12} = (G_{12:7} + P_{11:6} \cdot G_{6:-1}) \cdot p_{12} \quad (24)$$

$$c_{13} = (G_{13:8} + P_{12:7} \cdot G_{7:0}) \cdot p_{13} \quad (25)$$

$$c_{14} = (G_{14:7} + P_{13:6} \cdot G_{6:-1}) \cdot p_{14} \quad (26)$$

$$c_{15} = (G_{15:8} + P_{14:7} \cdot G_{7:0}) \cdot p_{15} \quad (27)$$

The above modified CLA equations are considered [13] and an 8-bit and 16-bit parallel prefix adders are implemented and shown in the Fig.9 and Fig.10 respectively.

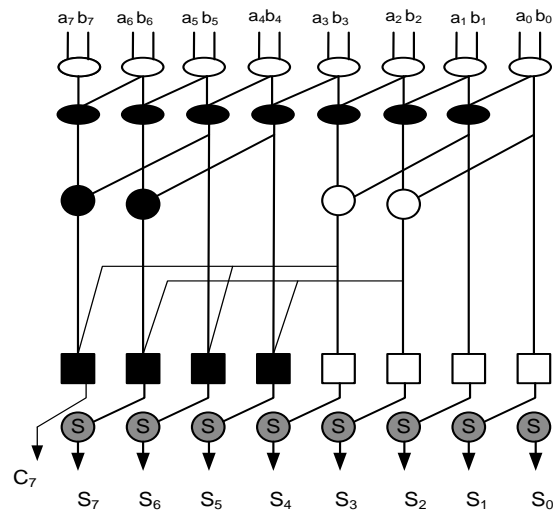


Fig.9. The 8-bit parallel prefix MCLA adder for multiplication

The logic cells required for the parallel prefix summation of 8-bit and 16-bit adder structures are shown in the Fig.11. All the logic cells are implemented by AND, OR and XOR logic gates.

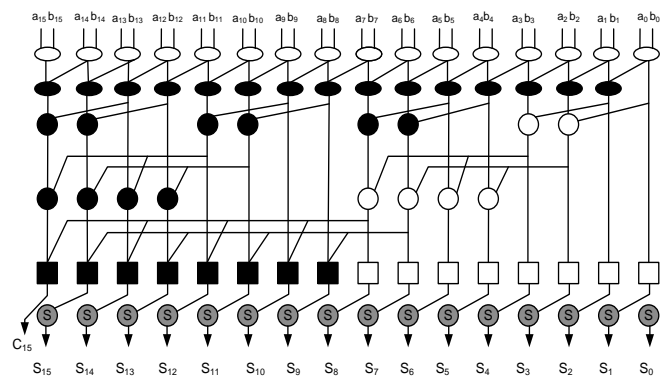


Fig.10. The 16-bit Parallel Prefix MCLA adder for filter outputs summation.

The implementation of each logic cell at transistor level is focused. The conventional CMOS logic is replaced with Transmission Gate Logic (TGL). The TGL logic reduces the number of transistors for the implementation of gates. The TGL AND/OR gates are shown in the Fig.12. The CMOS logic gates requires 4 transistors and whereas TGL gates can be implemented using 3 transistors only. Hence, total number of transistors for adder implementation is reduced thereby decreasing the switching activity and power dissipation. An 8-bit adder requires totally 48 AND/OR gates. Each gate is constructed by 4 transistors by conventional CMOS logic then totally 192 transistors are required. The TGL AND/OR gates used total of 144 transistors only. The area saving is 25% in one 8-bit adder.

This optimization can increase the area saving for higher bit adders. If transistors count reduced then power consumption also reduced in each adder and multiplier. The overall 2D FIR filter area and power saving is improved by TGL gates.

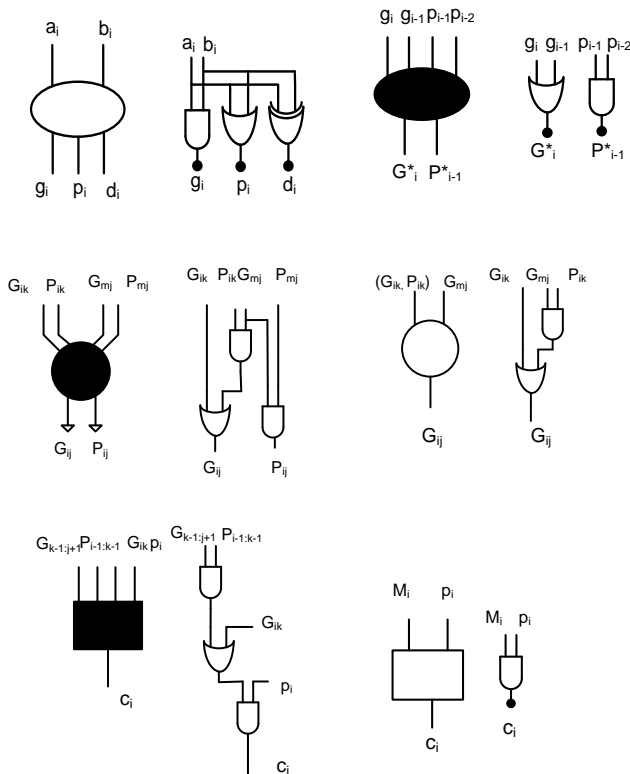


Fig. 11. Internal logic cells are used in MCLA adder

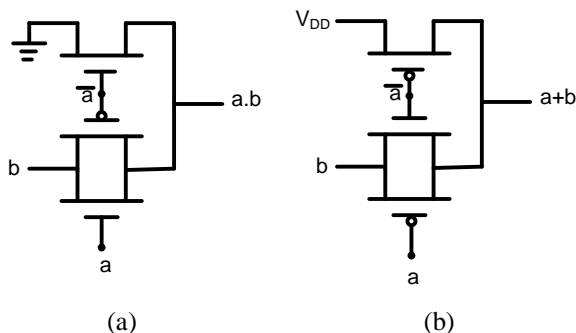


Fig. 12. (a) TGL-AND gate (b) TGL-OR gate.

The adder block consists of a special type of adder, i.e. MCLA. The MCLA adders are arranged in tree form is called as Adder Tree (AT) and used to compute the addition of IPC.

The final adder block of the FIR filter to produce an output of the filter which is the second block in the arithmetic module is designed as pipeline adder is called Pipeline Adder Unit (PAU). The PAU consists of D-FFs and MCLAs to do the final addition of the vectors from the FUs. The internal view of the PAU is presented in Fig. 13. The input data path is optimized by parallel processing and final output computation is pipelined. Pipelining and parallel processing are used to reduce the power consumption and reduce the critical path delay of the VLSI architectures [14, 15].

The output per one input block of 4 samples takes one clock cycle. Each clock cycle is defined using a minimum

clock period, which depends on all arithmetic blocks delay. The clock period for this architecture is $T = T_M + T_{PAU} + T_{MCLA}(2\log_2 N - 1)$, where T_M is one multiplier computation time, T_{PAU} is the time required for the PAU and T_{MCLA} is a delay of the MCLA adder in the adder tree. The single row of the input image takes 128 clock cycles and the entire image matrix can be completed in 128M cycles, where $M =$ image matrix size = 512.

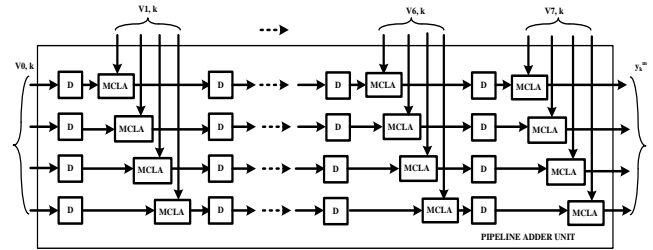


Fig. 13. Pipeline Adder Unit (PAU) of 2D FIR structure

IV. SYNTHESIS RESULTS

The block based non-separable structure comprises of $LN^2 = 4 \times 64 = 256$ multipliers and $L(N^2 - 1) = 4 \times 63 = 252$ MCLAs and $[(M + N)(N - 1)] = 512 + 8 \times 7 = 28672$ registers. This structure generates 4 outputs per each clock cycle. The memory reuse efficiency of non-separable structure is $L - 1 = 3$, and memory bandwidth per output (MBWPO) is $(L + N)(N - 1) / L = 21$. The MBWPO is 3 times less than the existing structures [10].

The proposed 2D FIR filter design is coded in HDL for block size $L = 2$ and 4 and filter sizes $N = 4$ and 8. The code is simulated in the 'NCSim' simulator from CADENCE tools. The simulated HDL code is synthesized using Encounter RTL compiler in the TSMC 90nm CMOS technology library from CADENCE tools. The generic building blocks library of the TSMC 90nm CMOS library is used for the synthesis of architecture and D-FFs are used as registers and shift registers. The input sample signal width is considered as $b = 8$ bits and the intermediate signal width is $d = 16$ bits.

The proposed non-separable 2D FIR filter design with a block size of $L = 2$ and 4 and filter lengths $N = 4$ and 8 is compared with existing 2D FIR filter architectures in Table II. For the comparison purpose $N=4$ with block size $L = 4$ FIR filter is also implemented. Fig.14 represents the power comparison plot of the proposed design with existing 2D FIR filter architectures.

Table II. Comparison of the area and power parameters of different non-separable FIR filter architectures ($L = 4$)

Structure	Length of the filter (N)	Area (μm^2)	Power (mW)		
			Static	Dynamic	Total
Proposed Non-separable	4	34166	0.3424	3.0834	3.4258
	8	55186	0.5766	4.3634	4.9401
Khoo [5]	4	1009878	3.9107	4.9441	8.8548
Mohanty et al [10]	4	791361	2.8016	3.2918	6.0934

Implementation of Low Power and Memory Efficient 2D FIR Filter Architecture

The total power for filter length $N=4$ is reduced by 44% comparatively structure [10], and even the length of the filter is increased to 8, the total power saving is 20% compared [10]. The proposed design power reduction is 62% compared with the structure of [5]. The area saving is more than the existing architectures as shown in Table II. The Table III shows the comparison between the Non separable FIR filter power with block sizes $L = 2$ and 4 for different filter orders $N = 4$ and 8.

Table. III Comparison of power for block size $L=2$ and 4

Structure	Length of the filter (N)	Input Block Size	Area (μm^2)	Power (mW)		
				Static	Dynamic	Total
Proposed Non-separable FIR filter	4	2	20182	0.2032	1.6233	1.8265
		4	34166	0.3424	3.0834	3.4258
	8	2	28602	0.2342	2.4869	2.7211
		4	55186	0.5766	4.3634	4.9401

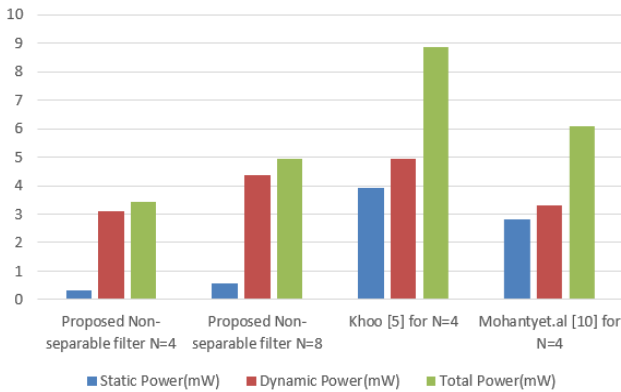


Fig.14. Graphical Comparison of power between proposed and existing structures.

The proposed design is investigated with MCLA adders used in multiplier and in the adder block and the same design with normal CLA adders in RTL compiler synthesis tool. The estimated synthesis results are shown in Table IV. The total power is reduced by 52% with MCLA adders with the area penalty of 2% only. The graphical comparison of power, area, and delay for the proposed design with MCLA and CLA is represented in Fig. 15 and Fig.16 respectively.

Table.IV. Comparison of the area, power and delay parameters with MCLA and with CLA in 2D FIR filter.

Design	Length of the filter (N)	Power (mW)			Area (μm^2)	No. of Cells	Delay (ps)
		Static	Dynamic	Total Power			
Proposed filter (with MCLA)	4	0.3424	3.0834	3.4258	34166	5770	783
	8	0.5766	4.3634	4.9401	55186	10793	887
Proposed filter (with CLA)	4	0.4869	5.7487	6.2356	38546	6206	956
	8	0.3997	9.8979	10.297	58574	12986	1109

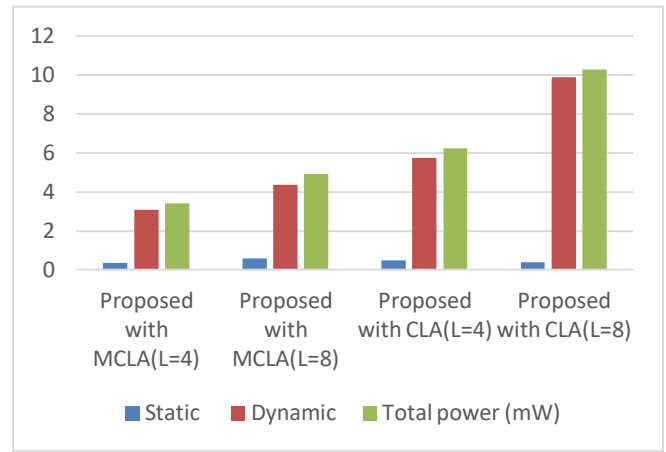


Fig.15. Comparison graph of power for the proposed design with MCLA and with CLA

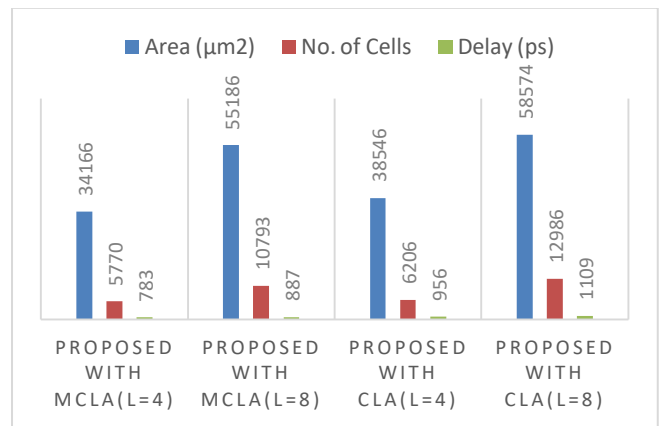


Fig.16. Comparison graph of area and delay for the proposed design with MCLA and with CLA for $N=8$

V. CONCLUSION

A systematic design is implemented to achieve low power, area and delay memory efficient 2D FIR non-separable filter architecture. The concurrent evaluation of output is achieved using block-based concept, so that throughput is increased to L times. The storage memory is reduced using memory reuse in fully direct form structure. The proposed filter design is implemented using low power BZ-FMD multiplier with parallel prefix adders. The MCLA addition concept is used to implement parallel prefix adder. Adder cells are optimized in terms of number of transistors to reduce the area, power and delay using TGL gates. The parallel processing and pipelining techniques in the final addition of the filter are used to reduce power consumption and critical path of the entire filter. The design is validated in two ways, with MCLA with TGL gates and with CLA adders. The power and area results of the non-separable 2D FIR filter with MCLA are better than the existing FIR structures. The input image is considered as 512×512 , the input block size is $L = 2$ and 4, and filter length is $N = 4$ and 8 for the implementation of the architectures, and design is elaborated and synthesized in RTL Compiler tools from TSMC 90nm CMOS library.



The 2D FIR Filter structure with proposed MCLA adders consumed 50% less power than the normal 2D FIR filter with 20% reduced delay. The experimental results show that the proposed architecture is better than the existing memory efficient architectures in terms of area, delay, and power.

REFERENCES

1. H. Mohammadzade, L. T. Bruton, "A simultaneous div-curl 2D Clifford Fourier Transform filter for enhancing vortices, sinks, and sources in sampled 2D vector field images," in Proc. IEEE International Symposium on Circuits and Systems, May. 2007, pp. 821-824.
2. T. Barbu, "Gabor filter based face recognition technique," in Proc. Rmanian Acad. Ser. A, 2010, vol. 11, no. 3/2010, pp. 277-283.
3. S. E. Grigorescu, N. Petkov, and P. Kruizinga, "Comparison of texture features based on Gabor filters," *IEEE Trans. Image Process.*, vol. 11, no. 10, pp. 1160-1167, Oct. 2002.
4. P. Y. Chen, I. D. Van, H. C. Reddy, and C. T. Lin, "A new VLSI 2-D four-fold-rotational-symmetry filter architecture design", in Proc. IEEE Int. Symp. Circuits Syst. (ISCAS), May 2009, pp. 93-96.
5. I. H. Khoo, H. C. Reddy, L. D. Van, and C. T. Lin, "Generalized formulation of 2-D filter structures without global broadcast for VLSI implementation", in Proc., *IEEE MWSCAS, Seattle, WA, USA*, Aug. 2010, pp. 426-529.
6. L. D. Van, "A new 2-D systolic digital filters architecture without-global broadcast", *IEEE Trans. Very Large Scale Integr. Syst.*, vol. 10, no. 4, pp. 477-486, Aug. 2002.
7. Van. Lan-Da, et al. "A new VLSI architecture without global broadcast for 2-D digital filters." 2000 *IEEE International Symposium on Circuits and Systems. Emerging Technologies for the 21st Century. Proceedings (IEEE Cat No. 00CH36353)*. Vol. 1. IEEE, 2000.
8. Mohanty, B. K., and P. K. Meher. "High throughput and low-latency implementation of a bit-level systolic architecture for 1D and 2D digital filters." *IEE Proceedings-Computers and Digital Techniques* 146.2 (1999): 91-99.
9. B. K. Mohanty and P.K. Meher, "A high-performance FIR Filter Architecture for Fixed and Reconfigurable Applications", *IEEE Trans. On VLSI Systems*, vol. 24, issue 2, pp. 444-452, 2016.
10. B. K. Mohanty and P.K. Meher, and A. Amira, "Memory Footprint Reduction for Power-Efficient Realization of 2-D Finite Impulse Response Filters", in *IEEE Trans Circuits Syst. I*, vol. 61, no. 1, Jan. 2014.
11. M. Mottaghi-Dastjerdi, A. Afzali-Kusha, and M. Pedram, BZ-FAD: A low-power low area multiplier based on shift-and-add architecture, *IEEE Trans. Very Large Scale Integration (VLSI) Systems*. (2009) 302-306.
12. Pinto, Rohan, and Kumara Shama. "Low-Power Modified Shift-Add Multiplier Design Using Parallel Prefix Adder." *Journal of Circuits, Systems and Computers* 28.02 (2019): 1950019.
13. Poornima N and V S KanchanaBhaaskaran, Area efficient hybrid parallel prefix adders, *J. Procedia Materials Science*. 10 (2015) 371-380.
14. A. P. Vinod and E.M. Lai, "Low power and high-speed implementation of FIR filters for software defined radio receivers" *IEEE Trans. Wireless Commun.*, vol. 7, no. 5, pp. 1669-1675, Jul. 2006.
15. O. Venkata Krishna, C. VenkataNarasimhulu and K. Satya Prasad "Design and Implementation of Block Based Transpose Form FIR Filter" in *IJCA*, Issue 8 Volume 1, Jan-Feb. 2018.

AUTHORS PROFILE



Mr. Venkata Krishna Odugu received B.Tech degree in Electronics and Communication Engineering from Acharya Nagarjuna University, 2004 and Master of Technology with specialization VLSI System Design from JNTU Hyderabad in 2009 and pursuing Ph.D. from JNTU Kakinada in the area of VLSI Signal Processing. Interested areas are VLSI Design and VLSI Signal Processing etc.



Dr. C. Venkata Narasimhulu received B.Tech degree in Electronics and Communication Engineering from S V University, Tirupathi in 1995 and Master of Technology in Instrumentation & Control Systems from REC, Calicut in 2000 and Ph.D. from JNTU, Kakinada in 2013 in the area of signal Processing. He has published more than 25

technical papers in national and international Journals and Conferences. His interested areas are Signal Processing, Image processing and medical image processing etc.



Dr. K. Satya Prasad received B Tech. degree in Electronics and Communication Engineering from JNTU college of Engineering, Anantapur, in 1977 and M. E. degree in Communication Systems from Guindy college of Engg. , Madras University, in 1979 and Ph.D from Indian Institute of Technology, Madras in 1989. He has published more than 139 technical papers in different National & International conferences and Journals and Authored one Text book. His areas of Research include Communications Signal Processing, Image Processing, Speech Processing, Neural Networks & Ad-hoc wireless networks etc.



Rice Grains Categorization using Neural Network

Dr. C V Narasimhulu¹, K. Divya Bhanu², P. Ludhiya³, G. Harish⁴

¹Professor Department of ECE Geethanjali College of engineering and technology

^{2,3,4}Bachelor of technology Department of ECE Geethanjali college of Engineering and Technology

Abstract: Rice is one of the most important food crop consumed by all the human beings. In this paper, an algorithm is used to classify three different varieties of rice based on their features. The proposed algorithm is a supervised learning algorithm which consists of five steps. The steps include image acquisition, image segmentation, feature extraction, neural network classifier and decision making. Fifty four color features and six texture features are extracted from each rice kernel. After passing these features to feed forward neural network, it identifies and counts the different types of rice kernels and displays the result. The overall classification accuracy rate is 98%.

Keywords: Acquisition, segmentation, neural network

I. INTRODUCTION

In the current grain-handling systems, grain type is assessed by visual inspection. The evaluation process for this is tedious and time consuming. The decision making capability of a person can be affected by different parameters like fatigue, eyesight and mental state caused by biases and work pressure and also working conditions such as improper lighting condition, etc. Hence, this needs to the automation of process by developing an imaging system that should acquire the rice grain images, rectify, and analyze it. In this project, we propose a simple, effective and high accuracy vision-based approach using pattern recognition techniques to identify rice varieties. The specific goal was to generate the optimal color and texture features for classifying the rice varieties with increased accuracy rate.

A. Software Components

- 1) Operating system: Windows XP/7
- 2) Coding Language: MATLAB
- 3) Tool: MATLAB R2015b

B. Proposed Method

In the proposed method, a new approach for classification of rice kernels variety using Feed-Forward Neural network is presented. Here three varieties of rice grains are taken namely Basmati, Masoori and Raw rice grains and the features of each type are calculated and trained to neural network.

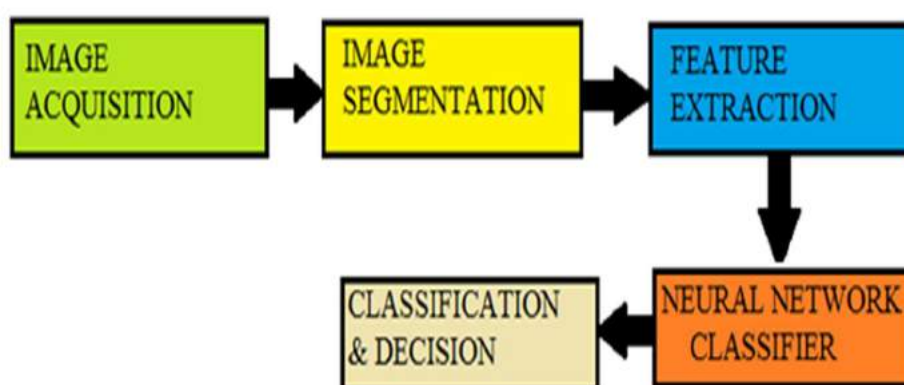


Fig 1: Block Diagram

The block diagram shown in figure-1 illustrates the procedure for recognition and classification of rice grains. It consists of following steps: Image Acquisition, Image Segmentation, Feature Extraction, Neural Network Classifier and Classification & Decision.

C. Working

The input image is first converted in to gray image and then to binary image as shown in figure 2.

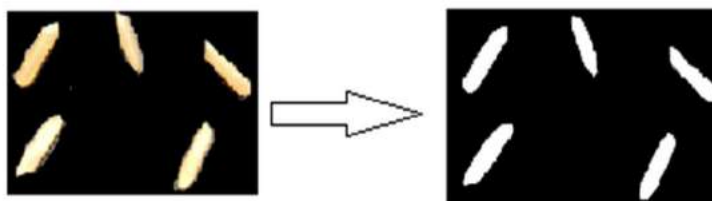


Fig 2: Image Acquisition & Conversion

During image segmentation, all the rice kernels in the image are segmented by thresholding as shown in figure 3.



Fig 3: Image Segmentation

The features are then extracted for each rice kernel and passed to neural network. The neural network then identifies and counts the number of different rice varieties as shown in figure 4. Based on the highest count, it displays the result in command window.

MATLAB Workspace 3 Apr, 2019	
Name ^	Value
<input checked="" type="checkbox"/> binaryImg	2250x4000 logical
<input type="checkbox"/> calregionProps	33x1 struct
<input type="checkbox"/> colorTransform	1x1 struct
<input type="checkbox"/> count_basmati	3
<input type="checkbox"/> count_masoori	2
<input type="checkbox"/> count_raw	0
<input type="checkbox"/> features	60x5 double

Fig 4: Workspace Window showing count variables

D. Feature Extraction

About fifty four color and six texture features are calculated for each rice kernel.

1) *Color Featues*: Currently the common color models are RGB, HSV, and L*a*b* models. The color features that are extracted from images of individual rice kernels are: Mean, Square of Mean, Standard Deviation, Kurtosis, Variance and Skewness as shown in figure 5. All these features were extracted on R, G and B in RGB color space. Also H, S, and V in HSV color space and luminance, a, and b in L*a*b* color space.

KURTOSIS	$\text{Kurt}[X] = \text{E} \left[\left(\frac{X - \mu}{\sigma} \right)^4 \right]$ (1)
STANDARD DEVIATION	$\sigma = \sqrt{\frac{\sum (X - \bar{X})^2}{n - 1}}$(2)
VARIANCE	$\sigma^2 = \sum \frac{(X - \mu)^2}{N}$(3)
SKEWNESS	$\gamma_1 = \text{E} \left[\left(\frac{X - \mu}{\sigma} \right)^3 \right]$(4)

Fig 5: Color Features Extracted

2) Texture Features: The texture features that are extracted from images of individual rice kernels are shown in figure 6.

- Mean (m): $\sum_{i=1}^{L-1} z_i p(z_i)$ --(5)

- Standard deviation (σ) : $\sqrt{\mu_2(z)}$ --(6)

- Entropy (e): $-\sum_{i=0}^{L-1} p(z_i) \log_2 p(z_i)$ --(7)

- Uniformity (U): $\sum_{i=0}^{L-1} p^2(z_i)$ --(8)

- Third moments: $\sum_{i=1}^{L-1} (z_i - m)^3 p(z_i)$ --(9)

- Smoothness (μ_3): $1 - 1/(1 + \delta^2)$ --(10)

Fig 6: Texture Features Extracted

E. Neural Network Classifier

A neural network is a computing model whose layered structure represent the networked structure of neurons in the brain, with layers of connected nodes. A neural network can learn from data so that it can be trained to classify data. A neural network breaks down the input into layers of abstraction. It can be trained over many examples to recognize patterns in speech or images. Its behaviour is defined by the way its individual elements are connected and by the strength or weights of those connections. These weights are automatically adjusted during training with respect to a specified learning rule until the neural network performs the desired task correctly.

Here Feed-forward artificial neural network is used to classify different varieties of rice grains. It allows signals to travel in one way only that is from input to output. There is no feedback (loops). Feed-forward ANNs are straight forward networks that associate inputs with outputs. They are extensively used in pattern recognition. This type of organisation uses bottom-up or top-down approach.

II. CONCLUSION

An algorithm was developed to identify varieties of rice grains based on their color and texture features. Sixty features were extracted which include fifty four color and six texture features. These features are then passed as inputs to the neural network to classify the rice kernels. In the test dataset, the total classification accuracy rate is 98%. If there is large amount of dataset then accuracy rate increases.

REFERENCES

- [1] Seyed Jaleleddin Mousavi Rad, Fardin Akhlaghian Tab, Kavch Mollazade "Classification of rice varieties using optimal color and texture features and BP Neural Network", IEEE,2011,Sanandaj, Iran.
- [2] Jagdeep Singh Aulakh, Dr. V.K. Banga "grading of rice grains by image processing" International Journal of Engineering Research & Technology (IJERT) Vol. 1 Issue 4, pp 1-4, June – 2012 ISSN: 2278-0181.
- [3] Harpreet Kaur, Baljit Singh "classification and grading of rice grains using multi-class SVM" IJSRP, Volume 3, Issued on 4 April 2013.
- [4] Yugashree Bhadane, Pooja Kadam "Identification and classification of grain using Image processing" IJIRCCE Vol 6 issued on 20 october 2018
- [5] S N. Sivanandam, S Sumathi, S N Deepa "INTRODUCTION TO NEURAL NETWORK USING MATLAB 6.0" McGraw Hill Education, First Edition published on 1 July 2017.
- [6] S N. Sivanandam "ARTIFICIAL NEURAL NETWORK" First Edition, published on 20 August 2003.
- [7] S Jayaraman, S Esakkirajan, T Veerakumar "DIGITAL IMAGE PROCESSING" published on 1 July 2017.
- [8] MATLAB can be downloaded by following the steps in this video <https://youtu.be/WOpjQouVIFg>
- [9] MATLAB can be installed by following the steps in this video <https://youtu.be/xSXW9SkETB4>

DESIGN AND ANALYSIS OF DUAL FREQUENCY PENTAGON SHAPED SLOTTED MICRO STRIP PATCH ANTENNA USING HFSS SOFTWARE

CH SURESH KUMAR,
Assistant Professor in
ECE, Geethanjali College
of Engineering and
Technology, Cheeryal

**RVNR SUNEEL
KRISHNA,**
Assistant Professor in
ECE, Geethanjali College
of Engineering and
Technology, Cheeryal

**K AMITH
NARAYANA,**
Student, Department of
ECE, Geethanjali College
of Engineering and
Technology, Cheeryal.

G UDAY BHASKAR YADAV,
Student, Department of ECE,
Geethanjali College of Engineering
and Technology, Cheeryal.

NAGAM SRIKANTH
Student, Department of ECE,
Geethanjali College of Engineering
and Technology, Cheeryal.

ABSTRACT

In this paper we give the design and analysis of dual frequency microstrip patch antenna. Instead of basic rectangular microstrip patch we introduce a pentagonal slot on the rectangular patch to get perfect impedance matching. Design and Simulation is performed using HFSS software. Obtained results reveal that, choosing a 50 ohm coaxial feed at perfect position the antenna operates at frequencies 7.95GHz and 9.48GHz respectively with corresponding bandwidths of 260MHz and 300MHz.

Different antenna parameters are measured and are compared in contrast with the single pentagonal slot microstrip patch antenna. The antenna has good resonance characteristics.

KEYWORDS: *Microstrip patch antenna, Dual frequency, coaxial feed.*

1. INTRODUCTION

Nowadays the most developing ways of communication is wireless communication. Antennas play a major role in wireless communication. They act as both transmitters and receivers. So, antenna performance is directly

proportional to the efficiency of wireless communication.

In the 1970s antenna technology was looking towards microstrip antennas. By the early 1980s the fabrication of microstrip antenna became quite popular. During the past ten years printed antennas have been largely studied. The advantages of the microstrip antenna is its highly stable structure, less weight, different feeding methods, small size, cost efficiency, compatibility with devices. A general microstrip patch antenna consists of a radiating patch on top of dielectric substrate and a ground plane on the bottom of the substrate. The patch is generally made of conducting material such as copper or gold. The patch is generally made up of a conducting material such as copper or gold and can take any possible shape like rectangular, circular, triangular, and elliptical or some other common shape. The radiation in microstrip antenna is mainly due to fringing fields between the patch edge and the ground plane. In the contacting method, the RF power is fed directly to the radiating patch using a connecting element such as a Micro strip line or probe feed. In the non-contacting scheme,

electromagnetic field coupling is done to transfer power between the Micro strip line and the radiating patch this includes proximity feeding and aperture feeding. They can be designed to have many geometrical shape. Recently even after the introduction various types and shapes of patches rectangular and circular Micro strip resonant patches have been used extensively in many applications.

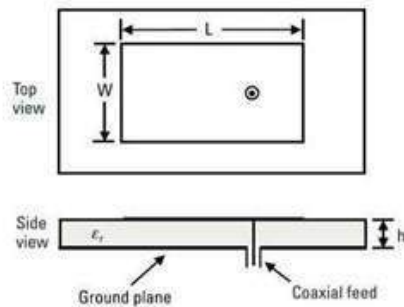


Figure 1: Micro strip patch Antenna

2. MICROSTRIP PATCH ANTENNA

The structure of the proposed antenna is shown in Figure 2.

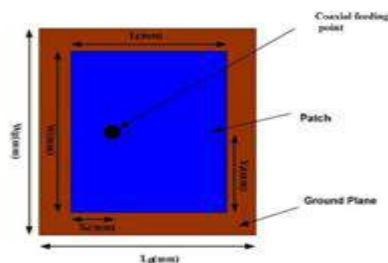


Figure 2: Dimensions of Rectangular patch Micro strip Antenna

Where,

- L=length of the patch
- W=width of the patch
- Lg=length of substrate
- Wg=Width of substrate
- Xf=feed point on x-axis
- Yf=feed point on y-axis

The dielectric substrate used is Taconic TLT. Its dielectric constant is 2.55.

Thickness of the substrate is 0.8mm. Length of the substrate is 1.55cm, Width of the substrate is 1.66cm, Length of patch is 8.9mm, Width of patch is 11mm. The location of the feed point is 2.7mm by 2.2mm on the patch.

3. PHYSICAL PARAMETERS OF ANTENNA

Antenna parameters can be calculated by the transmission line method.

3.1. Width of the patch

The width of the antenna can be calculated by the formula:

$$W = \frac{C}{2f_0 \sqrt{\frac{\epsilon_r + 1}{2}}}$$

3.2. Length of the patch

Length of the patch is given by

$$L = \frac{\lambda_0}{2} - 2\delta L$$

Where, δL is the dimension of the patch along its length that has been extended on each end.

3.3. Feed point

The feed position is given by (X_f, Y_f)

where

X_f and Y_f are given by equations:

$$X_f = \frac{L}{2\sqrt{\epsilon_{reff}}}$$

And

$$Y_f = \frac{W}{2}$$

3.4. Ground Plane Dimension

The ground plane dimensions is given by

$$\begin{aligned} L_g &= 6h + L \\ W_g &= 6h + W \end{aligned}$$

3.5. Antenna Dimensions

The designed parameters and its dimensions are given in table 1:

Table. 1: Antenna dimensions

Parameters	Dimensions
Length	8.9mm
Width	11mm
Thickness	0.8mm
X size	2.7mm
Y size	2.2mm

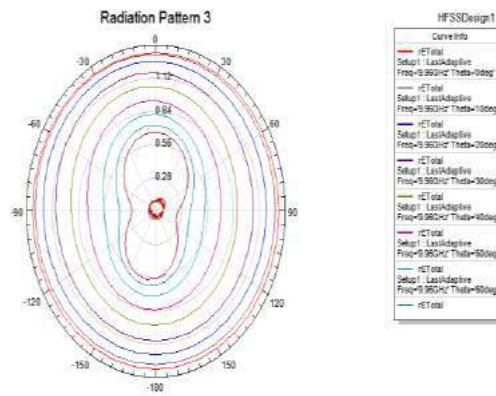


Figure 5: The radiation pattern

4. SIMULATION RESULTS

The antenna is designed using ansoft HFS simulator and the designed antenna is shown in figure 3.

4.1. Radiation Pattern

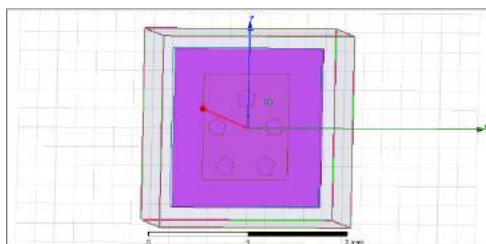


Figure 3: Design of Pentagonal slotted Micro strip patch Antenna

The 3D radiation pattern obtained for the designed antenna is shown in figure 4:

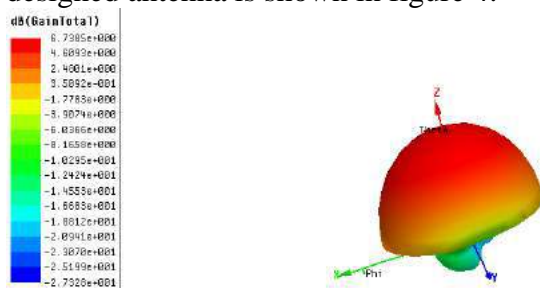


Figure 4: The 3D radiation pattern

4.2. Rectangular Plot

The rectangular plot for the micro strip patch antenna is shown in figure 6. It shows that the designed antenna operates at two frequencies.

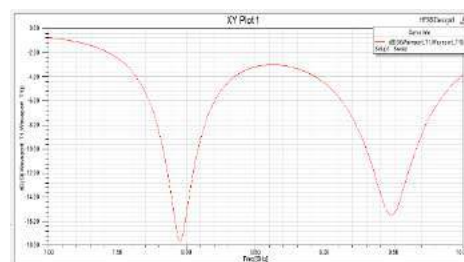


Figure 6: Rectangular plot

4.3. Comparison Table

The obtained parameters of the designed antenna are compared with various other antennas and the comparison results were furnished in table 2.

Table 2: Comparison Table

Properties	Single Pentagon Slot	Pentagon shaped pentagon slots
Operating Frequencies	7.5GHz, 9.11GHz	7.95GHz, 9.48GHz
Gain	8.64dB, 7.86dB	17.1dB, 15.2dB
Bandwidth	7.3GHz-7.9GHz, 8.55GHz-9.6GHz	7.82GHz-8.08GHz, 9.3GHz-9.6GHz

5. CONCLUSION

A pentagonal slotted microstrip patch antenna operates across two different frequencies. The lowest resonant frequency is 7.95GHz with bandwidth 7.82GHz-8.08GHz and highest resonant frequency is 9.48GHz with bandwidth 9.3GHz-9.6GHz. The simple feeding technique is used for the design of this antenna that makes this antenna a good choice in many communication systems in future.

The designed antenna is verified for its performance using Ansoft HFSS simulator and various parameters have been obtained.

REFERENCES.

- [1] LV HONG, Hua ZhiXiang, Sun Dengzhi, "DESIGN OF DUAL-BAND MICROSTRIP ANTENNA" , IEEE 2016 978-1-5090-4743-7/16.
- [2] P Naresh Kumar, CH Suresh Kumar, RVNR Suneel Krishna, "DESIGN AND ANALYSIS OF HIGHLY MINIATURIZED WIDE BAND PATCH ANTENNA", Anveshana's International Journal of Research in Engineering and Applied Sciences, VOL 3 ISSUE 2 (2018 FEB) ISSN-2455-6602.
- [3] Andrenko, I. Ida, T. Kikuzuki, "Dual-band patch antenna with monopole-like radiation patterns for BAN communications", 7th European Conf. on Antennas and Propag. (EuCAP), pp. 1922-1926, 2013.
- [4] Zhen-Hua Huang. Miniaturization of multifrequency research and design of microstrip antenna[D]. Shanghai Jiao Tong university, 2007.
- [5] Y. J. Wang & C. K. Lee, Design of dual-frequency microstrip patch antennas and application for IMT-2000 mobile handsets, Progress In Electromagnetics Research, PIER 36, 265-278, 2002.
- [6] Indra Surjati, "Dual Frequency Operation Triangular Microstrip Antenna Using A Pair of Slit, " 2005 Asia-Pacific Conference on communications, Perth Western Australia, 3-5, pp.124-126, October 2005.

An Effective Low Power Frequency Synthesizer for On-Chip Clock Generation

Thakur Sneha Maheshsingh¹, O.V.P.R. Shiva Kumar², B. Hari Kumar³

¹M.Tech, ECE, Geethanjali College of Engineering & Technology, Keesara Mandal, HYD, TS

²Professor, M.Tech, ECE, Geethanjali College of Engineering & Technology, Keesara Mandal, HYD, TS

³Professor & HOD, PHD, ECE, Geethanjali College of Engineering & Technology, Keesara Mandal, HYD, TS

Abstract: The variability and leakage current in nanoscale CMOS technology may debase the circuit exhibitions altogether. To suit the above issues in a wide-run stage locked circle (PLL), a self-healing prescaler, a self-healing voltage-controlled oscillator (VCO), and an aligned charge pump (CP) are displayed. This PLL is created in a 65-nm CMOS technology and its dynamic zone is 0.0182 mm. For the self-healing VCO, its deliberate recurrence run is from 60 to 1489 MHz. At the point when this PLL works at 855 MHz, the deliberate rms and crest to-crest nerves are 8.03 and 55.6 ps, separately. The deliberate reference goad is - 52.89 dBc. This PLL devours 4.3 mW from 1.2 V supply without supports. The proposed structure includes an engineering joining a LC quadrature voltage-controlled oscillator (VCO), two example and-holds, a stage interpolator, advanced coarse-tuning and rotational recurrence recognition for tweaking. Like multiplying delay-locked loops (MDLLs), this design limits jitter gathering to one reference cycle, as jitter amid one reference cycle does not add to the following reference cycles. Additionally, rather than utilizing multiplexer switches normally utilized in MDLLs, the reference clock edge is infused by stage interjection to help higher frequencies and

lower jitter. Usefulness of the recurrence synthesizer is approved between 8– 9.5 GHz, LC VCO's scope of activity. First-request dynamic of the procurement has been broke down and shown through estimation. The yield clock at 8 GHz has a coordinated rms jitter of 490 fs, top to-crest intermittent jitter of 2.06 ps and all out rms jitter of 680 fs. Diverse parts of jitter have been examined and separate estimations have been done to help the analysis.

Keywords: nanoscale CMOS technology, Leakage Current, clock multiplier, frequency synthesizer, interpolation.

1. INTRODUCTION

At the point when a CMOS technology ways to deal with a nanometer scale, the non-idealities [1], [2], for example, variability and leakage current, may altogether influence the circuit exhibitions. The procedure variability prompts the huge varieties to debase the gadget coordinating and exhibitions. It might result in just a couple of passes on a wafer to meet the objective execution details. The undesired leakage currents additionally debase the precision and goals of simple circuits and make advanced powerful circuits not to work appropriately [3], [4]. For a pMOS transistor

with 8 m 0.06 m in a 65-nm process, its source and entryway are associated with the supply voltage of 1.2 V. Fig. 1 demonstrates its reenacted channel current versus the channel voltage under various corners. The channel current, i.e., leakage current, is 687 nA, 0.12 uA, and 21 uA for the normal, moderate, and quick corners, separately, and 40 C. The leakage current is exceptionally reliant upon the procedure varieties. Demonstrates the reenacted channel current under various corners and the temperatures with a steady 1.2 V. The leakage current becomes quick in a high temperature condition. Regular multiplying stage locked circle (MPLL) engineering, appeared in Fig., has been the overwhelming design in this field for a long time [2]– [8].

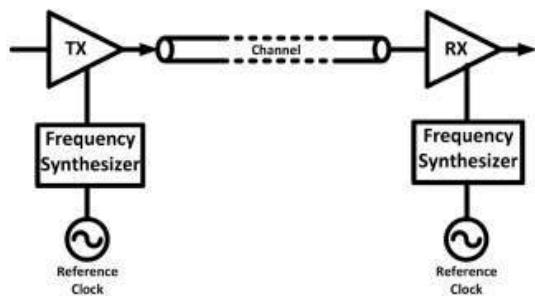


Fig. 1. Basic elements of a high-speed serial link.

PLLs are engaging for use as frequency synthesizers because of their low unpredictability and in light of the fact that their engineering can bolster a programmable augmentation rate. All the more as of late, delay-locked loop (DLL)- based frequency synthesizers have been under investigation [9]– [15].

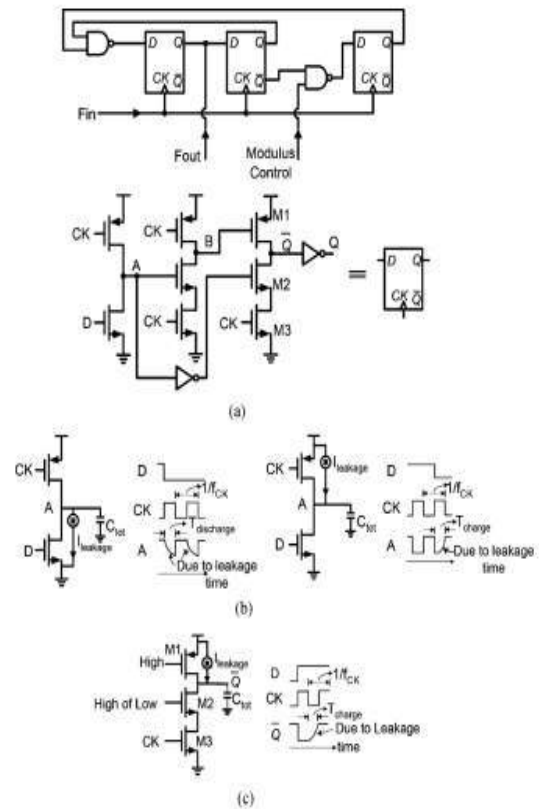


Fig. 2. (a) Conventional divide-by-4/5 dual-modulus prescaler using TSPC DFFs [7]. (b) Two kinds of malfunctions occurred at A. (c) The malfunction occurred at Q.

A traditional MPLL shows higher jitter than a multiplying DLL (MDLL) with same structure squares and clamor condition because of higher jitter amassing. In the MPLL of, a stage variety in the period of the ring oscillator gets incorporated over numerous cycles until the loop channel can react while it just motivations a consistent balance in a DLL. These outcomes in a significantly bigger pinnacle stage mistake for a customary PLL contrasted and DLL. Diminishing jitter collection, which has roused this work, is especially essential in frameworks with vast computerized exchanging commotion where a perfect reference is accessible. Preceding showing the proposed design, we

quickly audit other clock multiplying models and especially those that smother jitter collection.

Wide frequency extend limit the swaying frequency scope of a VCO and causes a VCO not to waver in a most pessimistic scenario. To understand a wide-go PLL, the divider following a VCO ought to work between the most elevated and least frequencies. At the point when a PLL works at a higher frequency which the static circuits can't work, dynamic circuits are required. A genuine single-stage timing (TSPC) divider is broadly used to understand a prescaler for this PLL. A TSPC prescaler must work over a wide frequency range to cover the procedure and temperature varieties. For a TSPC prescaler, the undesired leakage currents may restrict its frequency run or modify the first conditions of the drifting hubs to have a glitch. The leakage current and current bungle in a charge pump (CP) will debase the reference goad and jitter fundamentally. To relieve the above issues, a self-healing partition by-4/5 prescaler and a self-healing VCO are exhibited in this paper. An opportunity to-computerized converter (TDC) and a 4-bit encoder are utilized to quantize the stage mistake and carefully adjust the CP.

The fundamental activity of this framework can be broken into three primary components.. To begin with, we clarify the task of PI-based reference infusion. At that point, the calculation for computerized coarse tuning is examined. At long last, subtleties of calibrating rotational

frequency location are clarified. The PI-based reference infusion strategy is the quadrature tickers (and), with discretionary period of our inspected at the rising edges of the reference clock (and). These examples are then used to introduce between and utilizing the stage interpolator.

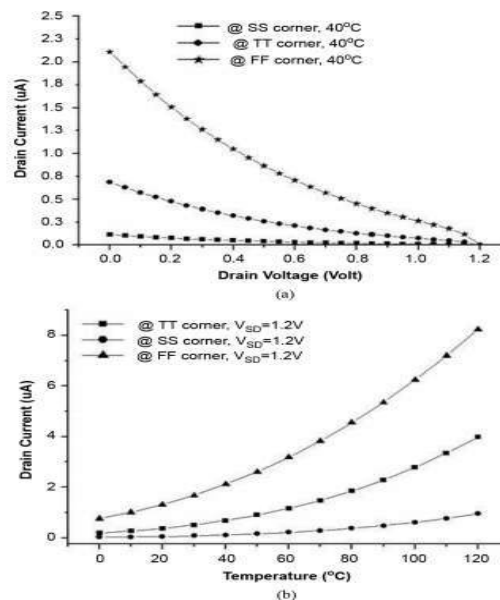


Fig 3: The simulated drain current versus (a) the drain voltage and (b) temperature for a PMOS with its source and gate connected to 1.2 V

2. PROPOSED SYSTEM

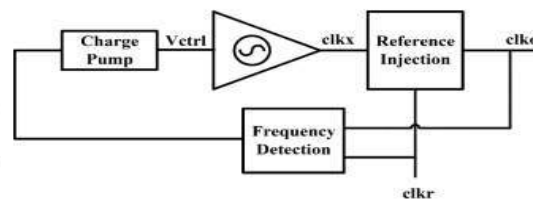


Fig 4: first-order frequency synthesizer.

Besides, there are different measurements that can be the bottleneck of frequency synthesizer's execution relying upon the application. For

instance jitter topping, which is the intensification of jitter exchange work over a specific frequency band, presents itself in customary second-request PLLs with a shut loop zero. Jitter topping in clock dissemination systems with a few PLLs or DLLs can cause critical execution debasement. Hence, a few systems have been proposed to limit or totally wipe out jitter cresting by evacuating the shut loop zero. Note that jitter cresting is portrayed by exchange capacity of reference to yield while jitter collection can be depicted as how the yield clock reacts to commotion on the control line of the VCO. Shows how particular sorts of MDLLs experience the ill effects of jitter topping while they display jitter amassing just amid one reference period. Another class of frequency synthesizer models is those abusing infusion locking. Infusion locked PLLs (ILPLLs), multiplying infusion locked oscillators (MILOs) are instances of such engineering. In the event that the characteristic running frequency of the VCO is near the n th consonant of the reference frequency, the VCO will bolt to that symphonious with the end goal that yield frequency progresses toward becoming N times the reference frequency. There is a key distinction between reference infusion wonders occurring in MDLL and ILO-based frequency synthesizers. While having a perfect reference a MDLL can totally clear jitter amassing each reference cycle, in ILO-based frequency synthesizers decrease in jitter gathering relies upon infusion quality and it achieves its pinnacle

when infused flag has a similar frequency as the characteristic frequency of the oscillator. Since PVT varieties can veer off characteristic frequency of an oscillator from frequency of intrigue, infusion locking may happen at the edge of the locking range with minor decrease in jitter gathering. For compelling infusion bolting, the VCO's common frequency must be held extremely near the n th consonant of the reference clock. In this manner, a different loop is important to change the VCO's common frequency. An elective methodology for decrease of jitter aggregation is displayed in this paper. This design straightforwardly infuses the rising edge of the reference clock to the yield clock, resetting jitter aggregation like a MDLL. Likewise, first-request frequency location and frequency adjustment is utilized, giving unqualified security. The main request frequency synthesizer engineering furnishes programmable clock increase with decreased jitter aggregation contrasted and regular PLLs and without difficulties in creating a select flag for open gap in a multiplying DLL [9], [12]. This engineering uses a stage interpolator (PI) based reference infusion proposed in for a burst-mode CDR application. PI-based reference infusion gives high-frequency feed-forward reference infusion without utilizing a MUX as in MDLLs [12]. As opposed to ILO-based reference infusion, in the PI-based reference infusion jitter amassing concealment does not debase as reference digresses from the VCO's common frequency (the yield rising edge is

viably supplanted with the reference rising edge). Additionally, not at all like MDLLs, the proposed engineering can use both a LC oscillator and inverter-based ring oscillator, contingent upon application and jitter prerequisites. In the model introduced in this paper, a LC VCO has been utilized for low stage clamor exhibition. Frequency securing is accomplished by a low-control usage of rotational frequency indicator, related to a computerized coarse-tuning. Reference of the proposed design must be kept clean since any jitter on this flag will pass legitimately to the yield. Since the execution of this frequency synthesizer is exceptionally subject to the nature of the reference clock, notwithstanding electrical reference clock, as an additional component, the model chip is equipped for accepting a low jitter optical reference clock created by a high-redundancy rate mode-locked laser. Additionally, any nonlinearity in the plan of reference infusion causes an efficient jitter at the yield clock. Along these lines, cautious regard for the plan of the example and-holds and stage interpolator for reference infusion is required. The proposed frequency synthesizer is actualized in a 65-nm CMOS technology. It works with a reference check in the scope of 400 MHz to 1 GHz to create a yield motion in the scope of 8– 9.5 GHz. The model is completely tried with electrical reference clock and its execution is estimated.

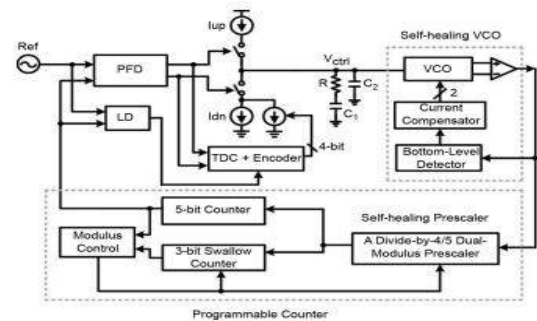


Fig 5: Programmable Counter

3. RELATED WORK

As complementary metal– oxide– semiconductor (CMOS) advances are downsized into the nanometer go, various real nonidealities must be tended to and defeat to accomplish an effective simple and physical circuit structure. The idea of these non idealities has been all around announced in the specialized writing. They incorporate hot transporter infusion and time-subordinate dielectric breakdown impacts constraining supply voltage, stress and lithographic impacts restricting coordinating exactness, electro movement impacts restricting transmitter lifetime, leakage and versatility impacts restricting gadget execution, and chip control dispersal limits driving individual circuits to be more vitality productive. The absence of simple plan and reenactment apparatuses accessible to address these issues has turned into the focal point of a huge exertion with the electronic structure computerization industry. Post layout recreation apparatuses are not valuable amid the structure stage, while technology PC helped plan physical reproduction devices are moderate and not in

like manner use by simple circuit fashioners. In the nanoscale period of simple CMOS plan, a comprehension of the physical elements influencing circuit unwavering quality and execution, just as techniques for alleviating or beating them, is winding up progressively critical. The initial segment of the paper presents factors influencing gadget coordinating, including those identifying with single gadgets just as neighborhood and long-remove coordinating impacts. A few dependability impacts are talked about, including physical structure constraints anticipated for future downscaling. Sometimes, it might be useful to surpass foundry-determined channel source voltage constrains by a couple of hundred millivolts. Models are introduced for accomplishing this, which incorporate the reliance on the state of the yield waveform. The condition $V_{sb} > 0$ is required for cascode circuit designs. The job of other terminal voltages is examined, as $V_{sb} > 0$ increments both hot and cold transporter harm impacts in exceptionally scaled gadgets. The second piece of the paper centers around patterns in gadget attributes and how they impact the structure of nanoscale simple CMOS circuits. Various circuit plan methods utilized to address the major non idealities of nanoscale CMOS innovations are examined. Precedents incorporate strategies for building up on-chip exact and temperature-uncaring predisposition currents, computerized alignment of simple circuits, and the structure of controller and high-voltage circuits.

Accomplishing high vitality proficiency in ICs equipped for pleasing 109 gadgets is ending up basically vital. This paper additionally displays an overview of the advancement of figure of legitimacy for simple to-computerized converters. An advanced procedure is embraced to adjust the current befuddle of the charge pump (CP) in stage locked frameworks. In this advanced alignment procedure, there is no additional imitation CP required. Moreover, it can align the CP under various control voltages on the circle channel to be safe to the channel-length adjustment. Because of the computerized nature, the extra power utilization and advanced changing clamor from the alignment circuits are killed once the adjustment is done. A 5 GHz recurrence synthesizer is utilized to legitimize the proposed adjustment method. The deliberate yield goad is smothered by 5.35 dB at 5.2 GHz after the adjustment circuits are dynamic. The deliberate yield goad levels are not exactly -68.5 dBc all through the entire yield recurrence go. The deliberate stage clamor is -110 dBc/Hz at a balance recurrence of 1 MHz.

Reasonable contemplations in the structure of CMOS charge pumps are examined. The non-perfect impacts of the charge pump by the leakage current, the confuse, and the delay counterbalance in the P/FD are quantitatively dissected. To utilize the fitting charge pump in different PLL applications, a few models are examined and their exhibitions are thought about. The improved plan of both the single-

finished and the differential charge pumps are given the reproduction result. A charge pump is broadly utilized in modern stage locked loops (PLL) for an ease IC arrangement as appeared in Fig. 1. Having the unbiased express, the perfect charge pump joined with the P/FD furnishes the boundless dc gain with aloof channels, which results in the unbounded draw in range for second request and high-request PLLs if not restricted by VCO input run [11]. For whatever length of time that the P/FD and the charge pump are perfect, the zero static stage blunder is accomplished. At the end of the day, the sort 2 PLL is conceivable with the detached channel when the charge pump is utilized. The charge pump, in any case, indicates non-perfect conduct when actualized in the circuit and its down to earth issues should be considered in the structure of the PLL. In this work, structure contemplations of the CMOS charge pumps are tended to and different models are explored.

4. CONCLUSION

A wide-extend PLL is manufactured in a 65-nm CMOS process. To manage the procedure variability and leakage current in nanoscale CMOS process, a self-healing prescaler, a self-healing VCO, and an adjusted CP are introduced. Exploratory outcomes are given to show the attainability. . Infusion of the rising edge of as far as possible jitter collection to one reference cycle, and first-request dynamic of the framework guarantees obtaining without strength concerns. Reference infusion is

actualized by means of stage interjection. The recurrence procurement comprises of computerized coarse-tuning and rotational recurrence recognition for tweaking. A model has been actualized in a 65 nm CMOS process, and has been completely checked through estimations and reenactments. Exploratory outcomes approved usefulness of the framework with an electrical information clock. The complete dynamic zone including inductors is 0.044 mm. The test chip works in the scope of 8– 9.5 GHz. At 8 GHz, with a duplication factor of 20, it expends 2.49 mW, and displays 490 fs rms incorporated jitter and 2.06 ps top to-top intermittent jitter. At this working recurrence, the reference goads are estimated to be 64.3 dB beneath the bearer recurrence. The principal request qualities of the recurrence procurement has been inspected and exhibited through estimation. Diverse components adding to the jitter have been examined and supporting estimations have been introduced. This engineering is appropriate for thick parallel connections and boisterous conditions where a perfect reference clock is accessible.

REFERENCES

- [1] L. L. Lewyn, T. Ytterdal, C. Wulff, and K. Martin, "Analog circuit design in nanoscale CMOS technologies," Proc. IEEE, vol. 18, no. 11, pp. 1687–1714, Oct. 2009.
- [2] J. M. Wang, Y. Cao, M. Chen, J. Sun, and A. Mitev, "Capturing device mismatch in analog

and mixed-signal designs,” *IEEE Circuits Syst. Mag.*, vol. 8, no. 4, pp. 137–144, Dec. 2008.

[3] K. Agawa, H. Hara, T. Takayanagi, and T. Kuroda, “A bitline leakage compensation scheme for low-voltage SRAMs,” *IEEE J. Solid-State Circuits*, vol. 36, no. 5, pp. 726–734, May 2001.

[4] R. Krishnamurthy, A. Alvandpour, G. Balamurugan, N. Shanbhag, K. Soumyanath, and S. Borkar, “A 130-nm 6-GHz 256 32b leakage-tolerant register file,” *IEEE J. Solid-State Circuits*, vol. 37, no. 5, pp. 624–632, May 2002.

[5] R. Holzer, “A 1 V CMOS PLL designed in high-leakage CMOS process operating at 10–700 MHz,” in *Proc. IEEE Int. Solid-State Circuits Conf.*, 2002, pp. 272–273.

[6] J. Maneatis, J. Kim, I. McClatchie, J. Maxey, and M. Shankaradas, “Self-biased high-bandwidth low-jitter 1-to-4096 multiplier clock generator PLL,” *IEEE J. Solid-State Circuits*, vol. 38, no. 11, pp. 1795–1803, Nov. 2003.

[7] C. Y. Yang, G. K. Dehng, J. M. Hsu, and S. I. Liu, “New dynamic flip-flops for high-speed dual modulus prescaler,” *IEEE J. Solid-State Circuits*, vol. 33, no. 10, pp. 1568–1571, Oct. 1998.

[8] P. Dudek, S. Szczepanski, and J. Hatfield, “A high-resolution CMOS time-to-digital converter utilizing a vernier delay line,” *IEEE J.*

SolidState Circuits, vol. 35, no. 2, pp. 240–247, Feb. 2000.

[9] C. N. Chuang and S. I. Liu, “A 1 V phase locked loop with leakage compensation in 0.13 μ m CMOS technology,” *IEICE Trans. Electron.*, vol. E89-C, pp. 295–299, Mar. 2006

[11] C. Kuo, J. Chang, and S. Liu, “A spur-reduction technique for a 5-GHz frequency synthesizer,” *IEEE Trans. Circuits Syst. I, Reg. Papers*, vol. 53, no. 3, pp. 526–533, Mar. 2006.

[12] C. Liang, S. Chen, and S. Liu, “A digital calibration technique for charge pumps in phase-locked systems,” *IEEE J. Solid-State Circuits*, vol. 43, no. 2, pp. 390–398, Feb. 2008.

[13] K. Wang, A. Swaminathan, and I. Galton, “Spurious tone suppression techniques applied to a wide-bandwidth 2.4 GHz fractional-N PLL,” *IEEE J. Solid-State Circuits*, vol. 43, no. 12, pp. 2787–2797, Dec. 2008.

[14] X. Gao, E. Klumperink, and G. Socci, “Spur reduction techniques for phase-locked loops exploiting a sub-sampling phase detector,” *IEEE J. Solid-State Circuits*, vol. 49, no. 9, pp. 1809–1821, Sep. 2010.

[15] C. Charles and D. Allstot, “A calibrated phase/frequency detector for reference spur reduction in charge-pump PLLs,” *IEEE Trans. Circuits Syst. II, Exp. Briefs*, vol. 53, no. 9, pp. 822–826, Sep. 2006.

- [16] W. Rhee, "Design of high-performance CMOS charge pumps in phaselocked loops," in Proc. IEEE Int. Circuits Syst. Symp., 1999, vol. 2, pp. 545–548.
- [17] J. Lin et al., "A PVT tolerant 0.18 MHz to 600 MHz self-calibrated digital PLL in 90 nm CMOS process," in IEEE ISSCC Dig. Tech. Papers, 2004, pp. 488–489.
- [18] X. Gao et al., "A 2.2 GHz sub-sampling PLL with 0.16 ps rms jitter and 125 dBc/Hz in-band phase noise at 700 W loop-components power," in Proc. IEEE Symp. VLSI Circuits, 2010, pp. 139–140.
- [19] W. H. Chiu, Y. H. Huang, and T. H. Lin, "A dynamic phase error compensation technique for fast-locking phase-locked loops," IEEE J. Solid-State Circuits, vol. 45, no. 6, pp. 1137–1149, Jun. 2010.
- [20] J. f. Dally et al., "Jitter transfer characteristics of delay-locked loopstheories and design techniques," IEEE J. Solid-State Circuits, vol. 38, no. 4, pp. 614–621, Apr. 2003.
- [21] B. Razavi, "A study of injection locking and pulling in oscillators," IEEE J. of Solid-State Circuits, vol. 39, no. 9, pp. 1415–1424, Sep. 2004.
- [22] J. Lee and H. Wang, "Study of subharmonically injection-locked PLLs," IEEE J. Solid-State Circuits, vol. 44, no. 5, pp. 1539–1553, May 2009.
- [23] B. Helal et al., "A low jitter programmable clock multiplier based on pulse injection-locked oscillator with a highly-digital tuning loop," IEEE J. Solid-State Circuits, vol. 44, no. 5, pp. 1391–1400, May 2009.



IMPLEMENTATION OF REMOTE MEDICAL NURSING MONITORING SYSTEM USING ARDUINO

T. Amulya

Student

Geethanjali College of Engineering and
Technology
Cheeryal.

tamulya.anu@gmail.com

Md. Shams Tabrez

Student

Geethanjali College of Engineering and
Technology
Cheeryal

shams17496@gmail.com

P. Uday Kumar

Student

Geethanjali College of Engineering and
Technology
Cheeryal

puppalaudaykumarr@gmail.com

B.L. Prakash

Professor

Geethanjali College of Engineering and
Technology
Cheeryal

prakashvignan4368@gmail.com

ABSTRACT

It is necessary to monitor the patient time to time by giving them proper attention. But it is missing in some hospitals. Hence in this paper we proposed an effective remote medical nursing monitoring system. If any patient of a particular bed need any medical assistance, the patient press that key which is present near the bed, then the key will be activated and the camera will be positioned towards the patient bed automatically if patient needs doctor's assistance, by pressing another key the message will be sent to the doctor through Bluetooth, after visiting the patient doctor has to press a special key, which means he visited the patient and it will be visible on LCD display. Finally, the project we designed for particularly taking care of general ward patients.

KEYWORDS: *Arduino, Blue-tooth, LCD, Motor, H-bridge.*

1. INTRODUCTION

The Subject of mechatronics which means a united frame work is constructed with mechanical part, Arduino, video monitoring, camera included in this project which is positioned towards the calling patient. LCD is to display the messages which are visible to patients, what key there have pressed. The current

technology, which involves the subject of mechatronics can restrict the motion of camera, it will be positioned at the middle of the two beds. For this purpose magnetic switches and limit switches are used and they are supposed to be installed near the beds. The video camera is arranged over the sliding channel mechanism and it will be moved horizontally within a specific span of time. In this paper we propose to arrange two mini beds near that beds three keys there are doctor calling, medicine, food and two keys are arranged for doctor and that key is pressed after visiting the patient.

If patient press any particular assistance key then the message will be send to that persons and the message will be displayed in LCD, by pressing key, camera will be moved from home position to particular patient bed and wireless video monitoring will be appear at the receptionist section. Finally, this project is designed for especially taking care of general ward patients in government hospitals; medical assistants

will not pay much attention to the poor patients.

Hence the purpose of this project work is to have a continuous vigilance over the staff of hospitals, i.e., whether they are serving the patients in proper manner or not, can be monitored by the concern higher official through wireless video monitoring system. The wireless video camera used in this project work can able telecast the live video to the monitoring station. The monitoring station is equipped with a synchronized video receiver and its output is fed to the small television set.

2. Block diagram

The entire system can be explained using the block diagram given below. It consists of Arduino Mega, Blue Tooth, LCD display, DC motor, H-Bridge and power supply. The patients are assumed to be arranged on 2 mini beds. The camera initially is in home position. Whenever the patient presses the key for calling the doctor, that information will be sent to the doctor via blue tooth. The Arduino will enable the H-bridge and DC motor which will focus the camera. It also stores programming instructions and displays the message on LCD.

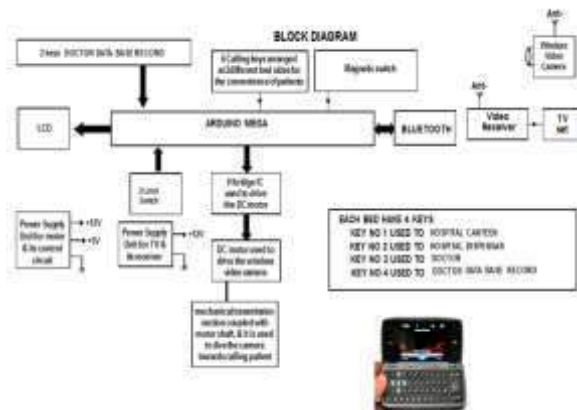


Fig.1 Block diagram of Remote Medical Nursing monitoring system

3. Circuit diagram

The circuit diagram shows the Arduino along with the power supply, the video camera, H-bridge and LCD display and the connectivity between them.

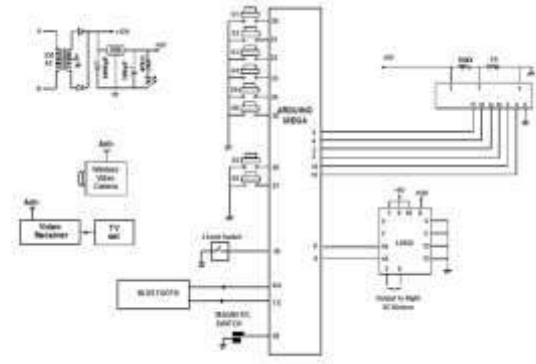


Fig.2. Circuit diagram of Remote medical nursing monitoring system

4. Description about various components used

4.1 Arduino Mega

Arduino Mega 2560 is a Microcontroller board based on Atmega2560. It comes with more memory space and I/O pins as compared to other boards available in the market. There are 54 digital I/O pins and 16 analog pins incorporated on the board that make this device unique and stand out from others. Out of 54 digital I/O, 15 are used for PWM (pulse width modulation). A crystal oscillator of 16MHz frequency is added on the board. This board comes with USB cable port that is used to connect and transfer code from computer to the board.



Fig.3 Arduino Mega 2560 Microcontroller

4.2 Bluetooth Module

The HC-06 Bluetooth module designed for transparent wireless serial communication. Once it is paired to a master Bluetooth device such as PC, smart phones and tablet, its operation becomes transparent to the user. All data received through the serial input is immediately transmitted over the air. When the module receives wireless data, it is sent out through the serial interface exactly as it is received. No user code specific to the Bluetooth module is needed at all in the user microcontroller program.



Fig.4. Blue Tooth module

4.3 L293D "H" Bridge IC

The motor driver package L293D is interfaced with ATMEGA 2560 microcontroller through IN1 to IN4 of H Bridge (L293D). Both the enable pins (EN1 and EN2) of motor driver L293D is combined together and fed to controller to access the command signals. Depending up on the command signals issued by the controller, the enable pins are activated to control all the four internal drivers of L293D respectively to drive the geared DC motor to which a wireless video camera is connected. Here H-Bridge is required, because the microcontroller output is not sufficient to drive the DC motor, so

current drivers are required for motor rotation.

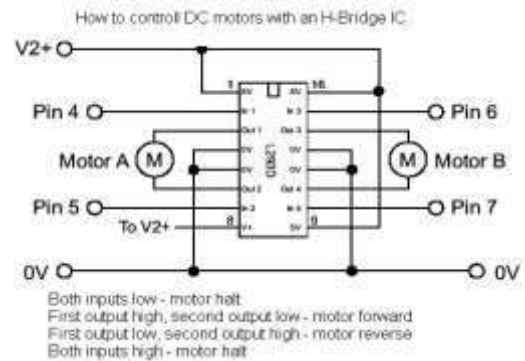


Fig.5. H-Bridge IC

4.4 Video Telecasting System

In television, light signals from the object are converted in to electrical signals by a video camera and transmitted through radio carrier waves. The television receiver separates the television signals from carrier waves and converts them in to light signals which form a picture of the televised object on the screen of the picture tube. However, in the television system sound signals are also to be transmitted along with the video signals. Separate carrier waves are used for the transmission of picture signals and sound signals, and are radiated by the same transmitting antenna. At the receiving end with the help of single receiving antenna both the carrier waves are received and later both the signals are separated. For the proper display of picture and reproduction of sound, several controlling signals also must be transmitted. Here, the wireless video camera arranged over a moving mechanism can broadcast both video and signals through a small antenna.

5. CONCLUSION

Various fields of technologies like wireless Video network, embedded



system, android platform, motor driving technology through H bridge device, display section etc. are included in this paper. Here a simple moving mechanism is constructed to position the video camera towards calling patient. The system equipped with wireless video camera can telecast the live video to the monitoring authority room. The main intention of this project work is to keep a continuous vigilance over the medical assistants for better service provided to the poor patients.

6. REFERENCES

- [1] *Design and Implementation of Remote Medical Nursing Monitoring System based on Computer Network* Luo Shi-yu Renhe Hospital; Hubei Yichang 443000, China.
- [2] *Pesola Aki, Serkkola Ari, Lahdelma Risto, Salminen Pekka, Multicriteria evaluation of alternatives for remote monitoring systems of municipal buildings, Energy and Buildings, 72, pp. 229-237, 2014.*
- [3] *Khan S., Usmani A., Remote patient monitoring system with a focus on antenatal care for rural population, Bjog-an International Journal of Obstetrics and Gynaecology, 121(2), pp.149-150, 2014.*
- [4] *Tina Giuseppe Marco, Grasso Alfio Dario, Remote monitoring system for stand-alone photovoltaic power plants: The case study of a PV-powered outdoor refrigerator, Energy Conversion and Management, TUNISIA, 78, pp. 862-871, 2014.*
- [5] *Takenaka Katsunobu, Hayashi Katsuhiko, Katoh Masayasu, Collaboration for Stroke Care (Medical Treatment/Nursing Service/Welfare) in the Remote Place, Such as Hida Area, in Northern Parts of Gifu, CEREBROVASCULAR DISEASES, 34(1), pp, 61-61, 2012.*
- [6] *Wang Huaqun, Wu Qianhong, Qin Bo, Domingo-Ferrer Josep, FRR: Fair remote retrieval of outsourced private medical records in electronic health networks, Journal of Biomedical Informatics, 50, pp. 226-233, 2014.*
- [7] *Howard A. Fuchsia, Smillie Kirsten, Turnbull Kristin, Zirul Chelan, Munroe Dana, Ward Amanda, Tobin Pam, Kazanian Arminee, Olson Rob, Access to Medical and Su ortive Care for Rural and Remote Cancer Survivors in Northern British Columbia, Journal of Rural Health, 30(3), pp. 311-321, 2014.*
- [8] *Bracken Hillar , Lohr Patricia A., Ta lor Jeanette, Morroni Chelsea, Winikoff Beverl , RU OK? The acce tabilit and feasibilit of remote technolo ies for follow-u after earl medical abortion, Contraception, 90(1), pp. 29-35, 2014.*

ROBUST VIDEO WATERMARKING USING A HYBRID ALGORITHM OF SVD AND DWT WITH SECURED QR CODE

¹D.S.Jaya Madhavi ²J.Sai Venkata Tarun ³C.Venkata Narasimhulu
^{1,2}UG Student, Department of Electronics and Communication
³ Ph.D,Professor, Department of Electronics and Communication
Geethanjali College of Engineering and Technology, Telangana, India.

Abstract : This paper discusses a new video watermarking scheme which is non-blind hybrid technique based on singular value decomposition (SVD) and discrete wavelet transform (DWT). The proposed hybrid algorithm partitions the host image into blocks and each of them is transformed into U, S and V components by SVD. And then, a set of blocks with the same size as watermark are selected according to the feature of the S component. To get better quality and to make less prone to noise and improve its robustness DWT is applied to both images and shown in LL band. In addition to this, it also uses a secret key which will improve its security by allowing an only desired person to insert or extract the watermark. The experimental results show that the proposed watermarking scheme is robust for video processing operations such as rotation and addition of noise and extracts the watermark more efficiently than the video watermarked schemes proposed recently.

IndexTerms - Watermarking, Discrete Wavelet Transform, Security, Robustness

I. INTRODUCTION

With the rapid development of network technology, vast multimedia data is communicated over the network. Every day lots of data in the form of emails, chats, images and videos are being transmitted over long distances in a span of a blink of an eye. One person sitting at one corner of the globe can communicate with another person sitting at any other corner of the globe. Digitization has dramatically changed the way one looks at his life and the way he has started leading their life. More and more digital multimedia data are available today, which can be perfectly copied and rapidly disseminated at large scale. Although network transmission is convenient and fast, the multimedia data passing through the network is often attacked and tampered by malicious attackers. This consequently has raised concerns from the content owners, when they realized that traditional protection mechanisms, such as encryption, were no longer sufficient. Sooner or later, digital content has to be decrypted and to be presented to human consumers. At this very moment, the protection offered by encryption no longer exists. As a result, digital watermarking, the art of hiding information in a robust and invisible manner, has been investigated as a complementary technology. Digital watermarking technology is an effective means to hide copyright information in the original content to protect the authenticity of the intellectual property. It is a concept which closely relates to steganography, in a way that they both hide a message inside a digital signal. However, it is the goal that separates them. Watermarking is used to hide a message related to the actual content of digital data, while steganography is used when the digital data has no link with the message, and it is used as an upper layer to hide its existence. Multimedia security has become extremely important for internet technology because of the ease with which the data can be manipulated, copied and distributed. Video watermarking differs from image watermarking. A video contains large spatial and temporal redundancy. There exists a complex trade-off between different parameters like imperceptibility, data payload and temporal synchronization of video frames. The data payload is the number of bits that are embedded by the watermark. The fidelity is another property of the watermark that tells about the distortion that the watermarking process is bound to introduce, which should remain imperceptible to a human observer. Finally, the robustness of a watermarking scheme can be seen as the ability of the detector to extract the hidden watermark from the altered watermarked data caused by various attacks. It finds its application in various domains and platforms such as fingerprinting, a technique to trace the source of illegal copies, Online Location, when Internet search services continuously look at the web for the watermarked video content and notify the owner of where their content was found. Broadcast monitoring, Copy and Control of playback and Content Filtering.

The aim of the paper is to achieve more security to the video and provide copyright protection to major extent, by providing an algorithm that is robust to various attacks and insert a watermark that is imperceptible and the temporal synchronization of frames is maintained. Each of the following section will give a glimpse of methods and the results obtained by it. The problem definition is given in Section I, the algorithms SVD and DWT have been discussed in Section II and III. Our proposed method is given in Section IV followed by the results and analyses in Section V. Finally, the paper is concluded in Section VI.

II.SINGULAR VALUE DECOMPOSITION

SVD is a technique that can be used to mathematically extract the singular values from a 2D image that represent the image's intrinsic algebraic image properties [3]. Considering that a frame (f) of a video sequence is a square matrix of size $M \times M$, its SVD is defined in Eq.2.1 as:

$$f = USV^T \quad (2.1)$$

where U and V are orthogonal (or unitary) matrices and S is a diagonal matrix, with the diagonal elements in the descending order of S , are called the singular values of f . SVD-based watermarking approaches, embed the watermark by modifying either U and V or S . SVD techniques are typically used in video watermarking due to the good stability of the singular values, that is, when a small perturbation is added to a frame, these values do not change significantly [4]. Although this characteristic of the SVD provides robustness to attacks, a limitation is that performing it on an image is computationally expensive [4]. An SVD-based non-blind watermarking scheme in which the SVD is applied to the host image using (1) to find the singular values was proposed by Liu and Tan [3]. In this approach, the singular values are modified by adding the watermark and then the SVD performed again on the resultant matrix to calculate the modified singular values. Finally, the original singular values are replaced by the modified values to obtain the watermarked image. An inverse operation is performed at the decoder to extract the watermark from the distorted watermarked image by applying the SVD on that image.

II. DISCRETE WAVELET TRANSFORM

Wavelet Transform: The DWT is a mathematical tool that decomposes an image or video frame into a lower resolution approximation image (LL) and three detail components, vertical (LH), diagonal (HH) and horizontal (HL).

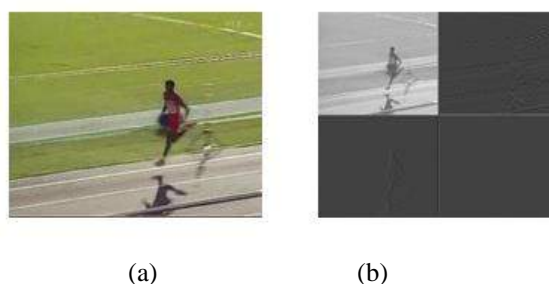


Fig.1 DWT for (a) Original Image
(b) Output image after 2-D DWT applied

The approximation image (LL) is the low-frequency part and detail components LH, HH and HL are the high-frequency part with decompositions able to be conducted at different DWT levels. A 2D DWT produces three sub-bands at each level oriented at angles of 0° , 45° , and 90° as shown in Fig.1. In a hybrid watermarking scheme based on the DWT and SVD introduced by Lai and Tsai [4], as the SVD transform of an image is computationally inefficient, the host image is decomposed into four different sub-bands (LL, LH, HL, and HH). The watermark is embedded in each sub-band and then an inverse IDWT is applied to these sub-bands to provide the watermarked image. Finally, the watermark is extracted from each sub-band.

IV. PROPOSED ALGORITHM

In the proposed hybrid algorithm,[5] the watermarked bits are embedded on the elements of the singular values of the frame of discrete wavelet low pass sub band which results from two level DWT.

4.1 Watermark Embedding

The proposed video watermark embedding algorithm is shown in Fig.2.

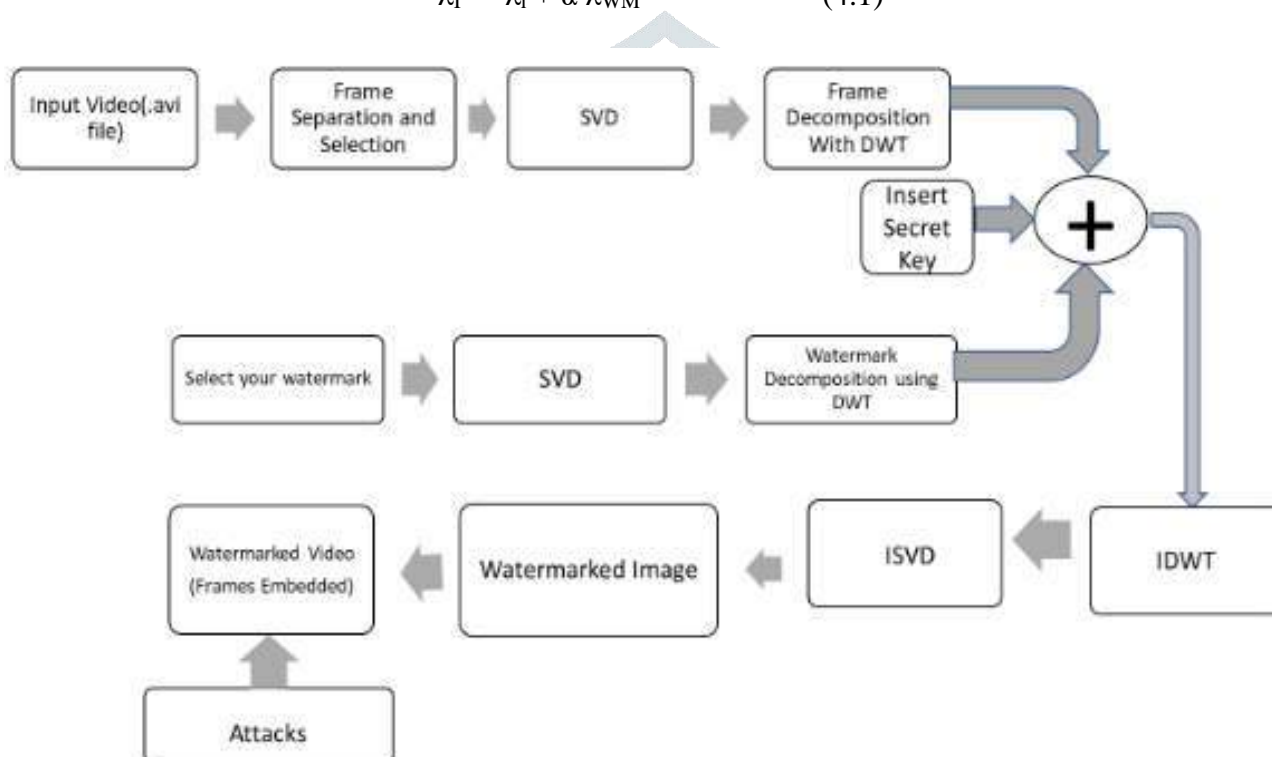
Fig.2 The watermark embedding process

Step1: Separate the original video into frames.

Step2: Apply SVD to a frame and a watermark image and apply 2-D DWT to decompose them into sub bands

Step3: Modify the singular values of low- level sub-band coefficients of the selected frame with the singular values of low pass sub-band coefficients of first watermark image using the additive algorithm. i.e.

$$\lambda_i^\# = \lambda_i + \alpha \lambda_{WM} \quad (4.1)$$



where α : scaling factor, λ_i is the singular value of the frame, λ_{WM} is the singular value of watermark and $\lambda_i^\#$ is the singular value of video

Step 5: Apply inverse SVD and IDWT to convert to the spatial domain.

Step 6: Insert the secret key and combine the frames to get the watermarked video.

4.2 Watermark Extraction

The proposed video watermark extraction algorithm is shown in Fig.3.

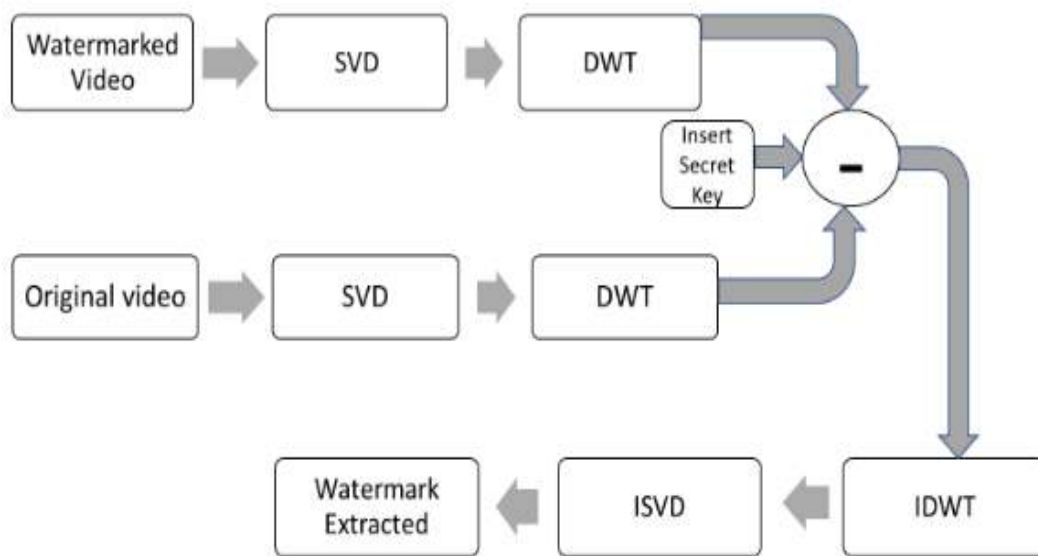


Fig. 3 shows the watermark extraction process

Step1: Separate the watermarked video into frames.

Step2: Apply SVD to a frame and a watermark image and apply 2-D DWT to decompose them into sub bands

Step3: Extract the singular values from low-level sub-band coefficients of frame of the watermarked and original video by using

$$\lambda_{WM} = (\lambda_i^{\#} - \lambda_i) / \alpha \quad (4.2)$$

Step4: Insert the secret code to extract the watermark

Step 5: Apply inverse DWT and inverse SVD on modified singular values.

V. EXPERIMENTAL RESULTS

The “input.avi” with 78 frames of size 256x256 is used as original video in our carryout tests. The original video is separated into frames and one frame, “31.bmp” is selected for insertion of a secret logo (i.e.,) binary images “jntu.bmp”, size 256x256 which is used as an original watermark, Table 1(b). The watermark, Table1(c) is embedded in all RGB colour spaces of any one frame chosen at random. The experiment is performed by taking scaling factor alpha (α) as 0.01, 0.1 and 1.5 as shown in Table 2.

The results show that there are no perceptible visual degradations on the watermarked video shown in table 1 and the watermark is extracted from the video scenes with an average NCC around unity and extracted watermark is also shown in Table 1(d). Upon adding attacks to the video, like rotation and adding salt and pepper noise NCC is calculated again and compared with the previous values as shown in Table2 and Table3. MATLAB 8.1 version is used for testing the robustness of the proposed method. The quality and imperceptibility of the watermarked image are measured by using PSNR which can be obtained using Eq.5.1 with respect to the original image.

Peak Signal-to-Noise Ratio

$$PSNR = 10 \log \left[\frac{\max(I(i, j))^2}{\sum_{N, M} (I'(i, j) - I(i, j))^2} \right] \tag{5.1}$$

The similarity of the extracted watermark with original watermark that is embedded is measured using NCC which is given in the Eq.5.2

Normalized Correlation Coefficient

$$Ncc = \frac{\sum_m \sum_n (A_{mn} - \bar{A})(B_{mn} - \bar{B})}{\sqrt{\left(\sum_m \sum_n (A_{mn} - \bar{A})^2\right) \left(\sum_m \sum_n (B_{mn} - \bar{B})^2\right)}} \tag{5.2}$$

JETIR

Table 1 shows the experimental results


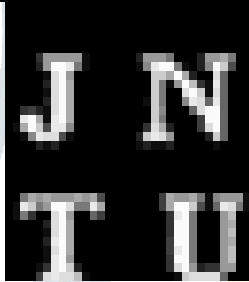



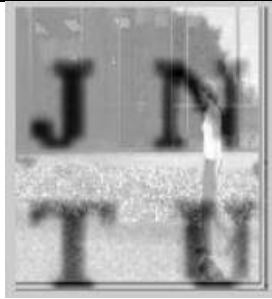


			
(a)Frame “31.bmp”	(b)Watermark “jntu.bmp”	(c) Watermarked Image	(d)Extracted “jntuh.bmp”
			
(e) Attacked Watermark by Rotation	(f)Extracted “jntu.bmp” after rotation	(g)Attacked Watermark by Salt and Pepper Noise	(h)Extracted “jntu.bmp” after salt and pepper noise attack

Table 2 shows how the PSNR values vary with different α values

ALPHA	PSNR (in dB)
0.01	49.5
0.1	29.3
1.5	5.67

Table 3 shows NCC for different attacks

ATTACK	NCC
ROTATION	0.87
SALT AND PEPPER NOISE	0.65

VI. CONCLUSION

A non-blind hybrid video watermarking technique is proposed for video authentication and its copyright protection using Discrete Wavelet Transform and singular value decomposition. In the existing methods, the watermark is embedded in all video scenes by modifying singular values of high sub band coefficients with respect to watermark high sub band coefficient with a suitable scaling factor. In this proposed algorithm, only in the selected frame for data hiding, and DWT processing is done for a video frame and secret logo to match the embedding criteria. The robustness of watermark is improved for common video processing operations by inserting a QR code as a secret for both embedding and extracting process of the watermarked image. This algorithm shows excellent robustness to attacks like JPEG, JPEG2000 compressions, Histogram equalization, Salt and Pepper Noise, Shearing, Cropping, Rotation, Weiner Filtering, Gaussian Noise, and Row Column Removal. It is also tested in different sub-bands for obtaining a better result of generating a watermark image without any visual degradation. The proposed method shows higher robustness to maximum no of attacks compared to any other algorithm.

REFERENCES

- [1] Kumar H.B.B. Digital Image Watermarking – at A Kumar H.B.B. Digital Image Watermarking – An overview. Orient J. Comp. Sci. and Technol;9(1). Available from: <https://www.computerscijournal.org/?p=3546>
- [2] Venkata Narasimhulu & K. Satya Prasad in 'A Novel Robust Watermarking Technique Based on Nonsampled Contourlet Transform and SVD', The International Journal of Multimedia & Its Applications (IJMA) Vol.3, No.1, February 2011.
- [3] R.Liu and T.Tan, "An SVD based watermarking scheme for protecting rightful ownership", IEEE Trans. Multimedia vol. 4, no. 1, pp. 121-128, Mar.2002
- [4] C.-C.Lai and C.-C.Tsai, "Digital image watermarking using discrete wavelet transform and singular value decomposition", IEEE Trans. Instrum. Meas., vol. 59, no.11, pp. 3060-3063, Nov.2010
- [5] Venkata Narasimhulu., Satya Prasad.K," A Non-Blind Hybrid Video Watermarking Scheme based on Singular Value Decomposition and Contourlet Transform", UACEE International Journal of Computer Science and its Applications - Volume 3: Issue 1 [ISSN 2250 - 3765]

SMART APARTMENT WITH AUTOMATIC WATER MANAGEMENT AND SECURITY ALERT SYSTEM

B. SREE LATHA

Associate Professor in
ECE, Geethanjali College Of
Engineering and Technology,
Cheeryal.

Y. SHRUTHI

Student, Department of
ECE, Geethanjali College Of
Engineering and Technology,
Cheeryal.

A. VANDANA

Student Department of
ECE, Geethanjali College Of
Engineering and Technology,
Cheeryal.

J. RAGINI RAMESH

Student, Department of
ECE, Geethanjali College Of
Engineering and Technology,
Cheeryal.

ABSTRACT

In this paper, we present a detailed model of a smart apartment with the use of Smart Water Management System and Security Alert System. Water Management concept is to measure and display the water consumption of individual flats. We adopt a pre-paid concept using smart card technology which is designed as detachable smart card, because it is supposed to be recharged when the debit is exhausted. Since security is prime concern in life these days. Every flat of the apartment is to be equipped with the MQ2 Sensor to sense gas leakage, IR Receiver to detect fire, MEMS to detect Earthquake and Limit Switch to measure the limit of dustbin.

KEYWORDS: Smart card, MQ2 Gas Sensor, IR Receiver, MEMS Sensor, Limit Switch

1.INTRODUCTION

The project “Smart Apartment with Automatic Water Management and Security Alert System” is a live project, prototype module constructed for the live demonstration. The system is designed for

domestic applications like apartments and individual colony’s where many families live together in one particular area. Generally, at these places, the source of water is from over headwater tank and the society or management of that particular colony or apartment collects some amount monthly as maintenance charge. Most of this amount is utilized for common electricity bill; this electricity bill is paid for energizing the water pumping motor and energizing the corridor or streetlights. In this regard, irrespective of water consumption, flat or lump sum amount is collected from the water consumers. This is a poor approach, because the consumption differs from consumer to consumer, a small family consumes less water, whereas the big family consumes more water and amount paid by both the families are same, this is injustice. To avoid this problem, this project work is taken up, which measures and controls the flow of water to the individual houses and according to the water consumption, amount will be charged from the house owners.

The demonstration module is designed with MQ2 Gas sensor has high sensitivity to

methane, propane and butane making it ideal for natural gas and LPG monitoring. This sensor is provided to detect the LPG Gas leakage. An IR detector is used for detecting the fire and an emergency situation is detected by the sensors in the apartment flat. In this regard the receiving part of the project work can be installed at the watchman or the security guard. This unit is designed to measure the garbage level in the bin through limit switch and earth quake is detected through MEMS sensor. This system uses the Arduino Mega microcontroller as the brain or center of operations which is also interfaced to the GSM for transmitting the SMS. Limit switch is one kind of force sensor. In this project, it is used to detect the maximum weight capability of the garbage bin and this switch is interfaced with Arduino microcontroller as input signal.

2.WATER MANAGEMENT USING SMART CARD DESIGNED WITH EEPROM:

Since it a proto type module, the system is designed with a pumping motor, means in other words the module is designed for one consumer only. In this concept, each and every flat or house should and must equip with one valve and two push-buttons for start and stop. Push buttons S1 and S2 are treated as start and stop the water flow, these are nothing but push to on type keys. Initially each and every consumer has to pay some amount to the organizer, according to the amount paid by the consumer, the organizer enters the data in to the Micro controller through keyboard to certain liters will be recharged into the smart card designed using EEPROM 93C46. During utilization of water, the consumer can energize and de-energize the valve as many times as he likes until the credit is exhausted. This is done through push buttons provided in his flat. Whenever the water is required; simply by

pressing the push button, the controller energizes his particular valve automatically by activating the pumping motor.

The water consumption of individual house can be displayed, as described above, according to the data entered into the micro controller, as the water is consumed, the display shows in decrement mode. When the total credit is exhausted, the display shows nil balance in the form of liters, and the smart card should be recharged again. In this condition if the consumer tries to energize the valve, the controller rejects the signal produced by the push button and it won't allow to energize the valve until the card is not recharged. Again, the consumer has to pay some amount to the organizer to recharge his card. The Figure of the smart card designed wuth EEPROM is shown in figure1.



Figure 1: Smart card designed with EEPROM

2.DETECTION OF GAS LEAKAGE USING MQ2 GAS SENSOR:

MQ2 is a general purpose Sensor that has good sensitivity characteristics to a wide range of gases. This device is designed to operate with a stabilized 5V heater supply and a circuit voltage depends up the design.

The most suitable application for the MQ2 is the detection of methane, propane and butane, which makes it an excellent Sensor for domestic gas or smoke detectors. The initial stabilization time of the MQ2 is very short and the relative and elapsed characteristics are very good over a long period of Operation. MQ2 has a very low sensitivity to 'noise-gases', which considerably reduces the Problem of nuisance alarming. The MQ2 is most practically employed in a circuit design, which maintains circuit voltages at fixed value of 5V. This voltage rating is very practical when determining design specifications because of the wide range of available components. This makes the use of the MQ2 an especially economical way to design low-cost, highly reliable gas detection circuits.

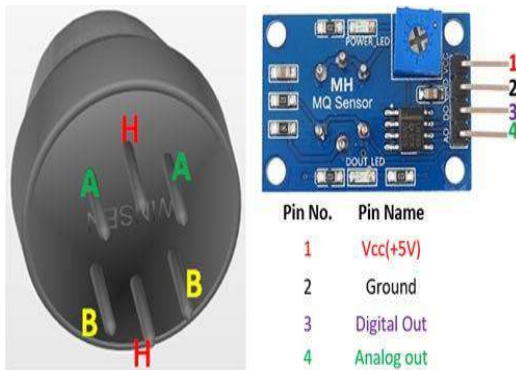


Figure 2: MQ2 Gas Sensor.

3.FIRE DETECTION USING IR RECEIVER:

IR diode is a simple and compact device used for sensing the presence of fire during any fire accident, hot gasses are emitted with the unique spectral pattern in the IR region. The module makes use of IR sensor and comparator to detect fire. The device weighing about 5 grams, can be easily mounted on the wherever required. It gives the high output on detecting the fire. An

appropriate action can be taken based on this output i.e., transmitting the information to the monitoring unit at the Security guard through Zigbee. The visual indication of output is provided by an on-board LED.



Figure 3: IR Receiver.

4.DETECTION OF EARTHQUAKE USING MEMS SENSOR:

Micro - Small size, micro fabricated structures

Electro - Electrical signal / control (In / Out)

Mechanical - Mechanical functionality (In / Out)

System Structures, Devices, Systems, Control

Earthquake early warning efforts aim to detect earthquakes and provide seconds of warning for surrounding populations. Here a working module rapidly detecting and characterizing earthquakes with the Quake-Catcher Network (QCN), which connects low-cost Micro Electro Mechanical Systems (MEMS) accelerometers to a volunteer network of an embedded system is designed.

Large magnitude earthquakes may cause significant losses of life and property. The concept is to detect the vibrations or jerks in the Earth, raise the alarm and alert the concern people by sending the information through the GSM technology to the mobile phone and Zigbee to the apartment flats. This concept can be proved practically with MEMS accelerometer mechanism.



Figure 4: MEMS (Micro electro mechanical system).

5. MEASURING OF MAXIMUM CAPABILITY OF GARBAGE BIN USING LIMIT SWITCH.

Limit switch is one kind of force sensor. In this project, it is used to detect the maximum weight capability of the garbage bin and this switch is interfaced with Arduino microcontroller as input signal. This limit switch is having long lever & when little pressure is applied to the lever, switch will be activated automatically. It is placed at the bottom of the garbage bin and if the weight reaches the maximum with standing capability of the garbage bin, it will be automatically pressed.

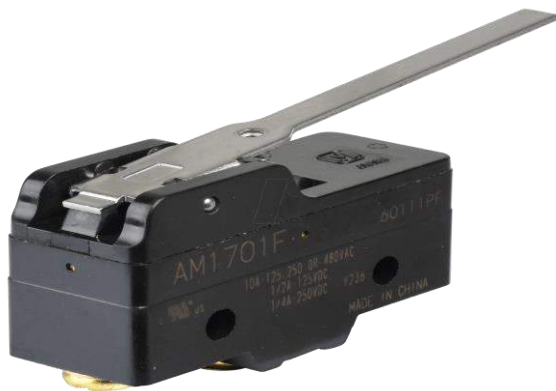


Figure 5: Limit Switch

6. CONCLUSION:

Because of deficiency of this kind of electronic monitoring systems, flat owners are in lot of confusion, and there is no vigilance about the consumption of water and safety and security systems. Irrespective of consumption, each flat owner is paying some fixed amount monthly as maintenance charge. By implementing this system, confusion can be avoided, and exact amount can be paid depending up on the water consumption. And also, the safety and security of the flats can be enhanced.

REFERENCES.

1. Linear Integrated Circuits – By: D. Roy Choudhury, Shail Jain
2. Digital Electronics. By JOSEPH J.CARR
3. Fundamental of Radio Communication: By A.SHEINGOLD
4. Basic Radio and Television: By S.P.SHARMA
5. Digital and Analog Communication System By: K. sam Shanmugam
6. Op-Amps Hand Book - By: MALVIND
7. The concepts and Features of Micro-controllers - By: Raj Kamal
8. The 8051 Micro-controller Architecture, programming & Applications - By: Kenneth J. Ayala
9. Programming and Customizing the 8051 Micro-controller - By: Myke Predko
10. Electronic Circuit guide book – Sensors – By JOSEPH J.CARR

Data Hiding using JPEG Steganography

Nidhi Singh¹, Shaik Karishma², S.Shiva Kumar³, R Odaiah⁴
 Guide⁴, Associate Professor⁴, ECE Department,
 Geethanjali College of Engineering and Technology, Hyderabad, India

Abstract:- Steganography and Steganalysis are two side of the same coin. This paper discuss about how a message or data can be hidden inside an image using JPEG Steganography. Along with this, RC5 encryption and Chaos cryptography are also used so that, an outsider is not able to access the data within the image. This paper also discuss about how a data is stored or hidden inside an image and how we can recover data from the same image. This type of systems are made to make our applications and data more secure from the threats. This paper focus on using lifting wavelet transform (LWT) instead of using old methods like DCT.

Keywords:- Steganography, RC5Encryption, Chaos Cryptography, Lifting Wavelet Transform.

I. INTRODUCTION

Security plays an important role in the world of information technology. It is necessary to secure our data from being access, stolen and manipulated. During communication there is a high risk that data can be accessed by the third party. We are able to hear many news about data hacking. The hackers are able to access the data and files because the security levels are low when they were implemented on the systems. To ensure high security we must use several techniques and methods to overcome these problems. It should be always keep in mind whenever we are implementing a system where we have to store a confidential data or files, we should implement high-quality level of encryption and decryption process which in turn make our system highly secure.

This paper mainly briefs about how a message or data can be conceal in an image with high amount of security level. The data or text are encoded and then they are stored into an image. The image in which data is embedded is known as Stego image. Whenever a person sees a stego image, it will look like a normal image, but the person cannot able to see the data hidden in that image. This is the quality of Steganography where a third party is not able to see the data and the image is also transferred securely from sender to receiver. To embed message into an image and to extract same message from that mage is not a huge process, but to prepare this system we should know how Chaos cryptography, RC5 encryption and Lifting Wavelet Transform are done. The security level of the system depends upon the algorithm we are preparing, so that third party is not able to extract our data.

II. DESCRIPTION

A. Steganography

Steganography means hiding or covering a text, image or file into another image, file or video. It's an art of hiding data where a sender and receiver knows a secret message is hidden into a file, where a third person cannot suspect that data is hidden into a image. Once a data is embedded into the image Its not an easy task to extract message from it.

Steganography has become more popular because, both data and communication between two parties are secured. This is the main advantage of steganography over cryptography.

B. Steganalysis

Steganalysis is a process of detecting data which is hidden into an image, video or another file. The main use of steganalysis is to identify any data which is hidden, if it is found that any data is covered or concealed by another file or image, the process will also help to recover the hidden data.

C. RC5 Encryption

Secret messages or data or not embedded directly into an image. With the help of RC5 encryption the original message is encoded. This encoded text is known as Cipher text. The obtained cipher text is then store into an image. RC5 is a symmetric key block cipher, which works fast when implemented. We use RC5 encryption because it has more number of iterations and strong key. Due to RC5 encryption data security level becomes more flexible.

D. Chaos Cryptography

Chaos cryptography is a study where a data is transferred from sender to receiver with high security in the presence of third party. Chaos cryptography algorithms are created in such a way that the result obtained from that algorithm produce confusion. This helps the quality of the security level of the system.

E. Lifting Wavelet Transform(LWT)

Lifting wavelet transform is commonly used because it design wavelets and perform discrete wavelet transform. By using this transform, it is very useful because two different works designing wavelet and DWT are done simultaneously. It is also easy to understand and can be used for irregular sampling.

III. LITERATURE REVIEW

The previous methods or techniques of Steganography of image were based on DCT(direct cosine transform).DCT have its drawbacks. In the present method we have used Lifting Wavelet Transform, RC5 encryption and Chaos cryptography.

IV. WORKING

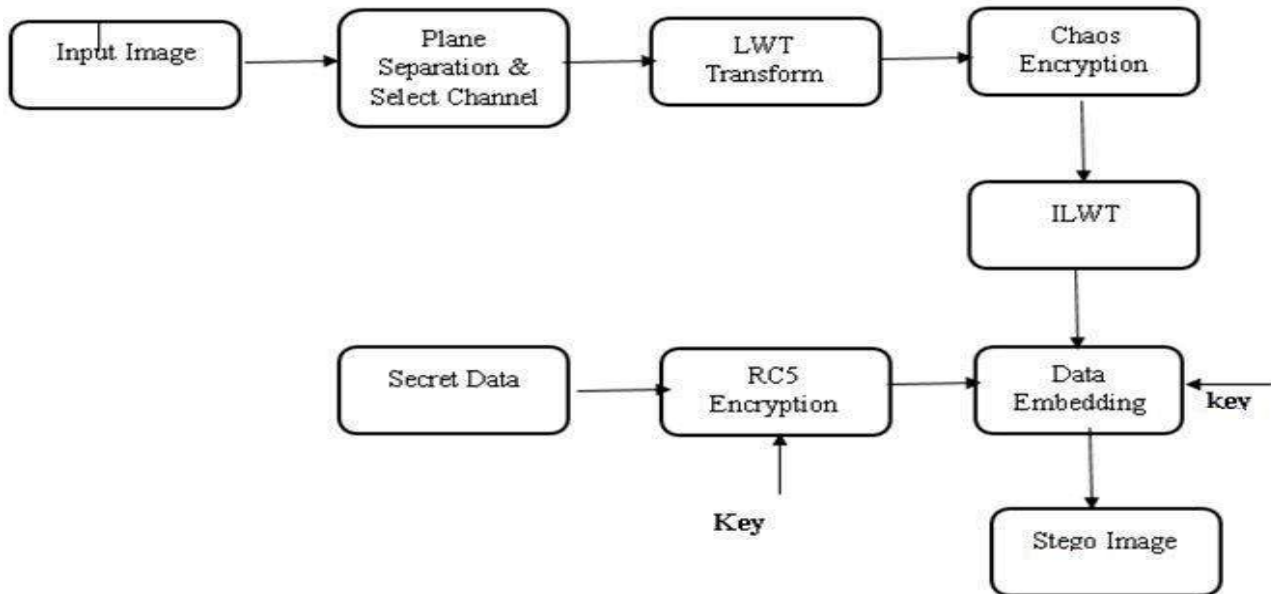


Fig 1:- Embedding Process of Steganography

The fig 1 shows how a secret data is embedded into an image. The first step is to take an image as an input which can be either in JPEG or PNG or bmp format. Then the input image is separated from its blue plane. This is done because data can be easily hidden at blue plane. With the help of LWT, samples of image are formed .In these samples we hide our secret data. Before hiding the data

should be converted into cipher text with the help of RC5 encryption. Chaos Encryption is done just to secure data from outside threats. After hiding the data inverse lifting wavelet transform is applied, so that image gain its original color. The image in which data is hidden is known as Stego image.

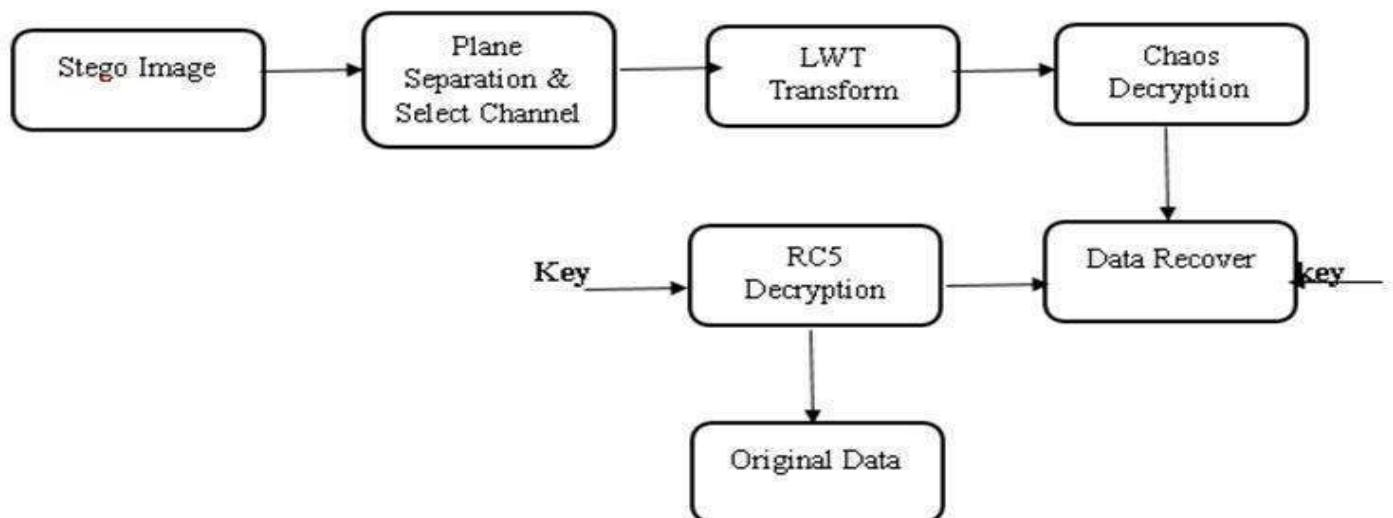


Fig 2:- Extraction Process of Steganography

The fig 2 shows how a hidden data is recovered from the stego image. First we should take the stego image as an input. Again the stego image is separated from its blue plane. Here also we will apply LWT to get the samples of the image. After getting the samples of image, extraction of

data can be done easily. But the data which we extract is in encoded form. With the help of RC5 decryption, the data in encoded form is decoded and we are able to recover the original data.

V. RESULTS

The process of embedding data into an image and to extract the same data from it, works on matlab. A required code should be written and dumped into the matlab which will successfully run the project.

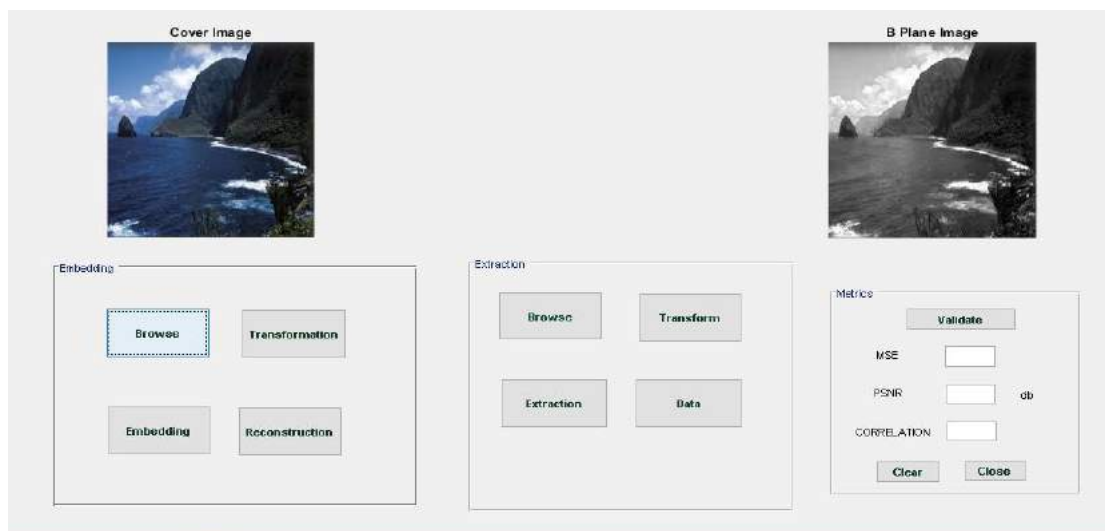


Fig 3:- Conversion of Input Image into Blue Plane

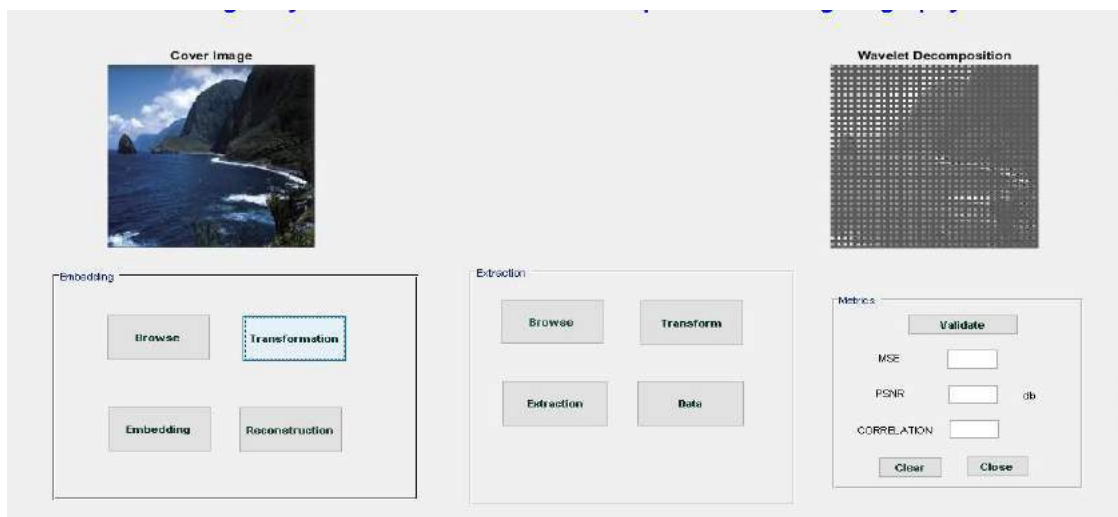


Fig 4:- wavelet Decomposition of Blue Plane Image

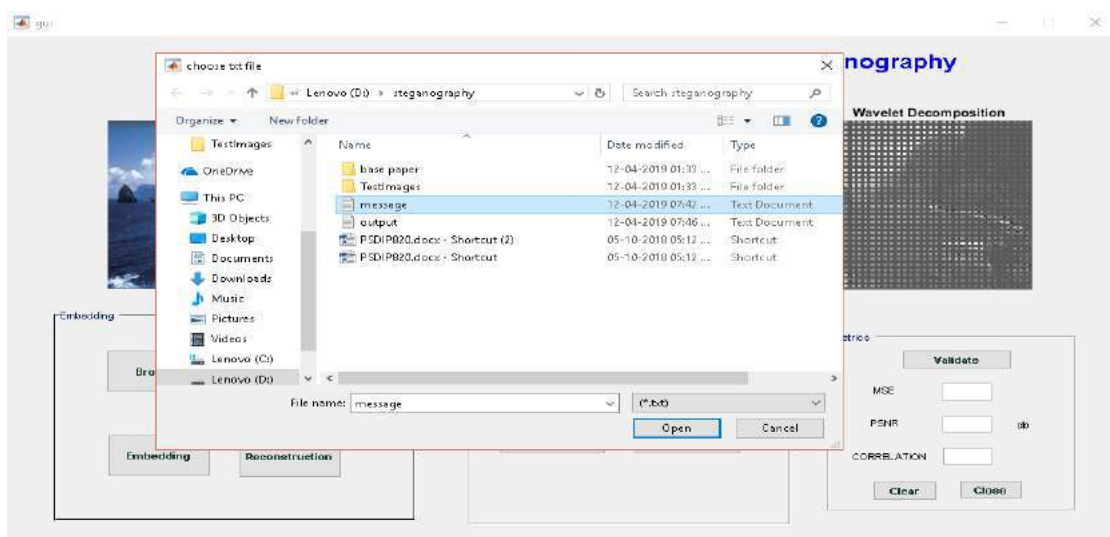


Fig 5:- Message is Browsed to keep inside the Image

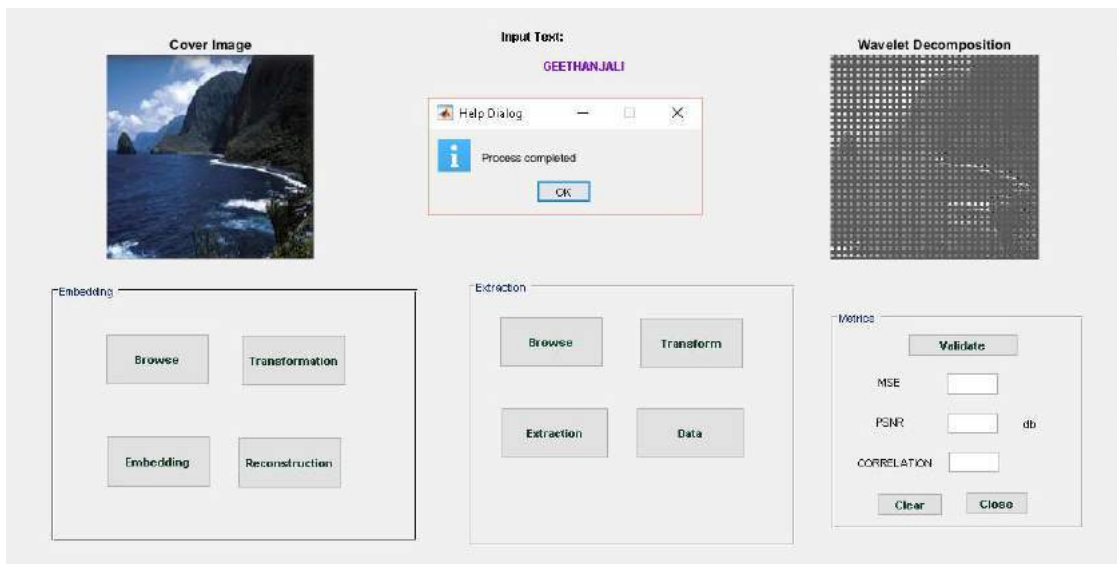


Fig 6:- After taking input Message it is Converted into Cipher Text



Fig 7:- Message in Cipher text is Stored into the Image

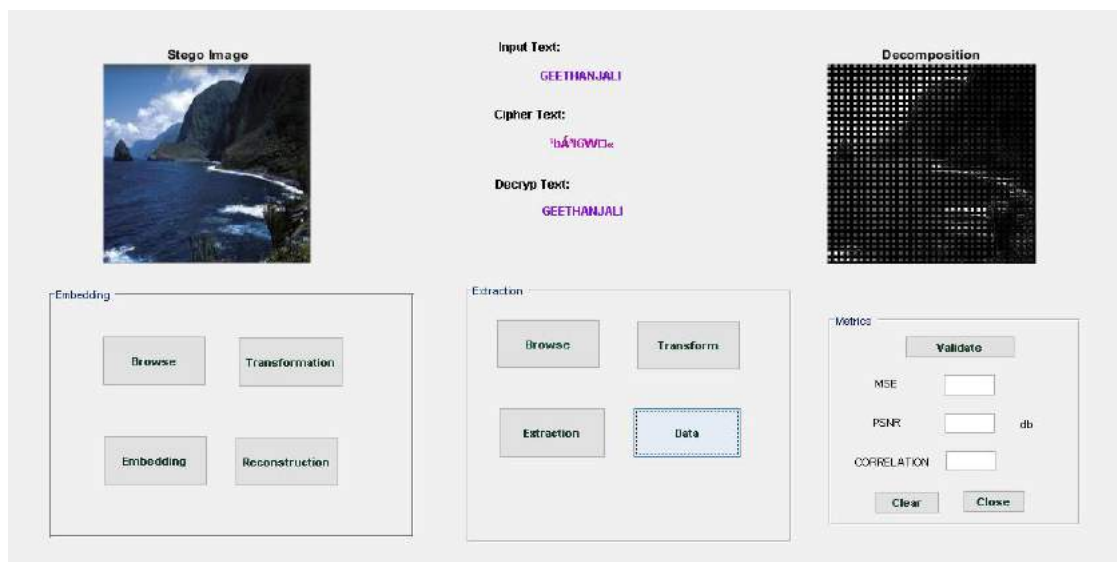


Fig 8:- Recovery of Original Data from the Cipher Text is done by taking the same Stego Image

VI. CONCLUSION

The main target behind this concept is the security of data, so that another people are not able to access, modify or delete our confidential data. This application is mainly useful in Military Service Medical information protection and Research Institutes where confidential data are protected with high security.

REFERENCES

- [1]. Image Steganography Based on Mantissa Replacement using LWT N Sathisha¹, K Suresh Babu², K B Raja², K R Venugopal³ ¹Department of ECE, Govt. S K S J Technological Institute, Bangalore, India. ²Department of ECE, University Visvesvaraya College of Engineering, Bangalore University, Bangalore, India. ³Principal, University Visvesvaraya College of Engineering, Bangalore University, Bangalore, India.
- [2]. T. Denmark and J. Fridrich, "Improving selection-channel-aware steganalysis features," in *Proceedings IS&T International Symposium on Electronic Imaging 2016* (A. Alattar and N. D. Memon, eds.), (San Francisco, CA), February 14–18 2016.
- [3]. Statistical Steganalysis for Content-Adaptive Steganography V.Gokula Krishanan¹, M.Deepak², S.Praveen Kumar³, B.Vinoth Kumar⁴ Assistant Professor¹, UG Scholar^{2, 3, 4} Department of CSE Panimalar Institute of Technology, Chennai, India



ACCIDENT DETECTION WITH MEMS AND ALERT SYSTEM FOR MEDICAL EMERGENCY

R.ODAIAH

Associate Professor

Geethanjali College Of Engineering And
Technology, Cheeryal
odaiahrece@gmail.com

I.NARESH

Student

Geethanjali College Of Engineering And
Technology, Cheeryal
ittaboina940@gmail.com

K.SAI KRISHNA REDDY

Student

Geethanjali College Of Engineering And
Technology, Cheeryal
saikrishnareddy.kskr@gmail.com

M.PRINCE TITUS

Student

Geethanjali College Of Engineering And
Technology, Cheeryal
princetitus14@gmail.com

ABSTRACT

The motor vehicle population is growing at a faster rate than the economic and population growth. Accidents and the death rate due to road accidents, especially two wheelers are also increasing at an alarming rate. most of the accidental deaths that happen due to lack of immediate medical assistance, on the facility for providing immediate medical assistance to accident area can reduce the fatality to greater extends. In this project the arduino microcontroller Atmega328 is interfaced with MeMs.This entire system should be placed on a moving vehicle

KEYWORDS: Accident detection; Mems; Gsm; Gps.

1. INTRODUCTION

With the increasing global demand for security, identification of people and assets and the merginations directive into unions, expansion and complexity of transport networks, raises the demand for Vehicle Tracking System. Vehicle Tracking System or Automatic Vehicle Location System (AVL) is now one of the most popular technological changes in all over the world that is going to make our personal and business life lot easier. As the term suggests, it enables one to track or monitor the location of vehicle in instant time. Primarily, the system

functions with the help of different technologies like the Global Positioning System (GPS), traditional cellular network such as Global System for Mobile Communications (GSM). But GPS is more effective and accurate in this field. As far as vehicle tracking in India is concerned, its uses and market are expected to increase within a couple of years.

The main concept of the proposed project work is to identify the crashed vehicle position (location Program has been developed which is used to locate the exact position of the vehicle and also to navigated track of the moving vehicle on Google Map.GPS provides highly accurate position information and can be used for a variety of land, sea, and air applications. GPS, which began as a military application, has become a viable tool for many commercial and personal applications. One such application has been a vehicle location tracking system (VLTS). These tracking systems incorporate a GPS receiver and a wireless transceiver that allow a remote unit to track the vehicle's position. GPS Tracking device acquire GPS signals from GPS

satellites and calculates its position on the earth. To acquire GPS information, a wireless receiver capable of the civilian L1 frequency (1575.42 MHz) is required. The GPS receiver measures distances to four or more satellites simultaneously. Using triangulation the receiver can determine its latitude, longitude, and altitude.

2. SYSTEM FEATURES

A. Architecture of the proposed system

The proposed system consists of accident detection system and a smart phone. The accident detection system continuously monitor the vehicle is in normal driving posture or met any accident. The system monitors the pulse rate of the driver continuously. if any abnormal condition is detected the alert will be sent to mobile numbers mentioned in the code written for arduino microcontroller. The system will have the details of the driver and the Gps coordinates send the alert. The high level architecture of the proposed system is shown in the figure 1

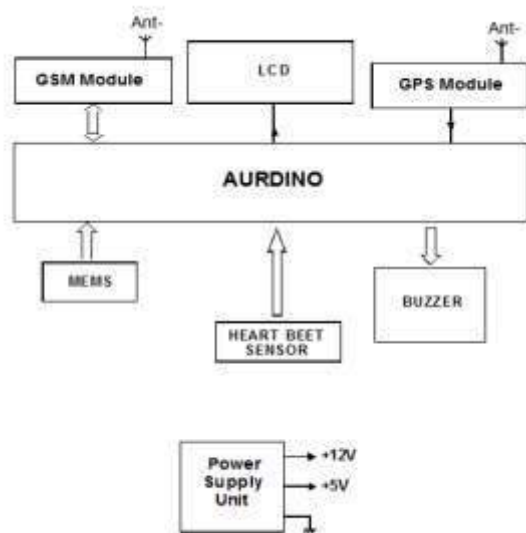


Figure 1:Block diagram of accident detection system

B.Accident detection system

Microcontroller used is ATMEGA 328. The code is written in the internal memory of Microcontroller i.e., in the ROM. With the help of instruction set it processes the instructions and acts as interface between GSM and GPS with help of serial communication and also used for selection of GPS or GSM through the switching transistors. The accident detection i.e. MEMS sensor is shown in the figure 2. With the help of transistor the microcontroller switches between GPS and GSM. GPS receives the data and GSM transmits and receives the data. So the GPS system will receive the Longitude and Latitude values corresponding collided vehicle position through the satellites. GPS TX pin and GSM TX pin are connected through two individual transistors that are controlled by the controller itself for switching the data that is to be read from the GPS or GSM.

3. DESIGN OF ACCIDENT DETECTION SYSTEM

A. Accelerometer (MEMS) sensor



Figure 2: Accelerometer sensor

Accelerometer (MEMS) sensor is used whose output values will be along X, Y and Z axes. Output of Accelerometer is input to the microcontroller. GPS receiver gives location of vehicle to microcontroller in each second. Message with location of accident is sent using GSM to preprogrammed numbers. GSM is connected to microcontroller through

MAX232. MAX232 IC synchronizes baud rates of microcontroller and GSM modem. Data is given to MAX232 through RS232 cable. The MEMS sensor is shown in the figure 2 Microcontroller supports TTL voltage levels. MAX232 is used to convert TTL voltage levels into RS232 voltage levels and vice versa.

B. Heartbeat sensor



Figure 3: Heartbeat sensor

It is the most popular technique which is used for measuring the heart rate. This technique is called as average calculation. A person average rate (i.e. beats per minute) can also be calculated by counting the no of pulses in a given time. In this method it is necessary to calculate Beat to Beat and no of beats per minute is calculated which is measured in this project. The heartbeat sensor is shown in the figure 3. When the blood volume at the finger tips is changed and it is monitored through IR sensor called as transmittance method. In this method Infrared light emitting diode and Infrared sensor are present which is closed in a region that fits over the tips of the finger. For designing of Heartbeat sensor we use technique called Plethysmography. If there is a change in the volume of blood this technique will respond. When the measured pulses go abnormal an SMS will be sent through GSM.

C. Buzzer

A buzzer is provided to alarm the nearby passengers that the accident has occurred,

thus, there will be more chances of exploring the help from the fellow passengers for the victim.

D. Arduino controller

Arduino is an open source electronics platform easy-to-use hardware and software. Arduino board designs use a variety of microprocessors and controllers. The boards are equipped with sets of digital and analog input/output (I/O) pins that may be interfaced to various expansion boards or breadboards (*shields*) and other circuits. The Arduino controller is shown in the figure 4. The boards feature serial communications interfaces, including Universal Serial Bus (USB) on some models, which are also used for loading programs from personal computers. The microcontrollers are typically programmed using a dialect of features from the programming languages C and C++.

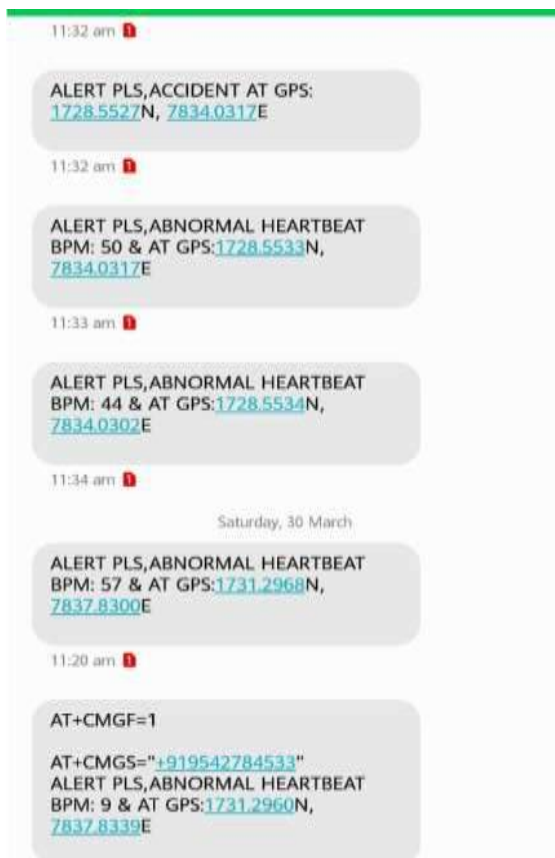
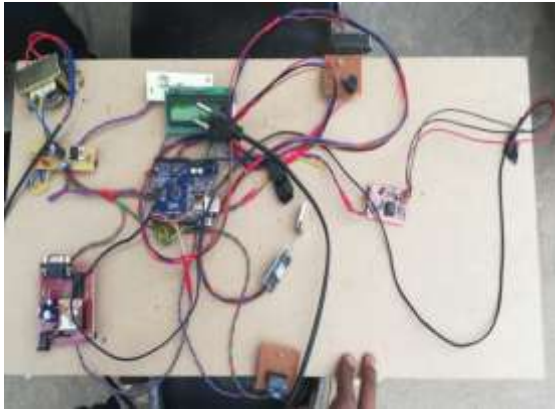


Figure 4: Arduino controller

4. FABRICATION, TESTING AND ANALYSIS

Buzzer will be activated when the heartbeat is in abnormal condition occurs the information is transferred to the registered number through GSM module. Using GPS the location can be sent through tracking system to cover the geographical coordinates over the area. Whenever accident of vehicle is occurred

then the device sends messages to given mobile number. The circuit diagram of this project is shown below in figure 5. As we know that if the accident occurs a message will be received to the registered mobile number. By knowing the longitude and latitude we can find the location of the person. The Output of this project is shown in the below figure 6



4. CONCLUSION

The Project titled “Accident detection with MEMS for Medical Assistance” using GSM, GPS, MEMS” is a model for Vehicle Tracking unit with the help of

Google maps and also with the help of GPS receivers and GSM modem.

The proposed system deals with the detection of the accidents. But this can be extended by providing medication to the victims at the accident spot. By increasing the technology we can also avoid accidents by providing alerts systems that can stop the vehicle to overcome the accidents

REFERENCES

1. Tanushree Dalai, “Emergency Alert and Service for Automotives for India”, *International Journal of Advanced Trends in Computer Science and Engineering (IJATCSE)*, Mysore, India, Vol.2, No.5, Pages: 08-12 (2013) Special Issue of ICETCSE2013.
2. Manuel Fogue, Piedad Garrido, Francisco J. Martinez, Juan-Carlos Cano, Carlos T. Calafate, and Pietro Manzoni, “Automatic Accident Detection: Assistance Through Communication Technologies and Vehicles”, *IEEE Vehicular Technology Magazine*, pp 90-100, Volume7, Issue 3 September2012.
3. Nitin Thakre, Nitin Raut, Abdulla Shaik, “Design and Development of Automatic Vehicle accident detection & Localization of Automobile Using Bluetooth Technology”, *International Journal of Advanced*
4. Amit Meena, Srikrishna Iyer, Monika Nimje, Saket JogJekar, Sachin Jagtap, Mujeeb Rahman, “Automatic Accident Detection and Reporting Framework for Two Wheelers”, *IEEE International Conference on Advanced Communication Control and Computing Technologies (ICACCCT)*, pp 962- 967, May2014
5. Megha Nirbhavane, Shashi Prabha, “Accident Monitoring System using Wireless Application”, *International Journal of Advanced Research in Computer Engineering & Technology (IJARCET)*, pp1532-1535, Volume 3 Issue 4, April 2014
6. Michael j. point “EMBEDDED C” Pearson education limited 2002 Programming and Customizing the 8051 Micro-controller By: Myke Predko
7. The concepts and Features of Micro-controllers - By: Raj Kamal The 8051 Micro-controller Architecture, programming & Applications By: Kenneth J. Ayala



A Unit Plane Edge on-off Slope Algorithm Based Fast LTVR Restoration Analysis

K. Praveen Kumar^{1*}, C. Venkata Narasimhulu², K. Satya Prasad³

¹Research Scholar, Department of ECE, JNTUK, Kakinada

²Department of ECE, GCET, Hyderabad

³Department of ECE, KL University, Vijayawada

* Correspondence Email: praveen416.kumar@gmail.com

Abstract

This research paper presents a Fast LTVR (Localized Total Variation Regularized) method for restoring the degraded images by white noise, while preserving the image edge details in a constructed unit plane edge model through a Unit Plane Edge ON-OFF Slope algorithm. The noisy image contains two details; one with high noise and the other with edge fine details. The edge fine details are restored using ON-OFF Slope algorithm. The denoised image and the edge fine details are used to reconstruct the final restored image. A Unit Plane Edge restoration method is proposed in this research work to estimate the edge-mapping with the fine details. Simulation results of proposed work shows an effective image restoration algorithm comparatively with different filter based restoration methods.

Keywords: : Image denoising; filter; ON-OFF; edge; restoration

1. Introduction

Image restoration has been in researching quite thoroughly to develop an effective denoising method that can retain the original image by removing the complete noise. During the process of image restoration, the edge is so precious, which is a challenging task in image processing techniques like compression, denoising and restoration. The image denoising technique so far implemented [1-5] could able to reconstruct the image area which is beyond the edges, and could able to restore with less quality and is the first challenging task in the present scenario of this research work. And the restoration of edge pixels using TV formulation is the second challenging task, which accomplishes the primal-dual method and min-max optimization, are the approaches implemented in this research work.

2. Previous Work

Form the literature survey, the methods to restore an image include non-linear and linear methods, for the fined and un-fined regions of the noised image, which was proposed in [4], [5] and [6] using different methods. The authors G. Gilboa, N. Sochen, and Y. Zeevi in [4], utilises a Adaptive Total Variation (ATV) method to denoise the fine regions of image and could able adaptively estimate the image reconstruction. The method in [5], utilises a Non-Local Means method (NLM) to eliminate the noise smoothen areas. The method in [6], utilises a inverse filtering method to eliminate the additive noise present in the smooth and non-smooth areas, which is a best technique for the fine image denoising technique in spatial [7-9] and frequency [10-11] domains. Moving further, [12-13] wavelet denoising techniques have been implementing in the present scenario to reduce the computation time [14] and precision of denoising [15], one among them is Lifting-based

wavelet domain adaptive Wiener filter (LBWDWF) [1] method to improve the image restoration by providing an increase in the computation time compared to traditional wavelets [16] [17]. Second among them is [8], to eliminate the neighbourhood local variance around the pixel region. Further subjective enhancement techniques proposed in have improved in estimating the noise variance in spatial and frequency domain.

The similar approach related to Total Variation (TV) proposed a minimal energy function to reduce the noise variation and total variation of the image adaptively. An approach in (FDWF)[2] Frequency Domain Wiener Filter provides a spectra power estimation through filter-based denoising method. In Edge map and Wiener Filter (EWF) [3], the denoising of details are preserved by reducing the noise levels.

3. Proposed Work

In this research work, comparing with the (LBWDWF)[1], (FDWF)[2], (EWF)[3], (ATV)[4] and (NLM)[5], the following are the key features:

- increased image pixel preservation
- fasten the computation performance
- increased the noise estimation
- a strong denoising in the smooth regions, a variant TV method is proposed
- to preserve the fine and edge details during the higher noise areas

The proposed Unit Plane Edge ON-OFF Slope algorithm is used to de-noise the edge details by preserving the neighbour pixels in the regions of image restorations. The image denoised area is considered as fine and non-fine regions. Across the fine regions, the unit threshold value restoration is estimated and across the non-fine regions, the plane threshold value restoration is estimated. And across the edges, ON-OFF slope threshold values are applied

to estimate the edge details in fine and non-fine regions. A new TV based method is derived and implemented in proposed method to visualise the fine and non-fine regions of the image. TV based method utilizes a corner-edge map decision to perform edge fining during the restoration process by taking the strong and weak threshold values across the fine and edge regions.

Total Variational (TV) models are widely used in this area of work and in analyzing image restoration. Fundamental image restoration problem define denoising, which takes a step ahead in computer vision applications for an image analysis. Total Variation based image restoration was explicitly used to restore the denoised sharp and plane edge discontinuous in an image while preserving edge details from the noise.

The paper in [1] gives the min-max problem as:

$$\left\{ \min_u \int_{\Omega} |\nabla b|; \|b - i\|_2^2 \leq v^2 \right. \quad (1)$$

in eq (1), Ω gives the bounded image values of the denoised region, i represent the input image, v is the noise variance in the image. The objective function in the eq. (1) is the Euclidean L2 semi-norm function of b . Eq. (1) fails at unconstrained minimization problems, to formulate the subsequent of (1), the authors [2] formulates the TV model as:

$$\left\{ \min_u P(b) := \int_{\Omega} |\nabla b| dx + \frac{\lambda}{2} \|b - i\|_2^2 \right. \quad (2)$$

by choosing proper λ value, the unconstrained minimization problem can be eliminated. The λ value can be maximized using a second order dual λ formulation [8], [4] and [5] as:

$$\int_{\Omega} |\nabla b| = \max_{\omega \in \mathcal{C}(\Omega)} \int_{\Omega} \nabla u \cdot \omega = \max_{\omega \in \mathcal{C}(\Omega)} \int_{\Omega} -[u \nabla \cdot \omega] \quad (3)$$

in eq (3) the ω give the range value extents as $\Omega \rightarrow \mathbb{R}^2$. The ω value define TV regularization requires the value of b only, to have dual λ formulation. The dual λ formulation needs a smooth edge denoising using bounded unit plane edge variations. In fact, this is the definition of proposed unit plane edge method for the space of bounded unit plane edge functions.

To derive the proposed unit plane edge method, the dual λ formulation with TV model for edge denoising is associated with the bounded value and minimum-and-maximum edge values using integrate and unit process, and becomes the following equation in the form:

$$\left\{ \min_u \int_{\Omega} \max_{\omega \in \mathcal{C}(\Omega)} \int_{\Omega} -u \nabla \cdot \omega + \frac{\lambda}{2} \|b - i\|_2^2 \right. \quad (4)$$

where (u, w) are p-d variables. The integration and unit process allows extracting the edge values to associate a minimization process, which reduces the blur intensity across them and allows the unit value representation to associate a maximization process, which increases the dual λ formulation effectively. The minimum-and-maximum edge values allows to interchange the edge unit values, to result

$$\int_{\Omega} \max_{\omega \in \mathcal{C}(\Omega)} \left\{ \min_u \int_{\Omega} -u \nabla \cdot \omega + \frac{\lambda}{2} \|b - i\|_2^2 \right. \quad (5)$$

The unit value representation is as follows:

$$b = i + \frac{1}{\lambda} \nabla \cdot \omega \quad (6)$$

resulting to following unit plane edge formulation:

$$\int_{\Omega} \max_{\omega \in \mathcal{C}(\Omega)} D(\omega) := \frac{\lambda}{2} \left[\|f\|_2^2 - \left\| i + \frac{1}{\lambda} \nabla \cdot \omega \right\|_2^2 \right] \quad (7)$$

the unit plane edge formulation method equivalent is:

$$\int_{\Omega} \max_{\omega \in \mathcal{C}(\Omega)} \frac{1}{2} \left\| i \lambda + \nabla \cdot \omega \right\|_2^2 \quad (8)$$

For a p-d unit plane edge variable (u, w) , ON-OFF Slope algorithm is defined through two steps, the Slope variation between ON and ON-OFF edge denoised image values and ON-OFF Slope representation. The first step can solve the dual λ formulation for differences in the primal and dual edge method, using the

$$R(u, w) = Pr(u)_{ON}^{OFF} - Du(w)_{ON}^{OFF} \quad (9)$$

The objectives of first step are:

$$Pr(u)_{ON}^{OFF} = \int_{\Omega} |\nabla \log_{10} u| + \frac{\lambda}{2} \|\max(u, f)\|_2^2 \quad (10)$$

And

$$Du(w) = \frac{\lambda}{2} \left[\|f\|_2^2 - \left\| i + \frac{1}{\lambda} \nabla \cdot \omega + f \right\|_2^2 \right] \quad (11)$$

The Slope variation bounds the ON and ON-OFF edges to optionally of the p-d objectives, is given as:

$$R(u, w) = \int_{\Omega} (|\nabla \log_{10} u| - \nabla \log u \cdot w) + \frac{\lambda}{2} \left\| \frac{1}{\lambda} \nabla \cdot \omega + f - u \right\|_2^2 \quad (12)$$

In Slope variation, if u and w are denoised specifics, the ON and ON-OFF edges are related to primal and dual problem, respectively results

$$0 \leq Pr(u) - O^* \leq R(u, w) \quad (13)$$

$$0 \leq O^* - Du(w) \leq R(u, w) \quad (14)$$

where O^* is p-d λ value. The primal λ variable u is calculated using,

$$\lambda_{TV}(u) = \sum_{1 \leq i, j \leq n} f + \frac{1}{\lambda} \nabla \cdot \|R(u, w)_{i,j}\| \quad (15)$$

& the dual λ variable w is calculated using,

$$\lambda_{TV}(w) = (\nabla \cdot \omega)_{i,j} = \omega_{(i,j)n+i} \mathbf{1} \leq i, j \leq n \quad (16)$$

The second step ON-OFF Slope is called in the following way:

Table 1: ON-OFF Slope approach

Input : $S_i=R x+u$, Process REPEAT Step 1 : Find R minimizing Φ with S_{ir} fixed; Step 2 : Solve $S_{iy}=\ S_i-R \Phi \alpha\ $, Step 3 : Solve ON-OFF_Slope $u_a=S_{ir}-S_i \approx \Phi S_{iy}-\Phi S_{ix}=\Phi S_{ux}$, Initialization : (λ, μ) REPEAT Step 1 : Solve $(\lambda, \mu)=\arg \max_{\lambda, \mu} \log G(S_{ux} S_{ix}, S_{iy}) + G(S_{ix}, S_{iy})$; Step 2 : Solve $S(S_{ix}, S_{iy})=S(\Phi)$ Step 3 : Solve $S S_{ux}=S G_i X$ UNTIL X_{ON-OFF} converges UNTIL G converges Output: ON-OFF Slope values

where x is the original image, i is the observed image for observation of ON-OFF and ON pixels, S_G is the pixel interspacing factor, Φ is the edge artifact, S_{ir} is the reconstructed image, S_{iy} is the predicted image, S_{ix} is the inter space image α is the slope variation factor, μ is image pixel state and S denotes the image ON-OFF pixels slope values near to the primal and dual λ estimations. The proposed ON-OFF Slope method provides the equality values of ON and ON-OFF estimation values, which are global variables

for dual λ formulation, thus the proposed image restoration analysis in providing a solution to $R(u,w)$ with fulfilling the ON-OFF and ON image object pixels using inter spacing providing proper interdependency in unit plane edges.

Proposed algorithms, in Table 1, would lead to a good edge representation solution to image reconstruction analysis in general. Proposed algorithm is very efficient in reliability and effective for image analysis.

Eq. 12 refers to the denoised ON-OFF pixel image model by approximating the second term under the assumption that interspacing, proposed method can retrieve Su_x in to the product of the ON-OFF pixel estimators, such equation is,

$$Slope(\varphi) = S(Six, Siy) = S_{ON}(\varphi|Six)S(Siy) = S_{OFF}(\varphi d|Six)S(Siy) \tag{17}$$

where $\Phi_d = \Phi|S_{ix} - \Phi$, defines the deviation between unit edge ON and ON-OFF image pixels. Such restoration can be viewed as a level of proposed algorithm strategy, so Φ_d is approximately independent from $\Phi|S_{ix}$.

4. Results and Discussions

Proposed algorithm is tested with Barbara, Building, Lighthouse, Text, Airplane, Girl, Lenna, Women and Boat gary scale test images (256x256). All images are tested with Gaussian white noise = 50, 100 and 200. Proposed work is compared with LBW DWF [1], FD WF [2], EWF [3], ATV [4] and NLM [5].

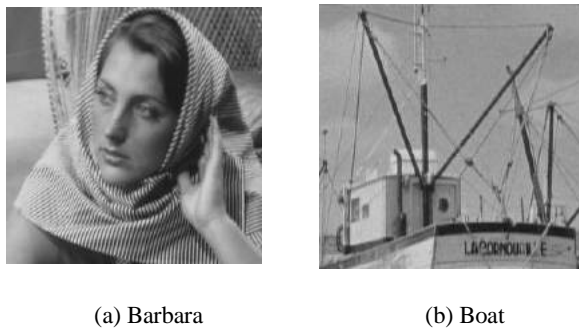


Fig 1: 2D images considered for proposed work analysis.

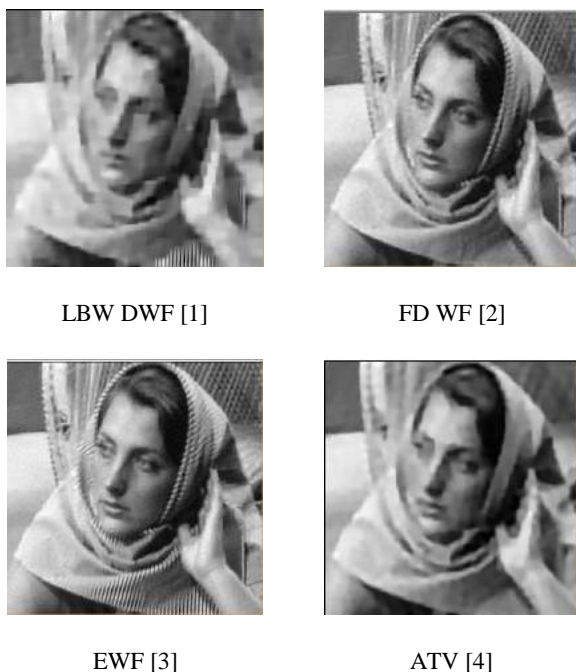


Fig. 2 : Restoration comparison of Barbara with low noise level (=50)

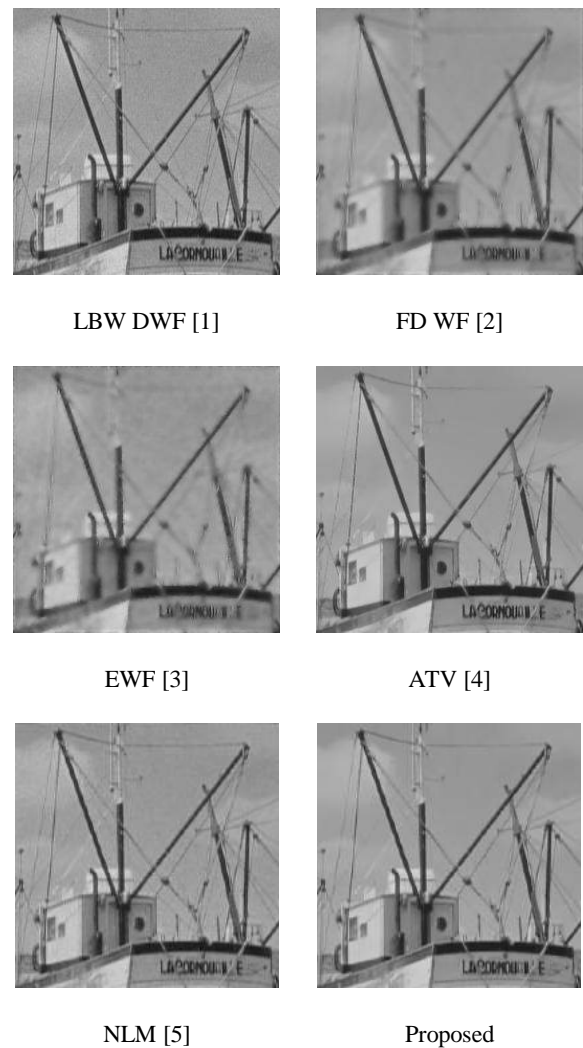


Fig. 3: Restoration comparison of Boat with low noise level (=50)

4.1. Comparative Image Reconstruction Results:

Figure 1 shows the input images considered for visual image reconstruction comparison. Figure 2 shows the image restoration comparison of input image Barbara with low noise level (=50) between comparative work and proposed work. Figure 3 shows the image restoration comparison of input image Boat with low noise level (=50) between comparative work and proposed work.

4.2. Comparative Image Reconstruction Quality Results

Table 2 and 3 give the performance evaluation in PSNR and MSSIM for Gaussian white noise = 50, between compared and proposed method. Table 4 give the average time execution comparison for Gaussian white noise = 50, 100 and 200 between compared and proposed method.

Table 2: Performance comparison in PSNR (=50)

Test Images	Boat	Barbara	Building	Lighthouse	Text	Airplane	Girl	Lenna	Women
PSNR (dB)	60	65	64	62	64	62	65	64	65

Table 3: Performance comparison in MSSIM(100%) (=50)

Test Images	LBW DWF [1]	FD WF [2]	EWf [3]	ATV [4]	NLM [5]	Proposed Work
Barbara	67	95	96	94	97	98
Building	62	96	96	96	96	97
Light-house	68	91	94	90	93	96
Text	68	95	96	95	93	97
Airplane	81	89	92	95	94	96
Girl	82	91	92	91	93	94
Lenna	83	91	94	96	96	97
Women	81	91	94	95	95	96
Boat	79	93	94	93	96	97

Table 4: Average time execution (s)

Test Images	Gaussian white noise	LBW DWF [1]	FD WF [2]	EWf [3]	ATV [4]	NLM [5]	Proposed Work
Barbara	50	0.60	0.31	0.93	23.33	67.31	0.28
	100	0.56	0.31	0.92	66.17	68.60	0.21
	225	0.57	0.30	0.93	751.49	67.82	0.20
Boat	50	0.58	0.30	0.89	21.01	65.22	0.26
	100	0.54	0.30	0.80	64.52	66.89	0.19
	225	0.55	0.28	0.91	721.55	68.23	0.18

5. Conclusions

Proposed an image restoration analysis in unit plane edge that is effective for denoising the image fine edges by reducing the noise in the reconstructed images. From the survey, it is clear that proposed method is fast for restoring images that are efficient in edge details.

References

- [1] E. Ercelebi and S. Koc, "Lifting-based wavelet domain adaptive Wiener filter for image enhancement " IEE Proc. Vis. Image and Signal Processing, vol.153, no.1, pp. 31–36, Feb. 2006.
- [2] S. Suhaila and T. Shimamura "Power spectrum estimation method for image denoising by frequency domain Wiener filter " in Proc. IEEE Int. Conf. Computer and Automation Engineering, Singapore, 2010, pp. 608–612.
- [3] S. Suhaila, and T. Shimamura, "Image Restoration Based on Edge-map and Wiener Filter for Preserving Fine Details and Edges", International Journal Of Circuits, Systems And Signal Processing, Issue 6, Volume 5, pp-618-626, 2011.
- [4] G. Gilboa, N. Sochen, and Y. Zeevi "Texture preserving variational denoising using an adaptive fidelity term " in Proc. IEEE Workshop Variational and Level Set Methods in Computer Vision, Nice, 2003, pp.137–144.
- [5] Buades, B. Coll and J M Morel "A non-local algorithm for image denoising " in Proc. IEEE Int. Conf. Computer Vision and Pattern Recognition, San Diego, 2005, vol.2, pp. 60–65.
- [6] W. Dong, G. Shi, Y. Ma, and X. Li, "Image Restoration via Simultaneous Sparse Coding: Where Structured Sparsity Meets Gaussian Scale Mixture," International Journal of Computer Vision (IJCV), vol. 114, no. 2, pp. 217-232, Sep. 2015.
- [7] Jian Zhang, Debin Zhao, Wen Gao, "Group-based Sparse Representation for Image Restoration," IEEE Transactions on Image Processing, 15-July-2015.
- [8] Vardan Papyan and Michael Elad, Multi-Scale Patch-Based Image Restoration, IEEE Transactions on Image Processing, vol. 25, no. 1, pages 249-261, January 2016.
- [9] Uwe Schmidt and Stefan Roth, "Shrinkage Fields for Effective Image Restoration," IEEE Conference on Computer Vision and Pattern Recognition (CVPR), Columbus, Ohio, June 2014.
- [10] Kheradmand and P. Milanfar, "A general framework for regularized, similarity-based image restoration," IEEE Transactions on Image Processing, vol. 23, no. 12, pp. 5136-5151, Dec 2014.
- [11] C. H. Hsieh, P. C. Huang and S. Y. Hung, "Noisy image restoration based on boundary resetting BDND and median filtering with smallest window " WSEAS Trans. Signal Processing, vol.5, no.5, pp. 178–187, May 2009.
- [12] V. Gui and C Caleanu "On the effectiveness of multiscale mode filters in edge preserving " in Proc. WSEAS Int. Conf. Systems, Rodos Island, 2009, pp. 190–195.
- [13] S. Suhaila and T. Shimamura "Power spectrum estimation method for image denoising by frequency domain wiener filter " in Proc. IEEE Int. Conf. Computer and Automation Engineering, Singapore, 2010, pp. 608–612.
- [14] Zhang Y, Pu Y-F, Hu J-R and Zhou J-L 2012 A class of fractional order variational image inpainting models. Appl. Math. Inf. Sc. Int. J. 2: 299–306
- [15] M. V. Afonso, J. M. Bioucas-Dias, and M. A. T. Figueiredo, "An augmented lagrangian approach to the constrained optimization formulation of imaging inverse problems," Image Processing, IEEE Transactions on, vol. 20, no. 3, pp. 681 – 695, Mar. 2011.
- [16] Beck and M. Teboulle, "A fast iterative shrinkage-thresholding algorithm for linear inverse problems," SIAM Journal of Imaging Science, vol. 2, no. 1, pp. 183–202, Mar 2009.
- [17] Y. Huang, M. Ng, and T. Zeng, "The convex relaxation method on deconvolution model with multiplicative noise," Commun. Comput. Phys., vol. 13, no. 4, pp. 1066–1092, 2013.

GEETHANJALI COLLEGE OF ENGINEERING AND TECHNOLOGY

(UGC Autonomous, Permanently Affiliated to JNTUH, Accredited by NAAC with 'A' grade)

Salient features of the Department

- Started in the year 2005
- Accredited by NBA three times in the years 2012, 2015 and 2018
- Accredited by NAAC with 'A' grade
- UGC autonomous from the year 2016
- SIRO Recognized
- DRDO/DST sponsored projects of more than Rs 1 Cr.
- Permanently affiliated to JNTUH
- Offers consultancy services to the industry
- Highly motivated and experienced Faculty
- State-of-the-art Infrastructure
- Student Centric Learning thorough
- Two Centers of Excellence (CoE) - VLSI Design and Embedded Systems and IoT

DEPARTMENT OF ELECTRONICS AND COMMUNICATION ENGINEERING

(Accredited by NBA in 2012, 2015 and 2018)

Cheeryala(V), Keesara(M), Medchal (Dist.), Telangana, INDIA, Pin Code-501301.